Geology and Geochemistry of the 'Caprocks' above VHMS Deposits at Myra Falls, Vancouver Island, British Columbia

by

Sarah A. Jones M.Sc.(Otago)

Sarah Anne

UNIVERSITY OF TASMANIA

Submitted as fulfilment of the requirements for the degree of
Doctor of Philosophy

November, 2001

Statement

This thesis contains no material that has been accepted for the award of any degree or diploma at any university. To the best of the candidate's knowledge this thesis contains no copy or paraphrase of material previously written or published by another person, except where due acknowledgement is made.

Signed: Sarah Jones

Date: 6-6-2002

Authority of Access

This thesis may be made available for loan and limited copying in accordance with the *Copyright Act 1968*.

Abstract

The aim of this thesis was to characterise and understand the evolution and significance of several large 'cap zones' that overlie Myra Falls mineralised zones. The Myra Falls volcanic hosted massive sulphide (VHMS) district is located in Strathcona Provincial Park in the middle of Vancouver Island, British Columbia, Canada. The orebodies are hosted by the Devonian Sicker Group, a volcano-sedimentary package which forms the basement rocks of Vancouver Island. The Cu-Pb-Zn deposits are located in two mineralised horizons, and this study concentrates on the lower ore horizon, which includes the Battle and HW deposits, located on or near the contact with the footwall Price Andesite. The orebodies are hosted by the HW horizon, a rhyolitic package, 5 to 200 m thick, of volcaniclastic and sedimentary rocks, and quartz-feldspar porphyry bodies. The HW horizon is overlain by an andesite-dacite volcano-sedimentary sequence, which is up to 450 m thick.

Paleoseafloor reconstructions indicate that the Battle and HW orebodies formed in small basins along a NW-trending ridge. Argillite deposits above the orebodies and in the South Flank area coincide with paleo-topographic lows and represent depocentres. The sequence has undergone multiple deformation events, including early extension and formation of growth faults; D_1 folding and development of an E-W oriented foliation; D_2 shear zones; D_{3a} and D_{3b} compression with steep strike-slip faults and shallow N-S dipping thrust faults; D_4 extension with steep planar normal faults; and D_5 compression resulting in large shallow N-S dipping thrusts and steep NE-oriented strike-slip faults.

Chert is best developed above the Battle orebody, where it appears to form a thick 'cap' (3-5m thick) above the massive sulphides. Chert horizons are also located above the Ridge and Extension ore zones. However, the HW orebody is overlain by a thick argillite sequence, with only minor chert.

The siliceous caprocks above the Battle deposit are replacement cherts (after mudstone), and these cherts share many sedimentological and petrological features with the adjacent unaltered argillite, including parallel laminations, interbedded turbidites, radiolarians, soft-sediment deformation and phosphatic concretions. Immobile elements indicate a closely related provenance for the argillite and chert, significantly different to the Price Andesite or rhyolitic rocks. Trace element geochemistry, and the spatial association of the cherts with the Battle orebody, indicate that the chert represents hydrothermal alteration of seafloor muds. There is a gradational transition, from white chert above the orebody, to black chert, 120m from the orebody, to unaltered argillite. Lateral metal zonation is observed in the chert, is interpreted to reflect precipitation from a cooling hydrothermal fluid, with a higher temperature Cu-Zn-Cd zone in the white chert, and a lower temperature Pb-Ag-Sb zone in the black chert.

Fluid inclusions in spherical megaquartz patches in the Battle chert, indicate temperatures between 135 to 250° C and salinities from 3 to 12.1 eq. wt % NaCl, which are similar to fluid inclusions in Battle orebody quartz (140 to 250° C, 3 to 12.4 eq. wt % NaCl). Densities, estimated from inclusion data, range from 0.88 to 1.05 g/cm^3 and are close to the density of ambient seawater at 2° C and 2000m depth (1.03 g/cm^3). These densities suggest that the hydrothermal fluids potentially displayed a range of behaviour types where they entered the submarine environment, from buoyant plumes to intermediate brines, which flowed laterally through porous seafloor sediments.

At the time of ore formation and caprock deposition, bottom water conditions in the Battle and HW basins were moderately anoxic to euxinic, indicated by DOP values > 0.90, Fe-sulphur-carbon relations, low Fe and Mn values, and high V/Cr, V/Ni and V/(Ni+V) ratios. Barite and haematite, which are common in VHMS caprocks globally, are absent in the caprock horizon, most likely reflecting low O_2 conditions. Zn, Pb, Cu, As, Ag, V, Ba and Cd are variably enriched in argillites from the Battle and HW basins, and these are attributed to a hydrothermal origin, because they are all enriched in the orebody. Argillites from the South Flank show no metal enrichment, interpreted to reflect a lack of hydrothermal activity in this area.

$\delta^{34}S$ values in the unaltered Battle basin argillite range from –35.2 to –10.3 ‰, which are much lighter than $\delta^{34}S$ values in the black chert (–18.4 to –5.3 ‰), and the Battle orebody (–1.1 to +4.1 ‰). The distinct shift from light $\delta^{34}S$ values in the unaltered argillite, to heavier $\delta^{34}S$ values in the black chert provides evidence that hydrothermal fluids, originally with Battle-like signatures, progressively leached regional argillites and so obtained intermediate $\delta^{34}S$ compositions.

A model for the formation of the Battle orebody and siliceous caprocks consists of 5 stages, including:

1) Basin formation and the onset of rhyolitic volcanism, followed by a period of tectonic and/or volcanic quiescence, with the deposition of several metres of laminated muds, silts, and minor interbedded turbidites in the Battle basin. Restricted circulation within the basin resulted in a stratified water column with low to fluctuating O_2 bottom water conditions.

2) The onset of hydrothermal activity during deposition of the seafloor muds resulted in the deposition of rutile, apatite and minor sulphides in primary pore space, principally by diffuse flow of hydrothermal fluids through the sediments. Buoyant venting also occurred, producing fine layers of sulphide-rich mud. In places, these layers were entrained into overlying sandstone turbidites.

3) Subsequent low to moderate temperature, silica-bearing fluids flowed laterally through porous seafloor muds to form the Battle chert. Silicification took place early in the depositional/diagenetic history of the muds, to account for the incorporation of chert into overlying mass flows. Ubiquitous bedding-parallel micro-stylolites indicate that silicification occurred prior to compaction. Low metal contents in the chert reflect relatively low fluid temperatures (<250° C) and likely prior deposition of sulphides in the underlying coarse-grained rhyolitic volcaniclastic layer. Low flow velocities combined with relatively high salinities and moderate temperatures may have enhanced subsurface

lateral fluid flow, rather than buoyant venting. Lateral fluid flow is consistent with the sheet-like form of the Battle orebody and caprocks, replacement textures, and lateral metal zonation in the chert. Plugging of the porous seafloor sediments by silica precipitation changed the hydrothermal flow regime from diffuse to more focussed flow, leading to enhanced lateral flow of subsequent ore-bearing fluids beneath the silica cap; the basal contact of the chert is crosscut by massive sulphides.

4) Formation of the siliceous caprocks was followed by renewed extension and volcanism, with the rapid deposition of rhyolitic mass flow units, interlayered with rhyolitic sandstones and volcaniclastic rocks. Finely bedded jasper clasts are common in the overlying mass flow units and most likely originated from Fe-Si deposits forming on the margins of Battle basin, above the anoxic-oxic boundary. The end of rhyolitic volcanism was marked by the intrusion of a massive quartz-feldspar porphyry body at the top of the rhyolitic sequence.

5) Ore deposition continued throughout the deposition of the HW Horizon rhyolitic volcaniclastic rocks and intrusion of the quartz-feldspar porphyry. The barite-rich Gap lens formed by upflow of a more focussed hydrothermal fluid, along the main growth structure at the northern edge of the basin. The upper ore lenses formed by diffuse fluid flow through the rhyolitic pile and ponding beneath the massive porphyry. A more oxygenated environment developed during deposition of upper zone sulphides, indicated by ubiquitous barite in upper ore lenses.

A similar structural and depositional environment is proposed for the HW orebody. However, the HW orebody formed prior to deposition of the caprock horizon. Massive sulphides were deposited within the coarse-grained rhyolitic detritus on the basin floor and the top surface of the HW orebody is eroded in places, with ore clasts common in overlying mass flows. Elsewhere, there is a sharp depositional contact between argillite and the orebody. This study indicates that the formation of siliceous caprocks required the interaction of hydrothermal fluids with a pre-existing carapace of fine-grained sediment.

Acknowledgements

I have greatly enjoyed working on this project, and am grateful to everyone who has helped and supported me over the last few years.

Firstly, I thank my supervisors, Bruce Gemmell and Garry Davidson, for setting up the project, assistance in the field, useful discussions, and chapter reviews. Garry's detailed reviews on the chert petrology and geochemistry were greatly appreciated. A special thanks to Ron Berry for his extensive help with the structure, the constructive discussions and thorough reviews of chapters. I am also grateful to Wally Herrmann for his reviews and help with the PIMA, and to Mike Solomon, for his helpful comments on the geological model.

This project was funded by Boliden-Westmin Ltd. I am grateful to all the staff at Myra Falls for making the fieldwork enjoyable, and in particular, thanks to the geological staff, Ivor, Rick, Cliff, Finley, Sean, Guy, Dean, Albert, Agzim, Hendrik and Mike. Thanks Amy for the great weekends in Campbell River, and Toni, thanks for making camp life comfortable and fun.

Thanks to Peter Cornish, Di Steffens, Lyn Starr, Chris Higgins and Lynne Vaudrey, for sorting out administration matters, and June Pongratz, for all her help and advice on printing matters. I am grateful for the technical assistance by Phil Robinson, Katie McGoldrick, Darren Turner, Alistair Chilcott, Phil Robinson, Zhongshou Yu, Simon Stephens, Dave Steele, Ashley Townsend, Graham Rowbottom, and Christine Cook. Special thanks to Nilar Hlaing for the long hours in the laboratory helping me with the sulphide sulphur analyses.

A big thankyou to my family for all their love and support. Thanks to my mum, Vanja; my sisters, Rachel and Amanda; my dad, David; stepmum, Ann; and aunts, Lolita and Jeanette. I couldn't have a better family.

One of the things I enjoyed most about CODES was socialising with the large number of postgrad students. Thanks for all the great Friday nights. There are too many to mention everyone, but I'd particularly like to thank my office mates, Karin and Andrew for making my final year so enjoyable. Many thanks also to my third floor office mates, Vanessa, James and Darryl; and thanks to Peter, Loreto, Cathryn, Mike, James, Briony, Glen, Catherine, Rohan, Steve, Peter, Andrew, Michael, Ollie, and Rick.

Finally, my biggest thanks goes to Mike. No matter how ratty I became (especially the last six months) he was there, providing lots of love and support. Thanks Mick.

Table of Contents

Abstract

Chapter 1: Introduction

1.1 Preamble 1
1.2 Project aims 2
1.3 Location and setting 2
1.4 Work plan 3
1.4.1 Field work 3
1.4.2 Laboratory work 6
1.5 Previous work 6
1.5.1 Documentation of geology 6
1.5.2 Past exploration 8
1.6 Organisation of the thesis 8

Chapter 2: Regional geology

2.1 Introduction 11
2.2 Tectonic setting 11
2.3 Stratigraphy of Vancouver Island 15
2.3.1 Sicker Group 16
2.3.2 Buttle Lake Group 19
2.3.3 Vancouver Group 20
2.3.4 Bonanza Group 21
2.3.5 Cretaceous rocks 21
2.3.6 Tertiary 22
2.4 Metamorphism 23
2.5 Structure 24
2.5.1 Early ductile deformation of Wrangellia 26
2.5.2 Mid to Late Triassic crustal dilation 26
2.5.3 Early to Mid Jurassic regional-scale warping of Vancouver Is. 26
2.5.4 Post Mid to pre-Late Cretaceous NW trending faults 27
2.5.5 Late Cretaceous to Eocene NW trending faults 27

2.5.6 Post Eocene faults 28
2.6 Metallogeny of Vancouver Island 29
2.6.1 Pre-accretionary deposits 29
2.6.2 Post-accretionary deposits 30
2.7 Summary 30

Chapter 3: Local Geology

3.1 Introduction 33
3.2 Local stratigraphy 33
3.3 Myra Formation – mine sequence 33
3.3.1 HW horizon 34
3.3.2 Hangingwall Andesite 40
3.3.3 Lower mixed volcaniclastic 40
3.3.4 Lynx-Myra-Price Horizon 40
3.3.5 Upper mixed volcaniclastic unit 42
3.3.6 Upper mafic unit 42
3.4 Tectonic and depositional setting of Sicker Group rocks 42
3.5 Local structure 44
3.6 Metamorphism and alteration 45

Chapter 4: Myra Falls structure

4.1 Introduction 49
4.2 Methods 51
4.2.1 Separation of brittle deformation events 51
4.2.2 Paleostress analysis 53
4.3 Deformation history of Myra Falls 54
4.4 Syn-depositional growth faults 55
4.5 D_1 folding 55
4.5.1 Macro-scale structure 55
4.5.2 Micro-scale structure 58
4.5.3 Strain estimate 62
4.5.4 Removing effects of the D_1 event 64
4.6 D_2 shear zones 66
4.7 D_3 faulting 71
4.7.1 D_{3a} strike-slip faults 71
4.7.2 D_{3b} thrust faults 73
4.8 D_4 normal faults 80
4.9 D_5 gouge-rich oblique thrust faults and strike-slip faults 88

4.10 Effects of deformation on stratigraphic sequence 96
4.11 Regional and tectonic correlation of Myra Falls deformation history 103
4.12 Summary and conclusions 106

Chapter 5: HW Horizon facies variation and paleoseafloor reconstruction

5.1 Introduction 111
5.2 Methods 112
5.3 HW Horizon facies variation 112
5.4 Paleoseafloor reconstruction 121
5.4.1 Structural domains 121
5.4.2 Removing the effects of late deformation (D_1-D_5) 121
5.5 HW mine area reconstruction 123
5.5.1 Location of growth structures 126
5.6 Battle-Ridge Zone reconstruction 132
5.6.1 Location of growth structures 132
5.7 Property scale paleoseafloor reconstruction 143
5.8 Comparison with modern VHMS systems 143
5.9 Summary and conclusions 146

Chapter 6: Chert and argillite 'caprocks'

6.1 'Caprocks' definition and distribution 151
6.2 Chert 153
6.2.1 Distribution 153
6.2.2 Macro-scale description 153
6.2.3 Mineralogy and textures 160
6.2.4 Sulphides 164
6.2.5 Interpretation of micro-textures in chert 166
6.3 Black chert 181
6.3.1 Distribution 181
6.3.2 Macro-scale descriptions 181
6.3.3 Mineralogy and textures 181
6.3.4 Sulphides 184
6.4 Argillite 184
6.4.1 Distribution 184
6.4.2 Macro-scale descriptions 184
6.4.3 Mineralogy and textures 186
6.4.4 Sulphides 186
6.5 Facies associated with the caprocks 186

6.5.1 Basal facies and ore contacts 188
6.5.2 Intercalated facies within the caprock horizon 190
6.5.3 Overlying facies 190
6.6 Discussion: Origin of siliceous caprocks 192
6.6.1 Mechanisms of chert formation 192
6.6.2 Origin of siliceous caprocks at Myra Falls 194
6.7 Depositional environment and origin of caprocks 206
6.7.1 Depositional environment 206
6.7.2 Battle deposit caprocks 208
6.7.3 HW deposit caprocks 210
6.8 Summary and conclusions 211

Chapter 7: SWIR spectral characteristics of the HW Horizon

7.1 Introduction 213
7.2 Methods 214
7.3 Alteration mineralogy 216
7.4 White mica and chlorite compositional and spectral characteristics 218
7.4.1 White mica compositional variation 218
7.4.2 White mica spectral characteristics 220
7.4.3 Chlorite compositional variation 220
7.4.4 Chlorite spectral characteristics 224
7.5 Previous work (SWIR analysis) 224
7.6 Results of SWIR analysis 225
7.6.1 White mica and chlorite compositions 225
7.6.2 Bulk rock control on white mica-chlorite spectral characteristics 226
7.6.3 White mica-chlorite compositional variation with proximity to ore 234
7.6.4 White mica and chlorite spectral variation maps 234
7.6.5 White mica compositional variation – microprobe analyses 238
7.7 Summary and conclusions 244

Chapter 8: Cap rock geochemistry

8.1 Introduction 247
8.2 Methods 248
8.3 Geochemistry of siliceous caprocks above the Battle orebody 250
8.3.1 Rationale of geochemical analysis for affinity and precursor determination 250
8.3.2 Siliceous caprocks geochemical features 251
8.3.3 Siliceous caprocks source 253

8.4 Caprock chemostratigraphy 257
8.5 Mass balance of siliceous caprocks above the Battle orebody 270
8.5.1 Mass balance equations 270
8.5.2 Battle chert/argillite mass balance 273
8.6 Rare earth elements 275
8.6.1 REE results 275
8.6.2 Interpretation of REE results 279
8.7 Argillite geochemistry 282
8.7.1 Introduction 282
8.7.2 Argillite characteristics 282
8.7.3 Metal enrichment 284
8.7.4 Metal sources – detrital, hydrothermal or hydrogenous 286
8.7.5 Summary and comparison of major and trace element behaviour in argillite from the Battle Basin, HW basin and regional areas 294
8.8 Paleoenvironmental analysis of sediment basins 295
8.8.1 Introduction 295
8.8.2 Organic carbon and sulphide sulphur 296
8.8.3 Degree of pyritization (DOP) 297
8.8.4 Degree of pyritization results 299
8.8.5 Organic carbon-sulphur-iron relations 300
8.8.6 Metal ratios – paleoenvironmental indicators 304
8.8.7 Phosphate nodules 308
8.8.8 Paleoenvironmental summary 309
8.9 Sulphur isotopes 310
8.9.1 Results 310
8.9.2 Sulphur sources 312
8.9.3 Interpretation of Myra Falls sulphur isotopes 315
8.9.4 Comparison with other VHMS systems 317
8.10 Summary and conclusions 318

Chapter 9: Fluid inclusion study of siliceous caprocks and Battle and HW orebodies

9.1 Introduction 321
9.2 Methods 323
9.3 Fluid inclusion characteristics 325
9.4 Results 325
9.4.1 Temperature of homogenisation (Th) 328
9.4.2 Temperature of melting (Tm) and salinity 330
9.4.3 Fluid densities 335

9.4.4 Eutectic temperature (Te) 336
9.5 Metamorphic effects 337
9.6 Discussion 338
9.6.1 Caprock fluid inclusions 338
9.6.2 Salinity 339
9.6.3 Water depth estimates 342
9.6.4 Fluid source 342
9.7 Summary and conclusions 344

Chapter 10: Geological and geochemical model for the origin of siliceous caprocks
10.1 Introduction 347
10.2 Structural and depositional setting of Myra Falls caprock horizon 347
10.2.1 Structural setting 348
10.2.2 Depositional environment 348
10.2.3 Metal distribution in the caprock horizon 350
10.3 Formation of siliceous caprocks 352
10.3.1 Siliceous caprock origin 352
10.3.2 Timing of silicification 353
10.3.3 Physiochemical conditions of Battle chert formation 355
10.3.4 Silica deposition 357
10.3.5 Metal zoning in Battle chert 362
10.3.6 Organic carbon degradation and metal complexes 367
10.3.7 Effects of low O_2 bottom water conditions 369
10.3.8 Fluid behaviour 372
10.4 Genetic model for Battle orebody and associated siliceous caprocks 375
10.5 Comparison with the HW basin 380
10.6 Comparison with other VHMS deposits 381

Chapter 11: Conclusions
11.1 Conclusions 383
11.2 Implications for exploration at Myra Falls 388
11.3 Future work 389

References 391

Appendix 1: Drill logs and underground maps 411

Appendix 2: Sample locations 433

Appendix 3: XRF analyses 439

Appendix 4: Rare earth analyses 453

Appendix 5: Sulphur-carbon-Fe analyses 457

5.1 Sulphide sulphur-carbon-Fe analyses 458

5.2 Sulphide isotopes 464

Appendix 6: Electron microprobe analyses 465

6.1 Apatite 466

6.2 White mica 476

6.3 Sphalerite 490

Appendix 7: Fluid inclusion data 491

List of Figures

Chapter 1

Fig. 1.1: Location map of Myra Falls VHMS camp 2

Fig. 1.2: Photos of Myra Falls VHMS camp and the Buttle Lake area 4

Fig. 1.3: Plan view and cross section of Myra Falls VHMS camp 5

Fig. 1.4: Underground mapping areas in the HW mine 7

Fig. 1.5: Underground mapping areas in the Battle mine 9

Chapter 2

Fig. 2.1: Tectonic setting of Vancouver Island 12

Fig. 2.2: Geology of Vancouver Island 14

Fig. 2.3: Schematic cross-section through southwestern Vancouver Island 15

Fig. 2.4: Stratigraphic column for Vancouver Island 16

Fig. 2.5: Comparative stratigraphy of the Paleozoic rocks of Vancouver Island 18

Fig. 2.6: Photo of Buttle Lake Formation overlying Karmutsen Formation 20

Chapter 3

Fig. 3.1: Regional geological map of the Myra Falls area 35

Fig. 3.2: Stratigraphic column of the Myra Falls area 36

Fig. 3.3: Photos of mine sequence rocks 39

Fig. 3.4: Photos of mine sequence rocks 41

Fig. 3.5: Tectonic and volcanic setting of the Myra Falls VHMS deposits 44

Chapter 4

Fig. 4.1: Contour map of the top surface of Price Andesite 50

Fig. 4.2: Criteria used to interpret sense of displacement on faults 52

Fig. 4.3: Map showing the areas where fault data was collected 52

Fig. 4.4: Photos and stereonets of D_2 folds 57

Fig. 4.5: Underground wall maps of D_2 folds, drives M148EX, ST183A, Battle mine 59

Fig. 4.6: Underground wall maps of D_2 folds, drive S335C, HW mine 60

Fig. 4.7: Map illustrating the pre D_{3-5}, S_1 foliation pattern 61

Fig. 4.8: Photomicrographs of S_0 and S_1 textures in HW Horizon lithologies 63

Fig. 4.9: Photomicrographs of S_0 and S_1 textures in HW Horizon lithologies 65
Fig. 4.10: Photos of deformed stringer veins, strain ellipse and principal strain axes 67
Fig. 4.11: Equal-area net and graphical solution for undeformed planes 68
Fig. 4.12: Stereonets illustrating deformed and undeformed stringer veins 69
Fig. 4.13: Underground wallmap, photos and stereonet illustrating S_2 foliation 70
Fig. 4.14: Quartz-epidote slickensides on steep D_{3a} fault 72
Fig. 4.15: Stereonets illustrating D_{3a} faults 74
Fig. 4.16: Interpretation of D_{3a} fault striations 75
Fig. 4.17: Stereonets illustrating D_{3b} faults 76
Fig. 4.18: Interpretation of D_{3b} fault striations 77
Fig. 4.19: Block diagrams of D_3 faulting 78
Fig. 4.20: Interpretation map of D_3 faults 79
Fig. 4.21: Stereonets illustrating D_4 faults 81
Fig. 4.22: Photos of D_4 faults 83
Fig. 4.23: Photos of D_4 faults 85
Fig. 4.24: Interpretation of D_4 fault striations 86
Fig. 4.25: Interpretation map of D_4 faults 87
Fig. 4.26: Stereonets illustrate D_5 faults 88
Fig. 4.27: Interpretation map of D_5 faults 90
Fig. 4.28: Photos of D_5 faults 92
Fig. 4.29: Photos of D_5 faults 93
Fig. 4.30: Underground map of drive C355DD, HW mine 94
Fig. 4.31: Interpretation of D_5 fault striations 95
Fig. 4.32: Section 1420E, Battle mine 97
Fig. 4.33: Section 2530E, Extension Zone, Battle mine 99
Fig. 4.34: Oblique 020 section, 23-428XN, HW mine 101
Fig. 4.35: Underground map, drives 23-427 and K424ACC, HW mine 104
Fig. 4.36: Interpretation of geology, drives 23-427, K424ACC, HW mine 105
Fig. 4.37: Summary map of major structures at Myra Falls 107
Fig. 4.38: Stereonets illustrating regional bedding 107

Chapter 5

Fig. 5.1: Fence diagram illustrating HW Horizon facies variation 113
Fig. 5.2: Map of quartz-feldspar porphyry bodies 115
Fig. 5.3: Isopach map of fine grained facies and footwall contours 117
Fig. 5.4: 3-d block diagram of footwall contours and major structures 116

Fig. 5.5: Isopach map of HW Horizon and Myra Formation 119
Fig. 5.6: Structural domains 121
Fig. 5.7: Thelwood Formation basal contours and photos 122
Fig. 5.8: HW mine footwall contours and argillite isopach map 124
Fig. 5.9: HW mine HW Horizon and Myra Formation isopach maps 125
Fig. 5.10: HW mine growth faults 127
Fig. 5.11: HW section 3500mE and restored section 129
Fig. 5.12: HW section 3050mE and restored section 131
Fig. 5.13: Battle mine footwall contours and argillite isopach map 133
Fig. 5.14: Battle mine HW Horizon and Myra Formation isopach maps 135
Fig. 5.15: Battle mine growth faults 136
Fig. 5.16: Battle section 1300mE and restored section 139
Fig. 5.17: Battle section 1000mE and restored section 141
Fig. 5.18: Footwall contour map and restored paleoseafloor 144
Fig. 5.19: 3-d block diagrams of footwall contours and restored seafloor 145
Fig. 5.20: Map of argillite depo-centres and block model of paleoseafloor 147
Fig. 5.21: Bathymetric maps depicting the sites of modern hydrothermal fields 149

Chapter 6

Fig. 6.1: Argillite-chert isopach map 152
Fig. 6.2: Battle mine fence diagram 154
Fig. 6.3: HW mine fence diagram 155
Fig. 6.4: Chert, black chert, argillite distribution, Battle mine 156
Fig. 6.5: Restored composite section 1260-1420E 157
Fig. 6.6: Lithological legend for graphic logs 156
Fig. 6.7: Graphic log and photos, drive ST183A, Battle mine 159
Fig. 6.8: Graphic log and photos, drive G171XS, Battle mine 161
Fig. 6.9: Graphic log and photos, drive S335C, HW mine 163
Fig. 6.10: Photos of chert clasts 165
Fig. 6.11: Photos of chert 167
Fig. 6.12: Photomicrographs of chert micro-scale textures 169
Fig. 6.13: Photomicrographs of quartz replacement textures 171
Fig. 6.14: Photomicrographs of chalcedonic spherules 173
Fig. 6.15: Photomicrographs of rutile in spherical megaquartz patches in chert and sericite 175
Fig. 6.16: Photomicrographs of type-1 and type-2 apatite in chert 177
Fig. 6.17: Scatter diagrams of type-1 and type-2 apatites 178
Fig. 6.18: SEM images and photomicrographs of sulphides in chert 179

Fig. 6.19: Photos of black chert 182
Fig. 6.20: Photomicrographs and SEM images of sulphides and black chert textures 183
Fig. 6.21: Photos of argillite 185
Fig. 6.22: Photomicrographs of argillite and radiolarians 187
Fig. 6.23: Photomicrographs of sulphides in argillite 189
Fig. 6.24: Photos of associated facies 191
Fig. 6.25: Section 1420mE, Battle mine 193
Fig. 6.26: Photos of chert and associated sulphides 195
Fig. 6.27: Photos of top ore contact, Battle mine 197
Fig. 6.28: Photos of top ore contact, HW mine 199
Fig. 6.29: Photos of sulphide-rich mud and overlying sandstone turbidite 201
Fig. 6.30: Photos of jasper clasts 203
Fig. 6.31: Comparison of argillite-chert textures 205
Fig. 6.32: Argillite-black chert-chert progression 207
Fig. 6.33: Photos of crosscutting fine-grained quartz veins 209

Chapter 7

Fig. 7.1: Photos of typical alteration textures in Myra Falls lithologies 215
Fig. 7.2: Photos of alteration textures in quartz-feldspar porphyry 217
Fig. 7.3: Photomicrographs of quartz-sericite alteration in felsic volcaniclastics 219
Fig. 7.4: Photomicrographs of weak sericite-chlorite alteration 221
Fig. 7.5: Typical SWIR spectra of white mica 222
Fig. 7.6: Typical SWIR spectra of chlorite 223
Fig. 7.7: Histograms of AlOH wavelength variation in white mica 227
Fig. 7.8: Histograms of FeOH wavelength variation in chlorite 228
Fig. 7.9: Graphic logs (20-675 and 18-1002-1003), Ti/Zr ratios, AlOH variation 229
Fig. 7.10: Graphic logs (S335C and G171XS) with AlOH wavelength variation 232
Fig. 7.11: Composite section 1260-1420mE and AlOH wavelength variation 233
Fig. 7.12: Graphic logs (14-680 and 18-1002-1003), Ti/Zr ratios, AlOH variation 235
Fig. 7.13: White mica AlOH wavelength map 237
Fig. 7.14: Chlorite FeOH wavelength map 239
Fig. 7.15: Scatter plots show mica compositions against AlOH wavelengths 240
Fig. 7.16: Triplots illustrating white mica compositions 241
Fig. 7.17: Scatter plots illustrate white mica compositions 243

Chapter 8

Fig. 8.1: Fe-Al-Mn and FeO-Al_2O_3-MgO plots of argillite and chert 254
Fig. 8.2: Fe/Ti vs Al/(Al+Fe+Mn) plot of argillite and chert 254
Fig. 8.3: ZnO-Al_2O_3-BaO and ZnO-Al_2O_3-CuO plots of argillite and chert 255
Fig. 8.4: Immobile element plots of caprocks vs QFP and Price Andesite 256
Fig. 8.5: Graphic log and chemostratigraphy of composite drillhole 18-1002-1003, 1420E, Battle mine 259
Fig. 8.6: Graphic log and chemostratigraphy of drillhole L14-680, 1260E, Battle south 261
Fig. 8.7: Lateral major and trace element variation in the caprock horizon 263
Fig. 8.8: Major and trace element variation of Battle Basin argillite and chert 266
Fig. 8.9: Major and trace element variation of Battle Basin argillite and chert 267
Fig. 8.10: Graphic log and chemostratigraphy of drillhole 23-503, HW mine 268
Fig. 8.11: Graphic log and chemostratigraphy of chert-siltstone sequence in drive S335C, HW mine 269
Fig. 8.12: Major and trace element variation of HW Basin argillite and altered argillite 271
Fig. 8.13: Mass balance diagrams for siliceous caprocks above the Battle orebody 274
Fig. 8.14: Chrondrite normalised REE plots of argillite and chert 277
Fig. 8.15: Shale normalised REE plots of argillite and chert 278
Fig. 8.16: Chrondrite normalised REE plots of seawater, endmember hydrothermal Fluids, chemical sediments, Kuroko tetsusukei, and Cyprus umbers 281
Fig. 8.17: Trace element variation in shale-normalised Myra Falls argillite 285
Fig. 8.18: Scatter plots of Myra Falls argillite 287
Fig. 8.19: Major and trace element variation of Battle Basin argillite and chert 289
Fig. 8.20: Major and trace element variation of HW Basin argillite 292
Fig. 8.21: Organic carbon vs sulphide sulphur plot of Myra Falls argillite 299
Fig. 8.22: DOP values for Myra Falls argillite 299
Fig. 8.23: Organic carbon-pyrite sulphur-iron relationships 301
Fig. 8.24: Organic carbon-pyrite sulphur-iron relationships for Battle Basin argillite 302
Fig. 8.25: Organic carbon-pyrite sulphur-iron relationships for HW Basin argillite 303
Fig. 8.26: Organic carbon-pyrite sulphur-iron relationships for regional argillite 304
Fig. 8.27: Histogram of sulphur isotope values in the Battle basin 313
Fig. 8.28: Spatial variation in $\delta^{34}S$ in the Battle basin 313

Fig. 8.29: Sulphur isotope compositional variation of marine sulphate during Phanerozoic time and Battle orebody sulphate 316
Fig. 8.30: Sulphur concentration vs $\delta^{34}S$ in Myra Falls argillite..... 316

Chapter 9

Fig. 9.1: Photomicrographs of inclusions in siliceous caprocks 322
Fig. 9.2: Photomicrographs of inclusions in quartz interstitial to massive sulphides 324
Fig. 9.3: Photos of late stage crosscutting quartz veins 326
Fig. 9.4: Photomicrographs of inclusions in crosscutting quartz veins..... 327
Fig. 9.5: Histograms illustrating salinity in Battle orebody samples 329
Fig. 9.6: Histograms illustrating homogenization temperatures in Battle orebody samples..... 331
Fig. 9.7: Histograms illustrating salinity in HW orebody samples 332
Fig. 9.8: Histograms illustrating homogenization temperatures in HW orebody samples 333
Fig. 9.9: Th-salinity plots of Battle and HW orebody samples..... 334
Fig. 9.10: Th-salinity plot of Myra Falls data vs other sulphide deposits..... 336
Fig. 9.11: Comparison of density data and ambient seawater 337
Fig. 9.12: Th-salinity plot with calculated fluid densities..... 341
Fig. 9.13: Schematic diagram illustrating Th-salinity trends due to fluid evolution processes..... 343
Fig. 9.14: Boiling point curves for H_2O liquid and for brine of constant composition 343

Chapter 10

Fig. 10.1: Block diagrams illustrating present day deformed paleoseafloor and restored paleoseafloor 349
Fig. 10.2: Block diagram of depositional environment of the Battle and HW Basins 351
Fig. 10.3: Argillite depocentres with paleoenvironmental indicators 351
Fig. 10.4: Battle chert distribution map with metal and $\delta^{34}S$ zonation 354
Fig. 10.5: Stability fields of selected minerals in the Battle orebody 356
Fig. 10.6: Silica solubility-temperature plot 358
Fig. 10.7: Quartz solubility as a function of pH and temperature..... 358
Fig. 10.8: Quartz solubility as a function of NaCl concentration and temperature..... 359
Fig. 10.9: Conductive cooling vs mixing resulting in precipitation of amorphous silica..... 361

Fig. 10.10: Lateral variation in metal concentrations in basal lens of Battle chert and argillite 363
Fig. 10.11: Pb-Zn-Cu solubilities as a function of temperature and distance from deposit 365
Fig. 10.12: Temperature-solubility model for sulphide mineral in Battle chert 366
Fig. 10.13: Model for the formation of bedded jasper deposits at the edge of Battle basin 371
Fig. 10.14a: Schematic representation of three fluid types (Sato, 1972) 373
Fig. 10.14b: Models for the genesis of sheet-style VHMS deposits (Large, 1992) 373
Fig. 10.15: Temperature vs salinity plot of Myra Falls inclusion data 374
Fig. 10.16a: Genetic model for the formation of the Battle chert 376
Fig. 10.16b: Genetic model for the formation of the Battle chert 377

List of Tables

Chapter 2

Table 2.1: Correlation table of deformation events in Vancouver Island 25

Chapter 3

Table 3.1: Comparison of mine sequence (Juras, 1987) and lithofacies (this study) 38

Table 3.2: Metamorphic mineral assemblages of Myra Falls lithologies 46

Chapter 4

Table 4.1: Crosscutting relations indicating relative fault ages 55

Table 4.2: Deformation sequence at Myra Falls 56

Chapter 7

Table 7.1: White mica and chlorite AlOH and FeOH wavelength variations 226

Table 7.2: Average AlOH wavelength and at. % of the main elements in white micas 242

Chapter 8

Table 8.1: Average major and trace elements for siliceous caprocks and argillite 252

Table 8.2: Rare earth elements in Myra Falls chert and argillite 276

Table 8.3: Average major and trace element values of argillite vs average shale values 283

Table 8.4: Average carbon, sulphur, iron values for Myra Falls argillite vs average shale values 300

Table 8.5: Average metal ratios for Myra Falls argillite vs average shale values 305

Table 8.6: Selected major and trace element variation in Myra Falls argillite vs other shale types 307

Table 8.7: Summary of $\delta^{34}S$ analyses 311

Chapter 9

Table 9.1: Comparison of Myra Falls fluid inclusion data with other VHMS deposits 341

Chapter 1
Introduction

1.1 Preamble

Fine-grained siliceous deposits are spatially associated with many VHMS orebodies, e.g., tetsusukei above the Kuroko deposits (Kalgeropoulous and Scott, 1983); iron stones associated with the Brunswick Horizon, Bathurst District (Peter and Goodfellow, 1996); or the silica-barite cap above the Hellyer Deposit (Sharpe, 1991; Gemmell and Large, 1992). Although there is a clear spatial association between surface and near-surface silica deposits and the massive sulphide deposits, the genetic relationship and the mechanisms of formation of the siliceous deposits are poorly understood.

The timing of silica deposition, relative to ore formation is important. For example, silica deposited in the near surface sediments, prior to massive sulphides, may form a porosity seal. This 'cap' could trap subsequent ore bearing fluids and aid in the formation of a VHMS orebody. Silica may also be deposited during ore formation, from venting hydrothermal fluids, to form exhalative deposits on the seafloor (e.g., white smokers, Hannington et al. 1998). These siliceous deposits typically have a much greater lateral extent than the associated orebody and commonly have a distinct geochemical signature. Mineralogical variations, major and trace element geochemistry and stable isotope studies of the exhalites can provide vectors to base metal orebodies.

The orebodies at Myra Falls VHMS camp are commonly associated with hanging wall siliceous zones and provide an ideal opportunity to examine the controls on silica deposition and their relationship to the underlying ore deposits. This thesis presents a reconstruction of the caprock depositional environment and a detailed petrological and geochemical study of the caprocks. A geological and geochemical model is then presented for the formation of the caprocks and their relationship to the underlying ore.

1.2 Project aims

The aims of this project are to:

1) Describe the geological and structural setting of the caprocks depositional environment by:
    - Mapping of volcanic and sedimentary facies in the caprock horizon;
    - Examination of detailed facies associations of the caprocks and the HW Horizon;
    - Identification of syn-depositional structures (growth faults) and their relationship to sites of caprock deposition; and
    - Recognition of post-depositional deformation (ductile and brittle) and the effects of this deformation on the present location of the caprocks.

2) Describe the mineralogy, textures, paragenesis and metal zoning in the siliceous caprocks in order to classify them as either 'true exhalites' or as alteration of pre-existing sediments or volcanic rocks by:
    - Identification of silicate, oxide and sulphosalt mineralogy in the caprocks; and
    - Detailed petrographic and textural studies.

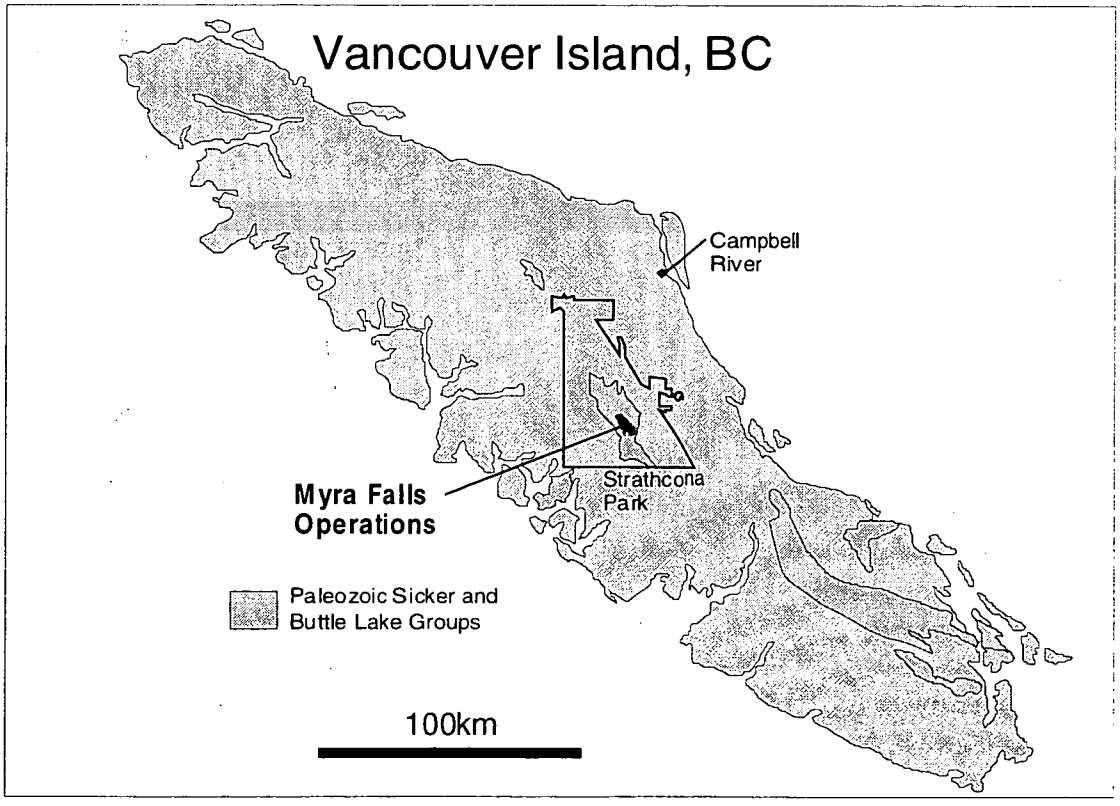

Figure 1.1: Location map of Myra Falls VHMS camp, Vancouver Island, BC. The VHMS deposits are hosted by the Paleozoic Sicker Group, which form the basement rocks of the island (see Figure 2.1 for a more detailed map of the area).

3) Determine the geochemical (trace element, stable isotope) characteristics and signature of the caprocks by:

- Examination of major and trace element variation
- Rare earth element analysis;
- Look at zonation within individual mineral phases;
- Examination of primary metal dispersion within the caprocks; and
- Sulphur isotope variation in the caprocks.

4) Determine the characteristics of the hydrothermal fluids associated with caprock formation by:

- a detailed fluid inclusion study of the caprocks and associated massive sulphides

5) Propose a model for the genesis of the caprocks.

6) Develop useful criteria, based on the caprocks for exploration in the Myra Falls district.

1.3 Location and setting

Myra Falls VHMS camp is located within Strathcona Provincial Park in the middle of Vancouver Island, British Columbia, Canada (Figure 1.1). The mine is located at the southern end of Buttle Lake (Figure 1.2a) in an area of rugged glaciated topography, with relief rising to 2200m above sea level. Access to the mine is via a 90 km paved road from Campbell River. Figure 1.2b and 1.2d shows the layout of Myra Falls VHMS camp in Myra Valley. Myra Falls, situated at the mouth of Myra Valley is shown in Figure 1.2c.

The Cu-Pb-Zn deposits at Myra Falls occur in two mineralized horizons, which have an approximate strike length of 5 km. The two horizons are the upper Myra-Lynx-Price horizon and the lower HW-Battle horizon, which also includes the Ridge East, Ridge West and Marshall Zones (Figure 1.3).

1.4 Work Plan

1.4.1 Field work

The fieldwork for this project was carried out over three field seasons, equating to about 7 months in the field. The fieldwork consisted of underground mapping in the HW, Battle and Lynx mines, logging of exploration and mine diamond drillcore, limited surface mapping on Price Hillside and Myra open pit, examination of exploration and

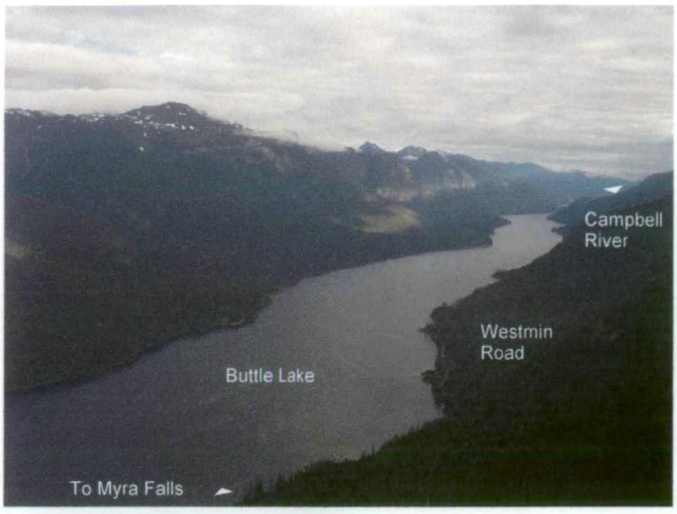

a

Figure 1.2: a) Aerial view looking north at Buttle Lake, with the mine access road on the eastern side of the lake (photo courtesy of F. Bakker).

b

Figure 1.2: b) Aerial view of Myra Falls VHMS camp (photo courtesy of F. Bakker).

c

Figure 1.2: c) Myra Falls, located at the mouth of the Myra River as it enters Buttle Lake.

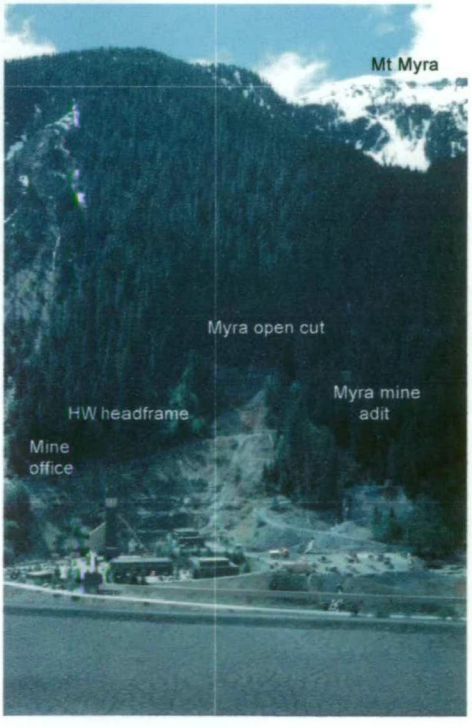

d

Figure 1.2: d) View across the tailings dam of the main HW shaft with the Myra open pit and Mt Myra in the background.

mining databases, and collection of data from exploration and mine sections, for the construction of footwall contour maps, isopach maps and facies maps.

The variation in HW Horizon facies across the property, and detailed facies associations within the caprock horizon were mapped by logging the HW Horizon in 80 drillholes (a full list of drillhole details and examples of drill logs are given in Appendix 1).

Detailed underground mapping was carried out in the Battle and HW mines (see Appendix 1 for examples of underground mapping). The areas mapped are shown in Figures 1.4 and 1.5 and include, drives S335C, B390C, K424ACC & 23-427, C355DD, S335A-D6 & D2, C353DD, N357RP, S335B-D15, N350B, and the 23 Shop in the HW mine; and drives ST183A, 18-Level ramp (near lunch room), M150DD, M172DD, G171XS, and M148EX in the Battle mine. Other underground areas were also examined, but in much less detail. These areas were examined for structural data and include, the Price mine, 24 and 21 Level in the HW mine, drive 23-331XN, HW mine, and the Gopher and Gap Zones in the Battle mine.

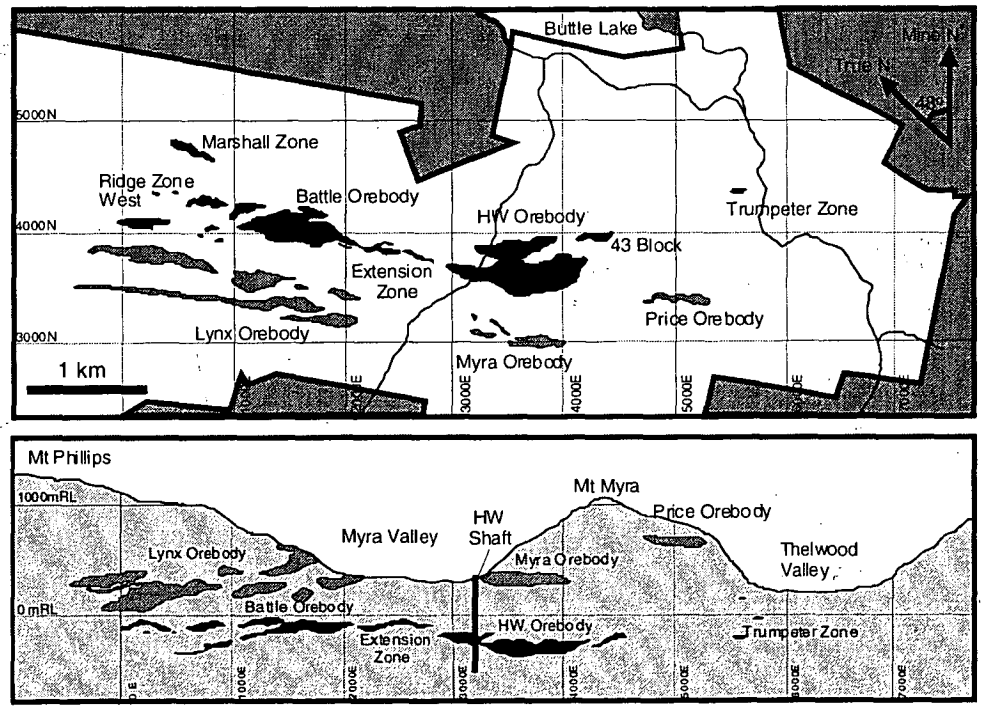

Figure 1.3: Plan view and cross section of Myra Falls VHMS camp. The massive sulphides occur in two mineralized horizons, which are the upper Lynx-Myra-Price ore horizon and the lower Battle-HW ore horizon.

1.4.2 Laboratory work

Laboratory work included the slabbing of drillcore and underground rock samples for polished thin sections; petrological analysis of thin sections; rock crushing and preparation of pressed powder pellets for trace element XRF and ICP-MS analysis; SEM analysis of chert and argillite samples; measurement of SWIR spectrum of rocks from the HW Horizon; electron microprobe analysis of white mica, chlorite, apatite and sulphides; extraction of sulphide sulphur (mono and di-sulphides) from argillites for sulphur isotope analysis; HCL-soluble iron measurements; organic carbon analysis by fusion; and fluid inclusion studies.

1.5 Previous Work

1.5.1 Documentation of geology

The first geological reconnaissance of the Buttle Lake area was in 1912 by Clapp, who identified and named the Sicker Series after Mt Sicker. Further mapping in the area was carried out by Gunning (1931), and by Jeffery (1970). Muller (1980) produced detailed maps and a stratigraphic sequence for the Buttle Lake area and renamed the Sicker Series, the Sicker Group (see Chapter 2).

Company geologists established a mine sequence at Myra Falls, which was described in field guides and company reports (e.g., Jeffery, 1970; Walker, 1985). Juras (1987) added to the local geology with a detailed examination of the volcanic stratigraphy (see Chapter 3). This work was undertaken for his PhD study and concentrated mainly on the Price Hillside. Further geological work by company geologists is written up in papers including, Juras and Pearson (1990), Pearson (1993) and McKinley et al. (1997).

A number of structural reports have been written for Myra Falls, describing the foliation and numerous fault styles. Reports include Benvenuto (1986), Glover (1990), Reid (1993), and Berry (1995, 1996, 1998 and 2000). Structural studies for the report (Berry, 2000) were undertaken during the final field season for this thesis, and data from this report is included in Chapter 4. A company report on district-scale metal zoning, was also carried out by Gemmell (1998).

Several Masters theses have been written on the property and include, Robinson, (1994), and Cresswell (1997). An honours thesis was also written on the Price Orebody (Dishaw, 1998). Several papers have been published on Robinson's work and include a paper on the geology, lithogeochemistry and alteration of the Battle Deposit by Robinson et al. (1996) and a lead isotope paper by Godwin et al. 1996. Barrett and Sherlock (1996) worked on the HW Deposit, giving a detailed description of the volcanic stratigraphy, lithogeochemistry and seafloor setting of the HW Deposit. The study also included fluid

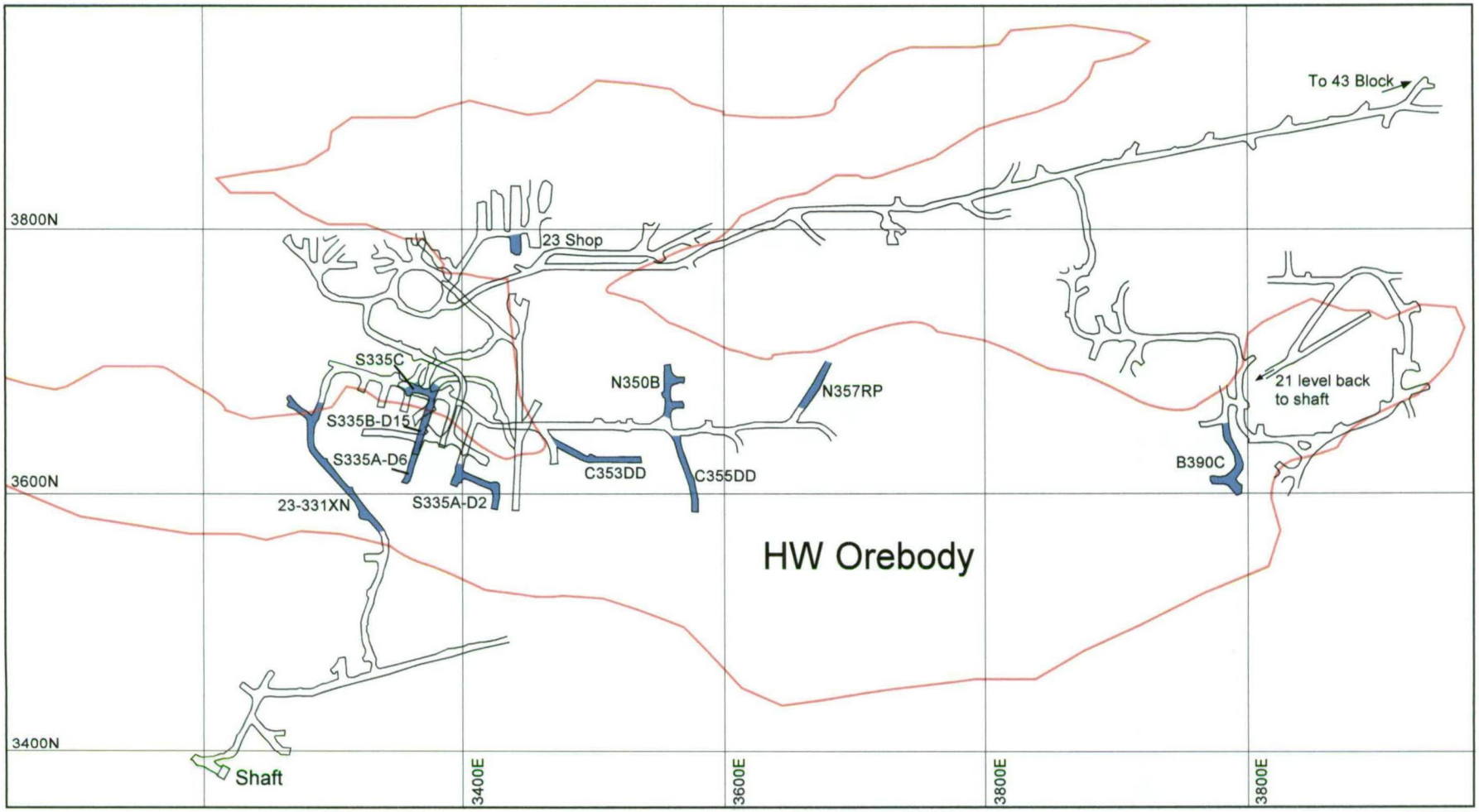

Figure 1.4: Map illustrating the underground areas mapped in detail (shaded blue) in the HW mine, 23 level.

inclusion data from the HW orebody, U-Pb dating of rhyolitic rocks immediately above the massive sulphides and whole-rock oxygen isotope data on footwall and hangingwall rocks.

The most recent work on the property, was a PhD study by Sinclair (2000), on the geology and genesis of the Battle Deposit, with particular emphasis on volcanic facies, metal zoning and sulphide speciation. This study was completed in 2000 and ran concurrently with this project.

1.5.2 Past exploration

Sulphide showings were discovered in the Buttle Lake area in the early 1900s, when Strathcona Park was opened for prospecting. The first claims were staked in 1917, near Price Creek and in Myra Valley, and include the Lynx, Price and Paw (Myra) claims (Juras and Pearson, 1990). Sporadic work was carried out on these claims until 1925, and after this date, work on the property ceased until 1946. The claims were acquired by Western Mines Ltd in 1961, and exploration was undertaken, mainly on the Lynx claim. Production in the Lynx deposit began in early 1967, with the development of open pits on the northern side of Myra Valley. This work continued until 1974, when production in the Lynx mine went underground. Production in the Myra Deposit began in 1972 and continued until 1985, including open pits on the southern side of Myra Valley and underground workings. The HW deposit was discovered in 1979 and underground production began in 1985. The Battle Deposit was discovered in 1991 and the Battle and HW deposits are currently being mined. Western Mines Ltd was acquired by Boliden in 1998, and is now known as Boliden-Westmin Ltd.

The historical production figures are 1.28 Mt Cu concentrate produced, and 1.65 Mt Zn concentrate produced from 1966 to 2000. The current proven and probable mining reserves are 11.9 Mt of ore, averaging 1.7 g/t Au, 53.3 g/t Ag, 1.5 % Cu, 0.59 % Pb, and 7.66 % Zn.

1.6 Organisation of thesis

The regional and local geology of Vancouver Island and the Buttle Lake area is given in Chapters 2 and 3. A detailed structural study of the Myra Falls area was undertaken and is presented in Chapter 4. The deformation history described in Chapter 4 is then used for the paleoseafloor reconstruction in Chapter 5.

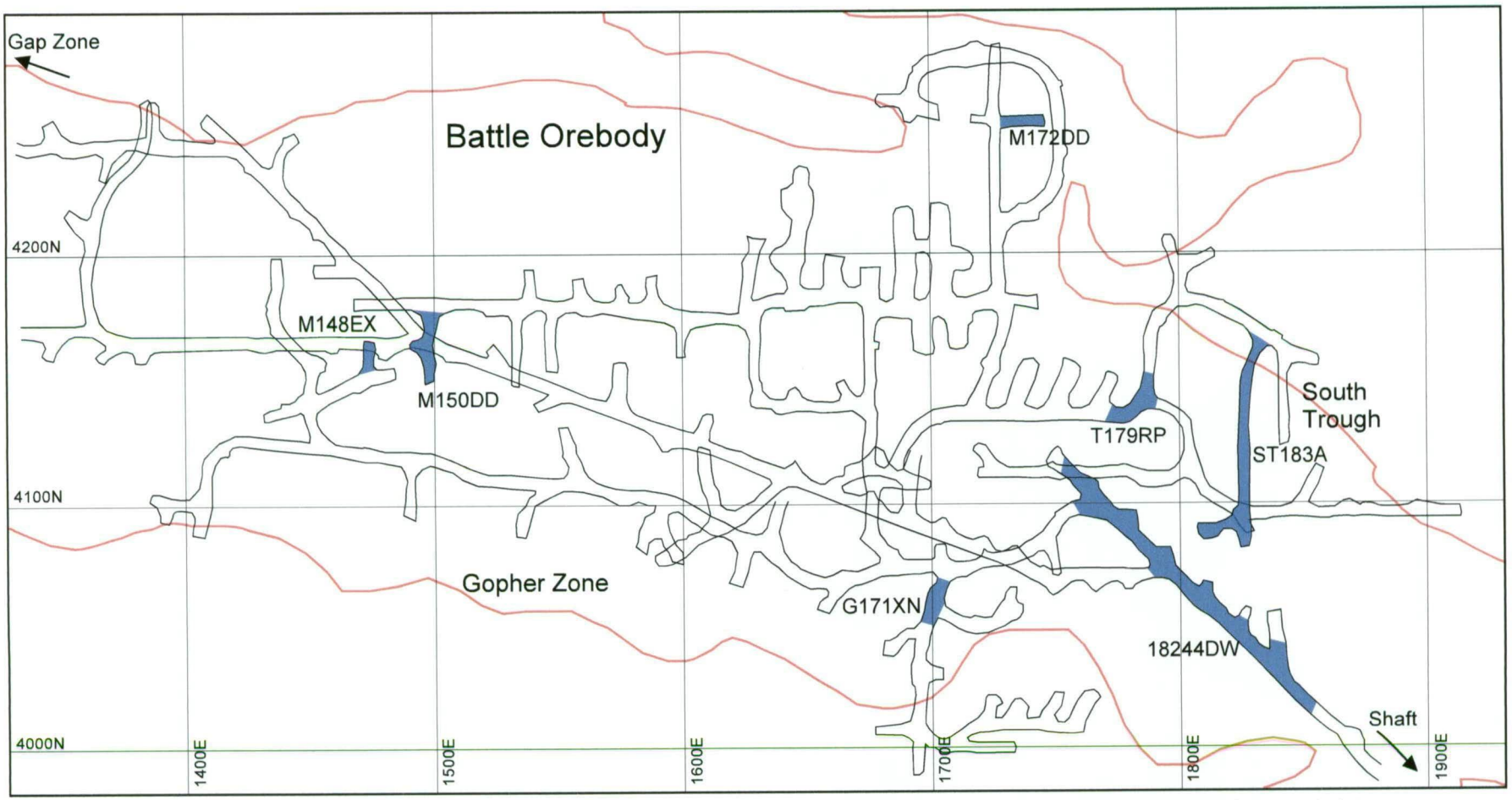

Figure 1.5: Map illustrating the underground areas mapped in detail (shaded blue) in the Battle Mine (lower mine levels of the Battle main lens omitted for clarity).

The caprocks and associated facies are described in Chapter 6, followed by an alteration study of the HW Horizon, in Chapter 7. This section uses SWIR analyses in combination with electron microprobe data to map out distinct alteration halos in white micas and chlorite in the hangingwall rocks across the property. The major and trace element geochemical characteristics of the caprocks and associated facies are then described in Chapter 8. A fluid inclusion data of the siliceous caprocks and the Battle and HW orebodies is presented in Chapter 9.

A geological and geochemical model for caprock formation is given in Chapter 10, and is followed by the conclusions, presented in Chapter 11. This chapter also includes the implications for exploration in the Myra Falls area and future research initiatives.

Chapter 2
Regional geology

2.1 Introduction

Vancouver Island is situated on the western edge of the Canadian Cordillera, forming part of a complex zone of accreted terranes, which make up the western coast of North America (Figure 2.1a). The basement rocks of Vancouver Island belong to the Wrangellia terrane, which consists of Paleozoic, Mesozoic to Cenozoic volcanic arc, oceanic and clastic wedge assemblages. The oldest rocks of the Wrangellia terrane are the Sicker Group, a Paleozoic volcano-sedimentary package, which hosts the VHMS deposits at Myra Falls (Figure 2.1b).

This chapter gives an overview of the tectonic setting, stratigraphy, metamorphism and structure of Vancouver Island.

2.2 Tectonic Setting

Vancouver Island forms part of the Insular Belt of the Canadian Cordillera. This belt is one of five NW trending zones, subdivided by distinct lithologies, internal structure and physiography to adjacent belts (Figure 2.1a). The Insular Belt is made up of a number of terranes, the largest being the Alexander and Wrangellia Terranes, often grouped as a Superterrane. This belt extends up the western coast of Canada and up into Alaska. The formation of these belts is the result of a long history of collision between exotic crustal fragments (allochthonous terranes) and the ancient margin of North America.

The Wrangellia Terrane, named after the Wrangell Mountains in SE Alaska (Jones et al., 1977), is an allochthonous terrane, based on paleomagnetic and paleontological evidence. Irving and Yole (1987), using paleomagnetic evidence, show that since the Late Triassic, there has been considerable northward movement of Wrangellia relative to the North American craton, indicating that Wrangellia originated in southern latitudes. This is consistent with paleontological data such as the tropical fossils found in limestone near

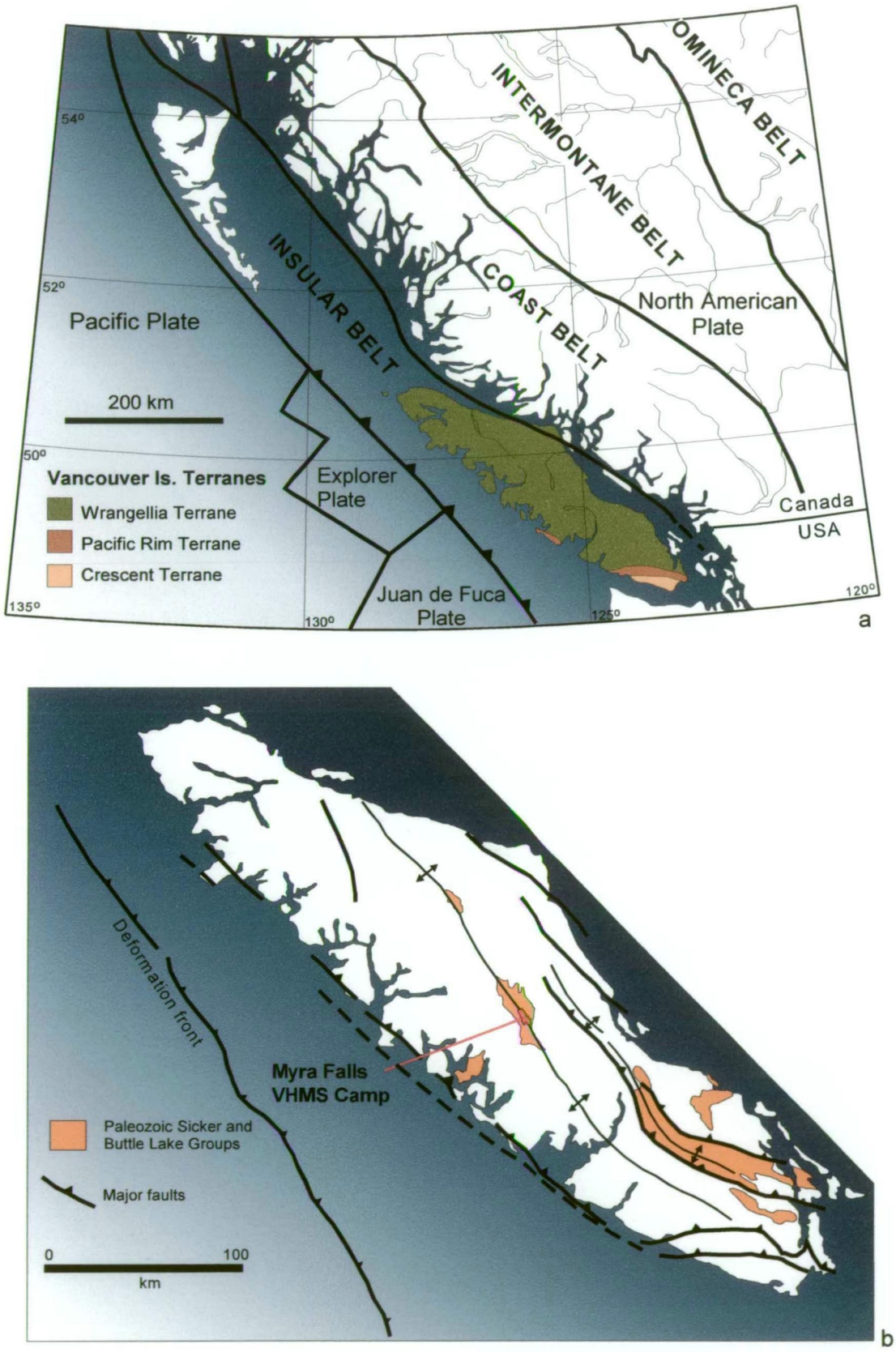

Figure 2.1: a) Tectonic setting of Vancouver Island; **b)** Regional geological setting of Myra Falls VHMS camp, Vancouver Island. Diagrams modified from Gabrielse et al. (1991) and Yorath et al. (1999).

the top of the Karmutsen Formation on Vancouver Island, which also indicate southern latitudes (Yorath and Nasmith, 1995).

In northern Wrangellia, the Upper Jurassic to Lower Cretaceous Gambier overlap assemblage suggests amalgamation with Alexander terrane just prior to deposition of these sediments (Gabrielse and Yorath, 1991). However, workers in Alaska have mapped a late Paleozoic pluton intruding both terranes, and suggest that "the terranes were together prior to Late Pennsylvanian time, or that they were never separate terranes" (R.B. Campbell, C.J. Dodds and G. Plafker, pers. comm., 1987, in chapter 18, Gabrielse and Yorath, 1991).

The time of amalgamation or collision of the resulting Insular Superterrane with the ancient margin of North America is also contentious. A widespread mid-Cretaceous paleomagnetic overprint for Wrangellia is in broad agreement with geological evidence for a mid-Cretaceous amalgamation (Irving and Wynne, 1991). However, Monger et al., (1982) suggest an early-Cretaceous time for collision, while Gabrielse and Yorath (1991) suggest that amalgamation may have occurred as early as Late Jurassic, due to the similarity of the stratigraphy across several small terranes in the southern Coast Belt.

The collision of Wrangellia with the ancient boundary of the North American continent has formed much of the structural and physiographical characteristics of Vancouver Island (Figure 2.1b). In the central part of the island, compression, caused by the collision, resulted in uplift and erosion, and deposition of Nainaimo Group sediments (Figure 2.2).

During the Cenozoic, younger terranes, the Pacific Rim and Crescent terranes, were emplaced beneath Wrangellia along prominent west and northwest trending thrust faults; Figure 2.3 (Hyndman et al., 1990; England and Calon, 1991). The western and southern margins of Vancouver Island were uplifted and eroded during these collisons, resulting in the exposure of gneiss complexes around Victoria. Folding and faulting of the Nanaimo Group sediments, during the collision events, resulted in the formation of the Gulf Islands.

Quaternary glaciations have also had a major effect on the physiography of Vancouver Island, with the formation of steep u-shaped valleys, till erratics, drumlins, grooves and striations.

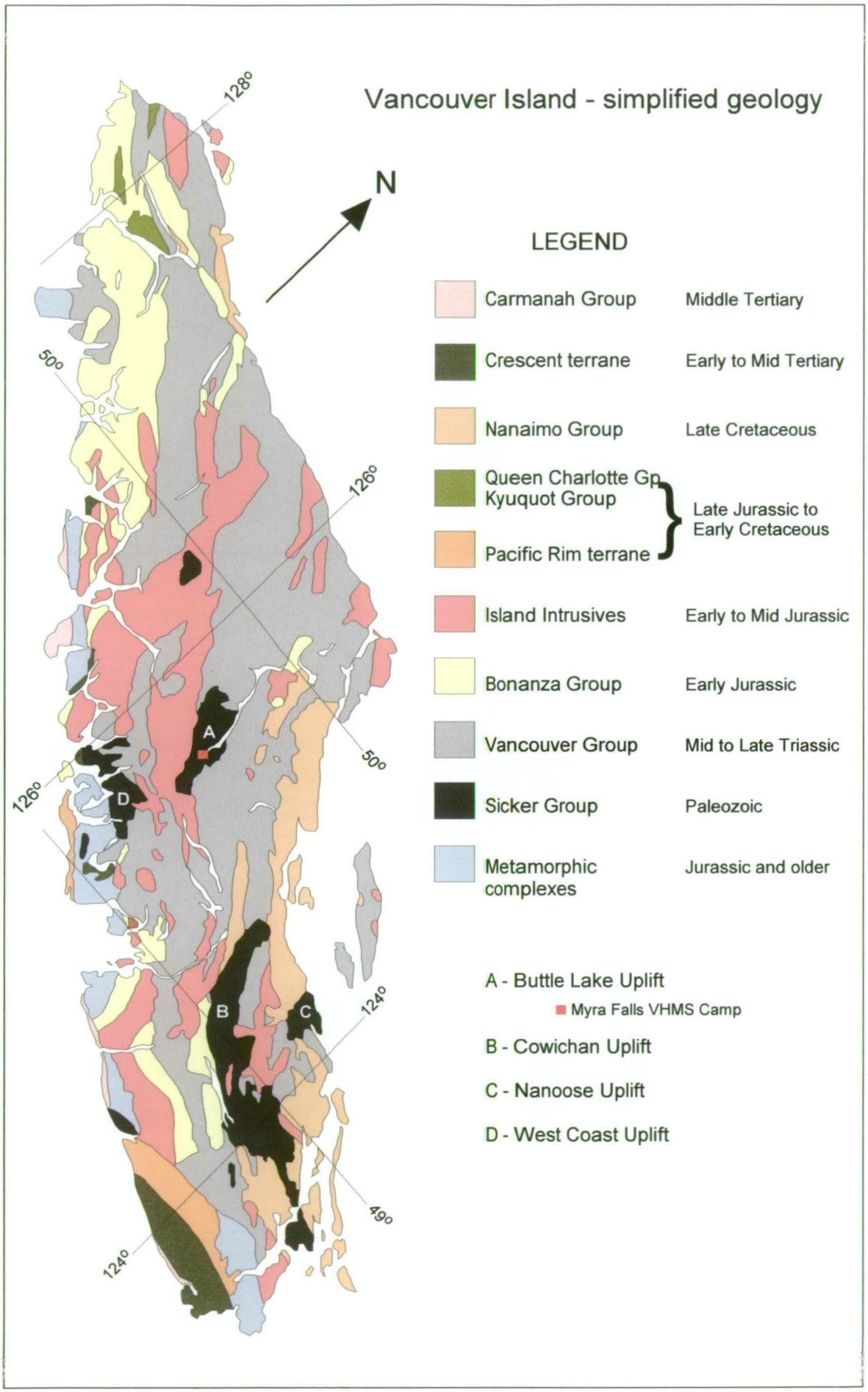

Figure 2.2: Geology of Vancouver Island, modified from Muller (1980).

Today, Vancouver Island lies about 200km east of the active Juan de Fuca spreading ridge (Figure 2.1a). The Juan de Fuca plate, comprising relatively young oceanic crust and a thin accumulation of sediments is at present being subducted beneath the North American plate, forming a new accretionary complex.

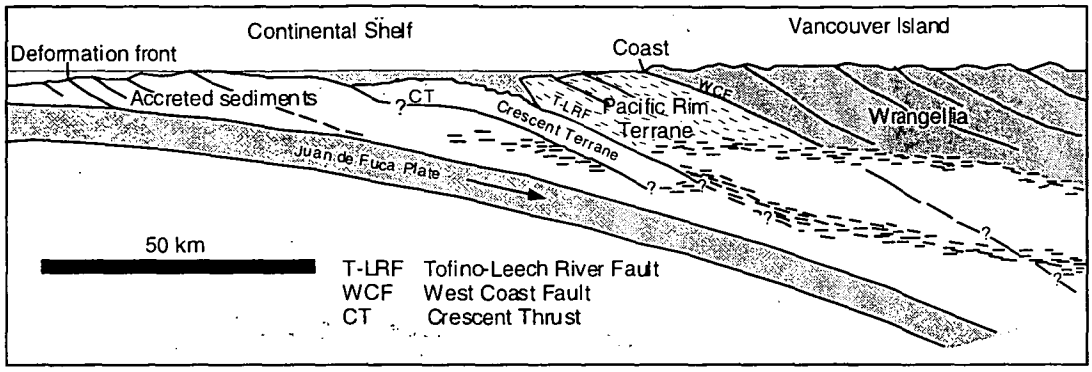

Figure 2.3: Schematic cross-section through the southwestern part of Vancouver Island, modified from Hyndman et al. (1990).

2.3 Stratigraphy of Vancouver Island

The majority of Vancouver Island is underlain by the Wrangellia terrane and these basement rocks are exposed in four major structural uplift zones, which are, the Buttle Lake, Cowichan, Nanoose and West Coast uplifts or anticlinoriums, shown in Figure 2.2. A simplified stratigraphic column, (Figure 2.4), illustrates the main units which make up Vancouver Island.

The distinctive rock sequence that defines Wrangellia represents the products of three cycles of volcanism, two with arc affinities and one rift-related. Following each cycle there was a change from marine to ultimately shallow subtidal or sub aerial deposition (Gabrielse and Yorath, 1991).

On Vancouver Island, the earliest period of volcanism, during the Paleozoic, is represented by the Sicker Group, which comprises calc-alkaline volcanics and volcaniclastics. The cycle ended with the accumulation of a shallow carbonate platform (Buttle Lake Group). The second cycle started in the Late Triassic, with the build-up of a thick succession of rift-related tholeiitic basalts (Karmutsen Formation) overlain by a carbonate platform (Quatsino and Parsons Bay Formations). The final phase of volcanism occurred in the Early Jurassic and is represented by the Bonanza Group, comprising subaerial lavas and granite intrusions with arc affinities. These intrusions were later upthrust to become the exposed plutons of the Island intrusives.

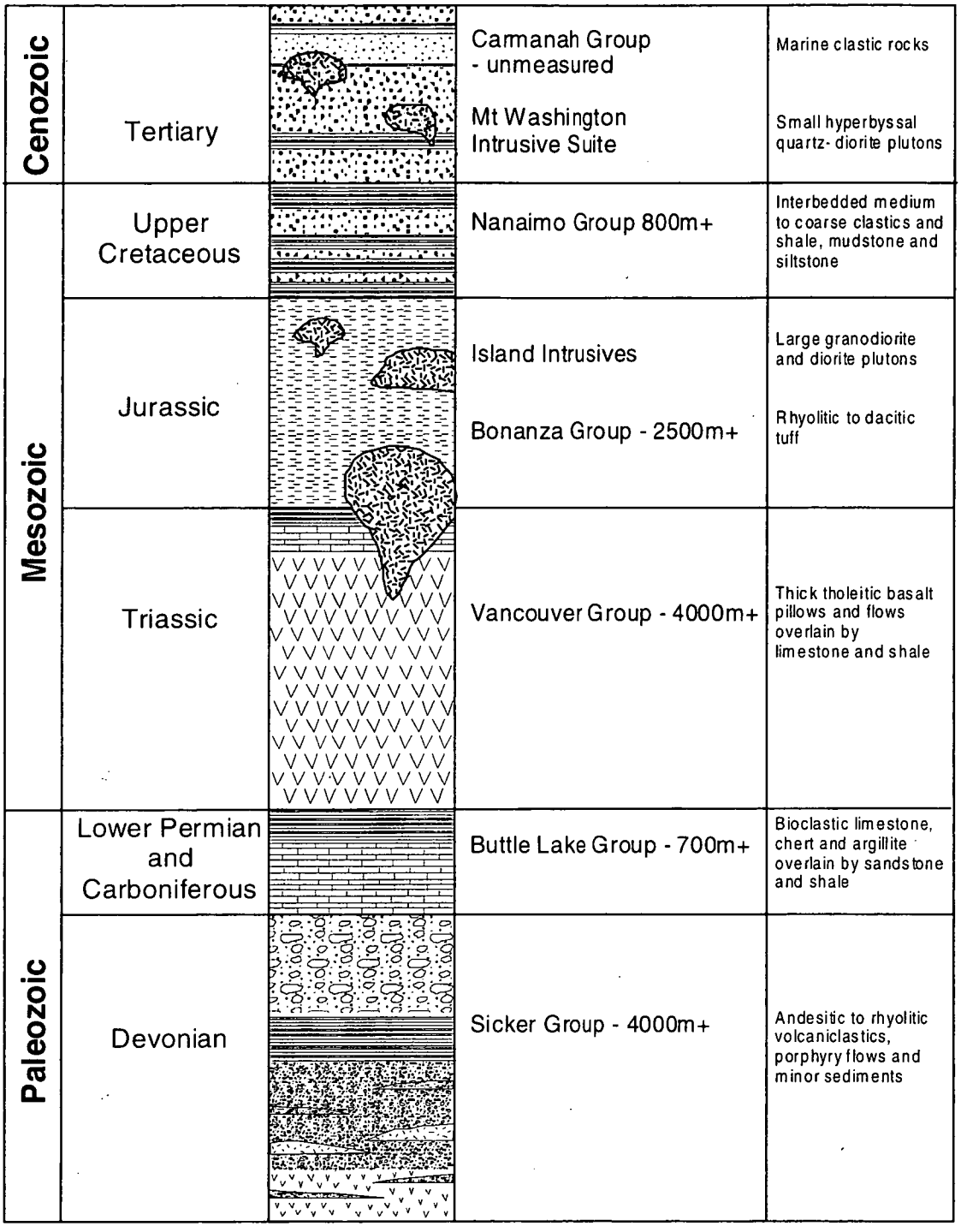

Figure 2.4: Stratigraphic column for Vancouver Island, modified from England and Calon (1991); Massey (1992); and Yorath et al. (1999).

2.3.1 Sicker Group

The Sicker Group, named after Mt Sicker (originally Sicker Series, Clapp, 1912) includes the most of the Paleozoic rock sequence of Vancouver Island. The economic importance of the Sicker Series was recognised by Clapp (1912), as the "country rock of various

copper deposits", which includes the Myra Falls VHMS deposits. The first major study of the Sicker Group was by Muller (1980), who mapped this group of rocks throughout Vancouver Island. He proposed four major subdivisions for the Sicker Group, which, in ascending stratigraphic order, are the Nitinat Formation, the Myra Formation, an informal sedimentary-sill unit and the Buttle Lake Formation. Later work by Juras (1987), in the Buttle Lake uplift, lead to the separation of the Paleozoic rocks into an older volcanic-dominated sequence of Devonian age, renamed the Sicker Group sensu stricto, and a younger Mississipian to Permian sedimentary sequence renamed the Buttle Lake Group.

Juras (1987), further subdivided the Sicker Group into four formations, which, in ascending stratigraphic order are: Price, Myra, Thelwood and Flower Ridge Formations. Elsewhere on Vancouver Island, such as the Cowichan and Nanoose uplifts, separate formation names are used to subdivide the Sicker Group, due to lithological diversity. The correlative units to rocks in the Buttle Lake Uplift are shown in Figure 2.5, and include the Duck Lake, Nitinat, and McLaughlin Ridge Formations (Massey, 1992, Yorath et al., 1999).

Duck Lake Formation represents the oldest rocks on Vancouver Island and the lowermost unit of the Sicker Group. This formation is only present in the Cowichan Uplift and has not been recognised in the Buttle Lake Uplift (Massey, 1992). It consists of dominantly pillowed amygdaloidal basalts with minor cherts and cherty tuffs, and the flows are dark grey-green, aphyric to feldspar phyric, variably altered to chlorite-epidote assemblages (Massey & Friday, 1989).

Price Formation is a volcanic package characterised by pyroxene-feldspar-porphyritic basalts and basaltic andesite flows and flow breccias (Muller, 1980; Juras, 1987). The unit has a minimum thickness of 300m (the base of the unit is not exposed in the Buttle Lake Uplift), and is moderately to strongly chlorite-epidote altered. It is characterized by alternating, 30-150m thick, massive lava flows, which are variably amygdaloidal, feldspar-phyric and pyroxene-feldspar-phyric; agglomerates, breccias, and lapilli tuffs, deposited from pyroclastic flows, mass debris flows and lahars (Juras, 1987). These are intercalated with minor fine laminated tuffaceous silt and sandstone. Abundant coarse-grained, dark green to black pyroxenes, which are often pseudomorphed by actinolite, give the rock a distinctive spotted appearance. A relatively sharp change into widespread rhyolitic volcanics and sedimentary rocks marks the boundary with the overlying Myra Formation.

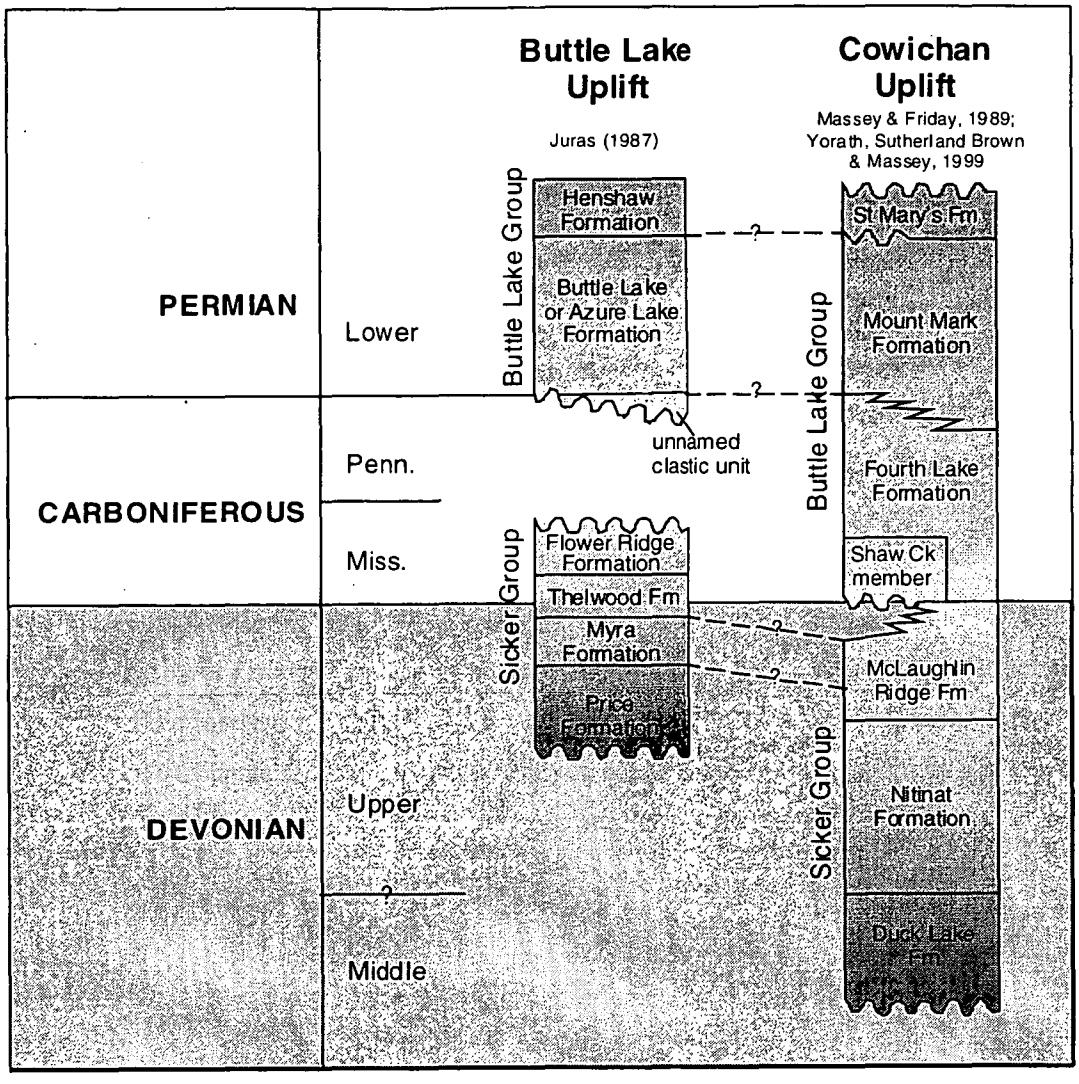

Figure 2.5: Comparative stratigraphy of the Paleozoic rocks of Vancouver Island (stratigraphic columns are not drawn to scale). Modified after Massey (1992).

Myra Formation is a thick succession (up to 500m thick in places), of rhyolitic, andesitic and basaltic volcanics and sedimentary rocks. The contact with the underlying Price Formation varies from a relatively sharp change up into monomict rhyolitic volcaniclastics, to a broad mixed zone, up to 3-5m thick, of andesite and rhyolitic volcaniclastics. The Myra Formation hosts the VHMS orebodies of the Myra Falls camp and is described in greater detail in Chapter 3. A late Devonian age (370 Ma) is indicated by U-Pb dating of zircons (Juras, 1987). Juras (1987) and Sinclair (2000) have further subdivided the formation into ten litho-stratigraphic units and these are described in the next chapter (Chapter 3, local geology). The top of the formation is marked by a generally conformable, gradational change, up into the finely bedded Thelwood Formation.

Thelwood Formation is a thick sequence (270-500m) of finely laminated mudstones, interbedded with fine to medium-grained volcaniclastics and penecontemporaneous mafic sills. The contact with the underlying Myra Formation is usually distinct, characterised by a sharp change up into the finely laminated mudstones. The unit is variably chlorite-epidote altered and the age of the formation is probably Early Permian, based on microfossil ages from equivalent rocks in the Cowichan Uplift (Brandon et al., 1986).

Flower Ridge Formation is composed of moderately to strongly amygdaloidal feldspar and pyroxene-phyric basaltic flows and volcaniclastics, tuffaceous siltstones, wacke, and argillite. The unit has a maximum thickness of 650m and is conformable with the underlying Thelwood Formation (Juras, 1987). The contact is characterised by the first appearance of abundant scoriaceous volcanic clasts. The age of the unit is estimated to be between late Devonian and Pennsylvanian, based on ages of the surrounding units.

A large unconformity separates the Sicker Group from the overlying Permian Buttle Lake Group (Massey, 1992).

2.3.2 Buttle Lake Group

The Buttle Lake Group is a dominantly epiclastic and bioclastic limestone sequence and consists of two formations, the Buttle Lake, or Azure Lake, and Henshaw Formations.

Buttle Lake Formation (or Azure Lake Formation) is a clastic limestone (up to 100-150m thick), consisting of interbedded medium-grained limestone and calcareous siltstone, with siliceous shell fragments, fossiliferous sandstone, coarse grained crinoidal limestone, fine grained limestone with chert nodules and some dolomitic limestone with abundant brachiopods and bryozoans (Muller, 1980; Massey, 1992). In the type area, near Azure Lake, west of Buttle Lake, the unit conformably overlies green and maroon mottled tuffaceous sediments and breccia at the base of the unit (Muller, 1980), this is the 'unnamed clastic unit' on Figure 2.5. Biostratigraphic ages range from Pennsylvanian to early Permian (Yole, 1969; Brandon, 1986).

Henshaw Formation comprises conglomerates, variably purple-coloured volcaniclastics and vitric tuff beds (Jeffery, 1967). A characteristic feature of this unit is the purple to red alteration of the volcaniclastics and the presence of crinoidal limestone clasts and boulders. The unit varies in thickness from 5-100m and the contact with the overlying pillowed lavas of the Karmutsen Formation, is unconformable in the Cowichan Uplift

(Massey, 1992; Yorath et al., 1999). The age of the formation is thought to be Permian (Jeffery, 1967; Juras, 1987).

2.3.3 Vancouver group

The Vancouver Group comprises volcanic rocks, limestone, flaggy argillite and quartzite and consists of four formations: Karmutsen, Quatsino, Parson Bay and Sutton Formations, all of Late Triassic (Carnian to Norian) age (Yorath et al., 1999).

Karmutsen Formation is the dominant formation of the Vancouver Group, and is a thick sequence (up to 4500m) of chemically and mineralogically homogenous tholeiitic basalt pillows, breccias, tuffs and comagmatic basalt dykes and sills (Figure 2.6). The formation is capped by a minor succession of subaerial basaltic flows with minor limestone interbeds (Yorath et al., 1999). Biostratigraphic ages ranging from Late Ladinian to Late Carnian at the top of the sequence, were derived from interlava sediments (Muller et al., 1974; Muller et al., 1981).

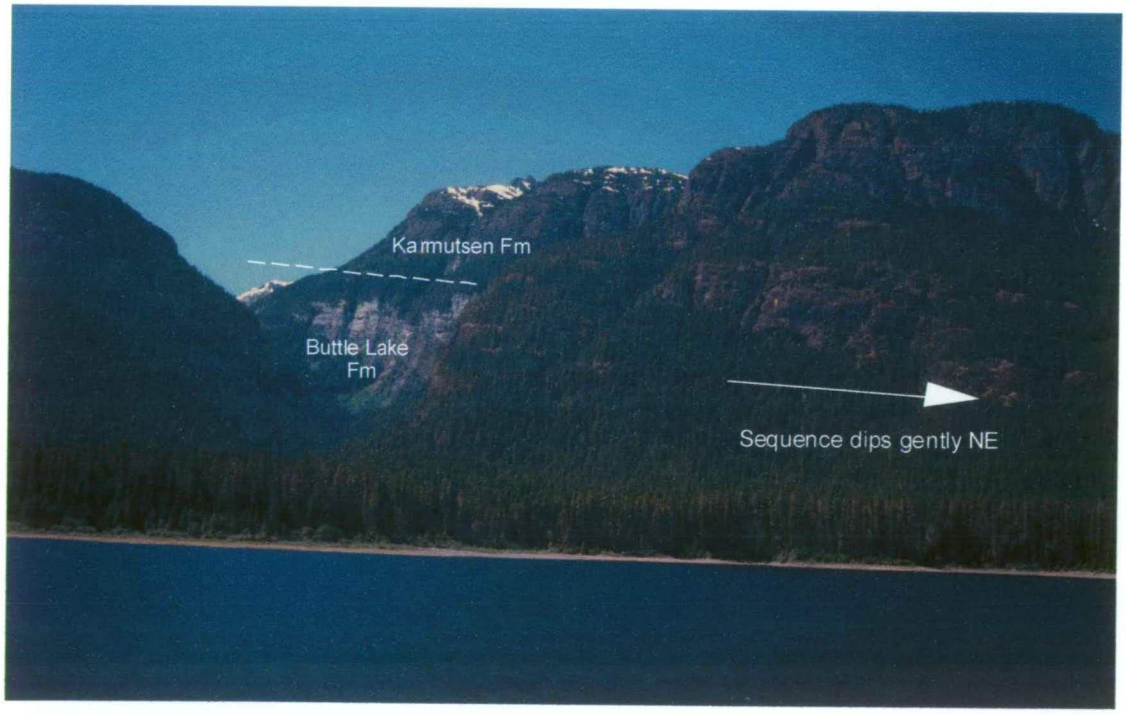

Figure 2.6: Buttle Lake Formation overlain by thick tholieitic flows of the Karmutsen Formation above Buttle Lake.

Quatsino Formation paraconformably overlies the basalt flows and pillows and consists of shallow water of carbonate platform limestone. It is thick-bedded and massive, and grades into the overlying sediments of the Parsons Bay Formation (Yorath et al., 1999).

The Formation has a late Carnian or Upper Triassic biostratigraphic age (Carlisle and Susuki, 1974).

Parsons Bay Formation marks a gradational change from carbonate to dominantly clastic deposition. The unit comprises carbonate rocks grading up into fine dark siliceous, carbonaceous, and calcareous shale, and calcareous arenite up to 300m thick (Gordey et al., 1991, Yorath et al., 1999).

Sutton Formation is the uppermost unit of the Vancouver Group on Vancouver Island, and is a thin, well bedded, richly fossiliferous and flaggy limestone unit with minor fine-grained clastic rocks. It has a gradational contact with the underlying Parsons Bay Formation (Yorath et al., 1999).

2.3.4 Bonanza Group

The Bonanza Group is a thick sequence of calc-alkaline volcanic rocks and minor interbedded sediments of Early Jurassic age (Gunning, 1932; Yorath et al., 1999). It is the youngest of the three volcanic cycles that make up the Wrangellia Terrane on Vancouver Island. The group comprises the Bonanza Volcanics and the Harbledown Formation and this sequence is intruded by abundant coeval hypabyssal rocks, of the Island Intrusive suite (Dawson et al., 1991).

Bonanza Volcanics consists of a thick sequence, up to 200m thick, of subaqueous to subaerial basaltic to rhyodacite flows, breccias and tuff with minor interbedded marine shales and siltstones. A characteristic feature of the Bonanza rocks is that the mafic and felsic volcanics are all plagioclase porphyritic.

Harbledown Formation is a 300m thick sequence of non-calcareous shale and tuff, which occurs in the northeastern part of Vancouver Island (Gordey et al., 1991; Nixon et al., 1994).

Island Intrusives are quartz diorite, granodiorite and quartz monzonite batholiths and plutons, which intrude the Sicker, Vancouver and Bonanza Groups throughout Vancouver Island.

2.3.5 Cretaceous Rocks

The Cretaceous and younger rocks on Vancouver Island were deposited after the collision of Wrangellia with the ancient margin of North America, and are therefore not

part of the Wrangellia Terrane (Gabrielse and Yorath, 1991). Three groups make up the Cretaceous rocks on Vancouver Island; the Kyuquot, Coal Harbour and Nanaimo Groups (Dawson et al., 1991). The Kyuquot Group represents an accretionary clastic succession while the Coal Harbour and Nanaimo Groups are post-accretionary deposits.

Kyuqot Group represents a minor accretionary sequence found on the central west coast of Vancouver Island. The sequence comprises a basal conglomerate, overlain by fine lithic sandstone, silt and minor limestone. It is of Lower Cretaceous age and unconformably overlies the lower Jurassic Bonanza Group (Muller et al., 1980; Dawson et al., 1991).

Coal Harbour Group of Mid Cretaceous age, is found on northern Vancouver Island. It comprises a coarse arenitic unit of greywacke, shale, silt, minor limestone conglomerate, limestone, and coal (Dawson et al., 1991).

Nanaimo Group of late Cretaceous to possibly early Tertiary age, underlies the coastal plain of southeast and south-central Vancouver Island, and the adjacent gulf islands. The group comprises a succession of terrigenous clastic rocks, including conglomerates, sandstone, mudstone, and shales deposited in a variety of settings, extending from neritic to at least upper bathyl depths (Yorath et al., 1999).

2.3.6 Tertiary

During the Tertiary, the Pacific and Crescent Terranes were accreted onto Vancouver Island on the southwest coast, along prominent west and northwest trending thrust faults, shown in Figures 2.1 and 2.3 (Hyndman et al., 1990; England and Calon, 1991; Yorath and Nasmith, 1995).

Pacific Terrane is a sequence of Lower Cretaceous melanges, overlying Uppermost Triassic fragmental calc-alkaline volcanics and diorite intrusions with minor limestone (Brandon, 1985; Yorath, 1991).

Crescent terrane comprises the Metchosin Igneous Complex and the Crescent Formation, and represents an ophiolite complex (Yorath, 1991). The Metchosin Igneous Complex was thrust beneath the Pacific Rim Terrane along the Leech River Fault.

Sedimentation continued throughout the Tertiary. In central and southern Vancouver Island, the Cretaceous Nanaimo Group is overlain by a Mid to Upper Eocene sequence of

nonmarine sandstone, mudstone and minor coal. These sediments are assigned to the Kitsilano and Burrard Formations of the Vancouver area (Yorath, 1991). On the southwestern coast of Vancouver Island, the middle Eocene to Oligocene Carmanah Group is in depositional and fault contact with the Jurassic Bonanza Group. The group comprises marine sediments including, calcareous sandstone, conglomerate, and shale (Yorath, 1991).

In mid to Late Paleogene and early Neogene, volcanism and plutonism re-occurred on Vancouver Island, with the Catface Intrusions. These comprise a suite of small hypabyssal bodies of broadly quartz diorite composition, which occur along many of the more important faults on the island (Yorath et al., 1999).

Quaternary sedimentation on Vancouver Island is largely a result of three major glaciations. The largest and most recent glacial event, the Fraser Glaciation, started about 29 000 yrs BP, with ice retreating about 13 000 years ago, followed by a period of glacial rebound (Clague, 1991). Earlier glacial and non-glacial events are either scoured away or buried by younger sediments.

2.4 Metamorphism

Metamorphism in the Wrangellian rocks of Vancouver Island is characterised by low grade regional metamorphism, up to greenschist facies. The Sicker Group includes chlorite and biotite zones, with minor zones of amphibolite facies, associated with plutons of the Island Suite (Juras, 1987; Greenwood et al., 1991). The overlying Karmutsen Formation has been metamorphosed to prehnite-pumpellyite to zeolite facies, while the Jurassic and Cretaceous strata are of zeolite facies mineralogy (Greenwood et al., 1991).

The increasing metamorphic grade of Sicker Group rocks in western and southern parts of Vancouver Island, may reflect a general increase in the depth of erosion and abundance of plutonic rocks towards the western side to the island. The timing and origin of this regional metamorphism is uncertain but there is evidence for both pre-early Triassic and post Late Triassic events. A minimum age for the metamorphism is provided by the unmetamorphosed Eocene to Oligocene clastic sediments of the Carmanah Group, exposed in the southwestern parts of the island (Greenwood et al., 1991).

The maximum temperatures reached during this regional metamorphism have been estimated by the conodont alteration index (CAI). In the Sicker Group, early Mississipian chert, and Permian limestone from the overlying Buttle Lake Group, have CAI values ranging from 5-7. This range indicates temperatures >300°C, which is consistent with chlorite-zone metamorphism (Brandon et al., 1986). In comparison, the overlying Upper Triassic Parson Bay Formation has CAI values from 3-7, and the average is significantly lower than those from the Sicker Group. The CAI data indicate that regional metamorphism of the Sicker Group took place pre-Late Triassic and post Permian (Brandon et al., 1986).

The intensity of deformation in the Sicker Group is highly variable. For example, Muller (1980) describes well preserved igneous clinopyroxes and a lack of penetrative fabrics in some locations, whereas in areas such as Myra Falls, the rocks are strongly cleaved and pyroxenes are strongly uralitized (Juras, 1987). The development of penetrative deformation appears to have occurred prior to the deposition of the Upper Triassic Karmutsen Formation, which lacks any deformation fabrics (Greenwood et al., 1991).

In summary, the lower to mid-greenschist metamorphic grade of the Sicker Group rocks reflects deep burial, and in areas such as Myra Falls, local hydrothermal alteration around VHMS deposits. The CAI values and lack of deformation fabrics in the overlying Karmutsen Formation suggests that metamorphism occurred in the early Triassic, predating the approximate 100 Ma collision of Wrangellia with the western coast of Canada (Brandon et al., 1986; Greenwood et al., 1991).

2.5 Structure

The structural style of Vancouver Island is complex, reflecting the Mesozoic and Cenozoic accretionary history. The island has a strong NW oriented structural fabric formed by large flexural folds, normal and reverse faults, strike-slip faults and broad belts of plutonic and metamorphic rocks.

Regional mapping indicates that an early phase of folding was followed by several distinct episodes of brittle deformation (Table 2.1). These separate deformation events reflect the complex tectonic history of the island. Massey (1992) suggests at least five major deformational events occurred, many of which have reactivated older structures.

	Late Devonian to earliest Mississipian	Middle Permian to pre-Middle Triassic (pre-Karmutsen Formation)	Late Triassic (syn-Karmutsen Formation)	Early to Middle Jurassic (Post Bonanza Group)	**Tertiary** Late Cretaceous to Eocene	post Eocene (?) NW-trending faults
Muller, 1980		NW trending assymetrical folds with axial planar cleavage variably developed; horizontal lineations; refolding of axial planar cleavage and lineations is rare; may postdate Buttle Lake Group (?)		A set of N to NE trending faults may predate the Eocene NW trending faults (these could also be 2nd order splays)	Major NW trending faults postdate deposition of the Nanaimo Group sediments, eg. Cowichan Lake Fault	
Gabrielse, 1991	Development of three major NW-trending anticlinoriums, cored by Paleozoic Sicker Group; Within these structures the Paleozoic rocks are commonly tightly folded				Large westward verging, NW-trending thrust faults of probable late Cretaceous to late Eocene age in southern Vancouver Island	
Massey, 1992 southern Vancouver Island (Cowichan Uplift)	Late Devonian to earliest Mississipian large scale open folds; Timing of deformation is indicated by an angular unconformitity between the Fourth Lake Group and the underlying Sicker Group in Cowichan Uplift	Middle Permian to pre-Middle Triassic W to NW trending, SW verging asymmetrical folds with abundant parasitic minor folds; axial planar cleavage with moderate to steep NE dips; lineations with horizonatal to shallow W to NW or E to SE plunges A crenulation cleavage (S2) is oblique to S1 and appears to be axial to broad open warps (possibly related to the regional-scale warping of Vancouver Island during late Jurassic?)	Extensive crustal dilation during the Late Triassic evolution of the Karmutsen volcanic sequence	Pre-Nanaimo Group deformation with regional-scale warping of Vancouver Island producing the three major anticlinal uplifts cored by Sicker Group rocks. Faulting, often axial, accompanied this deformation event	Large-scale W to NW trending thrust faults. Most are high angle reverse faults, with dips between 45-90°; in places, paralleling the earlier axial foliation in Paleozoic rocks. Faults become listric at depth	N-NE trending vertical cross faults, eg, Copper Canyon Fault,, offset NW-trending thrust faults with apparent sinistral sense; possible Miocene age
Nixon et al., 1994 northern Vancouver Island				Post Early Jurassic to pre-Cretaceous compressional event resulted in regional tilting and formation of the Victoria Arch, accompanied by flexural slip folding and faulting	Post Mid to Pre-late Cretaceous northerly directed compression produced NW trending strike-slip and lesser thrust faults with oblique-dextral movement on NW oriented faults and sinistral movement on NE oriented faults	NE to ENE trending normal faults formed during extension of Queen Charlotte Basin postdates deposition of Upper Cretaceous Nanaimo Group sediments; Reactivation of pre-existing strike-slip faults is observed Tertiary dikes intruded during this deformation event
Yorath et al., 1999 south-central Vancouver Island	Paleozoic Sicker Group rocks have two fold phases present (in comparison to the overlying Karmutsen Formation, which has only one). A moderate to strong foliation is developed axial planar to subsidiary folds within core zones of the major anticlinal structures (eg. Cowichan and Buttle Lake Uplifts). The fold axes of these subsidiary folds are parallel and oblique to the trend of the major anticlinal structures			One fold phase, comprising broad open folds is present in the Karmutsen Formation with dips on folded limbs ranging from 15-35°; The overlying Bonanza Group is also folded	Major NW trending faults developed during Eocene emplacement of the Pacific Rim and/or Crescent terranes beneath Wrangellia	N trending faults offset the NW trending faults suggesting post-Eocene movement; displacement sense is unclear
Tectonic Events	Early deformation of Wrangellia prior to collision with the N.A. plate margin			Regional scale warping and formation of major anticlinal structures during collision of Wrangellia and N.A. Intrusion of Island Intrusive Suite	Accretion of Pacific Rim and crescent terranes during NW movement of Pacific plate relative to N.A. plate	Opening of Queen Charlotte basin and continued NW motion of Pacific Plate

Table 2.1: Correlation table of regional deformation events from Northern, Central and Southern Vancouver Island.

2.5.1 Early ductile deformation of Wrangellia

Large NW trending, SW verging asymmetrical folds are common in the Paleozoic Sicker Group rocks, with abundant minor parasitic folds. A moderate to steeply north-dipping axial planar foliation is variably developed, with intense flattening in volcanic rocks, normal to the foliation (Muller 1980; Massey, 1992). Lineations generally plunge horizontal to gently W to NW, or E to SE. Refolding of lineations, and crenulations of the axial planar cleavage, are not common, but are observed in some Sicker Group rocks, indicating a second phase of folding (Muller, 1980; Massey, 1992; Yorath et al., 1999).

The timing and origin of folding in Paleozoic and younger rocks on Vancouver Island is contentious. Massey (1992) suggests that an initial phase of folding, comprising large-scale open folds in the Sicker Group, developed during late Devonian to earliest Mississipian deformation. This age is based on an angular unconformity at the base of the Fourth Lake Formation (Buttle Lake Group), on the SW limb of the Cowichan Uplift. The unconformity suggests subsequent uplift and erosion followed this early deformational event, prior to deposition of the Fourth Lake Formation.

The tighter folding associated with the development of a penetrative fabric is thought by some authors to be pre-Permian, owing to the lack of a fabric in the Permian Buttle Lake limestone. However, Muller (1980) suggests that there are some areas, such as Museum Creek and south of Horne Lake, where the limestone is closely folded together with the underlying strata. Massey (1992) suggests that the variation in fabric development may reflect rheological contrasts, with the Permian limestone acting more competently during deformation than the underlying Sicker Group volcanic rocks. Yorath et al. (1999), suggest a pre-Early Triassic age for the early folding and fabric development based on the fact that two phases of compressed folds are observed in the Sicker Group rocks, while only one fold phase, comprising broad open folds, is present in the overlying Triassic Karmutsen Formation.

2.5.2 Mid to Late Triassic crustal dilation

Massey (1992) suggests that extensive crustal dilation accompanied the intrusion and extrusion of the Karmutsen Formation lavas and gabbroic intrusives. Structures specifically associated with this magmatic event have yet to be documented.

2.5.3 Early to Mid Jurassic regional-scale warping of Vancouver Island

Regional-scale warping of Vancouver Island, during Early to Mid-Jurassic (pre-Nanaimo Group) N to NE directed compression, produced three major NW trending anticlinal

uplifts, including the Cowichan and Buttle Lake Uplifts. The Bonanza Group rocks, the Karmutsen Formation, and older rocks are gently folded into broad anticlinal uplifts with shallow dips of 15-35° on folded limbs in the Cowichan Uplift (Yorath et al., 1999). Faulting, often axial to the broad folds, accompanied the folding (Massey, 1992; Nixon, 1994). Regional scale warping, as a result of E to NE directed compression, is also observed in northern Vancouver Island. In this area, pre-Cretaceous Bonanza Group sediments and older, are folded to form the Victoria Arch (Nixon, 1994, 1995). A maximum age for this deformation is indicated by the angular unconformity between the Triassic to Jurassic and older sediments, and the overlying Cretaceous sediments of the Nanaimo Group.

This regional-scale warping most likely relates to the collision of Wrangellia with North America, during mid to late Jurassic. This is similar to the late Jurassic collision age suggested by stratigraphic evidence (Gabrielse and Yorath, 1991).

The development of a second foliation and crenulations in Sicker Group rocks, in the core zones of these uplifts, may in part, be the result of rheological contrasts during this second folding event. The overlying Karmutsen Formation is much more competent than the underlying Paleozoic volcanic rocks, and more intense localised deformation could develop in the less competent rocks of the core zones (England and Calon, 1991; Yorath et al., 1999).

2.5.4 Post Mid to pre-Late Cretaceous NW trending faults

A series of NW trending strike-slip faults and lesser thrust faults has been mapped in northern Vancouver Island (Nixon et al., 1994,1995). These faults postdate deposition of the Mid Cretaceous Coal Harbour Group and may predate the Upper Cretaceous Nanaimo Group. These faults form the dominant NW trending structures in the area and are thought to be the result of north directed compression. These faults appear to have oblique dextral motion. NE trending antithetic faults are also common and exhibit sinistral, NW side up displacement. Minor NW trending thrust faults, with a south up sense of motion have also been observed. Substantial strain has also been accommodated by flexural slip folding and bedding parallel shear (Nixon et al., 1994,1995).

2.5.5 Late Cretaceous to Eocene NW trending faults

Large NW striking, W verging thrusts and strike-slip faults, such as the Beaufort Range and Cowichan Lake fault zones, dominate the structural fabric of Southern Vancouver Island. These faults postdate the Nanaimo Group, with substantial offsets of these

sediments. The faults have dips of 45-90°, and in places, parallel the early axial foliation in the Paleozoic rocks (Massey, 1992). Wide schistose zones develop around these faults in receptive lithologies and some faults have up to 1-2 km offset. Regional mapping by Massey (1992) suggests that fault movements are directed to the W to SW, resulting in sinistral movement on steep E-W trending strike-slip faults and oblique movement on the NW-striking thrust faults. Multichannel seismic reflection profiles in southern and central Vancouver Island, indicate that these faults dominate the subsurface structure of the island and that they are listric at depth, see Figure 2.3 (Hyndman et al., 1990; England and Calon, 1991). The large W verging faults which subdivide the base of Vancouver Island are probably of late Eocene age, while older, high level thrust faults, which occur near the east coast, are of probable Cretaceous age (England and Calon, 1991; Massey, 1992). These large NW trending thrust faults and strike-slip faults most likely developed during NE-SW directed crustal shortening caused by the collision and accretion of Wrangellia and subsequent Pacific Rim and Cresent terranes, onto North America.

A set of N to NE oriented faults appear to predate the large NW trending faults, and these may represent an earlier brittle episode of deformation or could be second order splays (Muller, 1980).

2.5.6 Post Eocene faults

In many places the large NW trending faults are offset by N to NE trending vertical faults, such as the Copper Canyon and Yellows Creek faults in southern Vancouver Island (Massey, 1992; Yorath et al., 1999). Regional mapping suggests an apparent sinistral sense of displacement. The age of these faults is not known, however, similar NE striking faults in the southern coast belt, are early Miocene in age, although these faults have dextral offsets (Journeay and Csontos, 1989).

In northern Vancouver Island, Nixon (1994,1995) reports the most recent phase of deformation is represented by minor NE to ENE striking normal faults, with minor reactivation of pre-existing strike-slip faults. These faults are the result of NW to NNW directed extension, during the opening of the Queen Charlotte Basin (Riddihough and Hyndman, 1991), and postdate the deposition of the Upper Cretaceous Nanaimo Group sediments.

Tertiary to recent thrust and strike-slip faulting has continued throughout the island as a result of continued NW motion of the Pacific plate relative to the North American plate (Gabrielse, 1991). The emplacement and underplating of the Pacific Rim and Crescent

terranes, together with the effects of the modern subduction complex, has resulted in the uplift of western and southern Vancouver Island, and erosion of several kilometres of Wrangellian stratigraphy.

2.6 Metallogeny of Vancouver Island

Vancouver Island has a long history of diverse voluminous volcanism, related plutonism, intercalated reactive carbonates and repeated tectonic episodes, which has resulted in the formation of numerous mineral deposits and showings throughout the island (Dawson et al., 1991). They are predominantly small, sub-economic deposits and are grouped into pre-accretionary and post-accretionary deposit types.

2.6.1 Pre-accretionary deposits

Pre-accretionary deposits are characterised by syngenetic styles of ore formation, and this metallogenic episode is dominated by volcanic-hosted massive sulphide deposits, hosted by felsic volcanics of the Paleozoic Sicker Group. Known deposits include the Myra Falls district in the Buttle Lake Uplift; and the Mount Sicker (Twin J) mine, and the Lara Deposit in the Cowichan Uplift. The Duck Lake Formation contains iron formations dominated by iron oxide facies and minor sulphides, which may have an exhalative origin. Other jasper and oxide-rich cherts are found in the Nitinat and McLaughlin Ridge Formations, but appear to be of little economic value.

Skarn deposits rich in iron, some with significant copper and precious metals are also common. Most are near or partly in Jurassic plutons (Island Intrusives) at the top of the Karmutsen Formation, replacing it and/or limestones of the Quatsino or Kunga Formations. Known deposits include, Coast Copper, Kennedy Lake, Merry Wide, Nimpkish, Argonaut, and Zeballos (Dawson et al., 1991). Other copper skarns replace limestone of the Buttle Lake Formation (Thistle Lake deposit).

Porphyry copper deposits are also associated with Jurassic plutons of the Island Intrusive Suite. The single economic porphyry deposit is the Island Copper mine, in northern Vancouver Island, near Port Hardy, which was mined until 1996 by BHP Minerals Canada. Mineralistation and alteration are related to the intrusion of quartz-feldspar porphyry dykes into Bonanza Group volcanics (Mathias et al., 1995). Alteration consists of a high sulphidation assemblage consisting of pyrophyllite, dumortierite and diaspore and crosscuts the copper moly-gold rich ore shell (Mathias et al., 1991).

Other pre-accretionary deposits on Vancouver Island include three near Port Alberi, which are skarn and massive sulphides (Thistle mine), auriferous hematite and the Villatla prospect, and auriferous altered stockworks at the Debbie Prospect. There are also some small stratbound Cu(Ag,V) deposits near Menzies Bay and Quadra Island.

2.6.2 Post-accretionary deposits

Post-accretionary deposits are not as common as the pre-accretionary types and consist mainly of epigenetic veins, stockworks or porphyries. Most are small vein deposits in young fault zones that cut Wrangellian rocks and may have formed by the redistribution of pre-existing metal deposits. Some minor porphyry copper deposits also occur in plutons of the Eocene Catface Suite (Dawson et al., 1991).

Post-accretionary deposits include the Domineer-Lakeview zone at Mount Washington, and the Privateer at Zeballos. Domineer is a flat quartz vein-shear which crosscuts the Nanaimo Group, Catface sills and the Karmutsen Formation and contains pyrite-arsenopyrite and minor sulphides, tellurides, realgar and orpiment. Privateer occurs adjacent to the Zeballos stock of the Catface Suite and occurs as steep quartz veins containing pyrite and arsenopyrite, with minor sphalerite, chalcopyrite, gold and siliver (Dawson et al., 1991).

2.7 Summary

- Vancouver Island forms part of the Wrangellia Terrane, and together with the Alexander Terrane, forms the Insular Belt of the Canadian Cordillera. The time of collision between the Insular Superterrane and the ancient margin of North America is thought to be early Cretaceous.

- The Wrangellia Terrane consists of Paleozoic to Cenozoic arc-related rocks, and the Paleozoic Sicker Group, which hosts the VHMS orebodies of Myra Falls, forms the basement rocks of Vancouver Island.

- Metamorphism of Wrangellian rocks of Vancouver Island is characterised by low grade regional metamorphism, up to greenschist facies, with chlorite and biotite zones predominant, and minor zones of amphibolite facies associated with plutons of the Island Intrusives. The overlying Karmutsen Formation is prehnite-pumpellyite to zeolite facies, while Jurassic and Cretaceous strata are of zeolite facies.

- The structural style of Vancouver Island is complex, reflecting the Mesozoic and Cenozoic accretionary history. The island has a strong NW oriented structural fabric formed by large flexural folds, normal and reverse faults, strike-slip faults and broad belts of plutonic and metamorphic rocks.

- Mineral deposits on Vancouver Island can be divided into pre-accretionary and post-accretionary deposits. The pre-accretionary deposits are dominated by syngenetic styles of ore formation and include the Myra Falls VHMS camp. Post-accretionary mineral deposits are predominantly epigenitic veins, stockworks or porphyries.

Chapter 3
Local Geology

3.1 Introduction

This chapter gives an overview of the local geology of the Myra Falls area, with the main emphasis on the mine sequence, which hosts the VHMS orebodies. Figure 3.1 is a map of the geology of Strathcona Provincial Park. The mine property lies within the Sicker Group in the core of the Buttle Lake Uplift at the southern end of Buttle Lake. Large plutons of the Island Intrusive Suite dominate the area south and west of the property, with the thick basaltic flows of the Karmutsen Formation covering the rest of the area. Major E-W and NW trending structures are also shown, many with apparent sinistral offsets.

3.2 Local stratigraphy

The stratigraphy of the Myra Falls area, based on work by Muller (1980) and Juras (1987) is illustrated in Figure 3.2. The Devonian Sicker Group, a volcano-sedimentary sequence, is overlain by the younger Mississipian to Permian sedimentary sequence, the Buttle Lake Group. Juras (1987), further subdivided the Sicker Group into four formations, which, in ascending stratigraphic order are. the Price, Myra, Thelwood and Flower Ridge formations. As these formations have been described in the previous chapter, only the Myra Formation will be described here.

3.3 Myra Formation – mine sequence

The Myra Formation hosts the VHMS orebodies at Myra Falls and outcrops on the sides of Myra Valley and on Price Hillside, where the original sulphide showings were pegged in 1917. The formation has been separated into 10 main lithofacies, based on detailed mapping on the Price Hillside by Juras (1987), and stratigraphic interpretations by company geologists. These units make up the mine sequence and the initial sequence by Juras (1987) is shown in Table 3.1.

In this study, the sequence is combined into six main units. These units form the main mappable horizons across the property and include various facies and intercalated units (see Table 3.1). The lithofacies have been combined into these mappable units to aid geological interpretations and geological modelling, especially for paleo-reconstructions. The six main units are, in stratigraphic order, the HW Horizon, hangingwall andesite, lower mixed volcaniclastics, Lynx-Myra-Price Horizon, Upper mixed volcaniclastics, and upper mafic unit.

The basal contact of the Myra Formation at Myra Falls is marked by a change from andesitic volcaniclastic rocks to rhyolitic volcaniclastic rocks (see Figure 3.3d). The Price Andesite forms the footwall to the VHMS orebodies at Myra Falls and is altered to a quartz-sericite-pyrite assemblage beneath the massive sulphides, elsewhere the andesite is chloritized and epidotized.

3.3.1 HW Horizon

The oldest unit of the Myra Formation is the HW Horizon, which is a dominantly rhyolitic volcano-sedimentary package, comprising coarse volcaniclastics (Figure 3.3a), sandstones, and mudstones, with massive quartz-feldspar porphyry bodies near the top of the horizon. The horizon can be divided into 5 main facies, which include, massive to semi-massive sulphide, chert, argillite-silt, fine to medium-grained rhyolitic volcaniclastic rocks, coarse-grained rhyolitic volcaniclastic rocks, ore clast breccias, and quartz-feldspar porphyry.

Facies of the HW Horizon are described in greater detail than other units, as one of the aims of this study was to map facies variation within this horizon.

Massive to semi-massive sulphides occur in thick lenses, up to 35m thick, of massive and banded ore, forming the HW, Extension, Battle, and Ridge Zone orebodies, and the smaller more discontinuous Marshall and Trumpeter Zones. The ore is predominantly hosted by coarse-grained rhyolitic or mixed andesitic-rhyolitic volcaniclastics, close to the contact with the underlying Price Andesite. Chalcopyrite, sphalerite, pyrite and galena are the dominant sulphide species with lesser bornite and tetrahedrite, and accessory chalcocite, colusite, and gold (Figure 3.3b-d). Upper zone sulphides also occur in the mid-upper part of the HW horizon, above both the HW and Battle deposits. These upper zones differ from the main sulphide bodies at the base of the horizon, as they are predominantly Zn-Pb-barite-rich and pyrite-poor.

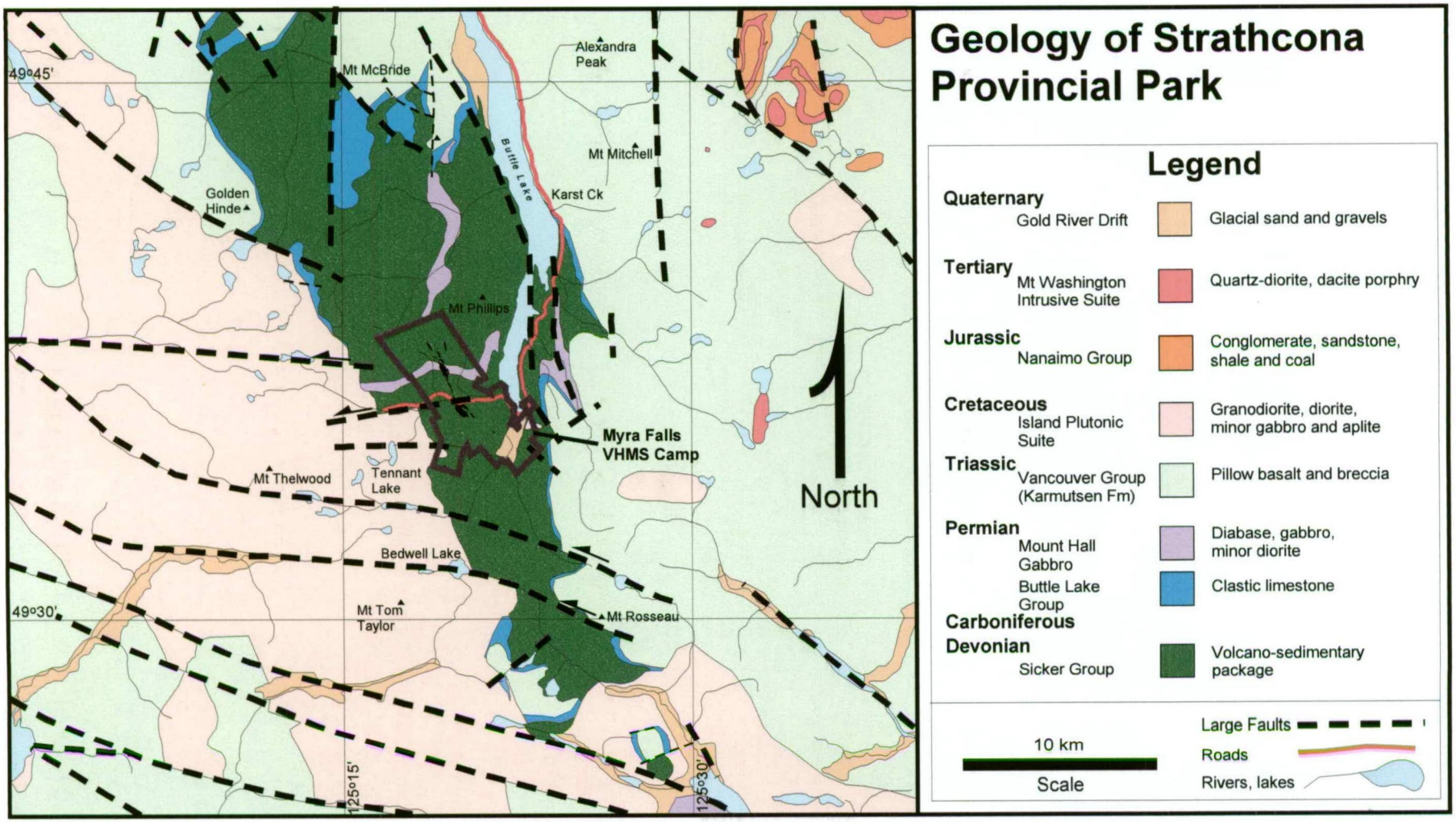

Figure 3.1: Regional geological map of the Myra Falls area, modified from Geological Survey of Canada information circular, 1995-7.

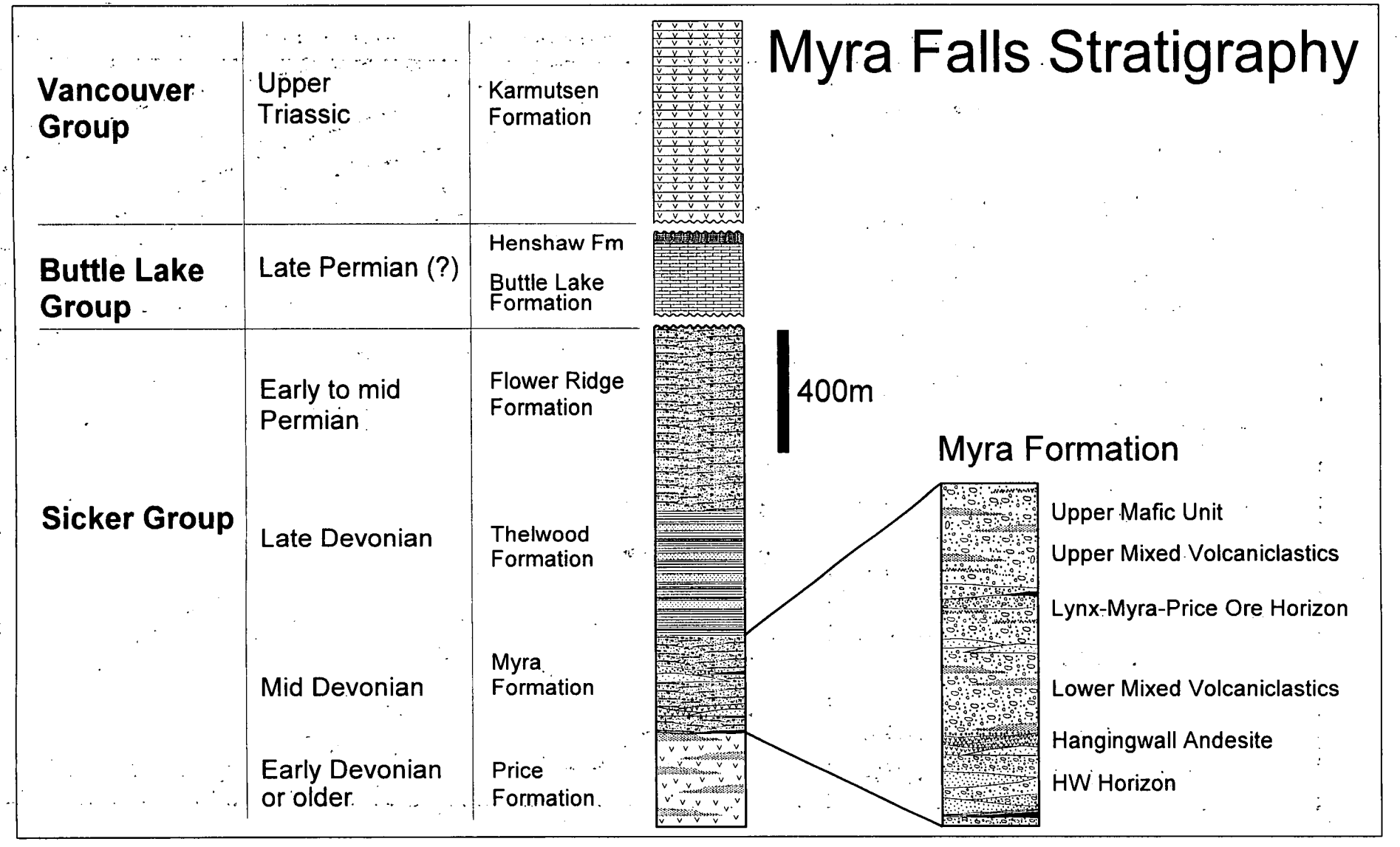

Figure 3.2: Myra Falls area stratigraphy, modified after Juras (1987) and Sinclair (2000).

Chert is common immediately above the Battle deposit where it appears to form a thick 'cap' above the ore. It is also present above ore in the Ridge and Extension zones, with minor localised occurrences above the HW orebody. The siliceous rocks are very fine grained, moderately to strongly laminated and occur in lenses up to 5m thick. This study examines these siliceous rocks in detail, with full descriptions given in Chapter 6, to determine their origin, whether or not they represent biogenic cherts, exhalites, or replacement cherts.

Argillite is found throughout the property, and thin argillite horizons are commonly intercalated with many units of the mine sequence. However, very thick sequences occur in the southern and eastern parts of the property, in the Thelwood Valley and south-flank areas. A thick argillite sequence also occurs above the HW deposit and to the south and west of the Battle deposit. The argillite is usually black to dark grey, massive to finely laminated and is often interbedded with fine rhyolitic sandstone and silt. Argillite also occurs as fine rip-ups in overlying sandstone units. The sandstone and silt commonly grade up into argillite and the argillite most likely represents the upper part of turbidite and/or background pelagic sedimentation. A detailed description of this unit is given in Chapter 6.

Fine to medium rhyolitic volcaniclastics occur throughout the HW Horizon and are often interbedded with the chert and argillite. Graded bedding is common with weak to moderately graded beds 0.5-5m thick and these units most likely represent turbidite deposits. The volcaniclastic rocks also occur in massive beds, commonly interbedded with much coarser units, and probably represent the finer portion of mass flow deposits.

Coarse-grained rhyolitic volcaniclastics are common throughout the HW Horizon, especially close to the basal contact with the underlying Price Andesite, often hosting ore, and in the upper half of the HW Horizon. The coarse-grained volcaniclastic rocks are typically very poorly sorted and matrix supported, with subangular to subrounded clasts, and most likely represent mass debris flows.

Ore clast breccia is common above the HW deposit, and form minor horizons above the Battle deposit and Ridge zones. The ore clast breccia comprises coarse-grained rhyolitic volcaniclastics with ore clasts scattered throughout. The ore-clasts usually make up a very minor proportion of the unit, and are generally less than 5cm, although can be up to 30cm immediately above the ore.

Stratigraphy (Juras, 1987)	Major lithofacies (modified this study)	Intercalated units
Upper mafic unit	**Upper mafic unit** Mafic volcaniclastics minor argillite and bedded jasper	
Upper Rhyolite Upper mixed volcaniclastics G-flow	**Upper mixed volcaniclastics** dominant facies: mafic and lesser felsic volcaniclastics minor argillite	G-flow- ultramafic lava flow
Lynx-Myra-Price Horizon	**Lynx-Myra-Price Horizon** dominant facies: rhyolitic sandstone to silt Sulphide breccia argillite-chert massive sulphides	
Upper Dacite Lower mixed volcaniclastics Oreclast breccia unit	**Lower mixed volcaniclastics** dominant facies: mafic volcaniclastics minor felsic volcaniclastics minor argillite	Upper Dacite- massive dacite porphyry Oreclast breccia unit- minor to moderately abundant sulphide clasts in mixed volcaniclastics
Hangingwall andesite	**Hangingwall andesite** Mafic lava and volcaniclastics	
HW Horizon	**HW Horizon** dominant facies: quartz-feldspar porphyry rhyolitic sandstone to silt Sulphide breccia argillite-chert massive sulphides	minor mafic sills often with peperitic margins minor mixed volcaniclastics

Table 3.1: A comparison of the mine sequence at Myra Falls from Juras (1987) with lithofacies used in this study.

Quartz-feldspar and feldspar porphyry is found predominantly near the top contact of the HW horizon and forms large flow-dome-like bodies and sills in the northern part of the property. There appears to be a distinct variation in the nature of porphyry bodies across the property. Quartz and quartz-feldspar phyric porphyry bodies are common in the western and northwestern areas, above the Battle orebody and Ridge zones, while feldspar-phyric porphyry bodies dominate the area north of the HW orebody and to the east, in the Price hillside and Thelwood Valley areas. Geochemical variations between these porphyry bodies are shown in Chapter 6.

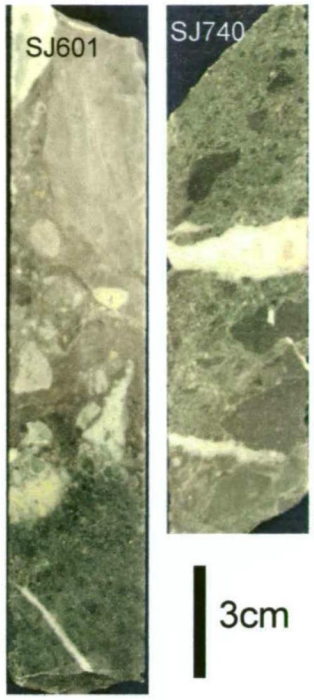

Figure 3.3: Typical examples of mine sequence rocks; **a)** Coarse-grained Price Andesite with a sharp contact up into rhyolitic volcaniclastic rocks of the HW Horizon (SJ601, 16-33, 26m, South Flank, and SJ740, 21-2072, 105.6m, HW mine); **b)** Chalcopyrite crystals on fracture plane in banded chalcopyrite-sphalerite-galena ore, Battle mine, Gap Zone, Battle mine; **c)** sphalerite-chalcopyrite-bornite-galena ore, Battle mine; **d)** Banded chalcopyrite, sphalerite and pyrite, C-sub, HW mine.

3.3.2 Hangingwall Andesite

Hangingwall Andesite comprises a thick basaltic andesite unit, which is typically massive, but also has thick zones of in-situ quench breccia and peperitic margins. The thickness varies from several metres to greater than 100m in places. The andesite is medium to dark grey-green, medium grained (1-3mm) and massive with a very uniform equigranular appearance in flow units.

3.3.3 Lower mixed volcaniclastic rocks

The lower mixed volcaniclastic package is a thick horizon, up to 200m in places, which is found across the property. The horizon consists of medium to coarse-grained andesitic, dacitic and rhyolitic volcaniclastic rocks, in poorly sorted, matrix supported units (Figure 3.4a). Andesitic clasts dominate with varying dacite, rhyolite and minor jasper clasts in a dominantly andesitic matrix. Minor argillite horizons occur throughout, and the argillite commonly occurs as rip-up clasts in adjacent coarser-grained units. The andesite clasts are medium to dark grey-green, subangular to angular, 0.5-3cm, and randomly oriented in a darker grey-green andesitic matrix. The rhyolite and dacite clasts are paler grey and grey-green and commonly subrounded to subrounded. Thin horizons of massive to finely laminated argillite, also occurs throughout the mixed volcaniclastic unit.

Ore clast breccia occurs in discontinuous zones in the lower half of the lower mixed volcaniclastic unit across the property. The ore clast breccia comprises coarse-grained andesite-rhyolitic volcaniclastics with ore clasts scattered throughout. The ore-clasts usually make up a very minor proportion of the unit, and are generally less than 5cm.

Upper dacite occurs close to the top of the lower mixed volcaniclastic unit above the HW orebody and in the Price area, and comprises massive dacite lava, forming large flow-dome complexes and sills. The dacite is commonly massive aphyric to strongly porphyritic, with euhedral feldspar phenocrysts dominating. The dacite is variably chlorite and epidote altered.

3.3.4 Lynx-Myra-Price Horizon

A discontinuous rhyolitic package occurs near the top of the Lower Mixed Volcaniclastic unit, and hosts the upper mineralized Lynx-Myra-Price Horizon. The thickness of the rhyolitic unit is highly variable, ranging from 1 to 45m thick. The unit consists of massive and bedded, fine to coarse-grained quartz-feldspar phyric rhyolitic

Figure 3.4: Examples of mine sequence lithologies at Myra Falls: **a)** Coarse-grained mixed andesitic and rhyolitic volcaniclastic rock overlying the HW Horizon in drive C353DD, HW mine (Lower Mixed Volcaniclastic Unit); **b)** Coarse-grained volcaniclastic rock on Price Hillside (Upper Mafic Unit, Jim Mitchell Road, Price Hillside); **c)** Epidote-chlorite altered coarse-grained volcaniclastic rock (SJ635, Upper Mafic Unit, Price Hillside); **d)** Epidote-chlorite altered laminated mudstone and fine sandstone of the Thelwood Formation, (SJ828) Westmin Road cutting above Buttle Lake.

UNIVERSITY OF TAS LIBRARY

volcaniclastics, laminated chert and massive and semi-massive sulphides in the Lynx, Myra and Price orebodies. The dominant sulphide species are chalcopyrite, pyrite, sphalerite and galena, and the orebodies of this horizon are characterised by abundant barite.

3.3.5 Upper Mixed Volcaniclastic unit

The Upper Mixed Volcaniclastic unit consists of andesitic, dacitic and rhyolitic volcaniclastic rocks (in decreasing order of abundance) and minor ore-clasts. The unit is medium to coarse grained with abundant pale to medium grey and green, subrounded to angular clasts, randomly oriented in a dark grey-green strongly sericite altered matrix. Clast sizes range from 2 to 30mm and the unit is very poorly sorted and predominantly matrix supported.

3.3.6 Upper Mafic Unit

The Upper Mafic Unit, or "P & G Unit" (purple and green unit) is the uppermost lithofacies unit of the Myra Formation. It is present throughout the property, and is thickest (>200m), in the southwest region, thinning to 5m in the northeast. The main rock types are basaltic volcaniclastic rocks with minor basaltic flow units (Figures 3.4b and 3.4c). Clasts are typically randomly oriented to jigsaw-fit within a finer matrix, and clast sizes range from 1 to 50cm. The main clast types are strongly pyroxene and feldspar-phyric basalt. Haematite and epidote alteration is common throughout this unit, giving it a distinct appearance.

The upper contact of the Upper Mafic Unit (and the Myra Formation), is marked by a relatively sharp change into the overlying finely laminated mudstones of the Thelwood Formation or "Sharp Banded Tuff" (SBT), see Figure 3.4d.

3.4 Tectonic and depositional setting of Sicker Group rocks

The Paleozoic Sicker Group rocks is thought to have formed in an intra-continental back arc setting, based largely on major, trace and rare earth element data, which indicate a transitional to mildly calc-alkaline arc affinity for the volcanic rocks (Juras, 1987; Barrett & Sherlock, 1996). The felsic volcanics at Myra Falls have similar geochemical characteristics to felsic rocks associated with the Kuroko Zn-Pb-Cu deposits (Juras, 1987; Barrett and Sherlock, 1996). Mafic volcanics also have marked similarities to intra-island arc rocks from several localities, such as the Okinawa Trough, a marine intracontinental back-arc basin south of Kyushu, Japan (Ishizuka et al., 1990), and the offshore Taupo Volcanic Zone, north of New Zealand. This is a transitional zone

between the Kermadec Ridge-Havre Trough system and the intracontinental Taupo Volcanic zone (Gamble et al., 1995).

The complex stratigraphy of the Myra Falls rocks reflects the varying roles of tectonism, volcanism and sedimentation during development of a continental island arc system that evolved from early to mature arc, and finally an incipient rift setting. The initial rift system may or may not have developed into a spreading centre. Juras (1987) gave a very detailed account of the changing tectonism and volcanism throughout the area and the section below is largely a summary of his work, with slight modifications resulting from this study.

In the Myra Falls area, early mafic and intermediate volcanism (Price Andesite), was followed by a period of syn-depositional rifting and widespread deposition of felsic volcaniclastic rocks (HW Horizon). The rifting was accompanied by regional sub-seafloor hydrothermal circulation and locally intense geothermal systems developed where fluid flow was focussed along growth structures. This resulted in the formation of VHMS orebodies, including the Battle and HW deposits, at outflow zones on or close to the seafloor. A period of volcanic and tectonic quiescence, indicated by widespread deposition of argillite, chert and fine tuffaceous silts, occurred during or just after (?) ore formation. A period of rhyolitic volcanism followed, with the deposition of thick rhyolitic mass flow deposits and the intrusion of large quartz-feldspar porphyry bodies near the top of the HW Horizon. Marked facies variations in the HW Horizon across the mine property reflect the development of significant seafloor topography and proximity to source regions such as seamounts or felsic centres. Topographic variations are probably the result of rift basin formation and the development of volcanic cones.

This episode of felsic volcanism was followed by repeated rifting, tectonism, and mafic-to intermediate-dominated volcanism, with only minor felsic volcanism, resulting in a thick accumulation of complexly intercalated volcaniclastic and epiclastic mass flow deposits. The extensive nature of these deposits and their complexity, reflects simultaneous activity of rift-related and arc-related volcanism, from a number of active volcanic centres. The likely position of mafic volcanic centres is indicated in Figure 3.5 (from McKinley et al., 1997).

A thin discontinuous rhyolitic volcaniclastic package in the upper part of the Myra Formation hosts the Lynx-Myra-Price orebodies, indicating that renewed hydrothermal activity occurred during a limited period of rhyolitic volcanism. Fine-grained sediments, including argillite and chert, are also associated with the Lynx and Myra orebodies and

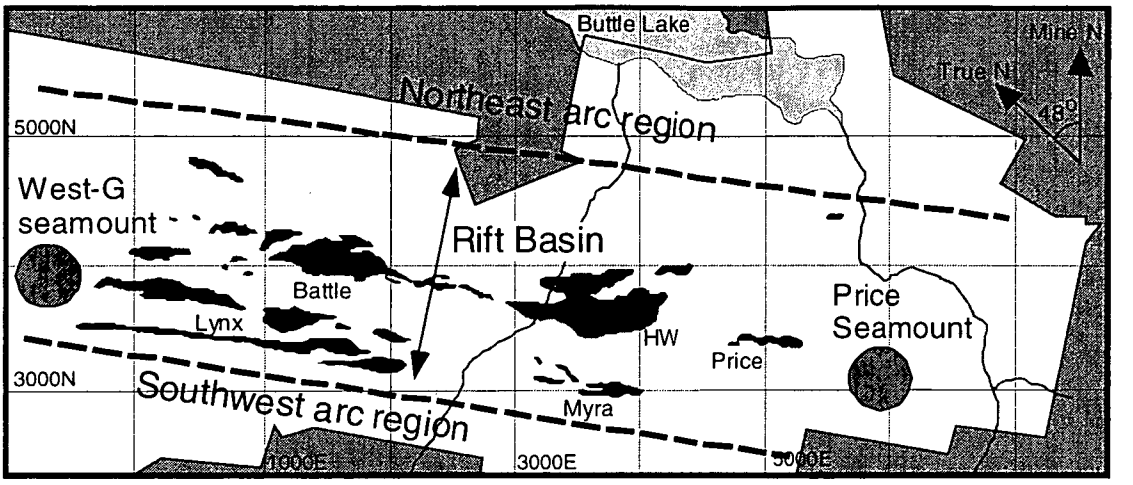

Figure 3.5: General tectonic and volcanic setting of the Myra Falls VHMS deposits (modified after McKinley et al. 1997).

indicate that hydrothermal activity was coeval with, or postdated (?) a period of tectonic/volcanic quiescence.

The onset of further mafic to intermediate volcanism is indicated by the overlying Mixed Volcaniclastic unit and the thick Upper Mafic Unit. A marked change in volcanic activity and sedimentation is indicated by the sharp change from the coarse-grained mafic volcaniclastics of the Upper Mafic Unit up into the fine-grained laminated mudstone and bedded sandstone of the Thelwood Formation. The much broader lateral extent of the Thelwood Formation and the fine-grained nature of the sediments, suggests more subdued topography and reduced volcanic activity in the area. Arc-related material decreases markedly up section in the Thelwood Formation, and the upper part of the unit is dominated by argillite and chert, reflecting increasing pelagic sedimentation.

3.5 Local structure

The structure of Myra Falls VHMS camp is complex, with several distinct episodes of ductile and brittle deformation affecting the area. For this reason, many structural reports have been written, including; Gunning (1931), Jeffery (1967), Walker (1980, 1983, 1985), Westmin Resources Ltd (company reports), Juras (1987), Berry (1995, 1996, 1998, and 2000) and Sinclair (2000).

The area is dominated by a N to NW trending structural fabric, formed by the Sicker Group rocks, in the large Buttle Lake anticlinal uplift. A major anticline extends through the mine property, and the hinge zone coincides with the Lynx-Myra-Price orebodies. The position of the hinge zone, most likely reflects the pre-existing anisotropy caused by

the strong alteration around the orebodies. Abundant parasitic folds are present throughout the property, and are generally open, upright folds with a weak to strongly penetrative axial planar cleavage. The cleavage has moderate to steep N-NE dips. Fold axes and lineations are generally horizontal or plunge gently E-W.

Abundant W to NW trending brittle faults disrupt the sequence, some with apparent sinistral offsets (Figure 3.1). Moderate to steeply dipping normal, reverse and strike-slip faults, flat faults, and bedding-parallel shearing, have been described in various reports (Walker, 1980, 1984, 1985; Juras, 1987; Berry, 1995, 1996, 1998 and 2000; and Sinclair, 2000). The majority of structures are thought to be post-Mesozoic, forming during compression and uplift during collision of Wrangellia with North America, or Tertiary (Muller, 1980; Massey, 1992; Yorath, 1999).

The most recent work by Berry (2000) and Sinclair (2000) outlined a deformation history for the area, and included results from this study (e.g., Jones and Berry, 2001). A more detailed structural history is reported in this thesis and includes the following deformation events:

Early growth faults, representing early basin-controlling structures and possible ore fluid conduits (?);

D_1: Folding and development of E-W-oriented cleavage;

D_2: Localised shear zones

D_3: Conjugate strike-slip faults and shallow thrust faults;

D_4: Normal faults; and

D_5: Thrust faults and steep strike-slip faults.

A detailed description of cross cutting fault relations, fault morphology, geometry and fault kinematics, which define the various brittle deformation events, is given in the following chapter.

3.6 Metamorphism and alteration

The Sicker Group rocks at Myra Falls have undergone lower greenschist metamorphism as a result of regional burial and submarine hydrothermal alteration. Juras, (1987) describes the typical metamorphic mineral assemblages for various lithologies throughout the sequence, with chlorite zone rocks dominant in the lower parts of the sequence and pumpellyite-actinolite facies assemblages dominant in the uppermost parts of the sequence (Table 3.1). Ubiquitous sericite alteration occurs in felsic and mafic rocks close to mineralized zones, obscuring much of the original volcanic and sedimentary features.

Formation	Rock type	Mineral Assemblage
Flower Ridge	basalt	chl + ep/clz + ab + q + act ±cc ±pp
Thelwood	intermediate tuffs	chl + ep/clz + q + ab
	mafic sills	chl + ab + ep
Myra	basalt	chl + q + ab
		chl + ep + ab + q ± act ± cc
		ep + q + ab + cc ± act
	basaltic andesite, andesite	ep + ab + q ± chl ± cc ± act
		chl + ab + q ± ep ± cc
	feldspar porphyry	ab + q + ep + ser ± chl ± hem
	quartz-feldspar porphyry	ser + q + ab ± chl
Price	andesite, basaltic andesite	chl + ep + ab + q + cc ± act
	high MgO basalt	act + chl + ab + ep
		chl + cc + ser + hem

Table 3.2: Metamorphic mineral assemblage of Myra Falls lithologies. Mineral abbreviations: chl=chlorite; ep=epidote; clz=clinozoisite; ab=albite; q=quartz; act=actinolite; cc=calcite; pp=pumpellyite; ser=sericite; and hem=haematite.

The metamorphic mineral assemblages are diverse, reflecting variations in factors such as, the bulk composition of rock types (e.g., ultramafic to felsic), rheological factors such as porosity and permeability, water/rock ratio and fluid compositions. The metamorphic mineral assemblages from Juras (1987) are discussed in the following paragraphs.

Chlorite and epidote-dominant assemblages are common in mafic lithologies of the Price and Myra Formations. Actinolite is also fairly common, and usually occurs as a pseudomorph after clinopyroxene. Mineral assemblages in felsic lithologies of the Myra Formation, are dominated by, white mica and quartz, with minor albite and chlorite. White mica, quartz and minor chlorite is also dominant in feeder zones in the Price Andesite beneath the HW and Battle orebodies. The chlorite content appears to increase away from the intensely altered feeder zone (Juras, 1987).

The Thelwood and Flower Ridge Formations, in the upper part of the sequence, are dominated by a metamorphic mineral assemblage of chlorite-epidote/clinozoisite-albite-quartz-actinolite-calcite-pumpellyite. Pumpellyite is only found in the upper to middle parts of the Flower Ridge Formation, implying that metamorphic grade increases with depth, from sub-greenschist facies at the top of the formation to lower greenschist facies

conditions in the lower parts of the Flower Ridge Formation. Silicification and minor epidote veining in the Thelwood Formation is thought to be a result of penecontemporaneous intrusion of mafic sills.

The slight increase in metamorphic grade with depth, from sub-greenschist facies in the upper parts of the stratigraphy to lower-mid greenschist facies conditions in the lower units, suggests the metamorphism is a result of regional burial. However, Juras, (1987) also suggests that the timing of some of the alteration in the sequence is early, ie., submarine seafloor alteration. For example, basaltic clasts, with markedly different alteration assemblages, often occur together in the same breccia unit. This implies that alteration occurred prior to phreatic fragmentation, when the basalt formed a more cohesive lava body.

A mid-Jurassic overprint of the regional burial metamorphism, as a result of intrusion of the Island Intrusive Suite, is indicated by reset K-Ar and to a lesser degree Rb-Sr isotopic dates (Juras, 1987). However, there is little evidence of contact metamorphic mineral assemblages in the Sicker Group rocks at Myra Falls. Within several hundred metres of the large plutons, biotite should start to appear in the intermediate and mafic rocks. However, biotite is not reported, even in the sequence in Thelwood Valley, which is located close to Island Intrusive Suite plutons. Metamorphic minerals are overprinted by the D_2 event, with an increase in the grainsize of phyllosilicates, and pressure shadow development around brittle minerals such as pyrite.

Chapter 4
Myra Falls structure

4.1 Introduction

The Sicker Group, which hosts the VHMS orebodies at Myra Falls, is strongly deformed by ductile and brittle deformation episodes. The sequence is folded and offset by numerous faults with a wide range of orientations, morphologies and kinematics.

To determine the overall effect of these deformation events on the sequence, a footwall contour map of the top surface of Price Andesite was constructed (Figure 4.1). This map highlights the major structures affecting the sequence, with marked offsets in the footwall used to estimate the position and orientation of the major structures. For example, a large topographic high in the southern part of the property, represents the hinge zone of the Myra Anticline. This topographic high is offset laterally by two large fault zones, the Myra-Price Fault Zone on the eastern side of the property and the Lynx-Phillips Fault Zone on the west. A large topographic low in the northern part of the property is related to down-throw on the North Fault Zone.

Smaller topographic lows, or basinal features occur beneath the HW orebody and southwest of the Battle orebody. These may represent the original basins formed contemporaneously with VHMS orebodies. Rapid changes in footwall elevation into these basins and associated stratigraphic thickening, most likely indicate the presence of syn-depositional growth faults. One of the aims of this project was to locate growth structures and determine their relationship to ore and the overlying caprocks. As these early basin-controlling structures are strongly overprinted by subsequent deformation, to locate these structures with any accuracy, a good understanding of the deformation history is necessary. For this reason, a detailed structural study was undertaken to determine the deformation sequence in order to reconstruct the paleoseafloor topography and locate early growth structures.

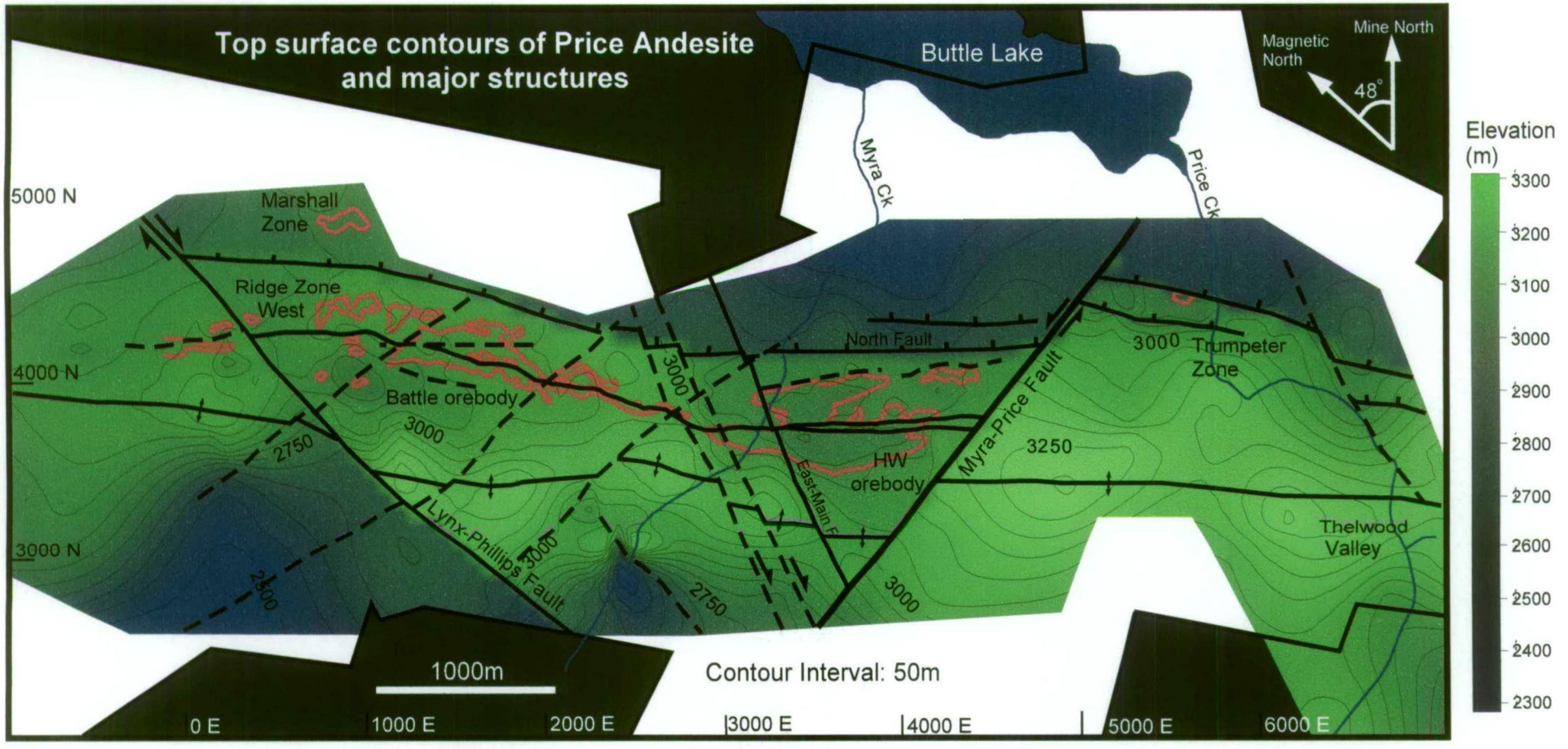

Figure 4.1: Contoured top surface of Price Andesite, which is thought to represent the deformed paleoseafloor (see discussion in text). Marked changes in the footwall contours highlight the major displacements resulting from the major structures. Only the lower mineralised horizon is shown as this horizon occurs on, or very close to the top contact of Price Andesite. Areas with no drillhole information are blanked out.

4.2 Methods

Structural measurements were collected during underground and surface mapping, over three field seasons at Myra Falls. Approximately 1000 fault planes and striations were measured, along with foliation, fold axes and mineral lineation measurements. Data was collected from underground in the HW, Battle Lynx and Price mines, and from surface measurements in the Lynx and Myra open-cut, Price hillside and Westmin Road cuttings. Fault striation data from previous work by Ron Berry (Berry, 1998, 2000) was also combined with this study. Structural interpretations on drillhole sections were constructed from detailed drillcore logging, noting bedding, cleavage and fault attitudes and styles. The location, orientation and displacement sense of some of the larger structures shown in Figure 4.1, such as the Lynx-Phillips, Myra-Price and North Fault Zones, are partly based on previous mapping and interpretations by company geologists, owing to a lack of suitable exposure. The orientation and location of other structures, such the Flat Fault (or Battle-Main Fault), and the East-Main Fault, are based on a combination of company data and underground measurements collected during the study.

Mine grid coordinates are used throughout this chapter, (mine north is +48° from true north). Where true north coordinates are given, such as in the regional correlation, Section 4.10, the true north coordinates are in bold italics ***(e.g., true north).***

4.2.1 Separation of brittle deformation events

A wide range of fault styles, orientations and kinematics were recorded at Myra Falls, making it difficult to determine a clear deformation sequence. Faults ranged in style from very planar, gouge-free faults with quartz-epidote-chlorite fibres, to wavy anastomosing faults with abundant gouge and only rare fibres. The faults were separated into groups based on the fault geometry, morphology and kinematics, and the criteria used to sort the faults included:

- Fault orientation;
- Displacement sense;
- Style of kinematic indicators, (e.g., coarse or fine quartz fibres, quartz-chlorite-epidote fibres, fine grooves in fault gouge, foliation or bedding drag adjacent to faults, and dyke offsets);
- Geometry, (e.g., wavy anastomosing faults, or planar faults);
- Presence or absence of fault gouge;
- Presence or absence of cleavage zones;
- Presence or absence of veining; and
- Type of veining, (e.g., quartz-carbonate, clear or milky quartz).

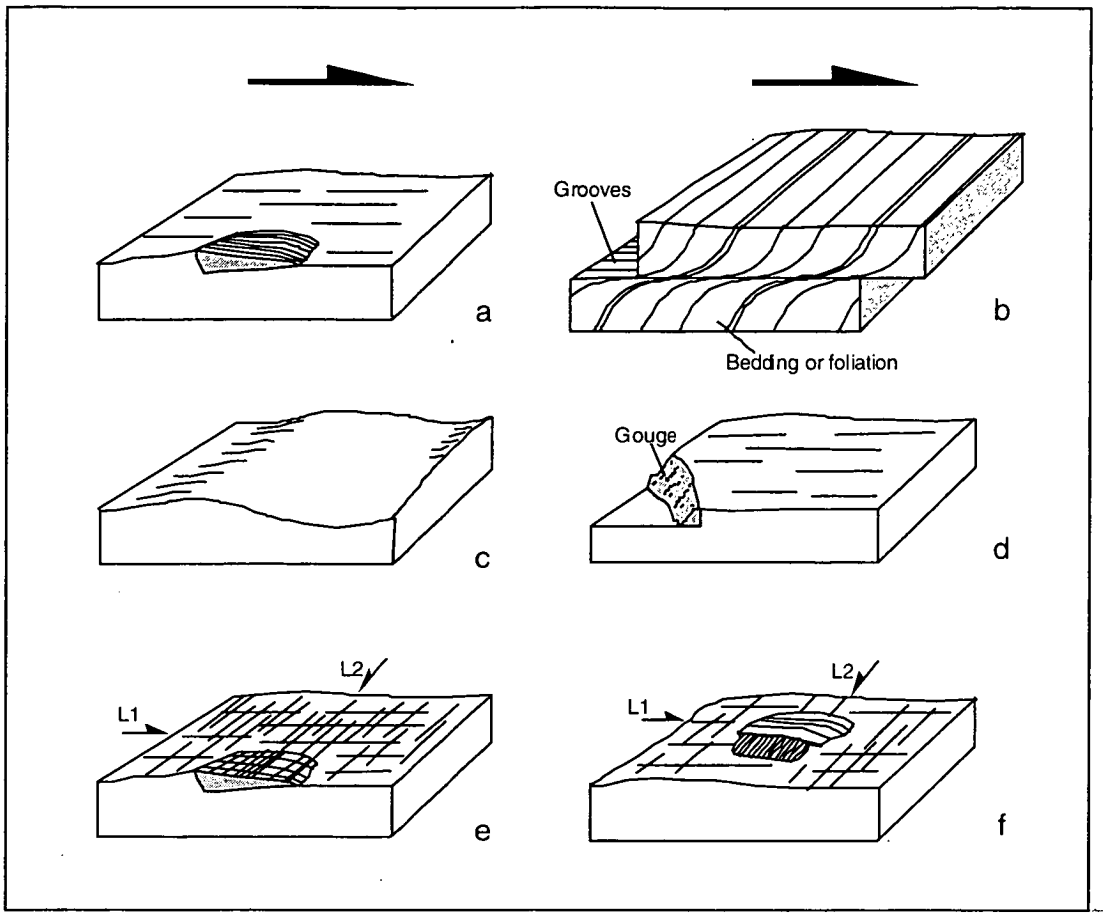

Figure 4.2: Criteria used to determine the sense of displacement (a-d) and relative age (f-g) from fault striations at Myra Falls (all diagrams are drawn with the top displaced to the right). Full explanations of displacement sense criteria are given in Petit (1987). **a)** Mineral fibres grow in the lee of a ledge on the fault surface; **b)** Fault drag of cleavage or bedding, where the planar fabric intersects the fault plane at a high angle to the striations; **c)** Striations on the upstream face of an irregular fault surface; **d)** Fault gouge collects on a ledge facing against the motion of the opposing block; **e)** Coarse fibres are overprinted by younger striations, leaving grooves in the older coarse fibres, indicating relative age; **f)** Fine fibres grow off older coarse fibres, indicating relative age.

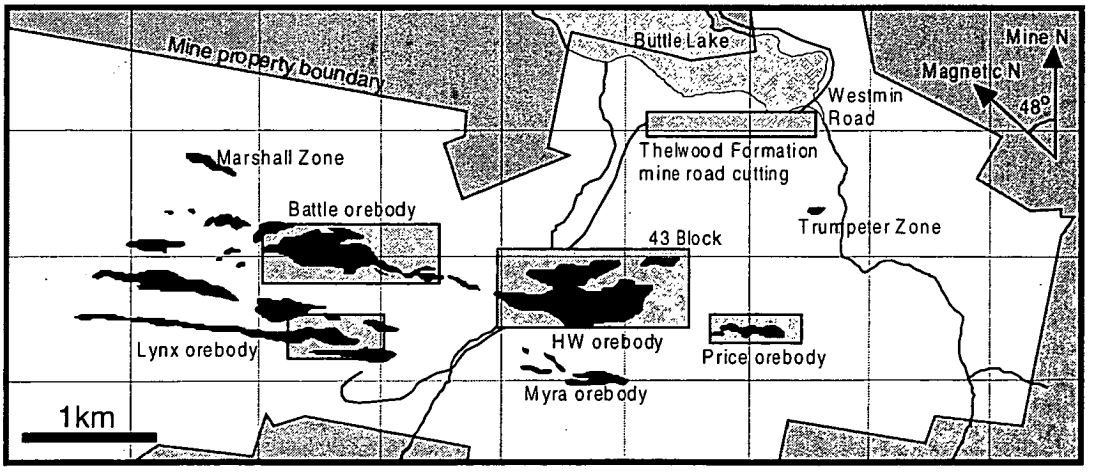

Figure 4.3: Fault data is separated into the areas shown above.

The sense of displacement on fault surfaces was determined by using criteria, summarized by Petit (1987). At Myra Falls the most reliable criterion were fibre veins attached to the back of ledges on the fault surface (Figure 4.2a). These were found on most faults, and were the most useful kinematic indicator. However, fibres were absent on many gouge-rich faults, instead the fault surfaces had fine grooves. The sense of displacement on these faults was determined mainly by fault drag of foliation and/or bedding (Figure 4.2b), shadowing of grooves across an undulating fault surface (Figure 4.2c), the presence of gouge in front of ledges (Figure 4.2d), and offsets of bedding and mafic dykes.

The relative timing of fault phases was determined by crosscutting relations observed in surface and underground exposures, by overprinting relations of striations on fault surfaces, including fibre overgrowths (Figure 4.2e), and grooves on older fibres (Figure 4.2f).

4.2.2 Paleostress analysis

Paleostress analysis was undertaken on each fault group to determine whether the faults were related to a single tectonic phase, and if so, what was the likely orientation of the stress field during deformation. Fault data was collected from many locations throughout the property, and the data was divided into five main areas to determine whether any significant changes in fault geometry and kinematics occurred in the different areas. The areas are as follows, Battle mine, Lynx mine and open-cut, HW mine, Westmin Road cutting above Buttle Lake, and the Price mine and hillside (Figure 4.3).

Striations from each fault group were interpreted using the method of Etchecopar et al. (1981). This method gives a quantitative interpretation of the stress field from striations observed on fault planes. The program minimises the errors between the observed slickenside measurements and the direction of maximum shear stress for a calculated stress field, as the orientation of slickensides on fault surfaces should be near-parallel to the maximum shear stress on the fault plane. The program then calculates the number of faults which have the correct orientation for failure in a given stress state. The fault data is displayed as a histogram, showing the residuals, or angular deviations between the actual and computed striations for a given stress state. The three dimensional stress state is shown with a Mohr circle, and the slickenside data are plotted to illustrate the calculated value of shear stress (τ) and normal stress (σ_n) for each fault. The nearest-exact solution of the orientation of the principal stress axes, for a given stress state, is shown by striation data plotting as points on a Schmidt net. The program is iterative, and does not require any information other than the observed striations. An initial solution is automatically provided by a random exploration of the data set. However, it is also possible to set various parameters, such as one or several of the principal stress axes, σ_1, σ_2 or σ_3. The proportion

of data used in the calculation, can also be specified. A satisfactory solution often results from lowering the percentage of fault data used, as it is rare that 100% of the data will fit a given stress state.

The program can also be used to separate fault data where only one or two tectonic phases are responsible for the striations. However, in an area affected by multiple tectonic phases, such as Myra Falls, it was not possible to separate the faults using this program. Instead, the fault data was separated prior to stress analysis, using criteria such as fault geometry, kinematics, and morphology.

4.3 Deformation history of Myra Falls

Four main fault groups were recognised at Myra Falls, and consist of, 1) steep planar NE-striking sinistral and NW-striking dextral strike-slip faults with coarse (2-5mm) shallow plunging quartz-epidote-chlorite fibres; 2) shallow to moderately dipping, wavy anastomosing thrusts, with narrow cleavage zones and minor gouge; 3) steep planar normal faults with fine quartz fibres, which are commonly associated with quartz-carbonate veining; and 4) wavy anastomosing gouge-rich faults, including steep NE-striking sinistral and NW-striking dextral strike-slip faults, and shallow to moderate N-dipping oblique thrusts, with top to the W-SW sense of displacement).

The relative age of the four main groups of faults are shown in Table 4.1. Planar strike-slip faults with shallow coarse quartz-chlorite-epidote fibres do not crosscut other fault groups and are therefore inferred to be the oldest fault group. Shallow dipping thrust faults crosscut the steep planar strike-slip faults and are in turn offset by steep planar normal faults. Gouge-rich thrusts and steep strike-slip faults crosscut all other fault groups and therefore represent the youngest fault group.

The fault history is combined with ductile deformation and evidence of early growth structures, based on stratigraphy and footwall contouring, to give a deformation sequence for Myra Falls (Table 4.2), and is as follows:

- Syn-depositional growth faults
- $\mathbf{D_1}$ – folding
- $\mathbf{D_2}$ – localised shear zones
- $\mathbf{D_3}$ – two-stage generation of steep strike-slip faults followed by shallow-dipping thrust faults
- $\mathbf{D_4}$ – planar normal faults
- $\mathbf{D_5}$ – gouge-rich thrust faults and steep strike-slip faults

1: Planar steep strike-slip faults with q-chl-ep fibres **crosscut: GROUP 1**	2:Shallow-dipping thrust faults with minor gouge **crosscut: GROUP 1**	3: Planar normal faults with fine steep quartz fibres **crosscut: GROUPS 1,2,3**	4: Gouge-rich wavy strike-slip faults and oblique thrusts **crosscut: GROUP 1,2,3,4**	
XXXXX XXX	XXXXX □□	X □□□□□ □□□□□ □□□□□ □□	XXXXX XXX	**GROUP 1** Planar strike-slip faults with q-chl-ep fibres
		XXXXX XXXXX XXXXX	XXXXX XXXXX XXXXX	**GROUP 2** Shallow-dipping thrust faults with minor gouge
		XXXX	XXXXX XXXXX XXXXX XXXXX XXX	**GROUP 3** Planar normal faults with fine steep quartz fibres
			XXXXX XXXXX	**GROUP 4** Gouge-rich wavy strike-slip faults and oblique thrusts

X Crosscutting faults
□ Crosscutting slickenfibres

Table 4.1: Crosscutting relations indicating the relative age of the four fault groups. Each X refers to an example of one fault offsetting another fault, and each □ equates to an example of overprinting fibres, which also indicates the relative age.

4.4 Syn-depositional growth faults

Syn-depositional growth faults are associated with basin formation. These faults are poorly preserved, and are overprinted and destroyed by subsequent deformation. For this reason, direct measurement of these structures was not possible, instead their location and orientation is inferred from rapid changes in footwall elevations accompanied by increased stratigraphic thickness and marked facies variation. The location and relationship of growth faults to VHMS orebodies and the overlying caprocks, is discussed in Chapter 5.

4.5 D_1 folding

4.5.1 Macro-scale structure

D_1 produced broad open upright folds with moderately to steeply north-dipping axial planar cleavage zones (S_1) that are variably developed. Figures 4.4a-c illustrate the typical open upright fold style associated with the D_1 event in folded siliceous caprocks and siltstone immediately above the massive sulphides in the Battle and HW mines (Figure 4.4a-b), and

Myra Falls deformation sequence

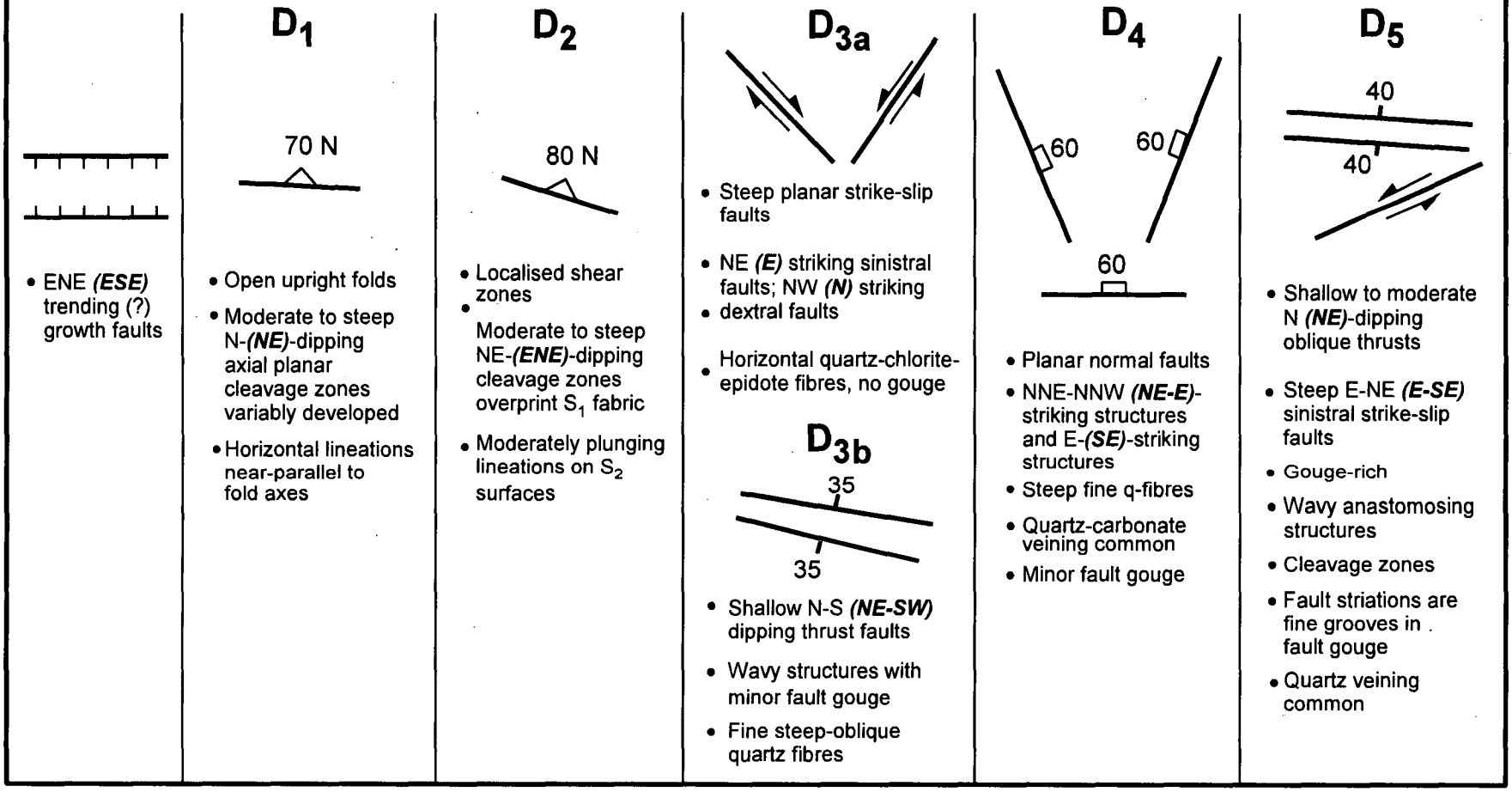

Table 4.2: Deformation sequence at Myra Falls.

a

b

c

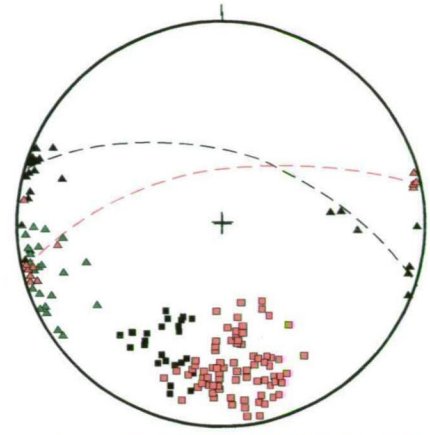

d

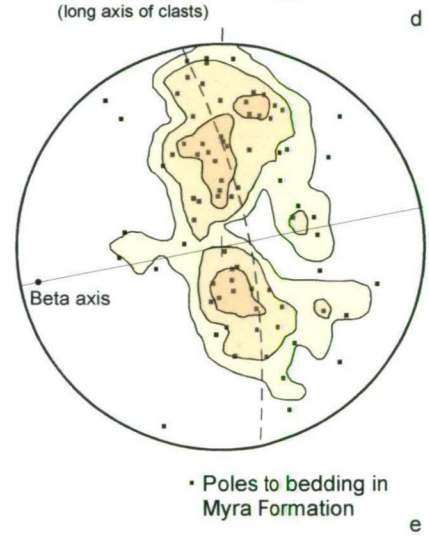

e

Figure 4.4: a) Folded chert and siltstone above massive sulphides, drive ST183A, Battle mine; **b)** Open folds in chert immediately above massive sulphides in HW mine, 20 level; **c)** Folded quartz-carbonate veins in HW mine, drive B390; **d)** Stereonet plot of D_1 and D_2 structural data from HW and Battle mines; **e)** Stereonet plot of bedding data measured in the Myra Formation from HW and Battle mines (see text for further discussion).

folded veins (Figure 4.4c). The stereonet (Figure 4.4d) shows the poles to S_1 foliations with the average S_1 foliation plane, F_1 fold axes and L_1 lineations. Stretching lineations (L_1) are predominantly horizontal to shallow WSW plunging and are generally parallel to F_1 fold axes. Figure 4.3e shows poles to bedding in the Myra Formation, based mainly on underground measurements in the Battle, Lynx, HW and Battle mines, and in surface areas across the property. These poles form a great circle with a beta axis near-parallel to measured F_1 fold axes and the long axes of stretched clasts (L_1).

The intensity of the S_1 fabric varies markedly, from zones of very weak cleavage, to to moderately sheared zones with weak S-C fabrics forming. The cleavage is best developed in strongly sericite-altered lithologies. Planar fabrics are dominant, but in places, SL fabrics (planar dominant over linear fabrics), to LS fabrics (linear dominant over planar fabrics), (Flinn, 1965) develop. The linear fabrics are defined predominantly by the aligned long axes of stretched clasts, which are approximately parallel to the F_1 fold axes and L_1 mineral lineations on the foliation surface.

Figures 4.5 and 4.6, illustrate typical underground wall maps of folded cherts and silt in the Battle and HW mine, disrupted by numerous faults. Ductile deformation predates most of the faulting in the area, with the exception of early syn-depositional faults.

The map, Figure 4.7, shows the orientation of the S_1 fabric across the property and the pre-D_3-D_5 position of a regional antiformal structure, the Myra Anticline, which is located south of the Battle and HW orebodies. The hinge-zone extends through the upper Lynx-Myra-Price orebodies, and the position may reflect a weak zone or anisotropy caused by strong sericite alteration around the VHMS orebodies. Abundant smaller parasitic folds, with similar orientations and wavelengths, approximately 1-5m, occur throughout the property.

4.5.2 Micro-scale structure

The S_1 foliation is defined predominantly by sub-parallel aligned muscovite and chlorite (Figures 4.8a-c), recrystallised quartz (Figure 4.8c), pyrite trails (Figure 4.8b), and wavy carbonaceous seams in argillaceous rocks (Figures 4.8d-f). The cleavage is weakly to moderately developed, and typically occurs as a spaced fabric of muscovite seams crosscutting weakly deformed rocks. Bedding is still visible in many rocks and cleavage is at a moderate to high angle to the bedding (Figures 4.8d-h).

Small quartz tails are common in strain shadows beside pyrite grains (Figures 4.9a-b) and detrital quartz grains commonly display undulose extinction, and are fractured and

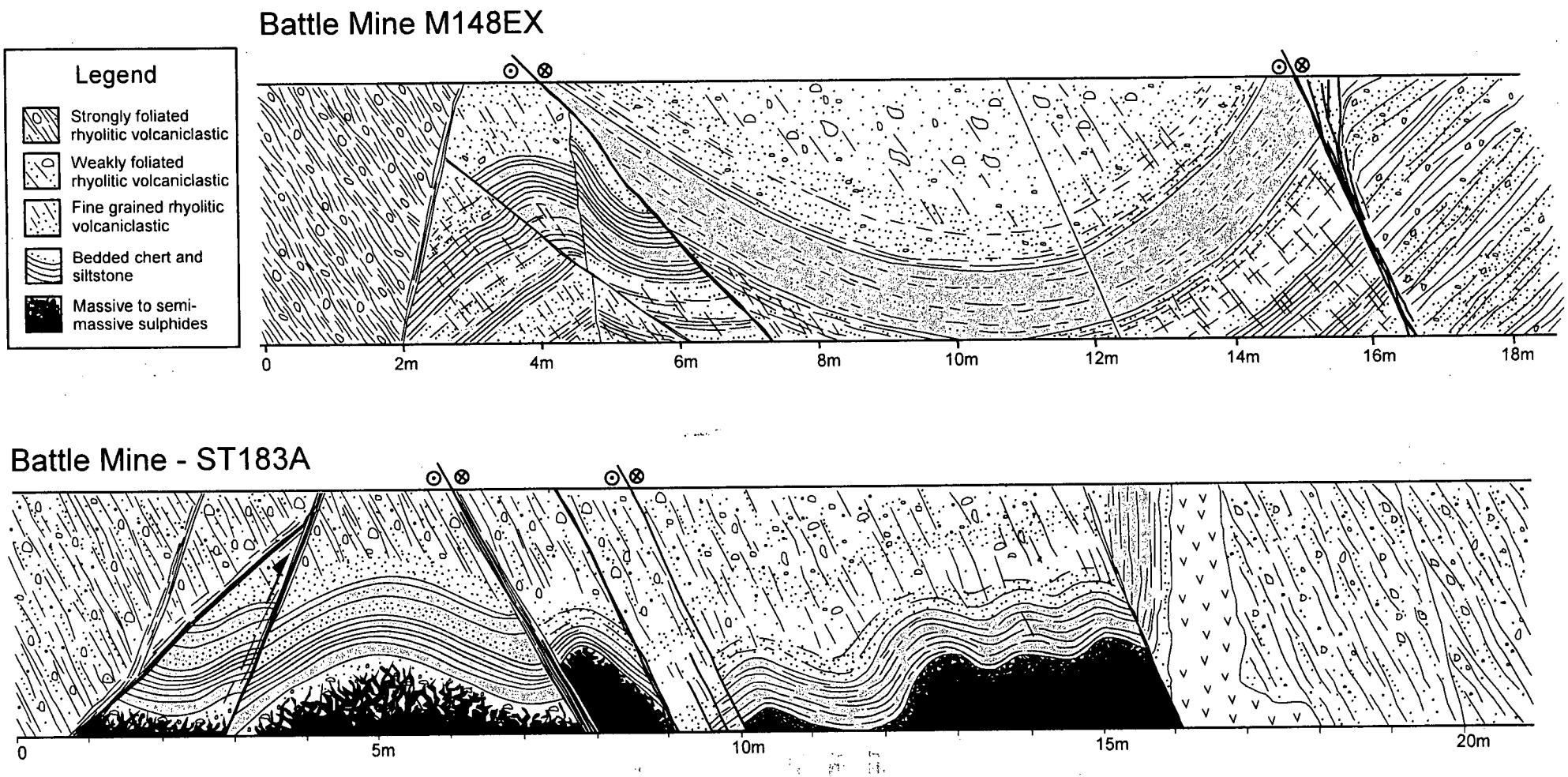

Figure 4.5: Underground wall maps illustrating typical open D_1 folds, offset by numerous faults in the Battle mine.

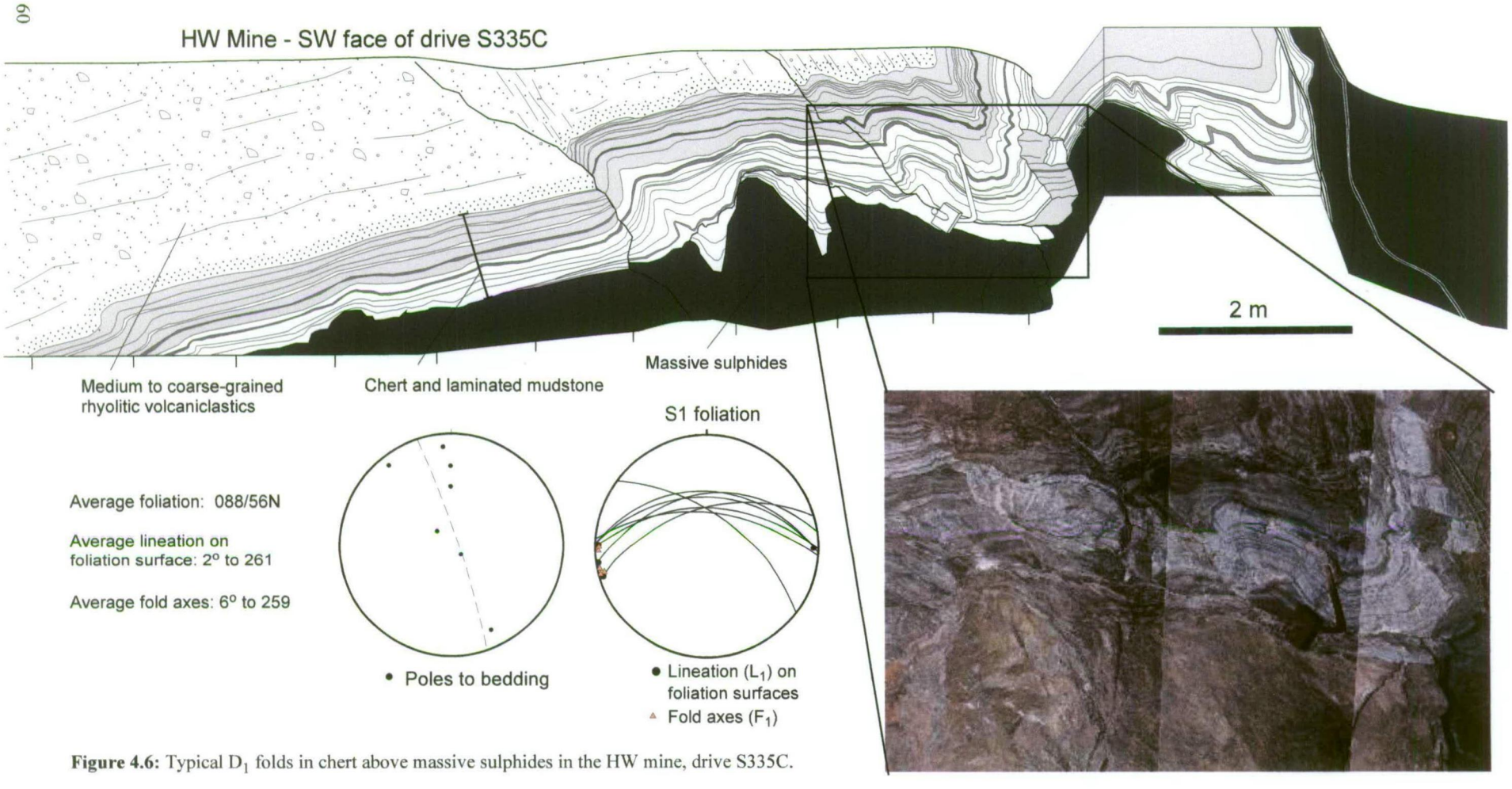

Figure 4.6: Typical D_1 folds in chert above massive sulphides in the HW mine, drive S335C.

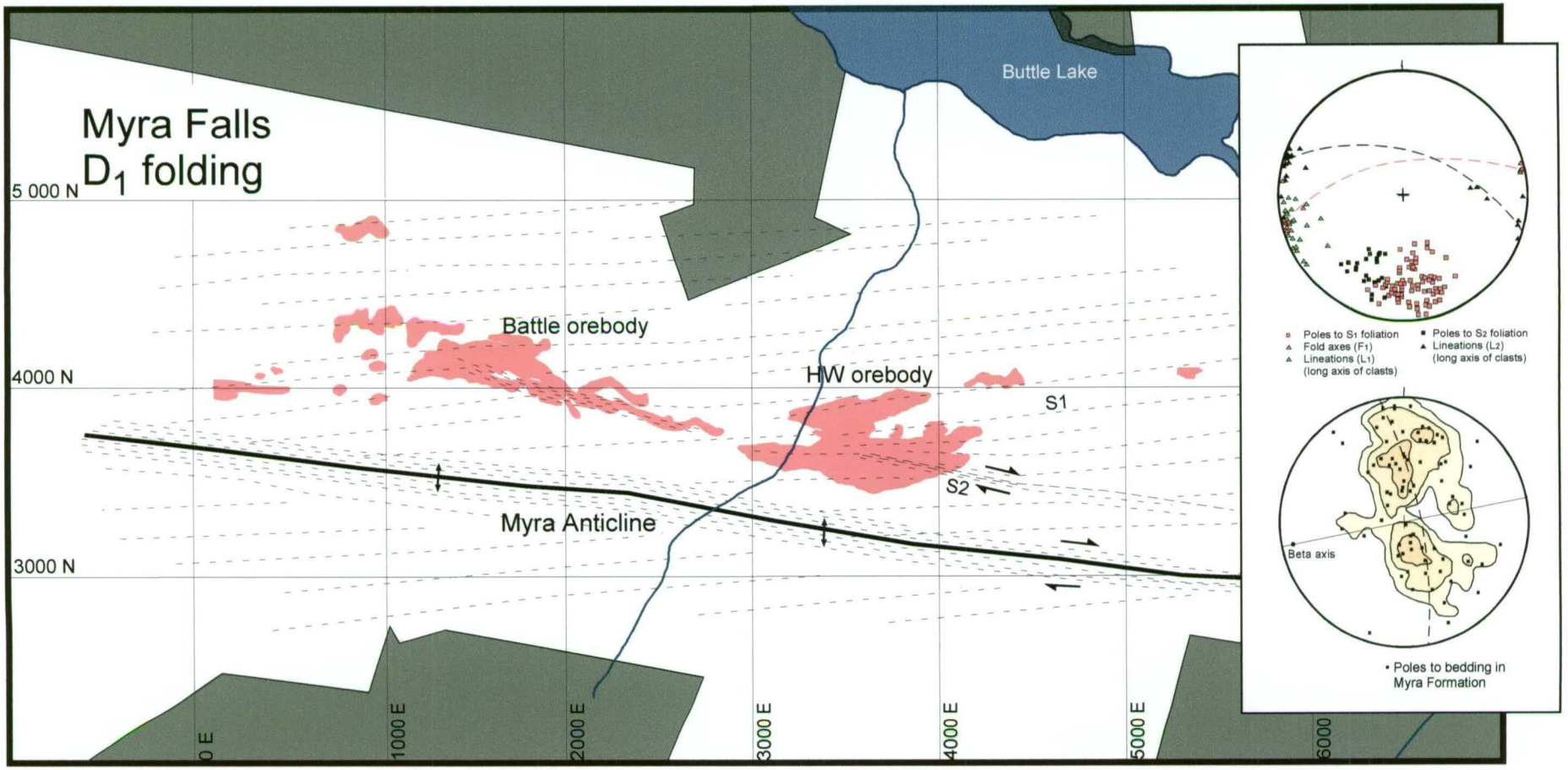

Figure 4.7: Map illustrating the pre-D_{3-5}, S_1 and S_2 foliation pattern at Myra Falls.

displaced along narrow shear bands (Figure 4.9c). Deformation lamallae are observed in larger white mica grains (Figure 4.9d). In areas of more intense cleavage development, fine shear bands are observed throughout (e.g., Figure 4.9e) and weak S-C fabrics are developed, shown in Figures 4.9f-h. The S_1 foliation, represented by the fine-grained aligned muscovite, is crosscut at a moderate angle by the C-planes. Measurement of the S-C fabric in oriented samples indicates a consistent dextral sense of shear (e.g., Figures 4.9f-h). The development of S-C fabrics may be related to the D_2 event discussed in Section 4.6.

4.5.3 Strain estimate

The distribution of strain tends to be uneven in areas of mixed lithologies and for this reason the strain is inhomogeneous at Myra Falls. The least competent lithologies accommodate the strain, resulting in a greater degree of fabric development, relative to the more competent units.

A finite strain ellipse for the principal strain axes has been estimated for the Myra Falls area, based on the average trends and ratios of stretched ovoid clasts, and the orientations of folded, flattened and boudinaged pyrite-stringer veins (Figure 4.10a-b). This is similar to the method of Talbot (1970), who used dykes as strain markers, by constructing stereographic plots of poles to shortened and extended dykes, assuming original random orientation. This enabled the determination of the *k* value, which describes the shape of the strain ellipsoid, and axial ratios of the finite strain ellipsoid. Limited data in this study only allow an approximation of the finite strain ellipsoid.

The poles to foliation, F_1 fold axes and L_1 lineations (long axes of stretched clasts) are shown on the stereoplot (Figure 4.10d), with the approximate principal strain axes, XYZ. The XY plane is sub-parallel to the average cleavage plane. The stereoplot below (Figure 4.10e) shows the poles to flattened, boudinaged and folded pyrite stringer veins. Stringer vein fold axes are near parallel to the L_1 lineations, or long axes of the stretched clasts.

The X-axis (maximum elongation direction), is estimated from the average trend of stretched, linear clasts, and plunges 0-2/267° (Figure 4.10c). The Z-axis (principal shortening direction) is perpendicular to the XY (foliation) plane, which has an average strike of 088/70°N. The stringer vein fold axes are parallel to the trend of stretched clasts and flattened and boudinaged veins are near-parallel to the foliation. The clear separation of poles to folded veins, from poles to boudinaged and flattened veins in Figure 4.10e, suggests that they were deformed during the same event, assuming they were originally

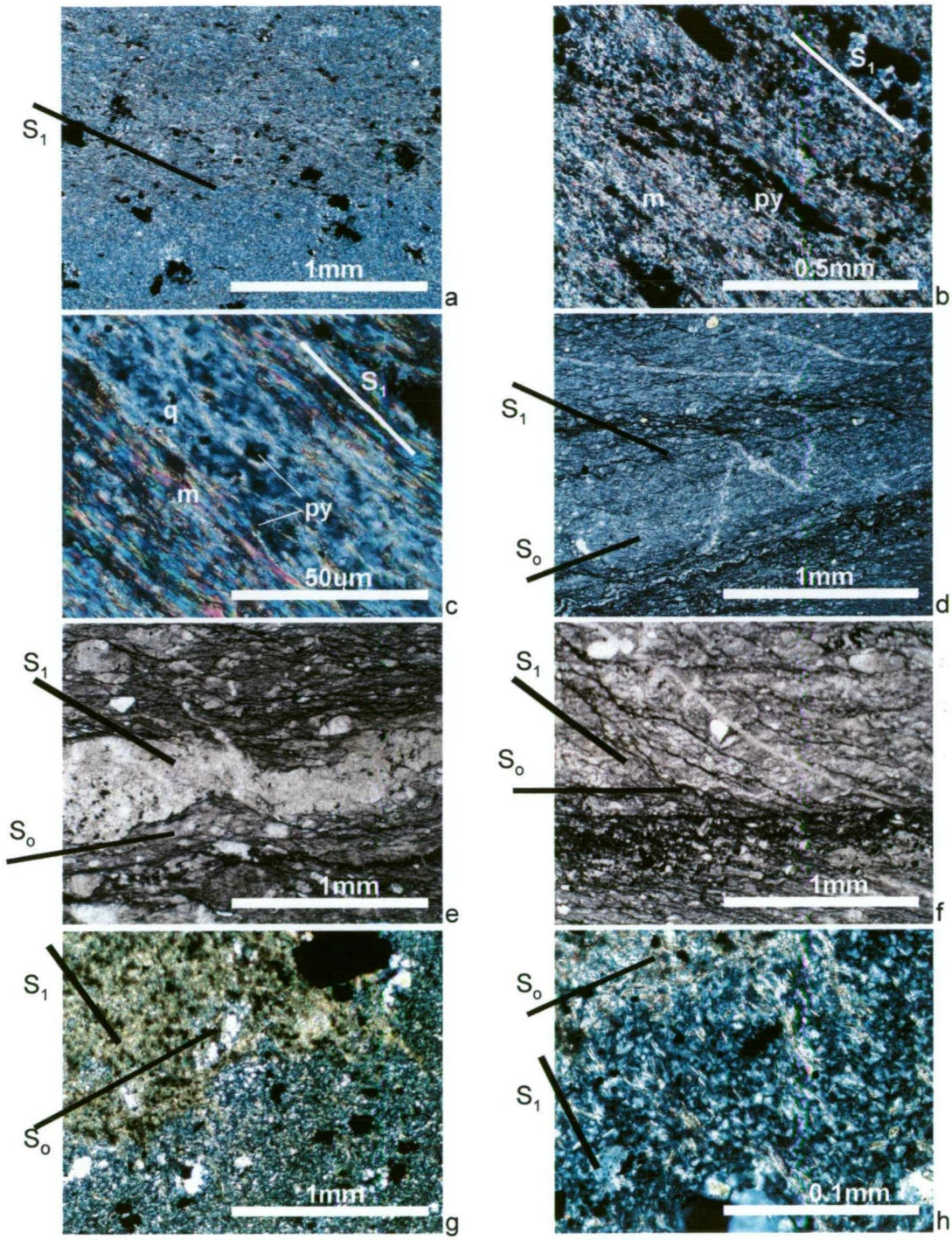

Figure 4.8: Typical micro-scale textures in HW Horizon lithologies: **a)** Weak S_1 foliation defined by aligned muscovite, XPL (SJ92, drive S335A-D6, HW mine); **b)** Well developed S_1 foliation defined by aligned muscovite, pyrite and recrystallized quartz, XPL (SJ319, drive 23-N350, HW mine); **c)** Close-up showing recrystallized, strongly aligned quartz and muscovite, XPL (SJ90, drive S335A-D6, HW mine); **d)** Weak S_1 foliation crosscuts the bedding defined by carbonaceous-rich layers in argillite, XPL (SJ47, drillhole 23-493, 17.6m); **e)** Sandy layer in laminated argillite crosscut by S_1 foliation, PPL (SJ47, drillhole 23-493, 17.6m); **f)** Carbonaceous-rich layers define the bedding and narrow wavy carbonaceous seams define the S_1 foliation, PPL (SJ47, drillhole 23-493, 17.6m); **g)** Bedding, defined by a phyllosilicate-rich layer is crosscut at a high angle by weak S_1 foliation, XPL (SJ150, drillhole 18-1086, Battle mine); **h)** Close-up of previous photo, showing the S_1 foliation defined by fine aligned muscovite, XPL (SJ150, drillhole 18-1086, Battle mine).

randomly oriented. The plot also indicates that the strain was irrotational at the outcrop scale, with no resolvable rotation of principal strain axes during the deformation event. Irrotational strain is also suggested by the consistent E-W strike of the S_1 foliation, with little or no swing in trend across the property and by the lack of refolded folds or boudinaged folds.

The predominance of SL to LS fabrics suggests a prolate ellipsoid with the LS fabric resulting from NNE-SSW shortening and WNW-ESE extension. The amount of strain was estimated from X-Y-Z ratios on elliptical argillite clasts in a rhyolitic conglomerate. The samples chosen for the strain ratio estimates, were from moderately deformed zones, rather than high strain zones, and are therefore more representative of the background strain. A rock sample, with abundant elliptical markers (argillite clasts) was sectioned to show the principal strain directions, allowing the maximum and minimum length ratios for the X, Y and Z axes to be estimated (Figure 4.10f). The average strain ratios estimated from these clasts was X:Y:Z, 3.3:1.8:1, suggesting about 25-30% shortening. This amount of shortening is similar to that estimated from restored geological sections (see Chapter 5).

4.5.4 Removing effects of the D_1 event

The orientation of stringer veins beneath VHMS deposits can provide information on the stress-state at the time of emplacement, which can then indicate the more likely orientations of growth structures associated with the orebodies. However, D_1 folding, with an estimated shortening of 25-30%, has greatly affected the original geometry of the stringer veins. A method used by Ramsay (1967) restores planar structures back to their original orientations using measured strain ratios from strain markers, such as ovoid clasts.

For the reconstruction the following strain was used:
Principal X axis of ellipsoid plunges 1° toward 266°
Principal Y axis of ellipsoid plunges 76° toward 356°
Principal Z axis of ellipsoid plunges 14° toward 176°
Principal axes of the ellipsoid have the ratio X:Y:Z = 3.3:1.8:1

The points representing the principal axes of the strain ellipsoid, and great circles representing the principal were then plotted on an equal area net. A deformed plane (stringer vein), was then plotted and the angles between the intersections of the deformed plane and the three principal planes were measured: θ_1', θ_2', and θ_3' (Figure 4.11a). Using these angles, together with the estimated strain ratios, the undeformed angles (θ_1, θ_2, and

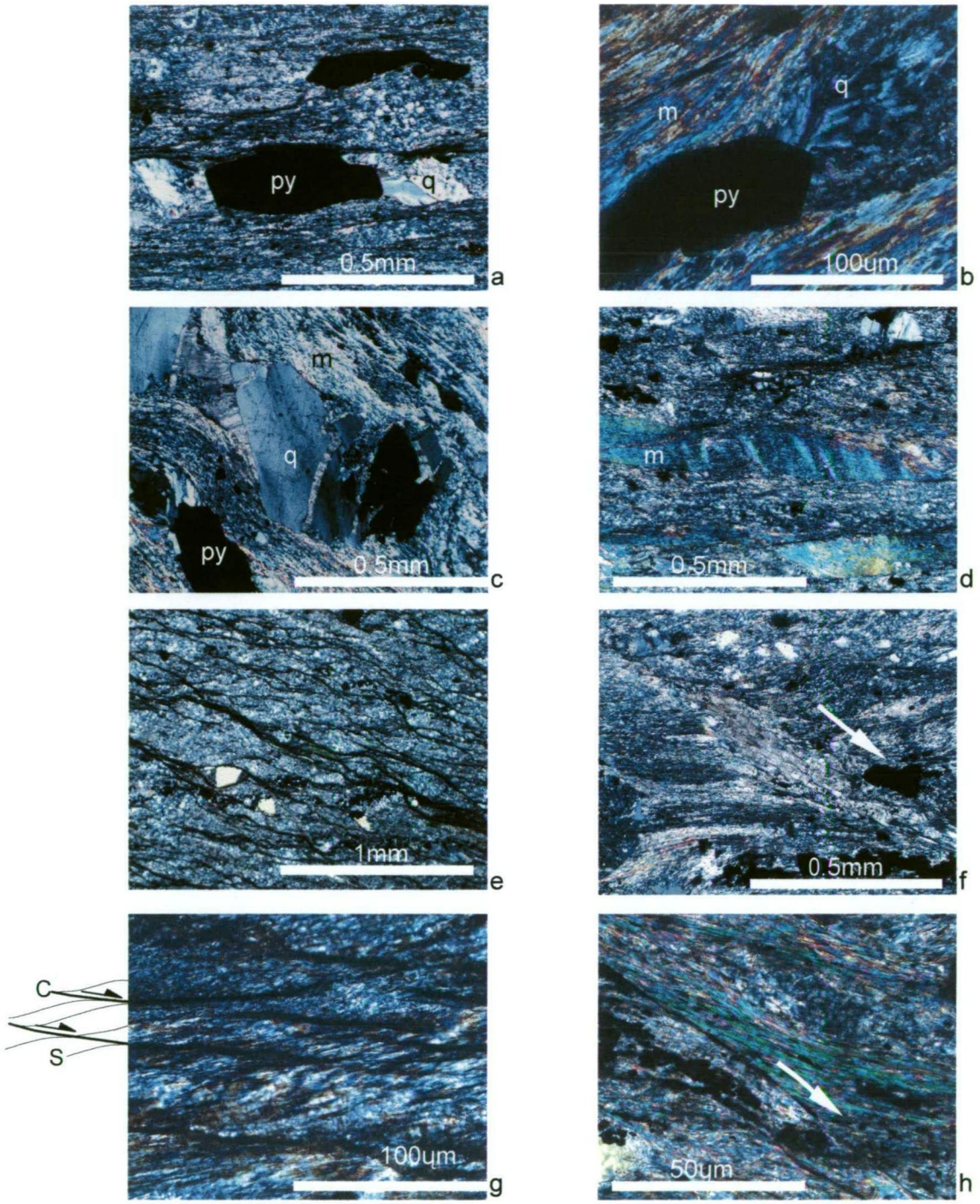

Figure 4.9: Micro-scale textures in rhyolitic volcaniclastic rocks at Myra Falls: **a)** Quartz tails in pressure shadows beside a pyrite grain, XPL (SJ92, drive S335A-D6, HW mine); **b)** Close-up of quartz tail growing in a pressure shadow, surrounded by strongly aligned muscovite, XPL (SJ90, drive S335A-D6, HW mine); **c)** Fractured detrital quartz grain showing undulose extinction, XPL (SJ90, drive S335A-D6, HW mine); **d)** Kink bands in a large detrital muscovite grain, XPL (SJ92, drive S335A-D6, HW mine); **e)** S_1 foliation defined by carbonaceous seams and fine aligned muscovite with a weak S-C fabric developing, (SJ90, drive S335A-D6, HW mine); **f)** Weak S-C fabric developed in rhyolitic siltstone (oriented sample indicates a dextral sense of displacement), XPL (SJ90, drive S335A-D6, HW mine); **g)** S-C fabric is well developed in oriented siltstone sample and indicates dextral offset, XPL (SJ319, drive 23-N350, HW mine); **h)** Close-up of weak S-C fabric in rhyolitic siltstone, indicating a dextral sense of displacement (oriented sample), XPL (SJ90, drive S335A-D6, HW mine).

θ_3), can be read off a graph (Figure 4.11b). The new points can be plotted on the stereonet, and will lie on a great circle representing the undeformed stringer vein.

The stereonets in Figure 4.12 illustrate the change in orientation of the stringer veins after using the method by Ramsay (1967). Stringer veins are separated into two areas, Myra open pit and drive 23-331XN, HW mine and in both areas, the undeformed stringer veins have a much wider range of orientations than the deformed stringer veins. However, two main trends are visible in both groups, with NE and ENE stringer veins dominant in the Myra area, and NNE and SE veins dominant in the HW mine. The stringer veins appear to form orthogonal sets, which may reflect either, normal faulting and the transfer direction, or equal extension in all directions. The original growth faults may have had similar orientations and are also likely to be rotated from their original orientations. The basinal structures now appear to be roughly E-W oriented, but this is most likely a result of shortening during D_1 folding.

4.6 D_2 shear zones

D_2 produced a second foliation (S_2), which is developed in localised shear zones, and overprints and/or rotates (?) the S_1 foliation. The S_2 fabric is generally steeply N-dipping to vertical with an ESE orientation. An underground wall map (Figure 4.13) in the HW mine (drive B390), illustrates the gradual change from the weakly developed S_1 foliation on the right side of the map, to a well developed S_2 foliation in the shear zone. The S_1 foliation and F_1 fold axes appear to be rotated by about 10-15° clockwise, and a slightly steeper lineation on the S_2 foliation surface has developed. The S_2 foliation is also observed in other shear zones throughout the HW and Battle mines and several of these zones are shown on the map, Figure 4.7.

The development of localised shear zones and the steep S_2 fabric most likely occurred during the late stages of ductile deformation. The shear zones may have developed by an increase in the strain partitioning and/or a slight rotation in the principle strain axes. The S_2 fabric is offset by the earliest brittle structures, which are the steep D_{3a} faults.

(text continued on page 71)

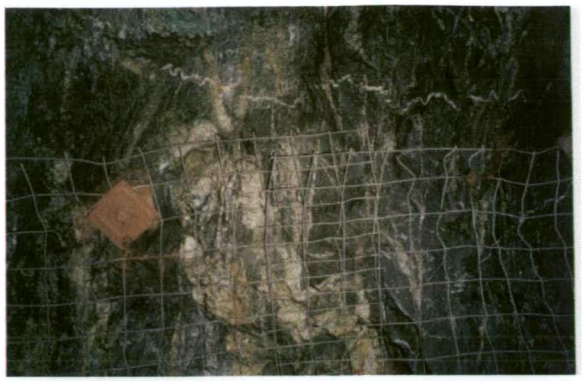

a

b

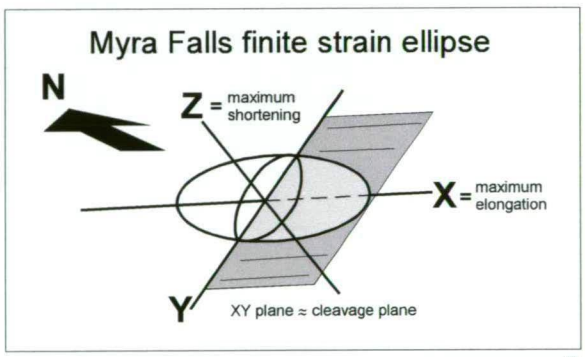

c

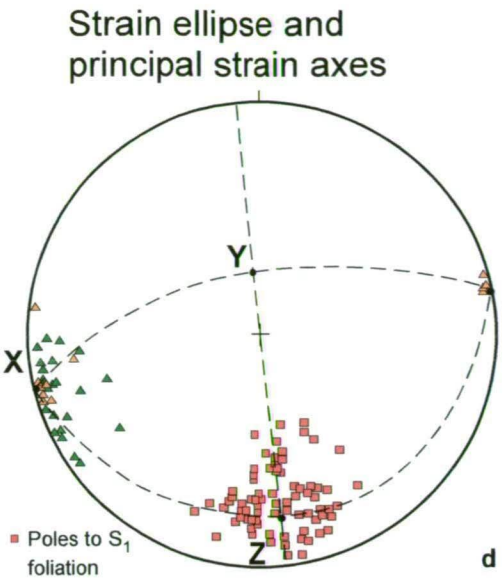

d

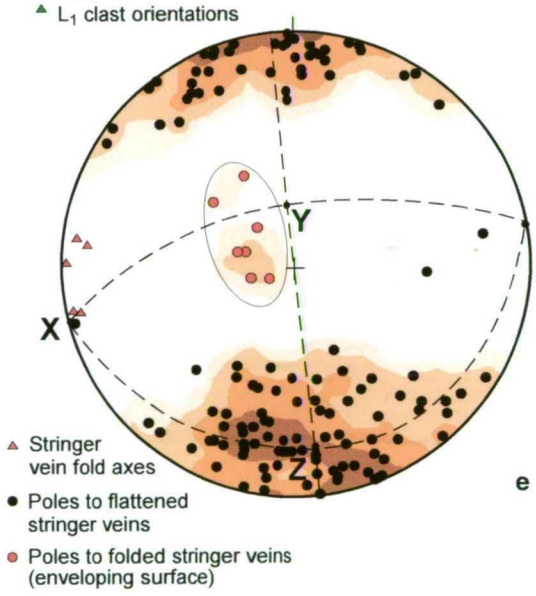

e

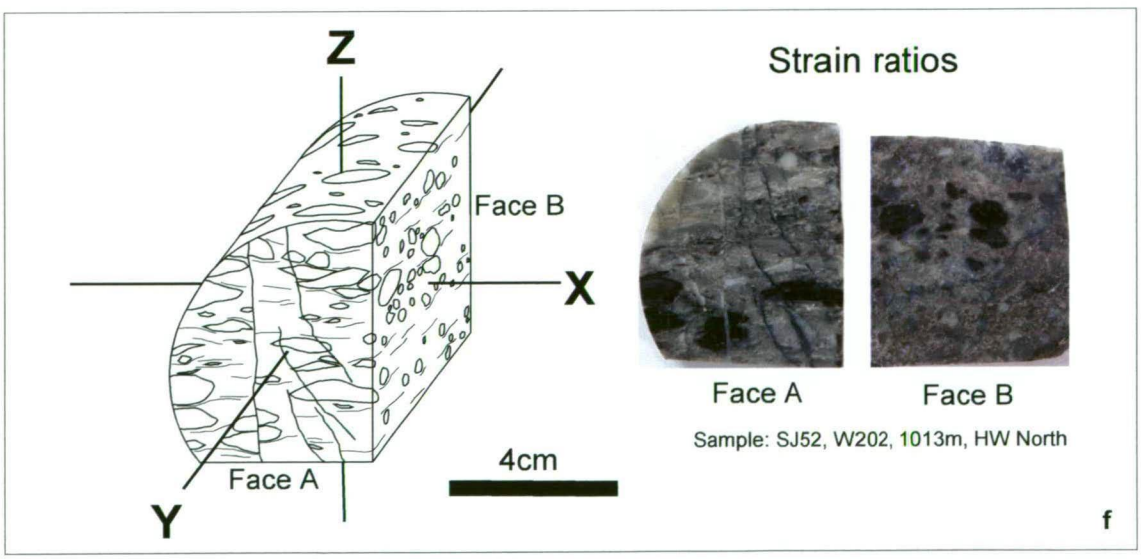

f

Figure 4.10a-b): Folded pyrite stringer veins in drive 23-331XN, HW mine; **c)** Strain ellipse for Myra Falls; **d)** Principal strain axes, with fold axes and L_1 clast axes parallel to X (maximum elongation), and the foliation sub-parallel to the X-Y plane; **e)** Stringer veins are sub-parallel to the S_1 foliation, whereas poles to boudinaged stringer veins plot at the X axis and poles to folded veins plot near the Y axis; **f)** A strain ratio of X:Y:Z =3.3:1.8:1 was estimated from stretched clasts (see discussion in text).

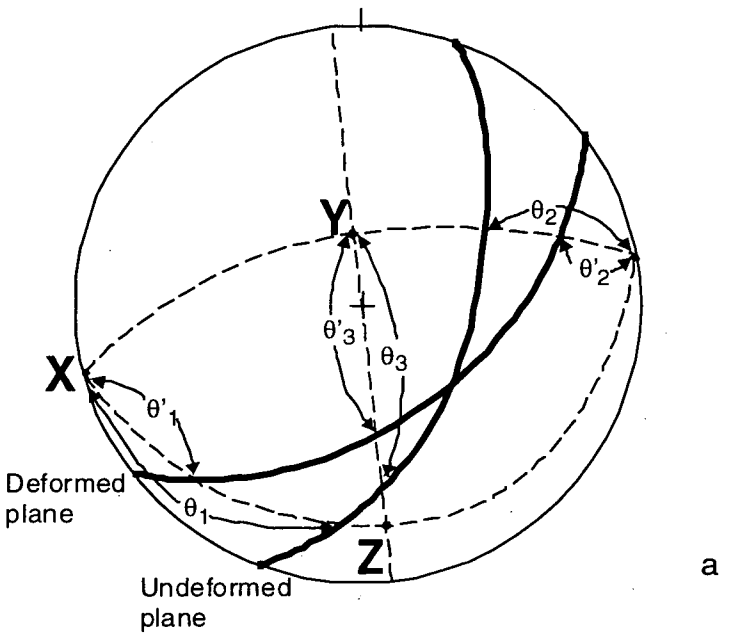

Figure 4.11a: Equal-area net construction of the spatial orientation of a plane before and after deformation.

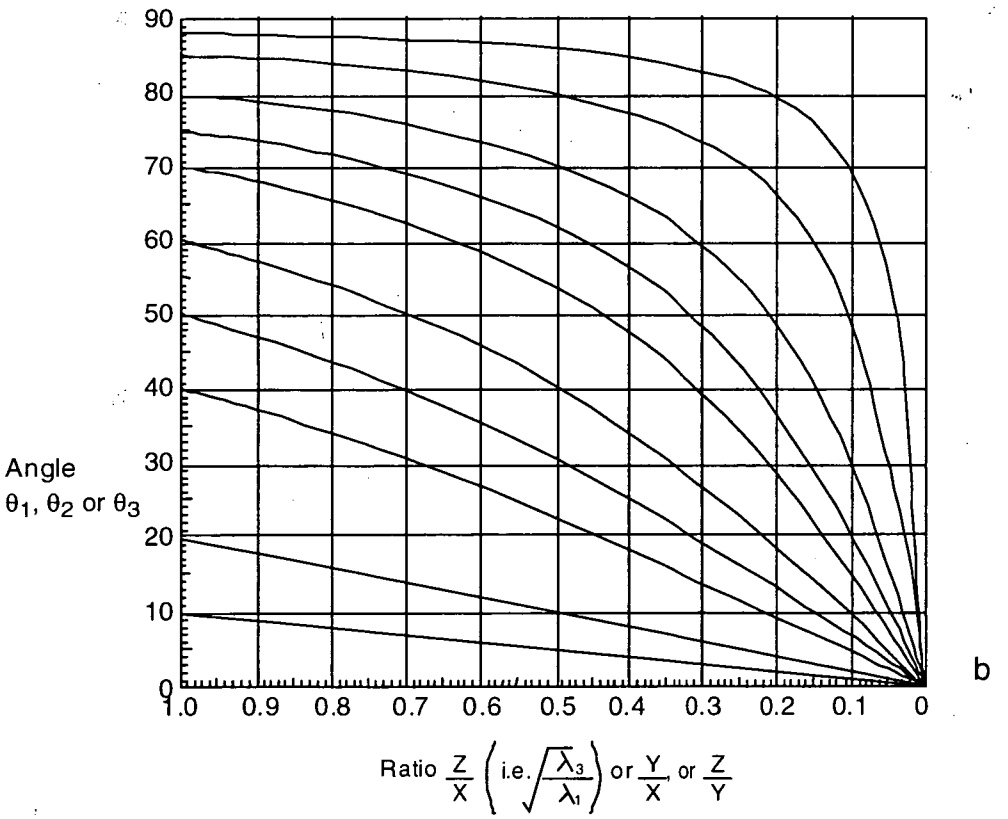

Figure 4.11b: Graphical solution of the relationships of θ_1 and θ'_1, θ_2 and θ'_2, θ_3 and θ'_3 of Figure 4.11a.

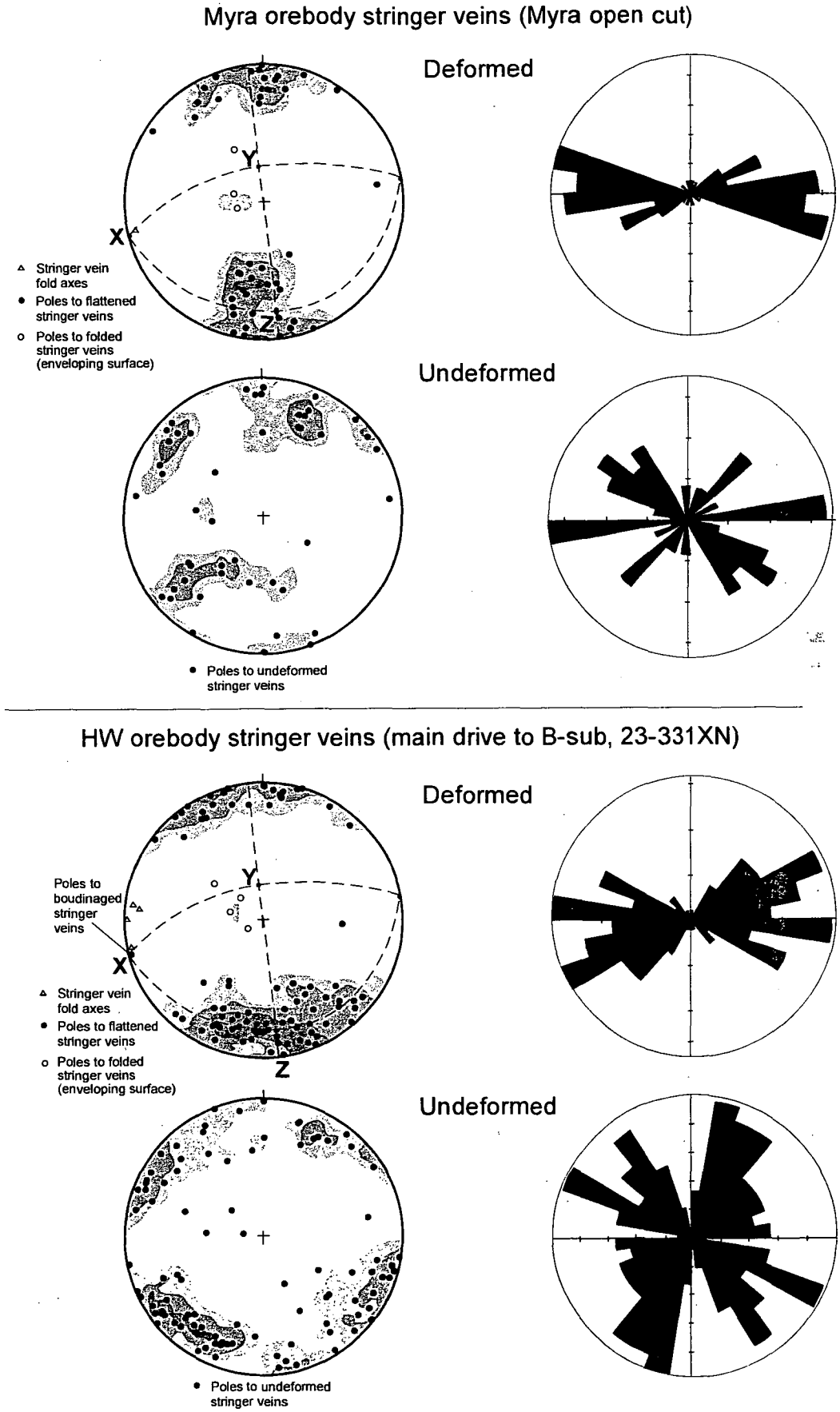

Figure 4.12: Stringer veins from the HW and Myra orebodies. For each area the effects of D_1 folding are removed and stringer veins are returned to their pre-D_1 orientations (see discussion in text).

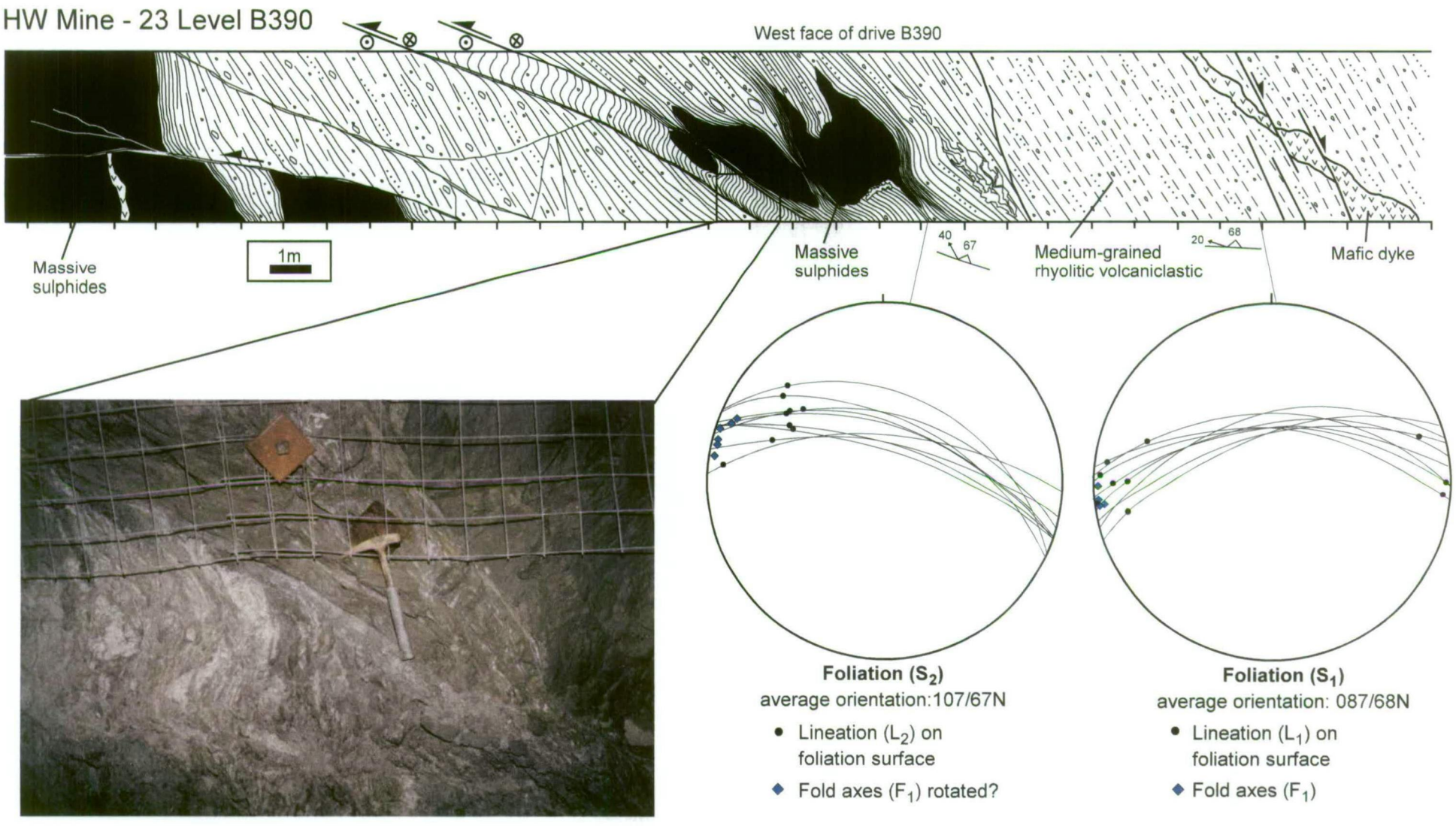

Figure 4.13: A second foliation develops in strong shear zones in drive B390, HW mine. This secondary fabric is observed in localised zones throughout the HW and Battle mines.

4.7 D_3 faulting

D_3 produced a two-stage evolution of faulting formed during N-S compression. Early steep, strike-slip faults are overprinted by shallow dipping thrust faults and bedding-parallel shears, similar to those described by Nixon et al. (1994), in northern Vancouver Island. Similar two-stage fault patterns are also described elsewhere. For example, Homberg et al. (1999), measured a large number of fault striations in the Jura Mountains in France, and managed to separate faults belonging to a single compressional event. These faults were generated in a two-stage evolution, with early steep strike-slip faults followed by shallow thrust faults, very similar to the patterns displayed by the D_{3a} and D_{3b} faults at Myra Falls.

4.7.1 D_{3a} strike-slip faults

D_{3a} faults are typically planar structures with well-developed coarse quartz-chlorite-epidote slickenfibres and chloritic polished surfaces (Figure 4.14). The fault striations are predominantly horizontal to shallow plunging and no fault gouge is associated with these faults. They are predominantly steeply dipping to vertical structures and have a very wide range of strike orientations. However, there is a consistent fault displacement pattern, with sinistral offsets occurring on faults striking NNE to E, and dextral offsets on faults striking W to NNW (Figure 4.15). There is slight variation in the dominant trends of the sinistral and dextral faults from area to area, but in general the fault pattern is fairly similar across the property. These faults are very common, and offsets are mostly minor, usually less than a metre. However, the large NE-oriented Myra-Price Fault and the NW-oriented Lynx-Phillips Fault may have formed during the D_3 event, with subsequent reactivation during the D_5 event. The timing of the large strike-slip displacements on these structures is unknown and could reflect both the D_3 and D_5 events.

The consistent fault pattern across the property, of NW-striking dextral faults and NE-striking sinistral faults, suggests that these faults may have formed during a single deformation event. Paleostress analysis of striations on faults from the areas outlined in Figure 4.3, was undertaken to determine whether the faults represented a single tectonic phase, and if so, the orientation of the stress field.

In an area affected by multiple deformation events, the orientation of the stress field predicted by striations from the oldest fault set, may not be correct if rotation occurred during subsequent tectonic phases. However, in the Myra Falls area, the oldest fault set, D_{3a}, is remarkably consistent across the property, with dominantly horizontal to shallow

Figure 4.14: Shallow plunging quartz-epidote fibres on a steep D_{3a} fault surface. Fault measured in Lynx open cut.

plunging slickensides resulting from a strike-slip regime. As these faults are steep to vertical, and slickensides are near-horizontal, this indicates that little or no rotation has occurred during subsequent tectonic phases, and paleostress analysis is appropriate. The HW mine area has the greatest number of measurements, and therefore, this area is discussed in the greatest detail for all fault groups.

N-S directed compressional is indicated by paleostress analysis of the D_{3a} striations. The histogram (Figure 4.16a) shows that a large proportion of the measured striations, fall within 18° error of the calculated striations for the given stress state. This suggests that the movement direction on these faults could be produced by a single regional stress field. The Mohr circle (Figure 4.16b) also indicates that most faults are favourably oriented for failure, as most striations plot in the area of high differential stress. The orientation of the nearest exact principal stress axes are shown on the Schmidt net (Figure 4.16c), indicating σ_1 is sub-horizontal with a N-S trend. This paleostress calculation was based on 85% of the fault data and the 85% were chosen using an initial orientation for σ_1 plunging 7° toward 168°.

4.7.2 D_{3b} thrust faults

D_{3b} faults differ markedly from the D_{3a} faults in their geometry, kinematics, and morphology. The D_{3b} faults predominantly strike E-W to NE-SW and have moderate to shallow N and S dips (Figure 4.17). They are common throughout the area, but are less visible than the steep D_{3a} faults, as they often develop parallel to bedding planes. They are predominantly wavy, slightly anastomosing structures with minor gouge. Slickenfibres are common, usually comprising quartz-chlorite and minor epidote fibres. Narrow cleavage zones, up to 5-10cm wide, are developed adjacent to these structures. D_{3b} faults consistently crosscut D_{3a} faults, and the displacement sense on most N-dipping D_{3b} faults is top to the S-SW and on S-dipping D_{3b} faults, top to the NE. Offsets on the D_{3b} faults are generally minor, up to 1-2m, where measured.

The D_{3b} faults most likely developed during NNE-SSW to NE-SW directed compression, based on analysis of D_{3b} striation data. Although this fault set is much smaller and less consistent than the D_{3a} fault set (possibly due to difficulties in separating some D_{3b} faults from D_5 faults), the histogram (Figure 4.18a) suggests that a large proportion of the measured striations fall within 18° error of the calculated striation direction for the given stress field. This suggests that the faults could be related to a single tectonic phase. The Mohr circle (Figure 4.18b) also indicates that most faults are favourably oriented for failure, with striations plotting in the area of high differential stress, although many have higher σ_n than optimal. Faults with high σ_n values, could represent P shears or reactivation of pre-existing surfaces, such as bedding. The orientation of the nearest exact principal stress axes are shown on the Schmidt net (Figure 4.18c), indicating σ_1 is sub-horizontal with a NNE trend. This paleostress calculation was based on 75% of the fault data, chosen using an initial orientation for σ_1 plunging 4° toward 058°.

The block diagram, (Figure 4.19) illustrates the change in stress states from D_{3a} to D_{3b} deformation and is modified from a model by Homberg et al (1999), who described a similar two stage evolution of strike-slip faults, followed by shallow thrust faults in the Jura Mountains in France. The fact that both the D_{3a} and D_{3b} faults have chlorite and epidote fibres, and little or no development of associated cleavage zones, indicates that these faults formed as early ductile-brittle fabrics, during N to NNE directed compression.

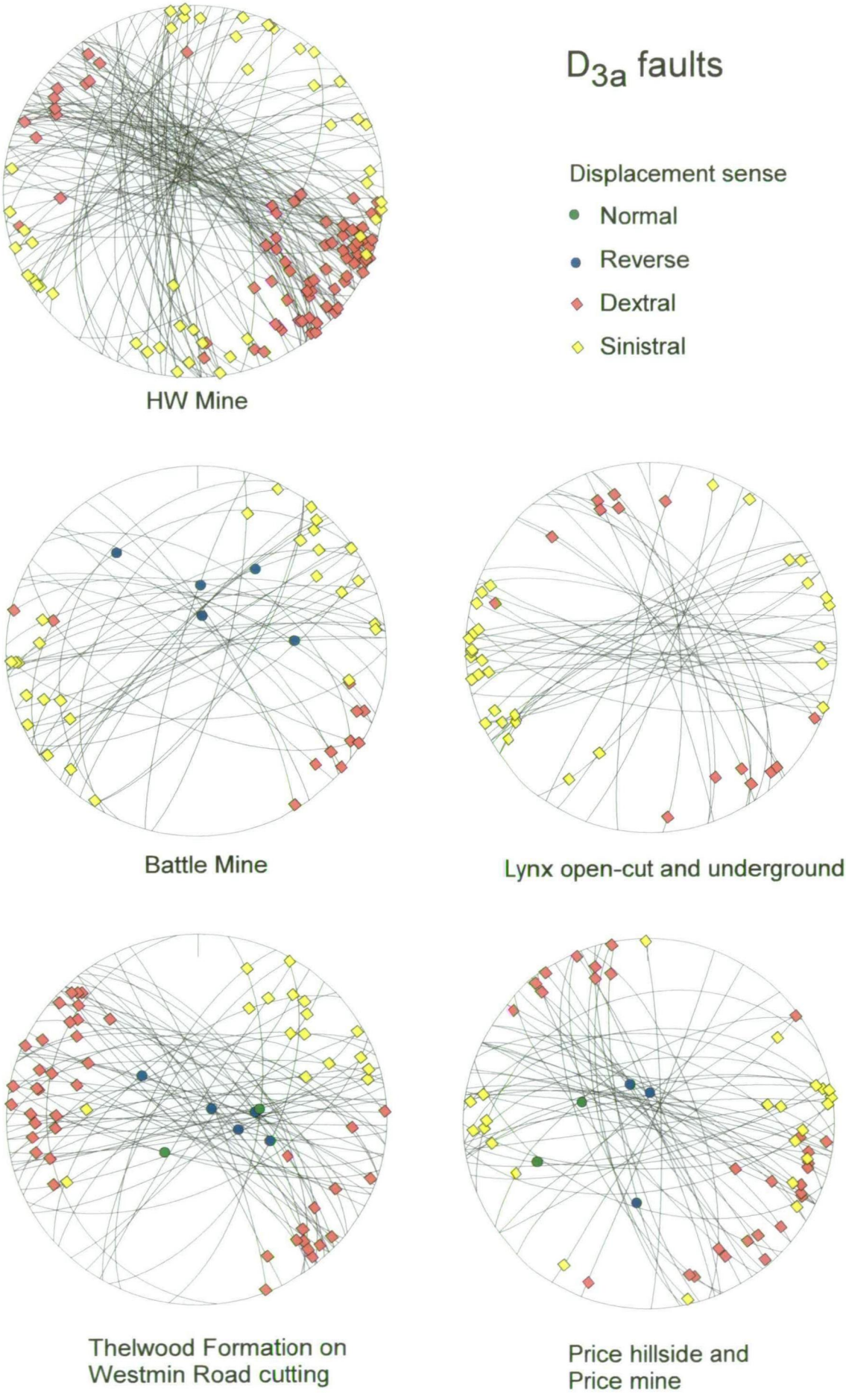

Figure 4.15: Stereonets illustrating the similar pattern of D_{3a} faults across the property, with NE-trending sinistral strike-slip faults and NW-trending dextral strike-slip faults.

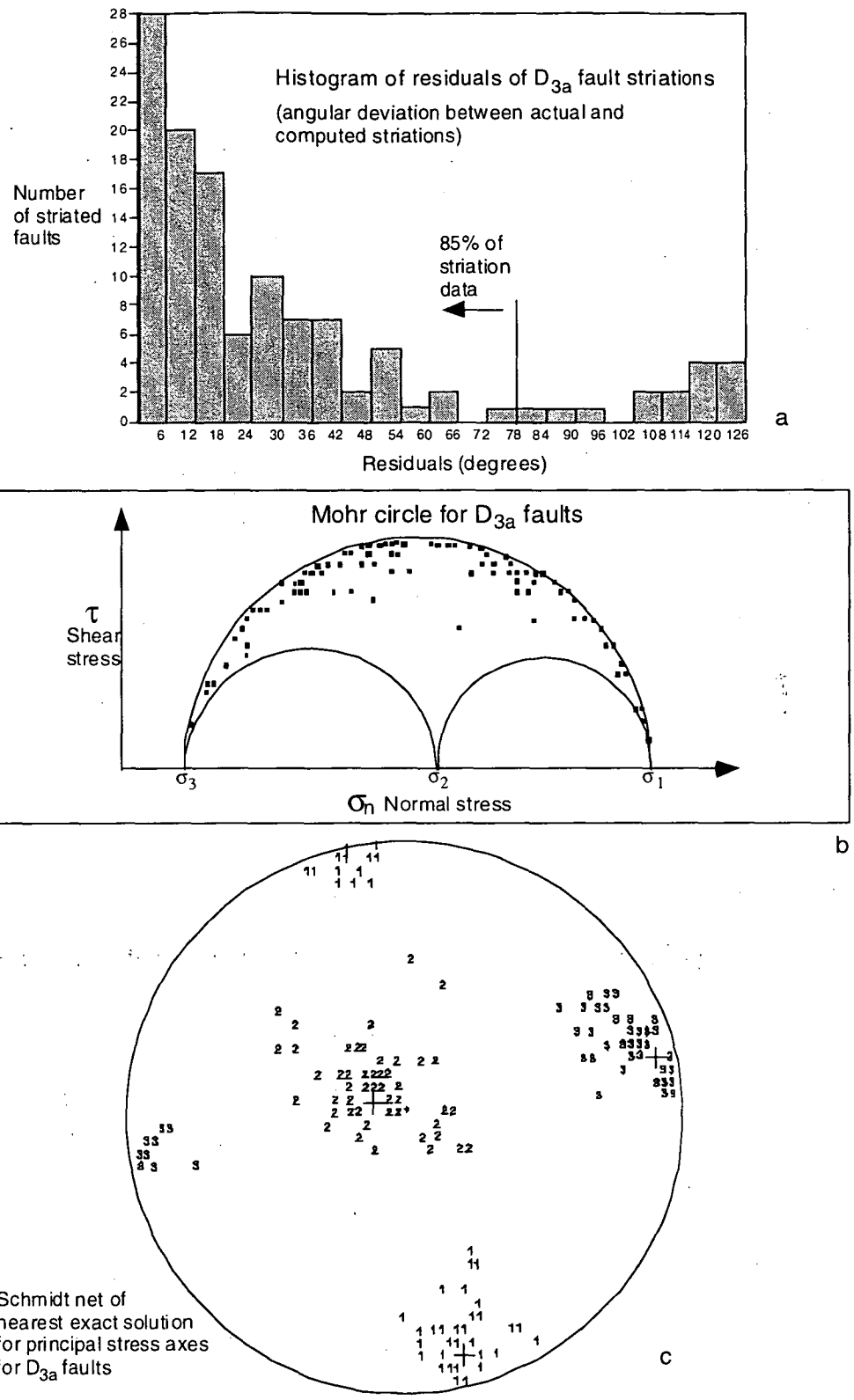

Figure 4.16: Interpretation of D_{3a} fault striations: **a)** Histogram of residuals, illustrating the angular deviation between actual and computed striations; **b)** The majority of D_{3a} faults are favourably oriented for failure on the Mohr plot; **c)** Schmidt net of the nearest exact solution for the principal stress axes, indicating σ_1 has a shallow plunge to SSE.

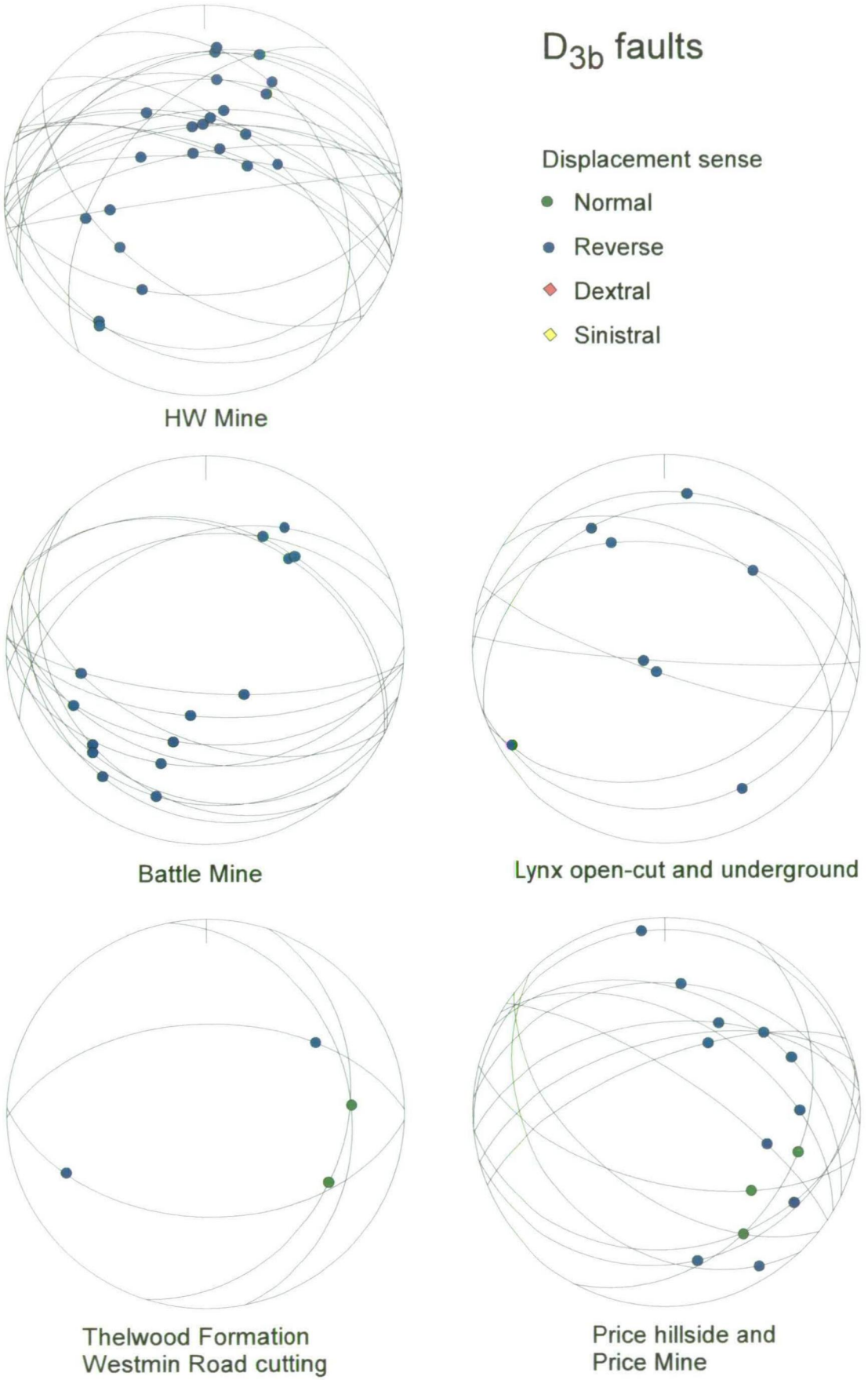

Figure 4.17: Stereonets illustrate D_{3b} faults at Myra Falls, which are typically E to ESE trending, shallow N and S dipping reverse faults.

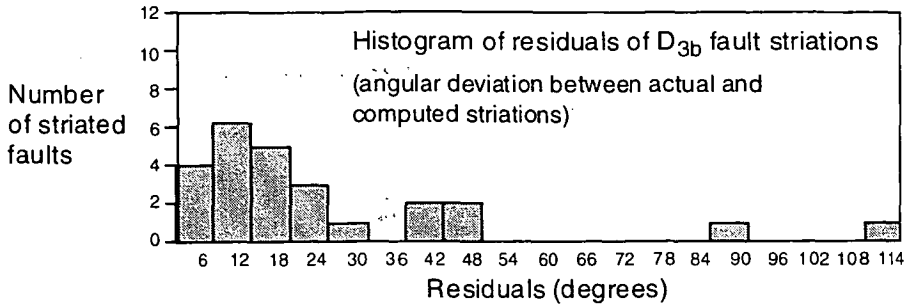

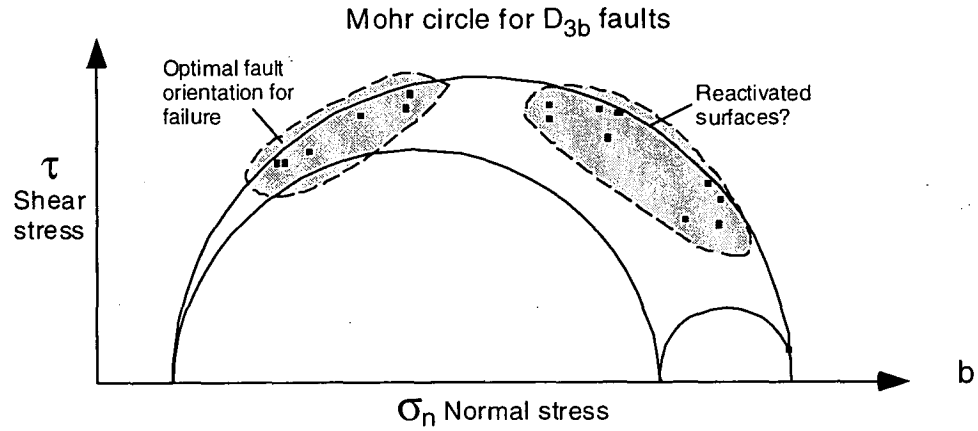

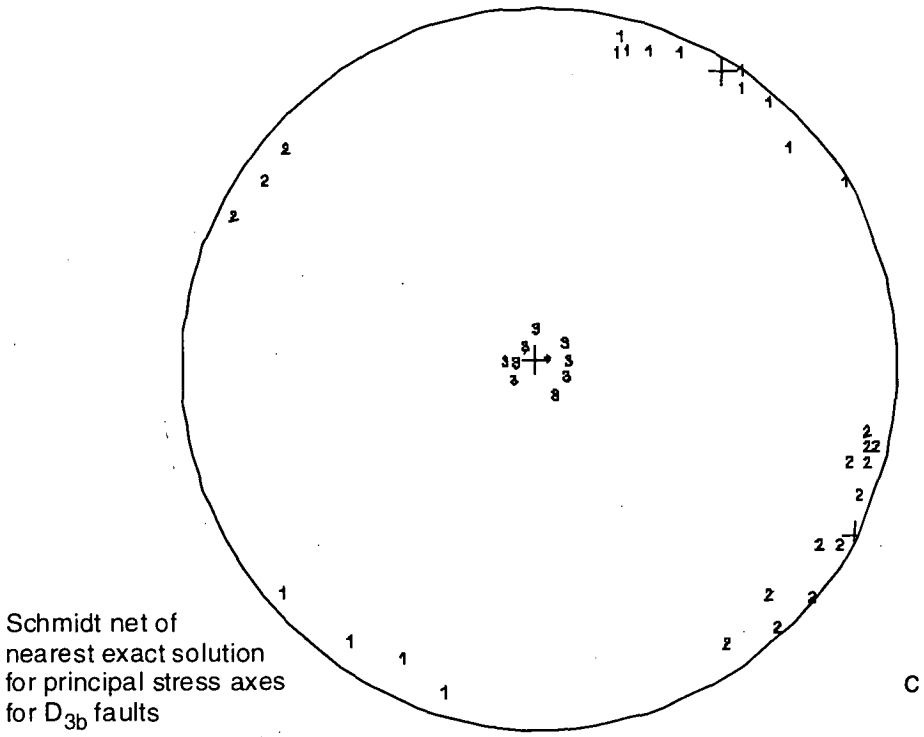

Figure 4.18: Interpretation of D_{3b} fault striations: **a)** Histogram of residuals, illustrating the angular deviation between actual and computed striations; **b)** Although many D_{3b} faults are favourably oriented for failure on the Mohr plot, many faults plot well below the failure envelope and may represent reactivated surfaces (see discussion in text); **c)** Schmidt net of the nearest exact solution for the principal stress axes, indicating σ_1 has a shallow NE plunge.

The interpreted D_3 fault pattern at Myra Falls is illustrated in the map, Figure 4.20. D_3 faults are mostly minor structures and are too numerous to show at the property-scale, with the exception of the Lynx-Phillips and Myra-Price Faults. However, the anisotropic pattern established by D_3 faulting is important, as it influences later deformation, with many D_3 structures, reactivated by the D_4 and D_5 events.

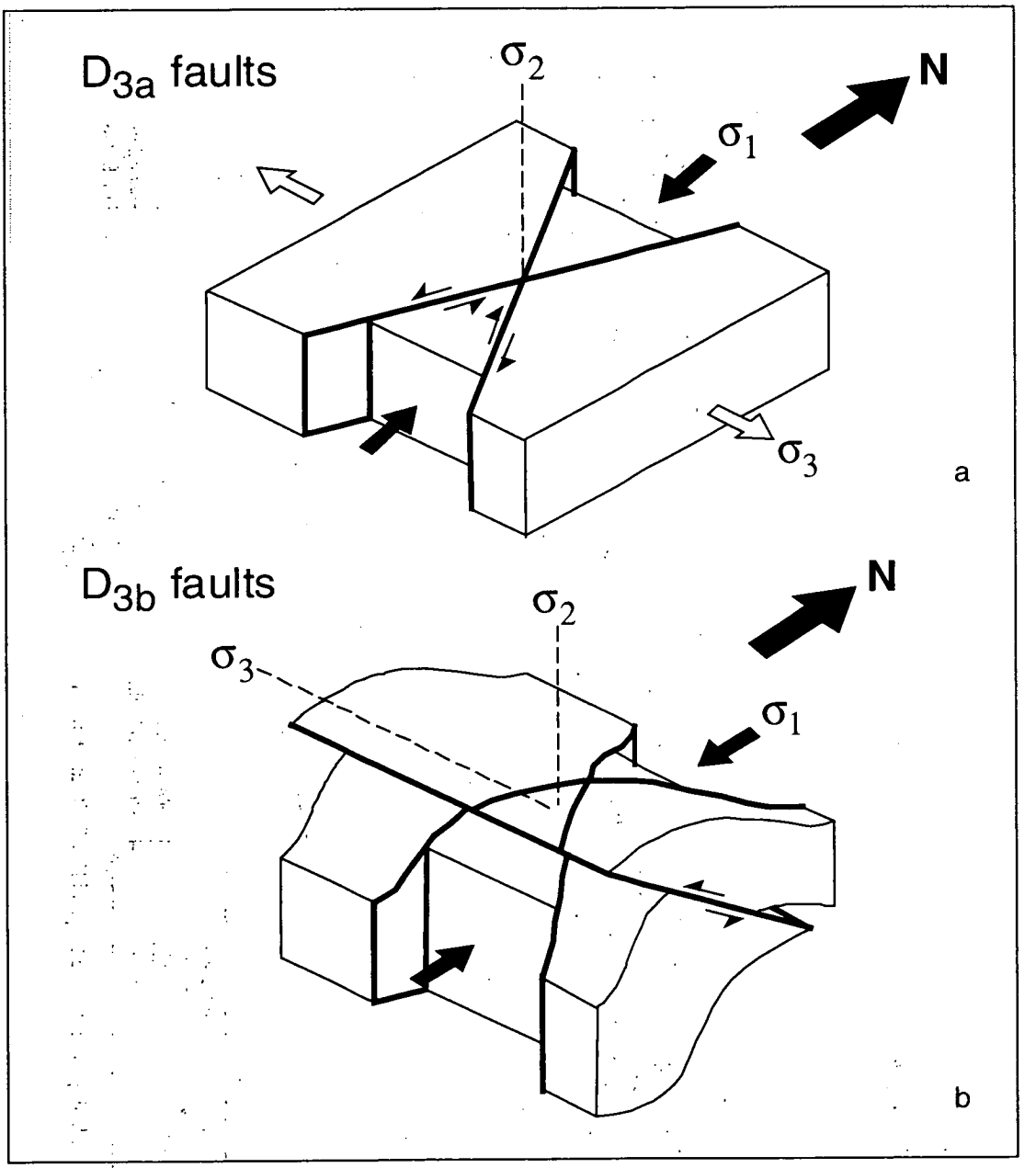

Figure 4.19: Block diagrams illustrating **a)** NE-trending sinistral and NW-trending dextral D_{3a} strike-slip faults, overprinted by **b)** E-W trending D_{3b} thrust faults (diagrams modified from Homberg et al., 1999).

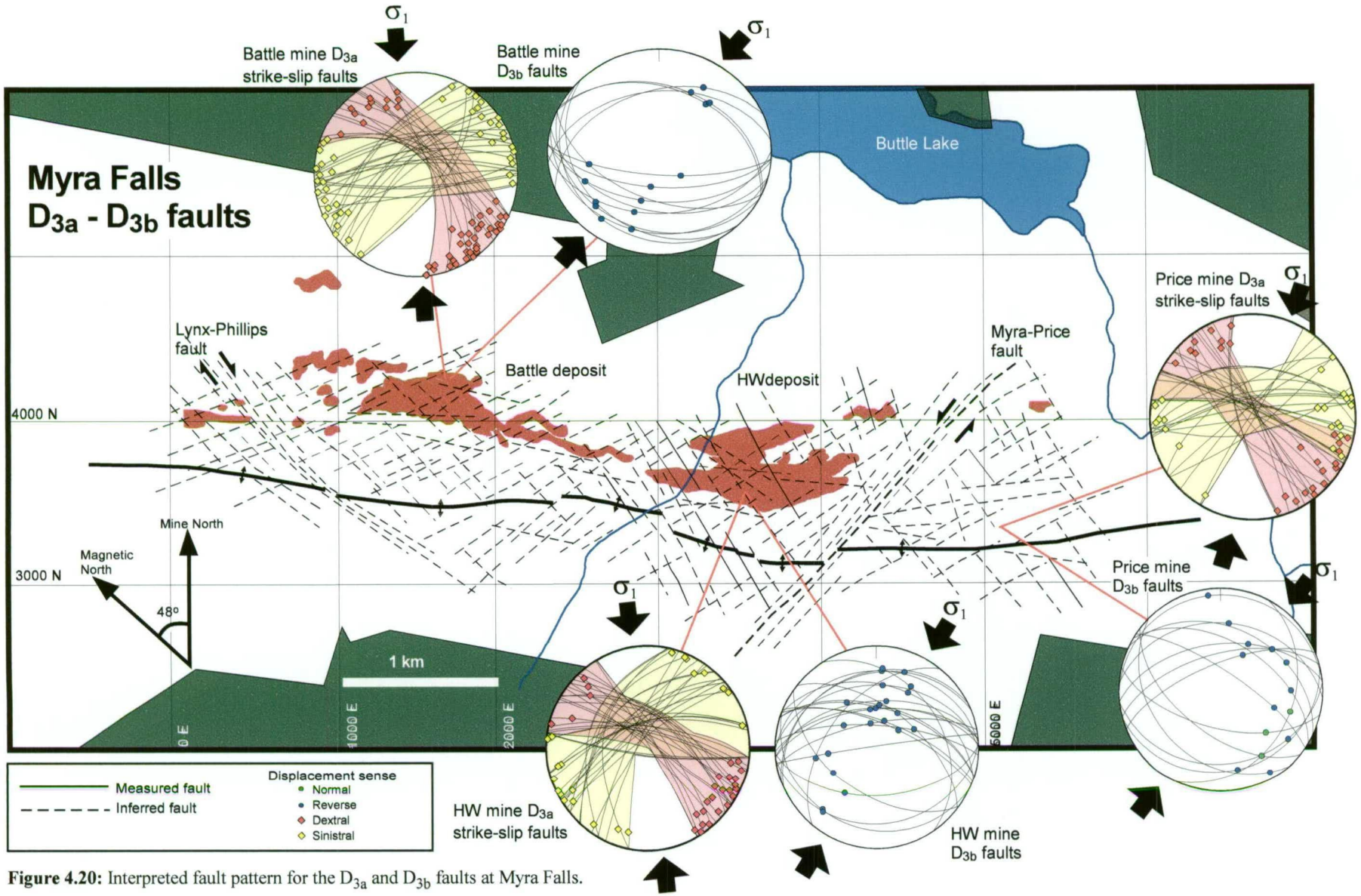

Figure 4.20: Interpreted fault pattern for the D_{3a} and D_{3b} faults at Myra Falls.

4.8 D_4 normal faults

D_4 produced steep normal faults with a wide array of orientations. D_4 faults are planar structures, with minor gouge and fine steep quartz fibres, and are often associated with quartz-carbonate veining. The stereonets in Figure 4.21 illustrate the variation in D_4 fault orientations across the property. D_4 faults predominantly strike NNW to NNE and are usually steeply dipping to vertical. The D_4 event commonly reactivates steeply dipping D_{3a} faults. Coarse shallow D_{3a} striations are commonly grooved and/or overgrown by the fine steep D_4 quartz fibres.

D_4 normal faults are common across the property, but are more abundant in localised zones, such as the East-Main Fault Zone on the western edge of the HW orebody, and the North Fault Zone, situated to the north of the Battle and HW orebodies. There is good evidence for the association of the East-Main Fault Zone with the D_4 event, with fine steep D_4 quartz fibres crosscutting and/or overgrowing horizontal coarse D_{3a} fibres on the East-Main fault planes, and the normal displacment of shallow D_{3b} faults. The steep East-Main Faults are then crosscut and displaced by steep NE-oriented sinistral strike-slip faults. However, no direct measurements were made of the North Fault Zone structures and this structure is interpreted as a D_4 fault based on the apparent sinistral offset of the North Fault Zone along the large NE-oriented D_5 Myra-Price Fault (Figure 4.1).

Although the overall displacement of a large fault zone may be quite substantial (e.g., greater than 100m in the North Fault Zone and approximately 50m East-Main Fault Zone), the offset on individual D_4 faults is minor, generally less than 10m. Faults are spaced 5-10m apart and Figure 4.22a shows an example of one of these structures in the HW mine. Massive sulphides of the main HW lens have been down thrown about 10m and now lie in fault contact with the andesitic footwall. Figure 4.22b shows abundant planar D_4 faults offsetting laminated mudstone of the Thelwood Formation in a Westmin Road cutting above Buttle Lake. D_4 faults are also abundant in the 43 Block area of the HW mine (Figure 4.23). Normal displacements are clearly indicated by quartz-chlorite slickenfibres (Figure 4.23a) and by fault drag adjacent to the steep structures (Figure 4.23b).

The consistent fault pattern seen across the property suggests that these faults formed during the same deformation event. E-W extension is indicated by paleostress analysis of the D_4 striations. The histogram (Figure 4.24a) shows that a large proportion of the measured striations, fall within 24° error of the calculated striations for the given stress state. This indicates that the movement direction on these faults can be produced by a single regional stress field. The Mohr circle (Figure 4.24b) also indicates that many faults

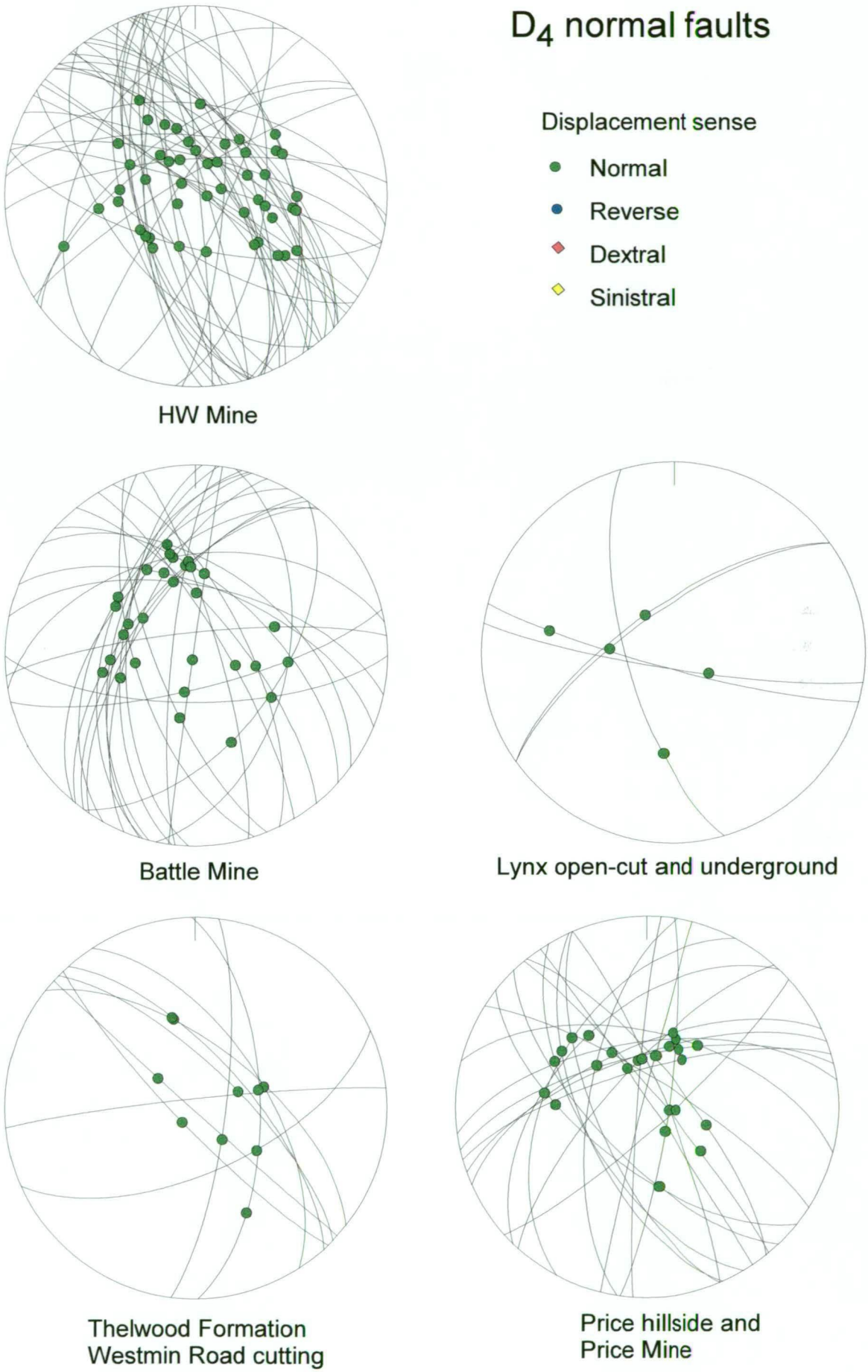

Figure 4.21: Stereonets illustrate D_4 faults at Myra Falls.

are favourably oriented for failure, as most striations plot in the area of high differential stress. However, faults, which plot well below the failure envelope may represent reactivated surfaces, such as bedding, or D_3 fault planes. The orientation of the nearest exact principal stress axes are shown on the Schmidt net (Figure 4.24c), indicating σ_1 is sub-vertical, whereas σ_3 trends E-W to ENE-WSW and is not as well constrained. This paleostress calculation was based on 80% of the fault selected using an initial orientation of σ_1 plunging 82° toward 192°.

The map, Figure 4.25, illustrates the inferred fault pattern for the D_4 event, with measured faults shown in solid lines and inferred faults by dashed lines. In many places the D_4 fault pattern is similar to the D_{3a} fault pattern, reflecting the previous anisotropy established by the D_3 event.

(text continued page 89)

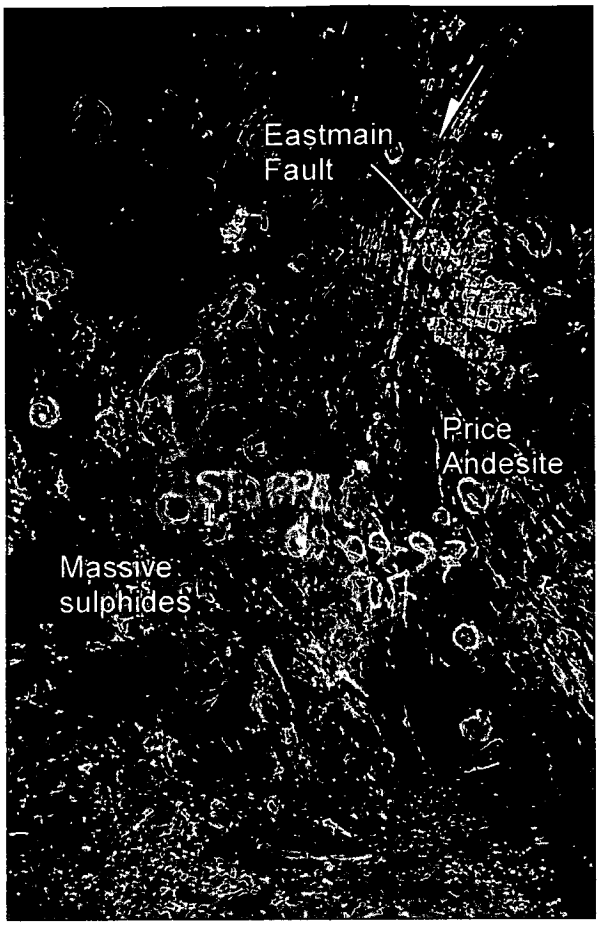

a

Figure 4.22: Examples of D_4 faults; **a)** Eastmain fault just off the main access drive to B-sub, HW mine (23-331XN). Massive sulphides are downthrown about 10m and are now in fault contact with the footwall, Price Andesite (for scale, rock bolts are 16cm wide); **b)** D_4 normal faults offset laminated mudstone of the Thelwood Formation in a road cut above Buttle Lake (roadcut is approximately 10m high).

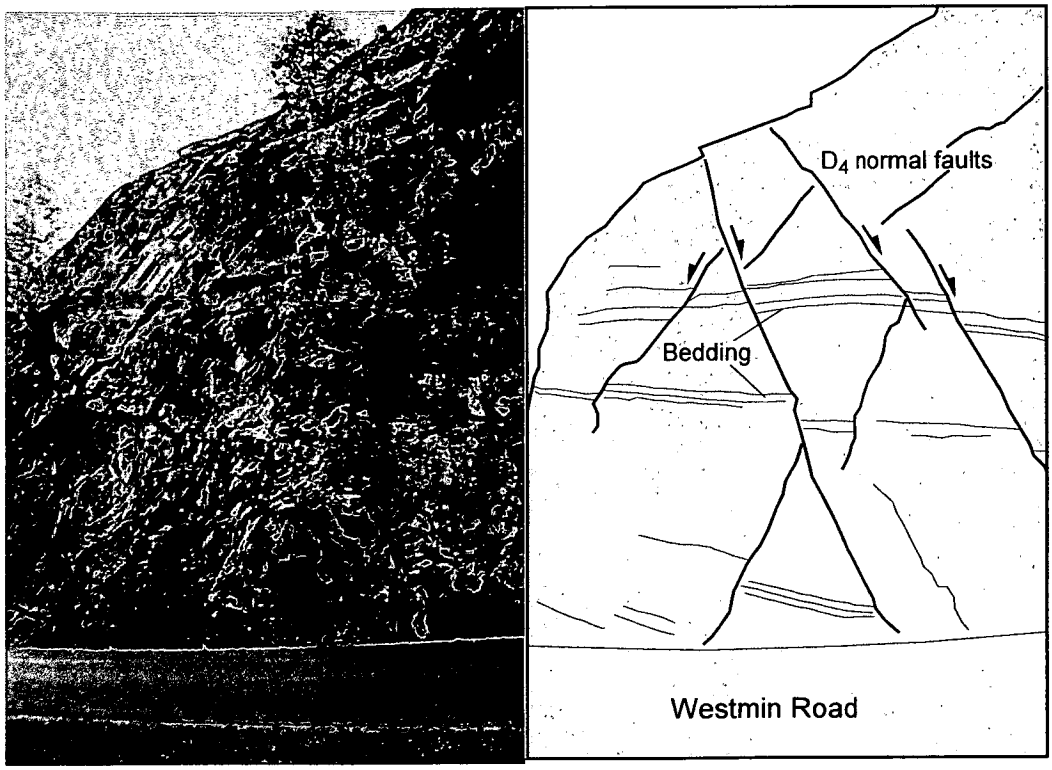

b

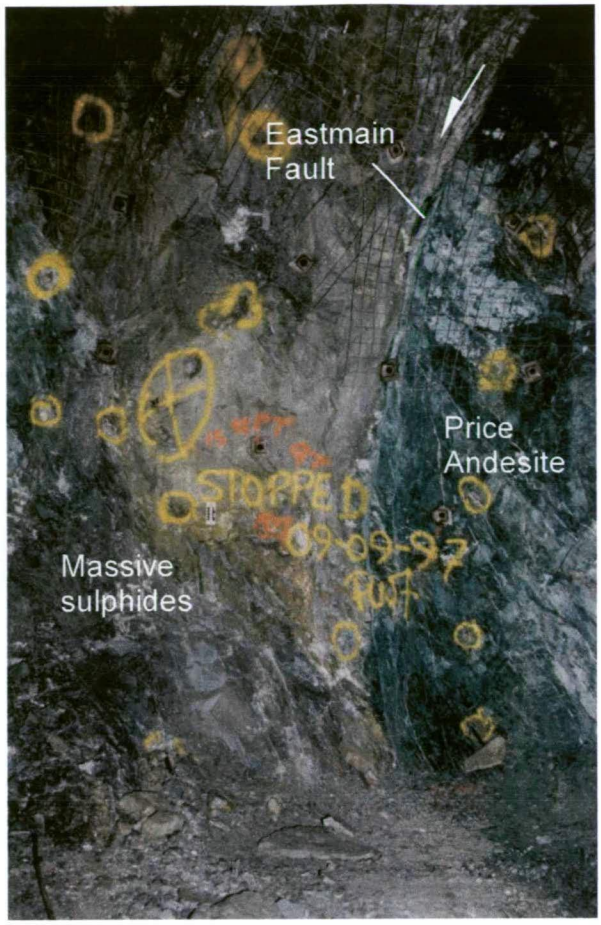

a

Figure 4.22: Examples of D_4 faults; **a)** Eastmain fault just off the main access drive to B-sub, HW mine (23-331XN). Massive sulphides are downthrown about 10m and are now in fault contact with the footwall, Price Andesite (for scale, rock bolts are 16cm wide); **b)** D_4 normal faults offset laminated mudstone of the Thelwood Formation in a road cut above Buttle Lake (roadcut is approximately 10m high).

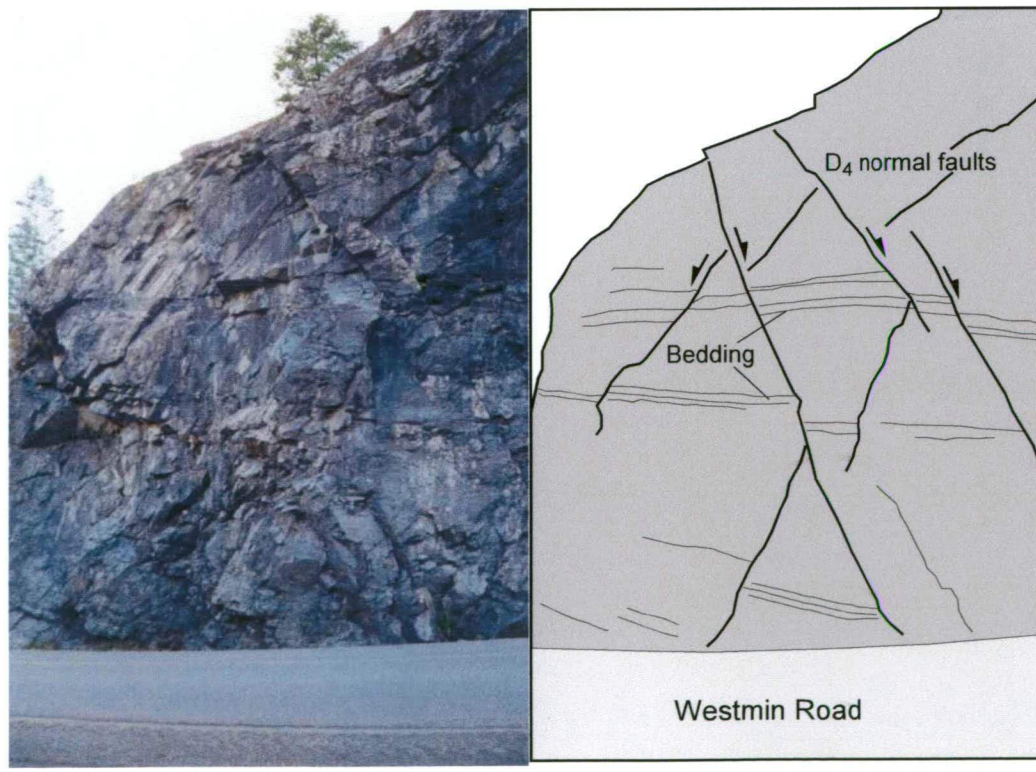

b

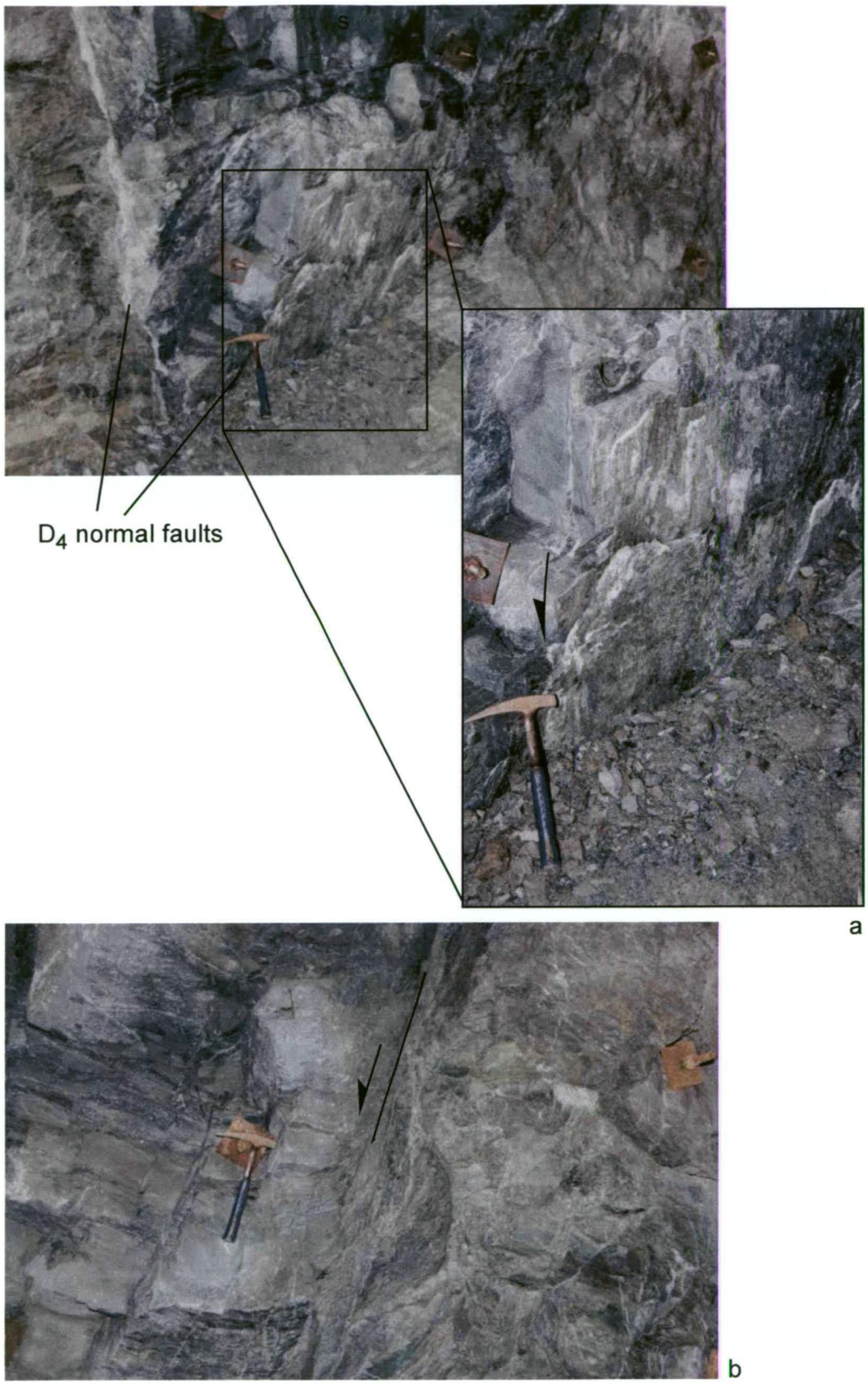

Figure 4.23: Typical D_4 normal faults in drive 23-427, 43 Block area of the HW mine. **a)** Two D_4 normal faults intersect at a high angle, and are associated with quartz-carbonate veining. The inset shows the development of quartz-chlorite slickenfibres on the fault surface, indicating normal displacement; **b)** Fault drag of bedding adjacent to a D_4 fault indicates normal displacement.

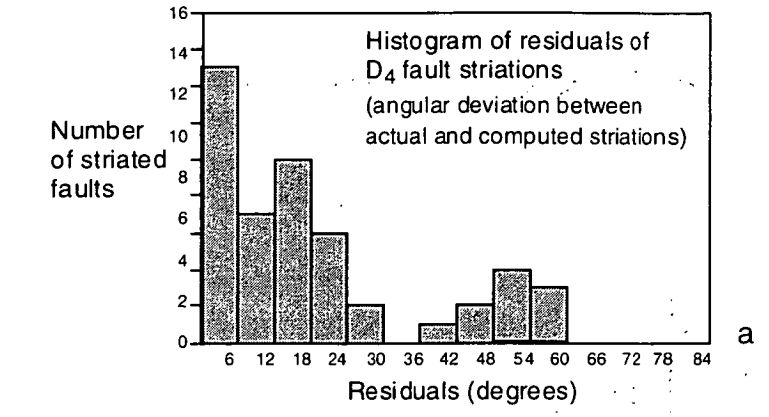

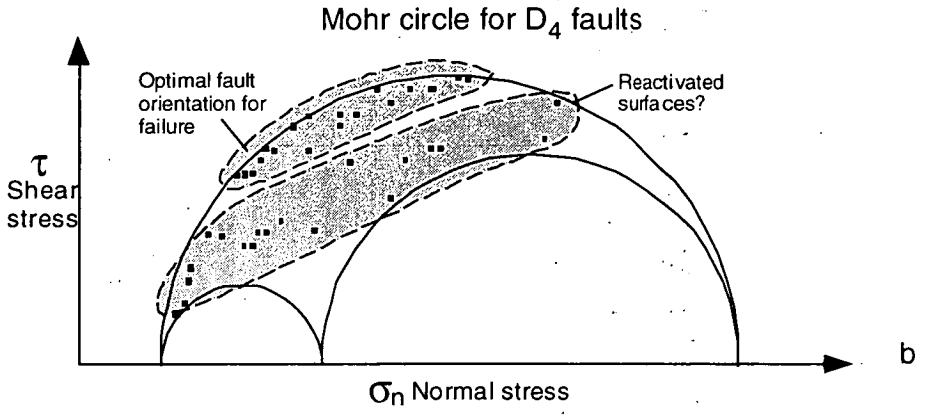

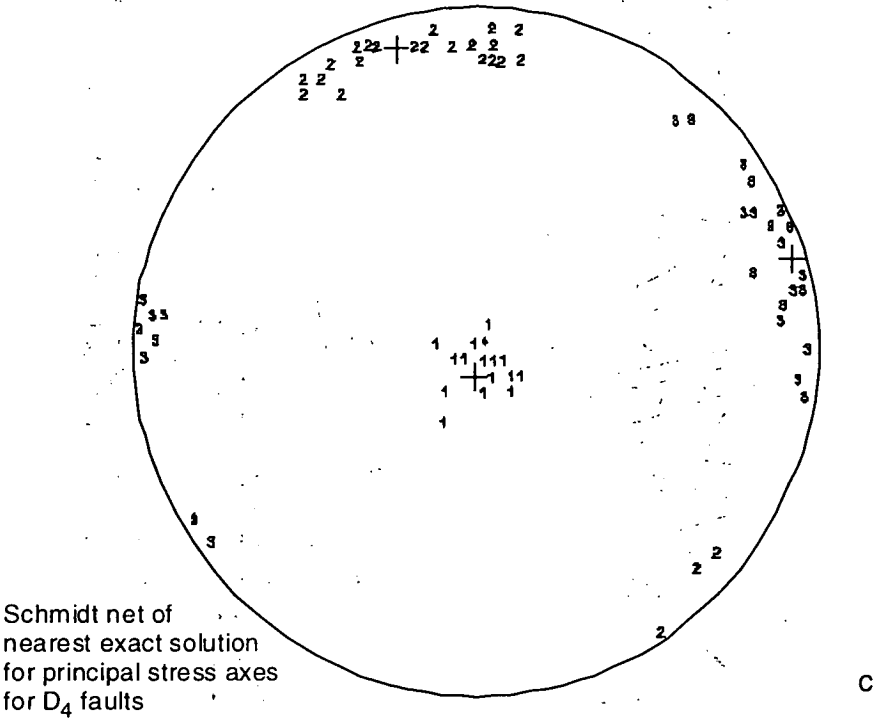

Figure 4.24: Interpretation of D_4 fault striations; **a)** Histogram of residuals, illustrating the angular deviation between actual and computed striations; **b)** The majority of D_4 faults are favourably oriented for failure on the Mohr plot; **c)** Schmidt net of the nearest exact solution for the principal stress axes, indicating $\sigma 1$ is close to vertical.

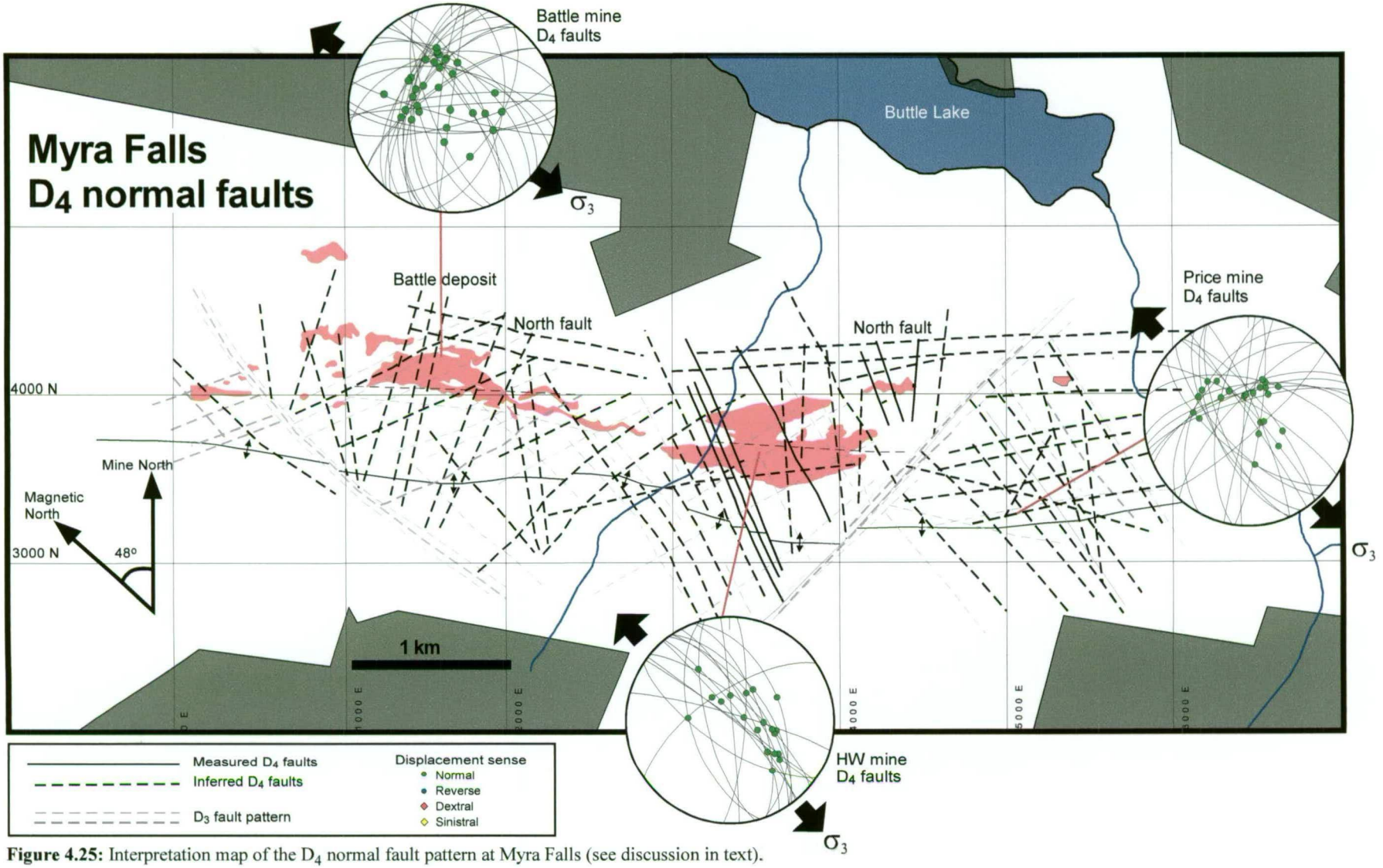

Figure 4.25: Interpretation map of the D_4 normal fault pattern at Myra Falls (see discussion in text).

4.9 D_5 gouge-rich oblique thrust faults and strike-slip faults

D_5 produced N-dipping oblique thrust faults and steep NE to E- and NW-oriented strike-slip faults. Large D_5 faults at Myra Falls include the reactivated Myra-Price Fault zone and the Flat Fault. D_5 structures differ markedly from structures formed during earlier deformation events. The faults are very gouge-rich, wavy, anastomosing structures, and are commonly associated with irregular, clear to milky quartz veins. Broad cleavage zones, up to several metres wide, are developed around these faults.

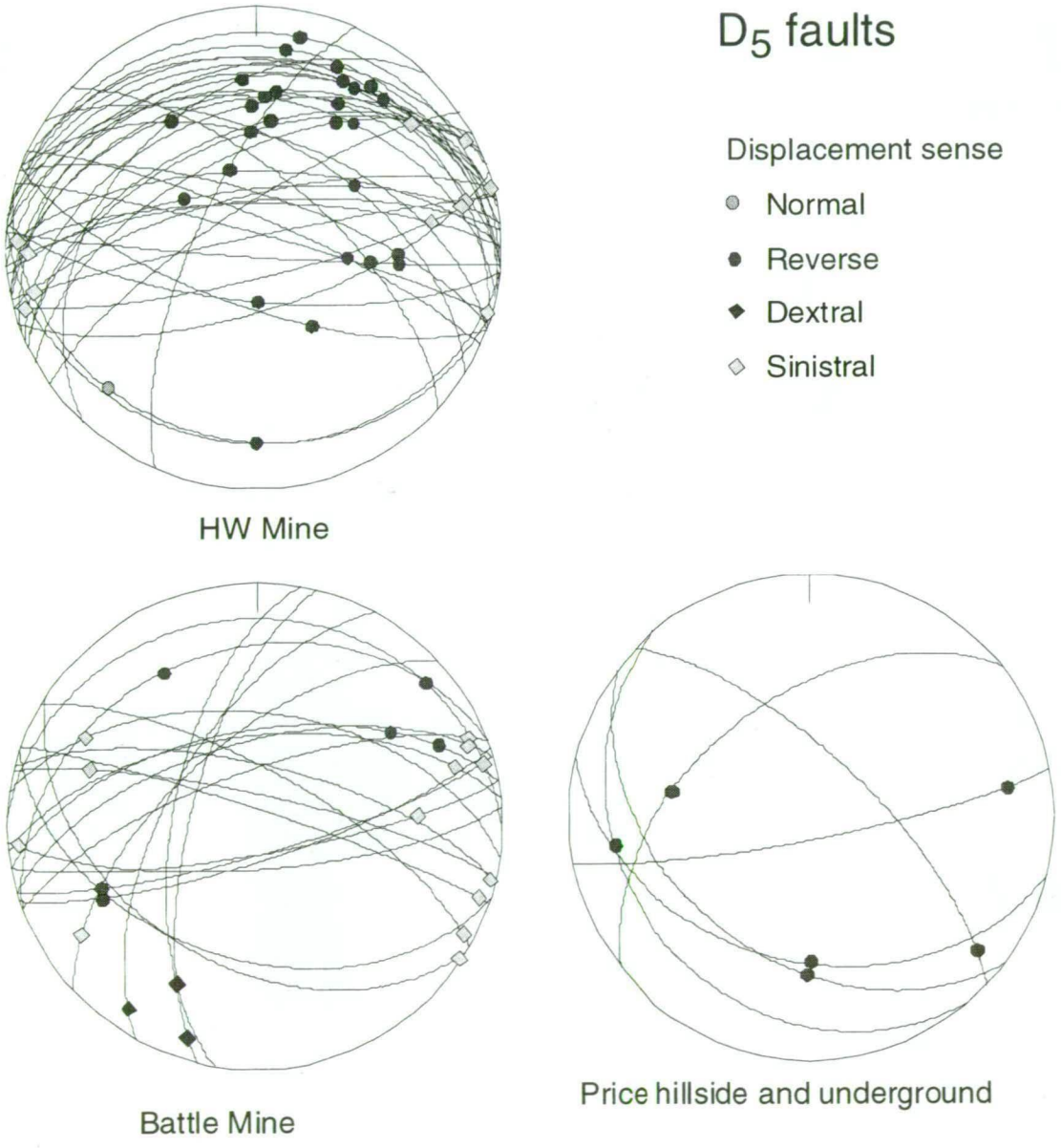

Figure 4.26: Stereonets illustrating D_5 faults at Myra Falls.

D_5 sinistral strike-slip faults most commonly strike NE to E, with moderate to steep N dips (Figure 4.26). D_5 thrust faults predominantly have shallow to moderate N and S dips, with a consistent displacement sense of top to the SW on N-dipping thrust faults and top to the NE on S-dipping faults (Figure 4.26). Fault striations on the steep strike-slip faults are shallow plunging to horizontal, and are oblique on the shallow to moderately dipping thrust faults. Slickenfibres are rare on these faults, instead, fault striations are mostly fine grooves in the fault gouge on fault surfaces. For this reason, the sense of displacement on these faults is estimated from foliation and bedding drag.

Major D_5 faults at Myra Falls are shown as in Figure 4.27, with inferred D_5 faults shown by dashed lines. The D_5 faults commonly occur as groups of faults, spaced 1-5m apart, and form wide disrupted zones. Although offsets on individual structures are typically 1-5m, the overall displacement across a large fault zone can be several 100s of metres. The largest D_5 fault zone is the NE-oriented Myra-Price Fault, which displays a significant displacement, up to 300m, making it clearly visible on the footwall contour map (Figure 4.1). The timing of this displacement is uncertain, as this structure is most likely a reactivation of an earlier D_3 structure.

Gouge-rich D_5 faults are ubiquitous throughout the Myra Falls area, and examples are shown in Figures 4.28 and 4.29. Figure 4.28a illustrates a steep anastomosing sinistral strike-slip fault in the Battle mine. The siliceous caprocks are displaced and fragmented by the steep fault, and are now in fault contact with the adjacent massive sulphides (an apparent down-throw). Another steep D_5 fault is shown in Figure 4.28b, with coarse-grained volcaniclastic rocks in fault contact with fine-grained andesite in drive 23-427, 43 Block HW mine. A close-up view of this fault is shown in Figure 4.28c, with abundant gouge and quartz veining associated with the structure. D_5 faults commonly offset D_4 normal faults and Figure 4.29a illustrates this relationship, with a steep D_4 normal fault, sinistrally offset on a steep D_4 fault. Figure 4.29b shows a gouge-rich flat fault in the HW mine (drive B390), with massive sulphides thrust over the rhyolitic hangingwall rocks. Strong foliation drag is commonly developed adjacent to these shallow to moderately dipping thrusts and is shown in Figure 4.29c (drive C355DD, HW mine). The foliation drag is consistent with an oblique thrust with a top to the west sense of displacement.

In many places, D_5 structures appear to have had the greatest effect on the sequence, and this is evident in the footwall contours (Figure 4.1). Underground maps also indicate the major effect of the D_5 structures. For example, a map of drive C355DD in the HW mine, shows that the position of ore and rhyolitic hangingwall rocks is controlled by shallow-

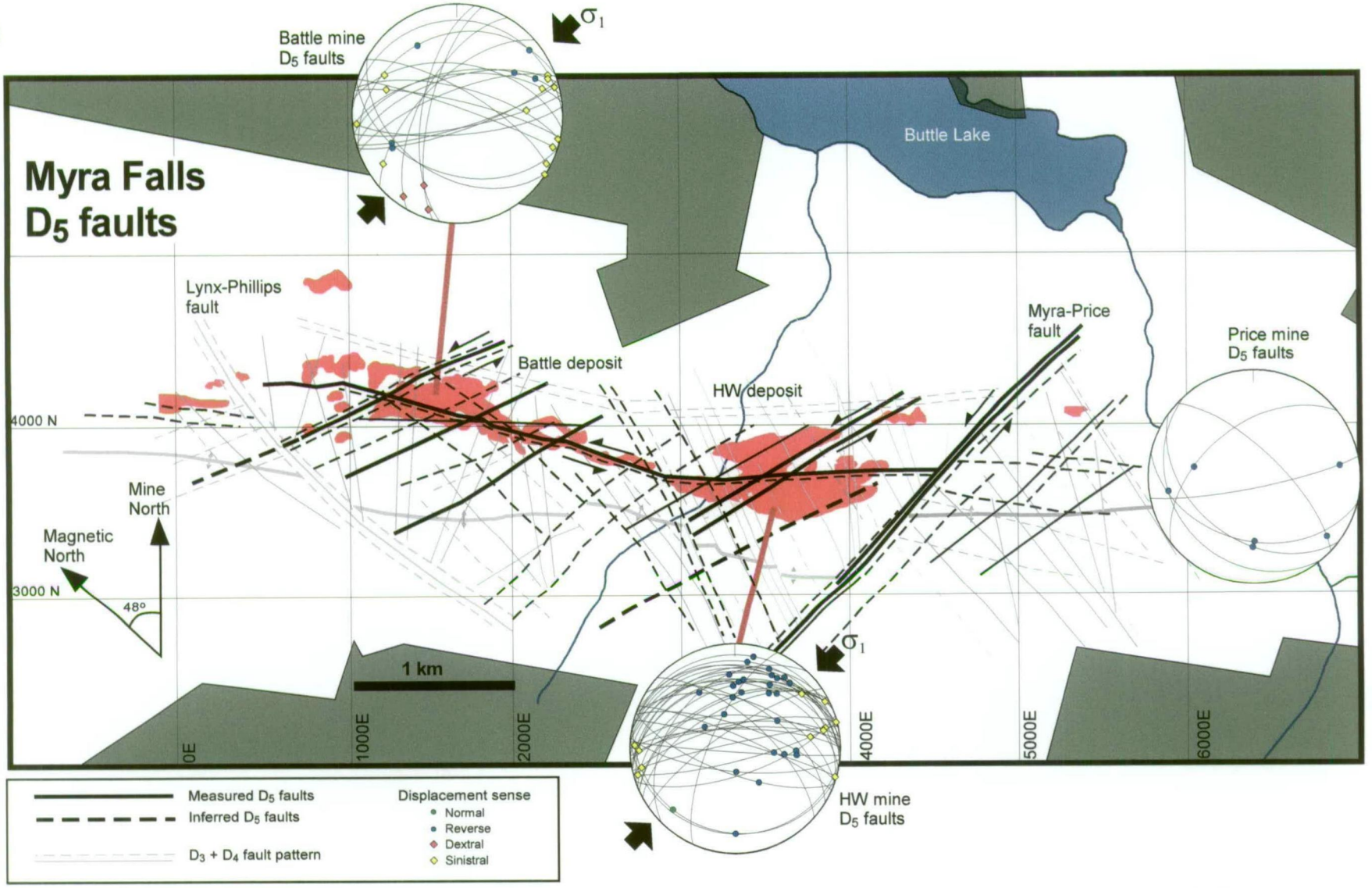

Figure 4.27: Major gouge-rich D_5 faults at Myra Falls, with steep NE-trending sinistral strike-slip faults, steep NW-trending dextral strike-slip faults, and shallow to moderately N-dipping gouge rich thrust faults (e.g., Flat Fault).

dipping oblique D_5 thrust faults, with a top to the west sense of displacement (Figure 4.30). These structures are the most recent in this area, offsetting many D_3 and D_4 faults.

The steep strike-slip faults appear to be coeval with the shallow thrusts as the structures commonly display mutually crosscutting relations. Paleostress analysis of D_5 striations also indicates that these structures could have formed during a single NE-SW compressional event. The histogram (Figure 4.31a) shows that the majority of measured striations fall within 30° error of the calculated striations for the given stress state, suggesting that they may be related to a single tectonic phase. The Mohr circle (Figure 4.31b) also indicates that many faults are favourably oriented for failure, as most striations plot in the area of high differential stress. The orientation of the nearest exact principal stress axes are shown on the Schmidt net (Figure 4.31c), indicating σ_1 is sub-horizontal with a NE-SW trend. This paleostress calculation was based on 85% of the fault data selected using an initial σ_1 plunging 4° toward 041°.

D_5 faults display a much greater degree of scatter on the Schmidt net of the nearest exact solutions for the stress tensor (Figure 4.31c) than previous events, and many faults plot well below the failure envelope on the Mohr circle (Figure 4.31b). However, the distinct morphology of D_5 faults and their consistent timing relations suggest that they are related to a single tectonic phase, even though the striation data is difficult to model. The largest faults at Myra Falls (Myra-Price and Lynx-Phillips Faults), belong to the D_5 event. These faults have displacements up to 300m, which are clearly evident on the footwall contours (Figure 4.1). In large fault systems it is difficult to get a good fit for the striation data because of rotation of local stress fields and local stress effects. The remarkably good fit of striation data for the D_3 and D_4 events indicates that the D_5 event did not rotate the earlier structures outside localised zones immediately adjacent to the D_5 structures. Care was taken when measuring faults, to avoid areas of obvious fault drag, which may account for the lack of evidence of rotation of the D_3 and D_4 faults in the database.

(text continued on page 96)

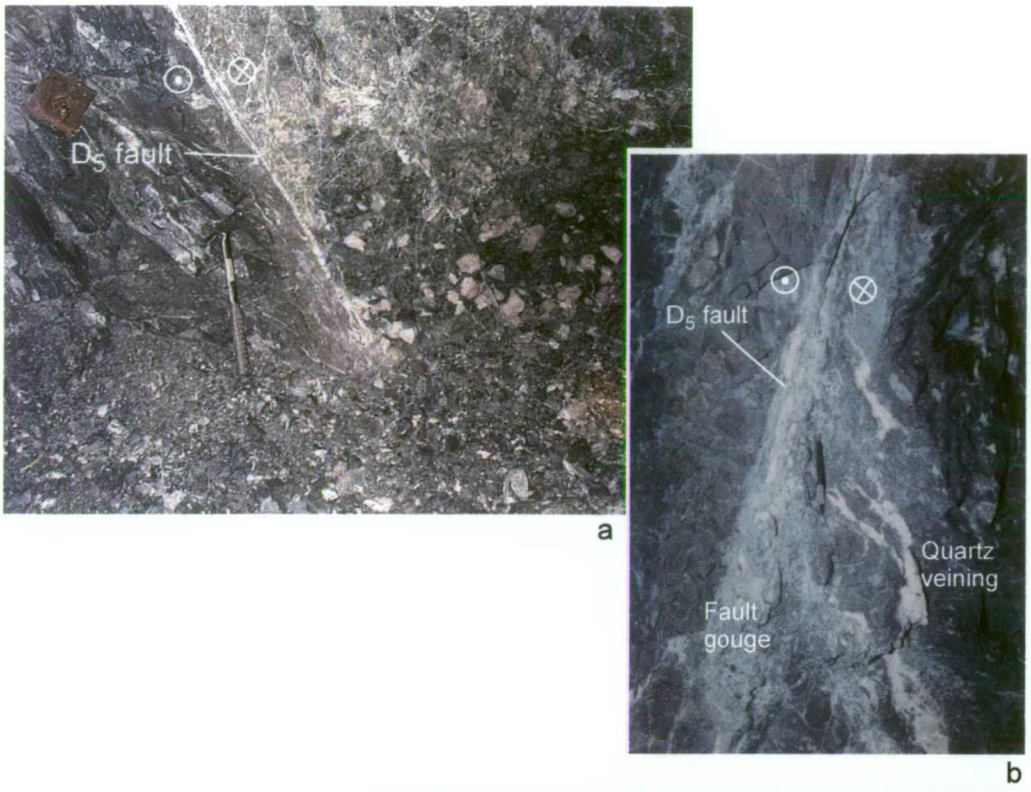

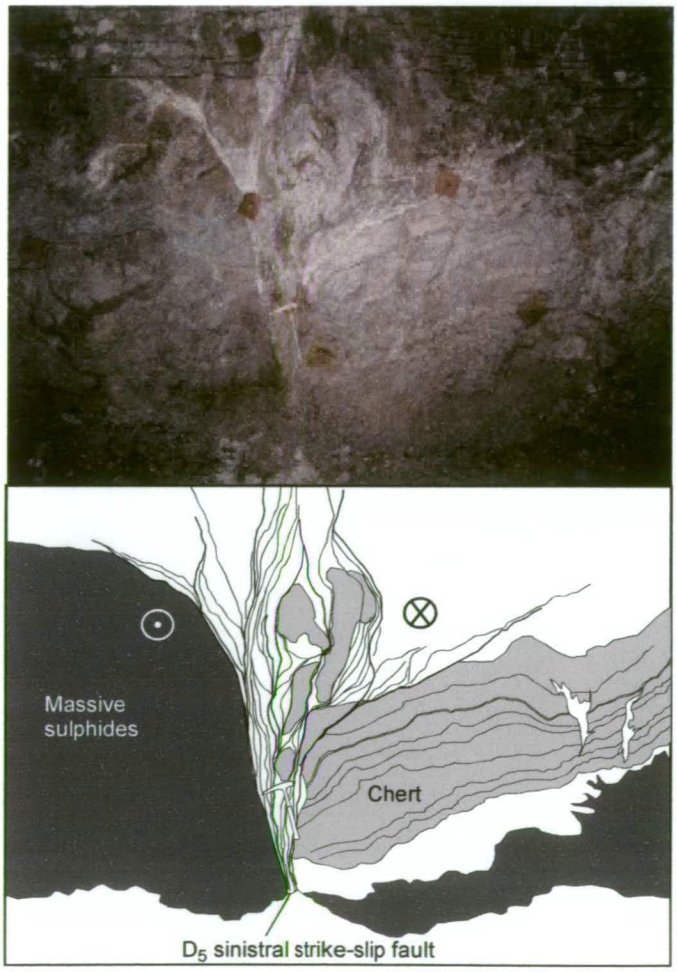

Figure 4.28: Typical gouge-rich D_5 faults in the Battle and HW mines. **a)** Sinistral strike-slip D_5 fault offsets a coarse-grained rhyolitic volcaniclastic unit in drive 23-427, 43 Block, HW mine; **b)** Fault gouge and quartz veining in a D_5 fault, veining indicates a sinistral sense of displacement; **c)** Steep anastomosing D_5 fault in drive ST183, Battle mine. The strike-slip fault offsets laminated chert, which is now in fault contact with the massive sulphides.

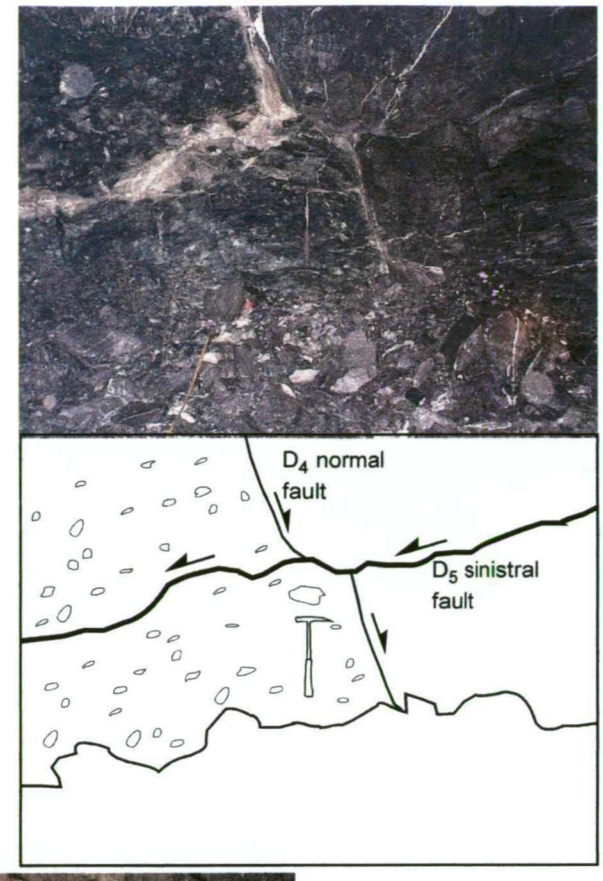

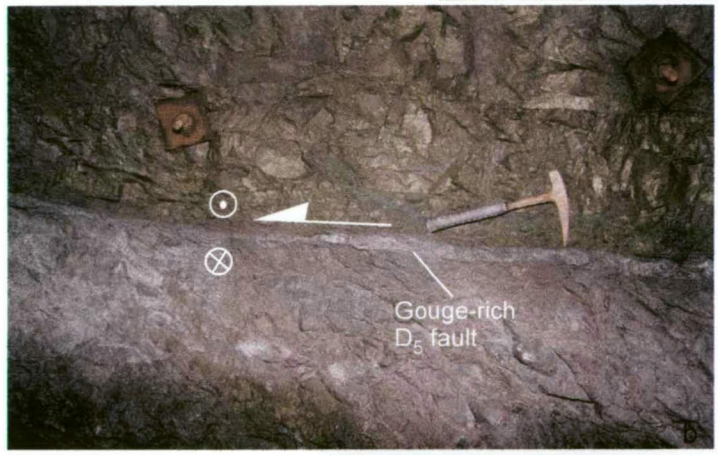

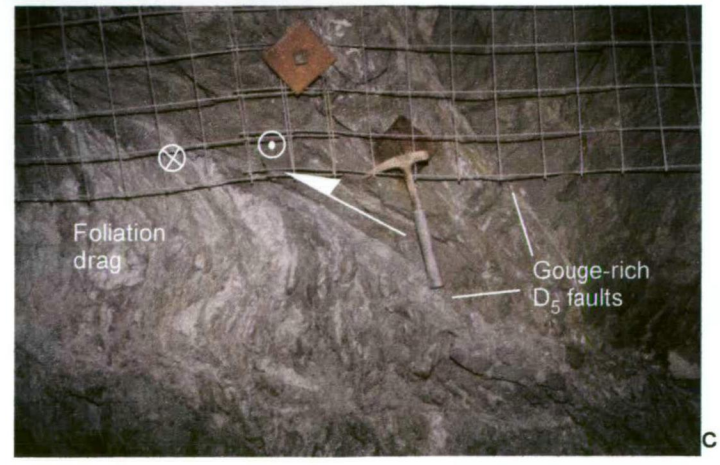

Figure 4.29: Typical D_5 faults in the HW mine. **a)** Gouge-rich wavy NE-striking D_5 fault offsets a steep D_4 normal fault, with a sinistral sense of displacement in the 43 Block area, HW mine; **b)** Gouge-rich 'flat-fault' with oblique top to the west displacement indicated by grooves on the fault surface and foliation drag (in drive B390, HW mine); **c)** Several gouge-rich D_5 faults with strong foliation drag adjacent to the structures indicating a top to the west sense of displacement (oblique thrust) in drive B390, HW mine.

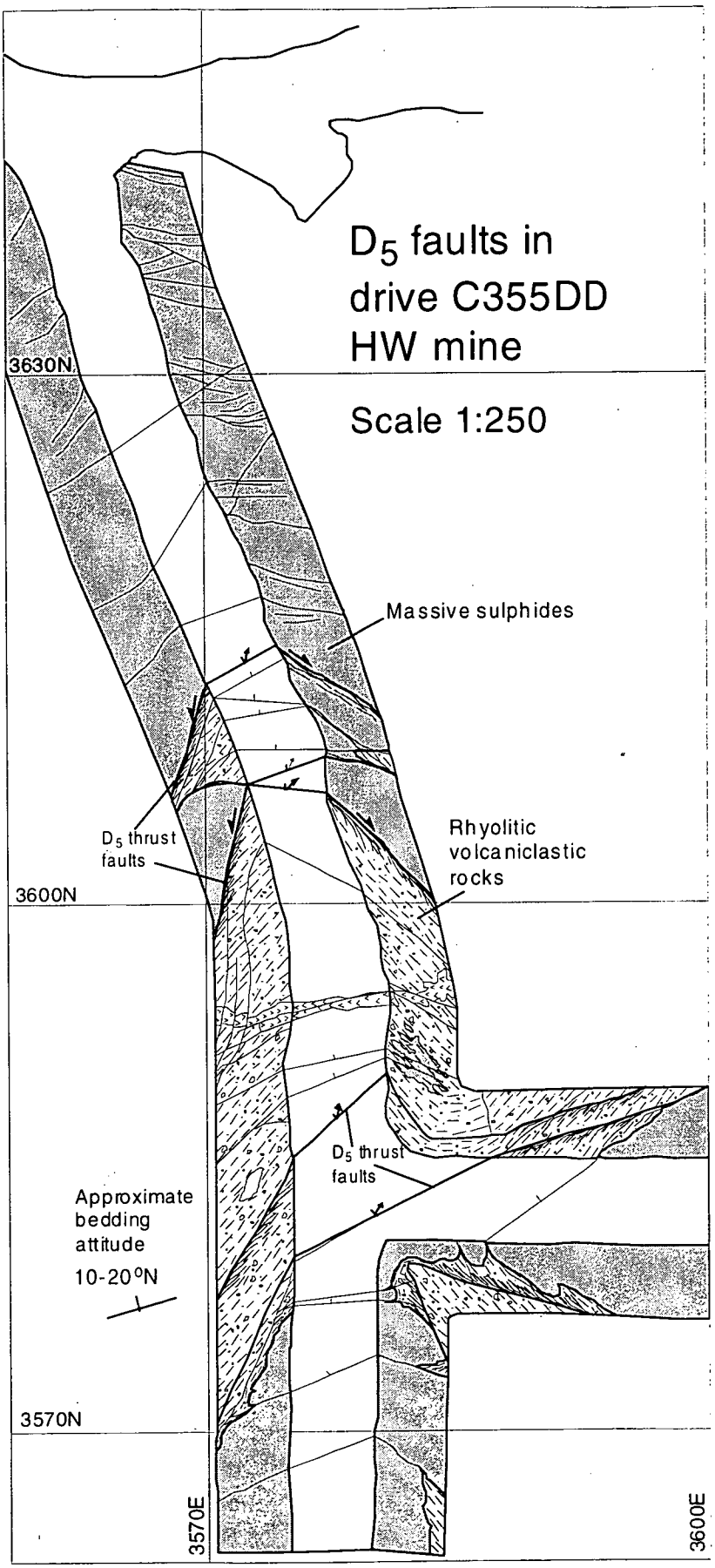

Figure 4.30: Underground wall map of drive C355DD, HW mine, illustrating the dominance of oblique D_5 thrust faults in this area.

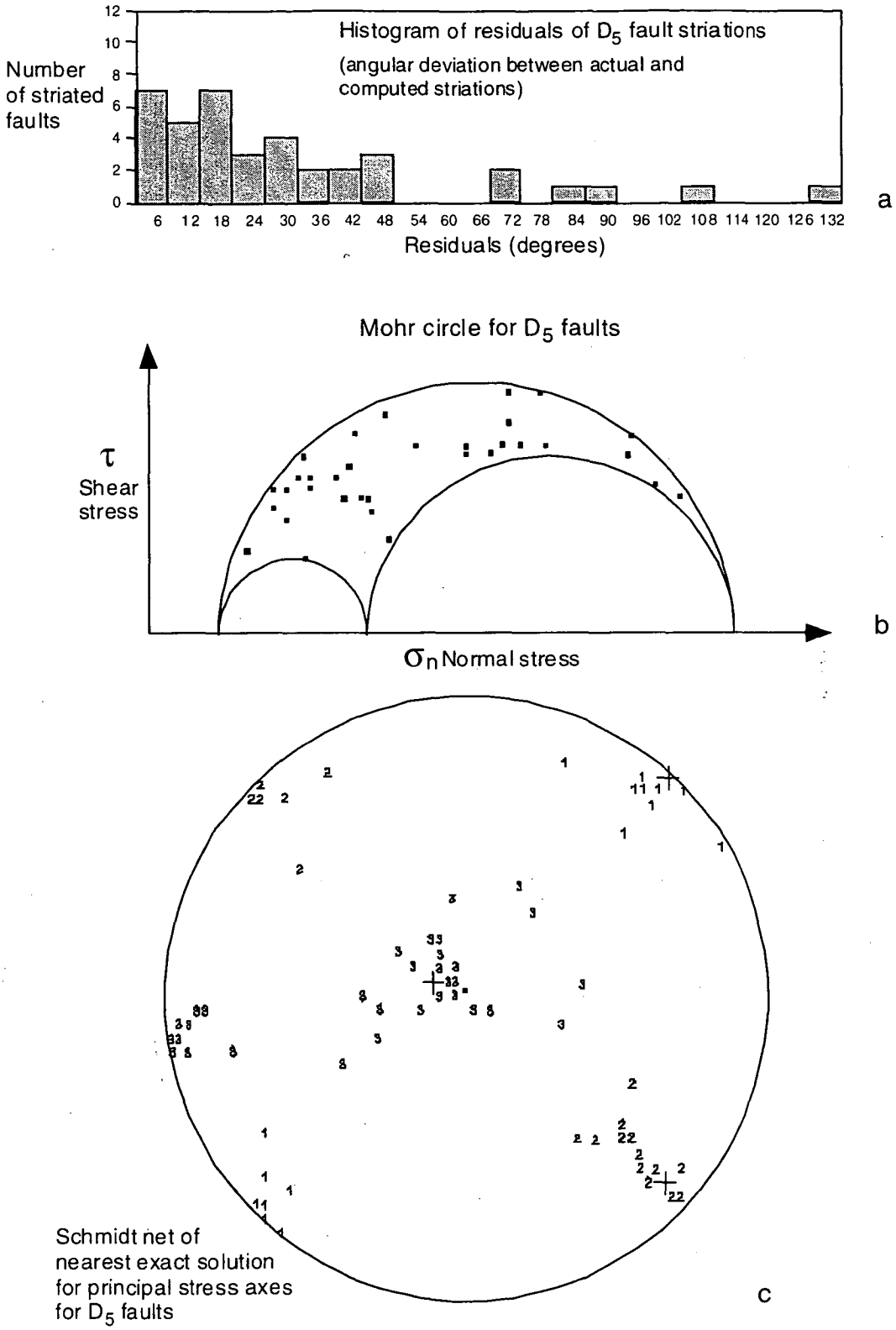

Figure 4.31: Interpretation of D_5 fault striations; **a)** Histogram of residuals, illustrating the angular deviation between actual and computed striations; **b)** many D_5 faults plot well below the failure envelope on the Mohr plot (see discussion in text); **c)** Schmidt net of the nearest exact solution for the principal stress axes, indicating σ_1 has a shallow plunge to the NE, although there is a lot more scatter in this diagram compared with the other deformation events.

4.10 Effects of deformation on stratigraphic sequence

The multiple deformation events have had a significant effect on the volcano-sedimentary sequence. However, it is still possible to reconstruct the geology in many places, with many units displaying good lateral continuity. Cross-sections 1420E, in the Battle mine (Figure 4.32), section 2530E in the Extension Zone (Figure 4.33), and oblique section 23-428XN, trending 020, in the 43 Block area of the HW mine (Figure 4.34), illustrate the effects of deformation on the sequence. Although these sections contain numerous faults, it is clear that the geology is relatively intact and individual units can still be traced.

Structures, which have the greatest effect on the sequence, include the D_1 folds, gouge-rich shallow-dipping D_5 thrust faults and steep D_3 strike-slip faults. However, in places, D_4 normal faults also have a significant effect on the sequence, such as the 43 Block area (Figure 4.34). The effect of the D_4 normal faults is best shown by underground wall maps (Figure 4.35) of the area adjacent to the oblique section shown in Figure 4.34, and an interpreted plan view of the area (Figure 4.36).

The underground map illustrates the abundant faulting with marked lithological changes across the faults (Figure 4.35). Faulting is dominated by steep D_4 normal faults, steep D_5 sinistral strike-slip faults and moderately north dipping D_5 thrust faults. The geological interpretation in Figure 4.36, indicates that the complex nature of the geology is most likely a result of D_4 normal faulting. The sequence is only shallow to moderately SW dipping and small normal displacements result in large apparent lateral offsets. Subsequent displacement on steep sinistral D_5 strike-slip faults appears to have been minor, but the moderately NW-dipping D_5 thusts (top to the south sense of displacement) had a major effect on the sequence, as shown in the oblique section in Figure 4.34.

A structural summary map, Figure 4.37, provides an interpretation of the major structures, which affect the sequence, and is based on offsets shown by the footwall contours (Figure 4.1). The relative importance and timing of the deformation events is indicated by the footwall contours, and this deformation history is used in the following chapter for the reconstruction of the paleoseafloor.

(text continued on page 103)

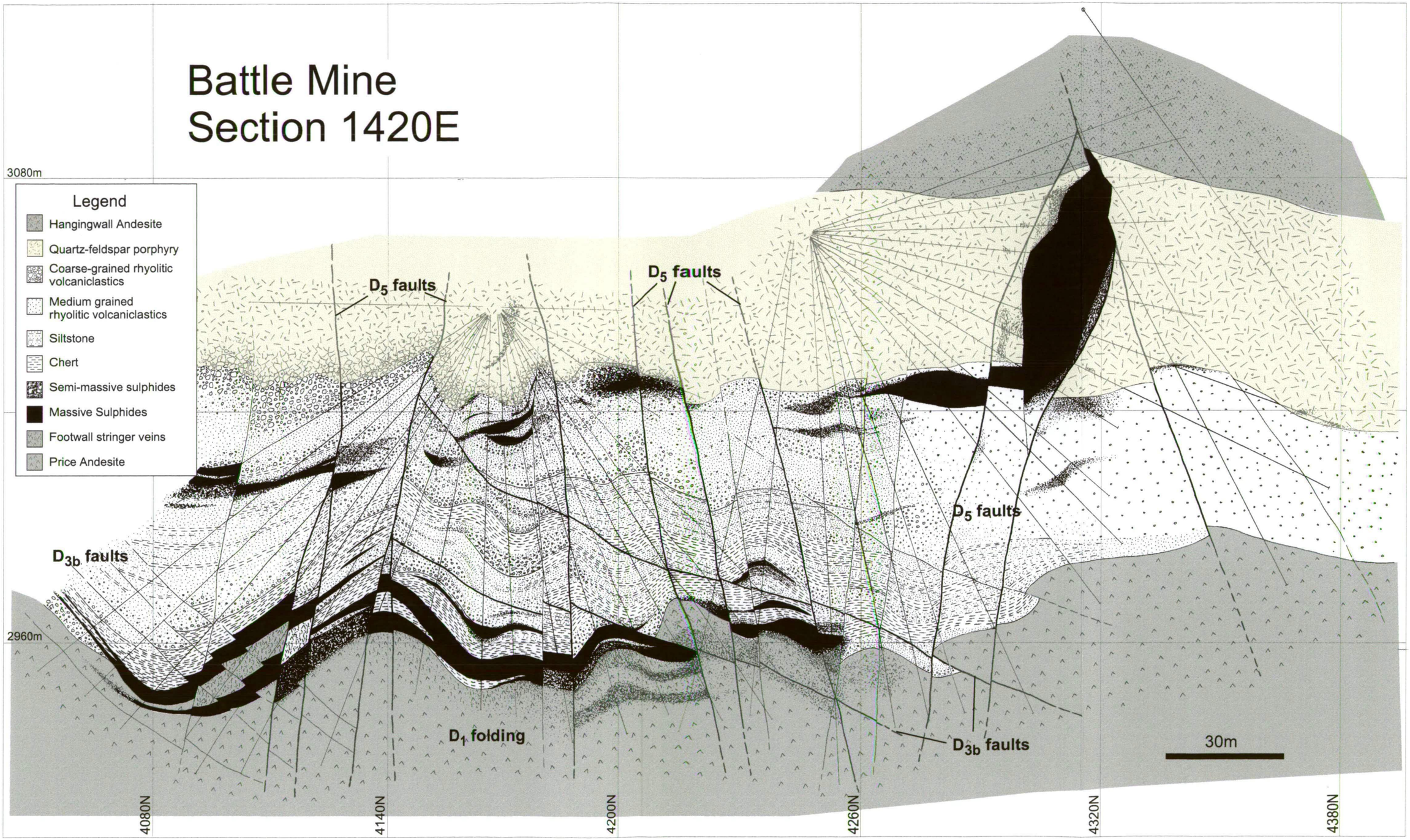

Figure 4.32: Detailed geology of HW Horizon, section 1420E, Battle Mine. The siliceous caprocks and associated facies are folded and dissected by D_1 to D_5 events, but at a broad scale the stratigraphy is preserved (see discussion in text).

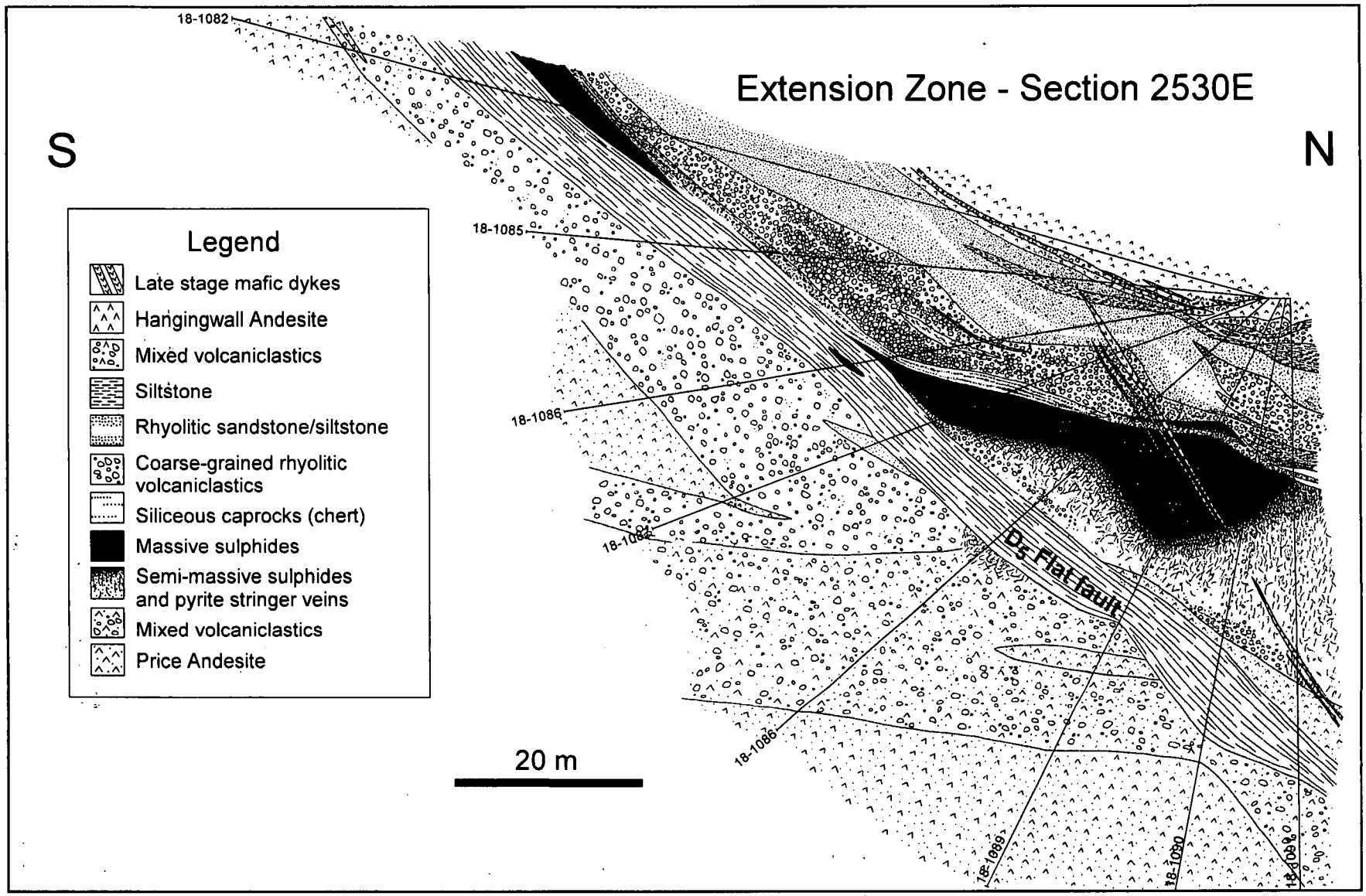

Figure 4.33: Extension Zone section 2530E illustrating the large D_5 oblique thrust, which is the dominant structure in this area.

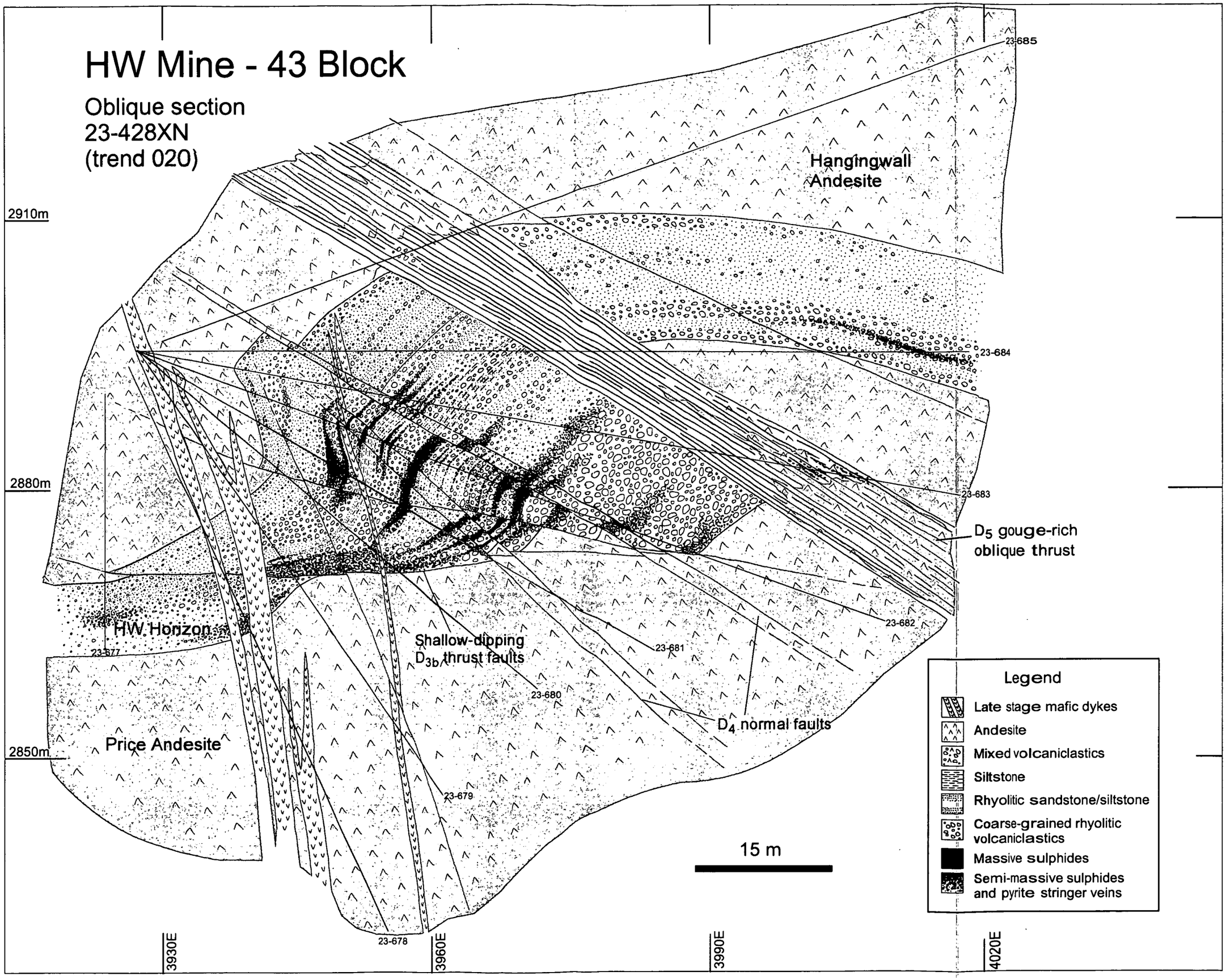

Figure 4.34: Oblique cross-section through the HW Horizon in the 43 Block area, illustrating the effects of D1 folding and D3-D5 faulting (see discussion in text).

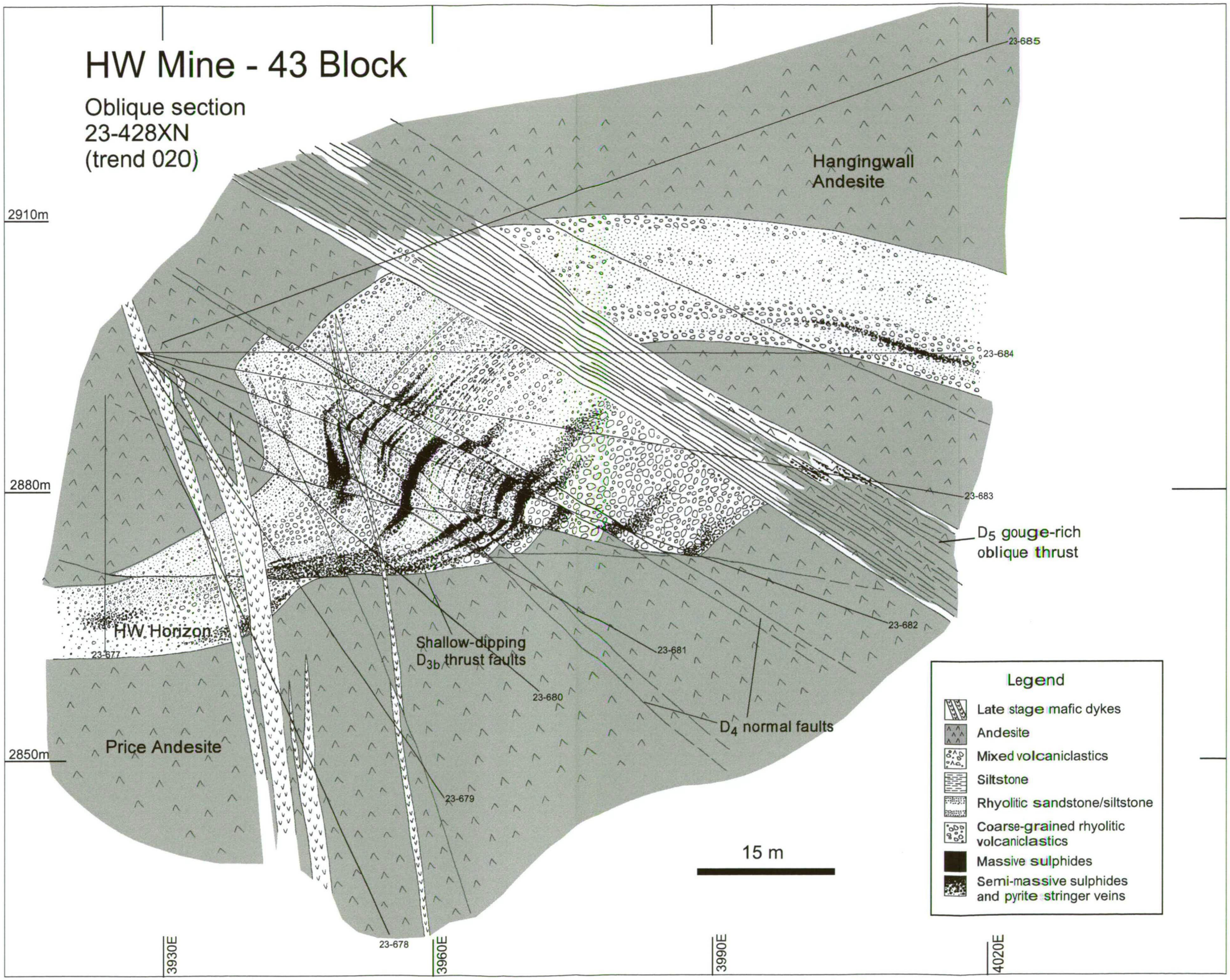

HW Mine - 43 Block
Oblique section
23-428XN
(trend 020)
Hangingwall Andesite
Price Andesite
HW Horizon
Shallow-dipping D_{3b} thrust faults
D_4 normal faults
D_5 gouge-rich oblique thrust
2910m
2880m
2850m
3930E
3960E
3990E
4020E
23-677
23-678
23-679
23-680
23-681
23-682
23-683
23-684
23-685
15 m
Legend
Late stage mafic dykes
Andesite
Mixed volcaniclastics
Siltstone
Rhyolitic sandstone/siltstone
Coarse-grained rhyolitic volcaniclastics
Massive sulphides
Semi-massive sulphides and pyrite stringer veins

Figure 4.34: Oblique cross-section through the HW Horizon in the 43 Block area, illustrating the effects of D1 folding and D3-D5 faulting (see discussion in text).

4.11 Regional and tectonic correlation of Myra Falls deformation history

The structure of the Myra Falls VHMS camp reflects the complex tectonic history of Vancouver Island, described in Chapter 2 and 3. Five deformational events were recognised in the Myra Falls area. The large number of deformation events observed in this area is mainly a result of good underground exposure on the mine property.

D_1 and D_2 clearly predate most of the faulting in the area, with the exception of early syn-depositional structures. D_1 fabrics are present in the Thelwood Formation and poles to bedding give a very similar pattern to those from the Myra Formation. However, it is unclear whether this deformation event affected younger rocks of the Buttle Lake Group. Bedding measurements were collected from the Buttle Lake Limestone, and indicate broad open folding (Figure 4.38). This data matches the orientation of folding in the Sicker Group but the folding in the limestone appears to be more open. However, not enough measurements were made to reach a formal conclusion. Muller (1980) suggests that Buttle Lake Group rocks are affected by this fold phase, because in several locations the Buttle Lake Group rocks are infolded with the underlying Sicker Group rocks. Other authors, such as Massey (1992) and Yorath et al. (1999), suggest that the ductile deformation occurred pre-Karmutsen Formation (i.e., Pre-Triassic) as only one phase of folding is recognised in the Karmutsen Formation, while two fold phases are present in the older Sicker Group rocks (Table 2.1). Although the timing of D_1 folding is still unclear, the deformation is the result of N-S ***(NE-SW true north)*** directed compression, which occurred within the Wrangellia terrane, prior to collision of Wrangellia and the ancient margin of North America.

D_3 faulting resulted from later N-S ***(NE-SW true north)*** directed compression. Nixon et al. (1994), describes a similar two-stage evolution of strike-slip faults and thrust faults during post-Mid to (?) pre-Late Cretaceous time, in northern Vancouver Island (Table 2.1). At Myra Falls, the D_3 faults display a similar displacement pattern and could be correlated with these faults. The lack of any significant cleavage zone development around D_3 faults, and the presence of epidote-chlorite slickenfibres suggests that these structures represent early ductile-brittle faults, associated with relatively hot fluids, as epidote is thought to grow at or above 240-260°C (Browne, 1978). The N-S compressional direction estimated for the D_3 faults is similar to that estimated for the D_1 and D_2 events. However, D_{3a} faults with epidote fibres, crosscut igneous rocks of the Island Intrusive Suite (Berry, 2000). This suggests that they do not represent a final brittle phase of the N-S ductile deformation event, instead, D_3 faulting represents a much later N-S compressional event. The relatively

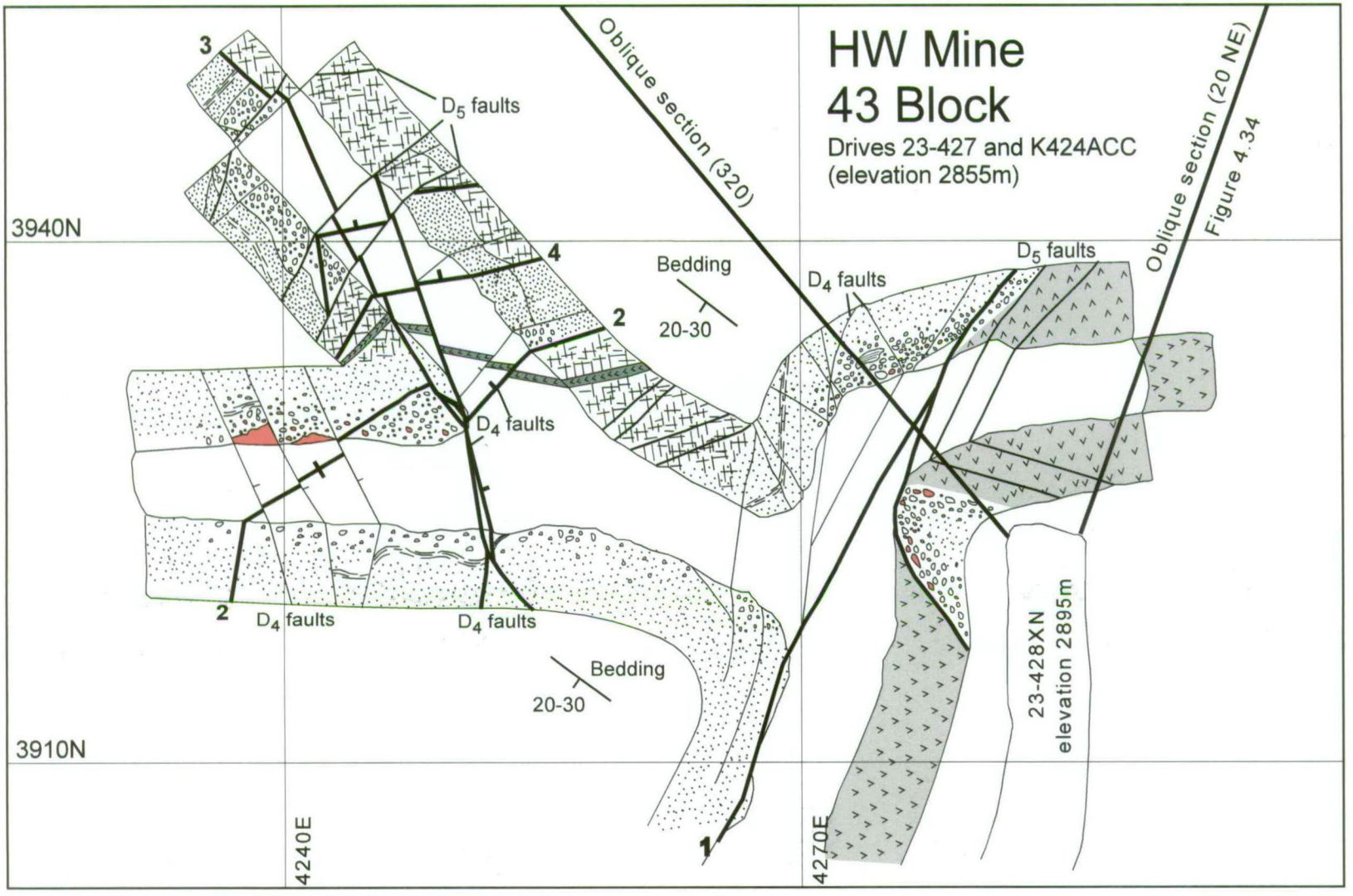

Figure 4.35: Underground wall maps of drives 23-427 and K424ACC, illustrating the effects of D_1 folding and D_3-D_5 faulting. An interpretation of the geology (and legend) is provided in the next map (Figure 4.36).

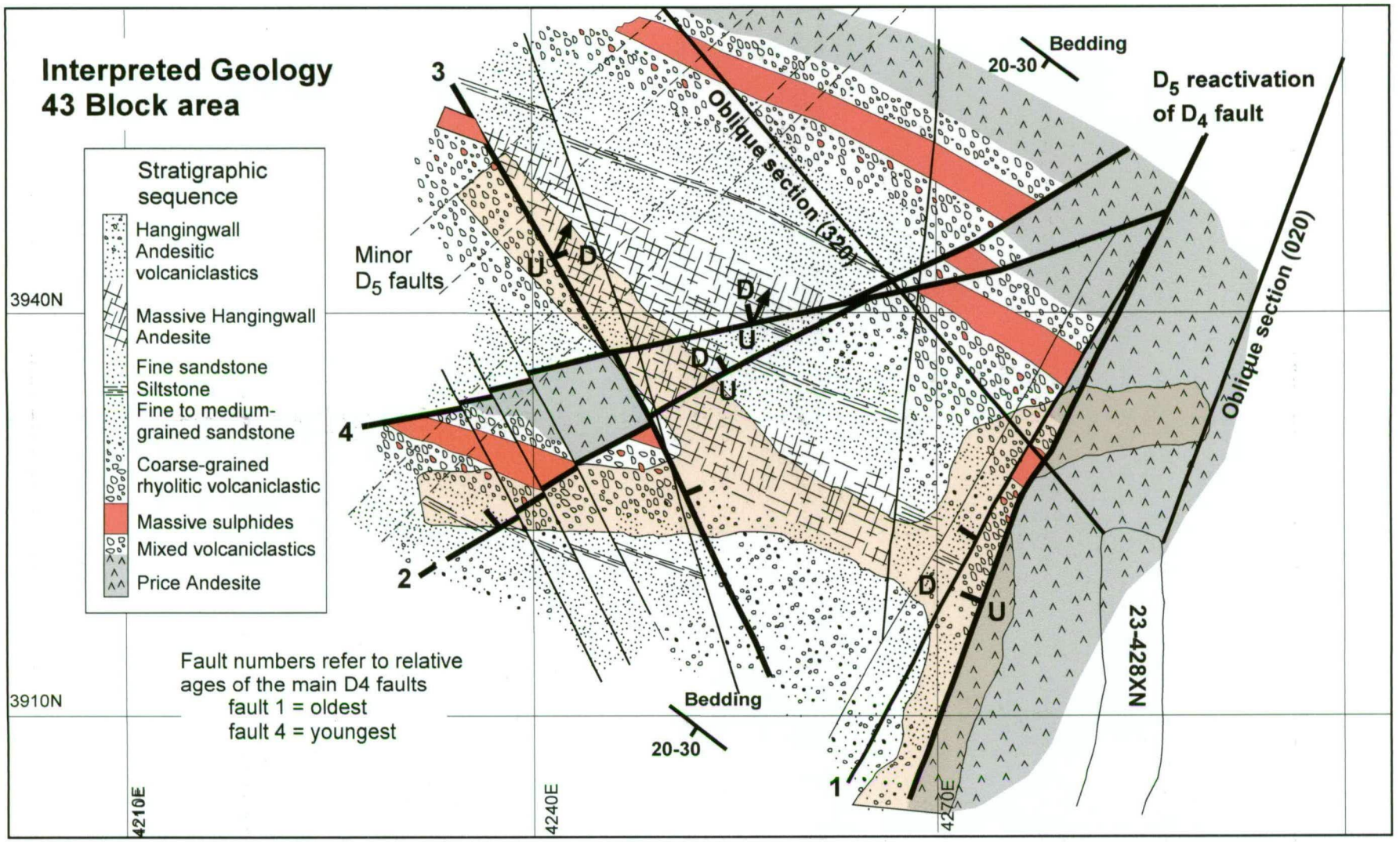

Figure 4.36: Interpreted geology from underground wall maps (Figure 4.35) and oblique cross sections from drive 23-428XN (section 020 shown in Figure 4.35). The interpreted geology illustrates how D_4 normal faulting affects the shallow SE-dipping sequence, with large offsets resulting from relatively small dip-slip movements on normal faults.

hot fluids associated with the D_3 faults may indicate formation during or just after emplacement of the Island Intrusive Suite.

Underground mapping and fault striation data indicate that the D_4 normal faults postdate D_3 faults and are consistently offset by D_5 faults. Although the D_4 faults are common in the Myra Falls area, they are not described on regional maps. With the exception of the D_4 North Fault Zone, displacement on the D_4 structures is relatively minor and this may account for their absence on regional maps. However, Muller (1980) does report a set of NW to N ***(N to NE)*** striking faults that appear to predate the large NW trending thrust faults (D_5?). These structures could correlate with the Myra Falls D_4 faults.

The shallow N ***(NE)***-dipping gouge-rich D_5 thrusts and coeval NE ***(ENE-WSW)*** trending D_5 strike-slip faults have a major effect on the stratigraphy of the Myra Falls area. These large faults can be correlated with major north-dipping thrust faults described in the Cowichan Uplift by England and Calon (1991), Massey, (1992), Yorath et al., (1999). These structures dominate the structural fabric of southern Vancouver Island and are probably of Cretaceous to late Eocene age (England and Calon, 1991; Massey, 1992). The faults most likely developed during crustal shortening caused by the collision and accretion of Wrangellia and subsequent Pacific Rim and Cresent terranes, onto North America. The strike-slip component of these large faults is a result of NW movement of the Pacific Plate relative to the North American plate.

4.12 Summary and conclusions

- The deformation history for Myra Falls VHMS camp includes:

  Syn-depositional growth faults
  D_1 folding
  D_2 shear zones
  D_3 strike-slip faults and shallow thrust faults
  D_4 normal faults
  D_5 strike-slip and thrust faults

- Syn-depositional growth faults are not directly measured, instead they are recognised by rapid changes in footwall elevation, thickness changes on isopach maps, and facies variation.

- D_1 produced broad open upright folds with moderately to steeply N-dipping axial planar cleavage zones (S_1) that are variably developed. Stretching lineations (L_1) are

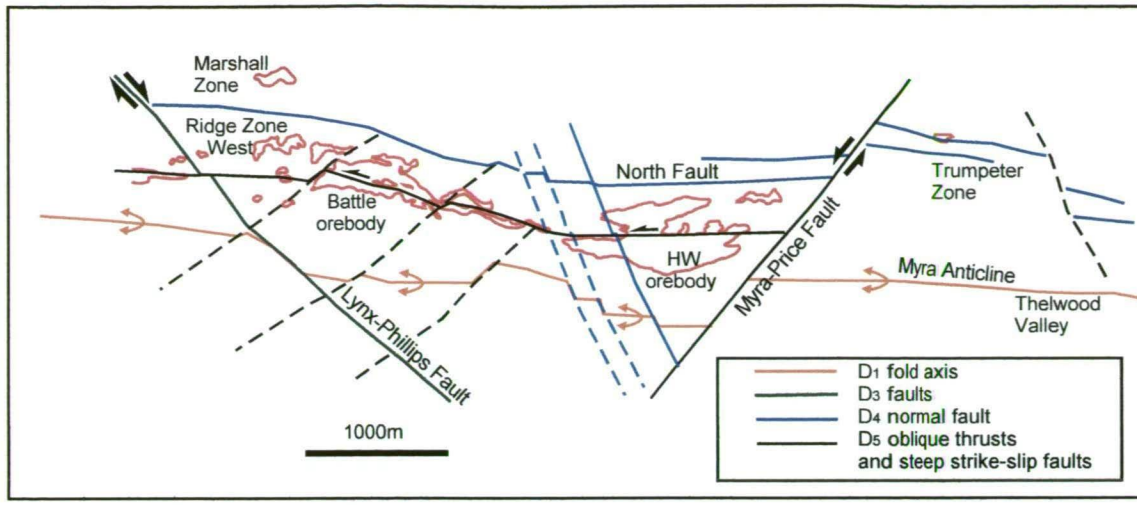

Figure 4.37: Summary map of the major structures, which affect the sequence at Myra Falls. The relative ages of the structures are also shown. This map is used for the removal of the D_1 to D_5 events in the paleoseafloor reconstruction in the following chapter (Chapter 5).

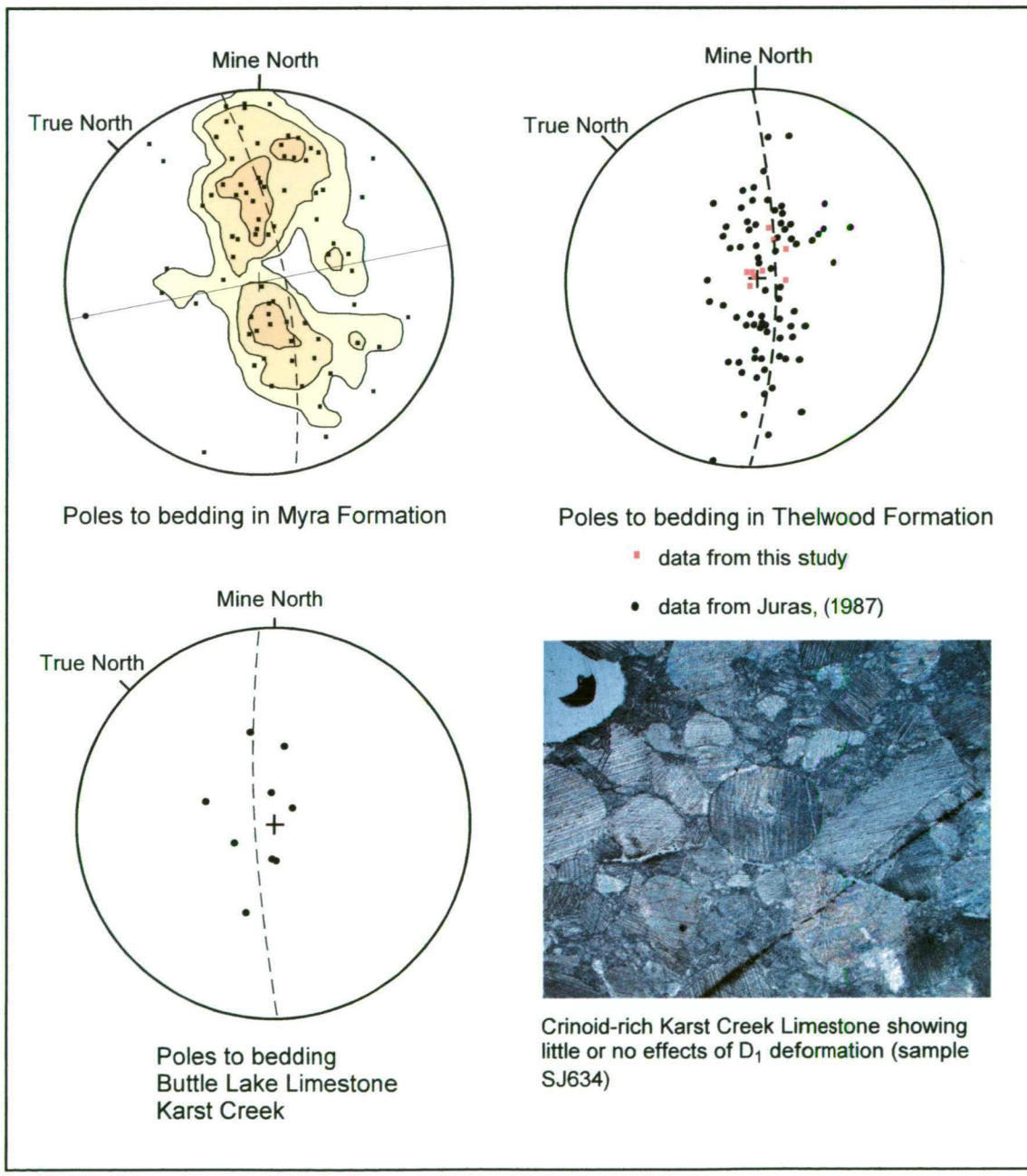

Figure 4.38: Regional bedding measurements in Thelwood Formation and Buttle Lake Limestone.

horizontal to shallow WSW plunging and are generally parallel to F_1 fold axes. D_1 folds developed during N-S compression.

- D_2 produced a second foliation (S_2), which is developed in localised shear zones, and overprints and/or rotates (?) the S_1 foliation. The S_2 fabric is generally steeply N-dipping to vertical with an ESE orientation. The development of the steep S_2 fabric most likely occurred during the late stages of ductile deformation. The shear zones may have developed by an increase in strain partitioning and/or a slight rotation in the principle strain axes. The S_2 fabric is offset by the earliest brittle structures, which are the steep D_{3a} faults.

- D_3 produced a two-stage evolution of faulting during N-S compression. Early steep strike-slip faults (D_{3a}) are overprinted by shallow N and S dipping thrust faults and bedding-parallel shears (D_{3b}).

- D_{3a} faults are typically steep planar structures with well-developed coarse quartz-chlorite-epidote slickenfibres and chloritic polished surfaces. Fault striations are predominantly horizontal to shallow plunging and fault gouge is not present. Sinistral strike-slip offsets occur on NNE to NE oriented faults, while dextral offset is observed on W to NNW oriented faults.

- D_{3b} faults strike E-W to NE-SW and have moderate to shallow N and S dips. They are wavy anastomosing faults, with minor gouge. Fine quartz slickenfibres are common and indicate oblique top to the west displacement on shallow N-dipping faults, and top to the NE displacement on shallow S-dipping faults.

- D_4 produced steep normal faults, which are planar structures with minor gouge and fine steep quartz fibres. They are commonly associated with quartz-carbonate veining and predominantly strike NNW to NNE. The D_4 event commonly reactivates D_{3a} faults, with coarse D_{3a} striations commonly grooved and/or overgrown by the fine steep D_4 quartz fibres.

- D_5 produced N-dipping oblique thrust faults and steep NE to E-oriented strike-slip faults. D_5 faults are gouge-rich, wavy anastomosing structures, commonly associated with irregular quartz veins. Broad cleavage zones, up to several metres wide, are commonly developed around D_5 faults. The NE to E-oriented steep strike-slip faults

display sinistral offset, with top to the west displacement on shallow N-dipping thrust faults.

- Multiple deformation events have had a significant effect on the volcano-sedimentary sequence at Myra Falls. However, it is still possible to reconstruct the geology in places, with many units displaying good lateral continuity.

- The deformation history of the Myra Falls area can be related to regional structural mapping on Vancouver Island. The D_1 fold event has been mapped in Sicker Group rocks throughout Vancouver Island, while a two-stage brittle event, similar to the D_3 event has been recognised in northern Vancouver Island. The large gouge-rich D_5 faults at Myra Falls are most likely related to the large NW-oriented (true north orientation) thrust faults, which dominate the structural fabric of Vancouver Island.

Chapter 5
HW Horizon facies variation and paleoseafloor reconstruction

5.1 Introduction

The HW Horizon occurs at the base of the Myra Formation and hosts both the Battle and HW orebodies. The horizon is mainly composed of rhyolitic volcaniclastic rocks and marks an abrupt change from andesitic volcanism to rhyolite dominated volcanism. The VHMS orebodies occur on or very close to the contact with the underlying Price Andesite and this contact is thought to represent the paleoseafloor surface at or near the time of ore formation.

The aims of this chapter are as follows:

1. Describe the facies variation within the HW Horizon, with particular emphasis on facies associated with the siliceous caprocks
2. Remove the effects of deformation to reconstruct the paleoseafloor and identify early vs late structures, using isopach maps, footwall contours, facies maps and the deformation history (from Chapter 4)
3. Describe the depositional and structural setting of the VHMS orebodies at Myra Falls and compare with modern analogues.

Juras (1987) and McKinley et al. (1997) suggest that the shape of the present orebodies is "governed by the configuration of the hosting extensional depressions (trough structures)". However, in many cases the extensional depressions are controlled by late structures (e.g., D_4 and D_5 faults) which overprint and obscure the original growth faults. Early vs late structures are identified in this thesis, by a combination of footwall contouring, isopach maps, facies maps and the deformation history. In order to gain an accurate picture of the depositional and structural setting of the VHMS orebodies at Myra Falls, the effects of the

D_1-D_5 events were removed. All orientations in this chapter are in local mine grid (mine N is 48° east of true N).

5.2 Methods

To describe the facies variation and changing stratigraphic thickness of the HW Horizon and Myra Formation various maps and sections were constructed, including:

1. Footwall contours (top surface of Price Andesite). The major structures have been included to allow representative contours to reflect the fault pattern;
2. Contour map of the top surface of the HW Horizon;
3. HW Horizon isopach map;
4. Basal contour map of the Thelwood Formation;
5. Myra Formation isopach map;
6. Facies maps – (fine-grained facies and porphyry bodies); and
7. Cross sections through the HW and Battle orebodies.

The data used to construct the maps was collected from exploration and mine sections. Contour maps were constructed from drillhole pierce points and plotted on maps with drillhole traces for greater accuracy. The thickness of units on facies maps and sections is based on the true thickness measured from sections, rather than from drillhole intersections.

Footwall, isopach maps and facies maps were initially contoured by hand, as computer modelling was not possible, due to lithological naming inconsistencies in the exploration and mine databases. The data was then gridded and contoured using the minimum curvature method with Golden Software Surfer 7.0. Isopach maps were produced using the grid-math function, with additional points added to footwall and hangingwall contour maps to eliminate zones of negative values. Map areas without drillhole information were blanked out.

5.3 HW Horizon facies variation

Marked facies variation occurs throughout the HW Horizon and is shown in a series of N-S sections in Figure 5.1. There is a noticeable facies change from north to south with the northern part of the property dominated by coarse-grained, proximal rhyolitic volcaniclastic rocks and massive porphyry intrusives and flows. In the south, the horizon is dominated by finer grained lithologies such as, mudstone, siltstone and fine sandstone. The massive intrusives and flows mainly occur at the top of the HW Horizon with quartz-feldspar porphyry common in the western part of the property, and feldspar-porphyry and dacite more common in the east. Figure 5.2 illustrates the distribution and isopachs of the quartz-

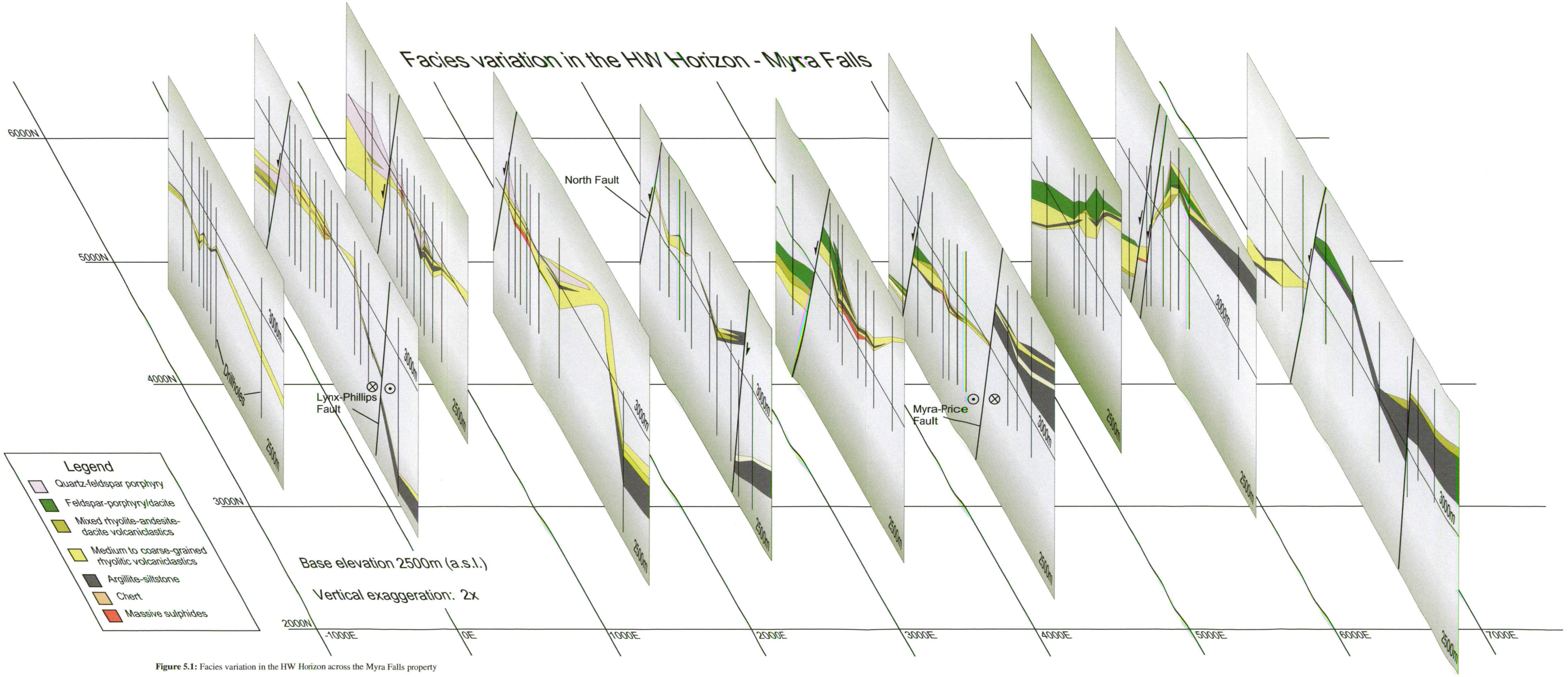

Figure 5.1: Facies variation in the HW Horizon across the Myra Falls property

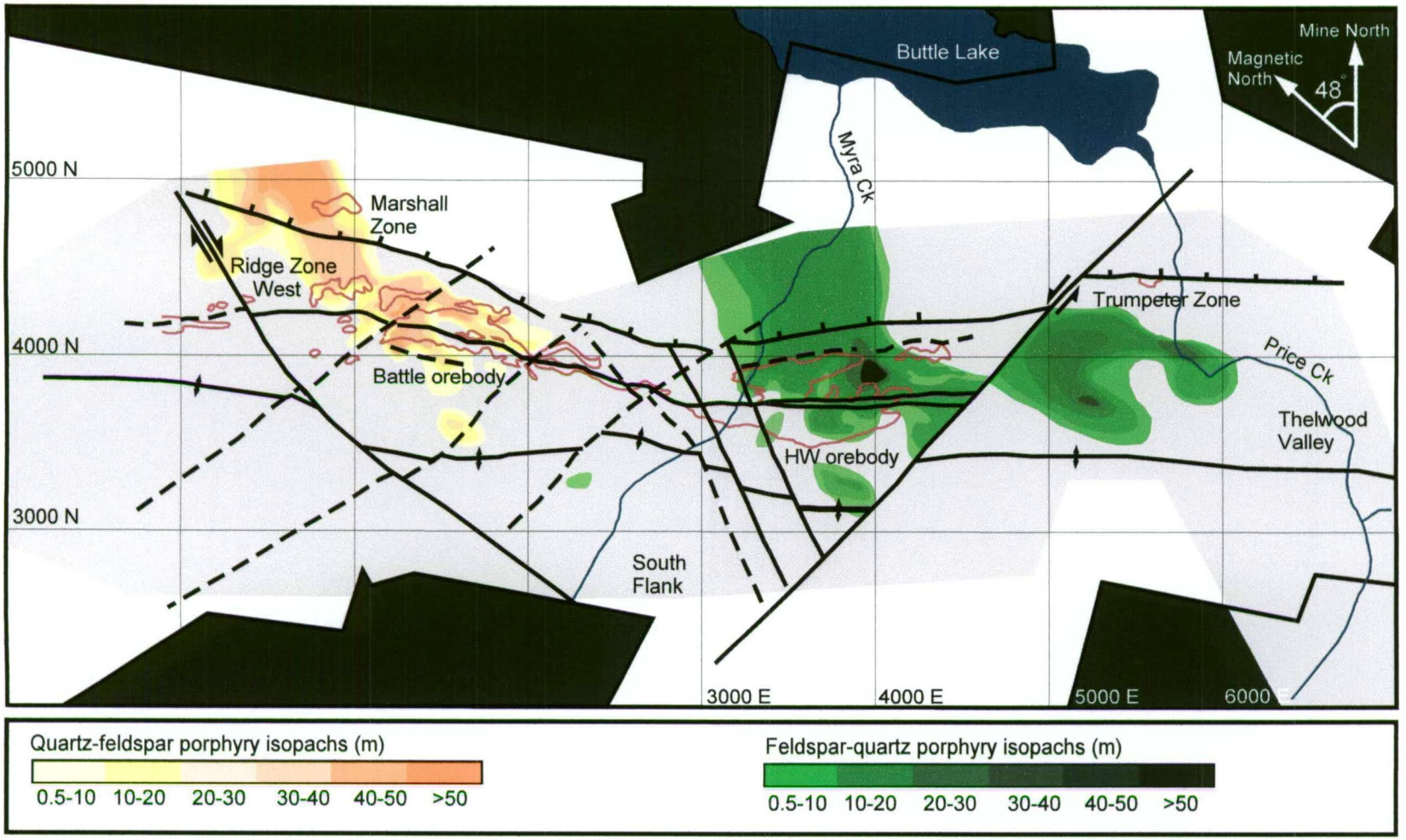

Figure 5.2: Location of quartz-feldspar porphyry bodies in Myra Falls VHMS camp. The porphyry bodies are located above the VHMS orebodies, at the top of the HW Horizon.

feldspar and feldspar porphyry bodies. The massive porphyry bodies become thicker to the north, and are absent in the south. This distribution most likely reflects the presence of a volcanic centre to the north (see further discussion in Section 5.7).

The distribution and isopachs of fine-grained facies, which occur near the base of the HW Horizon is illustrated in Figure 5.3a. Argillite is the dominant lithology across the property, and is commonly interbedded with siltstone, and fine sandstone. The siliceous caprocks, or chert, are well developed above the Battle orebody, and in the Ridge and Extension zones, with minor patches above the HW orebody. Argillite and siltstone are also common in the Battle and Ridge zones, and form thick deposits, up to 25m thick, above the HW orebody. However, the thickest argillite deposits are located in the southern part of the property, in the South Flank area, with argillite and interbedded siltstone deposits greater than 100m thick in places. Fine-grained facies are rare or absent in the northern part of the property.

The map below, Figure 5.3b, shows the present day footwall geometry, represented by the contoured top surface of Price Andesite. A 3-d view of the footwall geometry is also shown in Figure 5.4. The presence of scoriaceous breccias and pillowed flows in the andesite suggest that this surface represents the deformed paleoseafloor, at the time of HW Horizon deposition (Juras, 1987; Juras and Pearson, 1990). This contact is therefore a

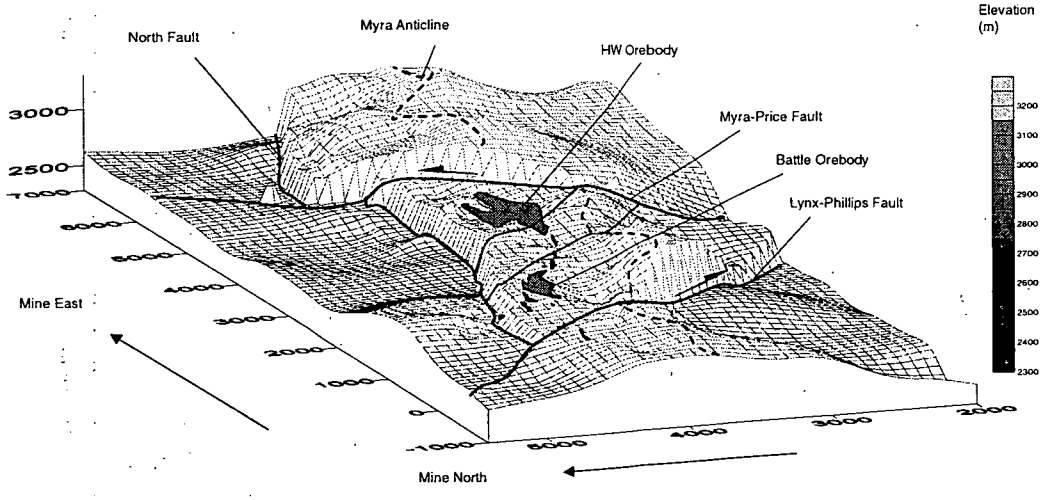

Figure 5.4: Present day top surface contours of Price Andesite (or paleoseafloor) showing the effects of deformation. The large topographic high in the centre of the block diagram is largely a result of D_1 folding (Myra Anticline), and the large topographic low to the north is due to large down throw on the North Fault. Uplift and lateral displacements also occur along the Myra-Price and Lynx-Phillips Faults.

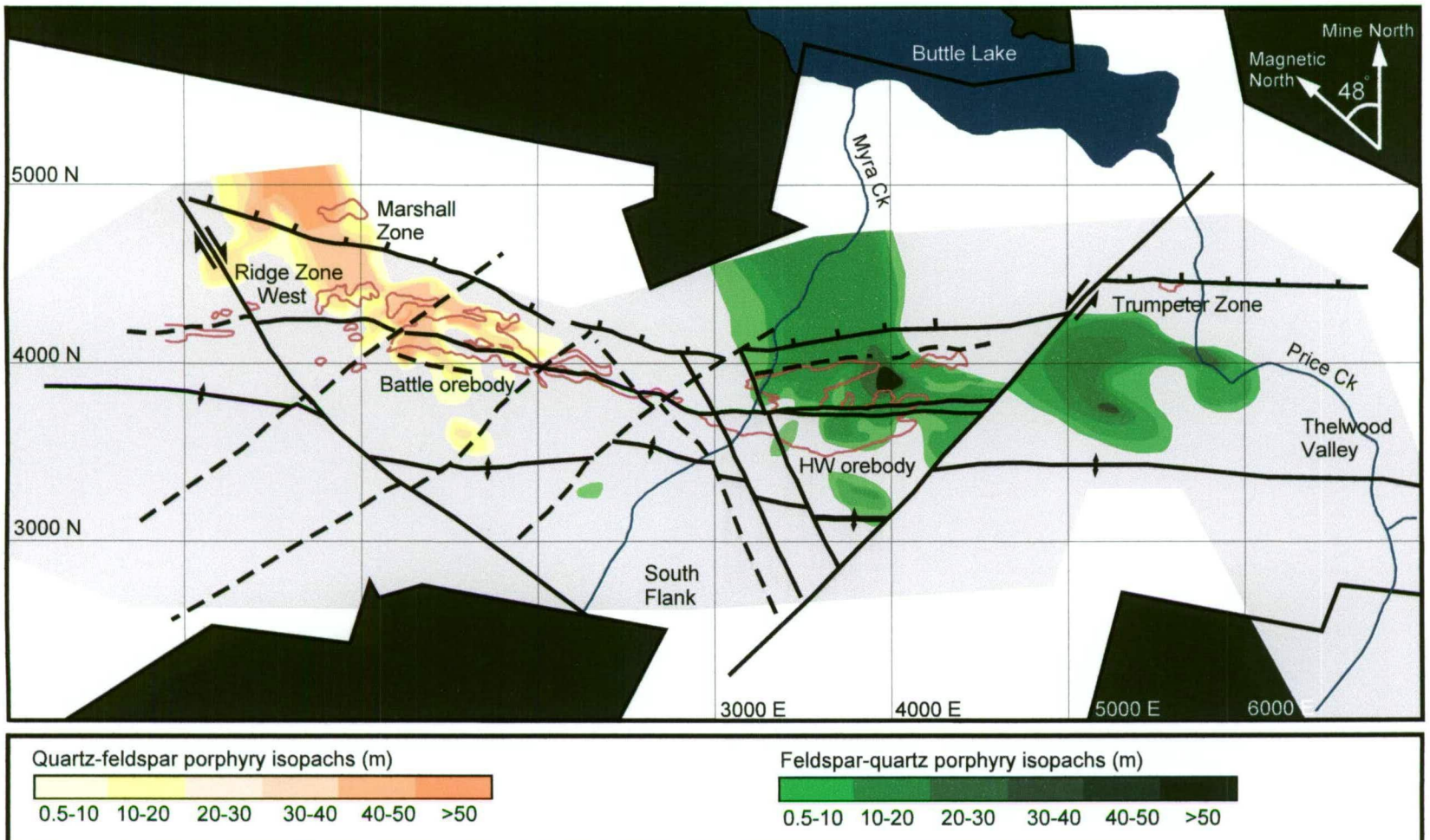

Figure 5.2: Location of quartz-feldspar porphyry bodies in Myra Falls VHMS camp. The porphyry bodies are located above the VHMS orebodies, at the top of the HW Horizon.

feldspar and feldspar porphyry bodies. The massive porphyry bodies become thicker to the north, and are absent in the south. This distribution most likely reflects the presence of a volcanic centre to the north (see further discussion in Section 5.7).

The distribution and isopachs of fine-grained facies, which occur near the base of the HW Horizon is illustrated in Figure 5.3a. Argillite is the dominant lithology across the property, and is commonly interbedded with siltstone, and fine sandstone. The siliceous caprocks, or chert, are well developed above the Battle orebody, and in the Ridge and Extension zones, with minor patches above the HW orebody. Argillite and siltstone are also common in the Battle and Ridge zones, and form thick deposits, up to 25m thick, above the HW orebody. However, the thickest argillite deposits are located in the southern part of the property, in the South Flank area, with argillite and interbedded siltstone deposits greater than 100m thick in places. Fine-grained facies are rare or absent in the northern part of the property.

The map below, Figure 5.3b, shows the present day footwall geometry, represented by the contoured top surface of Price Andesite. A 3-d view of the footwall geometry is also shown in Figure 5.4. The presence of scoriaceous breccias and pillowed flows in the andesite suggest that this surface represents the deformed paleoseafloor, at the time of HW Horizon deposition (Juras, 1987; Juras and Pearson, 1990). This contact is therefore a

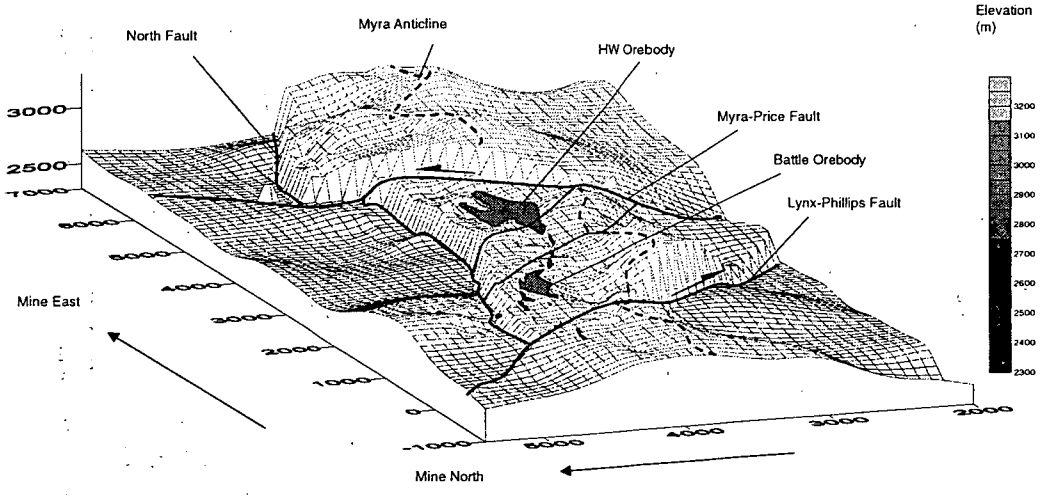

Figure 5.4: Present day top surface contours of Price Andesite (or paleoseafloor) showing the effects of deformation. The large topographic high in the centre of the block diagram is largely a result of D_1 folding (Myra Anticline), and the large topographic low to the north is due to large down throw on the North Fault. Uplift and lateral displacements also occur along the Myra-Price and Lynx-Phillips Faults.

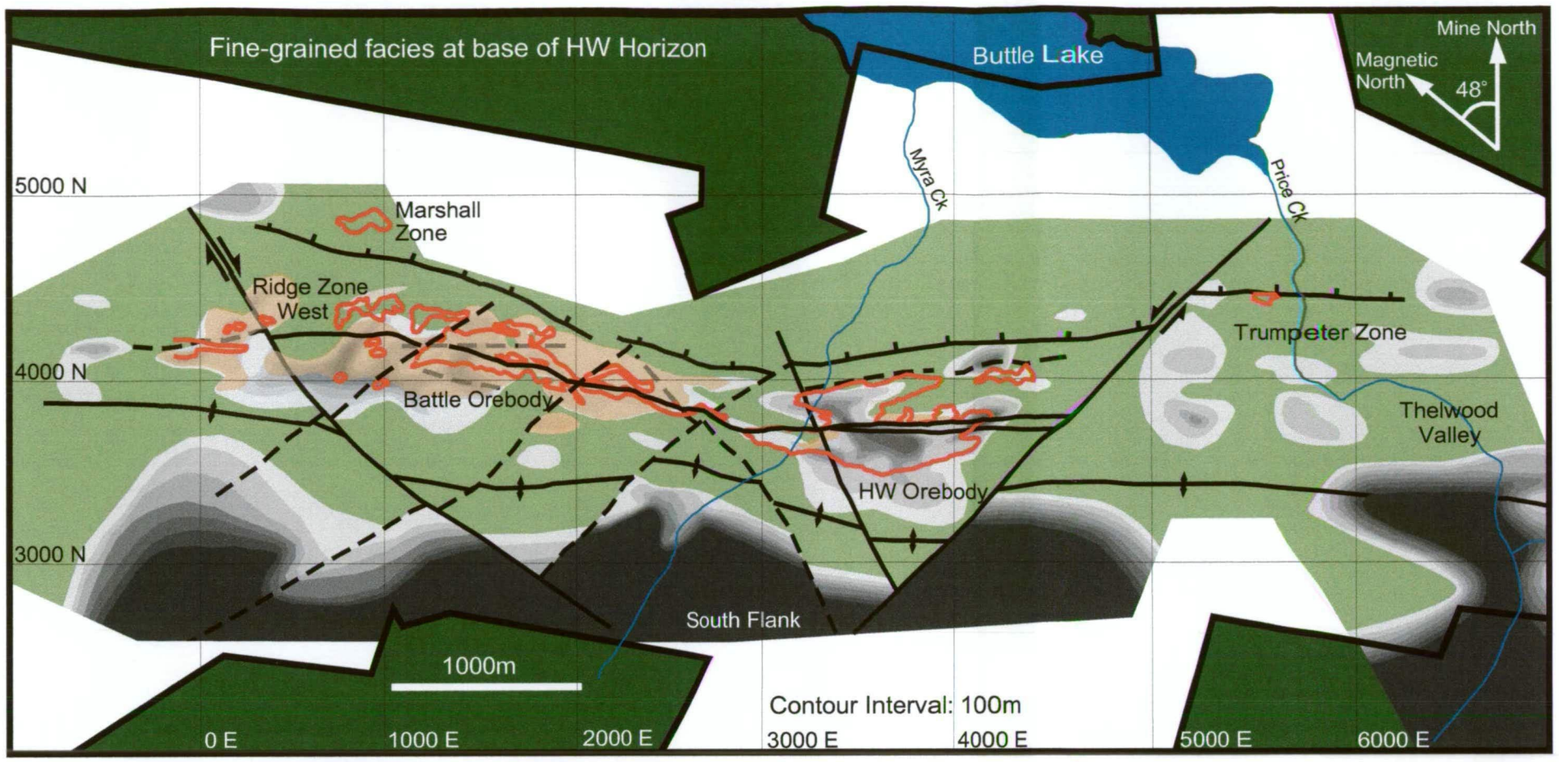

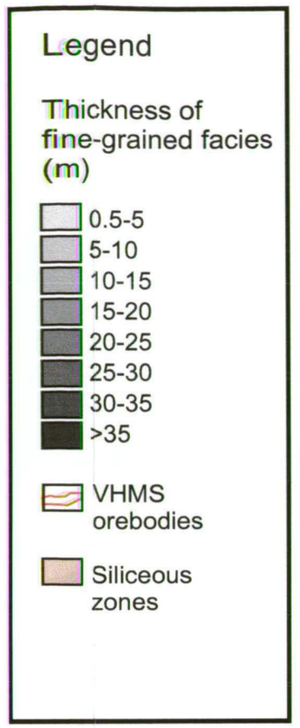

a

Figure 5.3: a) Isopach map of the fine-grained facies at the base of the HW Horizon; **b)** Footwall contours (deformed paleoseafloor) and major structures which affect the sequence. Thick zones of argillite coincide with many topographic lows in the footwall contour map (see discussion in text).

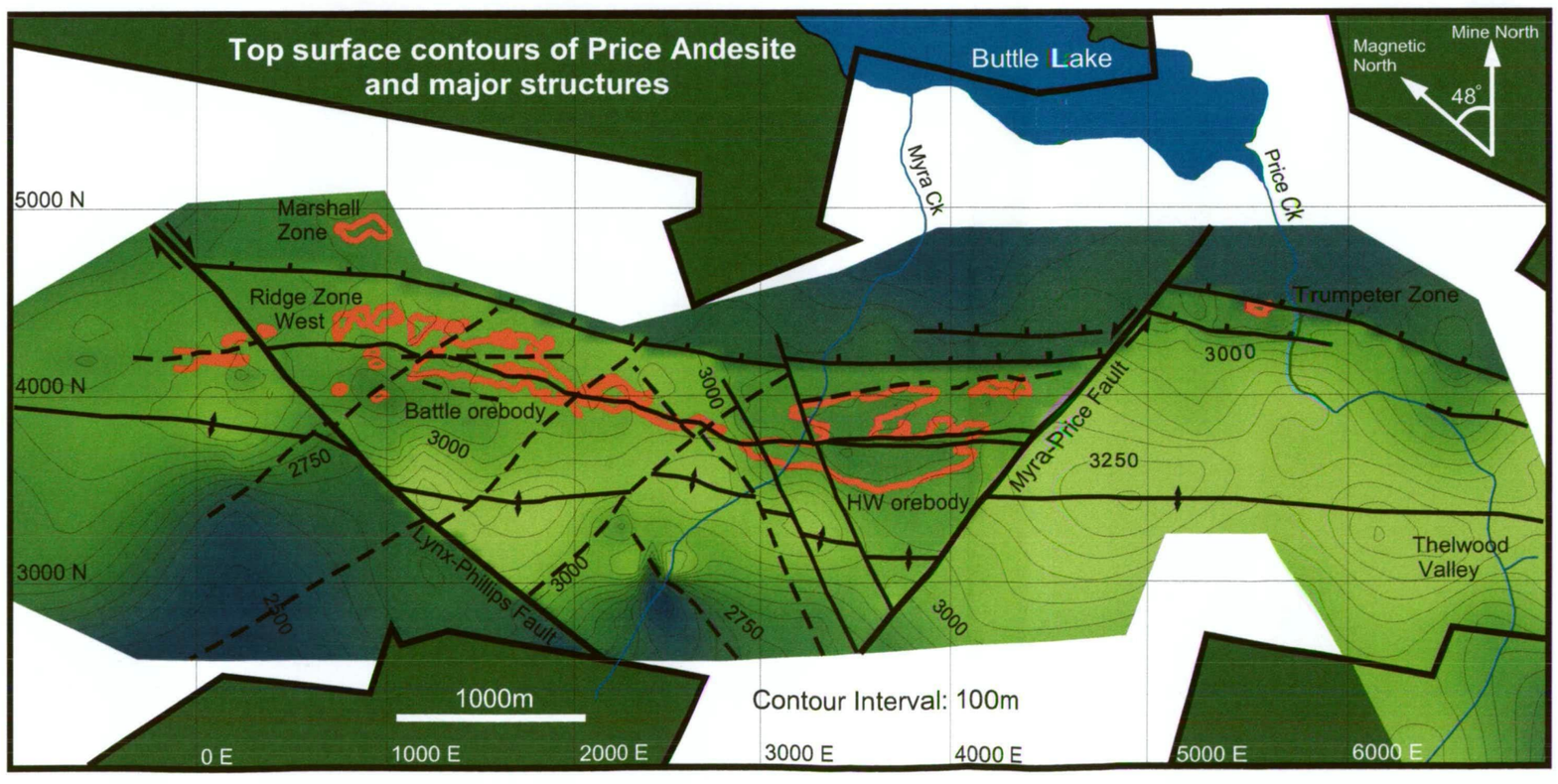

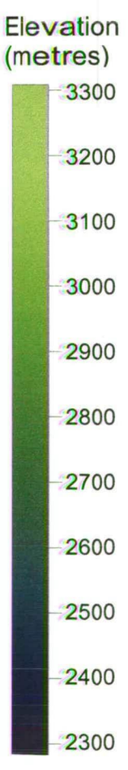

b

UNIVERSITY OF TAS LIBRARY

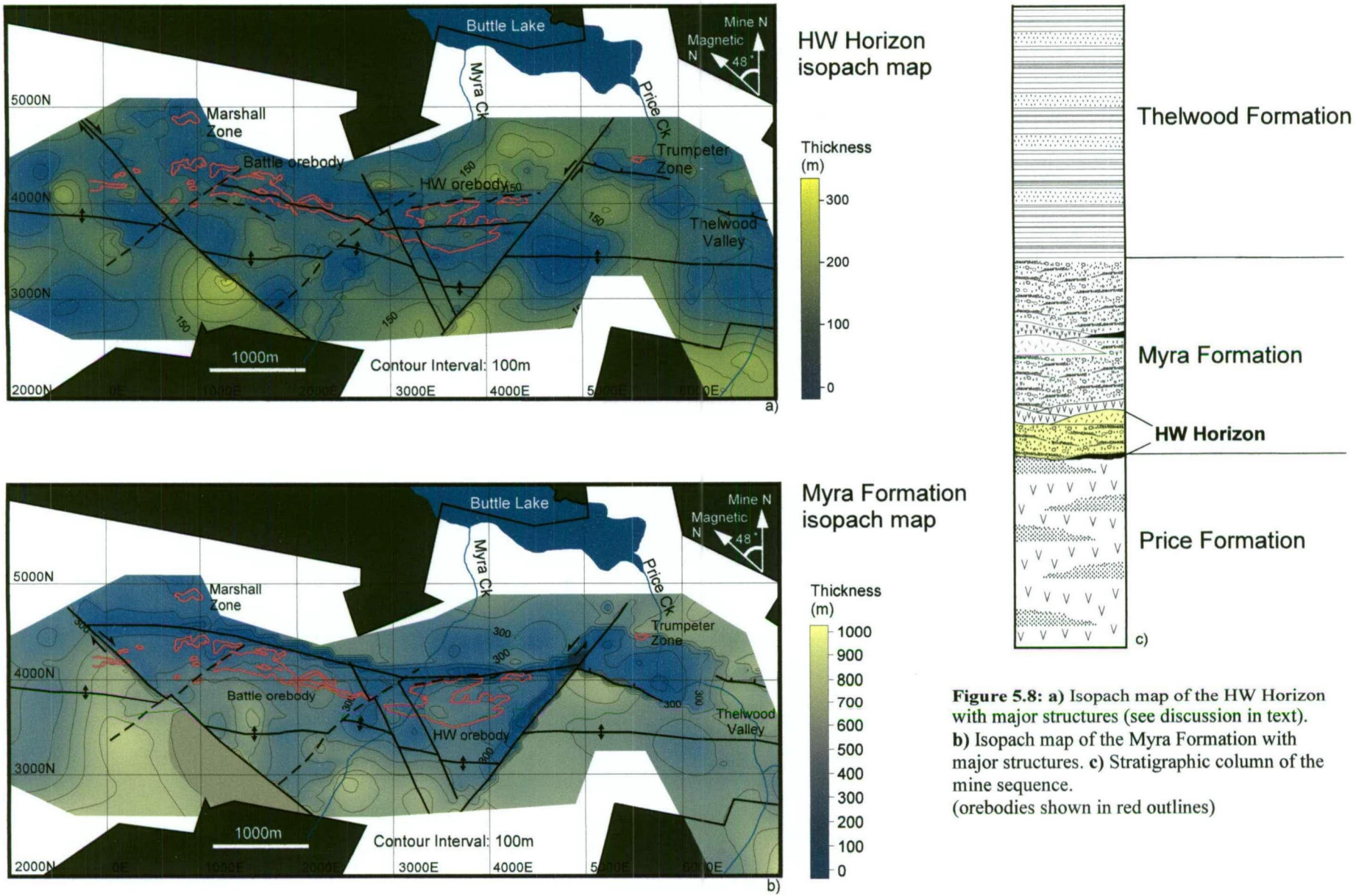

Figure 5.8: a) Isopach map of the HW Horizon with major structures (see discussion in text). **b)** Isopach map of the Myra Formation with major structures. **c)** Stratigraphic column of the mine sequence.
(orebodies shown in red outlines)

useful marker to illustrate the paleoseafloor topography and the likely position of early growth structures. However, much of the topographic variation present in the map (Figure 5.3b and 5.4), is the result of late deformation. For example, the large topographic high in the centre of the map, reflects the hinge zone of the Myra anticline, whereas the topographic low in the north, is the result of a large down throw on the North Fault (see previous chapter for detailed discussion on fault displacements). Although deformation has significantly disrupted the sequence, there are some areas where the original seafloor topography appears to be preserved. Several distinct basinal structures occur, such as the one beneath the HW orebody and another immediately south and west of the Battle orebody.

A number of topographic lows in the deformed paleoseafloor, Figure 5.3b, appear to coincide with the distribution of fine-grained facies shown in Figure 5.3a. This coincidence suggests that some features of the paleoseafloor topography may be preserved, and that mudstone-rich areas may represent original topographic lows. Potter (1999) suggests that "mud and shale-rich deposits ranging from a few to 100s metres thick, whether restricted in size or widespread, represent topographic lows, some shallow, some deep, that had minimal bottom currents or waves". Other areas of the facies map, which are devoid of fine-grained facies, may have originally been topographic highs, where fine-grained sediments were eroded or never accumulated.

The isopach map, Figure 5.5a illustrates variation in total stratigraphic thickness of the HW Horizon, which ranges from 1-300m thick. The map below, Figure 5.5b, shows variation in thickness of the Myra Formation, which includes the entire mine sequence. This formation ranges in thickness from about 100m to greater than 900m. Thin linear zones adjacent to large faults, such as the Myra-Price Fault, indicate fault thinning and are not representative of the true thickness. In general, the HW Horizon and Myra Formation increase in thickness to the south, and both units thicken slightly above the HW deposit and south of the Battle deposit. A detailed examination of the stratigraphic variation and footwall geometry around the orebodies, is discussed in later sections.

The isopach maps indicate that although the sequence at Myra Falls is strongly deformed, at a broad scale, original features of the VHMS environment appear to be preserved. Variations in facies, footwall contours, and stratigraphic thickness, reflect changes in the depositional environment and proximity to volcanic centres.

5.4 Paleoseafloor reconstruction

5.4.1 Structural domains

The sequence is strongly deformed with ubiquitous faults at all scales. However, displacements on many faults are relatively minor (<1-2m) and at a property scale have little effect on the overall sequence. For this reason, the property is divided up into a number of structural domains, separated by major structures (Figure 5.6). Within each of these domains the geology is relatively coherent and the major effects of deformation can be removed from each block or domain. In general, only faults or fault zones with total displacements greater than about 50m are recognized in the reconstruction process. Individual faults (with displacements <10-15m) do not show up on the footwall contours, and most likely do not have a dramatic effect on the sequence.

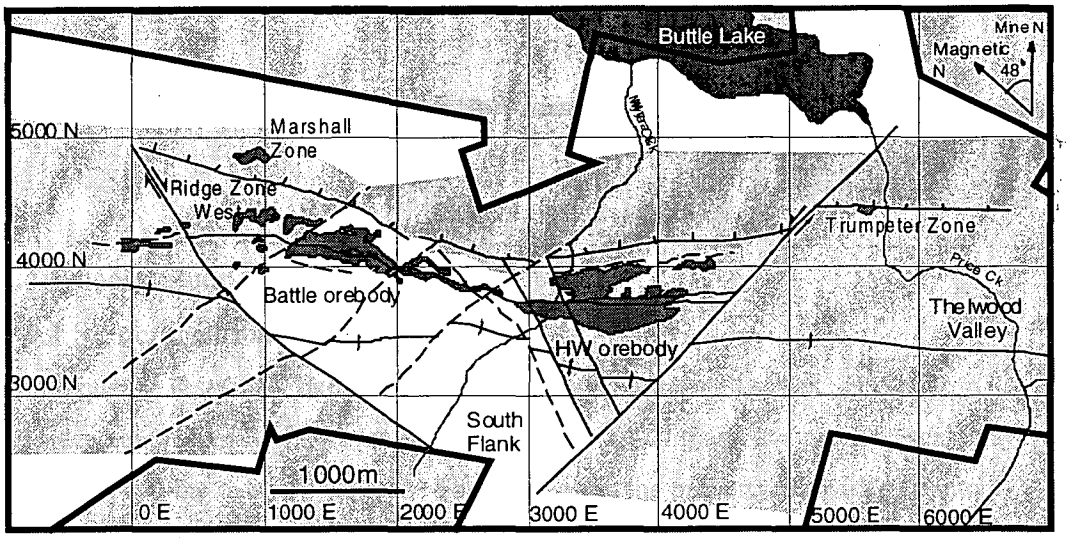

Figure 5.6: Structural domains in the Myra Falls area. Domains are separated by major structures and deformation is relatively minor within each domain.

5.4.2 Removing the effects of late deformation (D_1-D_5)

A planar marker horizon is used to remove vertical displacements across the property, by restoring the marker to a consistent elevation. The basal contact of the Thelwood Formation with the underlying Myra Formation is used as the marker horizon, and the contoured basal contact is shown in Figure 5.7a. The Thelwood Formation is mainly composed of horizontal, laminated mudstone, with interbeds of massive fine to medium-grained sandstone and mafic sills. The dominance of laminated mudstone, the very planar nature of the bedding and the lateral extent of this unit, suggests that it was deposited during a time of subdued relief (Figure 5.7b-c).

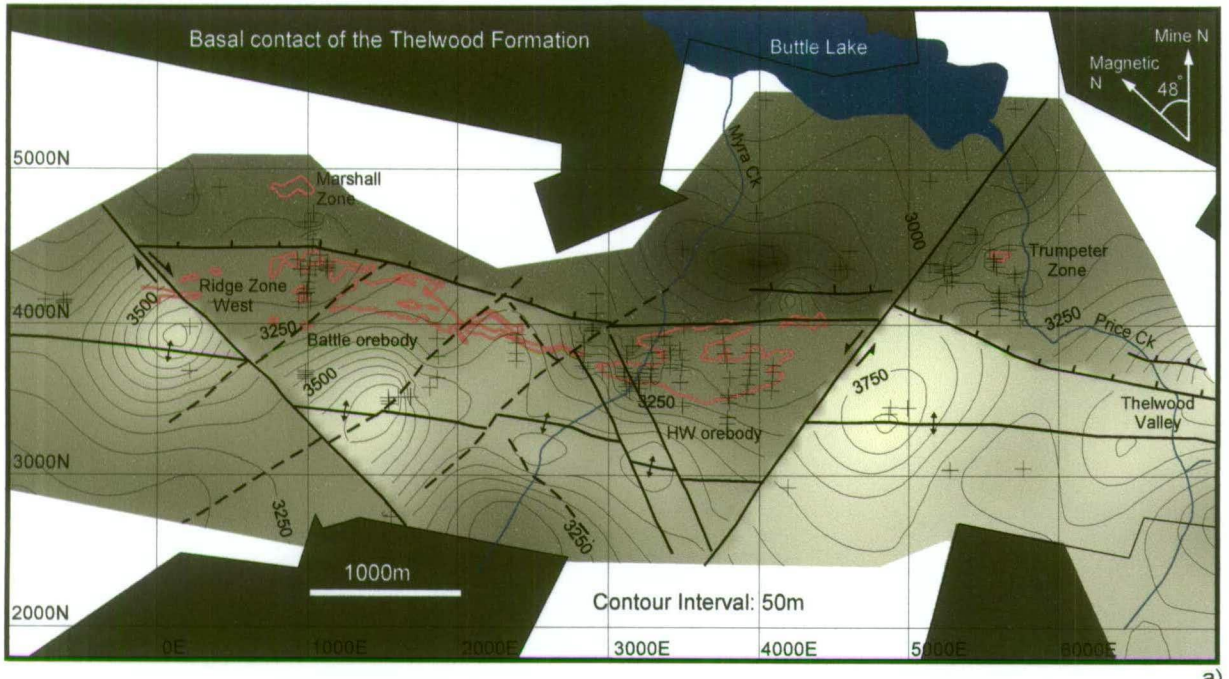

a)

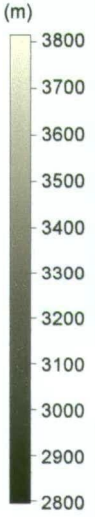

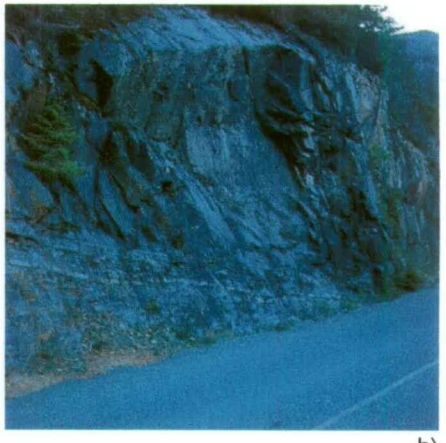

b)

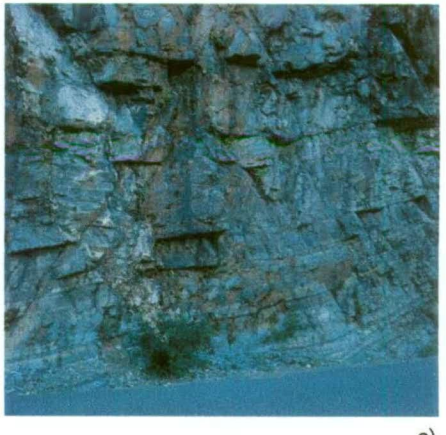

c)

Figure 5.7: a) The basal contact of the Thelwood Formation, shown by the contour map, provides an important marker for the paleoseafloor reconstruction. The very planar nature of the bedding and lateral extent of this unit, suggests that the Thelwood Formation was deposited during a time of subdued relief. Marked topographic variation in the basal surface indicates that this formation is also affected by deformation. The topographic highs represent the hinge zone of the large D_1 fold (Myra Anticline), with significant lateral shifts along D_5 structures, including the Myra-Price and Lynx-Phillips Faults, and large down throw in the northern part of the property along the D_4 North Fault system. Although the unit is moderately deformed, the elevation of the basal contact is relatively level above the Battle and HW orebodies, even though the underlying there is marked topographic variation in the underlying Price Andesite in these areas (orebodies shown in red outline).
b) Thelwood Formation in a roadcut on the Westmin Mine Road, illustrating the planar nature of the bedding.
c) Photo of Thelwood Formation at the same road cutting, illustrating the laminated mudstone which dominates the unit.

The contour map, Figure 5.7a, indicates that the basal contact of the Thelwood Formation has significant relief across the property. Much of this relief is due to late deformation, with topographic highs in the centre of the map reflecting the hinge zone of the Myra Anticline, and the deep low in the north, representing down throw on the North Fault. However, the basal contact appears to have a similar and consistent elevation of 3200m, above both the HW and Battle-Ridge zones. In both of these areas the underlying footwall, or paleoseafloor, shows marked relief. This suggests that the structures responsible for rapid changes in the paleoseafloor elevation, did not affect the Thelwood Formation, and may represent growth faults.

Vertical and lateral displacements of the paleoseafloor were removed by a series of steps using the grid-math function in Golden Software Surfer 7.0. These steps involved:

1. Separating the data into the major structural blocks and removing the lateral displacements for each block. The strike-slip component of fault displacement was estimated from offset markers, such as the hinge zone of the Myra Anticline, and offset porphyry bodies and footwall contours;
2. Subtracting the present day Thelwood Formation basal contact contours from a plane at 3200m elevation to create a residuals file; and
3. Addition of residuals to the footwall contours to restore the paleoseafloor topography.

Paleoseafloor reconstruction was first undertaken at a deposit scale for the HW and Battle-Ridge zones to identify the possible location and orientation of growth structures. These structures were then added to a paleoseafloor reconstruction for the entire property. This reconstruction gives an overview of the depositional and structural setting for the VHMS orebodies at Myra Falls.

5.5 HW mine area reconstruction

The footwall contours in the HW mine area are shown in Figure 5.8a. Major structures, which affect the footwall elevation are also shown. The West Main Fault is a zone of steep normal faults, which dissect and uplift the western side of the orebody. The total displacement across this zone is approximately 50m, however, individual normal faults in this zone generally show only 5-10m displacement. The faults are spaced 10-20m apart and for this exercise, the zone is represented by only 2-3 faults. Other major structures in the area are the North Fault and the Myra Anticline, which result in the deep topographic low in the north and the ridge to the south respectively. The Myra-Price Fault displays sinistral movement, offsetting the Myra Anticline axis to the north. Although these structures dominate the footwall topography of this area, a distinct basinal feature is still visible beneath the HW orebody.

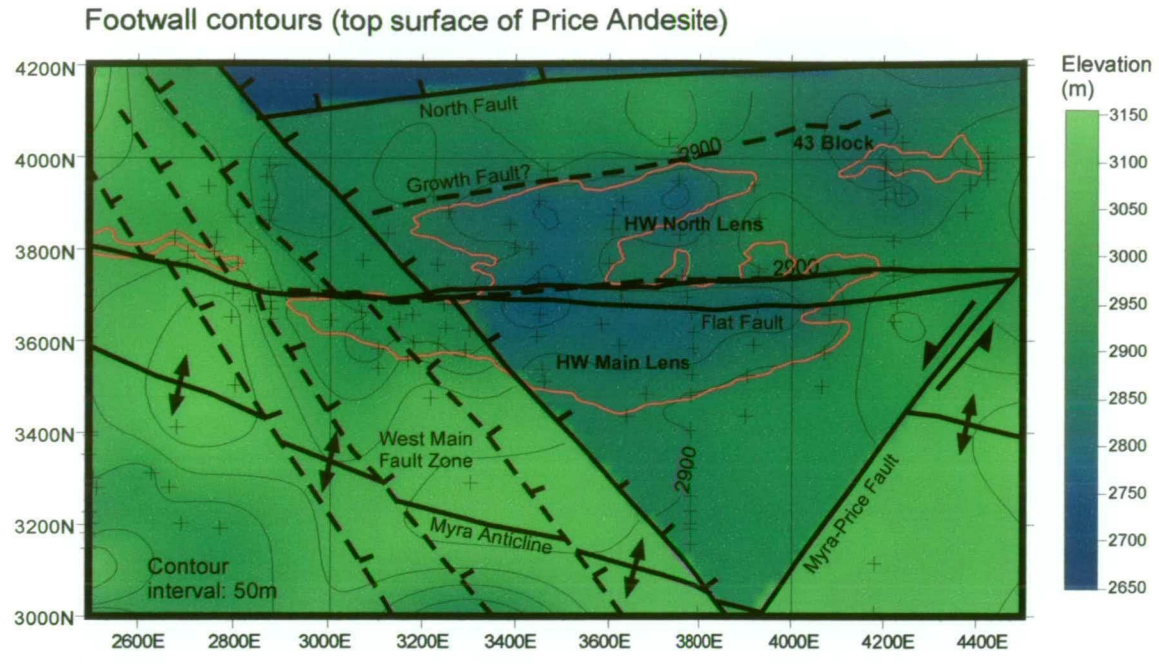

Figure 5.8: a) HW mine contour map of the top surface of Price Andesite (footwall to VHMS ore). The effects of the major structures are shown by marked changes in footwall elevation (see discussion in text).

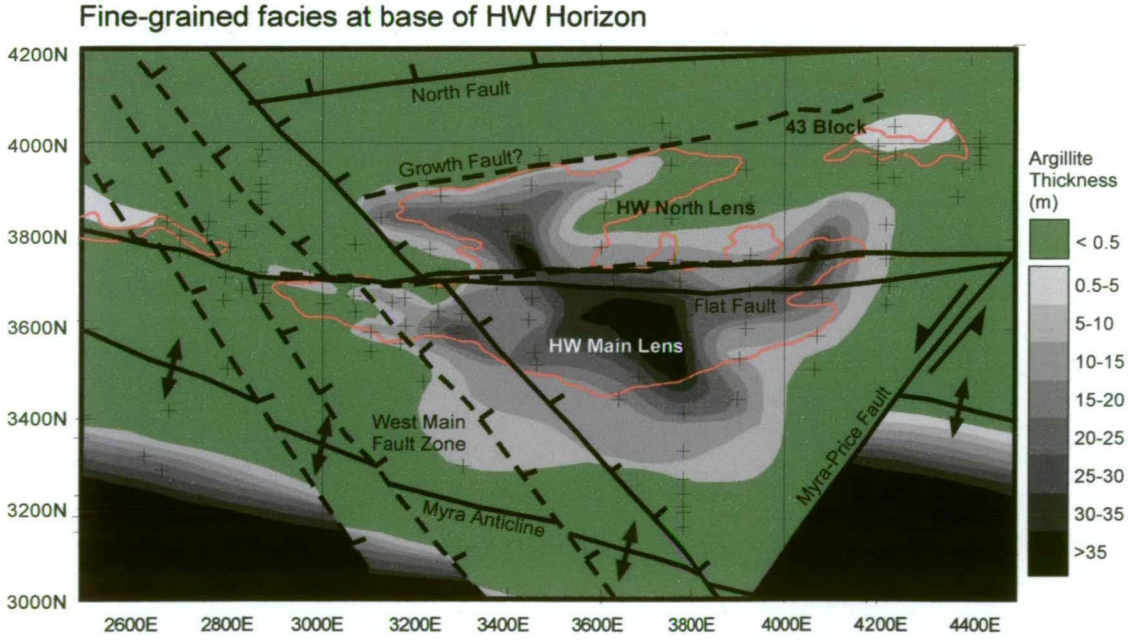

Figure 5.8: b) Facies map of the HW mine area illustrating the distribution of fine-grained facies in the basal part of the HW Horizon. Argillite, interbedded with fine sandstone is the dominant fine-grained facies in this area, and appears to coincide with the topographic lows in the southern part of the area and beneath the HW orebody.

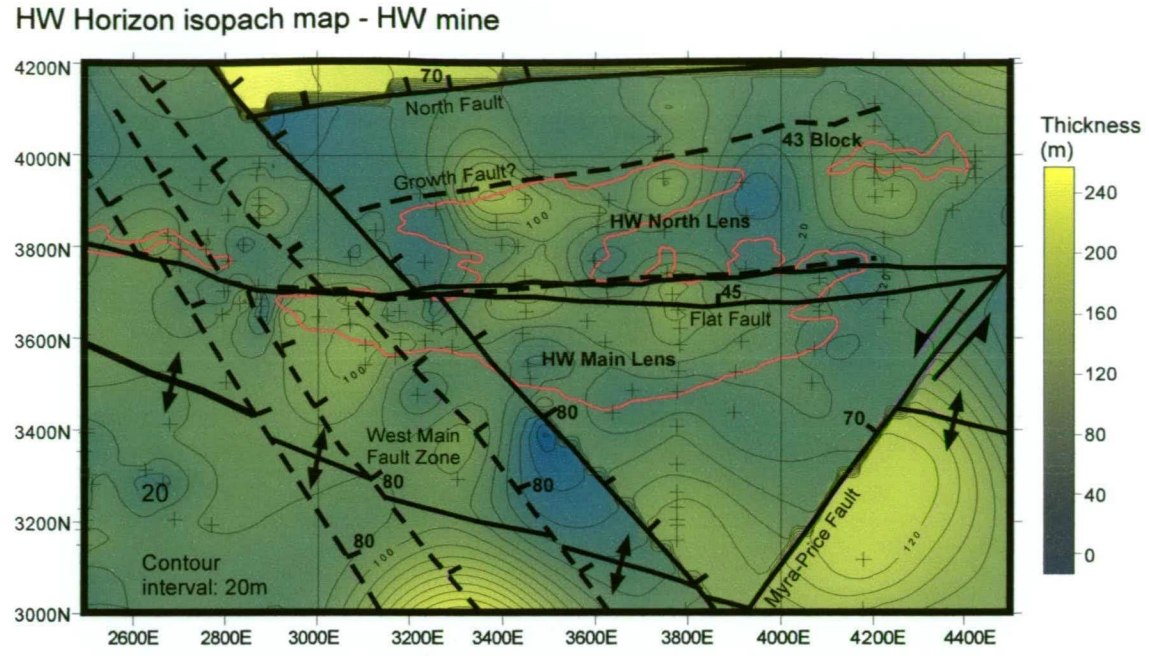

Figure 5.9: a) HW mine isopach map of the HW Horizon illustrating the variation in thickness above the orebody and the surrounding area. The thickest zones are generally in the south, which is dominated by thick mudstone sequences. The Myra-Price Fault displaces this thicker part of the HW Horizon to the north. A slight thickening in the HW Horizon is observed above the orebody, with thinner zones to the north and south. These changes in stratigraphic thickness may be related to syn-depositional growth faults.

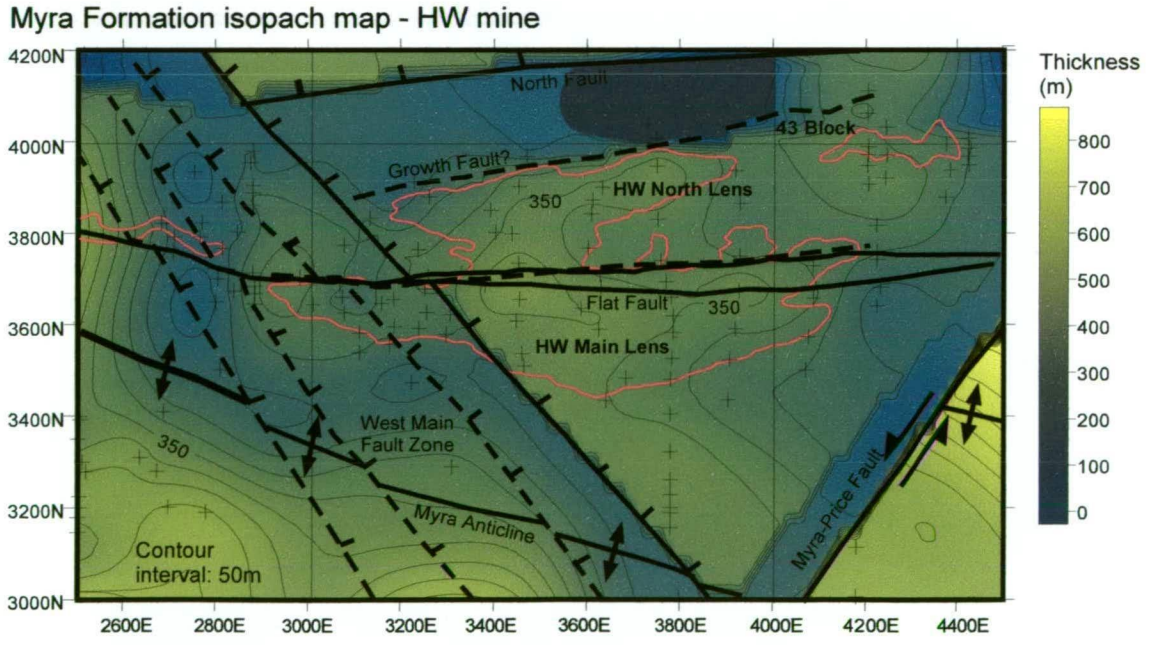

Figure 5.9: b) HW mine isopach map of the Myra Formation. A marked decrease in the thickness of the Myra Formation immediately north of the orebody is most likely a result of a syn-depositional growth fault (see text for discussion). Other thin zones reflect fault thinning along major structures such as the Myra-Price Fault and the West-Main Fault Zone.

The basinal feature coincides with a moderately thick zone of argillite, shown in the isopach map below (Figure 5.8b). The presence of argillite indicates that this zone was a topographic depression or depo-centre. Thick argillite deposits are also common in the south, and have been displaced northwards on the eastern side of the Myra-Price Fault.

The isopach map of the HW Horizon, Figure 5.9a, indicates that the HW Horizon becomes slightly thicker into the basinal structure, with thinner zones on the periphery of the structure. Myra Formation isopachs also indicate an increase in stratigraphic thickness into this basinal structure (Figure 5.9b). The formation thins rapidly to the north of the HW orebody, with the thickness varying from 400m over the orebody to less than 200m in the northern area. Thinner zones are also associated with the large faults, such as the Myra-Price Fault, and reflect fault thinning.

5.5.1 Location of growth structures

Figure 5.10a is an isopach map of coarse-grained mixed rhyolitic and andesitic material, which occurs beneath the HW orebody. The dark green areas, with no contours, are zones where the orebody is in direct contact with the underlying Price Andesite. The northern part of the orebody and the southwestern edge, have rhyolitic material beneath the ore, up to 50m thick in places. Early growth structures are shown on this map, and their position and orientations are based on a number of criteria, including the location of thick rhyolitic deposits beneath the ore, marked changes in footwall elevation and the thickness of the HW Horizon and Myra Formation. Footwall contours and isopach maps suggest that the basal coarse-grained mixed volcaniclastic deposits may represent early basin infill adjacent to growth faults, prior to ore formation. Figure 5.10b illustrates the reconstructed paleoseafloor in the HW mine area, with the growth faults from Figure 5.10a.

The most obvious growth structure is growth fault 1, which has an ENE trend and is located at the northern margin of the HW orebody (Figure 5.10a). There is a relatively sharp drop in footwall elevation into the HW basin, with a rapid drop of about 100m. For example, on section 3400E the footwall elevation changes from 2900 down to 2800 between W129 and W127, and on section 3800E, from about 2890m down to 2800m between drillholes P13-307 and P13-306 (Figure 5.10b). The thickest zone of rhyolitic-andesitic debris beneath the orebody is located adjacent to this structure (Figure 5.10a), and a marked increase in stratigraphic thickness of the HW Horizon and the Myra Formation also indicates the presence of an early growth structure (Figure 5.10a). For example, on section 3400E, the thickness of the HW Horizon increases southward, from 35 to 80m, and the Myra Formation increases from about 100 to 300m thick, between drillholes W129 and W127. On section 3800E, the HW Horizon increases southward, from 20 to 100m thick, and the

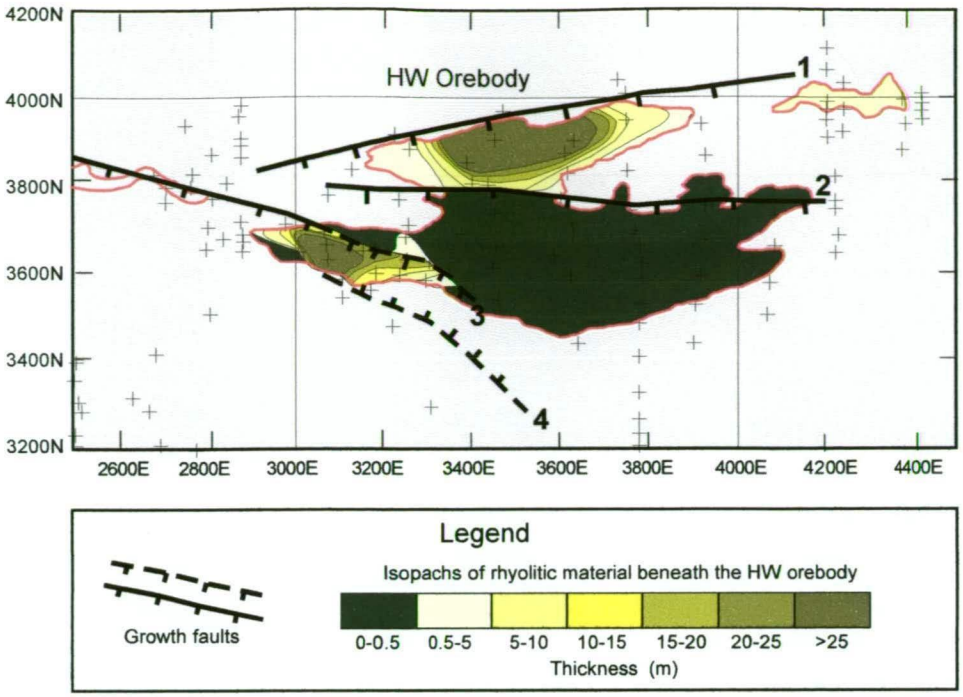

Figure 5.10: a) Isopachs of coarse-grained mixed rhyolitic-andesitic material beneath the HW orebody and inferred position of early growth faults (see text for further discussion).

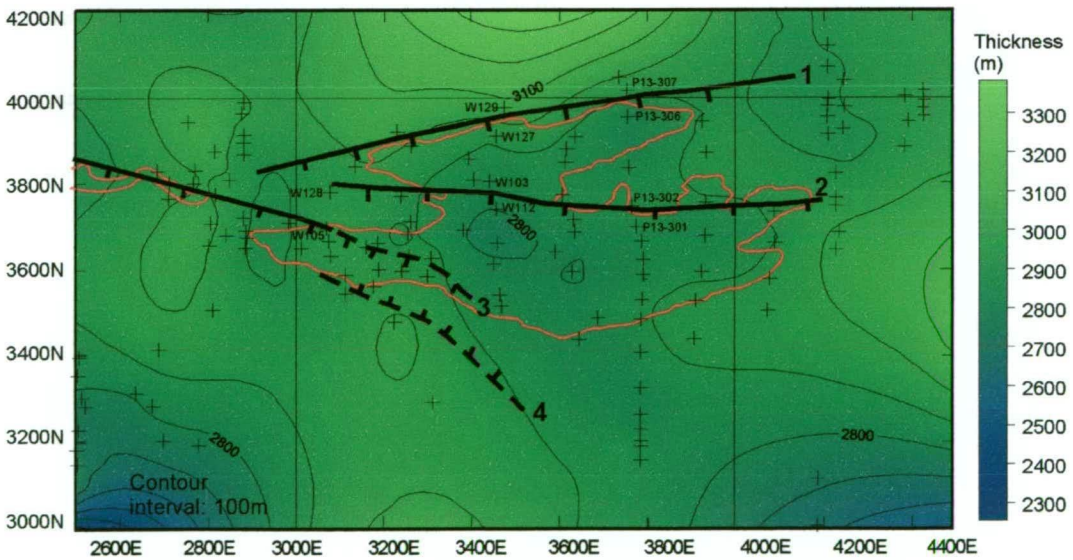

Figure 5.10: b) Restored paleoseafloor with the estimated location and orientation of growth faults from the diagram above. The location of growth faults is based on: 1) rapid changes in footwall elevation; 2) marked facies variation in the coarse-grained rhyolitic units beneath the orebody; 3) marked increases in the thickness of the HW Horizon and Myra Formation (see text for further discussion).

Myra Formation increases from 100 to 300m thick, between drillholes W129 and W127 (Figure 5.9a and 5.9b).

The second structure (fault 2) has a similar orientation, and its position is indicated by variation in footwall elevation, stratigraphic thickness, and by the change in the position of the ore horizon, relative to the underlying Price Andesite (Figure 5.10a). South of this structure, the ore horizon lies in direct contact with Price Andesite, whereas to the north, the orebody is located above a thick pile of coarse-grained mixed rhyolitic and andesitic detritus. A much broader zone of argillite occurs in the southern area, suggesting a larger, deeper depo-centre. A smaller change in the footwall elevation is seen across growth fault 2, generally, less than 30m. On section 3400E the footwall elevation decreases southward from 2820 to 2795m between drillholes W103 and W112 (Figure 5.10b). The thickness of the HW Horizon increases southward across the structure, by about 30m (Figure 5.9).

Faults 3 and 4 were not as obvious as faults 1 and 2, as they do not show up clearly on the footwall contours. This suggests that the total offset on these structures may have been less than 50m. The faults also occur in an area disrupted by the West Main Fault zone, making interpretation more difficult. Although footwall contours do not indicate the position of fault 3, the orientation of the structure is estimated to be an extension of the WNW trend of the Extension Zone orebodies (Figure 5.3). This is based mainly on the presence of coarse-grained mixed rhyolitic-andesitic material beneath the orebody (Figure 5.10a), and HW Horizon isopachs (Figure 5.9a). There is a marked increase in the thickness of the HW Horizon to the south, from 20 to 100m, between drillholes W128 and W105, on section 3100E (Figure 5.9a) suggests the presence of a growth structure. The position of fault 4 is estimated from the rapid increase in footwall elevation to the south (Figure 5.10b) accompanied by a slight decrease in stratigraphic thickness of the HW Horizon and Myra Formation (Figure 5.9).

The growth faults and associated changes in stratigraphic thickness and footwall elevation are best illustrated by N-S oriented sections. Figure 5.11a, shows section 3500mE, which extends through the centre of the HW orebody. The section shows the present day geology with the major structures, which affect the sequence. The large uplifted zone on the southern side of the section is the result of D_1 folding (Myra Anticline) and D4 normal faulting in the West Main Fault zone. A deep topographic low in the north is the result of large down throw on the North Fault. Displacement on the Flat Fault is relatively minor at this scale. The section below, Figure 5.11b, illustrates the restored geology, with the base of the Thelwood Formation returned to 3200m elevation. The most noticeable effect of the reconstruction is that the footwall topography is greatly reduced. However, there is still a

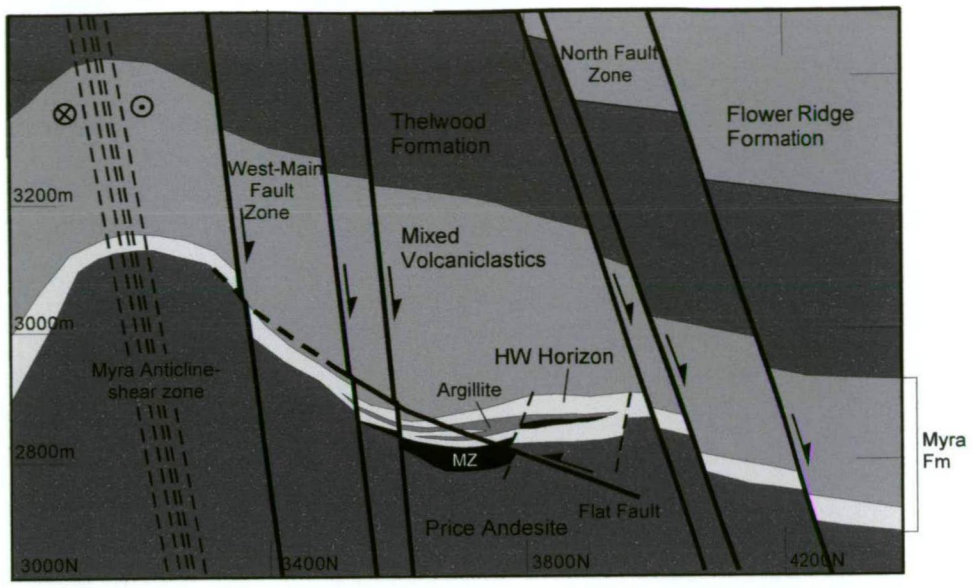

Figure 5.11: a) This section shows the present day geology of section 3500mE in the centre of the HW mine. Major structures affecting the area are shown and include the D_1 Myra Anticline, D_4 West-Main and North Fault Zones, and the D_5 Flat Fault (MZ = orebody).

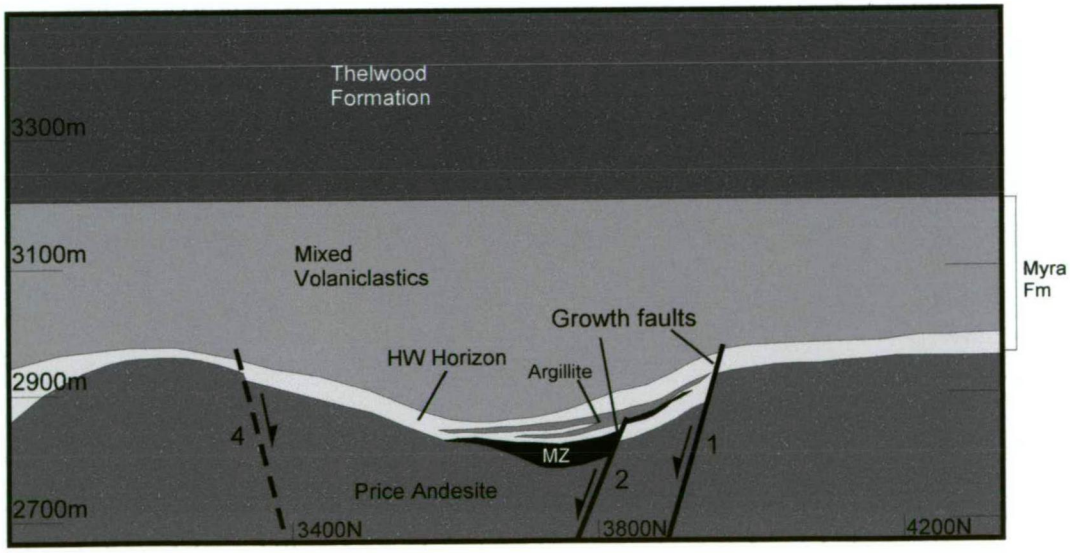

Figure 5.11: b) Restored geology of HW mine section 3500E. The base of the Thelwood Formation is restored to a planar feature at 3200m elevation and this correction is applied to the underlying units to remove vertical displacements. The reconstruction greatly reduces the topographic variation in the footwall (or paleoseafloor), but there is still a distinct thickening into a basinal structure associated with the VHMS orebody (MZ = orebody)

distinct basinal structure beneath the orebody and the HW Horizon and Myra Formation show a marked increase in thickness. The growth faults from Figure 5.10 are located at the northern edge of the HW basin.

The present-day geology of the western edge of the HW orebody is shown on N-S oriented section, 3050mE (Figure 5.12a). Similar structural features, to the previous section are seen, with major uplift resulting from D_1 folding and D_4 normal faulting. The large down throw on the North Fault can also be seen on the northern side of the section. The section below, Figure 5.12b, illustrates the restored geology, with the base of the Thelwood Formation returned to 3200m. Growth faults 3 and 4, from Figure 5.10, are located adjacent to the thick zone of rhyolitic material beneath the orebody. These structures were most likely active well before ore formation, with rhyolitic debris infilling the early fault depression, as it did adjacent to fault 1. The restored cross section, (reconstructed manually) shows a rapid drop in footwall elevations across the growth structures 3 and 4. However, these marked changes in footwall elevation are not observed in the footwall contour map. This is most likely due to the structural complexity of the area (West Main Fault zone), resulting in slight inaccuracies of the paleoseafloor model.

The WNW trend of faults 3 and 4 is similar to the trend of the Extension Zone orebodies and the eastern edge of the Battle orebody (Figure 5.3). This alignment may represent a major fault trend for the area. In contrast, growth faults 1 and 2 (Figure 5.10) appear to splay off the WNW trending faults, and these splays may represent a bend in the main fault trend. If so, this zone would form an ideal locus for fluids, and ore formation.

(text continued on page 132)

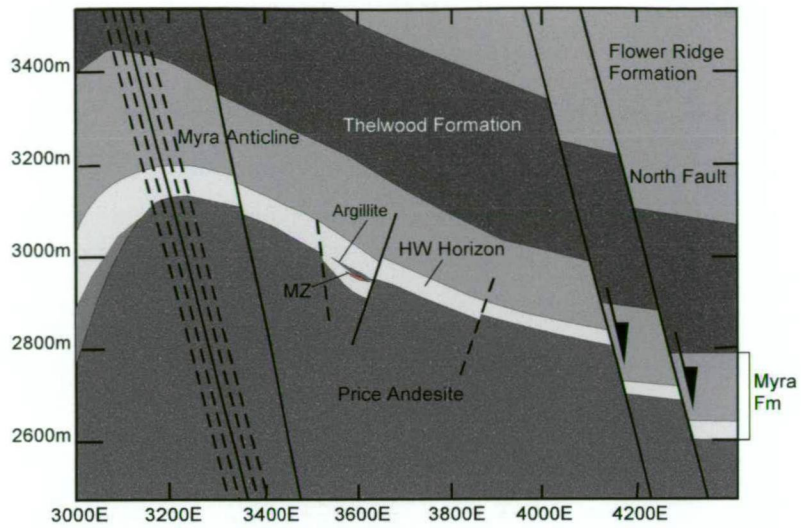

Figure 5.12: a) Section 3030E, at the western edge of the HW orebody illustrates the dramatic effect of late deformation on the sequence. A possible growth structure from Figure 5.10 is shown adjacent to the mineralized horizon (MZ = orebody).

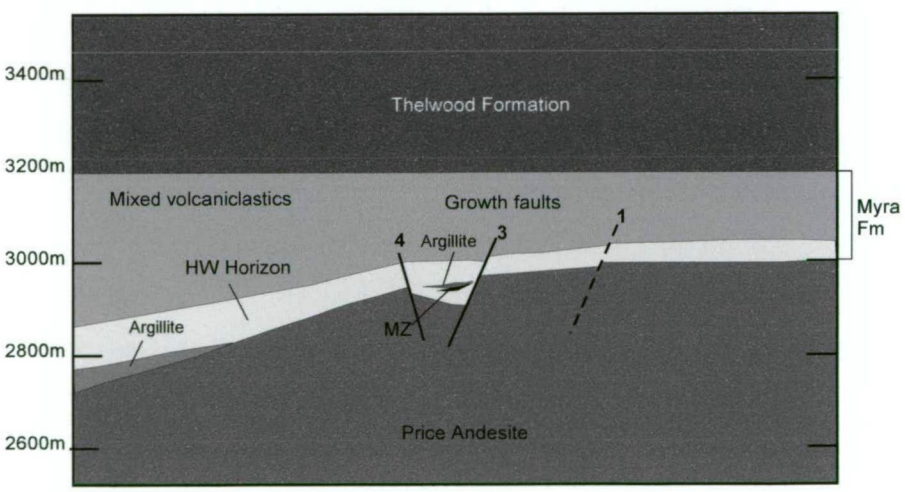

Figure 5.12: b) Restored section 3050E shows the likely position of the growth adjacent to a sharp drop in the footwall contours and marked thickening in the HW Horizon (MZ = orebody).

5.6 Battle-Ridge Zone reconstruction

Reconstruction of the paleoseafloor and identification of growth structures in the Battle-Ridge Zone was more difficult, mainly due to a greater degree of deformation. Figure 5.13a illustrates the present day footwall contours of the Battle-Ridge area and the major structures, which affect the sequence. The deep topographic low in the north is a result of down throw on the North Fault, and the topographic high on the south edge of the map is close to the hinge zone of the Myra Anticline. A series of NE oriented D_5 faults displace the western edge of the Battle orebody. The Flat Fault extends throughout the orebody with top to the west displacement. The footwall contours suggest that a broad topographic low or basinal feature occurs immediately south and west of the Battle orebody. The topographic low coincides with a relatively thick zone of argillite and chert in the isopach map below (Figure 5.13b). The fine-grained facies appear to lie in several NE oriented deposits and this trend may reflect the orientation of original basin controlling structures. The isopach map of the HW Horizon (Figure 5.14a) shows a slight increase in stratigraphic thickness into the basinal feature. A more marked increase in stratigraphic thickness is shown by the Myra Formation isopachs (Figure 5.14b), with the formation increasing from just over 100m to greater than 300m thickness within the basinal structure.

5.6.1 Location of growth faults

A reconstruction of the paleoseafloor and growth structures in the Battle-Ridge zone is illustrated in Figure 5.15. The position and orientation of these early structures is based on the restored paleoseafloor contours, isopach maps of the HW Horizon and Myra Formation, and facies maps. However, the interpretation of early growth structures here, is not as reliable as those mapped around the HW orebody, mainly due to a greater degree of deformation in the Battle area. The Battle structures may also have had smaller total displacements, therefore, not showing up as well on footwall contours and isopach maps.

Growth fault 1 is the most readily recognised structure, and is located adjacent to a NE trending zone of argillite (Figure 5.13b), and a sharp drop in footwall contours (Figure 5.15). On section 1000E, footwall elevation decreases rapidly from 3000 to 2960m, and the thickness of Myra Formation increases from 240 to 310m, between drillholes L15-346 and L15-342.

The interpretation of growth fault 2 is the least reliable of the faults and is based mainly on a rapid increase in footwall elevation and decreasing stratigraphic thickness on restored composite section 1260-1420E, illustrated in the following chapter (Figure 6.5). The fault is located at about 4280E and may have acted as a ore-fluid conduit for the Gap orebody.

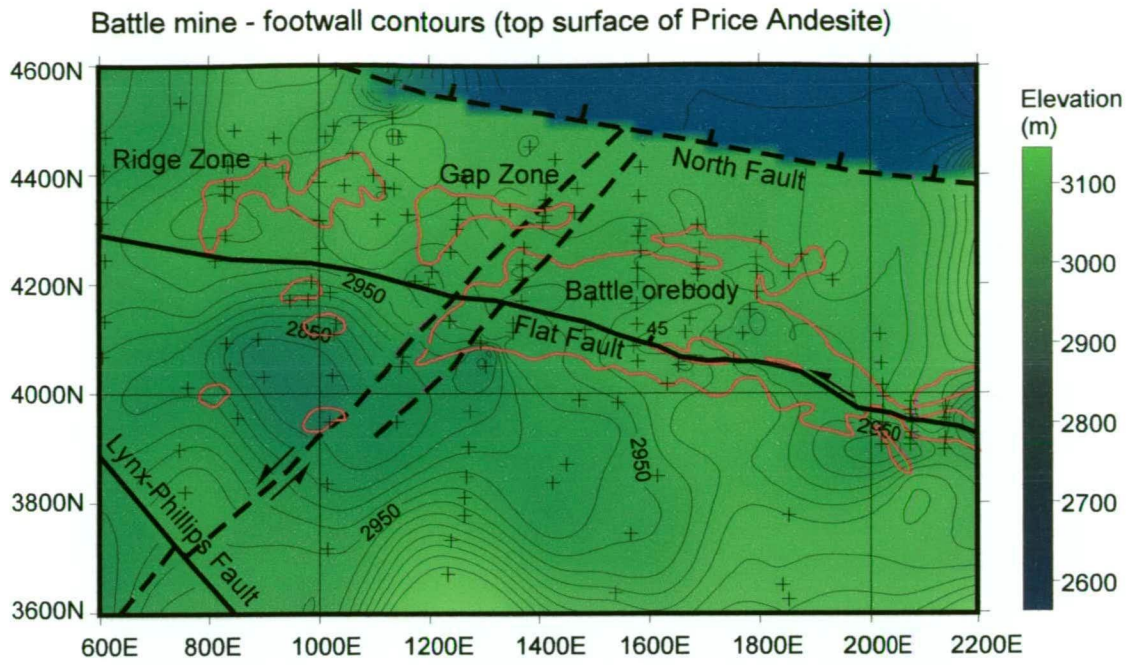

Figure 5.13: a) Footwall contours (top surface of Price Andesite) in the Battle mine area. A large basinal structure occurs southwest of the orebody and coincides with thick argillite deposits (see facies map below).

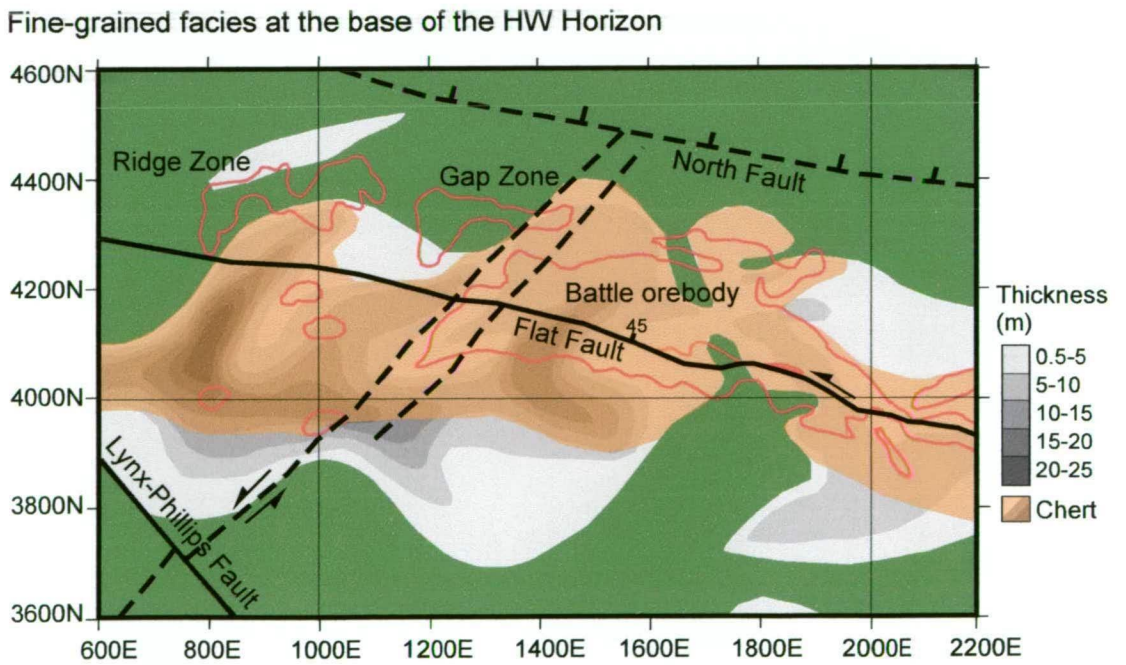

Figure 5.13: b) Facies map of the Battle mine area, showing the distribution of fine-grained facies which occur at the base of the HW Horizon. Siliceous caprocks (or chert) are best developed in this area, and appears to be spatially associated with the orebody.

Growth fault 3 is clearly indicated by a sharp drop of about 60m in footwall elevations on section 1260E, between drillholes L14-753, L14-707 and L14-683 (Figure 5.15). The thickness of the Myra Formation also increases southward, across this structure, from 250 to 320m (Figure 5.14b). The isopach map (Figure 5.13b) also indicates that a thick zone of argillite displays a NE trend, adjacent to this structure.

Growth faults 1, 2 and 3 have an ENE orientation and appear to splay off the WNW trending structure, which extends through the Extension Zone and up to Battle orebody. Sinclair (2000) examined metal zonation throughout the Battle orebody and found linear trends of high Cu and Fe at the base of the orebody and suggested that they represent feeder zones. These linear trends have ENE to NE orientations and line up approximately with growth faults 1, 2 and possibly 3.

The paleoseafloor reconstruction and the effects of growth faults are best illustrated by N-S oriented sections. Figure 5.16a, shows the present day geology of the western side of the Battle orebody on section 1300E. The sequence is strongly deformed by D_1 folding (Myra Anticline), D_4 normal faulting (North Fault) and D_5 shallow oblique thrusts (Flat Fault). Figure 5.16b, below, illustrates the reconstructed geology, with the base of the Thelwood Formation returned to 3200m elevation. The footwall (or paleoseafloor) topography is greatly reduced and the basinal feature, immediately south of the Battle deposit is more visible. The position of growth faults 2 and 3 is based largely on marked increases in the thickness of the Myra Formation from north to south. Only slight changes in the thickness of the HW Horizon are visible and the majority of movement on these growth faults may have postdated deposition of the HW Horizon. A more detailed view of the HW Horizon in this area, is shown in restored composite section 1260-1420E in the following Chapter (Figure 6.5). In this section, there is a marked change in stratigraphic thickness and footwall elevation at about 4350N, which coincides with growth fault 1. However the horizon shows only a gradual decrease in thickness to the south, accompanied by a slight rise in the footwall topography. Deposition of the HW Horizon and Battle ore formation most likely predates movement on growth faults 2 and 3.

The present-day geology of the western edge of the Battle orebody and the Ridge Zone is shown on section 1000E (Figure 5.17a). The effects of late deformation are similar to the previous section, with major vertical displacements resulting from D_1 folding and D_4 normal faulting. The section below (Figure 5.17b) shows the restored geology with the base of the Thelwood Formation returned to 3200m elevation. The Ridge Zone orebodies are still located on a steep slope at the northern margin of a large basin. The marked increase in thickness of the Myra Formation coincides with the drop in the footwall

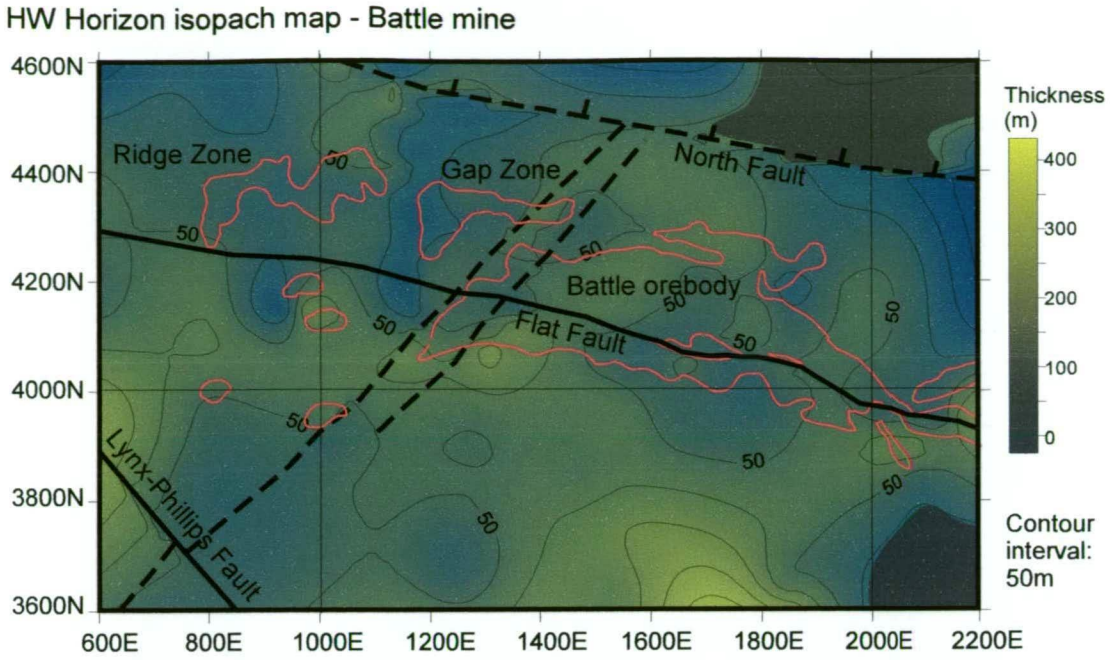

Figure 5.14: a) Isopach map of the HW Horizon in the Battle mine area. Although there is not a lot of variation in the thickness of the HW Horizon across the area, the unit does appears to thicken slightly to the south and west of the orebody and this area coincides with a topographic low on the footwall contours and the thickest zone of argillite/chert on the facies map. The stratigraphic thickening to the south most likely reflects the paleoseafloor topography.

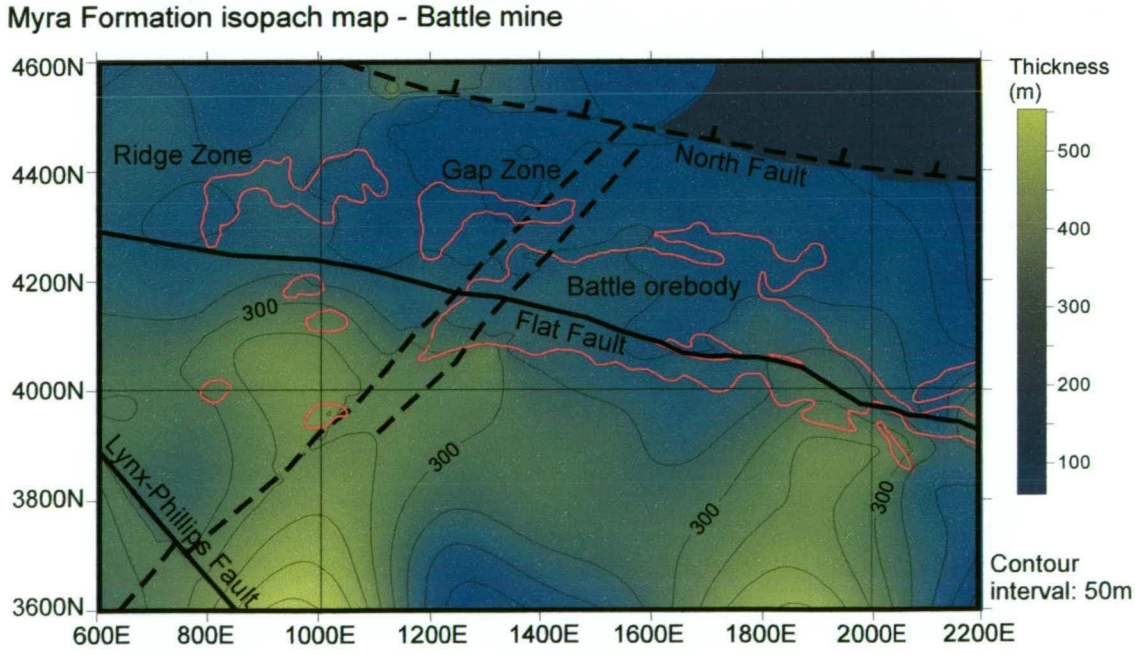

Figure 5.14: b) Isopach map of the Myra Formation in the Battle mine area. The unit thickens to the south and west of the Battle orebody, most likely reflecting the lower topography of the underlying footwall Price Andesite. The marked thinning to the north of the orebody also coincides with elevated footwall topography.

elevation, indicating that growth faults were active during deposition of the Myra Formation. However, the HW Horizon maintains a similar thickness throughout this zone and movement on the major growth faults controlling basin formation, most likely postdates deposition of the HW rhyolitic facies and ore formation (?).

In general, the reliability of the paleoseafloor reconstruction and the interpreted growth faults depends on drillhole density, the intensity of late deformation, and the total displacement on each structure. In most places, marked changes in the elevation of the reconstructed paleoseafloor indicate the position of the growth faults. However, in zones of strong deformation, such as the western edge of the HW orebody in the West Main fault zone, the accuracy of the reconstruction is diminished, making the interpretation of growth faults difficult. In this case, manual construction of restored cross sections was necessary to locate the growth structures. The assumption about the planar nature of the basal contact of the Thelwood Formation also has a major effect on the accuracy of the reconstruction. Ideally the top contact of this formation should be used, however, a large proportion of the drillholes were collared within the Thelwood Formation and the upper contact is therefore poorly constrained.

(text continued page 143)

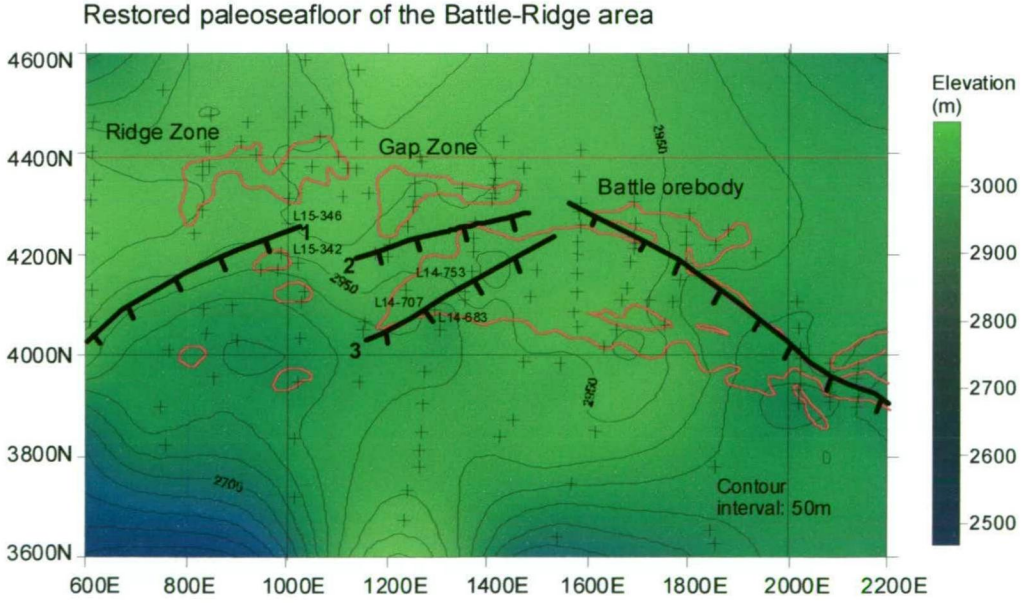

Figure 5.15: Restored paleoseafloor of the Battle-Ridge area with growth structures. The orientation and position of growth faults is estimated from footwall contours, isopach maps of the HW Horizon and Myra Formation and facies maps.

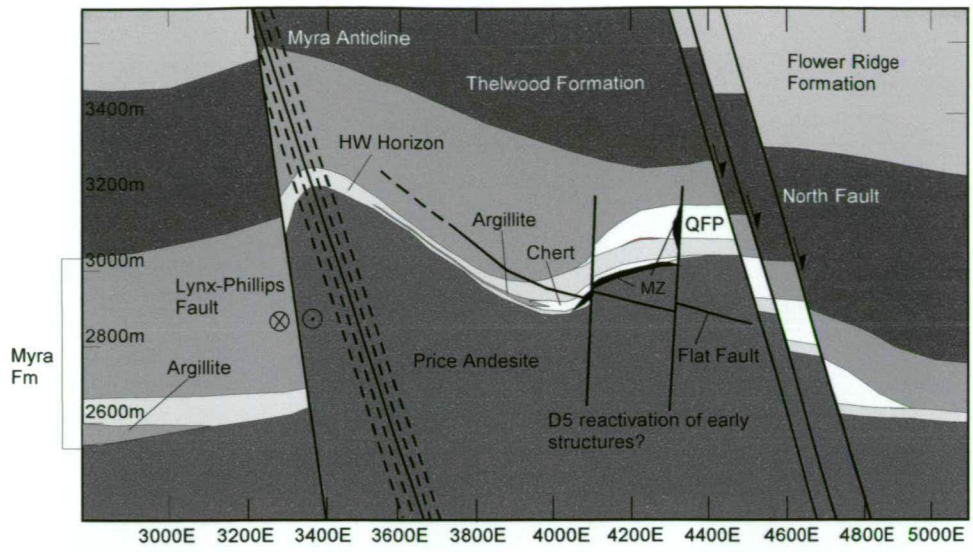

Figure 5.16: a) Section 1300E is located on the western side of the Battle deposit. The sequence is strongly disrupted by major structures including the Myra Anticline, Lynx-Phillips Fault and North Fault. The effects of these structures are removed in the restored section below (MZ = orebody).

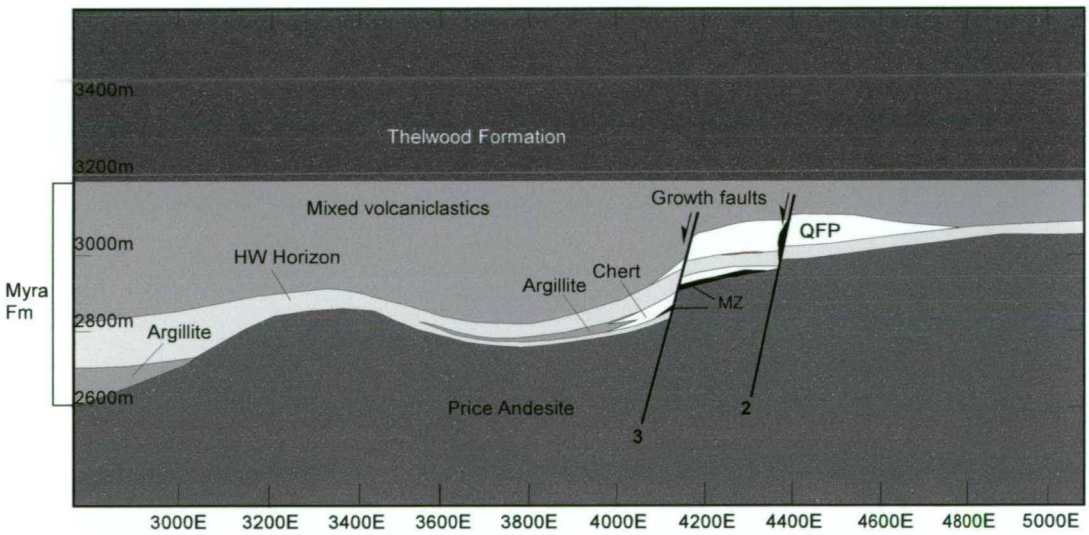

Figure 5.16: b) Restored geology of the Battle deposit (Section 1300E). This section also shows a marked increase in the thickness of the Myra Formation, coinciding with a drop in the elevation of the underlying Price Andesite. The HW Horizon thins slightly adjacent to growth fault 2 and this may be the first active growth structure. The thickness of the HW Horizon does not change over fault 2, suggesting that this fault was active after deposition of the HW Horizon, and ore formation (MZ = orebody).

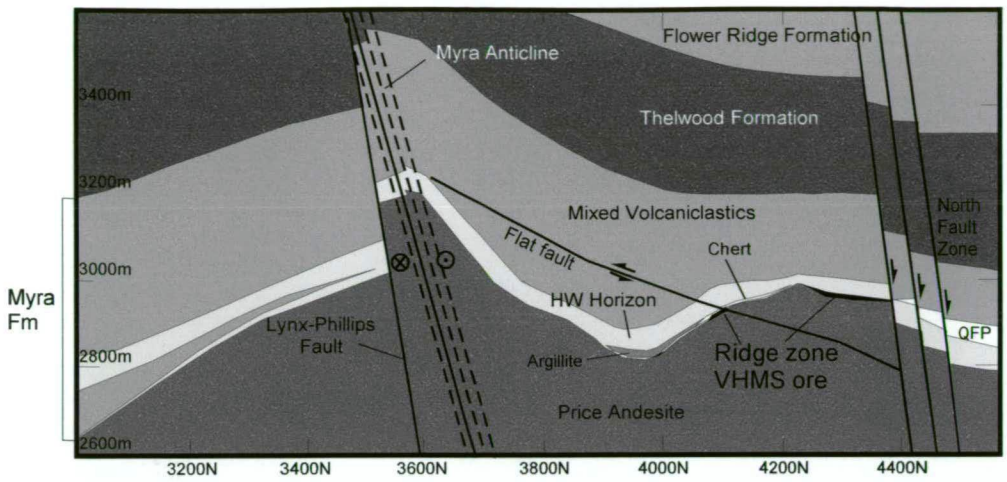

Figure 5.17: a) Section 1000E is located just west of the main Battle orebody and was chosen to illustrate the geological reconstruction because of the number of drillhole pierce points through the Thelwood Formation. Major structures are shown and include the Myra Anticline, which has a major effect on footwall topography, the Lynx-Phillips Fault and the North Fault zone.

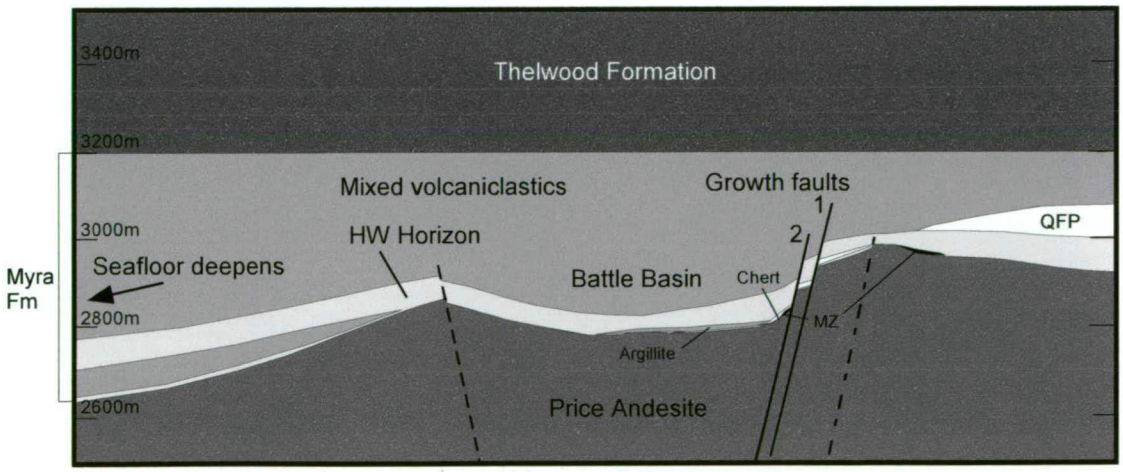

Figure 5.17: b) Restored geology of Battle (Ridge Zone) section 1000E. A marked increase in thickness of theMyra Formation coincides with a significant drop in the elevation of the footwall, Price Andesite, which suggests growth faults were active during deposition of the Myra Formation. However, the HW Horizon maintains a similar thickness throughout this zone, and the major growth faults controlling the basin formation most likely postdate deposition of the HW rhyolitic facies and ore formation (?). MZ = orebody.

5.7 Property scale paleoseafloor reconstruction

The present day deformed paleoseafloor of the Myra Falls property is shown in Figure 5.18a. In comparison, the reconstructed paleoseafloor is shown below in Figure 5.18b. The most noticeable change in the reconstructed paleoseafloor is the removal of the deep topographic low in the north. Instead, this is now an area of elevated topography. The large topographic high associated with the Myra Anticline, and the eastern side of the Myra-Price Fault is also removed. Two distinct basinal structures are present beneath the HW orebody and south and west of the Battle orebody and are referred to as the HW and Battle basins. Growth faults are spatially associated with the orebodies and their positions and orientations are based on the detailed mine-scale paleoseafloor reconstructions.

A 3-d view of the effect of the paleoseafloor reconstruction is also shown in the wire-frame diagrams, Figures 5.19a and 5.19b. Large faults and the D_1 Myra Anticline are clearly visible in Figure 5.19a, whereas the topography is much more subdued in the restored paleoseafloor, Figure 5.19b. The orebodies appear to occupy small sub-basins along a WNW-trending ridge. The topography appears to drop away rapidly to the south and increases slightly to the north.

The distribution of the fine-grained facies, which reflects depressions or depo-centres is shown in Figure 5.20a. The fine-grained facies coincides with topographic lows in the restored paleoseafloor (Figure 5.18b). Fine-grained facies are absent from areas of elevated topography, such as the northern part of the property. Instead, this area is dominated by coarse-grained volcaniclastic rocks, which are more typical of zones, proximal to volcanic centres. The block diagram, Figure 5.20b, illustrates the paleoseafloor topography and the position of the HW and Battle basins. The HW and Battle basins appear to be small, restricted basins, quite separate from the broad deep basin in the south. A volcanic centre is interpreted to be located in the north, due to the rising elevation of the paleoseafloor, the marked increase in coarse-grained volcaniclastic rocks and massive porphyry flows and intrusives, and the absence of fine-grained facies.

The coincidence of fine-grained facies and topographic lows, indicates that at a broad property-scale, the footwall reconstruction is a good approximation for the paleoseafloor topography during deposition of the HW Horizon.

5.8 Comparison to modern VHMS systems

Bathymetric maps of several modern hydrothermal fields in back-arc basins are shown in Figure 5.21, with examples from the North Fiji Basin (Bendel et al., 1993), eastern Manus

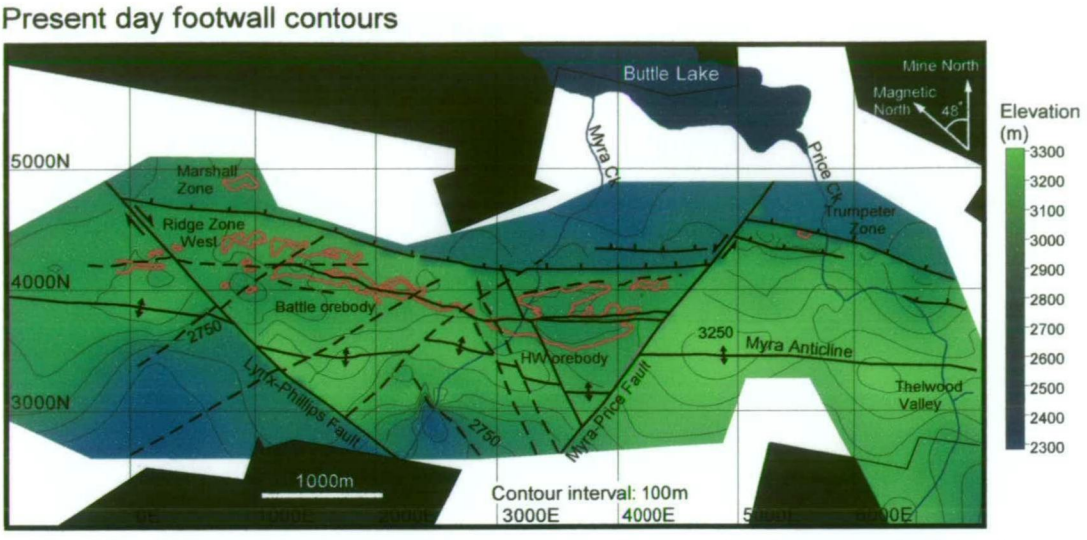

Figure 5.18: a) Present day footwall contours showing the effects of major structures on the footwall elevation.

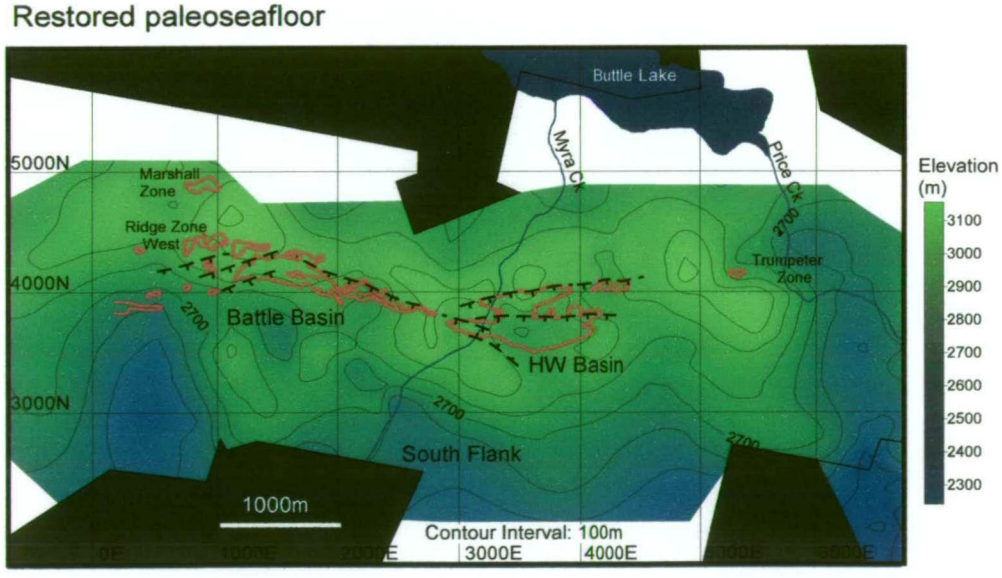

Figure 5.18: b) Restored paleoseafloor (top surface of Price Andesite), with major growth faults shown at the margins of the HW and Battle Basins. The paleotopographic reconstruction suggests that the Battle and HW orebodies formed within small basins on the edge of an area of elevated topography, with the seafloor elevation rapidly decreasing into the south flank area.

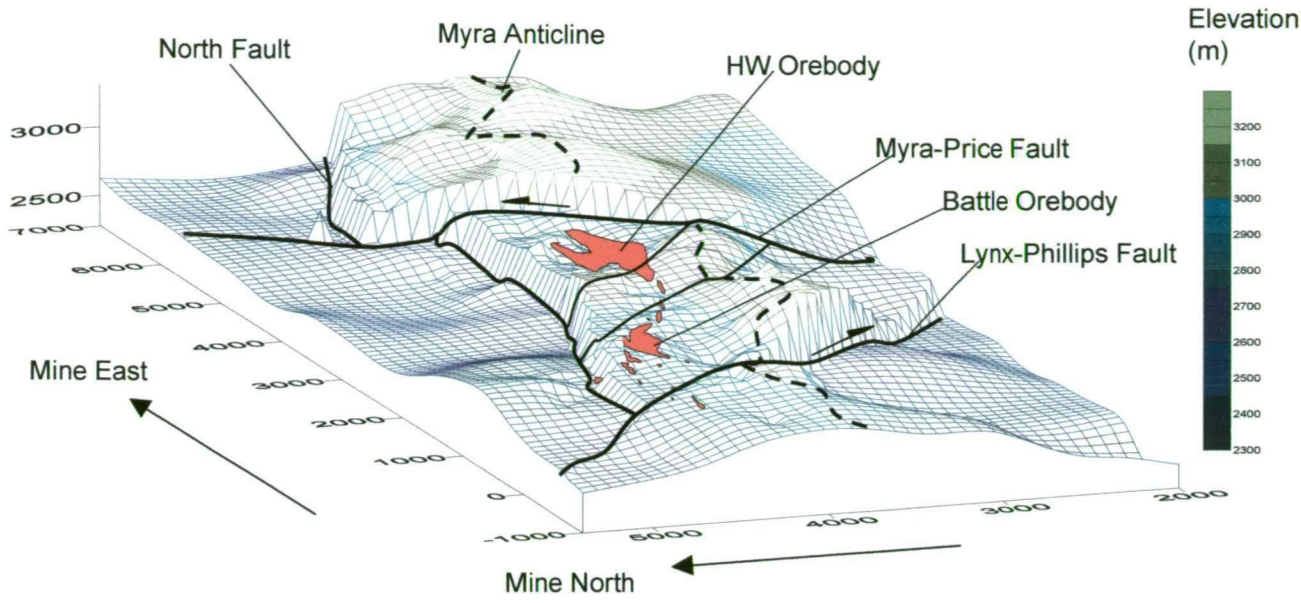

Figure 5.19: a) Present day surface contours of Price Andesite (or paleoseafloor) showing the effects of deformation. The large topographic high in the centre of the block diagram is largely a result of D_1 folding (Myra Anticline), and the large topographic low to the north is due to large down throw on the North Fault. Uplift and lateral displacements also occur along the Myra-Price and Lynx-Phillips Faults.

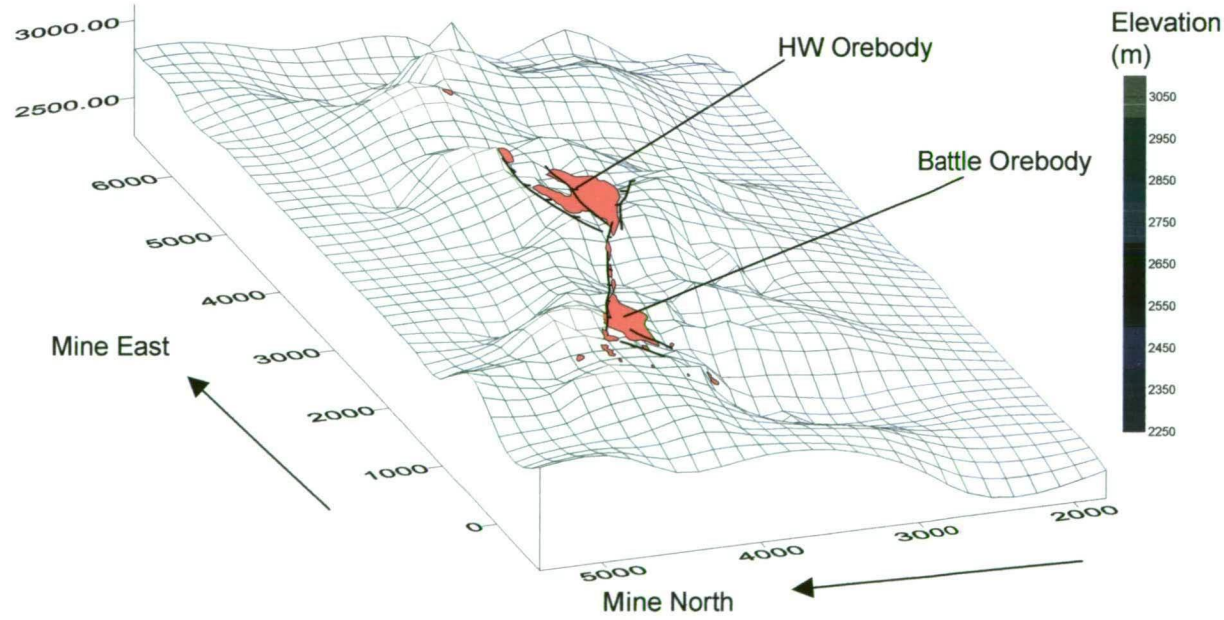

Figure 5.19: b) Restored paleoseafloor (at time of deposition of the Thelwood Formation) showing the location of growth faults and VHMS orebodies. The orebodies are spatially associated with the growth faults and these structures most likely acted as ore fluid conduits. The HW orebody is located within a small basin, separated from the large topographic low to the south. The Battle orebody is also associated with a small basin, but appears to be located on the steep northern edge of the basin. Isopach maps indicate that the location of the orebody, (on a slope) is most likely a result of subsequent uplift on younger growth faults at the edge of the basin.

Basin and the Central Okinawa Trough (Halbach and Pracejus, 1993). These examples illustrate some of the wide variation in structural and depositional settings of modern hydrothermal fields, with deposits forming along linear troughs, e.g., White Lady hydrothermal field (Bendel et al., 1993), along linear ridges, e.g., Pual Ridge in the Manus Basin (Binns et al., 1995) or on the margins of deep caldera structures such as the Central Okinawa Trough (Halbach and Pracejus, 1993).

The Pacmanus hydrothermal field, Eastern Manus Basin (Binns et al., 1995) is particularly interesting as a modern analogue for Myra Falls VHMS orebodies. The paleoseafloor reconstructions indicate that the Myra Falls orebodies formed in small basins along a ridge, similar to the Pacmanus hydrothermal field. These small basins are quite separate from the larger basin to the south, where the depth progressively increases. This suggests that the deepest basins in this area, are not necessarily prospective for VHMS ore, instead, smaller sub-basins which occur along the WNW-trending ridge are more likely sites of VHMS ore deposition.

5.9 Summary and conclusions

The results of facies mapping and paleoseafloor reconstruction can be summarised as follows:

- The sequence is strongly disrupted by D_1 folding, D_4 normal faulting and D_5 oblique thrusts and strike-slip faults;

- Marked north-south facies variation occurs within the HW Horizon, with coarse-grained felsic volcaniclastics dominating in the north and thick mudstone and siltstone deposits in the south. Quartz-feldspar porphyry bodies are common in the west, feldspar porphyry and dacite are more common in the east;

- The footwall contours, or deformed paleoseafloor, clearly shows the effects of late deformation, but two basinal features associated with the HW and Battle deposits appear to be preserved. The distribution of fine-grained facies, dominantly composed of argillite, coincides with many of the topographic lows in the footwall contours. As mudstone deposits commonly represent depressions or depo-centres, this indicates the preservation of at least part of the original seafloor topography;

- Stratigraphic thickness of the HW Horizon varies from 2 to 300m, while the thickness of the Myra Formation varies from 100 to 1000m;

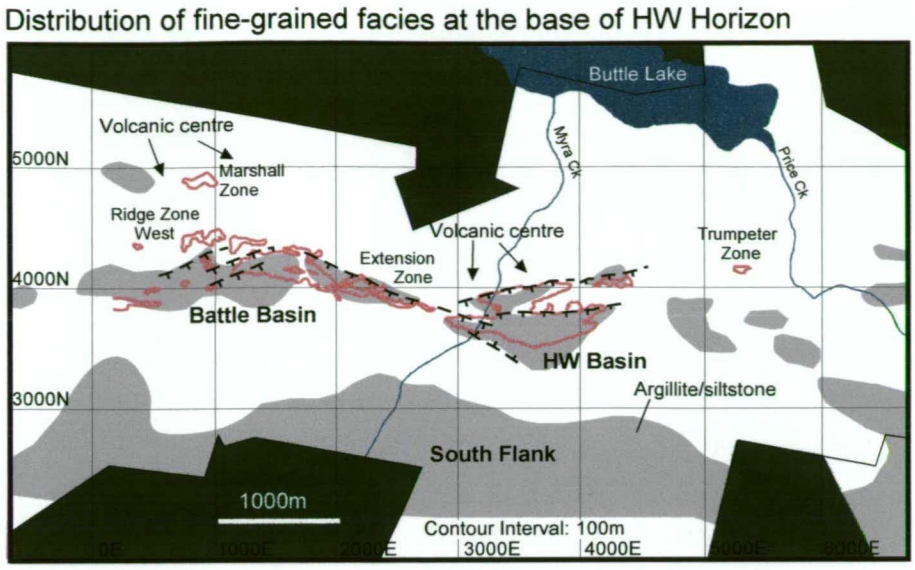

Figure 5.20: a) Distribution map of the fine-grained facies which occur at the base of the HW Horizon. Fine-grained facies (predominantly argillite, chert and siltstone) usually accumulate in depo-centres and coincide with the topographic lows in the reconstructed paleoseafloor in the map above and provide further evidence for the presence of smaller basins associated with the Battle and HW orebodies. Major growth faults are also shown as dashed lines.

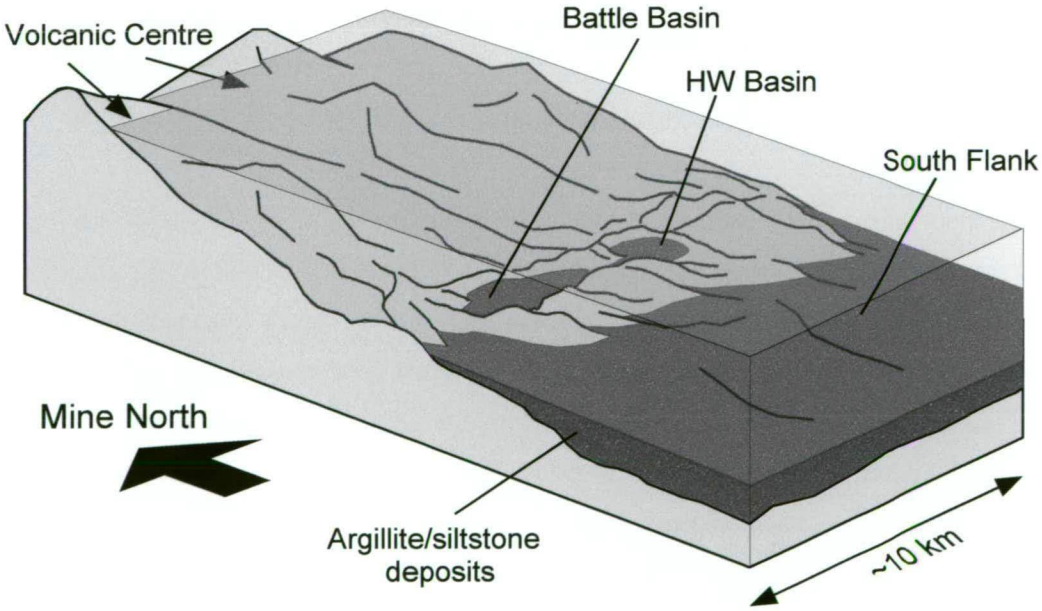

Figure 5.20: b) Interpreted paleogeography of the Myra Falls area, based on the paleoseafloor reconstruction and facies mapping.

- The paleoseafloor reconstruction indicates that the VHMS orebodies occur within or at the edges of small basins, which occur along a NW oriented ridge. The depositional and structural setting of the orebodies at Myra Falls appears to be similar to the Pacmanus hydrothermal system; and

- Although early growth faults are obscured by late deformation, paleoseafloor reconstructions, isopach maps and facies maps can be used to locate possible growth structures. The growth faults identified appear to have a slightly different trend to the main NW oriented ridge and may represent splays off the main trend. If so, these zones would form an ideal locus for fluids and may be the controlling factor for the position of the two largest orebodies in the area.

In conclusion, the reconstruction of the paleoseafloor is possible, at least at a broad property scale. However, the reliability of the reconstruction will vary across the property with changing drillhole density and intensity of late deformation. At this scale, only large fault displacements are recognised by footwall contouring. The effects of individual faults, with offsets less than about 30-40m, are not observed in the footwall contours. The assumption about the planar nature of the basal contact of the Thelwood Formation also has a major effect on the accuracy of the reconstruction. Ideally, the top contact of this formation should be used. However, a large proportion of the drillholes, were collared within the Thelwood Formation and the upper contact was therefore poorly constrained.

Although there will always be some inaccuracies with any reconstruction, the combined use of facies mapping, isopach maps and an understanding of the deformation history, add to the reliability of this reconstruction. The coincidence of the fine-grained facies with the topographic lows, suggest that the reconstruction provides a good approximation for the original paleoseafloor, and aids the comparison with modern analogues such as the Pacmanus hydrothermal system, Eastern Manus Basin. The depositional and structural setting of the orebodies at Myra Falls has important implications for the chemistry of the fine-grained facies and/or caprocks, which occur immediately above the VHMS orebodies, and a detailed discussion will be given in Chapter 8.

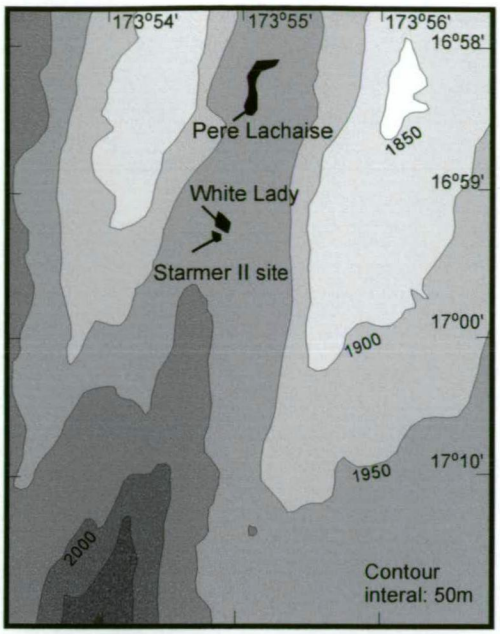

a

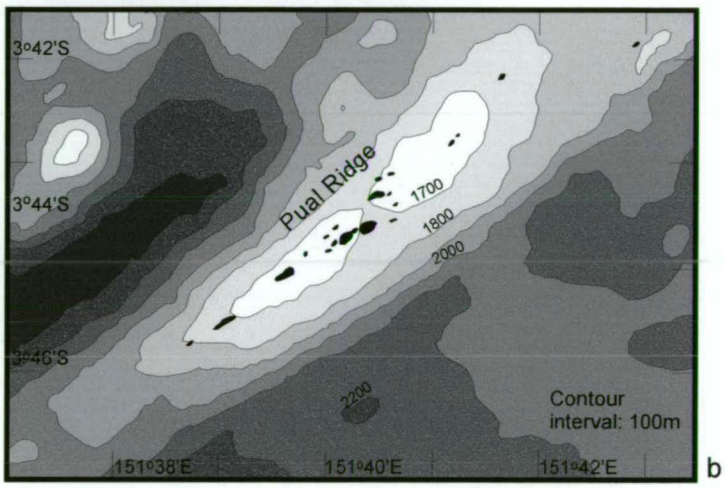

b

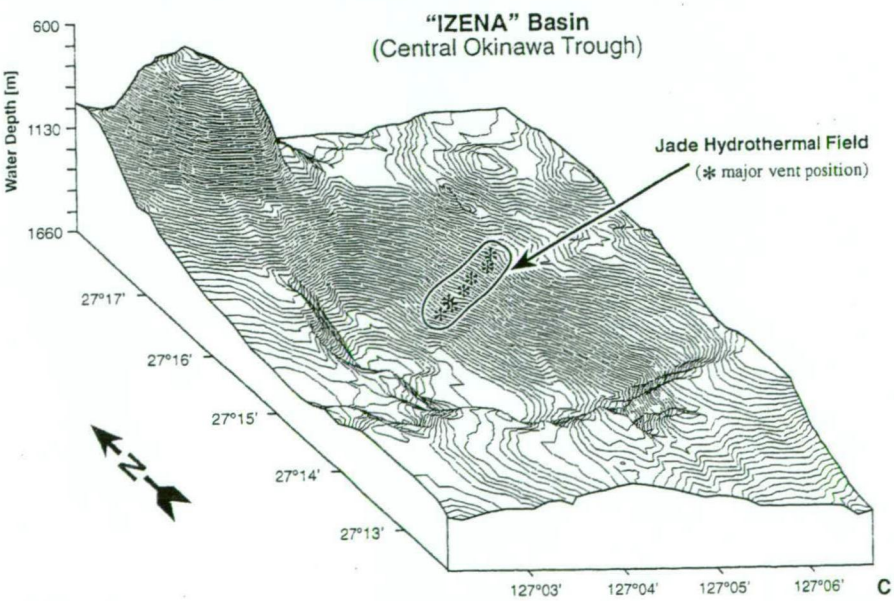

c

Figure 5.21: Bathymetric maps depicting the sites of modern hydrothermal fields: a) North Fiji back arc basin (Bendel et al., 1993); b) Paul Ridge at PACMANUS (Binns et al., 1995); c) Jade hydrothermal field, Central Okinawa Trough (Halbach et al., 1993).

Chapter 6
Chert and argillite 'caprocks'

6.1 Introduction and 'Caprocks' definition

The VHMS orebodies at Myra Falls are in many places 'capped' by a fine-grained sequence of chert and argillite. For instance, in the Battle mine, siliceous facies dominate above the ore and are referred to as the siliceous 'caprocks' or chert. In this study the term 'chert' is defined non-genetically, as any rock containing greater than 75% microcrystalline quartz (Folk and Weaver, 1952).

One of the main aims of this study is to determine the distribution, nature and origin of the 'cap rocks'. Detailed analysis of geological sections, drillcore and underground mapping has shown that the 'cap rocks' form a distinct fine-grained horizon across the property. This horizon commonly occurs immediately above, or within 1-2m above the ore horizons, and close to the contact with the Price Andesite in areas distal to ore. Although the fine-grained rocks form a distinct horizon, substantial lithological variation is present within the horizon. Pale grey chert is common above the Battle orebody, and grades into black chert at the edge of the siliceous zone. Elsewhere, the caprock horizon consists predominantly of finely laminated black argillite with siltstone interbeds.

The caprocks are divided into three main facies: 1) Chert; 2) Black chert; and 3) Argillite. Other facies associated with the fine-grained caprocks are siltstone, fine to medium grained rhyolitic sandstone and conglomerates, rhyolite, mixed andesite-dacite-rhyolite volcaniclastic rocks and massive to semi-massive ore horizons. The facies map (Figure 6.1) illustrates the distribution of the caprock facies, and the stratigraphic position of the caprock horizon is shown in the fence diagrams (Figures 6.2 and 6.3).

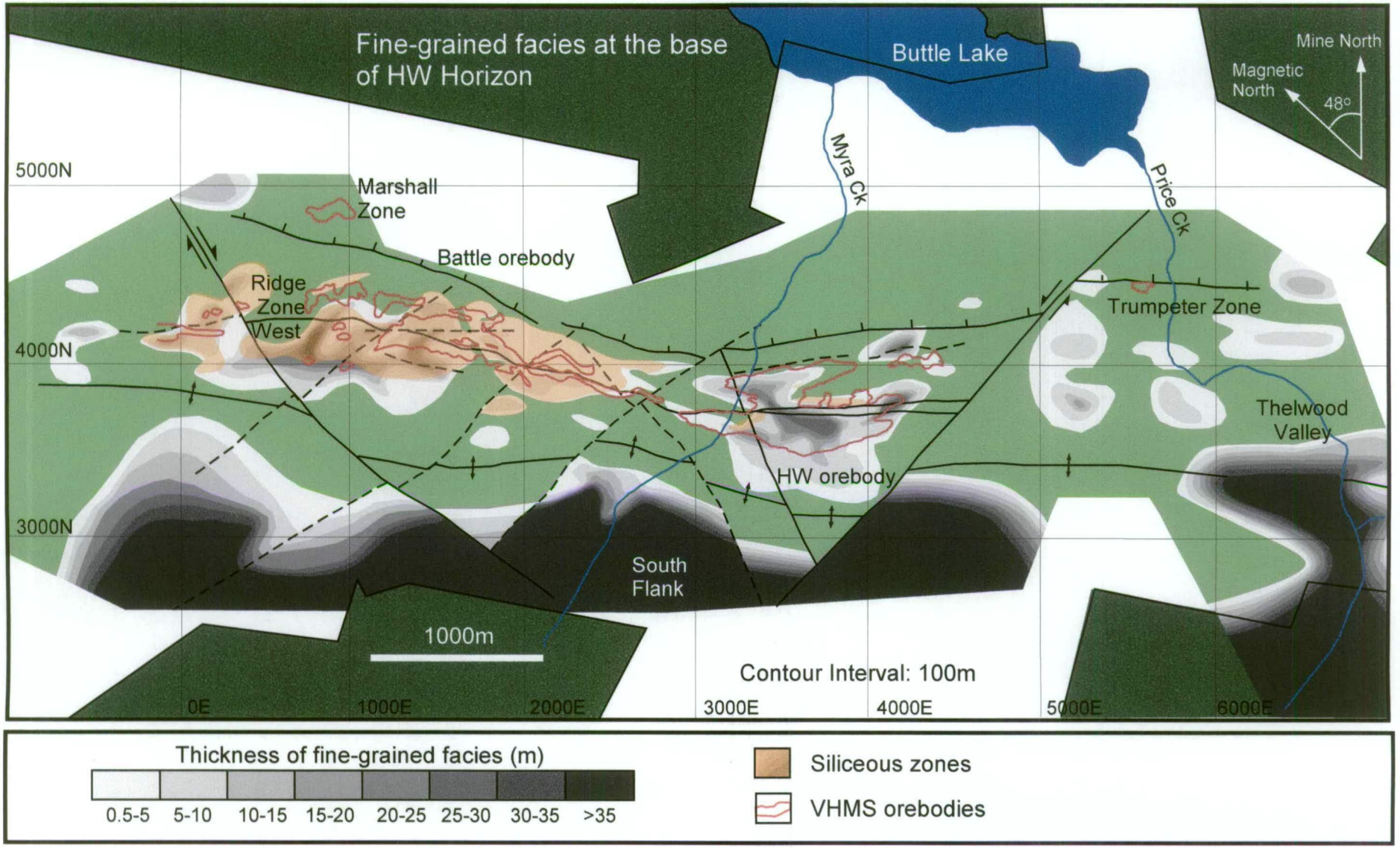

Figure 6.1: Distribution of argillite and chert which occurs near the base of the HW Horizon.

6.2 Chert

6.2.1 Distribution

The pale grey chert is best developed above the Battle orebody, where it appears to form a thick 'cap' (3-5m thick) above the massive sulphides. Chert horizons are also located above the Ridge and Extension ore zones, with minor chert zones above the HW mine (Figure 6.1). Instead, the HW orebody is overlain by a thick argillite sequence, up to 35m thick.

Although the pale grey chert is spatially associated with massive sulphides, the chert extends over a much broader area than the ore horizons. The distribution of the Battle chert is illustrated in Figure 6.4, and shows that the chert extends up to 250m south of the Battle orebody. In other places, such as the Extension Zone or the HW orebody, the chert has a more limited distribution and is generally located immediately above the massive sulphides.

6.2.2 Macro-scale description

The chert is usually very fine-grained and pale, to medium grey. Pale brown, green and pink varieties are also present but are much less common. The white to pale grey-pink chert is located immediately above the Battle ore, whereas the green chert predominantly occurs on the southern and eastern periphery of the Battle orebody (Figures 6.4 and 6.5). The white to pale grey chert commonly has a smooth glassy appearance with a conchoidal fracture, but with increasing clay content the chert or porcellanite (clay content >25-50%) has a dull or matte lustre, similar to unglazed porcelain (Bramlette, 1946; Hesse, 1990a, 1990b). With a slight increase in grain-size, this material develops a grainy appearance.

The chert occurs in massive centimetre to metre scale beds, or in strongly laminated horizons with mm to 0.5cm scale parallel laminations. The chert horizons can be 1-5m thick and are commonly interbedded with coarser sandstone, silt and volcaniclastic units. The basal contact of the chert is commonly very sharp against the underlying ore or coarse-grained volcaniclastic rocks (e.g., Figure 6.7b). The upper contact is less defined, and consists of an interlayered zone of chert, rhyolitic sandstone and volcaniclastics. Individual chert layers, mm-cm wide, also occur within coarser-grained sandstone units. A typical sequence of pale grey to pink chert is shown in Figure 6.7, from drive ST183A in the Battle Mine. A sequence of green chert from drive G171XS in the southern edge of the Battle deposit is shown in Figure 6.8, while Figure 6.9 illustrates a chert sequence from one of the few chert localities in drive S335C, in the HW mine. In the overlying mass flow units and coarse-grained rhyolitic volcaniclastic rocks, chert clasts (up to 10-20cm) and large blocks of laminated chert (up to 1-2m) are present in places (e.g., Figure 6.10).

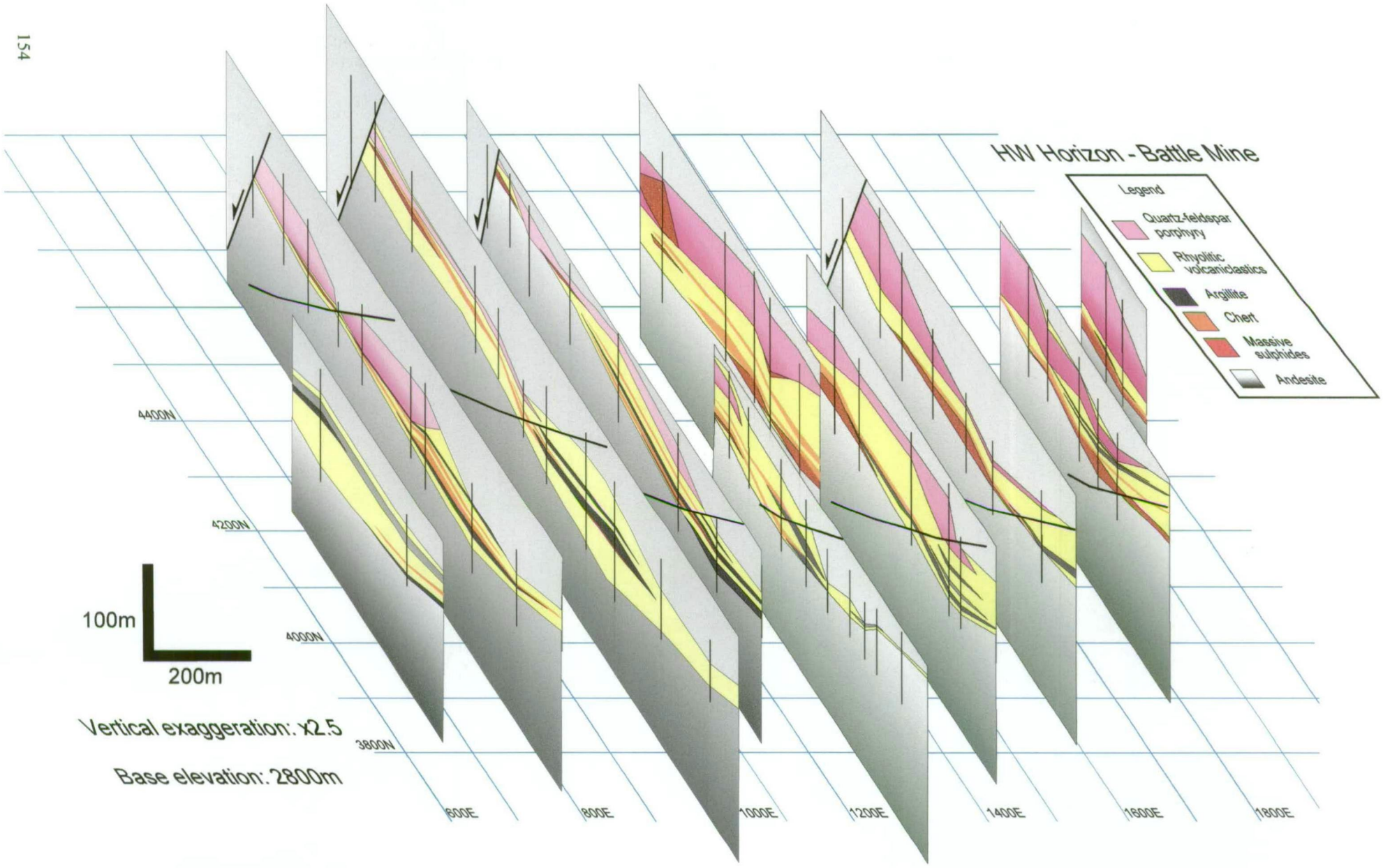

Figure 6.2: North-south oriented sections illustrate facies variation of the HW Horizon in the Battle mine area, and shows the location of chert and argillite above the massive sulphides.

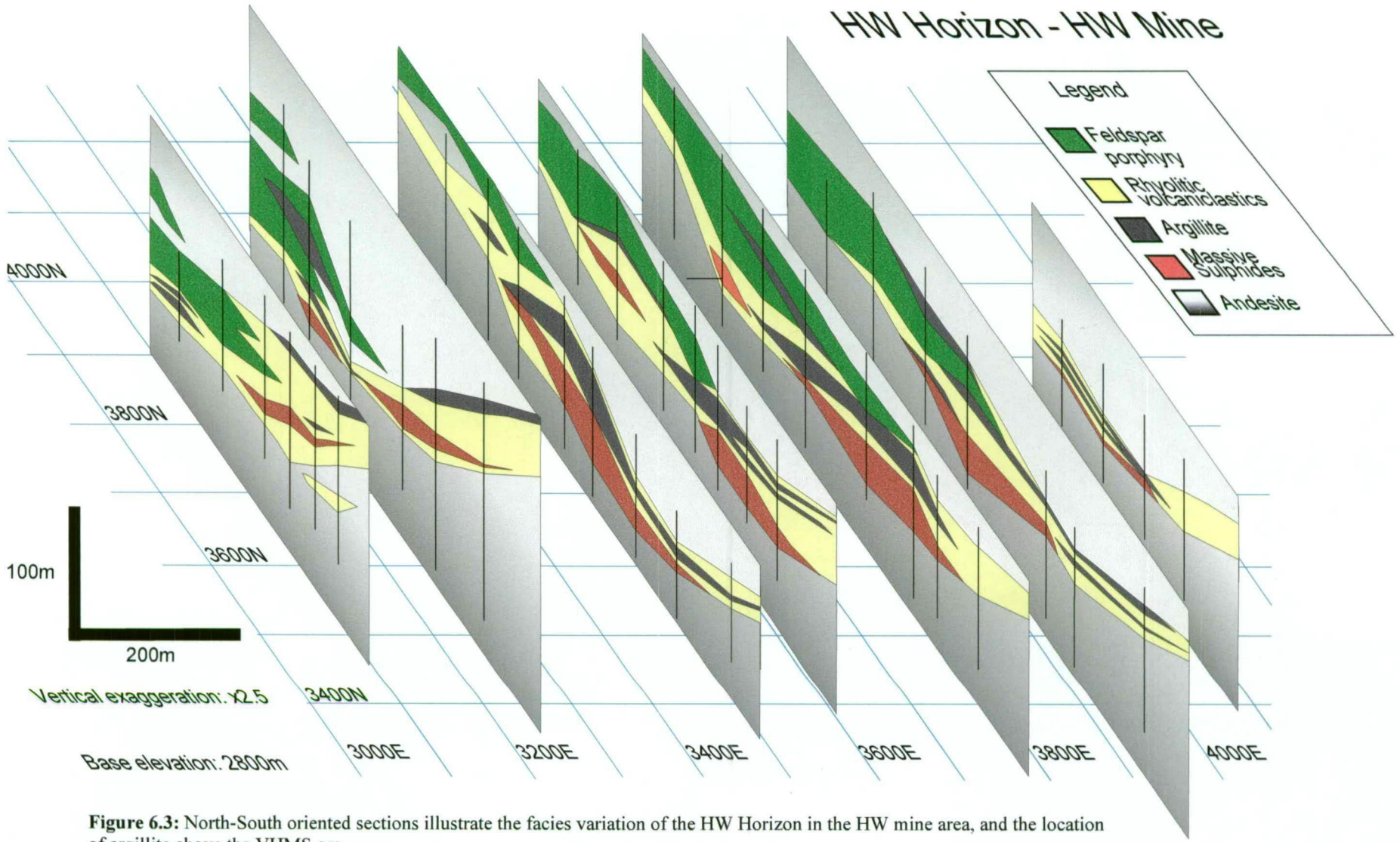

Figure 6.3: North-South oriented sections illustrate the facies variation of the HW Horizon in the HW mine area, and the location of argillite above the VHMS ore.

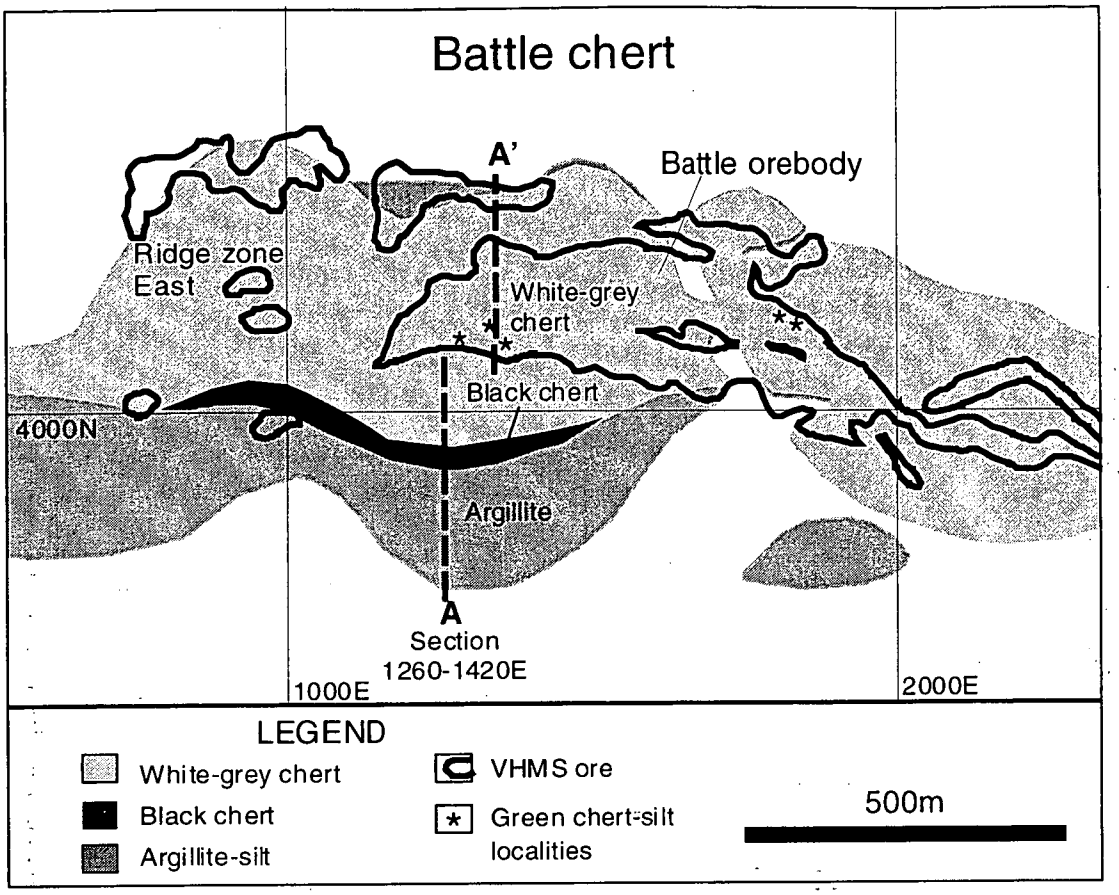

Figure 6.4: Chert distribution map of the Battle mine area. Pale grey to white chert dominates in the area immediately above the Battle orebody. Black chert occurs at the edge of the pale grey chert, south of the Battle orebody. The contact is gradational with the adjacent pale grey-white chert and the argillite to the south.

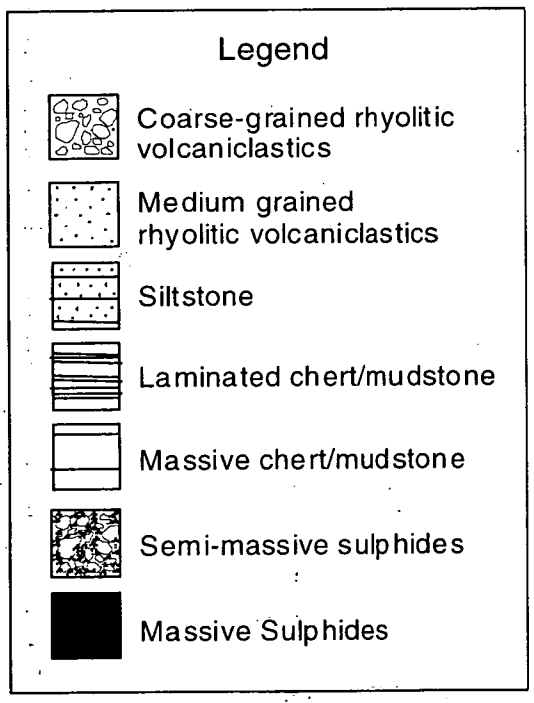

Figure 6.6: Lithological legend for the following graphic Logs (Figures 6.7, 6.8 and 6.9).

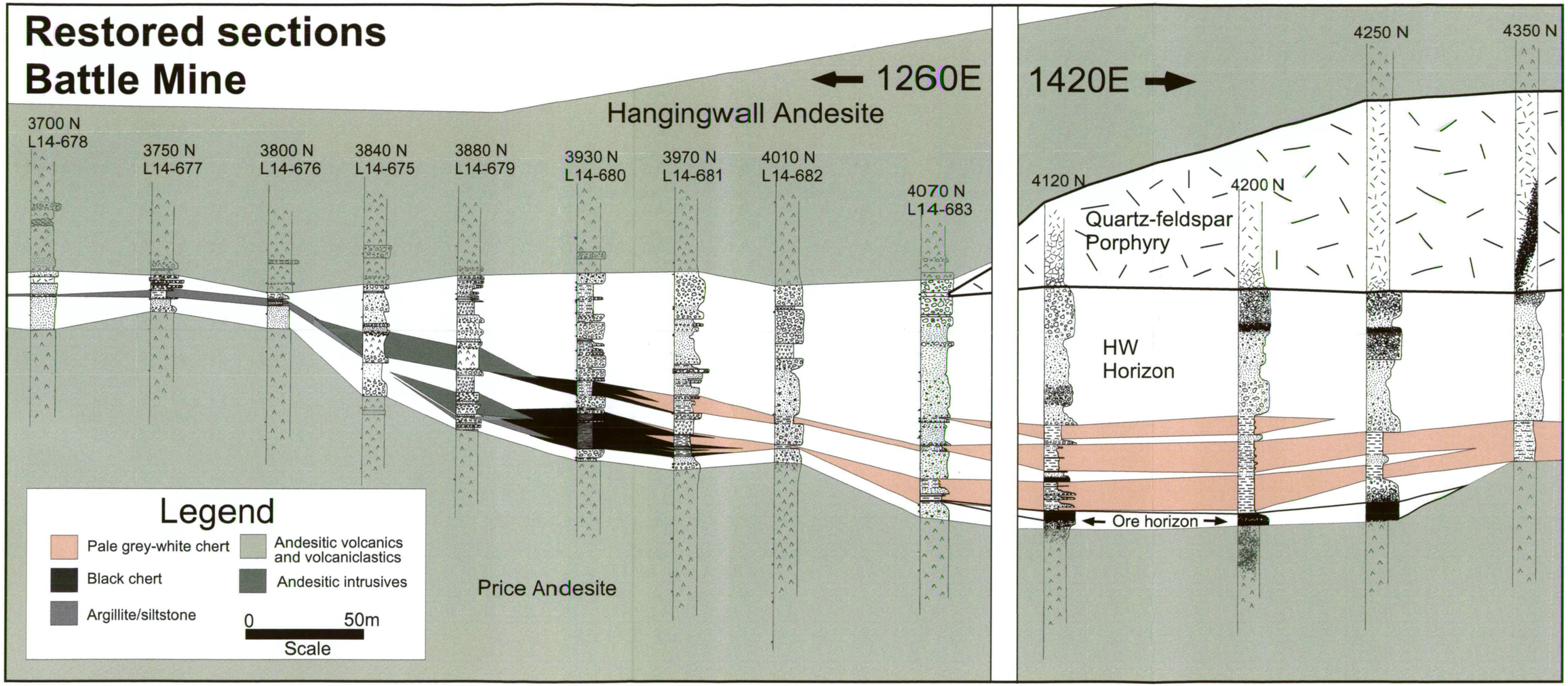

Figure 6.5: Restored composite section, 1420-1260E, Battle Basin.

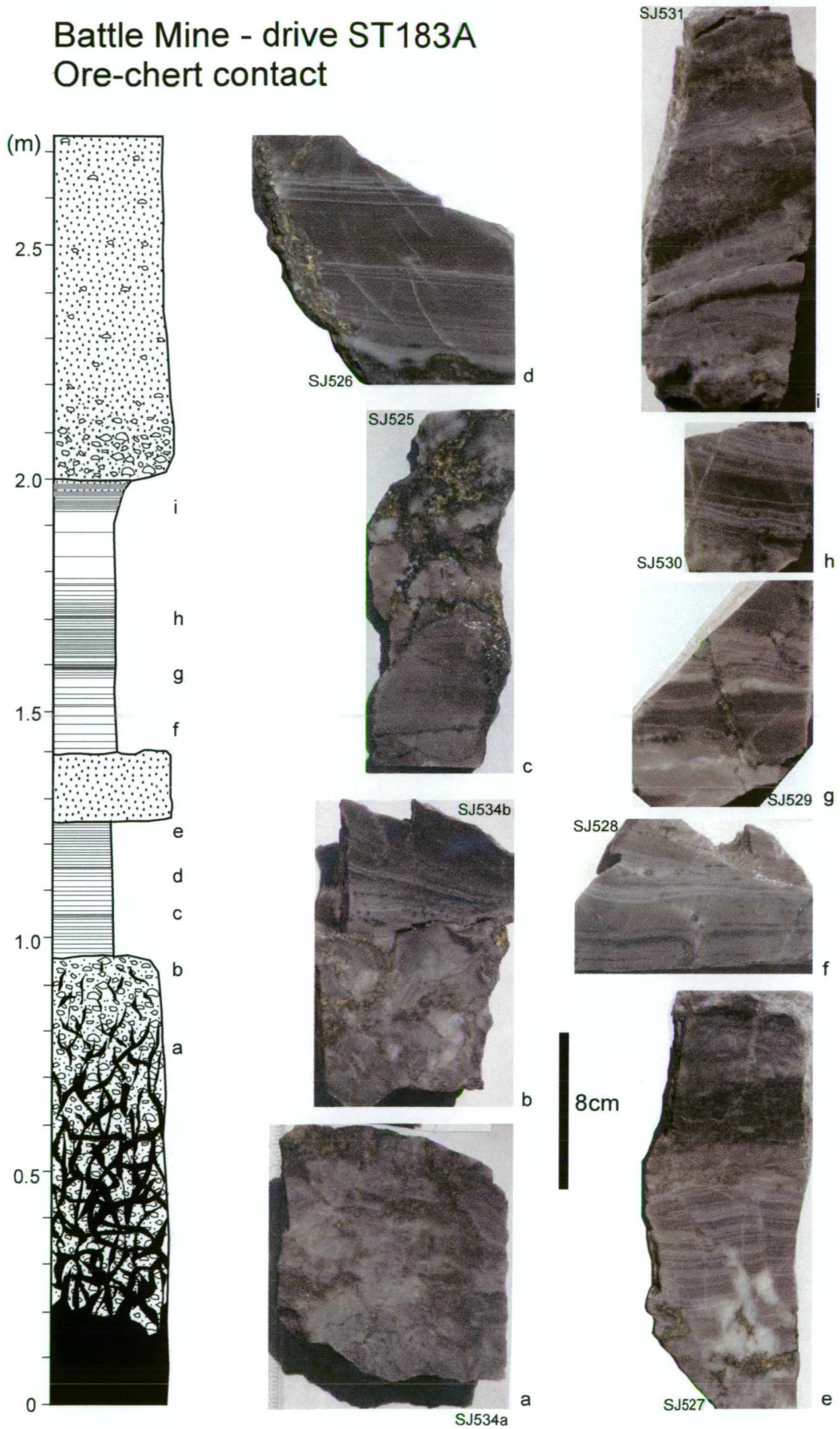

Figure 6.7: Laminated chert sequence overlying massive sulphides in the Battle mine, drive ST183A (see Figure 6.5 for legend)

6.2.3 Mineralogy and textures

The chert consists of 75-90% microcrystalline quartz and 10-25% sericite with variable contents of fine impurities (including clays and carbonaceous material), scattered fine sulphides (up to 1-5%), and carbonate (calcite and dolomite), up to 5% in some cherts. The majority of chert is white to pale grey, but a few Battle chert samples have a faint pink hue and this could be due to a fine dusting of haematite (?) on microquartz boundaries (the extremely fine grain-size of the mineral prevented identification, even with SEM). Other fine impurities, such as clay and goethite, most likely account for the pale brown colour of some cherts, and the green cherts generally have a greater proportion of sericite.

Typical chert textures consist of an inequigranular micro-mosaic of interlocking anhedral to subhedral quartz grains and sericite plates, with a grainsize of 2-10μm. The quartz and sericite commonly display a 'felted' texture (Figure 6.12a) but in more deformed rocks the sericite becomes aligned to the S_1 foliation (Figure 6.12b). Bedding and laminations (mm-cm scale) are recognisable in thin section, and are defined by: subtle variations in grainsize; changes in the phyllosilicate content; increases in the abundance of carbonaceous material and other impurities; or the presence/absence of sulphides (Figures 6.12c-g). Bedding-parallel micro-stylolites are also common, and enhance the laminated appearance of many cherts (Figures 6.12d, g, h).

Three types of quartz are recognised in the chert; microcrystalline quartz, megaquartz (defined by Folk, 1950), and chalcedony.

Microcrystalline quartz is the dominant form of quartz (80-90%), and occurs as a fine dense micro-mosaic of interlocking grains. The grain-size ranges from 1 to 50 μm, but the average grain-size is generally 8 to 10μm, (Figure 6.12a). Individual microquartz grains mainly show random extinction, although domain extinction also occurs in places, where clusters of quartz crystals exhibit a diffuse sweeping extinction as defined in Simonson (1985).

Megaquartz, refers to quartz crystals with well defined crystal shapes and terminations, which usually display unit extinction. Megaquartz makes up about 5-10% of the chert and is present as larger grains (up to 50-100 μm diameter), which are commonly present in irregular, rectangular or spherical patches (20 to 400μm diameter) scattered throughout the fine microcrystalline groundmass (Figures 6.13a-c, 6.13i-j). The elongate, rectangular megaquartz patches (e.g., Figure 6.13d-f) are rare, but in one sample (from drillhole, 18-480, about 2m above the Battle main lens), forms a dense layer of elongate megaquartz grains, generally oriented parallel to bedding. In detail,

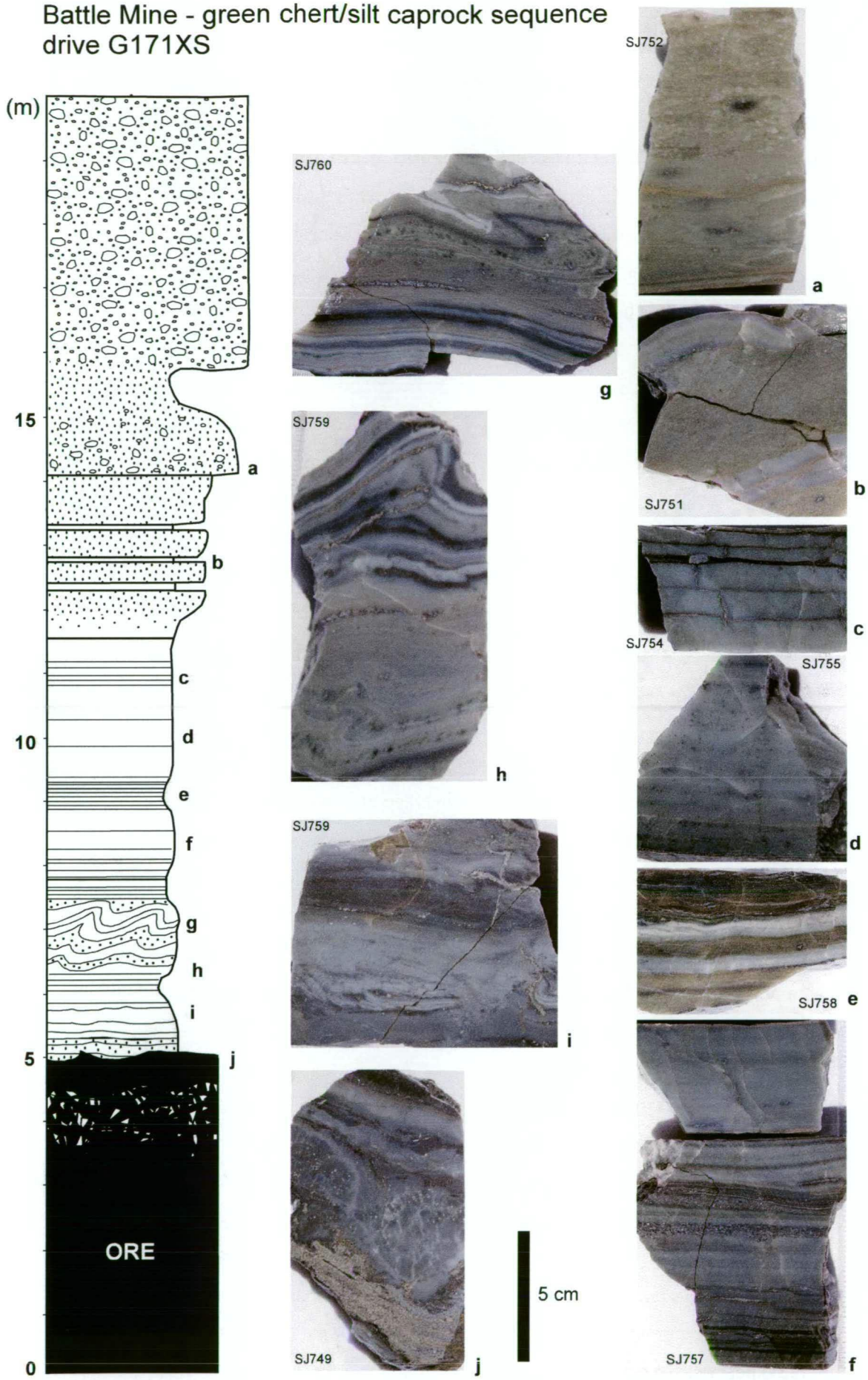

Figure 6.8: Green chert-silt sequence above massive sulphides from drive G171XS in the Gopher Zone, Battle mine. Sample a is from the overlying sandstone, while sample b shows fine chert layers within a sandstone-siltstone horizon. Note the changing colour down sequence from green (a-h) to pale grey (i-j) as the silica content increases and the sericite content decreases.

the grains have sharp terminations. Spherical megaquartz patches, typically 50 to 200μm diameter and inclusion-rich, are common in very fine-grained layers throughout the chert (e.g., 6.13a and 6.13i-j). In layers with abundant spherical megaquartz patches the chert has a distinct finely mottled or spotted appearance in hand specimen. Megaquartz textures are interpreted in the discussion in Section 6.6.2. Detrital quartz grains, up to 0.1 to 0.6mm also occur, some with resorbed and embayed margins. The size and density of detrital quartz grains increases markedly in silty horizons within the chert (Figure 6.12e).

Chalcedony is the fibrous variety of quartz, and is only a minor component of the chert (<1-2%). Chalcedony grains vary from 10 to 200μm in length and occurs, 1) in a radial habit within circular patches in the microcrystalline groundmass (Figures 6.13g-h), and 2) in a radial habit forming wedge shaped mammillated growth structures and spherulites within phosphate nodules (Figures 6.14a-f). The chalcedonic spherulites are best seen in crossed polars (e.g., 6.14d, f), where they form spherulitic figures, as defined by Simonson (1985). Rare patches within the microcrystalline quartz groundmass of some cherts contain 'ghostly' spherulitic forms similar to those described above (Figures 6.14g-h). All chalcedony observed in the chert was length fast.

The sericite in chert forms a felted interlocking texture with the microcrystalline quartz and sericite grains are generally very fine, with an average grainsize of 2 to 10μm. With increasing sericite and clay content, the S_1 foliation commonly becomes visible, defined by an alignment of sericite blades, which are commonly at a high angle to bedding (Figures 6.12f). Sericite also occurs as fine granular masses replacing larger feldspar grains (Figure 6.15a); and as larger detrital grains up to 30μm long. Late crosscutting quartz-sericite veins are common throughout the chert (Figure 6.15b), and sulphides in the chert commonly have a sericite overprint (Figure 6.15c).

Carbonate rhombs and irregular blebs or patches (0.5-2mm) are common in the chert immediately above the Battle orebody (Figure 6.15d). The carbonate is commonly zoned, with calcite overgrowing dolomite (Sinclair, 2000). Where there is abundant carbonate, the chert develops a slightly speckled appearance.

Fine euhedral rutile grains (10 to 100 μm) are common within the spherical megaquartz patches, and display good open space growth textures, with the crystals growing inwards from the outer walls of the spherical megaquartz patches (Figure 6.15e-i). Minor subhedral

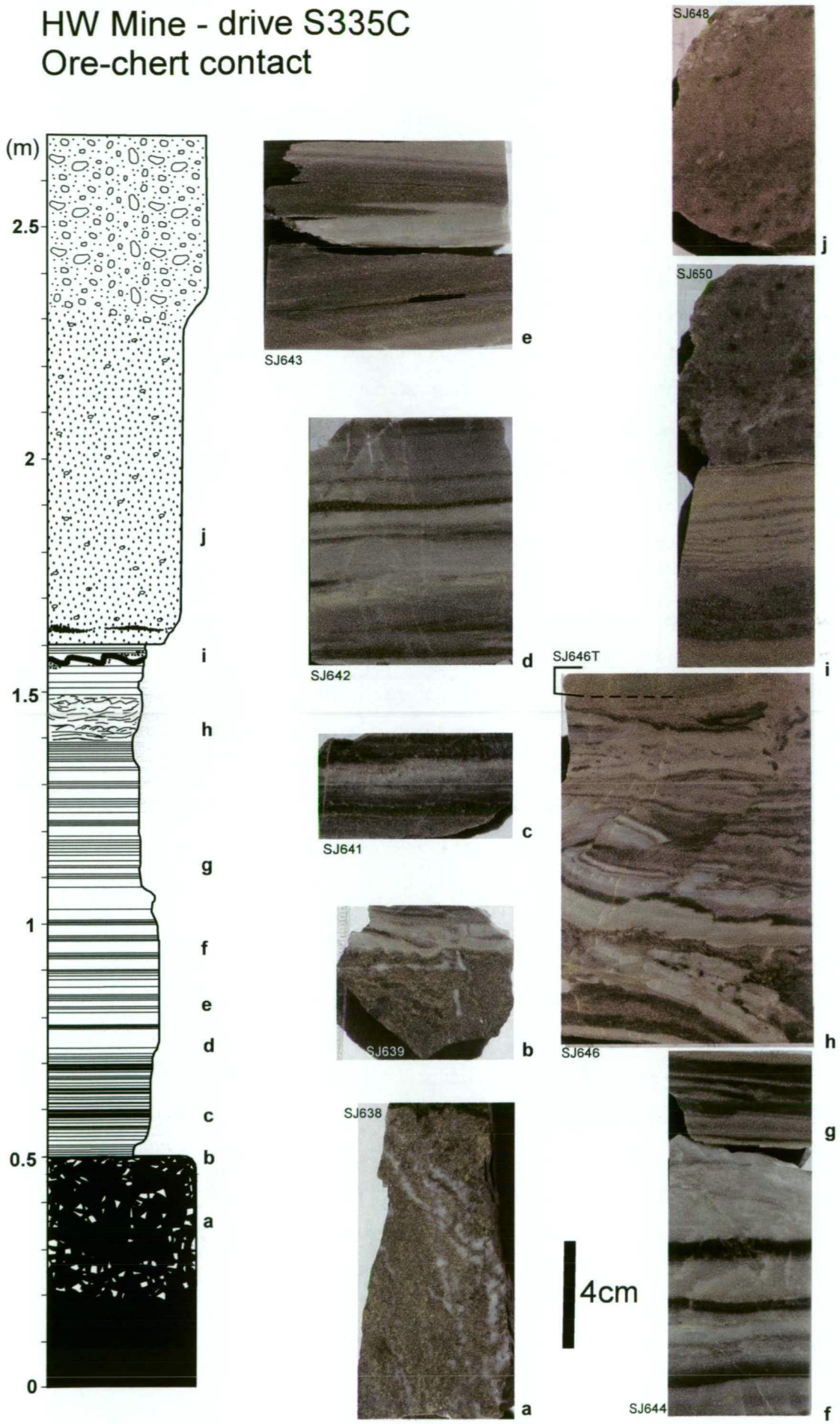

Figure 6.9: Chert-mudstone sequence overlying massive sulphides in the HW mine, drive S335C (see Figure 6.6 for legend). Sample i and j show the overlying sandstone unit.

rutile grains (10 to 100 μm) are also observed in the microcrystalline quartz groundmass around the spherical megaquartz patches.

Minor apatite is observed in the Battle chert, but is not found throughout, instead it occurs in distinct apatite-rich layers. Two types of apatite are observed, 1) fine euhedral apatite grains (2-15 μm) form the groundmass of phosphate nodules and replace radiolarian tests within the nodules (Figures 6.16a-d). These fine apatite grains are referred to as type-1 apatite, and 2) coarser-grained euhedral apatite (10-600 μm), is observed in spherical megaquartz patches with rutile, and in the surrounding microcrystalline quartz groundmass of minor apatite-rich horizons in the chert. Coarser-grained euhedral apatite is also found on the chalcedony spherules within the phosphate nodules (Figure 6.14e-f). This coarser-grained apatite (referred to as type-2) displays open space growth textures, and some grains contain fine pyrite ± chalcopyrite inclusions.

Microprobe analyses of type-1 apatite grains in a number of phosphate nodules, and type-2 apatites from phosphate nodules and numerous spherical megaquartz patches are shown in scatter plots in Figure 6.17, and indicate that the type-1 and type-2 apatites are very similar. Both types are fluorapatites, $Ca_5(PO_4)_3F$, with only negligible Cl (see data in Appendix 6.1). However, the scatter diagrams (Figure 6.17) do indicate slight differences between the two varieties, with the type-1 apatites forming a much tighter cluster than the data for type-2 apatites. The type-2 apatites also appear to have slightly greater S, Na, Sr, Y and Ba contents than type-1 apatites. Zoning was not observed in either variety of apatite.

6.2.4 Sulphides

Pyrite, sphalerite, chalcopyrite and galena are the dominant sulphides in the white to pale grey chert. Minor bornite, chalcocite and electrum are also present, predominantly as fine inclusions in sphalerite and chalcopyrite. The sulphide content in the chert varies from 1 to 10%. Fine (2-40 μm) anhedral to subhedral sulphides, including pyrite, sphalerite, chalcopyrite and galena, are generally finely disseminated through the microcrystalline quartz matrix (Figures 6.18a-g). Coarser sulphides commonly occur throughout the chert in crosscutting and bedding parallel quartz-sericite veins and patches (Figure 6.18h). Late cross-cutting quartz veins also contain tetrahedrite associated with chalcopyrite and pyrite.

Pyrite occurs in three main habits: 1) as fine framboids (Figures 6.18a-b); 2) equant, almost circular grains in places, with relict framboidal textures (Figures 6.18b-c); and 3) as isolated euhedral cubes, or clusters of cubic grains (Figures 6.18d).

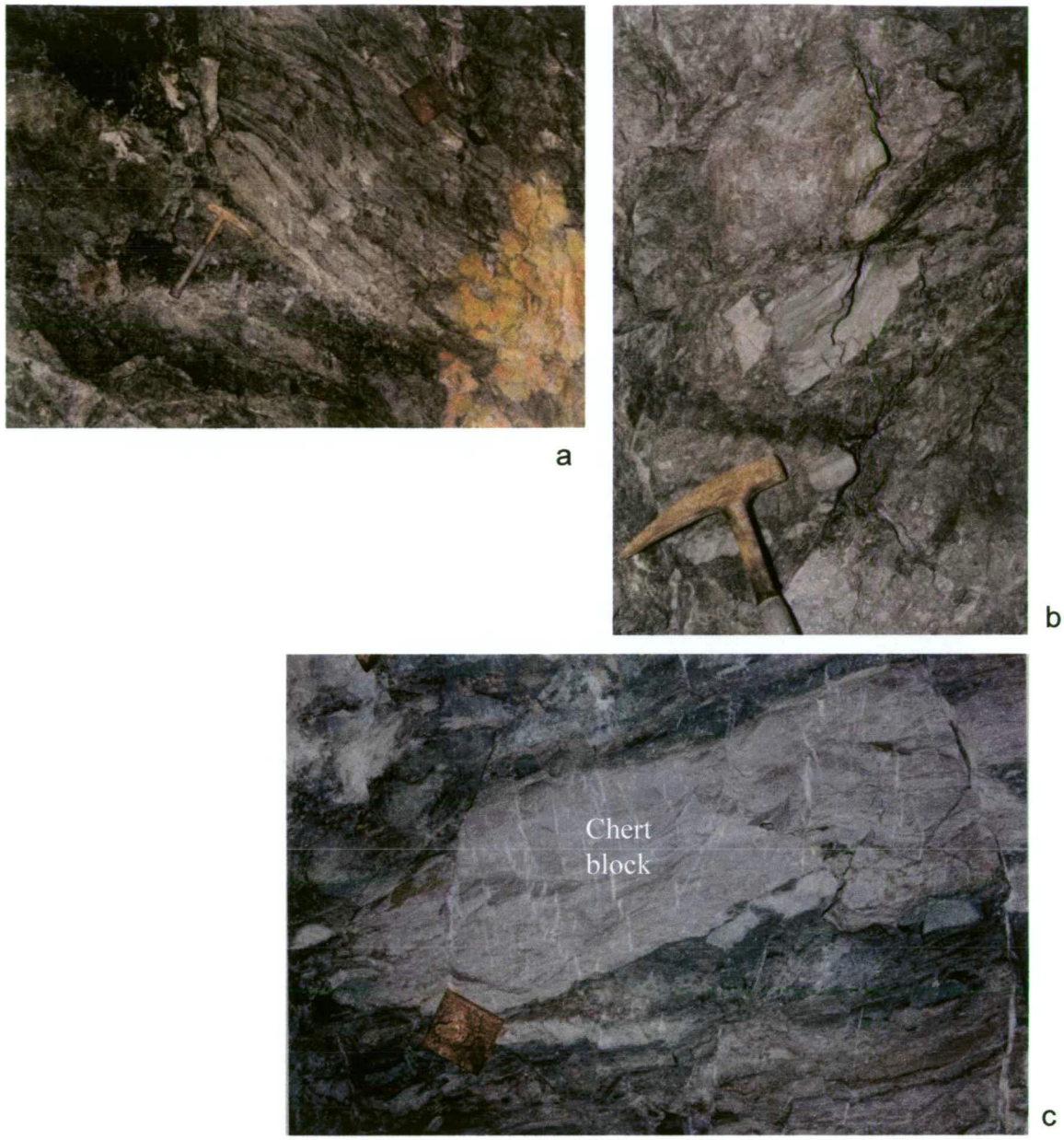

Figure 6.10: Laminated chert clasts in coarse-grained volcaniclastic rocks above the HW orebody; **a)** large chert clast in drive C355DD, HW mine; **b)** smaller laminated chert clasts in drive B390, HW mine; and **c)** large block of laminated chert in drive 23-427, 43 Block area, HW mine (for scale, bolt plate is approximately 24cm wide).

In most chert horizons the sulphide mineralogy is relatively consistent. However, variation is observed in the green chert in the southern part of the Battle Mine, G171XS in the Gopher Zone, ~1700E, 4220N (Figure 6.4). Figure 6.8 illustrates the green chert sequence. Sphalerite, chalcopyrite and minor to rare pyrite are the dominant sulphide species in the upper green and brown part of this sequence. However, pyrite increases down sequence, and in the basal 1-1.5m immediately above the ore it is the dominant sulphide species present, with only minor sphalerite and chalcopyrite. This zone is a pale to medium grey, a colour which reflects the increasing silica and decreasing sericite content of the chert.

6.2.5 Interpretation of micro-textures in the chert

This section provides an interpretation of the micro-scale textures observed in the chert. Megaquartz is relatively common throughout the chert and occurs in irregular, rectangular and spherical patches. Spherical megaquartz patches, which are often inclusion-rich and typically 50-200μm, most likely represent quartz replacement of radiolarian tests, (e.g., Kneller, et al., 1968; Adachi et al., 1986; Pollock, 1987). They could also be a replacement or infilling of algal cysts, e.g,, Tasmanites (Schieber, 1996; 1998), which have similar scales. The microfossils are not randomly distributed throughout the chert, instead, they occur within distinct horizons, usually the finest grained horizons, with little or no detrital quartz grains. The chert in these horizons has a distinct finely mottled or spotted appearance in hand specimen.

Elongate, rectangular megaquartz patches (e.g., Figure 6.13d-f) are rare, but can form a dense layer, with grains generally oriented parallel to bedding. In detail, the grains have sharp terminations. These rectangular megaquartz patches occur in distinct horizons and may represent quartz pseudomorphs after feldspar or anhydrite (?).

(text continued on page 181)

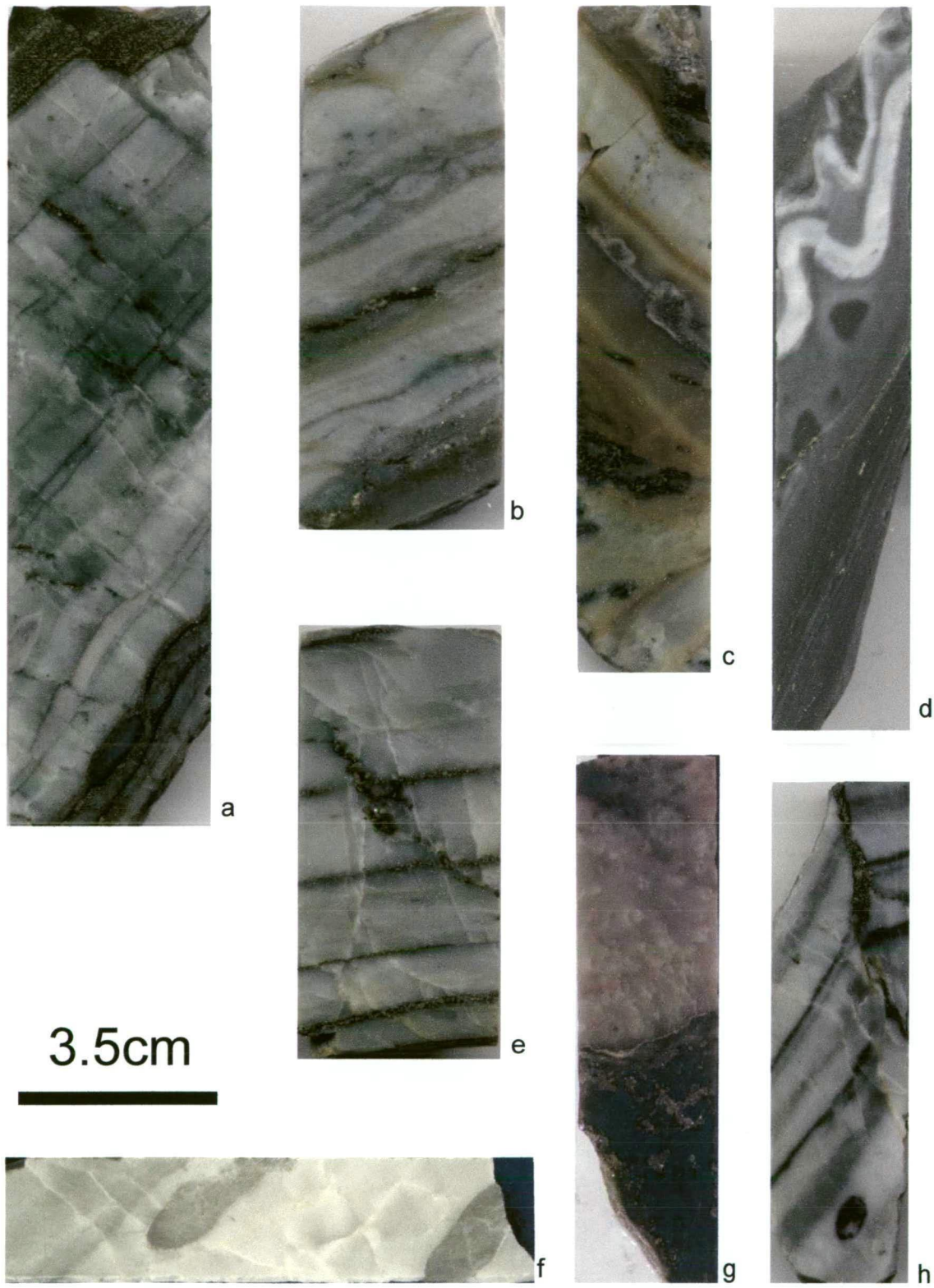

Figure 6.11: a) Typical fine parallel laminations in chert above the massive sulphides, Ridge Zone (sample SJ287, 15-431, 252.2m); **b)** interbedded chert and silt with relatively sharp contacts (sample SJ287, 15-431, 252.2m); **c)** white-cream and tan laminations in chert above the Battle orebody (SJ399, 18-1003, 77m); **d)** soft-sediment deformation preserved in chert layers interbedded with siltstone (sample SJ440, 18-1004, 70.6m); **e)** bedding-parallel and crosscutting pyrite veins in chert immediately above massive sulphides, Ridge Zone (sample SJ285, 15-431, 251.2m); **f)** ovoid phosphate concretions lie parallel to bedding in chert above the Battle orebody (sample SJ441b, 18-1004, 73.8m); **g)** weakly laminated to massive chert in sharp contact with dark green sericite-rich siltstone, immediately above the Battle orebody (sample SJ403, 18-1003, 83.35m); **h)** diffuse parallel laminations in chert above the Battle orebody with a small phosphate concretion near the base, and a steep crosscutting sulphide vein (sample SJ434, 18-1004, 49.5m).

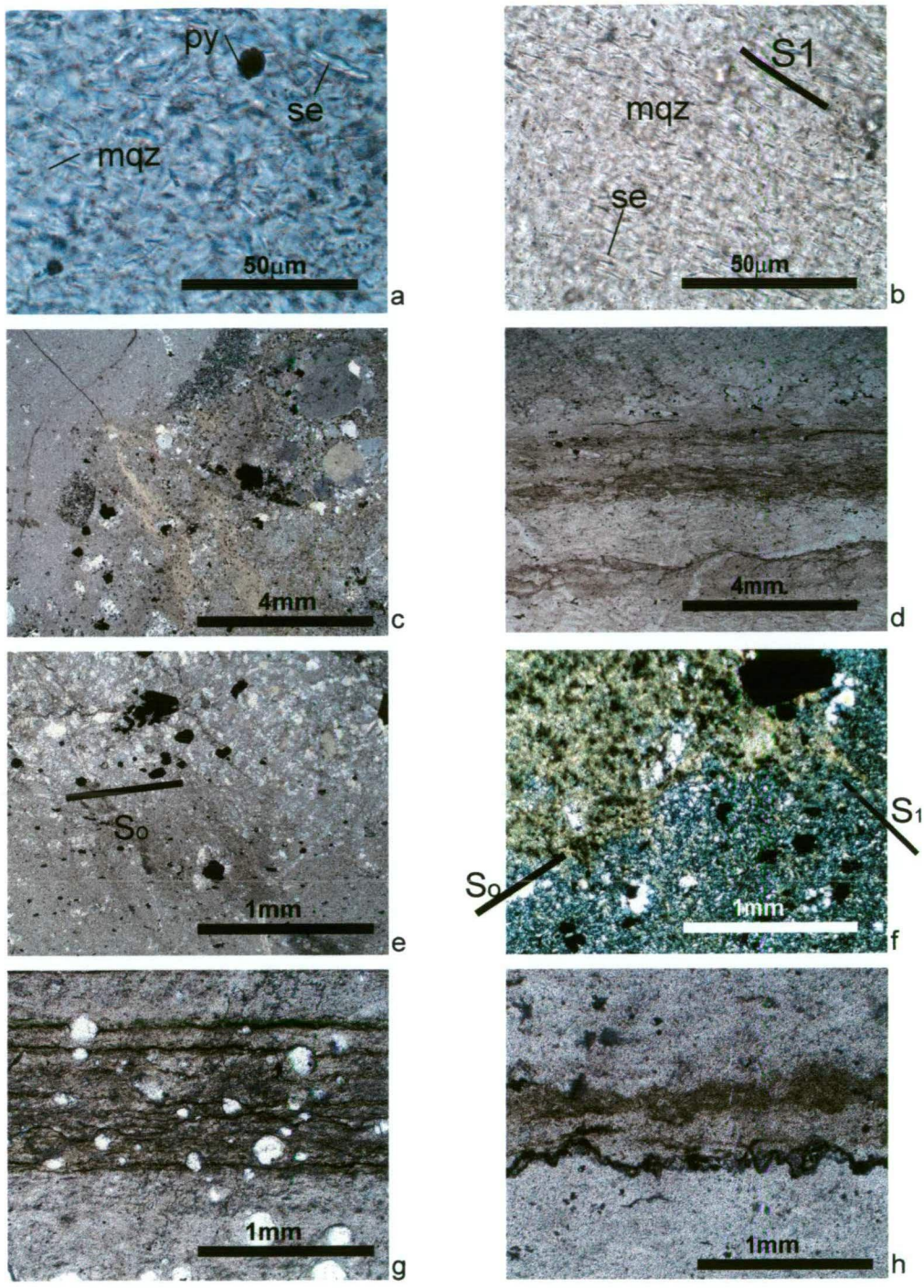

Figure 6.12: a) typical texture in pale grey-white chert consisting of interlocking microquartz (mqz), sericite (se) and pyrite (py), PPL (SJ160, 18-1127, 39m); **b)** Microquartz with abundant sericite (se) blades, strongly aligned parallel to the S_1 foliation, PPL (SJ134, 18-483, 36m); **c)** laminations in chert appear to drape over coarse sandstone layer, PPL (SJ158, 18-1127, 38m); **d)** bedding in chert defined by fine carbonaceous layers, PPL (SJ129, 18-480, 37m); **e)** bedding in chert defined by a slight increase in grainsize, PPL (SJ179, 18-1091, 18.5m); **f)** chert-silt bedding defined by an increase in the phyllosilicate content. S_1 foliation crosscuts bedding at a high angle to bedding, XPL (SJ150, 18-1086, 40.5m); **g)** parallel laminations and bedding-parallel micro-stylolites defined by carbonaceous material with abundant radiolarians, PPL (SJ159, 18-1127, 39m); **h)** bedding parallel stylolite along a carbonaceous-rich lamination in chert, PPL (SJ159, 18-1127, 39m).

Figure 6.13: Micro-scale textures of quartz in Battle chert; **a**) inclusion-rich megaquartz (mgq) forms a spherical patch, after radiolarian test, PPL (SJ327, 14-633, 293.4m); **b**) megaquartz (mgq) replaces a square grain, possibly feldspar? XPL (SJ158, 18-1127, 38m); **c**) megaquartz (mgq) replaces a rhomb, after carbonate? XPL (SJ608, 10-2024, 845m); **d**) megaquartz replaces elongate grains, which are generally oriented parallel to bedding, defined by the thin carbonaceous seams, PPL (SJ129, 18-480, 37m); **e**) close up of previous photomicrograph illustrating the regular form of the grains, PPL (SJ129, 18-480, 37m); **f**) megaquartz replaces elongate rectangular grains, after anhydrite? XPL (SJ129, 18-480, 37m); **g**) spherical inclusion-rich quartz, replacing a radiolarian test, PPL, (SJ753, G171XS); **h**) same view as previous photomicrograph but in XPL, which illustrates that the radiolarian test is replaced by chalcedony with a radial habit (length fast), (SJ753, G171XS); and **i-j**) spherical megaquartz (mgq) patches in chert, XPL, (SJ723, L14-682, 350.8m, Battle south).

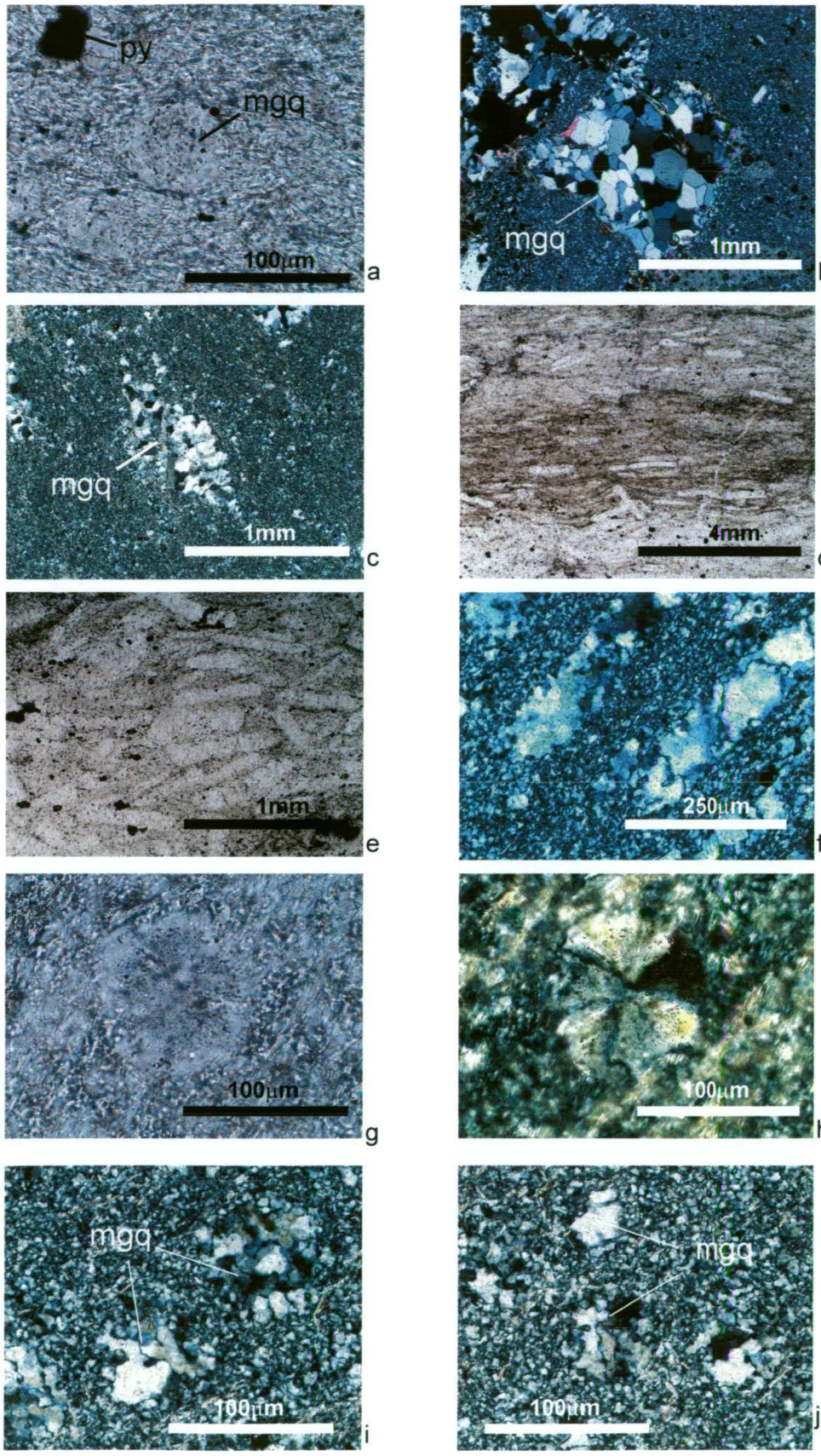
py
mgq
100µm
a
mgq
1mm
b
mgq
1mm
c
4mm
d
1mm
e
250µm
f
100µm
g
100µm
h
mgq
100µm
i
mgq
100µm
j

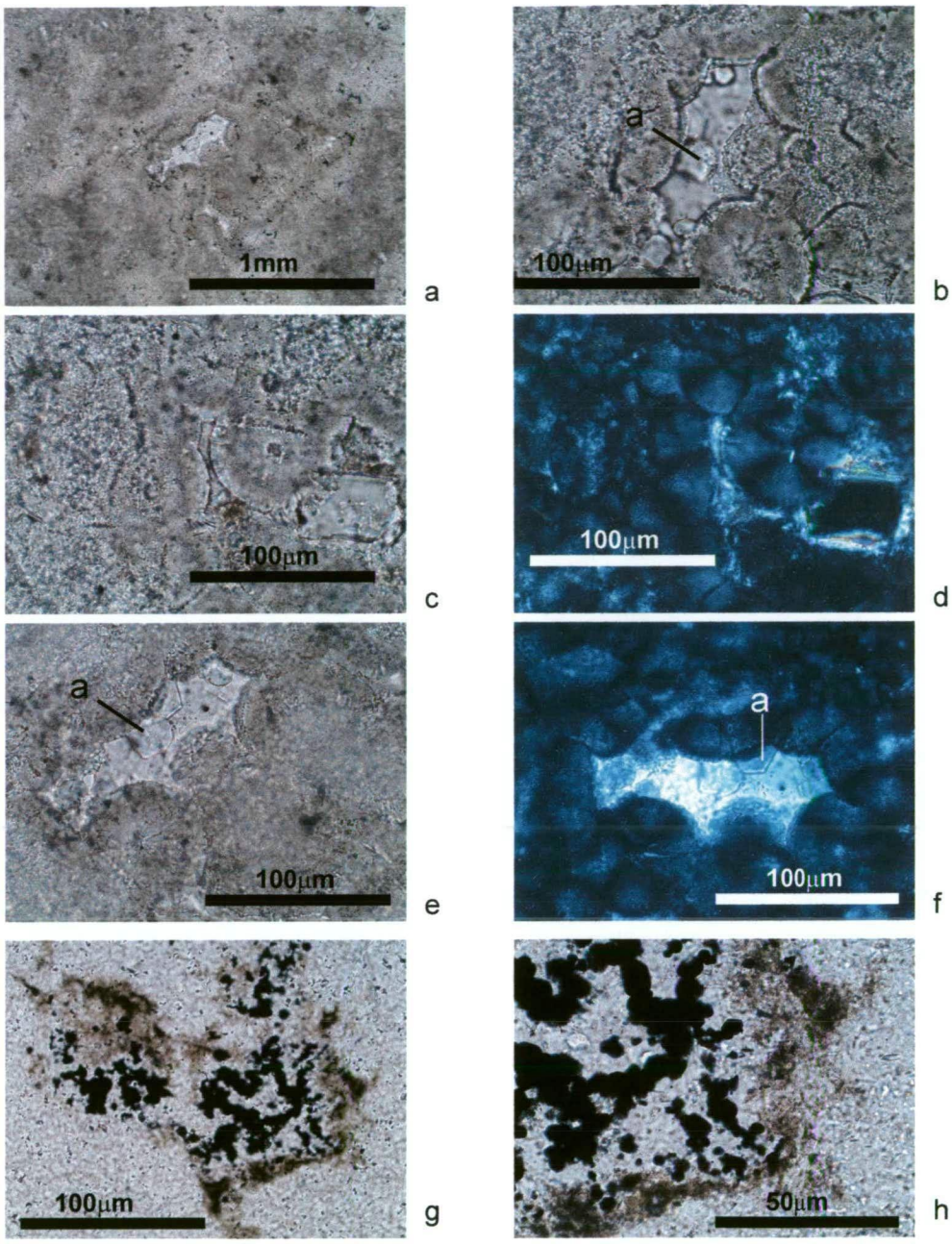

Figure 6.14: a) Chalcedony spherules infill a rectangular void, after anhydrite or carbonate(?) within a phosphate concretion in chert, PPL (SJ446, 18-1004, 82m); **b)** fine euhedral apatite (a) grains occur on the chalcedony spherules, PPL (SJ446, 18-1004, 82m); **c)** tightly packed chalcedony spherules, form the groundmass of the concretion, PPL (SJ446, 18-1004, 82m); **d)** same view as previous photomicrograph but in XPL to illustrate the spherulitic figures (SJ446, 18-1004, 82m); **e)** fine euhedral apatite (a) grains on chalcedony spherules, PPL (SJ446, 18-1004, 82m); **f)** same view as previous photomicrograph but in XPL (SJ446, 18-1004, 82m); **g)** rare ghostly forms of possible chalcedony spherules (replaced by microcrystalline quartz) with fine pyrite in chert, PPL (SJ151, 18-1126, 59.5m); **h)** close up of the previous photomicrograph, PPL (SJ151, 18-1126, 59.5m).

Figure 6.15: a) Feldspar grain replaced by a fine granular mass of sericite (se), XPL (SJ24, 18-1032, 92.7m); **b)** sericite veins crosscut faint laminations (So) in chert, XPL (SJ161, 18-1127, 39.5m); **c)** sericite partially replacing pyrite (py) grain, XPL (SJ760, G171XS); **d)** carbonate (cc) rhomb in microcrystalline quartz groundmass of chert, XPL (SJ776, L14-683, 400.2); **e)** spherical megaquartz (mgq) patches after radiolarians. Note opaques infilling radiolarian test near base of photomicrograph, PPL (SJ754, G171XS); **f)** euhedral rutile (ru) grows into primary pore space (radiolarian test) in green silt-chert PPL-RL (SJ754, G171XS); **g)** euhedral rutile (ru) displaying good open space growth textures, PPL (SJ754, G171XS); **h)** reflected light shows rutile (ru) that grew within a radiolarian test in green chert, RL (SJ158, 18-1127, 38m); **i)** euhedral rutile (ru) and megaquartz (mgq) within a radiolarian test in pale grey-white chert, PPL (SJ158, 18-1127, 38m); **j)** pyrite (py) and sericite (se) have replaced a radiolarian test in pale grey chert above the Battle deposit, PPL (SJ160, 18-1127, 38.5m).

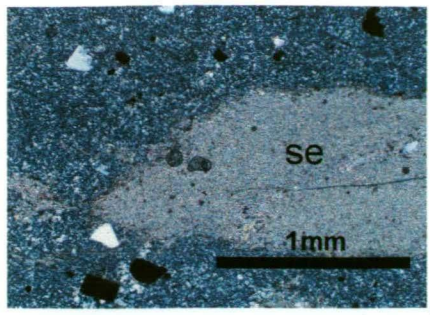
se
1mm
a

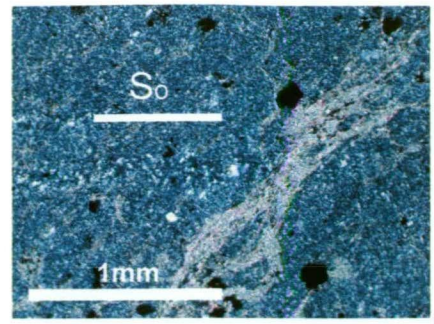
So
1mm
b

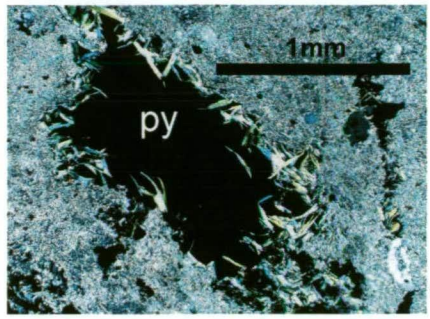
1mm
py
c

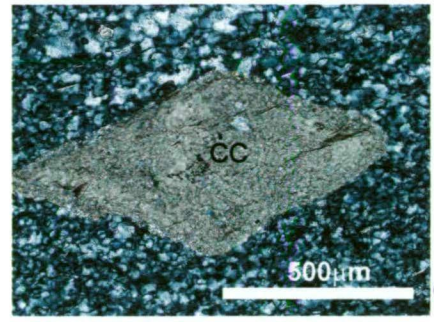
cc
500µm
d

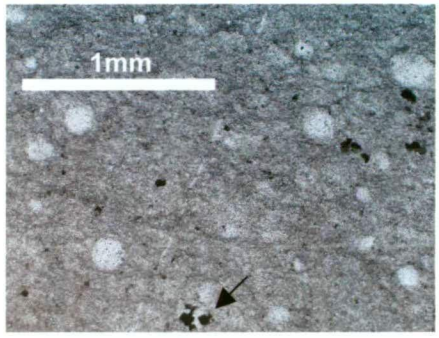
1mm
e

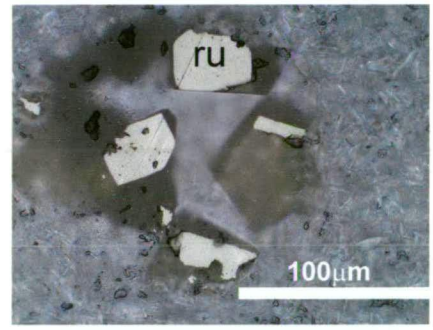
ru
100µm
f

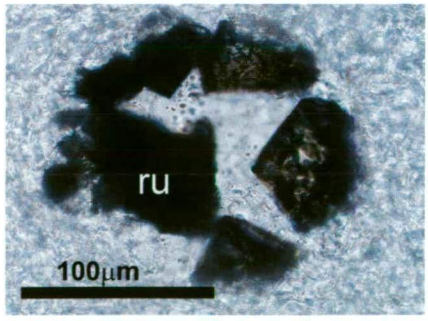
ru
100µm
g

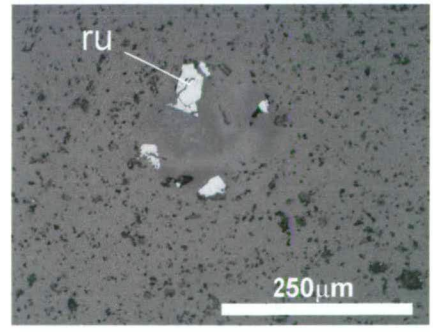
ru
250µm
h

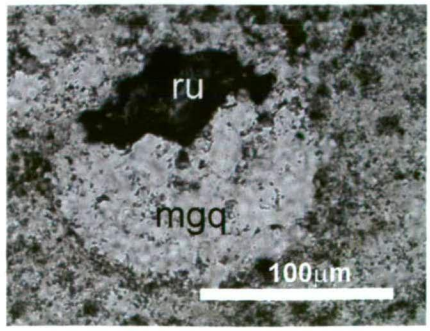
ru
mgq
100µm
i

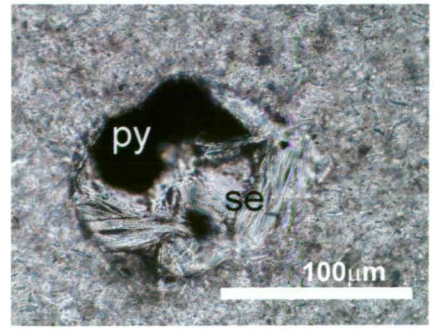
py
se
100µm
j

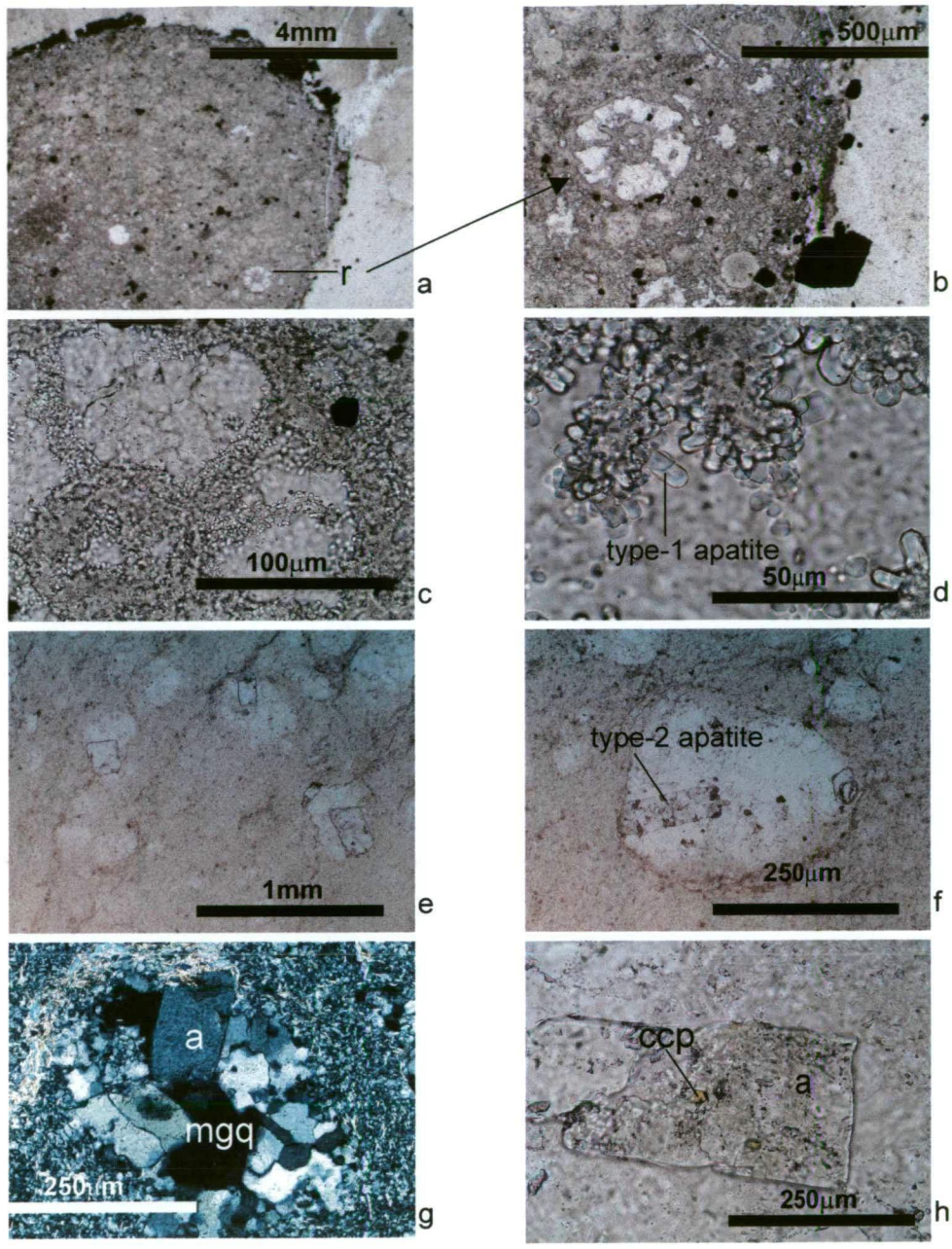

Figure 6.16: a) Ovoid concretion (phosphate nodule?) in chert above the Battle deposit, note the small radiolarian (r) in bottom right hand side, PPL (SJ441b, 18-1004, 73.8m); **b)** edge of 6.17a concretion, with radiolarian, PPL (SJ441b, 18-1004, 73.8m); **c)** close up of radiolarian test, replaced by fine euhedral apatite (a) grains (type-1), PPL (SJ441b, 18-1004, 73.8m); **d)** fine euhedral apatites (type-1) form most of the groundmass of the concretion, PPL (SJ441b, 18-1004, 73.8m); **e)** coarser-grained euhedral apatite grains (type-2) growing in primary voids in chert, PPL (SJ161a, 18-1127, 39m); **f)** close up of type-2 apatite, displaying good open space crystal habit, PPL (SJ161a, 18-1127, 39m); **g)** type-2 apatite and megaquartz (mgq) within a primary pore (after radiolarian?), XPL (SJ161a, 18-1127, 39m); **h)** fine chalcopyrite (ccp) within euhedral type-2 apatite (a), PPL (SJ161a, 18-1127, 39m).

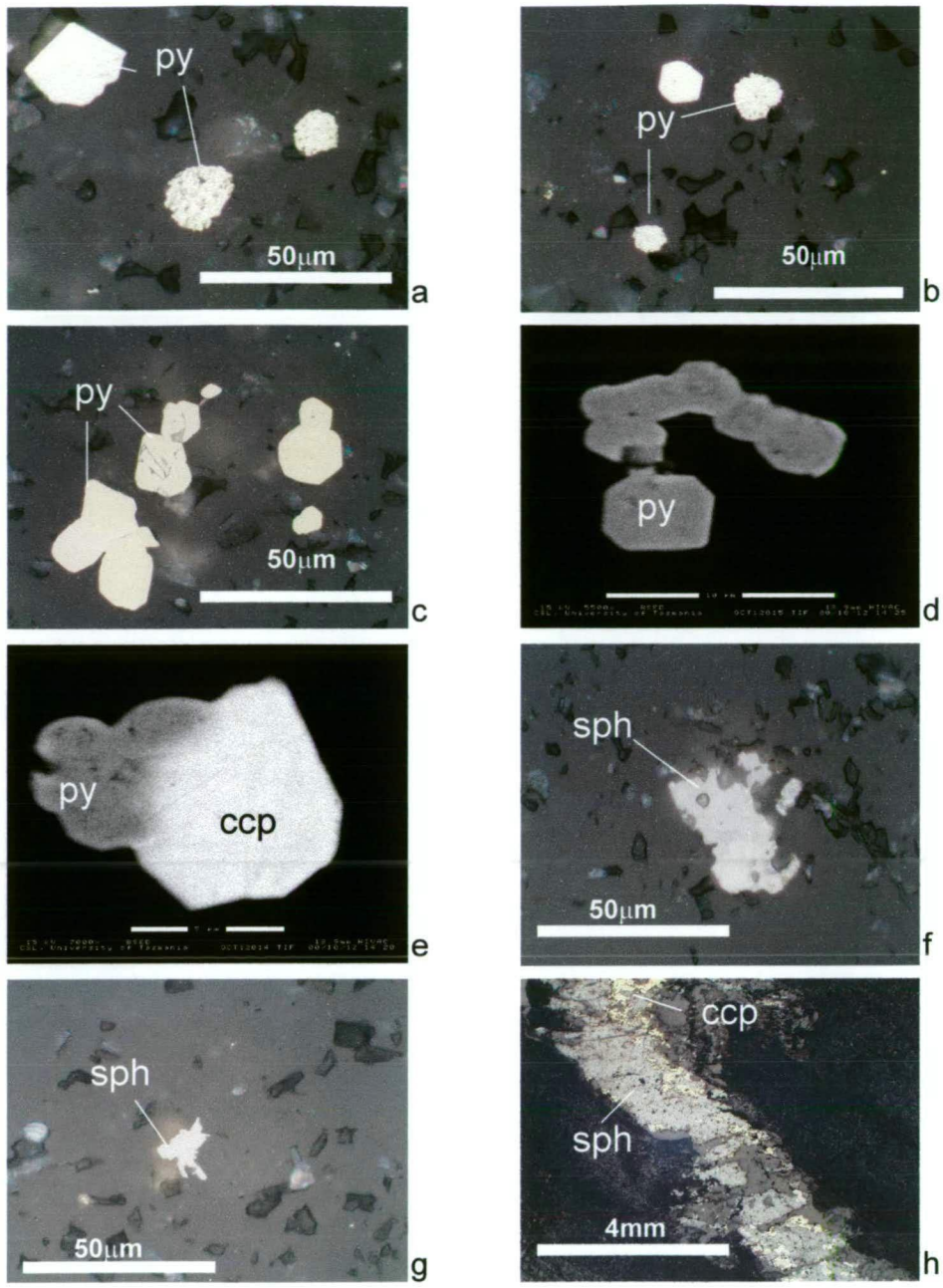

Figure 6.18: a) Fine pyrite (py) in chert above the Battle deposit displaying relict framboidal textures and euhedral crystal forms, RL (SJ327, L14-633, 293.4m); **b)** fine pyrite (py) framboids in chert, RL (SJ327, L14-633, 293.4m); **c)** relict pyrite (py) framboids and euhedral crystal forms are commonly scattered throughout the microcrystalline quartz groundmass of chert above the Battle deposit, RL (SJ434, 18-1004, 49.5m); **d)** possible relict pyrite framboids and cubic pyrite (py) in SEM image, (SJ34, 18-1101, 40m); **e)** SEM image showing chalcopyrite (ccp) overgrowing relict pyrite (py) framboids in chert, (SJ17c, 18-1032, 76.1m); **f)** fine anhedral sphalerite (sph) in microcrystalline quartz groundmass in chert above the Battle deposit, RL(SJ434, 18-1004, 49.5m); **g)** typical fine anhedral to subhedral sphalerite in microcrystalline quartz groundmass, RL (SJ441, 18-1004, 73m); **h)** sphalerite (sph) -chalcopyrite (ccp)-pyrite (py) vein crosscutting chert, RL (SJ434, 18-1004, 49.5m).

6.3 Black Chert

6.3.1 Distribution

Black chert occurs in an area south and west of the Battle Deposit (Figure 6.4). There is a gradational transition from the pale grey chert above the Battle orebody, to the black chert, approximately 200m from the orebody. In the contact zone between the pale-grey chert and the black chert, the cherts are interlayered with very diffuse boundaries.

The basal contact of the black chert is commonly very sharp against the underlying coarse-grained volcaniclastics. The upper contact is less well defined, consisting of an interlayered zone of black chert, rhyolitic sandstone and coarser volcaniclastics.

6.3.2 Macro-scale description

Black chert is a dark grey to black, very fine-grained argillaceous chert or ludite, as defined by Hesse (1990a). The chert predominantly has a glassy appearance and conchoidal fracture and occurs in massive metre-scale beds or as strongly laminated horizons (Figure 6.19a-c). The laminations are much fainter than those in the pale grey chert, due to a lack of colour contrast, but sedimentary structures such as scours and graded beds are still visible. Coarser rhyolitic sandstone and silt interbeds occur throughout the black chert sequence, with relatively sharp contacts.

6.3.3 Mineralogy and textures

The black chert consists of quartz, up to 80-90%, with 10-20% sericite, abundant carbonaceous material, minor sulphides (usually <1-2%), accessory apatite, monazite and rutile. The black nature of this chert is attributed to the carbon content of the rock. Total organic carbon in the black chert was measured, using the 'ashing' method of Krom and Berner (1980), and ranged from 0.07 to 0.38 wt.% (see Appendix 5.1 for results).

In thin section, the black chert has a distinctive texture of wispy black carbonaceous seams and fine sericite blades (up to 10-15 μm long), wrapping around abundant spherical to slightly flattened quartz filled radiolarian tests and scattered detrital quartz and feldspar grains (Figure 6.20a-b). Massive beds versus fine laminations are distinguished by, variations in the carbonaceous content, subtle grainsize variations and changes in the phyllosilicate content.

In places, a weak to moderate S_1 fabric, defined by sericite and carbonaceous seams is developed, commonly at a high angle to bedding. Bedding-parallel micro-stylolites are common, defined by fine wavy carbonaceous-rich layers

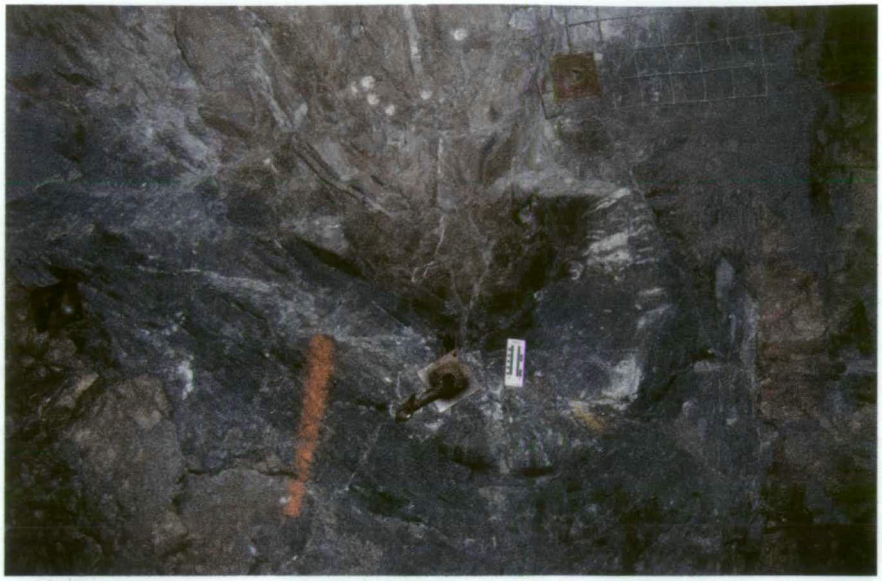

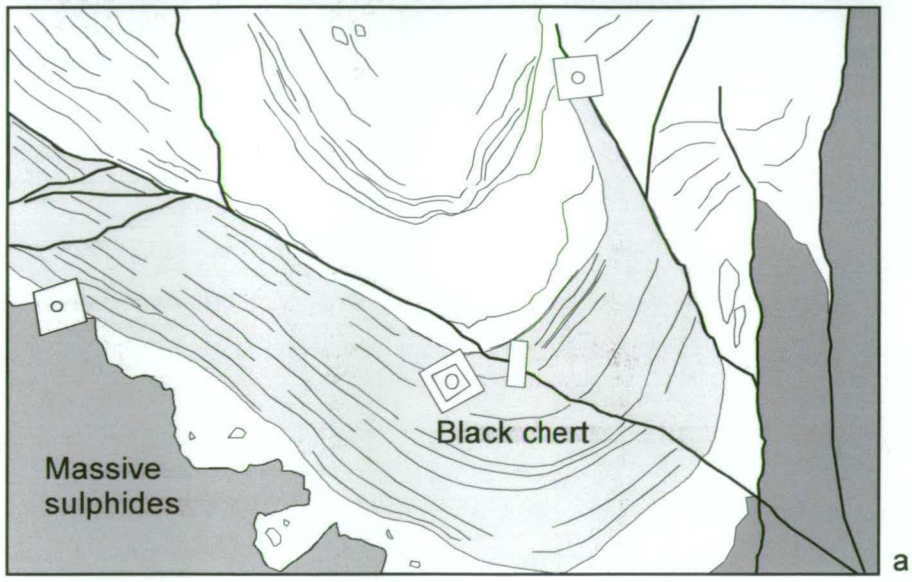

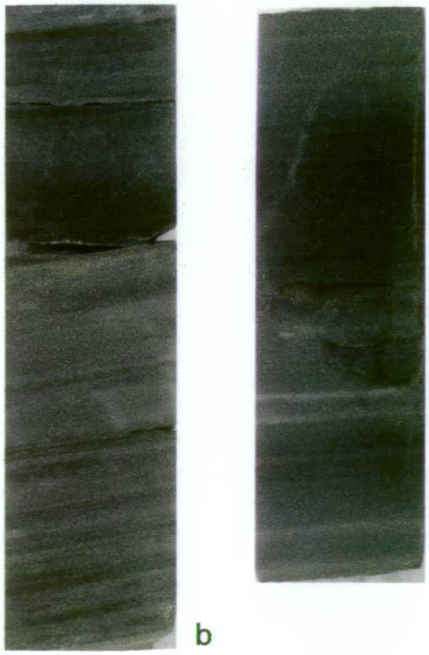

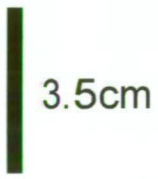

Figure 6.19: Black chert in the Battle mine; **a)** folded black chert in the Gopher Zone (G158DD, 1600E, 4050N, Battle mine); **b-c)** diffusely laminated black chert and interlayered medium grey chert (SJ788, L14-681, 365.2m and 366.5m).

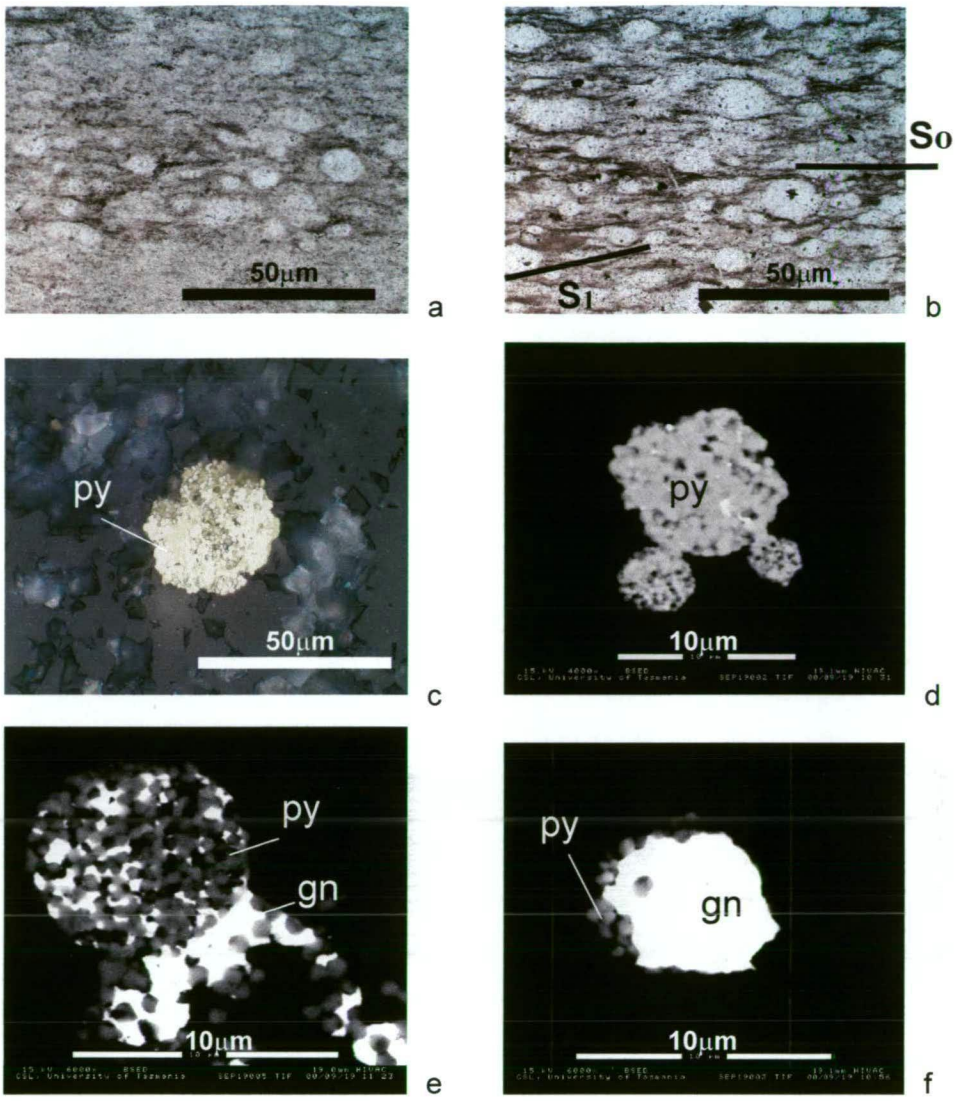

Figure 6.20: a) Typical micro-scale texture of black chert with carbonaceous seams wrapping around spherical megaquartz patches, which are after radiolarian tests, PPL (SJ788, L14-681, 365.2m); **b)** similar texture with a greater amount of carbonaceous material preserved. Carbonaceous seams define the bedding and the crosscutting S_1 foliation, PPL (SJ788, L14-681, 365.2m); **c)** pyrite (py) commonly occurs in black chert as fine framboids, RL-PPL (SJ317, L14-680, 352m); **d)** SEM image of fine pyrite (py) framboids in black chert, (SJ317, L14-680, 352m); **e)** SEM image showing a cluster of fine pyrite (py) framboids, with intergrown galena (gn) (SJ317, L14-680, 352m); **f)** SEM image of pyrite framboids, overgrown or replaced by galena (gn) (SJ317, L14-680, 352m).

Quartz predominantly occurs as, 1) fine anhedral to subhedral grains in the microcrystalline groundmass; 2) as coarser detrital grains; and 3) as spherical megaquartz patches. Fine sericite grains (2 to 10 μm long) occur throughout the microcrystalline groundmass and also as larger detrital grains (up to 50 μm grain-size) and fine granular masses after feldspar grains.

6.3.4 Sulphides

Pyrite is the dominant sulphide in black chert, with very minor fine anhedral to subhedral sphalerite, chalcopyrite and galena finely disseminated throughout the microcrystalline groundmass. The pyrite mainly occurs as fine framboids and minor cubes scattered throughout the chert (Figures 6.20c-d). Galena commonly occurs as an overgrowth on the framboids (Figures 6.20e-f).

6.4 Argillite

6.4.1 Distribution

Argillite occurs in large deposits, up to 100m thick, in the southern and eastern parts of the mine property, in the South Flank and Thelwood Valley areas (Figure 6.1). Thinner argillite sequences also occur above the HW deposit and to the south and west of the Battle deposit. The argillite has a similar stratigraphic position to the chert, occurring immediately above, or 1-3m above the HW orebody, and close to the contact with the underlying Price Andesite in areas distal to the orebodies. In the Battle basin, the argillite has a gradational contact with black chert, and is interlayered with the black chert with very diffuse contacts.

Throughout the property, the basal contact of the argillite is consistently very sharp against the underlying coarse-grained volcaniclastics and ore horizons. The upper contact, although sharp in places, is a less well defined, interlayered zone of argillite, rhyolitic siltstone and sandstone and coarser volcaniclastic rocks.

6.4.2 Macro-scale description

The argillite is dark grey to black, very fine-grained and occurs as massive metre-scale beds, to strongly laminated horizons (Figure 6.21a). Pale rhyolitic siltstone and sandstone interbeds (mm to cm scale) are common throughout (Figures 6.21b-c). The argillite is variably silicified and is strongly graphitic in places. Sedimentary structures such as scours, graded beds, flames, convolute laminations and soft sediment deformation are present (Figures 6.21d-f). Small round to ovoid phosphate nodules and concretions (0.5-

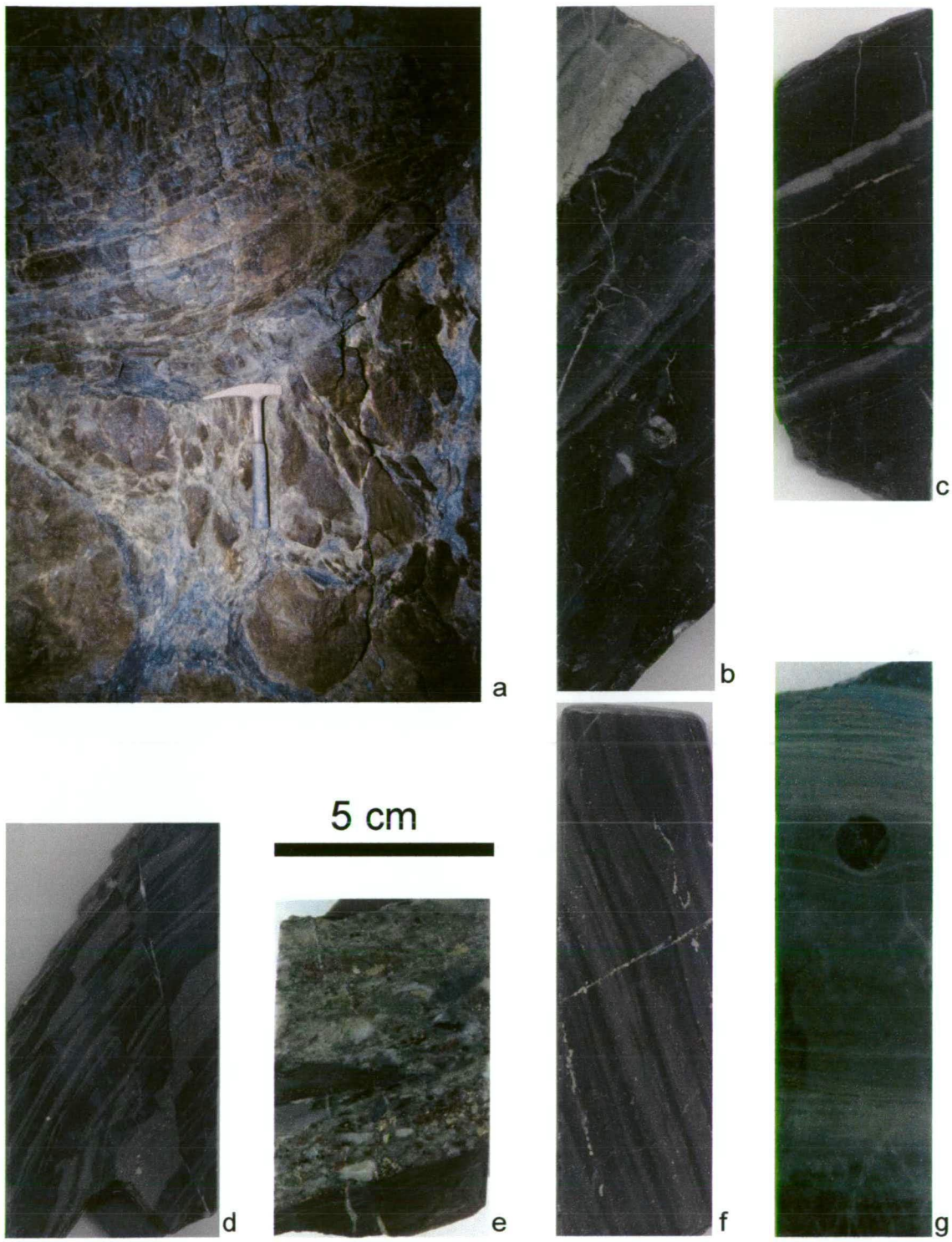

Figure 6.21: a) Laminated argillite in sharp contact with the underlying massive sulphides in the HW mine (23 shop); **b)** laminated argillite with interbedded rhyolitic sandstone layer with a sharp, scoured basal contact (sample SJ716, L14-641, 773.5m, South Flank area); **c)** fine (mm scale) rhyolitic sandstone layers in argillite (sample SJ719, L14-641, 782.2m) **d)** finely interbedded argillite and sandstone disrupted by small normal faults (probably D4); **e)** argillite rip up clasts in coarse-grained rhyolitic conglomerate-sandstone above massive sulphides in HW mine (sample SJ261, 23-503, 135m); **f)** strongly laminated argillite with a small concretion (phosphatic?) with diffuse margins, near the top of the sample (sample SJ824, 16-43, 481.6m, South Flank area); **g)** spherical concretion in strongly laminated argillite/siltstone (sample SJ566, 20-675, 28m).

3cm long) occur in scattered horizons throughout the argillite sequence (Figures 6.21f-g). The argillite is interbedded with coarser rhyolitic sandstones, conglomerates and volcaniclastic rocks, and is commonly found as rip-up clasts in the overlying coarser-grained units.

6.4.3 Mineralogy and textures

The argillite consists of fine quartz (30-50%), sericite (30-40%), abundant carbonaceous material, detrital feldspar and carbonate, and minor sulphides, predominantly 1-2%. Accessory detrital apatite, monazite and rutile grains are also observed.

The argillite has a texture of abundant detrital quartz and feldspar grains, lithic clasts and radiolarian tests, scattered in a dark carbonaceous-clay rich matrix (Figures 6.22a-b). Bedding is defined by variations in the carbonaceous content, grainsize and phyllosilicate content. In places, a strong S_1 fabric is developed, defined by sericite and carbonaceous seams and is commonly at a high angle to bedding. This fabric can give the rock a false mylonitic appearance (Figure 6.22b).

Quartz is present as, 1) scattered detrital grains, up to 0.5-2mm diameter; 2) fine grains in the granular matrix; and 3) spherical megaquartz patches, which most likely represent quartz pseudomorphs after radiolarian tests. The internal structure of the radiolarians is variably preserved, although they are much better preserved than those in the chert (Figures 6.22c-h). Late silica-carbonate veining is common throughout the argillite, and commonly forms a fine network of veins through the rock.

6.4.4 Sulphides

Pyrite is the dominant sulphide in argillite, and is most commonly present as, 1) fine framboids (10-100 μm) scattered thoughout the fine granular matrix; and 2) as isolated cubes and clusters. The pyrite content is most argillite samples is only 1-2%, but increases up to 10-15% in argillite samples above the HW orebody. In the HW argillite, the pyrite occurs as framboids and euhedral cubic grains, and many pyrite framboids appear to have grown inside radiolarian tests, along with length-fast chalcedony (Figures 6.23a-h). Minor fine anhedral sphalerite and chalcopyite are also observed in the argillite above the HW orebody, as fine disseminated grains in the carbonaceous matrix.

6.5 Facies associated with the caprocks

Variation in facies associated with the caprocks reflect changing depositional environments, proximity to ore, and the timing of ore formation relative to the deposition of the caprocks.

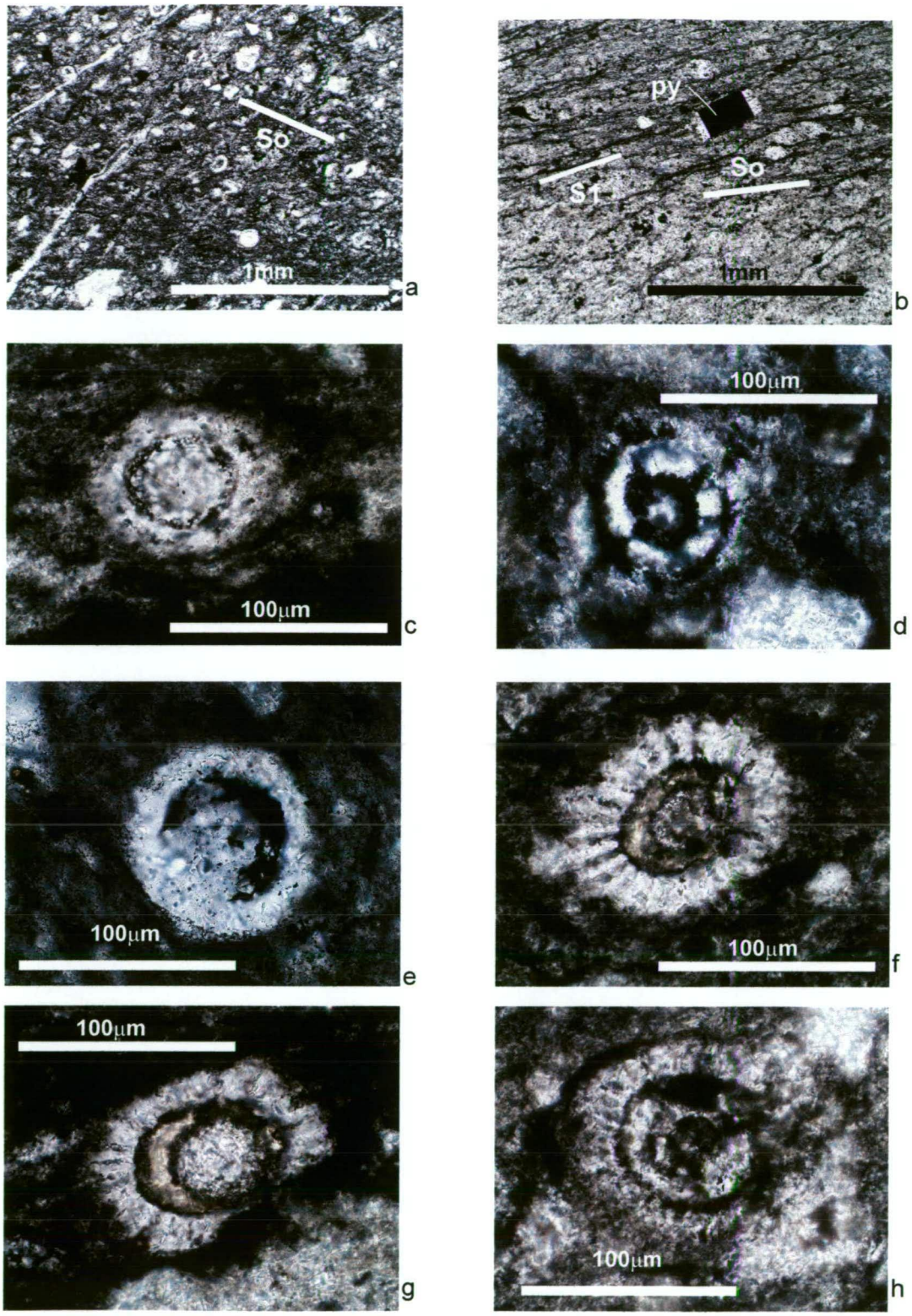

Figure 6.22: a) Typical micro-scale texture of argillite with fine detrital quartz grains scattered in a carbonaceous-clay matrix. Carbonaceous seams define bedding (So) and the S_1 foliation, PPL (SJ260, HW23-503, 140m) **b)** bedding (S_o) is defined by carbonaceous-rich laminations, which are crosscut by the S1 foliation defined by wavy carbonaceous seams, PPL (SJ47, 23-493, 17.6m); **c-h)** radiolarians in argillite above the HW deposit, infilled by megaquartz and length-fast chalcedony, with internal structure variably preserved,PPL (SJ260, HW23-503, 140m).

Facies associated with the caprocks include rhyolitic siltstone, sandstone and conglomerate, rhyolitic volcaniclastic rocks; mixed andesitic/dacitic/rhyolitic volcaniclastic rocks; ore-clast breccias; and the massive to semi-massive ore horizons (Figures 6.24a-k). Facies variation of the HW Horizon above the Battle and HW orebodies, is illustrated in a series of N-S oriented sections in Figures 6.2 and 6.3. Section 1420E (Figure 6.25) provides a detailed illustration of the facies associated with a thick zone of chert above the Battle orebody. The facies associated with the caprocks are divided into three sections based on stratigraphic position relative to the caprocks.

6.5.1 Basal facies and ore contacts

The basal contact of the fine-grained 'caprocks' is predominantly very sharp against either coarse-grained rhyolitic volcaniclastic rocks and/or massive to semi-massive sulphides. This boundary is largely a depositional contact, although, where chert lies immediately above the massive sulphides in the Battle mine, there is evidence of replacement of the chert by the underlying sulphides. This indicates that at least some ore was emplaced after chert formation (Figure 6.26a-b,f).

The coarse-grained volcaniclastic rocks below the caprocks hosts the Battle orebody and parts of the HW orebody, and contains good ore replacement textures of the coarse-grained rhyolitic volcaniclastic rocks (Figure 6.26c-e). This unit was deposited on the Price Andesite and indicates a rapid change from andesitic volcanism into dominantly rhyolitic volcanism. The unit consists of subangular to subrounded rhyolitic clasts in a finer granular matrix. The unit is commonly very poorly sorted and predominantly matrix supported. In places, the unit is composed of 10 to 20% angular andesitic clasts (2-10cm diameter). In many places this coarse-grained unit becomes very thin, and the fine-grained facies (or caprock) is deposited close to, or directly on the Price Andesite.

In the Battle mine, the siliceous caprocks predominantly lie immediately on the orebody with a very sharp contact (Figures 6.27b-v). Massive sulphides also crosscut the chert in places (e.g., 6.26a-b and f). The top contact of the massive sulphides is commonly irregular and the sulphides appear to die out within the coarse volcaniclastic unit, up to 1-2m below the sharp basal contact of the caprocks, and a depositional contact is preserved (Figure 6.27a).

The nature of the ore-caprocks contact is markedly different in the HW mine. Here, the caprocks consist of argillite with only minor chert, and the argillite is commonly in sharp contact with the underlying massive sulphides. The ore-hangingwall contact in the HW mine, is commonly an erosive one, with ore clasts entrained in the overlying coarse

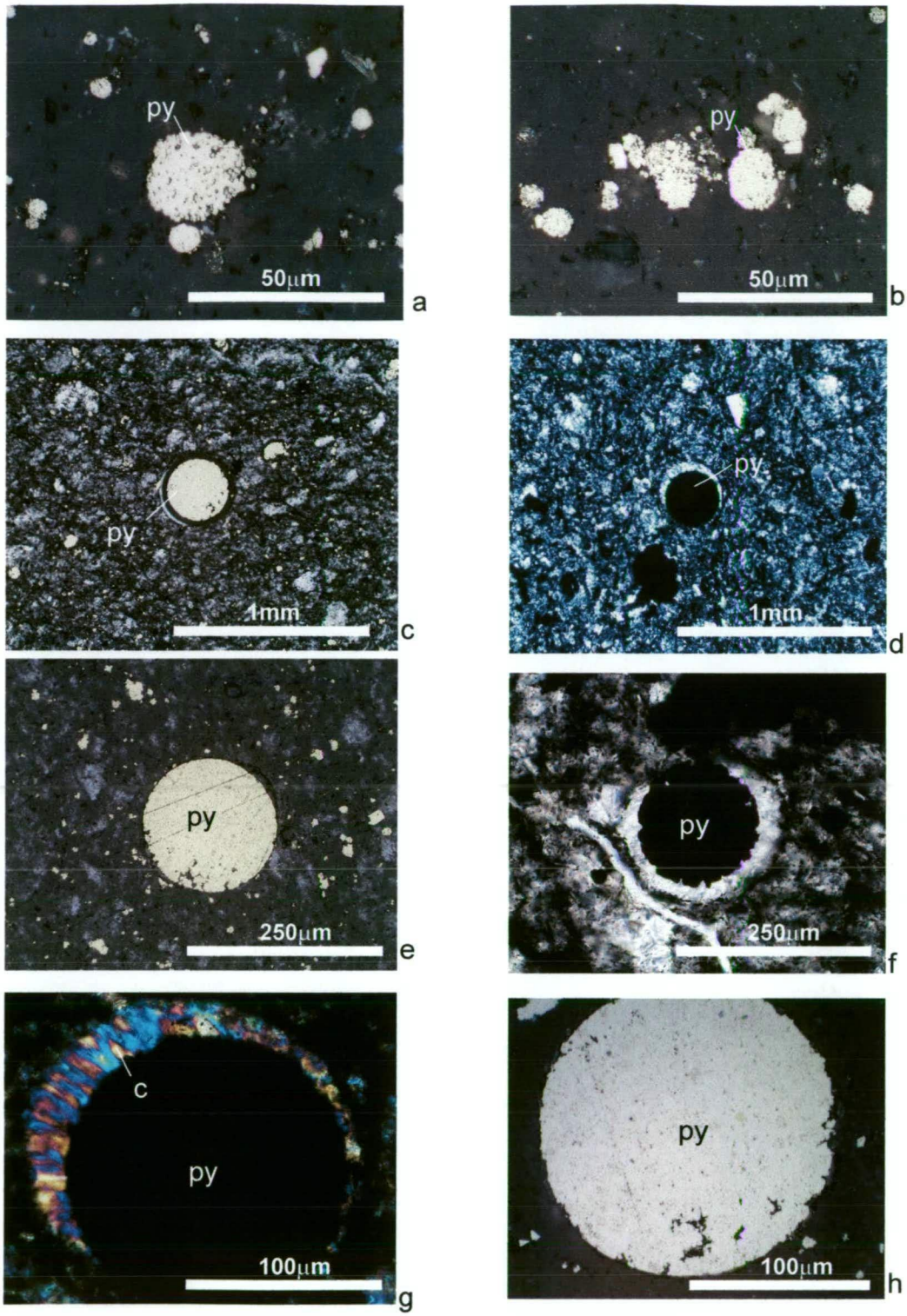

Figure 6.23: a) Pyrite (py) framboid in argillite above the HW orebody, RL (SJ670, 23 Shop); **b)** pyrite framboids often form clusters in argillite, RL (SJ670, 23 Shop, HW mine); **c)** unusual circular pyrite, possibly replacing a radiolarian test, RL-PPL (SJ670, 23 Shop); **d)** pyrite (py) appears to incompletely replace a radiolarian test. The random orientation of the pyrite infill indicate that they are not geopetal structures, PPL (SJ670, 23 Shop); **e)** circular pyrite replacing a radiolarian test, RL-PPL (SJ670, 23 Shop); **f)** pyrite framboid with an irregular margin incompletely replaces a radiolarian test, PPL (SJ670, 23 Shop); **g)** length-fast chalcedony (c) with a radial habit forms a rim around circular pyrite (py), XPL (with gypsum plate), (SJ670, 23 Shop); **h)** close-up of the circular pyrite (py), in detail, the edges are irregular and most likely represent framboidal growth within a radiolarian test, RL (SJ670, 23 Shop).

rhyolitic detritus (Figures 6.28a). The top contact of the massive sulphides is commonly brecciated and in many areas, the argillite is in sharp contact with the underlying ore (Figure 6.28c). Laminated chert and siltstone overlies the massive sulphides in a few locations in the HW mine (Figure 6.28b). The presence of rip-up mud clasts and laminated chert clasts in coarse-grained mass flow units above the HW orebody (e.g,, Figure 6.10), indicate erosion of the caprock horizon. The caprock horizon above the HW orebody may have been much more extensive, prior to the influx of mass flows.

6.5.2 Intercalated facies within the caprock horizon

The main facies intercalated with the caprocks are fine rhyolitic siltstones, sandstones and minor conglomerates. Basal contacts of these coarser grained units are commonly sharp, with scour structures and occasional rip-up clasts visible. The sandstones are commonly graded, with fine tops grading sequentially into silt-sized grains, mudstone and then chert. Above the ore deposits, these sandstone beds commonly contain a greater sulphide content (up to 10-15%) than the surrounding fine-grained caprocks (1-5%).

In the Battle mine, a turbidite bed, with a sharp scoured base, overlies sulphide-rich siltstone and mudstone at the edge of the chert horizon in the South Trough zone (drive ST183, Figure 6.29). In detail, the nature of the basal contact zone of the turbidite, indicates that the mudstone was most likely semi-consolidated prior to turbidite deposition. The underlying mudstone forms clasts near the contact, and also occurs as matrix in the overlying sandstone. Sulphides only occur in the mud clasts near the contact and in the mud matrix, and are totally absent from the silicilastic grains. The siliciclastic grains in the overlying sandstone turbidite, contain relatively fresh feldspar grains. In the adjacent chert, feldspar is commonly overprinted or in places totally replaced, by quartz and/or sericite.

6.5.3 Overlying facies

The upper contacts of the caprock are more poorly constrained than the sharp basal contacts. The upper boundary is generally an interlayered zone of rhyolitic siltstone, sandstones and coarser grained rhyolitic and minor mixed volcaniclastic rocks with the finer chert and argillite. In the coarser volcaniclastic units, clasts are mainly 1 to 40cm diameter, subangular to subrounded and are matrix supported. Pale to dark red jasper clasts, are common throughout this unit, above both the Battle and HW orebodies, although they are more common above the HW orebody (Figure 6.30). Subsequent silica alteration commonly overprints the jasper clasts, leaving relics.

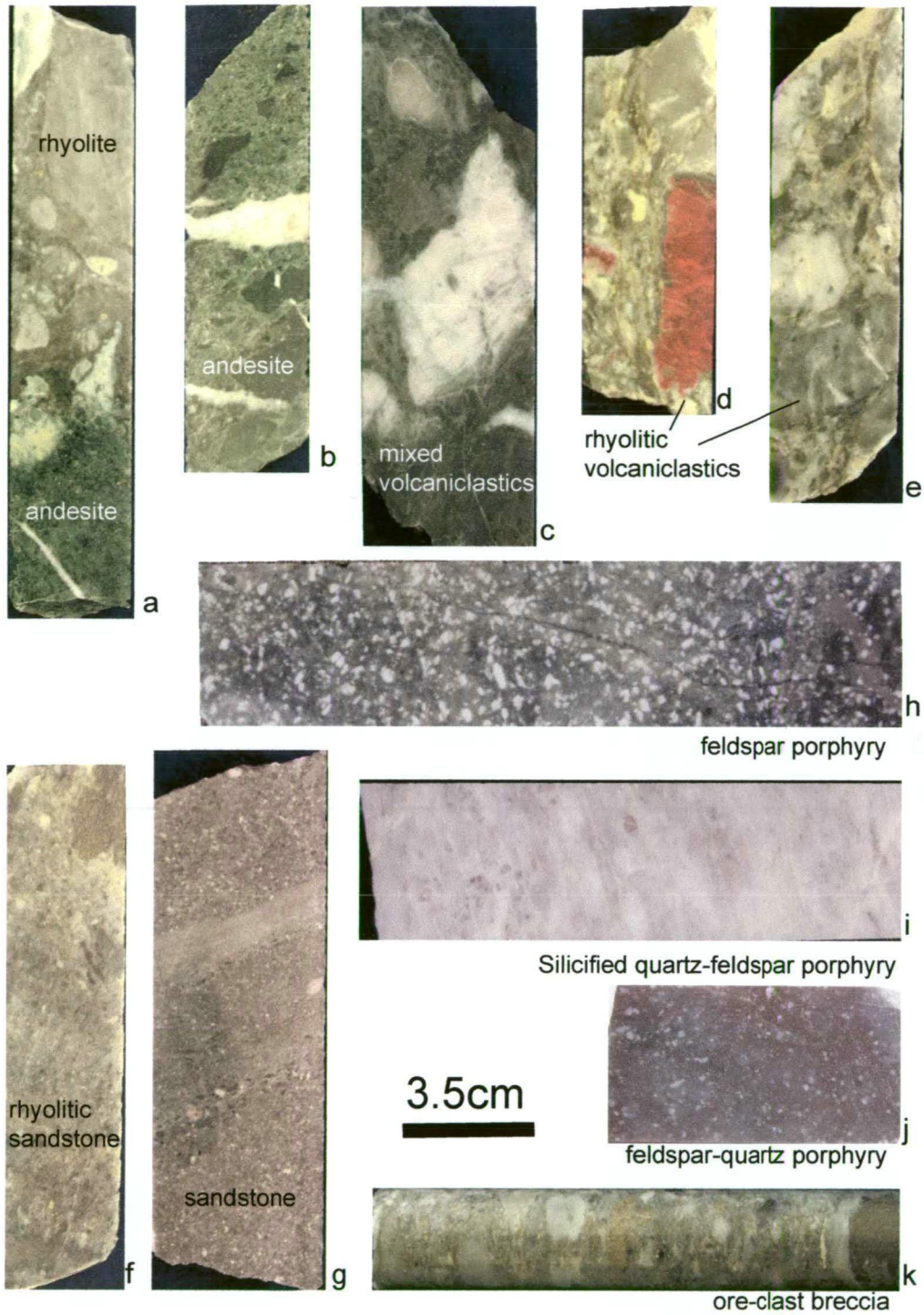

Figure 6.24: a) Contact between Price Andesite and HW Horizon rhyolitic volcaniclastic rocks in the South Flank area (SJ601, 16-33, 9.6); **b)** weakly altered Price Andesite (SJ545, 20-845, 11.3m); **c)** mixed rhyolite-andesite-dacite volaniclastic rocks (SJ50, W202, 1009.9m); **d)** coarse-grained rhyolitic volcaniclastic rocks with jasper clasts (SJ782, L14-681, 317m); **e)** quartz-sericite altered coarse-grained rhyolitic volcaniclastic rocks (SJ782, L14-681, 317.5m); **f)** medium-grained rhyolitic sandstone/volcaniclastic rocks (SJ782, L14-681, 318m); **g)** graded beds in rhyolitic-dacitic sandstone (SJ48, W202, 999.5m); **h)** feldspar porphyry above the HW orebody (SJ796, P13-304, 407m); **i)** quartz-feldspar porphyry above the Battle deposit (SJ696, 18-976, 24m); **j)** feldspar-quartz porphyry in the Marshall Zone (SJ588, L15-501, 365m); **k)** ore-clast breccia above the HW orebody (SJ477, HW23-514, 10.2m).

6.6 Discussion: Origin of siliceous caprocks

This section examines the origin of the siliceous caprocks at Myra Falls to determine whether they represent exhalative deposits or silicification of pre-existing fine-grained sediments. An exhalative origin has important implications for exploration models, as exhalites can provide very useful marker horizons, with trace element variations providing good vectors to ore (e.g., Kalogeropoulos and Scott, 1989).

6.6.1 Mechanisms of chert formation

There are a number of ways in which chert can form. These include: 1) maturation of a primary inorganic siliceous ooze; 2) maturation of a biogenic siliceous ooze; 3) post-depositional silica replacement of sediments; 4) or a combination of these. The source of silica can be, 1) biogenic (e.g., radiolarian tests, diatoms, or spicules); or 2) inorganic, such as modified silica-rich pore water, high temperature hydrothermal fluids or the devitrification of volcanic glass (Simonson, 1985; Adachi et al., 1986; Pollock, 1990). High temperatures are not necessary (Knauth, 1994), as illustrated by the observation of low temperature (20°C) modern silica precipitation (Mackenzie and Gees, 1971).

The most widely known mechanism for chert formation is the transformation sequence from opal-A (xray-amorphous silica) to opal-CT (low ordered cristobalite-trydimite) to microquartz (well ordered α-quartz) (Williams et al., 1985). Opal-A is precipitated at low temperatures to form a siliceous ooze. With progressive burial opal-A transforms to less soluble opal-CT. The opal-CT recrystallizes to lower solubility microquartz. The crystallinity of such quartz progressively increases with burial and metamorphism (Williams et al., 1985). As a result of this transformation, opal-A is normally not present in sediments older than about 20 My, although it has been found in sediments as old as 85 Ma (late Cretaceous), but only at shallow subsurface depths (Hesse, 1990a). In comparison, opal-CT can persist in sediments 100-120 my old, but no opal-CT has been found in pre-Cretaceous sediments older than 144 Ma (Hesse, 1990a).

Although the transformation process from opaline silica to quartz is a well known phenomenon of chert formation, Knauth (1994) suggests that it is likely that many of the common cherts in the ancient record formed by direct diagenetic precipitation of microquartz without any precursor opaline phases. As Mackenzie and Gees (1971) showed in experiments, quartz can precipitate directly without the precursor opaline phases. However, it is commonly very difficult to texturally differentiate between sedimentary fabrics of opal-CT cherts and quartz cherts (Williams et al., 1985). However, some quartz

Battle Mine
Section 1420E

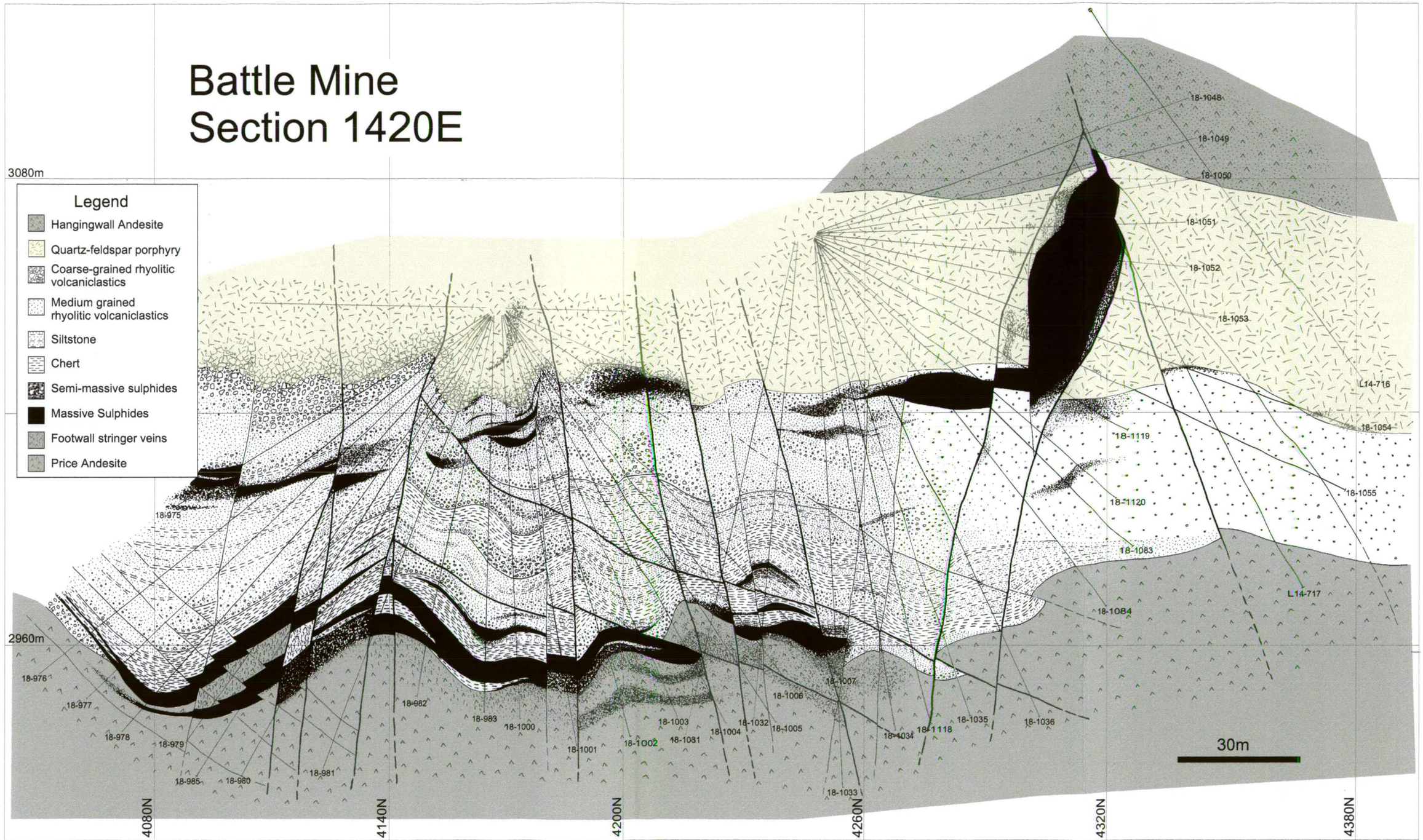

Figure 6.25: Detailed geology of HW Horizon, section 1420E, Battle Mine. The siliceous caprocks and associated facies are folded and dissected by numerous faults, however, at a broad scale, the stratigraphy is preserved.

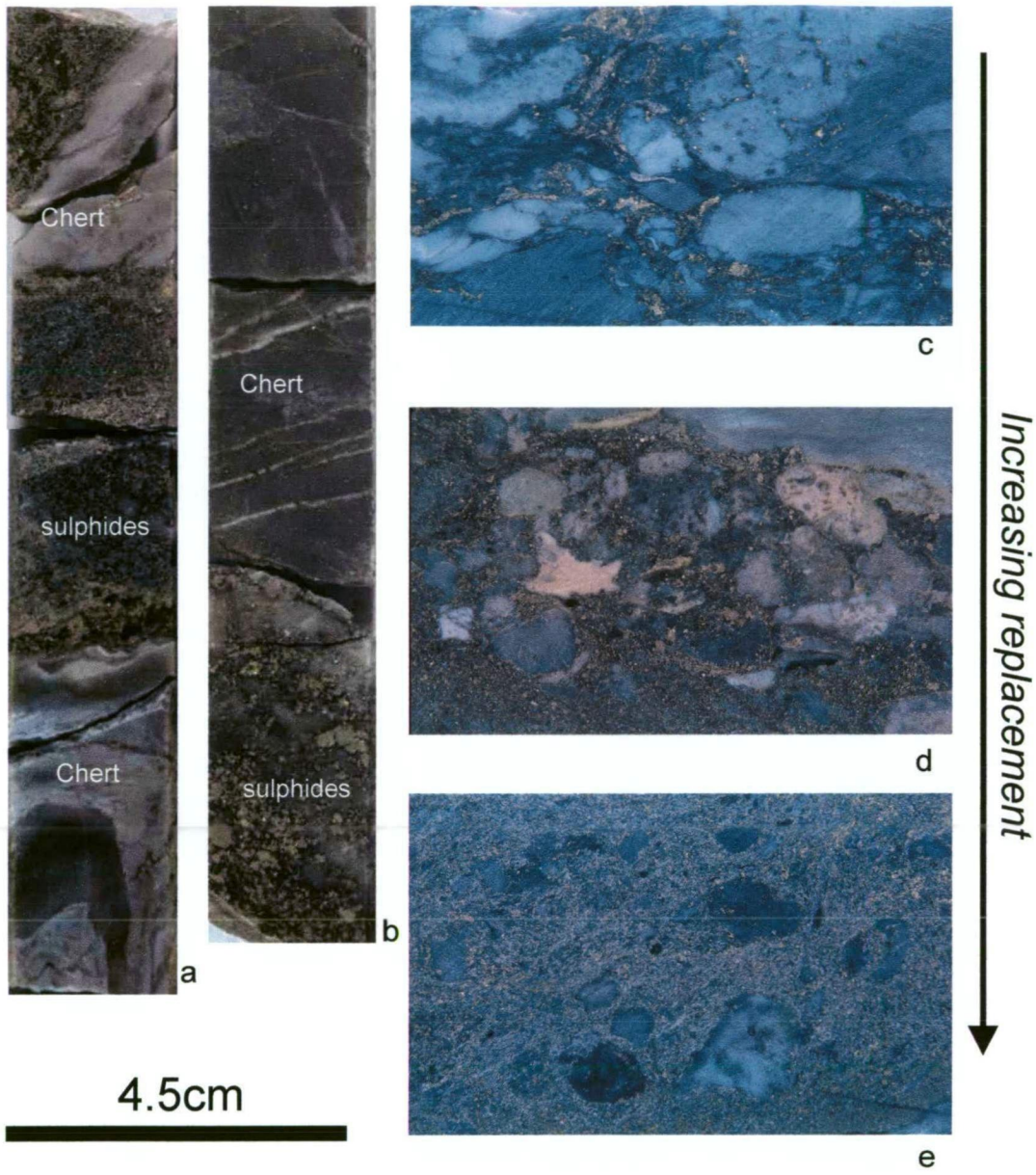

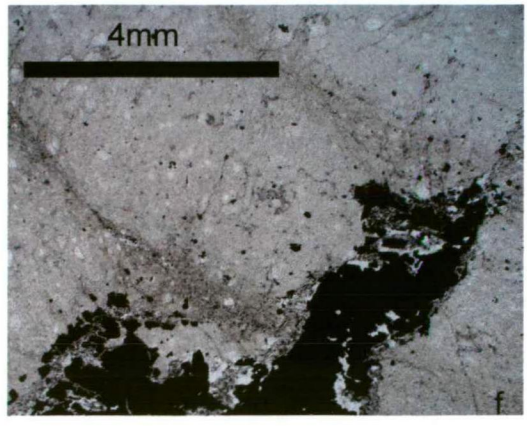

Figure 6.26: a) Chert-ore contact with sphalerite-rich ore crosscutting laminations in chert (SJ129, 1818-480, 37m); **b)** pink chert-ore contact in the Battle mine (SJ151, 18-1126, 59.5m); **c-d)** progressive replace-ment of coarse grained rhyolitic volcaniclastics by massive sulphides in the Ridge Zone (photos courtesy of B. Gemmell); **f)** photomicrograph showing a sulphide stringer vein crosscutting laminated chert above the Battle orebody, PPL (SJ158, 18-1127, 38m).

cherts do have distinctive pore-filling opal-CT lepisphere pseudomorphs indicating early opaline precursors (e.g., Duhig et al., 1992).

Finely bedded siliceous deposits are relatively common above many VHMS systems. An inorganic source for such silica is most likely, from hydrothermal emanations and the breakdown of volcanic glass. Petrological features of such silica deposits are important in determining whether the silica was deposited as a primary amorphous silica accumulation, or whether it represented silicification of pre-existing sediments. Silicification could occur from syn-depositional silicification through low-temperature sediment-water interactions on the seafloor and/or post-depositional recirculating hydrothermal fluids.

6.6.2 Origin of siliceous caprocks at Myra Falls

The abundance of radiolarians in the chert at Myra Falls requires that they be considered as a possible silica source. However, as concentrations of radiolarians are generally less than 10% the cherts cannot be classified as radiolarites (Pollock, 1987; Hesse, 1990a). Although they may contribute silica, the dominant source of silica is more likely to be from volcanic emanations and the breakdown of volcanic glass, due to the proximity of volcanic vents.

The sequence at Myra Falls has undergone significant burial and metamorphism (lower to mid-greenschist facies) over a long period of time, and therefore, less ordered forms of silica, such as opal-CT are not observed. Instead, only α-quartz occurs, as microquartz, megaquartz and chalcedony (see section 6.2.3 for detailed descriptions).

In the Battle chert, many features suggest that the chert formed as a replacement of the pre-existing sediments rather than as a primary accumulation of amorphous silica, such as a hydrothermal exhalative deposit. These features include:

- The chert has many sedimentological and petrological similarities to the adjacent argillite, such as fine laminations, soft-sediment deformation, convolute bedding, interbedded turbidites, the presence of radiolarians and phosphate nodules (Figure 6.31a-e);
- As radiolaria are pelagic organisms, a similar density of radiolaria in the chert and adjacent argillite, indicates similar pelagic sedimentation rates in both units.
- Argillite and chert occur at the same stratigraphic level, see section 1260E (Figure 6.5);
- Diffuse contacts between the argillite, black chert and pale-grey chert;

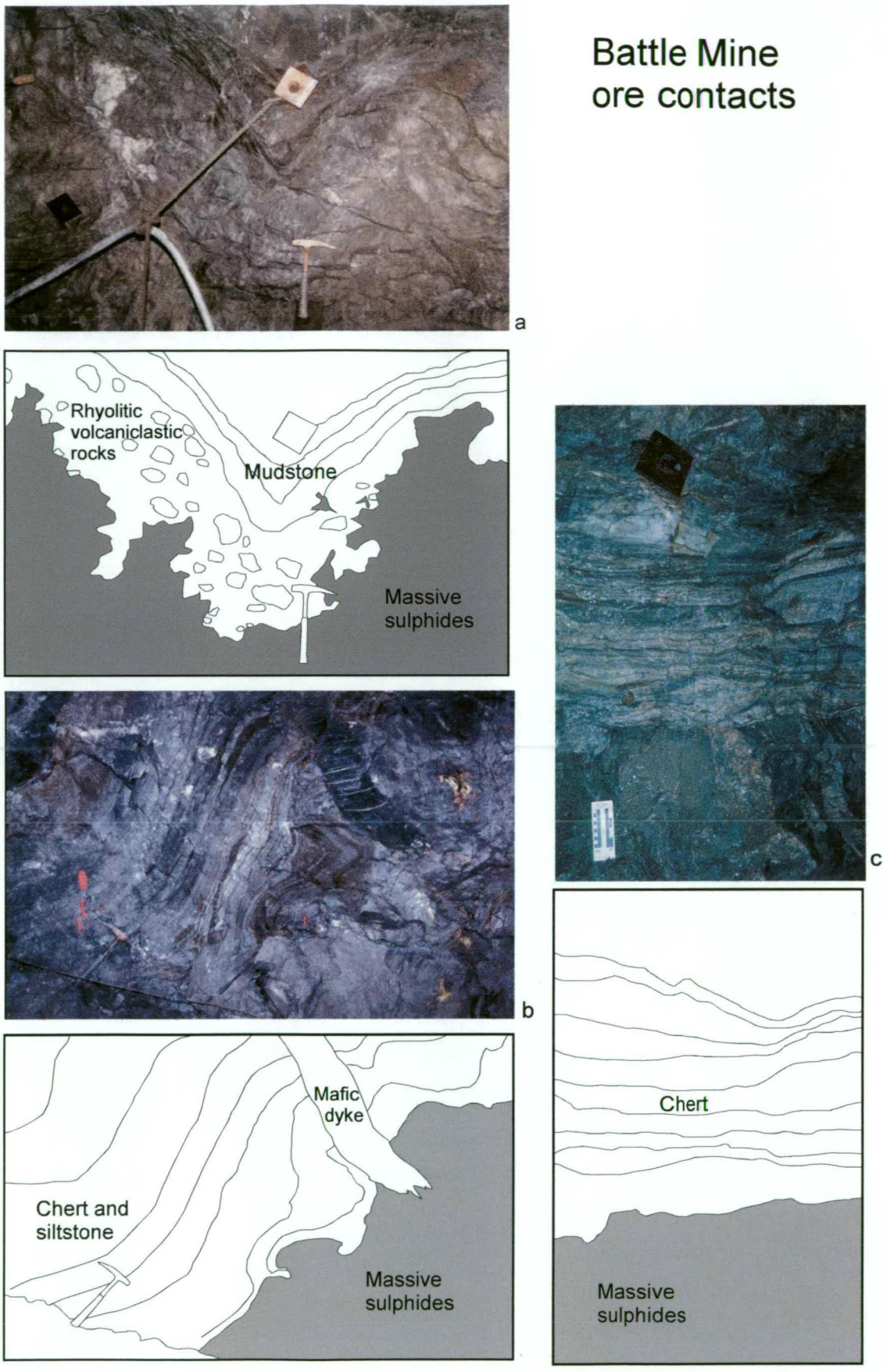

Figure 6.27: Typical ore contacts in the Battle mine: **a)** sharp, folded contact of laminated silt and the underlying coarse-grained rhyolitic volcaniclastic unit, which hosts the massive sulphides, drive ST183A, Battle mine; **b)** strongly laminated green silt-chert overlies massive sulphides with a sharp, irregular contact in drive G171XS, Gopher Zone, Battle mine; **c)** laminated chert overlies massive sulphides with a sharp relatively planar contact, drive M150DD, Battle mine (photo courtesy of B. Gemmell);

- Relict pyrite framboids are still visible in the chert, although most appear to be recrystallised to equant forms. Framboids are the dominant form of pyrite growth in the adjacent argillite;
- Progressive destruction of carbonaceous material from the argillite into the more siliceous units (Figure 6.32). In the argillite, dark carbonaceous seams wrap around spherical radiolarian tests. This texture becomes increasingly faint, almost ghostly, in the adjacent chert units and is only visible in crossed polars. A marked decrease in the total organic carbon from the argillite to the chert, also indicates that the organic matter is destroyed by silicification;
- The presence of convolute laminations in the chert, this texture mainly develops in silty to sandy clastic sediments (Sugitani et al., 1996);
- The microcrystalline groundmass overprints earlier lithological variation, such as increases in grainsize of detrital elements. Contacts are diffuse with no discrete siliceous layers;
- A silicic alteration front is seen on the periphery of the chert, with chert grading out into muds. In these areas, e.g., southern margin of the chert (Figure 6.32) and G171XS (Figure 6.33a), bedding parallel to slightly discordant microquartz veins, 0.5-2cm wide, are common. Microcrystalline quartz veins or stringers also crosscut massive sulphides beneath the chert sequence in location S335C, in the HW mine (Figure 6.33b);
- In some chert layers, silt and occasional sand-sized detrital grains float in a chert matrix, Sugatani (1996) suggests this is evidence for silicification of a pre-existing sediment; and
- Quartz replaces detrital feldspars, possible anhydrite and larger detrital quartz grains often have resorbed and embayed margins.

Although these features suggest that silicification was the dominant process of chert formation at Myra Falls, there is some evidence that surface precipitation of amorphous silica may have also occurred. Unusual silica textures preserved in radiolarian tests, in phosphate nodules, and in rare patches within the microcrystalline groundmass, suggest that an earlier phase of amorphous silica deposition may have occurred prior to silicification.

Relict silica textures include:

- Spherical radiolarian tests are infilled with microcrystalline quartz and length-fast chalcedony with a radial habit in chert above the Battle mine (Figure 6.13g-h). Other minerals that infilled radiolarian tests include rutile, apatite and pyrite (Figures 6.15 and 6.16e-h);

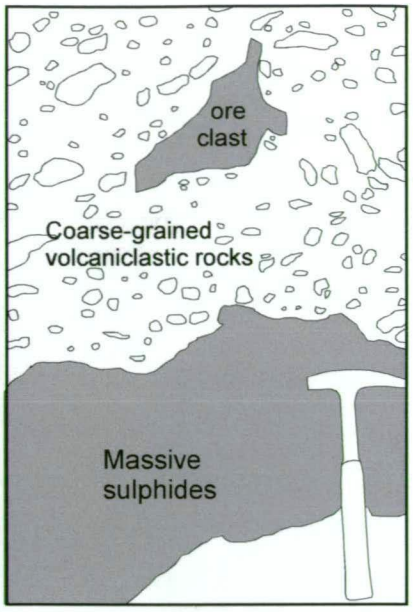

HW mine
ore contacts

a

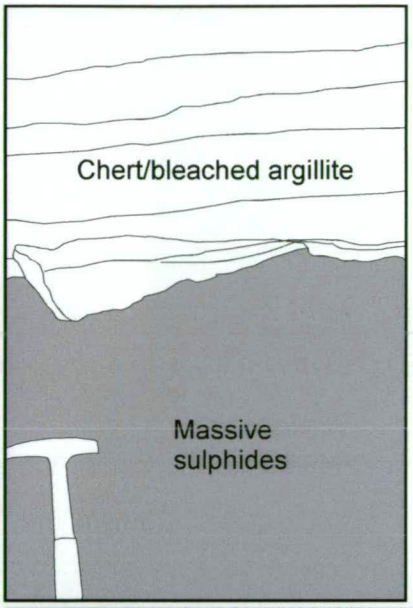

b

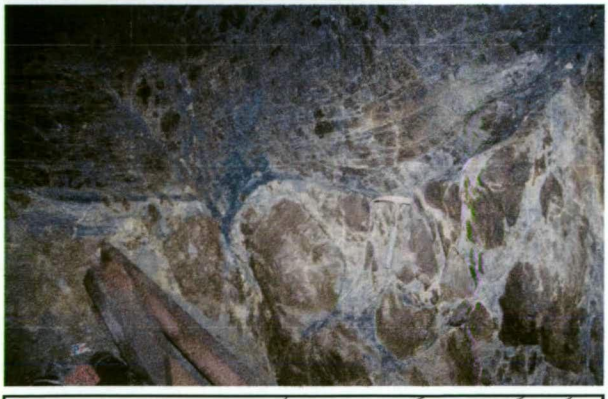

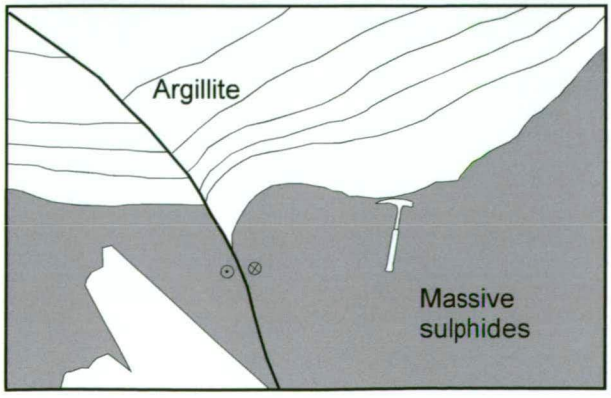

c

Figure 6.28: Typical ore contacts in the HW mine. **a)** erosional ore contact with oreclasts common in the overlying coarse-grained rhyolitic volcaniclastic unit (drive 23-427, 43 Block area, HW mine); **b)** sharp relatively planar contact between chert and bleached argillite and the underlying massive sulphides (drive S335C, HW mine); **c)** laminated black argillite directly overlies the massive sulphides with a sharp, irregular contact. The upper part of the massive sulphides appears to be brecciated (23 Shop, HW mine).

- Inclusion-rich, very fine-grained chalcedony occurs in a radial arrangement, forming wedge shaped mammillated and spherulitic growth structures within phosphate nodules (Figures 6.14a-f); and
- Rare quartz pseudomorphs of spherulitic growth structures occur within the microcrystalline groundmass of the chert (Figures 6.14g-h).

The spatial association of the chert horizons with the underlying VHMS orebodies suggests, but does not prove, that the source of the silica was from hydrothermal fluids circulating through the sediments. The distribution of chert also appears to coincide with the location of growth faults shown on paleoseafloor reconstructions in Chapter 5 (Figure 5.19). These early faults most likely acted as hydrothermal fluid conduits, and silicification was best developed proximal to these zones. The degree of silicification dies out markedly away from these structures. For example, this is well illustrated by the progressive destruction of carbonaceous material in the pale-grey chert to black chert and argillite in section 1260E on the southern margin of the Battle deposit.

Radiolarian tests, infilled by microcrystalline quartz and length-fast chalcedony, are typically interpreted as an early *in situ* diagenetic feature (Folk and McBride, 1978; Pollock, 1990). Spherical uncompacted tests are evidence that resistant quartz infills developed prior to significant compaction. These quartz-filled tests are a common feature in many layers of Myra Falls chert, and indicate that the early diagenetic history of the chert involved the selective early replacement of amorphous biogenic silica by microcrystalline quartz and/or chalcedony. The partial to total infill of radiolarian tests by rutile, apatite and pyrite are also interpreted to be an early syn-depositional precipitate (Adachi et al., 1986; Schieber, 1996).

The regular, circular form of the spherulitic figures in the phosphate nodules (Figure 6.14a-f), are typical of spherulites formed by competitive growth during void-filling precipitation of fibrous crystals in radiating aggregates (Simonson, 1985; Roedder, 1968). Although silica spherulites can form as a replacement of other material, their forms are generally more irregular, as the radial-fibrous aggregates do not tend to nucleate solely on pore edges. As a result, their mutual boundaries and extinction patterns are more irregular (Simonson, 1985). Weaver and Wise (1972) suggest that very regular spherulitic figures can form by neomorphism of opaline silica. During diagenesis, voids in microfossil molds and microcavities are commonly filled with bladed spherules of silica about 5-12 μm in diameter. Bulk x-ray analyses indicate that these lepispheres appear to consist of opal-CT (Weaver & Wise, 1972).

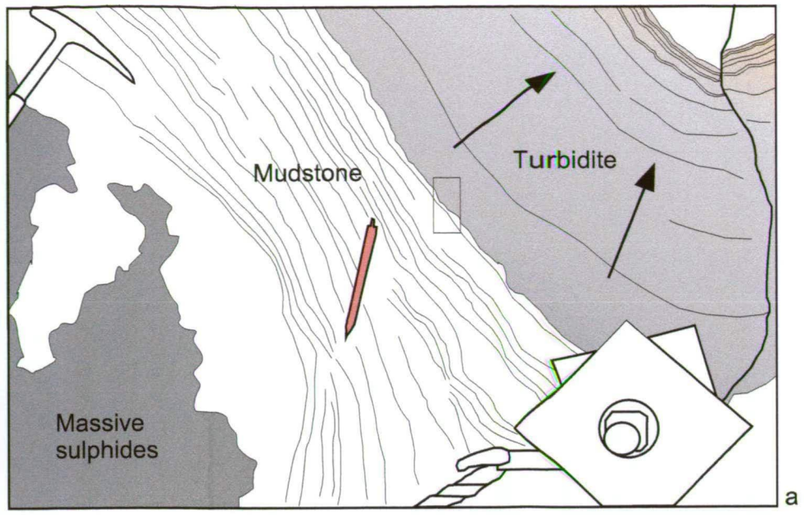

a

Sulphide-rich mudstone entrained into a sandstone turbidite
Battle mine - drive ST183A

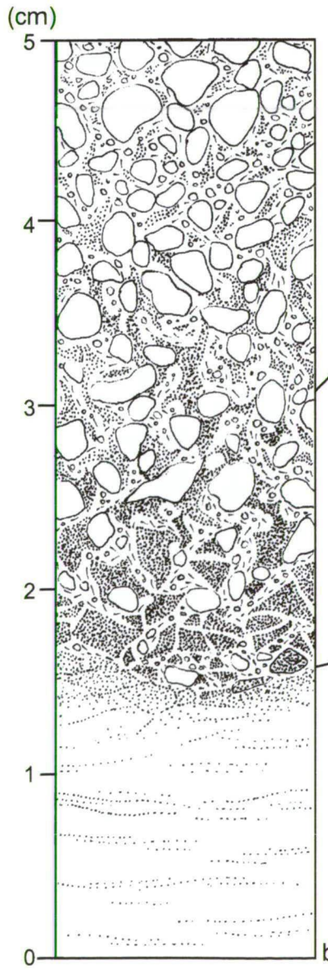

b

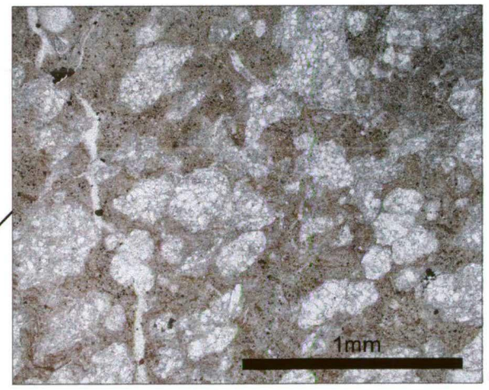

c

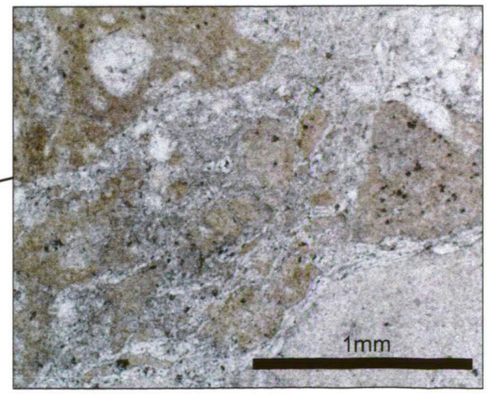

d

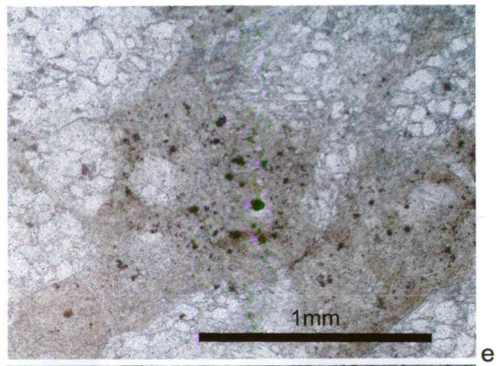

e

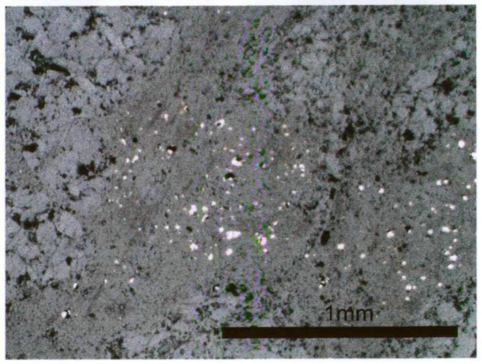

f

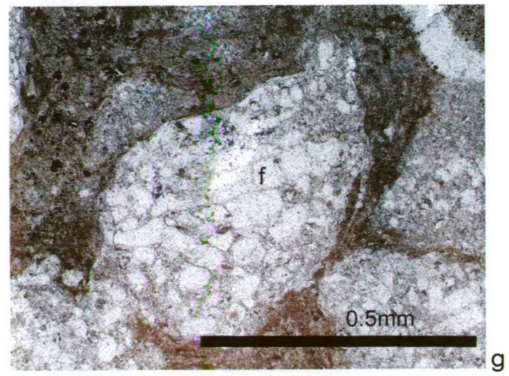

g

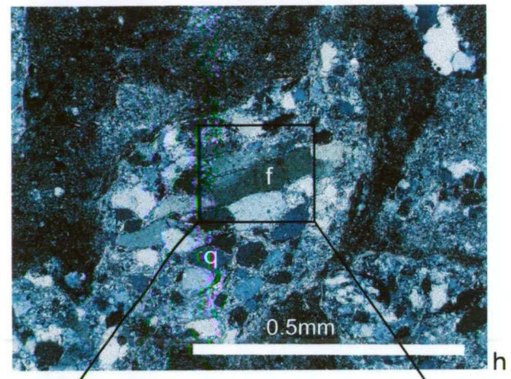

h

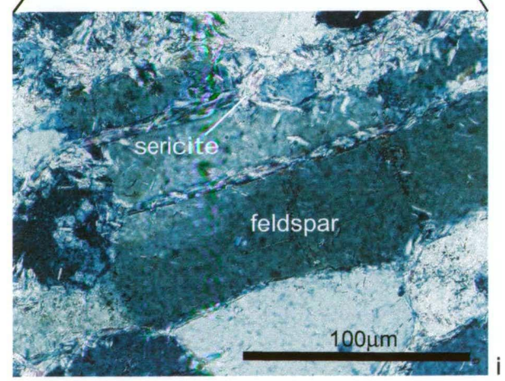

i

Figure 6.29: A semi-lithified sulphide-rich mud layer entrained into the overlying sandstone turbidite, in drive ST183A, Battle mine; **a)** graded base of the sandstone turbidite overlying strongly laminated muds. Small box in centre represents the sample location (SJ535, ST183A); **b)** schematic drawing of entrained sulphide-rich mud and quartz-feldspar sandstone; **c)** sulphide-rich mud is entrained by the turbidite and now forms the matrix (PPL); **d)** semi-lithified sulphide rich mud layer is brecciated during deposition of the turbidite (PPL); **e)** sulphide-rich mud matrix and felsic clasts (PPL); **f)** same view but reflected light illustrates that the sulphides are only present in the matrix, none are observed in the felsic clasts (RL); **g-h)** feldspar (f) grains are well preserved in the felsic clasts (PPL, XPL); **i)** close-up of fresh feldspar grain with very weak sericite alteration along the cleavage planes (XPL).

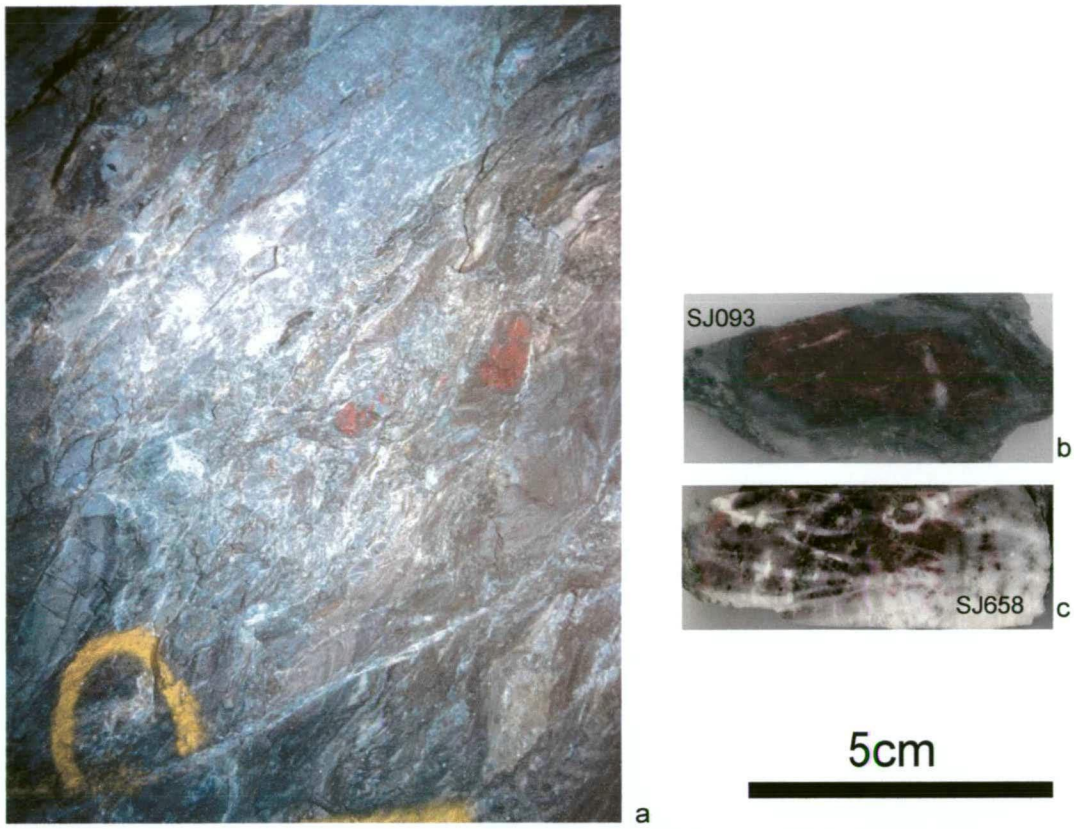

Figure 6.30: Jasper clasts in the coarse-grained volcaniclastic unit above the caprock horizon; **a)** Jasper clasts, (about 5-10cm long) with large chert clasts in a poorly sorted mass flow unit above the HW orebody, drive B390, HW mine; **b-d)** close-up of jasper clasts variably replaced by silica, leaving jasper relics (samples from drive S335A, HW mine).

The ghostly forms seen in rare patches in the microcrystalline quartz groundmass (Figures 6.14g-h) also appear to have a spherulitic habit and similar dimensions to those shown in Figure 6.14a-f). Microcrystalline quartz in the ghostly spherical forms (Figures 6.14g-h), are full of fine inclusions, very similar to the spherulites in the phosphate nodules (Figures 6.14a-f). These spherical forms could also represent microcrystalline quartz pseudomorphs after early diagenetic opal-CT infill of microcavities.

Although chalcedony is a relatively stable form of silica, its presence only in rare patches in the microcrystalline quartz groundmass and in phosphate nodules suggests that these early diagenetic features were overprinted by later silicification. The fact that microcrystalline quartz clearly pseudomorphs early diagenetic features (e.g., 'ghostly' spherulitic forms replaced by microcrystalline quartz, Figure 6.14g-h), and overprints compaction features, such as the carbonaceous seams wrapping around spherical radiolarian tests, suggests that most silicification was post-depositional. At least some compaction had occurred prior to this event, to account for the minor compaction features preserved in the chert.

Although silicification is interpreted as post-depositional, the ubiquitous presence of bedding-parallel microstylolites throughout the chert indicates that silicification occurred prior to substantial compaction. Chert rip-up clasts in overlying coarse-grained volcaniclastic layers support this view. Erosion of chert was not extensive, as chert clasts are only a minor component of the overlying coarse-grained units.

Silicification mainly affected the finer-grained units. However, silicic alteration of jasper clasts in the coarse-grained volcaniclastics, which overlie the chert, indicate that siliceous fluids also percolated through this unit. The observed grain-size control on silicification may have been due to differences in permeability and grain surface area between the muds and overlying coarse-grained volcaniclastics (Lowe, 1999). In the highly permeable coarser units, hydrolysis would have been slower than in the muds, because of the low surface area of larger grains, and the rapid flushing by pore fluids would have inhibited the development of silica-supersaturated pore fluids. In the adjacent muds, the higher surface area of the finer grains and the lower permeability, would have enhanced the development of silica-supersaturated pore waters and silica precipitation.

The presence of crosscutting, quartz-sulphide-sericite veins throughout the chert indicate that siliceous fluids continued to flow through the sedimentary sequence, well after chert had consolidated by maturation.

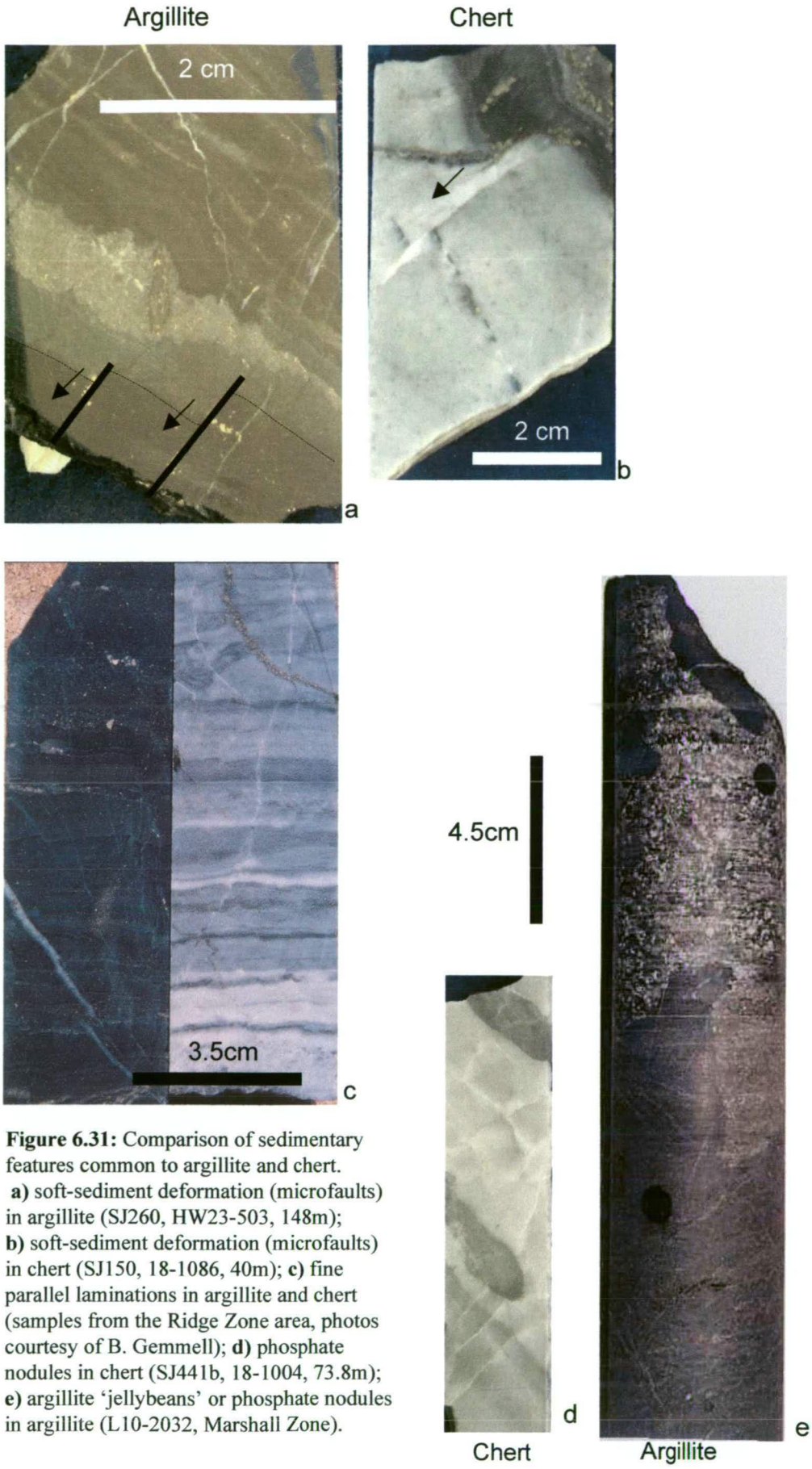

Figure 6.31: Comparison of sedimentary features common to argillite and chert. **a)** soft-sediment deformation (microfaults) in argillite (SJ260, HW23-503, 148m); **b)** soft-sediment deformation (microfaults) in chert (SJ150, 18-1086, 40m); **c)** fine parallel laminations in argillite and chert (samples from the Ridge Zone area, photos courtesy of B. Gemmell); **d)** phosphate nodules in chert (SJ441b, 18-1004, 73.8m); **e)** argillite 'jellybeans' or phosphate nodules in argillite (L10-2032, Marshall Zone).

6.7 Depositional environment and origin of caprocks

6.7.1 Depositional environment

Sedimentary features within the argillite and chert, such as the fine parallel laminations indicate that deposition occurred in response to reduced current energy. The clay- to silt-size of the siliclastic detritus in the laminated chert (e.g., detrital quartz in Figure 6.12e) indicates, via hydraulic equivalence, that the chert was originally deposited as mud (Simonson, 1985). Interbedded sandstone turbidites and radiolarians in the argillite and chert also suggests a relatively deep, quiet depositional environment, at least below storm wave base, >80-100m (e.g., Jones and Desrochers, 1992; Einsele, 2000).

Mud and shale rich deposits, ranging from a few to 100s of metres thick, whether restricted in size or widespread, represent topographic lows. Some of these would be shallow and some deep, with minimal bottom currents or waves (Potter, 1998). The paleoseafloor reconstruction in Chapter 5, identified growth faults and associated paleo-topographic lows which coincide well with the argillite and chert locations. The fine-grained deposits are absent in areas of elevated topography, suggesting that the argillite ponded in topographic lows such as the Battle and HW basins and the south flank area.

The lack of bioturbation, with good preservation of fine laminations, indicates an absence of benthic fauna. The only fauna present were planktic radiolarians which give few clues to the nature of the benthic environment. However, the abundance of radiolarians in some layers of the argillite and chert indicate very low sedimentation rates. If sedimentation rates were high, the concentration of radiolarians would have been much lower, being diluted by detrital material.

The presence of phosphate nodules in some horizons of the argillite and chert also suggests that low sedimentation rates prevailed. Phosphate accumulations are commonly associated with condensed section or sediment-starved shales in modern sediments, because the slow rate of sedimentation allows completion of chemical reactions (Schutter, 1998). O'Brien et al., (1990) suggest that phosphate nodules form within the anoxic zone in the sediments at depths of approximately 10-18cm below the sediment-seawater interface, based on studies of phosphate deposits on the East Australian continental margin.

The low sedimentation rates indicated for the argillite-chert caprock horizon, suggest that its deposition corresponded to a hiatus in the volcanic activity of the area. The chert horizon is similar in many ways to thin finely bedded siliceous sediment that are present above many VHMS systems. Examples include, the Main Contact Tuff in the Noranda

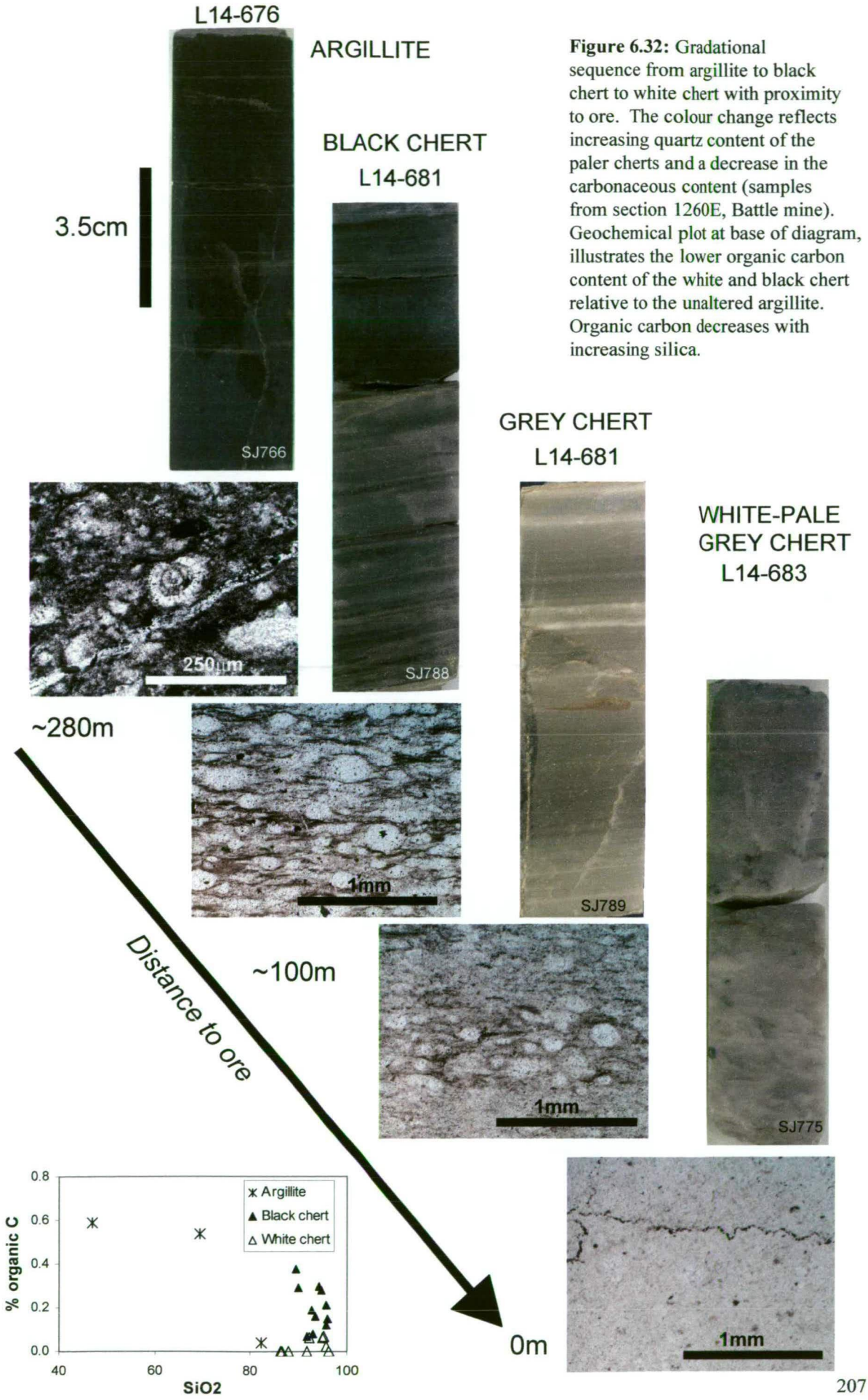

Figure 6.32: Gradational sequence from argillite to black chert to white chert with proximity to ore. The colour change reflects increasing quartz content of the paler cherts and a decrease in the carbonaceous content (samples from section 1260E, Battle mine). Geochemical plot at base of diagram, illustrates the lower organic carbon content of the white and black chert relative to the unaltered argillite. Organic carbon decreases with increasing silica.

district (Kalgeropoulos & Scott, 1989); tetsusukei in the Horoku system (Kalgeropoulous and Scott, 1983); and siliceous deposits around white smokers, (Hannington et al., 1998). These sedimentary deposits are thought to represent primary accumulation from siliceous exhalites, which could only form during times of slow sedimentation. However, not all global siliceous caprocks represent siliceous exhalites, instead, many are likely to be silicified sediments, which may or may not have an exhalative component. A detailed examination of petrological and geochemical features of the local caprocks is necessary to determine the nature of the siliceous sediments above VHMS deposits.

6.7.2 Battle deposit caprocks

The close spatial association between the chert and the underlying VHMS orebodies suggests a genetic link between the mineralising event and silicification in the Battle deposit. In the Battle basin, galena, sphalerite and chalcopyrite are mainly present in the silicified zones, proximal to ore and are not observed in the non-silicified Battle basin argillite.

Although the massive sulphides appear to crosscut the chert in places in the Battle mine, there is evidence that some ore deposition predated chert formation. Euhedral rutile and apatite, with fine sulphide inclusions, partially infill radiolarian tests, and occur within cavities of closely packed chalcedony spherules in phosphate nodules. These most likely represent early syn-depositional mineral growth in voids, prior to compaction. Rutile growth is thought to be indicative of temperatures greater than 180°C in geothermal systems (Reyes, 1990). Microprobe analyses indicate that the large euhedral apatites (type-2) occurring within radiolarian tests have higher S, Ba, Na and Sr contents than the fine apatites (type-1) which form the groundmass of the phosphate nodules (Appendix 6.1). This suggests that although they are similar in composition, the type-2 apatite, with the greater S and Ba contents, may have had a hydrothermal input, compared to the diagenetic apatite in the phosphate nodules. Apatite is also present in quartz-sulphide veins within the Battle orebody. Reyes, (1990) suggests that apatite growing in veins and vugs in geothermal systems, formed at temperatures ranging from 80 to 220°C. Adachi et al (1986) describes similar infilling of radiolarian tests, with barite, in fine siliceous metalliferous sediments in areas of hydrothermal activity in the northern Pacific. At Myra Falls, the syn-depositional minerals, some with sulphide inclusions, indicate that early moderately hot fluids percolated through the semi-consolidated sediments.

Radiolarian tests with rutile, apatite and sulphide infills are only found in fine sediments immediately above the Battle orebody. This includes the mudstone on the periphery of the

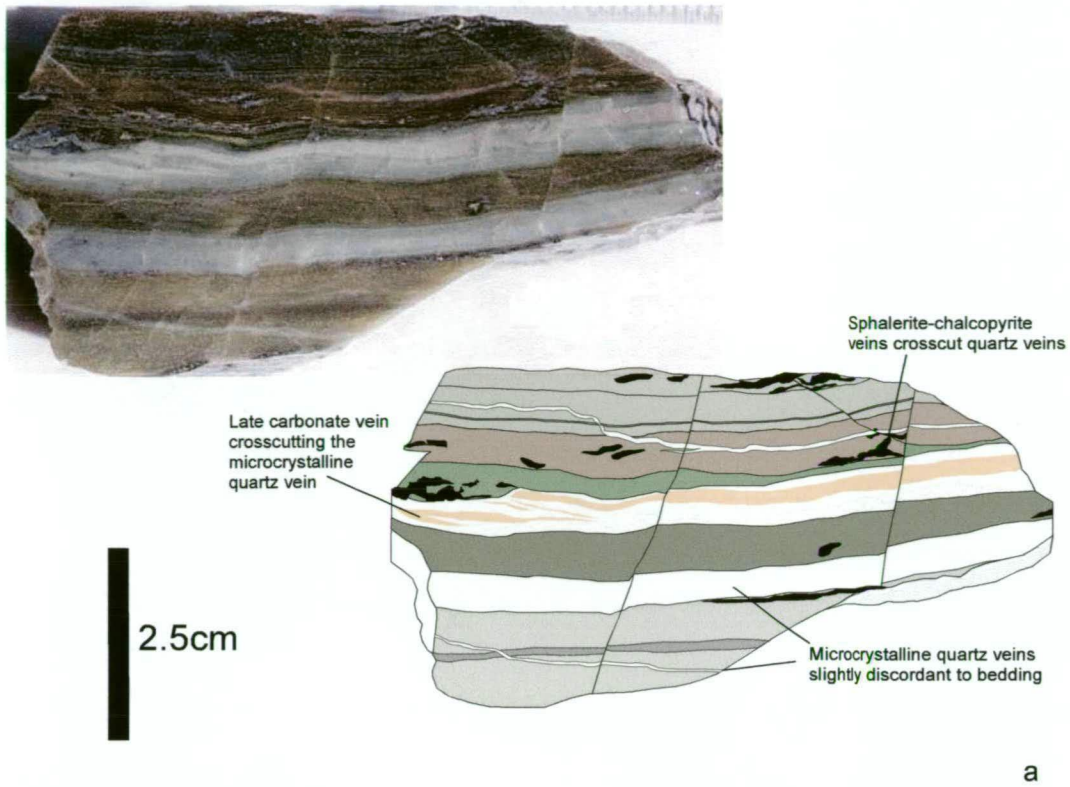

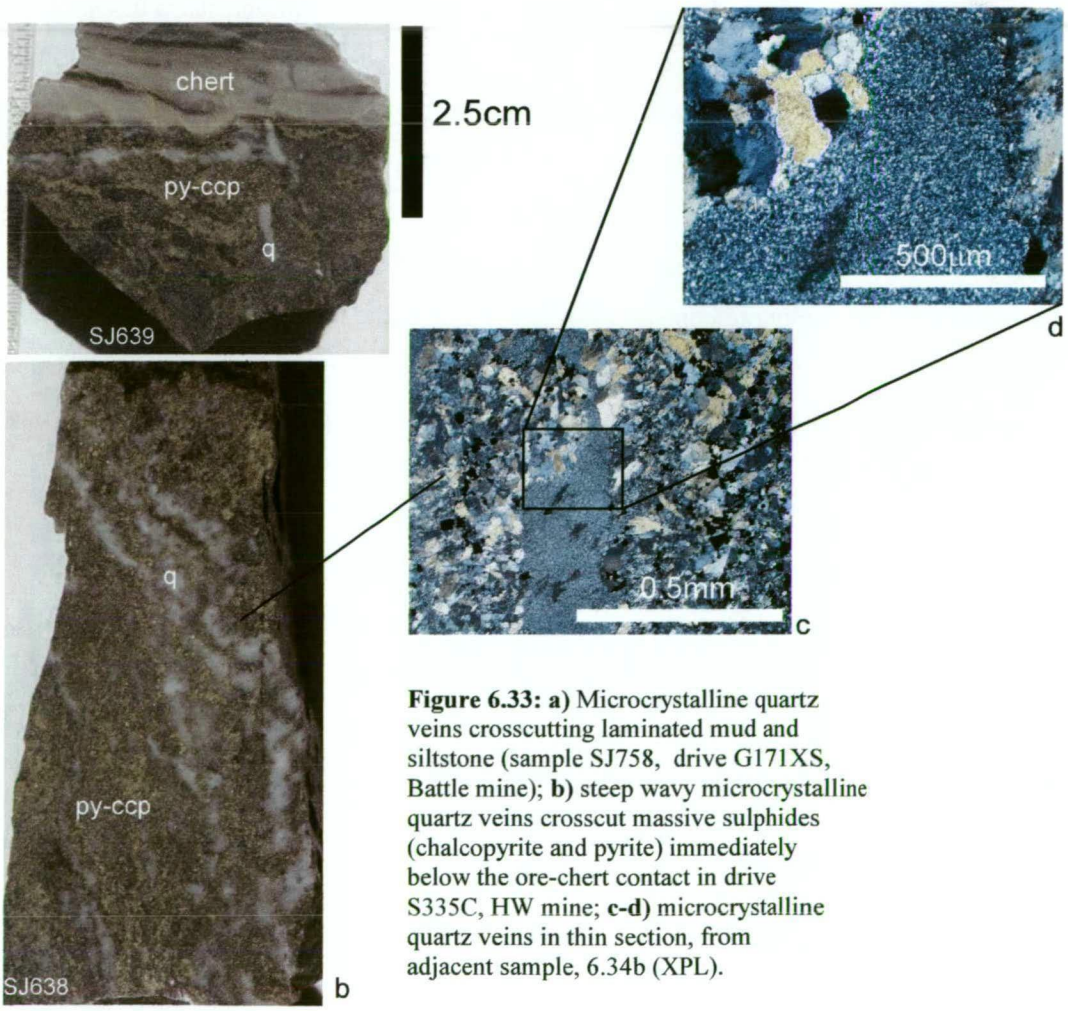

Figure 6.33: a) Microcrystalline quartz veins crosscutting laminated mud and siltstone (sample SJ758, drive G171XS, Battle mine); **b)** steep wavy microcrystalline quartz veins crosscut massive sulphides (chalcopyrite and pyrite) immediately below the ore-chert contact in drive S335C, HW mine; **c-d)** microcrystalline quartz veins in thin section, from adjacent sample, 6.34b (XPL).

chert, and throughout the chert overlying the ore horizon. Quartz is the only mineral present in radiolarian tests in fine-grained sediments away from the orebody. The silicification event, resulting in the formation of the chert horizon, may have post-dated early syn-depositional ore fluids, which were much more localised, or represented later silicification by cooler, more widespread fluids. Further evidence that at least some ore deposition predated silicification, is provided by primary textures in sulphide-rich muds overlain by a turbidite deposit, in the Battle mine, drive ST183A (Figure 6.29). The overlying sandstone turbidite scoured out a semi-consolidated sulphide-rich mudstone, which became entrained into the overlying clastic unit. These primary textures are well preserved because the area is located on the periphery of the chert, and was not greatly affected by silicification (evidenced by fresh feldspar grains). These features indicate that at least some deposition of sulphides occurred on the seafloor, possibly as an exhalative deposit (?). The occurrence of minor ore-clast breccias, near the base of the HW horizon, to the south of the Battle deposit provides evidence that at least parts of the Battle orebody were exposed on the seafloor.

Ore deposition continued after chert formation, with quartz-sulphide veins commonly crosscutting the chert. In many places, massive sulphides overprint the sharp basal depositional contact of the chert.

6.7.3 HW deposit caprocks

Only minor chert occurs above the HW orebody. Instead, the caprocks are dominated by strongly laminated argillite. Pyrite is the dominant sulphide in the argillite and there is a marked increase in the pyrite content immediately above the HW deposit. Framboidal pyrite has commonly grown within radiolarian tests, as an early diagenetic mineral, similar to pyrite infills described by Schieber (1998). Minor sphalerite, chalcopyrite and galena also occur in the argillite immediately above the ore horizon.

Chert formation is much more localised above the HW deposit, compared with the Battle chert, with only minor occurrences on the western and northern margins of the orebody. These locations coincide well with the position of growth structures identified in the paleoseafloor reconstruction in Chapter 5. As these zones of silicification, overprint the massive sulphides and argillite, they may represent the last stages of hydrothermal activity in the system.

The varying degree of silicification of the caprocks above the HW and Battle deposits, could reflect the timing of ore formation and the deposition of the caprocks. Markedly different mineral assemblages infill and replace radiolarian tests in the fine sediments above

the two deposits (quartz and pyrite in radiolarians above the HW orebody; quartz-rutile-apatite-sulphides in radiolarians above the Battle orebody).

In the HW mine there is good evidence for the deposition of argillite directly upon a sulphide mound. The orebody has an eroded top surface in many places, indicating that the ore was forming on or very close to the seafloor. These contact relationships imply that the argillite was deposited well after most of the sulphide mound had formed. The very localised nature of silicified argillite-chert horizons in the HW mine, and coincidence with growth structures, suggests that these may represent the last outflow zones of the hydrothermal system. The predominance of primary void-filling quartz and pyrite, compared with the syn-depositional minerals seen above the Battle deposit, could have reflected the lower temperatures of percolating fluids from a dying hydrothermal system.

In comparison, the fine sediments above the Battle deposit were much more strongly affected by hydrothermal fluids, with widespread silicification, and the presence of early void-filling minerals such as rutile and apatite with sulphide inclusions. These minerals were clearly deposited from syn-depositional hydrothermal fluids, indicating that formation of the Battle orebody was occurring during deposition of the fine-grained caprocks. The extensive silicification, overprinting these early textures, indicates that silica-rich hydrothermal fluids percolated through the sediments after deposition of the caprocks. However, silicification occurred early in the depositional history, evidenced by the presence of chert rip-up clasts in the overlying coarse-grained units and ubiquitous microstylolites throughout the chert. Ore formation clearly continued long after chert formation, as massive sulphides crosscut the chert, and stacked ore lenses are present above the chert (see section 1420E, Figure 6.5).

6.8 Summary and conclusions

The following points summarise the results of Chapter 6:

- The caprocks at Myra Falls can be separated into three types, chert, black chert and argillite. The chert is most commonly developed above the Battle mine with only localised occurrences above the HW mine. Instead, the HW orebody is overlain by, thick argillite deposits. Black chert occurs to the south of the Battle orebody, with a gradual transition into the white-pale grey chert above the orebody;

- The chert consists of three types of quartz, microquartz, megaquartz and chalcedony with no low-ordered forms of silica, such as opal-CT observed;

- Petrological features indicate that the chert above the Battle deposit formed mainly from the silicification of pre-existing fine-grained sediments;

- The dominant source of silica was most likely hydrothermal emanations from volcanic vents and the breakdown of volcanic glass, with a minor contribution from the dissolution of radiolarian tests;

- The silicification event above the Battle orebody overprints early syn-depositional features, such as primary pore-space infills of silica, rutile, apatite and minor sulphides. The syn-depositional infills, and the presence of minor ore-clast breccias above the orebody indicate that although the Battle deposit formed largely by sub-seafloor replacement, at least parts of the orebody were very close to, or exposed on the seafloor;

- The chert, which occurs in small localised zones above the HW orebody, represents post-depositional silicification of argillite, probably during the waning stages of hydrothermal activity. The erosional top contact of the HW orebody and the occurrence of argillite immediately overlying the orebody, are consistent with the HW orebody forming on the seafloor; and

- A deep, quiet depositional environment, at least below storm wave base, is estimated for the caprocks, based on sedimentological features such as fine parallel laminations, interbedded sandstone turbidites, and the presence of radiolarian fossils.

Chapter 7
SWIR spectral characteristics of the HW Horizon

7.1 Introduction

The alteration mineral assemblage at Myra Falls is relatively simple, consisting of white mica, quartz, pyrite, carbonate and minor chlorite in felsic lithologies, with white mica, chlorite, pyrite, carbonate, epidote and minor quartz in the mafic lithologies. The mineral assemblages reflect the regional metamorphism (lower to mid greenschist facies) and local hydrothermal alteration associated with VHMS orebodies. Alteration textures and mineralogy have been described in detail by Juras (1987) and Sinclair (2000). This study, provides a brief summary of the alteration mineralogy and emphasises the construction of property-scale alteration maps of the HW Horizon.

The simplicity of the alteration suite and the dominance of white mica, has made alteration mapping at Myra Falls very difficult, as mineral isograds are absent or only weakly developed. However, SWIR (Short-Wavelength Infrared) spectral analysis can be used to measure subtle compositional variations within individual hydrous mineral species, such as chlorite and white mica. Recent studies, based on SWIR analyses in VHMS districts, show that the composition of these minerals can vary systematically with proximity to ore (e.g., Pontual et al., 1997b; Huston et al., 1999; Thompson et al., 1999; Herrmann et al., 2001). Alteration maps, based on subtle compositional variations, can then be constructed, even in fine-grained rocks. However, metamorphic and structural effects must also be considered to properly understand the alteration system.

This study presents property-scale alteration maps, based on subtle compositional variations in white mica and chlorite, from SWIR analyses, in combination with probe analyses, detailed drillcore logging and mapping. The main aims of this study are:

1. Determine SWIR spectral characteristics and variations of white mica and chlorite in background and proximal areas and in different lithologies, to identify the controls on white mica and chlorite compositions.

2. Use microprobe analyses to test compositional variation indicated by SWIR analyses.
3. Locate and determine the size and intensity of alteration halos associated with VHMS orebodies.
4. Identify any systematic trends in mineral compositions, and if present, establish whether they can be used as vectors to target VHMS ore horizons.

7.2 Methods

In this study, the majority of samples were collected from the HW Horizon, with only a few selected from Price Andesite and the overlying Mixed Volcaniclastic unit. Rock samples were analysed by the PIMA-II spectrometer (Portable Infrared Mineral Analyser), and PIMA VIEW 3.1 software, which measured the infrared (1300-2500nm wavelengths) radiation reflected from illuminated samples. Hydrous minerals such as clays, white mica, chlorite and epidote have characteristic absorption features. Spectral parameters such as the wavelength and depth of absorption features, were calculated from hull quotient-corrected spectra by 'the Spectral Geologist 2.0' software and The Spectral Assistant (TSA) (Pontual et al., 1997a; Merry and Pontual, 1998). This software also identified the minerals present, by comparing the wavelengths of absorption features (absorbed from the reflected light), to a reference library. Minerals identified by SWIR, were generally consistent with the mineral assemblage observed by detailed petrographic studies, microprobe and XRD analyses.

Sample preparation for the PIMA-II spectrometer was minimal, with SWIR readings taken on clean, flat (sawn) surfaces of dry rock or drillcore. Rock samples were predominantly pale, with few opaque minerals, such as magnetite, to suppress spectral features. However, dark-grey to black argillite samples were too dark to give reasonable spectra. The relatively simple mineralogy and absence of clays, such as kaolinite, aided the identification of minerals, and absorbtion features in the AlOH band were clean and clearly visible.

White micas and chlorite from selected samples were analysed by the author on the Cameca SX-50 electron microprobe at the Central Science Laboratory, University of Tasmania. Mineral formulae were calculated on the basis of 22 oxygens for white mica and 28 oxygens for chlorite and microprobe analyses are listed in Appendix 6.2.

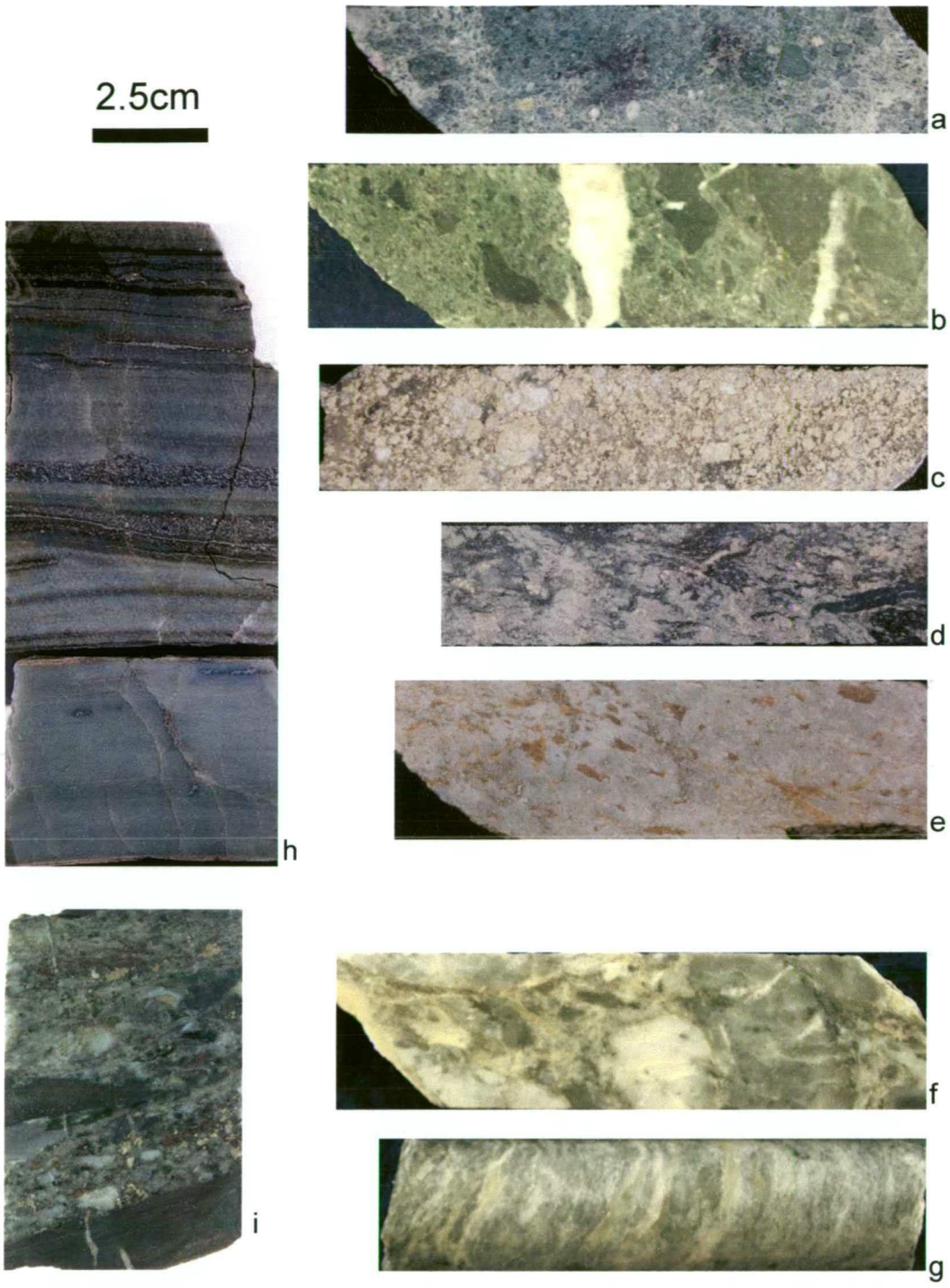

Figure 7.1: Typical alteration textures in rhyolitic and andesitic rocks at Myra Falls; **a)** chlorite-epidote altered Hangingwall Andesite (SJ740, drillhole 21-2072, 105.6m); **b)** chlorite altered Hangingwall Andesite (SJ545, drillhole 20-845, 11.3m); **c)** sericite-pyrite altered Price Andesite (SJ409, drillhole 18-1003, 103m); **d)** chlorite-sericite-pyrite altered Price Andesite (SJ447, drillhole 18-1004, 95.6m); **e)** quartz-pyrite-sericite altered Price Andesite (SJ778, drillhole L14-683, 427.6m); **f)** weakly sericite-quartz altered HW rhyolitic volcaniclastic rock (SJ782, drillhole L14-681, 345.2m); **g)** strongly sericite altered HW rhyolite volcaniclastic rock (SJ113, drillhole 18-1033, 56.5m); **h)** sericite-rich green chert/siltstone (SJ754, G171XS, Battle mine); **i)** weak sericite altered conglomerate and argillite (SJ261, drillhole PR124, 135m).

7.3 Alteration mineralogy

The alteration mineral assemblage for the volcano-sedimentary sequence at Myra Falls is shown in Table 3.2 from (Juras, 1987). The alteration mineral assemblages vary with changes in the bulk rock composition (i.e.,, mafic or felsic) and the intensity of hydrothermal alteration, reflecting fluid/rock ratios. A detailed description of alteration minerals and textures, is given by Juras (1987) and Sinclair (2000), and a brief summary of these studies is outlined below.

The most common alteration minerals are white mica, quartz, pyrite, chlorite, epidote and carbonate. Chlorite is common in mafic rocks of the volcano-sedimentary sequence, but is rare in rhyolitic units, such as the HW horizon (Figure 7.1a-b). White mica (or sericite) is present in all rock types across the property, but dominates over chlorite in felsic rocks and in the strongly quartz-sericite and quartz-sericite-pyrite altered zones around the Battle and HW deposits. In these areas, white mica, quartz and pyrite often overprint and obscure original features of the rock such as bedding and clast boundaries (Figures 7.1c-g). Figure 7.1h shows silt-chert layers immediately above the ore, which commonly have a distinct green appearance resulting from abundant white mica with higher Fe and/or V contents (see Table 7.2, and Appendix 6.2). Microprobe analyses indicate that Fe and V contents not high enough to be celadonite or roscoelite respectively, as maximum Fe and V values are significantly lower than 1 wt.% (Wells and Brannock, 1946; Ernst, 1963; Velde, 1965; Miyashiro and Shido, 1985).

In areas not affected by the strong sericite alteration, clast boundaries are distinct in volcaniclastic rocks (Figures 7.1a-b, i), and crystal boundaries are sharp in quartz and feldspar porphyries (Figures 7.2a, d). Epidote is only present in the mafic units of the sequence and is absent in the strongly altered zones proximal to ore. Figure 7.2e, shows strong epidote-chlorite alteration of dacite in the 43 Block area of the HW mine. Carbonate has a very sporadic distribution but appears to be most common in the strongly altered zone around the Battle deposit, with dolomite-calcite rhombs commonly up to 1-2mm, giving the rocks a slightly spotted appearance (Sinclair, 2000). Calcite is common in background samples, predominantly occurring in fine veins, and is also common as irregular patches in the groundmass of andesitic units.

Typical petrologic features of the strongly quartz-sericite-pyrite altered rocks in zones near to the Battle and HW orebodies are shown in Figures 7.3a-f. Sericite dominates and the rocks are often moderately to strongly foliated, with sheared and fragmented lithic clasts

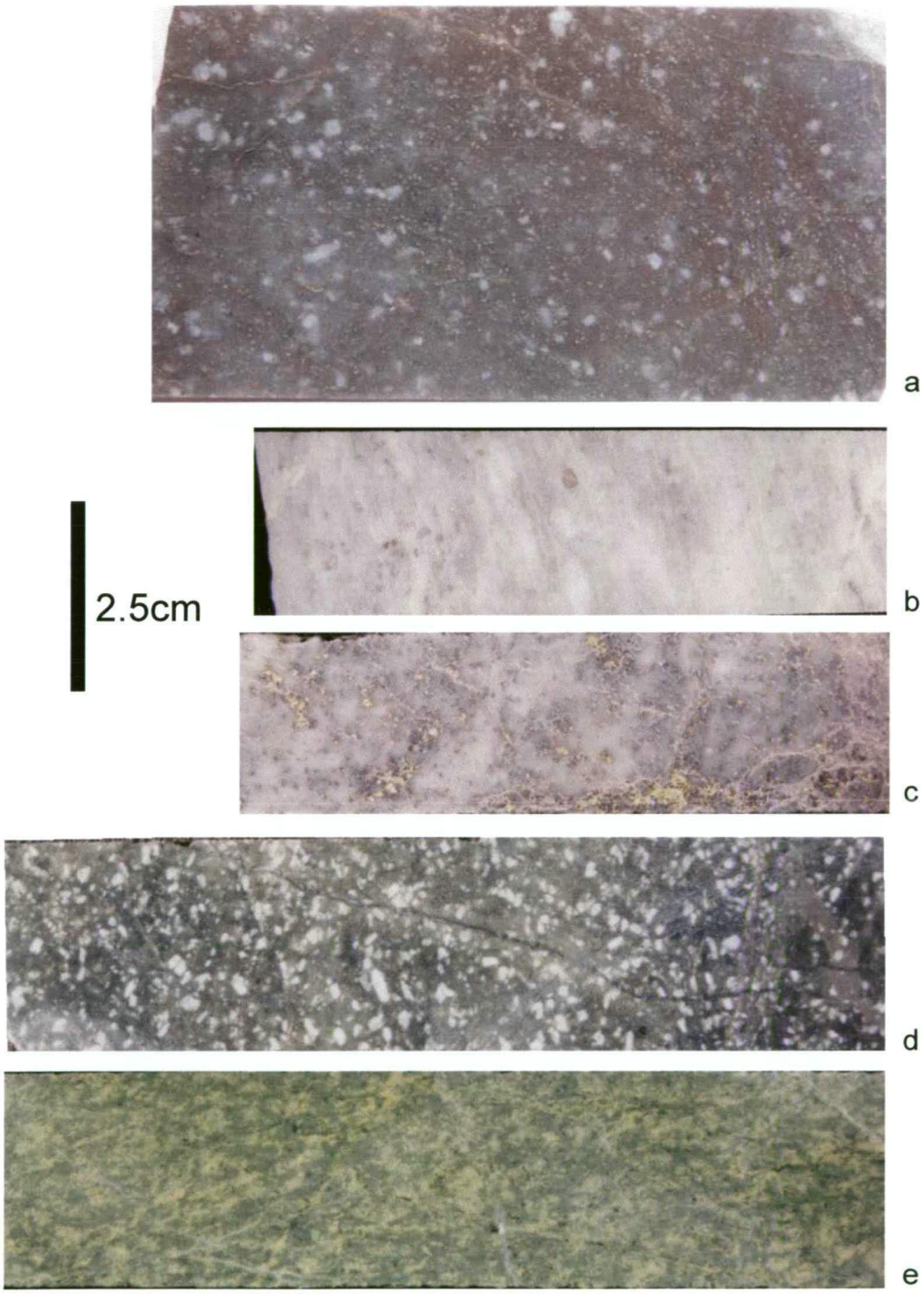

Figure 7.2: Typical alteration textures in quartz-feldspar and feldspar porphyry rocks at Myra Falls; **a)** weakly quartz-sericite altered feldspar-quartz porphyry (SJ588, drillhole L15-501, 365m, Marshall Zone); **b)** strongly silicified quartz-feldspar porphyry (SJ696, drillhole 18-976, 24m, Battle mine); **c)** sphalerite-chalcopyrite stringer veins in sericite-altered quartz-feldspar porphyry (SJ427, drillhole 18-1004, 14.6m, Battle mine); **d)** weakly sericite altered feldspar porphyry (SJ796, drillhole P13-304, 407m, HW mine); **e)** strongly chlorite-epidote altered dacite (SJ550, drillhole 20-845, 43 Block).

scattered in a strongly aligned matrix of sericite and quartz (Figure 7c-f). Fine pyrite is ubiquitous and feldspar grains are rare, usually occurring as relict feldspar cores in a sericite pseudomorph (Figure 7a-b). In comparison, weakly altered rocks in Figures 7.4a-h, from areas distal to ore, have a markedly different appearance. Feldspar grains are albitised and only weakly sericite altered, and original textures, such as igneous quartz crystals with lobate margins, and tube pumice clasts are clearly visible (Figures 7.c-d). These features are completely obscured or destroyed in strongly quartz-sericite altered zones, proximal to ore.

7.4 White mica and chlorite compositional and spectral characteristics

7.4.1 White mica compositional variation

White micas are a very common alteration mineral in VHMS systems and their complex chemical structure allows for a wide range of compositions. White micas can be expressed as:

$$(K, Na)^{it}_2(Al, Fe, Mg)^{vi}_4(Si, Al)^{iv}_8O_{20}(OH)_4$$

where it, iv and vi represent the interlayer, tetrahedral and octahedral sites respectively (Yang, 1998).

Na-rich micas, or paragonite, result from Na substitution for K in the interlayer site. Minor Ca can also occur in the interlayer site. In low to moderate temperature hydrothermal systems (<600°C), K-rich micas dominate because of the limited substitution between K and Na at relatively low temperatures. The limited substitution results in a wide miscibility gap between the Na and K-rich white micas (Eugster & Yoder, 1955; Guidotti et al., 1994). Although not as common as K-white micas, paragonite is reported in VHMS districts and geothermal systems, and is often present in zones proximal to ore (Pontual et al., 1997b; Herrmann et al., 2001).

Compositional variation in white micas is predominantly a result of the Tschermak substitution, a coupled substitution of Mg and/or Fe for Al in the octahedral site and Si for Al in the tetrahedral site:

$$Si^{iv}(Mg,Fe)^{vi} = Al^{iv}\ Al^{vi}.$$

The Tschermak substitution results in phengite, with a Si:Al ratio >3:1 and elevated Fe and/or Mg contents. The substitution results in a range of phengitic mica compositions from endmember muscovite, $K_2Al_4(Si_6Al_2)O_{20}(OH)_4$ to endmember celadonite, $K_2(Mg,Fe^{2+})_2(Al,Fe^{3+})_2Si_8O_{20}(OH)_4$. However, complete solid solutions do not form between all endmembers, instead there are miscibility gaps (Velde, 1965).

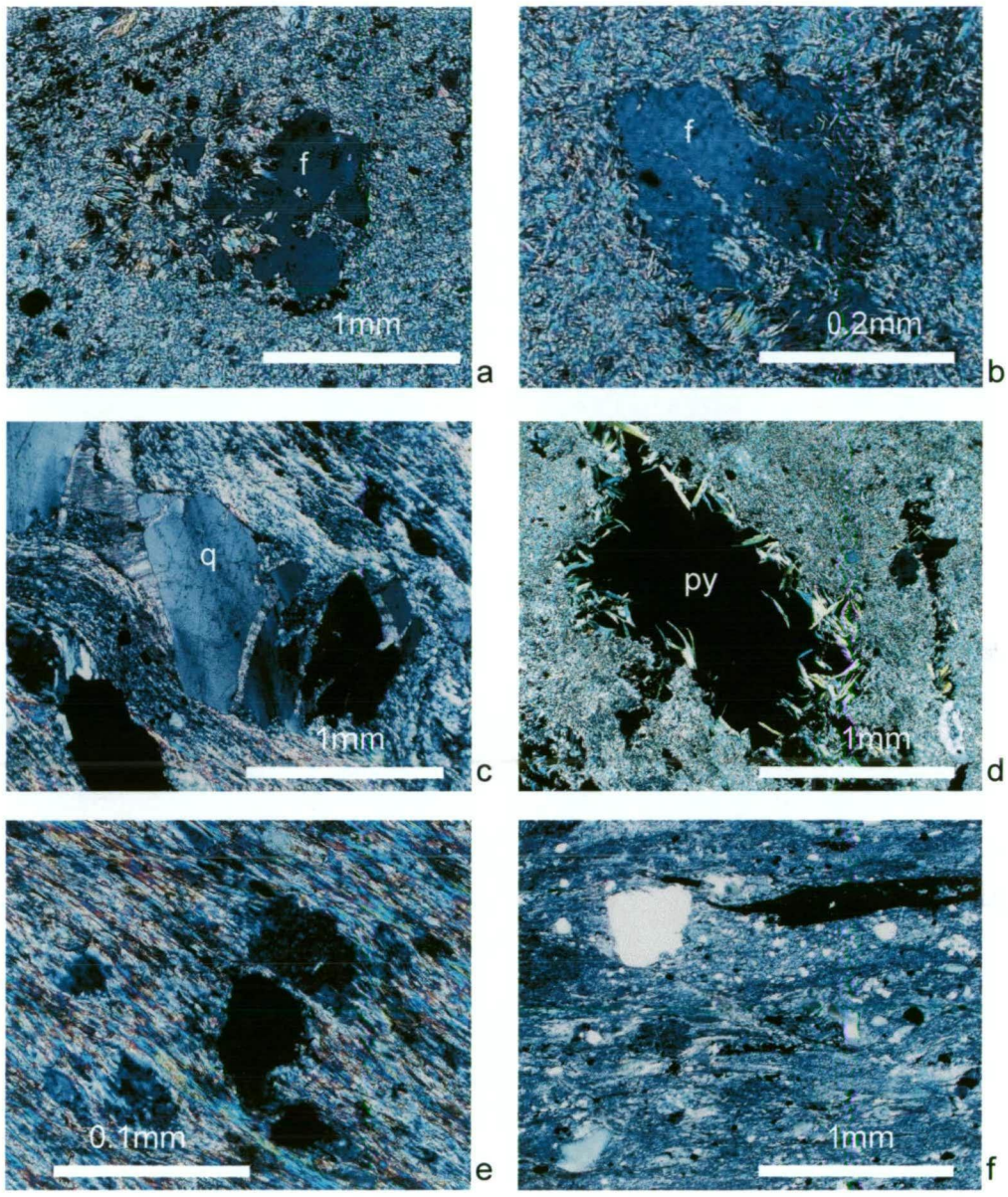

Figure 7.3: Typical strong alteration textures in samples proximal to ore at Myra Falls; **a)** strongly sericite altered feldspar in a sericite-rich groundmass, XPL (SJ92, S335A-D6, HW mine); **b)** relict feldspar with strong sericite alteration, XPL (SJ55, S335A-D6, HW mine); **c)** strong sericite altered and foliated matrix with detrital quartz grain, XPL (SJ90, S335A-D6, HW mine); **d)** sericite altered pyrite grain, XPL (SJ760, G171XS, Battle mine); **e)** strongly sericite altered matrix in rhyolitic volcaniclastic rock, XPL (SJ90, S335A-D6, HW mine); **f)** strong sericite alteration in rhyolitic volcaniclastic rock, XPL (SJ92, S335A-D6, HW mine).

Phengites are always K-rich micas, due to the reluctance of natural Na-white micas to accommodate a greater amount of Si than the ideal 6 atoms per formula unit (Yang, 1998). For this reason, there is an inverse correlation between the Na and Tschermak content $(Mg,Fe^{2+})Si^{iv}$. Other elements, which commonly substitute for Mg-Fe in the octahedral site, include V, Mn, Cr and Ti.

Another important variation in K-white micas, especially at low temperatures, is the formation of illite, by the substitution of Si^{iv} ^{it} for $Al^{iv}K^{it}$, where ^{it} represents an interlayer cation vacancy (Cathelineau, 1988; Yang, 1998). The illite substitution results in the interlayer cation number becoming < 2 p.f.u. With increasing temperature this substitution becomes less important and is thought to cease at about ≥ 300°C (Cathelineau, 1988).

7.4.2 White mica spectral characteristics

White micas have a number of absorption features, with a deep, sharp AlOH absorption feature occurring between 2180-2228nm, and moderate secondary AlOH features near 2344nm and 2440nm. The main AlOH peak (2180-2228nm) is commonly evident even in noisy spectra, making it a useful feature for mineral identification.

The shifts in the wavelengths of the AlOH feature, have been shown to be related to subtle changes in white mica compositions, with varying proportions of octahedral Al in the mineral structure, resulting in AlOH wavelength shifts. For example, AlOH wavelengths <2195nm result from high proportions of octahedral Al (and a low Fe-Mg content), while AlOH wavelengths >2216nm reflect low proportions of octahedral Al (and higher Fe-Mg content). Generally, paragonite has AlOH wavelengths 2180-2195nm; phengite has AlOH wavelengths 2216-2228nm; and muscovite/illite (normal potassic micas) have AlOH wavelengths between 2200-2208nm (Post & Noble, 1993; Hermann et al., 2001). Samples with more than one white mica phase, or intermediate white mica compositions, result in intermediate AlOH wavelengths.

7.4.3 Chlorite compositional variation

Chlorite is a very common mineral in VHMS systems, and in low to moderate grade metamorphic rocks formed at temperatures up to about 400°C and a few kilobars pressure (Deer et al., 1996). Chlorite often replaces primary mafic minerals in hydrothermal systems

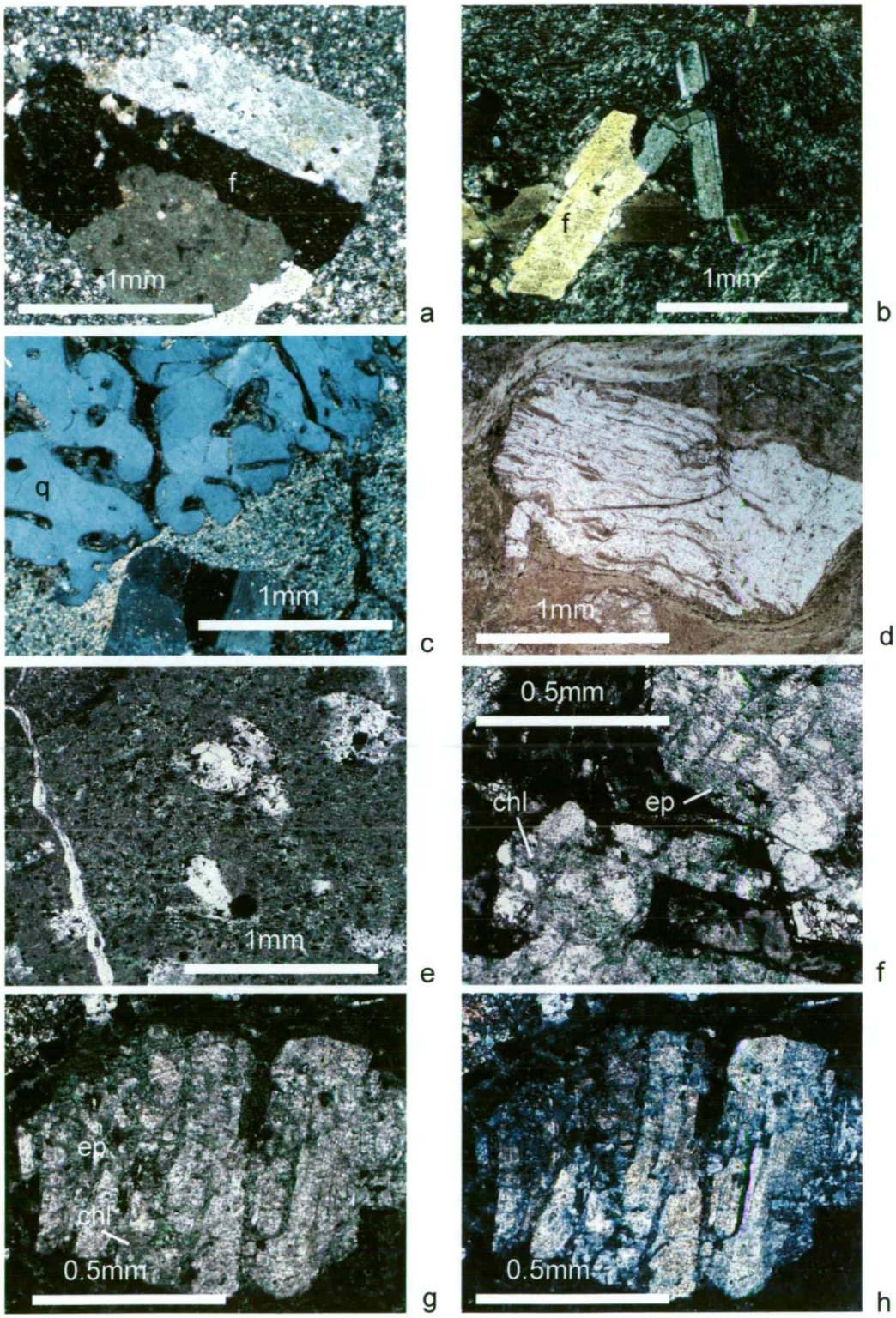

Figure 7.4: Typical weak alteration textures in background mafic and felsic rocks at Myra Falls; **a)** weak sericite alteration with relatively fresh feldspars in quartz-feldspar porhphry, XPL (SJ792, drillhole L14-683, 329.5m); **b)** fresh plagioclase in dacite, Price-Thelwood area, XPL (SJ620, drillhole PR13-68, 30.4m); **c)** well preserved primary volcanic texture, with embayed quartz, QFP, XPL (SJ792, drillhole L14-683, 329.5m); **d)** well preserved flow banded rhyolite clast in Thelwood Valley area, PPL (SJ629, drillhole CR88-4, 551.7m); **e-h)** chlorite (chl)-epidote (ep) rich Hangingwall Andesite, 43 Block area, XPL (SJ558A, drillhole 20-675, 5.9m).

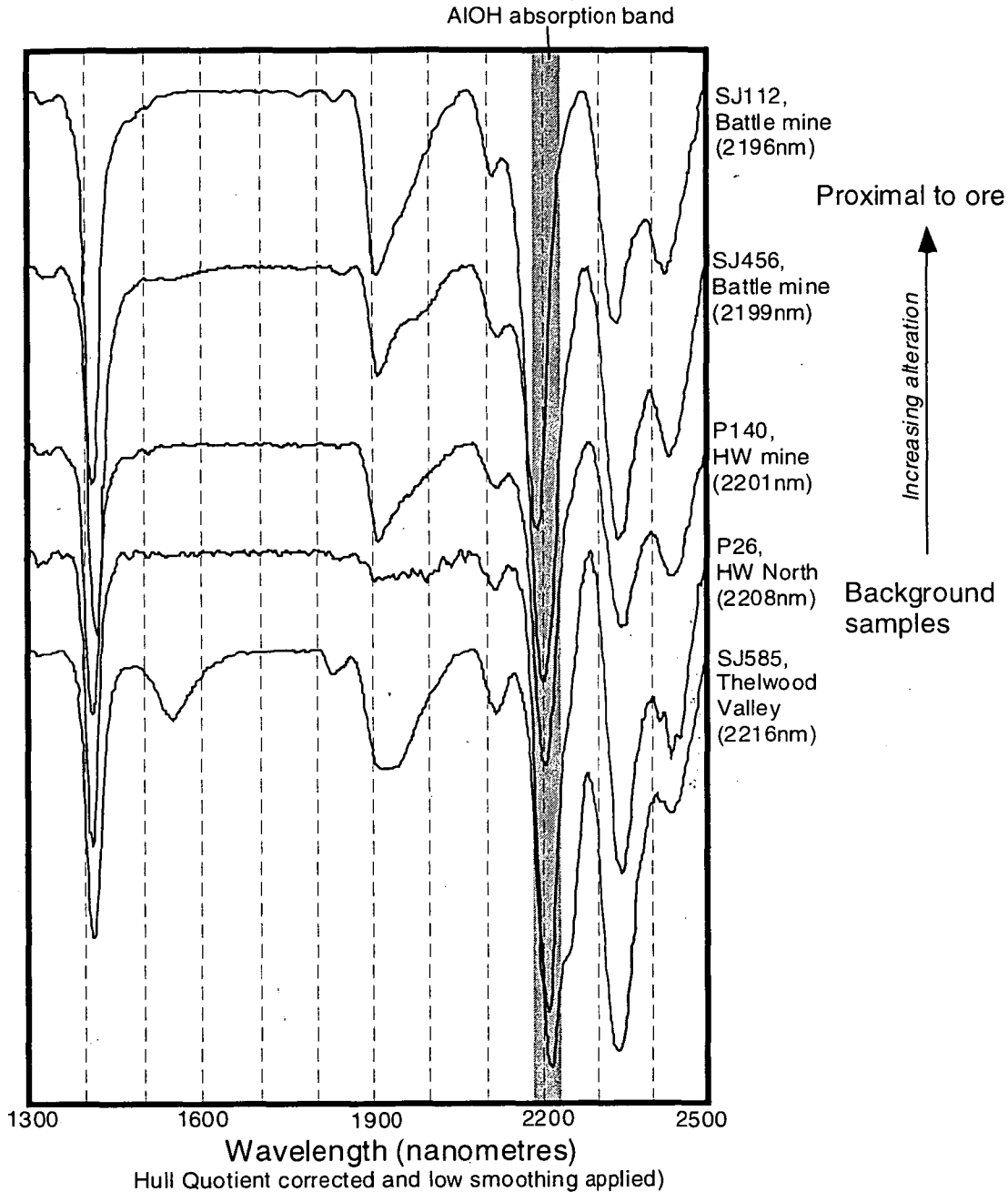

Figure 7.5: Typical SWIR spectra, illustrating the range of AlOH wavelength values of white mica in regional samples and samples proximal to ore, Myra Falls VHMS camp.

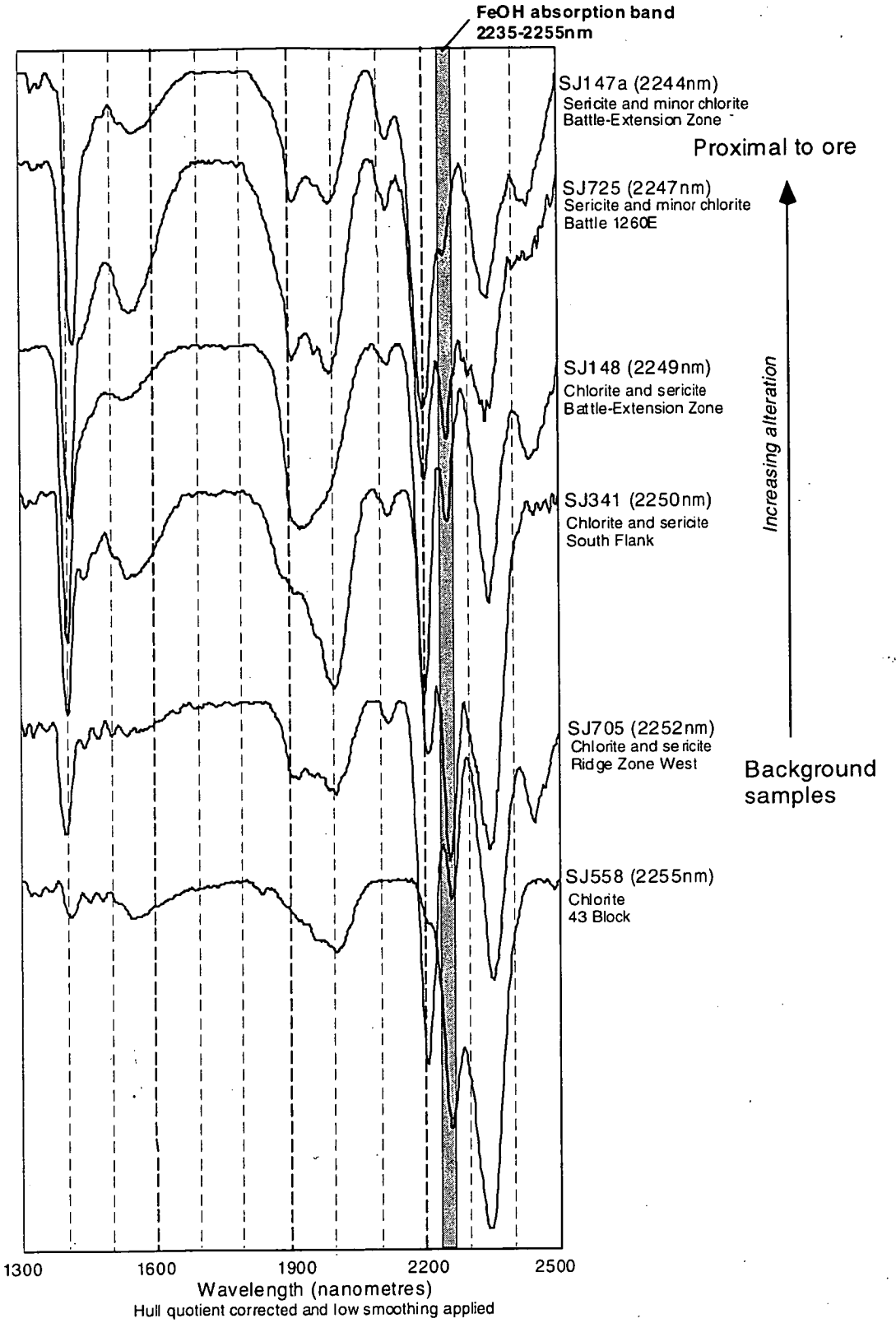

Figure 7.6: Typical SWIR spectra, illustrating the range of FeOH wavelength values of chlorite in regional samples and samples proximal to ore, Myra Falls VHMS camp.

and a wide variety of chlorite compositions can occur due to the large number of substitutions. Chlorite can be expressed as:

$$(Mg,Fe^{2+},Fe^{3+},Mn,Al)_{12}[(Si,Al)_8O_{20}](OH)_{16}$$

The main varieties of chlorite include, clinochlore, chamosite and pennantite as the names for Mg-rich, Fe-rich and Mn-rich chlorites respectively (Deer, et al., 1996). The structure of the common chlorites consists of regularly alternating negatively charged talc-like layers comprising tetrahedral-octahedral-tetrahedral, 2:1, layers with $Y_6Z_8O_{20}(OH)_4$; and positively charged interlayer brucite-like layers with composition $Y_6(OH)_{12}$, (Y and Z represent octahedral and tetrahedral sites respectively).

The Mg↔Fe substitution results in a very wide range of compositions and most chlorites can be approximately expressed as combinations of the chlinochlore $(Mg_{10}Al_2)(Si_6Al_2O_{20})(OH)_{16}$, and chamosite $(Fe^{2+}{}_{10}Al_2)(Si_6Al_2O_{20})(OH)_{16}$ end-members. Other types of chlorite include Mn, Cr, Ni, Li and Zn-rich varieties.

7.4.4 Chlorite spectral characteristics

The two main diagnostic spectral features of chlorite occur between 2235-2255nm, associated with FeOH absorption, and 2320-2360nm, associated MgOH absorption. The wavelengths of these absorption features vary with chlorite composition, with the shortest wavelengths occurring in the most Mg-rich chlorites and the longest wavelengths occuring in more Fe-rich chlorites (Pontual et al., 1997b).

Systematic variations in chlorite compositions with proximity to ore have been reported in a number of studies (e.g., Pontual et al., 1997b; Herrmann et al., 2001). In these cases, the chlorite became more Mg-rich towards the ore, and these subtle compositional changes were shown by distinct shifts in the FeOH and MgOH wavelengths. These absorption features can also be used to discriminate metamorphic/regional chlorite from hydrothermal chlorite, as the regional chlorites are often relatively more Fe-rich than hydrothermal chlorites.

Although chlorite absorption features are easily recognisable, in many samples where white mica dominates over chlorite, the chlorite MgOH peak is often masked by a white mica absorption feature at 2340nm. For this reason, estimates of chlorite compositions in this study are predominantly based on the FeOH wavelengths.

7.5 Previous work (SWIR analysis)

Sinclair (2000) used SWIR analysis to identify the dominant alteration minerals and compositional variation in white mica and chlorite in rocks from the Battle deposit. The mineral assemblages identified by SWIR in felsic rocks, comprised white mica and minor chlorite and carbonate. Strongly sericite-quartz altered mafic rocks, comprised white mica, chlorite and carbonate; and weakly altered mafic rocks contained chlorite, white mica, epidote, and carbonate.

White mica AlOH wavelengths were between 2196 to 2215nm, with interpreted compositions ranging from muscovite to phengite. Chlorite compositions were interpreted to range from Mg-rich chlorite, intermediate chlorite, to Fe-rich chlorite. FeOH wavelengths were measured between 2244 to 2255nm and MgOH wavelengths between 2339 to 2352nm.

White mica and chlorite spectral characteristics from strongly altered rocks in the Battle mine were compared with several regional samples to determine the presence of any systematic variation with proximity to ore. A shift in the chlorite and white mica absortion wavelengths was detected, which suggested phengitic white mica and Fe-chlorite occurring in the background samples, and muscovite and Mg-rich chlorite in proximal samples.

7.6 Results of SWIR analysis

This study extends the alteration study carried out by Sinclair (2000), by providing analyses of over 1000 samples across the property, and characterising the alteration mineralogy associated with the Battle and HW orebodies. Initially, the bulk rock control on alteration mineralogy is examined. The background white mica and chlorite spectral features are then defined and compared to spectral characteristics of minerals in zones, proximal to ore. In general, SWIR spectra were of good quality and the relatively simple mineralogy, dominated by white mica and chlorite, resulted in easily recognisable absorption features.

7.6.1 White mica and chlorite spectral variation

Typical SWIR spectra collected for white mica and chlorite are shown in Figures 7.5 and 7.6, and illustrate the shifting AlOH and FeOH wavelengths with subtle changes in mineral composition. A wide range of compositions were recorded for white mica and chlorite, with the AlOH feature for white mica, ranging from 2194-2218nm, suggesting a range in compositions from paragonite, muscovite to phengitic micas. The chlorite FeOH absorption feature also displayed a range of wavelengths, from 2238-2255nm, indicating compositions from Mg-rich, intermediate to Fe-rich chlorites (Table 7.1).

Formation and location	Mineral assemblage	White mica AlOH wavelengths	Chlorite FeOH wavelengths
Price Andesite (proximal to ore)	Quartz, muscovite, Mg-Int chlorite, pyrite, carbonate	2196-2218nm average: 2201nm	2238-2254nm average: 2246nm
Price Andesite (regional samples)	Int-Fe chlorite, epidote, muscovite-phengite, minor carbonate, sericite, quartz	2198-2218nm average: 2204nm	2236-2252nm average 2246nm
HW horizon rhyolite (Battle orebody)	Quartz, paragonite-muscovite, pyrite, minor Mg-Int chlorite and carbonate	2194-2204nm average: 2198nm	2238-2252nm average: 2241nm
HW horizon rhyolite (HW orebody)	Quartz, muscovite, pyrite, minor Mg-Int chlorite and carbonate	2196-2214nm average: 2201nm	2238-2254nm average: 2246nm
HW horizon rhyolite (regional samples)	Quartz, muscovite-phengite, pyrite, minor Mg-Int chlorite and carbonate	2194-2218nm average: 2206nm	2238-2255nm average: 2247nm
Hangingwall andesitic rocks (Battle orebody)	Int-Fe chlorite, epidote, muscovite-phengite and carbonate	2204-2218nm average: 2207nm	2242-2253nm average 2250nm
Hangingwall andesitic rocks (regional samples)	Int-Fe Chlorite, epidote, muscovite-phengite and carbonate	2203-2217nm average: 2210nm	2238-2253nm average: 2250nm

Table 7.1: White mica and chlorite AlOH and FeOH wavelength variations. Mg-Int = Intermediate to Mg-rich chlorite, Fe-Int = Intermediate to Fe-rich chlorite.

The histograms in Figures 7.7 and 7.8, show the full range of AlOH and FeOH wavelengths measured, and illustrate the differences in AlOH and FeOH wavelengths for white mica and chlorite in felsic and mafic samples. In general, white mica AlOH and chlorite FeOH wavelengths appear to be longer in the more mafic lithologies. The histograms also illustrate the marked difference in AlOH and FeOH wavelengths in samples from areas proximal to ore, to distal or background samples. For example, AlOH wavelengths measured in HW horizon rhyolite samples from the Battle mine, have an extremely narrow range of values (most within 2196-2200nm). In comparison, background samples, have a much broader range of AlOH wavelengths, with the majority between 2198-2216nm.

The histograms suggest that white mica and chlorite compositions are influenced by, the bulk rock composition and/or the proximity to ore. Changes in mineral compositions probably reflect varying water/rock ratios. Background samples are rock buffered (low fluid/rock ratios, while samples, proximal to ore, are fluid buffered (high fluid/rock ratios).

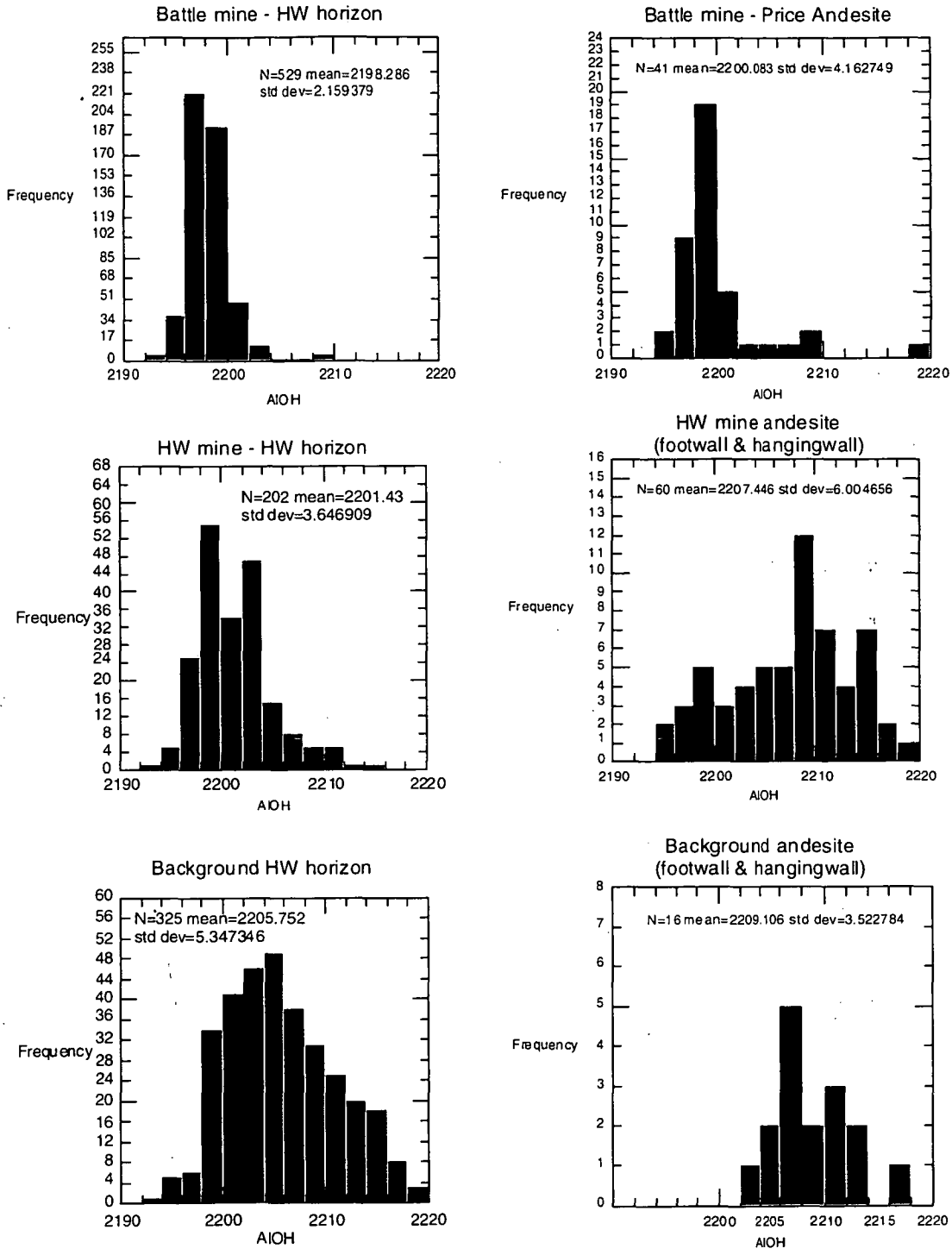

Figure 7.7: Histograms illustrating the variation in AlOH wavelengths of white micas in proximal and background samples in the HW Horizon rhyolitic units, Price Andesite and Hangingwall Andesite.

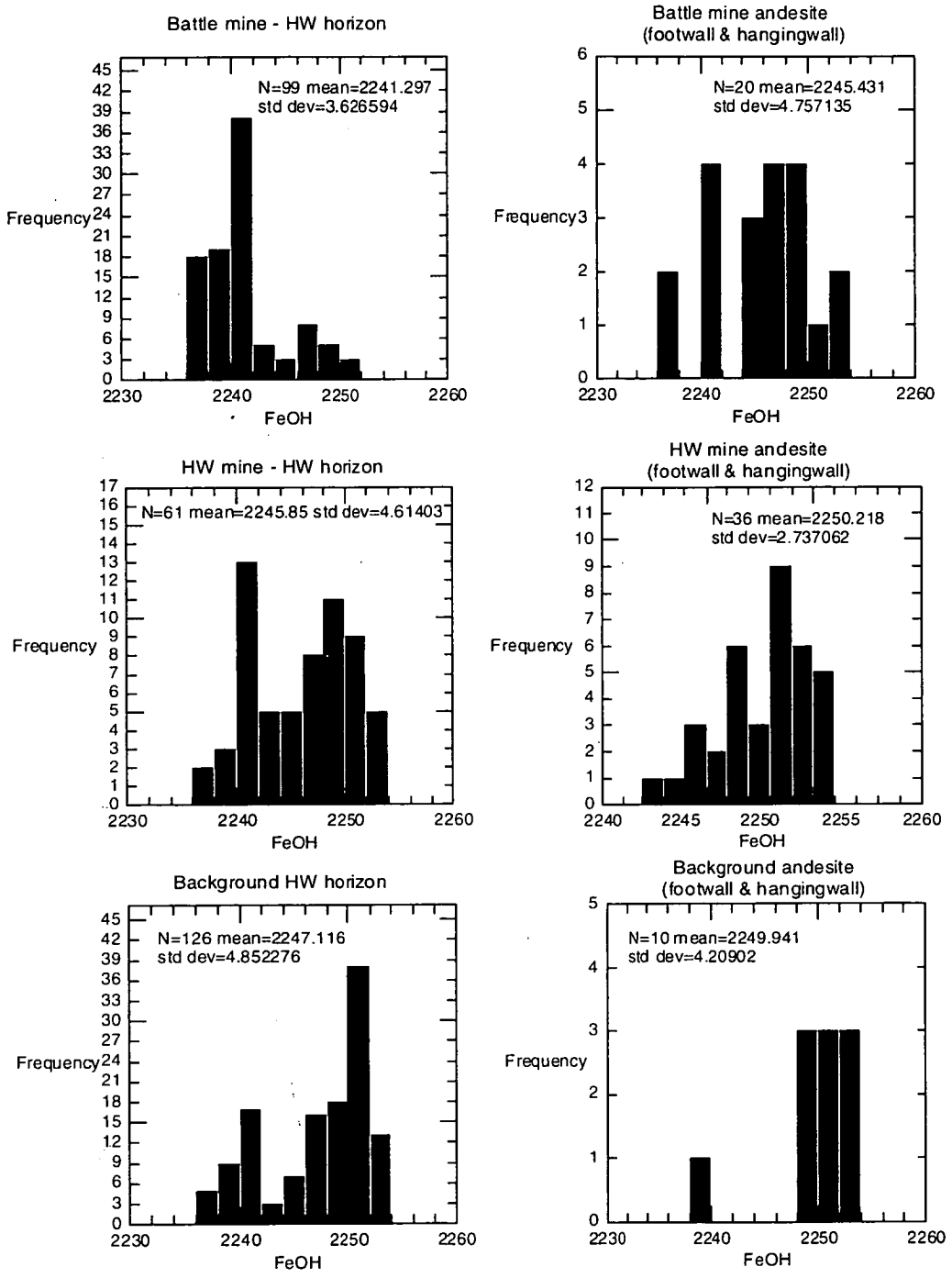

Figure 7.8: Histograms illustrating the variation in FeOH wavelengths of chlorite in proximal and background samples in the HW Horizon rhyolitic units, Price Andesite and Hangingwall Andesite.

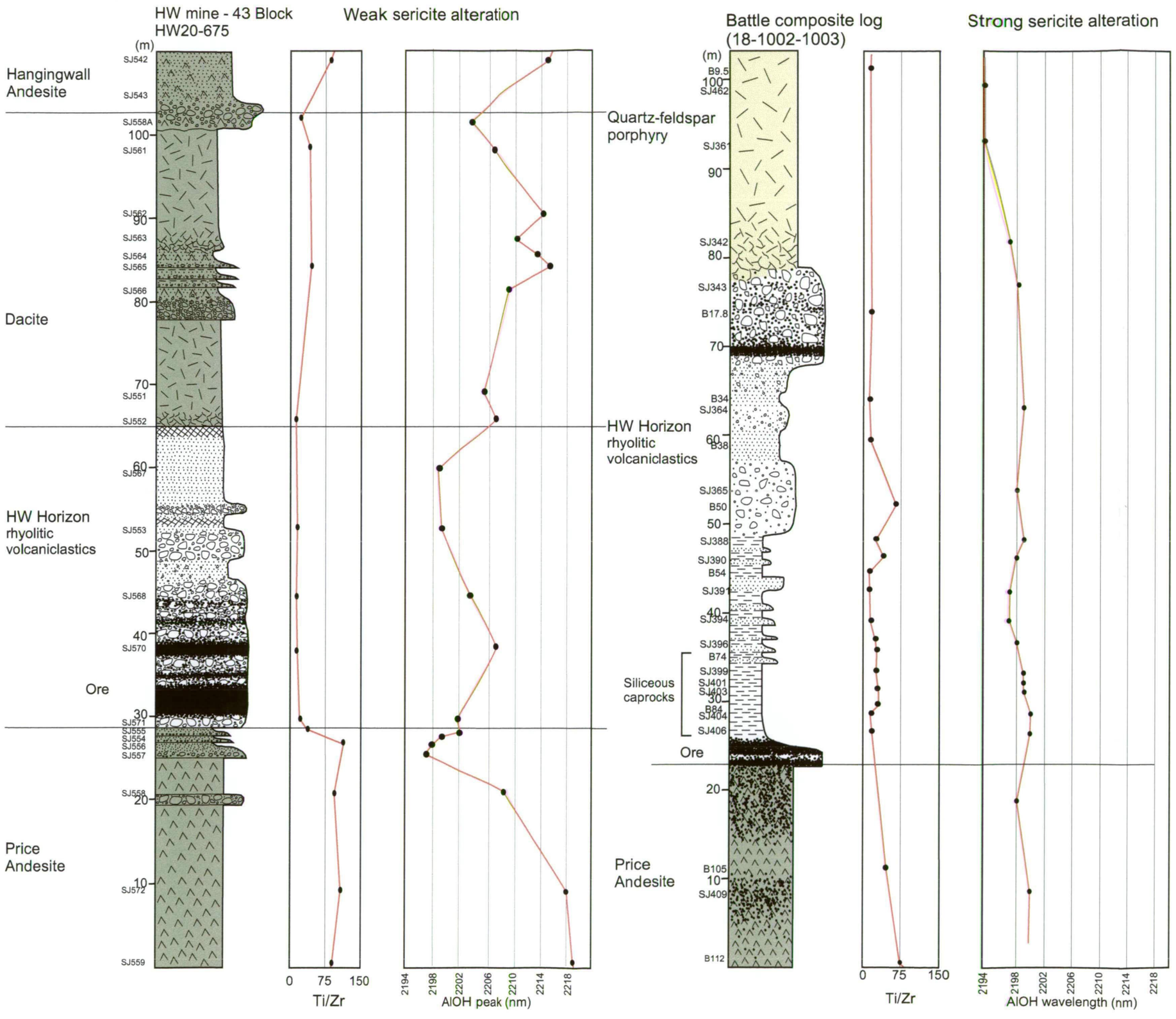

Figure 7.9: Graphic logs and plots illustrating the effect of changing lithology on white mica composition and AlOH wavelengths.

1) The drillhole HW20-675 (43 Block) is in an area of weak sericite alteration, confined to the HW Horizon and about 5m wide zone in the footwall Price Andesite immediately beneath the massive sulphides. Marked lithological changes are shown by the Ti/Zr plots and shifts in AlOH wavelengths appear to match the lithological changes, with lower AlOH wavelengths (2198-2206) in the rhyolite and AlOH wavelengths >2206nm in andesite and dacitic lithologies, except in the strongly altered zone beneath the massive sulphides where the andesite has similar AlOH wavelengths to the altered rhyolite. Note the higher AlOH wavelengths in samples within the semi-massive sulphides.

2) The second log illustrates a sequence in the strongly sericitic altered zone above the Battle orebody (from section 1420E). The Ti/Zr plot illustrates the marked lithological change from footwall Price Andesite up into the rhyolitic lithologies. However, the AlOH wavelengths remain relatively consistent throughout the sequence (2194-2200nm). This illustrates that in these strongly altered zones, hydrothermal alteration is the controlling factor on white mica composition, rather than original lithology.

7.6.2 Bulk rock control on white mica-chlorite spectral characteristics

The bulk rock control on white mica-chlorite spectral features appears to be greatest in distal or background samples. Figure 7.9 shows two graphic logs, one from a zone of weak sericite-quartz alteration (drillhole HW20-675 from the 43 Block area of the HW mine), the other from the Battle mine (composite log 18-1002-1003), in a very strongly quartz-sericite altered zone.

In the first log (HW20-675), the white mica AlOH wavelengths show marked variation with changes in the bulk rock composition, which are indicated by shifts in the Ti/Zr ratios. In the dacitic and andesitic lithologies, AlOH wavelengths are generally between 2207-2214nm, except for the strongly altered zone immediately beneath the massive sulphides (AlOH =
2197-2202nm). The andesite and dacite AlOH wavelengths are distinctly higher than those measured in the adjacent rhyolitic units (predominantly 2198-2200nm, excluding the high zone over the ore horizon, which is discussed below). Chlorite and epidote are common in the dacite and andesite, but are rare in the rhyolite. In comparison, the adjacent log (Battle 18-1002-1003) shows little change in AlOH wavelengths throughout the andesite and rhyolite sequence, apart from minor highs over the mineralised zones. AlOH wavelengths consistently lie between 2194-2200nm. These plots suggest that the bulk rock composition is an important first order control on white mica compositions in weakly altered zones or regional areas, but is less important in strongly hydrothermally altered zones.

Within the rhyolitic HW horizon, AlOH wavelengths are usually highest within and immediately above ore horizons. In log HW20-675 (Figure 7.9), AlOH values increase to 2207nm, far higher than the surrounding rhyolite. This increase in AlOH values in samples associated with ore, is also shown in Figure 7.10, with two graphic logs illustrating measured sections from HW drive S335C and Battle drive G171XS. In both sections there is a marked increase in AlOH wavelengths toward the massive sulphides. In S335C, AlOH wavelengths increase from 2198nm to 2204nm, and in G171XS, AlOH values increase from 2197 to 2203nm. This shift in the white mica AlOH feature appears to be a very localised phenomenon (metre-scale), and has little effect on the regional alteration maps.

Other studies also show similar shifts in white mica compositions with changing host lithologies. For example, in the Los Azufres geothermal field in Mexico, illites in andesite are reported to be systematically more Fe-Mg rich than those from rhyolites (Cathelineau & Izquierodo, 1988). McLeod and Stanton (1984) also report that the Mg/(Mg+Fe+Mn) content of white micas changed in sympathy with that of coexisting phyllosilicates, based on studies from several volcanogenic stratiform deposits, including Captain flat, Colo

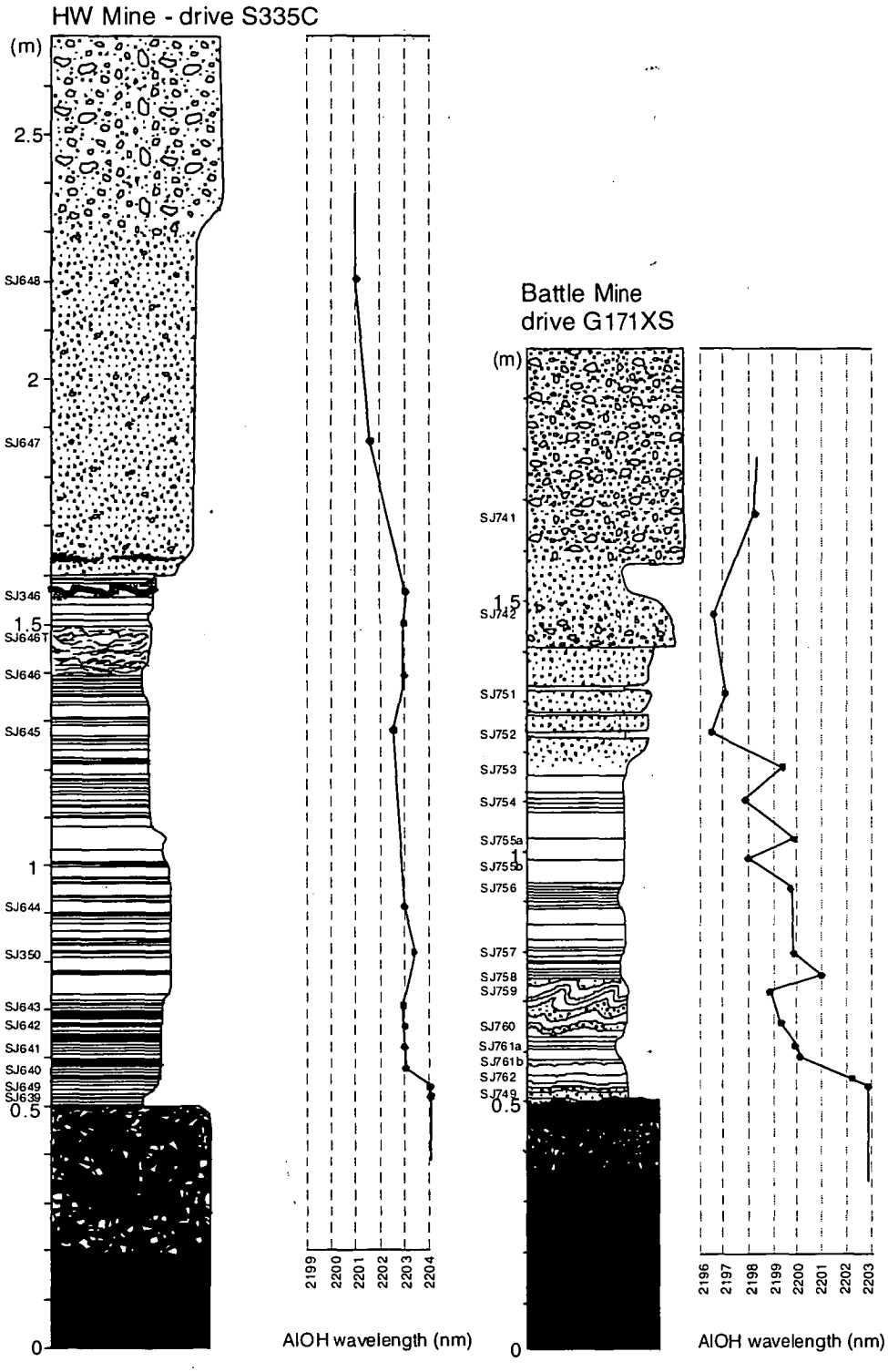

Figure 7.10: Graphic logs illustrating the increasing AlOH wavelength of samples proximal to massive sulphides above the Battle and HW deposits. In the G171XS sequence above the Battle deposit, AlOH wavelengths increase from background values of 2196-2198nm to 2200-2203nm in samples proximal to ore. AlOH wavelength values are higher in the fine sediments above the HW deposit, with most about 2198-2201nm, but still show a distinct shift to values of 2202-2204nm in samples proximal to ore. Fine sulphide bands occur throughout the S335C sequence and may account for the consistently high AlOH wavelength values (2203nm) in the caprocks of this area.

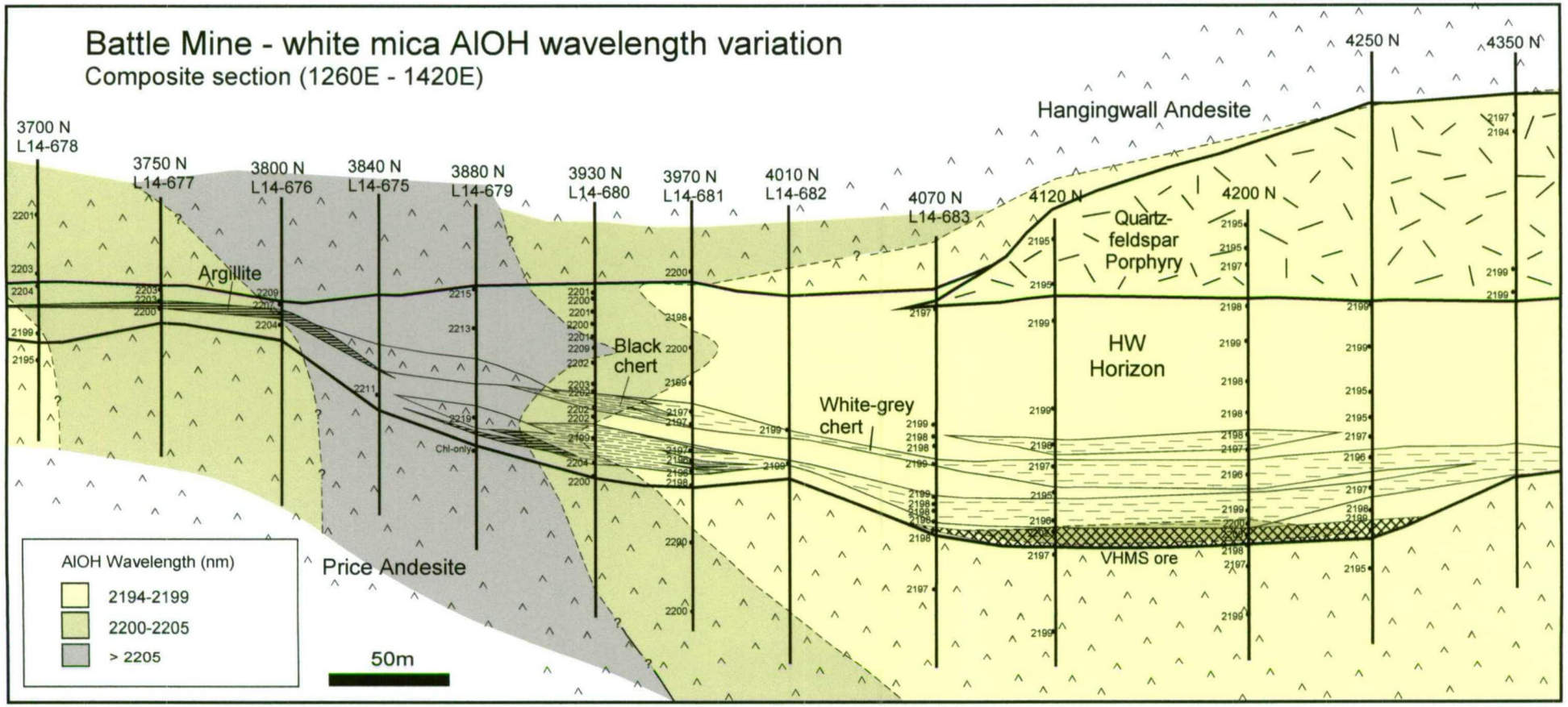

Figure 7.11: White mica AlOH wavelength variation on restored composite section 1260-1420E, Battle Basin (see discussion in text).

Creek, Que River, Roseberry and Woodlawn in southeastern Australia. In larger, district scale studies, using imaging spectroscopy, the octahedral aluminium content of white micas was also shown to vary with changing host lithologies (Clark et al., 1998).

Clearly, in rocks not strongly affected by hydrothermal alteration, the bulk rock composition is an important first order control on white mica compositions, and must be carefully considered when constructing alteration maps.

7.6.3 White mica-chlorite spectral variation with increasing sericite alteration

Composite section 1260-1420E, from the Battle mine, illustrates the shifts in white mica AlOH wavelengths with proximity to strong sericite-quartz alteration associated with VHMS ore (Figure 7.11). White mica AlOH wavelengths are predominantly between 2194-2199nm in the strongly altered zone, close to ore, but rapidly increase to values >2205nm over a distance of about 100m away from ore. The anomalously low AlOH values at the southern edge of the section may represent part of the feeder zone for the Lynx orebody.

The systematic variation in white mica AlOH wavelengths provides a useful exploration vector in alteration zones, and can be used to construct alteration maps for the property. The sequence at Myra Falls is relatively flat-lying and is ideal for showing hangingwall alteration. However, in order to reduce or eliminate the effects of changing bulk rock compositions, alteration maps are best constructed from spectral data from HW horizon rhyolitic samples only.

Figure 7.12 illustrates the changing AlOH wavelengths in the HW Horizon, with distance from ore and decreasing sericitic alteration. Drillhole L14-680 is located on the edge of the sericite alteration halo outlined in Figure 7.11, while drillholes 18-1002-1003, are located within the strongly altered zone in the Battle mine. Ti/Zr ratios give a good indication of the original lithology, with the rhyolitic units having Ti/Zr ratios approximately 8-23, mudstones and chert, slightly higher 25-43, and andesites >70 Ti/Zr (full results listed in Appendix 3). The consistent Ti/Zr ratios through the HW Horizon, indicate the dominance of rhyolitic material in this unit. A marked increase in AlOH wavelengths (>2201nm and up to 2209nm) occurs in samples from drillhole L14-680, and most likely reflects a shift towards more background or regional white mica compositions.

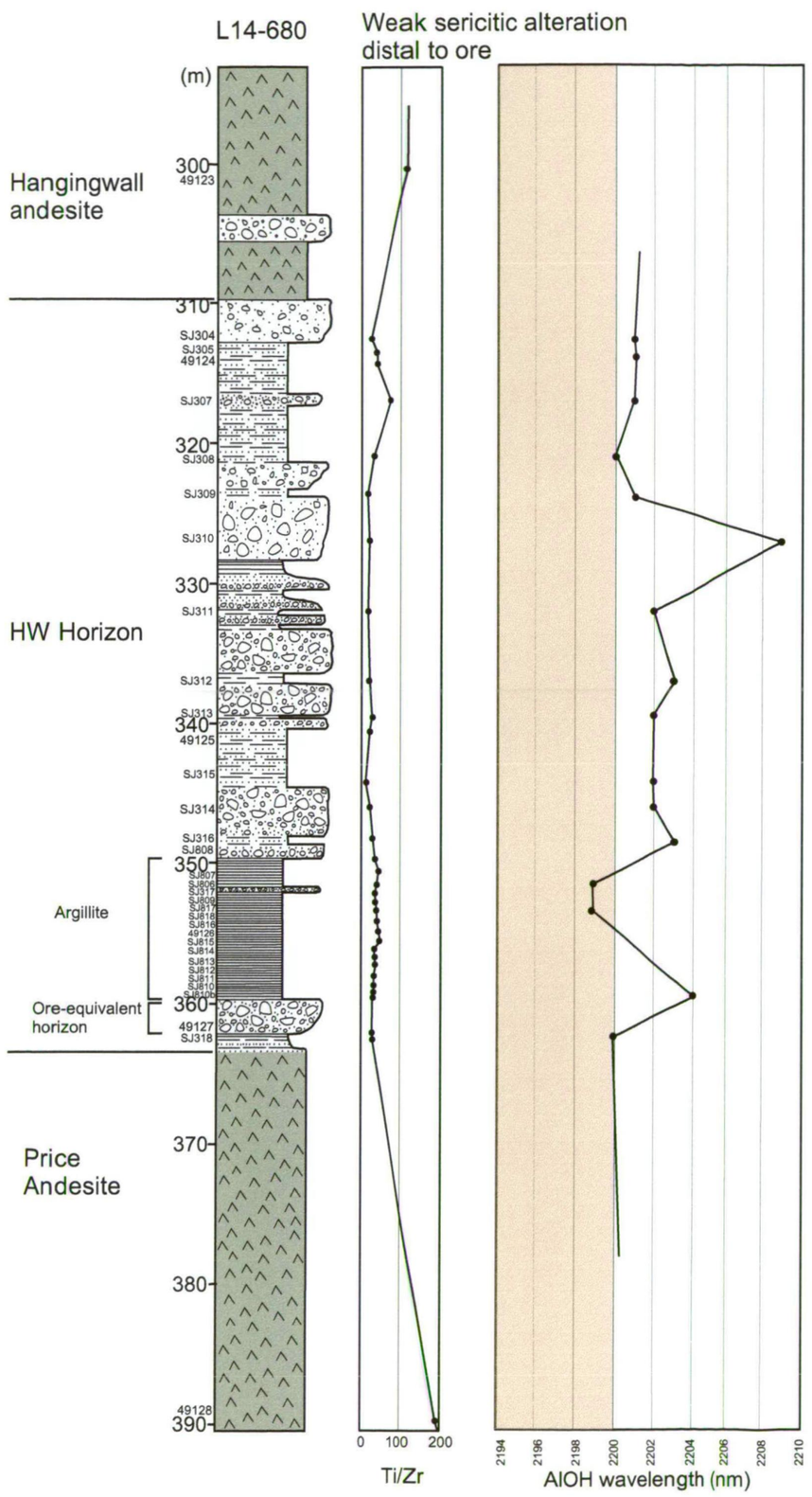

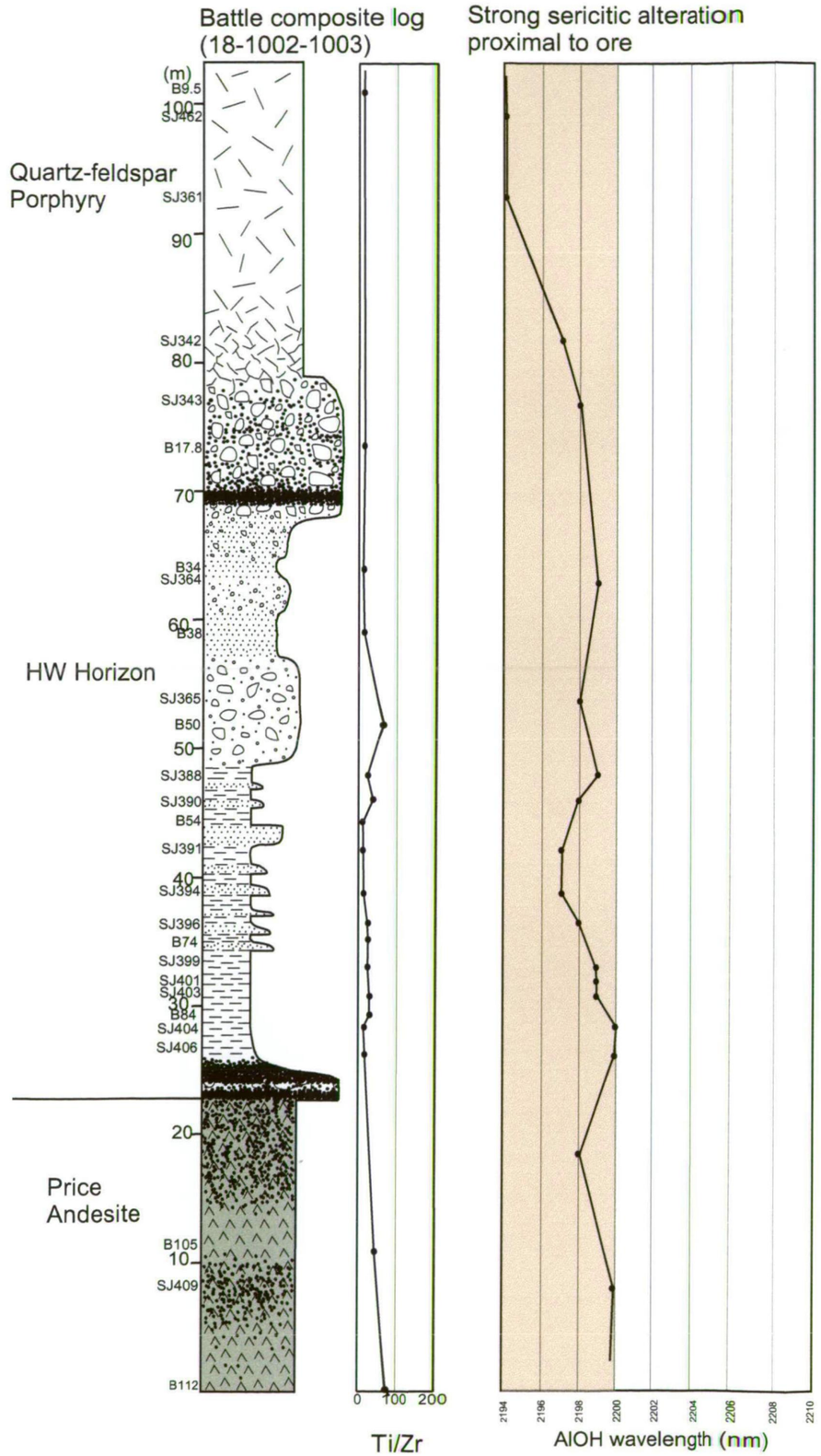

Figure 7.12: Plots illustrating the shift in AlOH peaks with increasing sericitic alteration, from L14-680, 120m away from ore to 18-1002-1003, proximal to ore.

L14-680: The Ti/Zr ratios increase from <20 for rhyolitic material, to 20-40 in the argillite and >100 in the andesite. In this weakly altered zone the AlOH wavelengths are generally >2200nm.

In comparison, the AlOH wavelengths are much lower (<2200nm) in the strongly sericitic altered zone, shown by composite drillhole 18-1002-1003 in the Battle mine. The changing Ti/Zr ratios reflect the rhyolitic and argillite lithologies of the HW Horizon and the footwall, Price Andesite (see discussion in text).

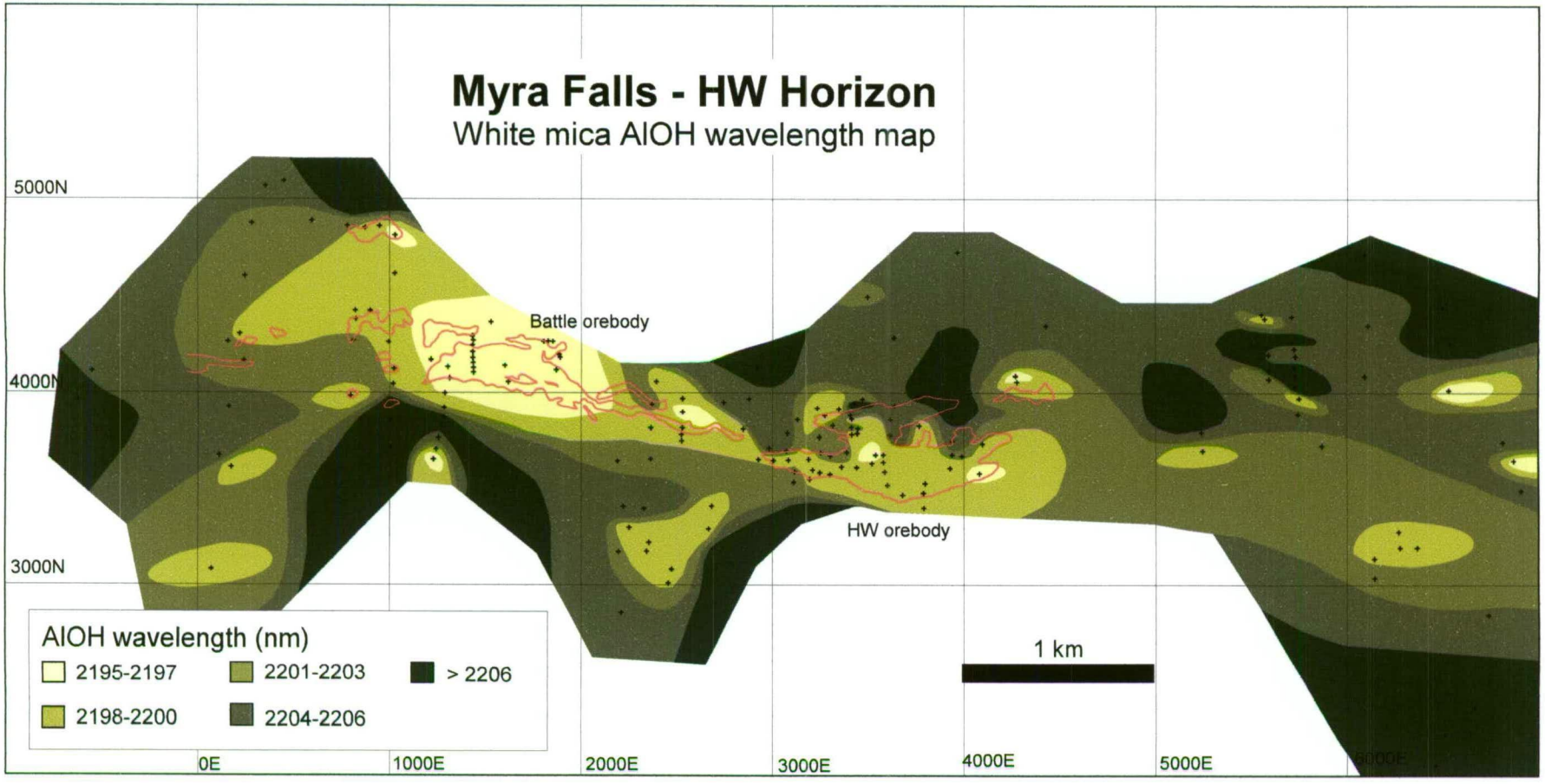

Figure 7.13: White mica AlOH wavelength variation in the HW Horizon at Myra Falls VHMS camp. Note the distinct increase in AlOH wavelength away from the orebodies.

7.6.4 White mica and chlorite spectral variation maps

The spectral characteristic maps of the HW horizon (Figure 7.13 and 7.14) illustrate the spatial variation in white mica and chlorite AlOH and FeOH wavelengths. As chlorite is only a minor component of the rhyolitic rocks, chlorite spectral features were weak and often masked by white mica AlOH features. For this reason, the chlorite FeOH wavelength map (Figure 7.15) is based on much less data, but still gives a broadly similar zonation pattern.

The white mica AlOH wavelength map (Figure 7.13) was constructed by consistently choosing the lowest AlOH wavelengths from samples in the HW horizon. This method was chosen to highlight and emphasise any possible hydrothermal alteration in peripheral zones. During construction of the map, individual spectra were examined, and only spectra with distinct AlOH features and a TSA error <140 were used. The TSA error is the standardised residual sum of squares or the "goodness-of-fit" measure for each match between an individual spectra and the reference library (Pontual et al., 1997a). In general, spectra with a TSA error of 250 or less are considered viable (Pontual et al., 1997a). The lowest AlOH values (≤ 2197nm) were found in a broad zone above the Battle deposit and in small patches above the HW mine. Small zones of low AlOH wavelengths were also found in regional samples in the Thelwood Valley-Price area. This area contains several small mineralised zones within the HW horizon, (e.g., the Trumpeter zone). In general, regional or background white mica AlOH wavelengths were consistently higher (>2204nm) than proximal samples, which were predominantly <2000nm.

Chlorite has a more sporadic distribution in the HW horizon, but also shows a shift in FeOH wavelengths with proximity to ore (Figure 7.14). In general, there is a broad shift from Mg-rich chlorites (FeOH wavelengths <2240nm) immediately over the Battle mine, and parts of the HW mine, to more Fe-rich chlorites in distal or background areas (FeOH wavelengths >2243nm). Microprobe analyses of chlorite by Sinclair (2000), confirm variations in the Fe-Mg content of the chlorites, with Mg-rich chlorites in proximal samples (average Mg# = 0.82), and intermediate to Fe-rich chlorites in regional samples (average Mg# = 0.55).

7.6.5 White mica compositional variation – microprobe analyses

White micas in proximal and distal HW horizon samples, were analysed by electron microprobe to determine the compositional changes related to shifts in AlOH wavelengths and analyses are listed in Appendix 6.2. Average white mica compositions are shown in Table 7.2. Although white mica compositional variation is subtle, electron microprobe

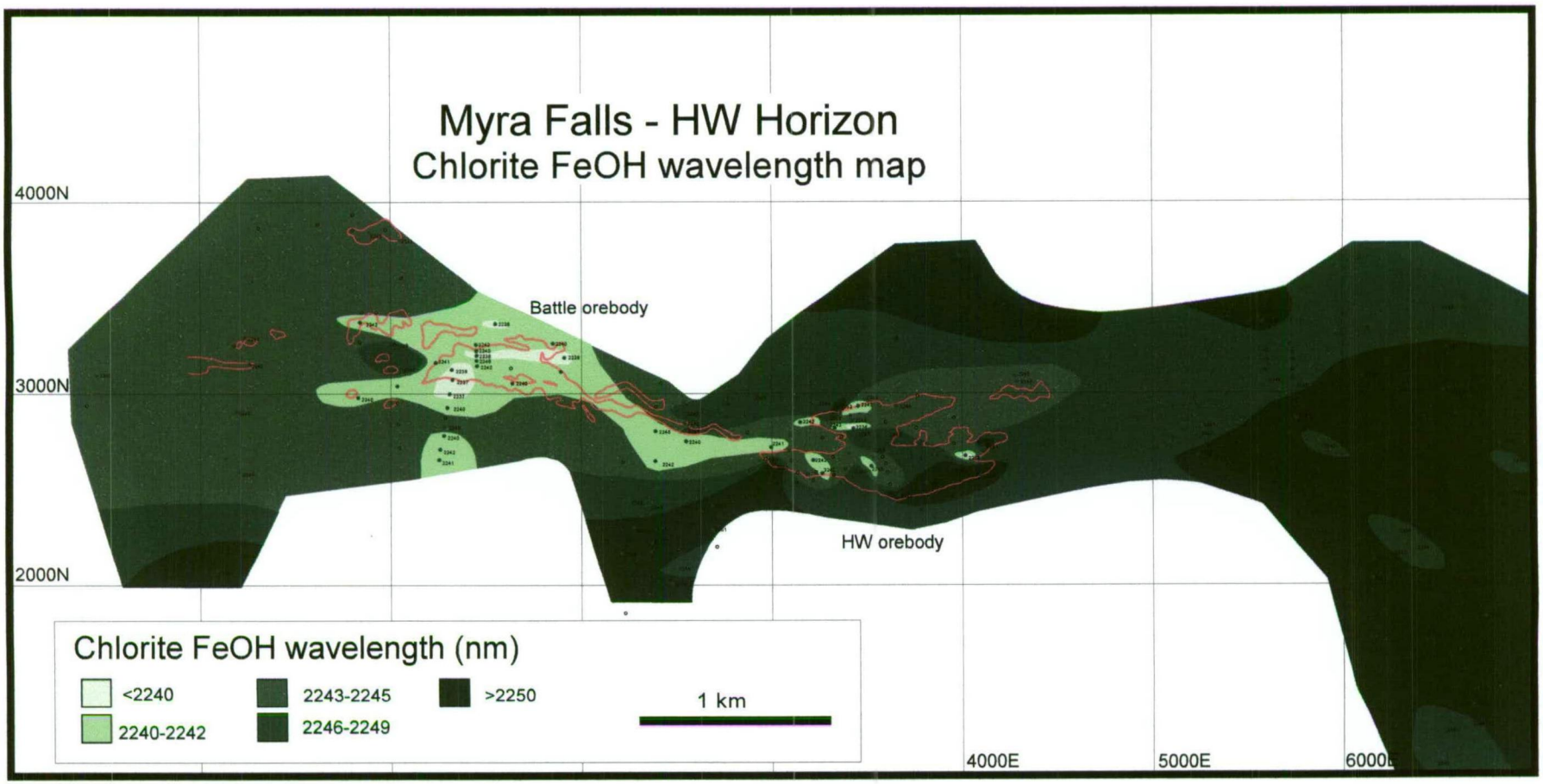

Figure 7.14: Chlorite FeOH wavelength variation in the HW Horizon at Myra Falls VHMS camp. Note the distinct increase in FeOH wavelength away from the orebodies.

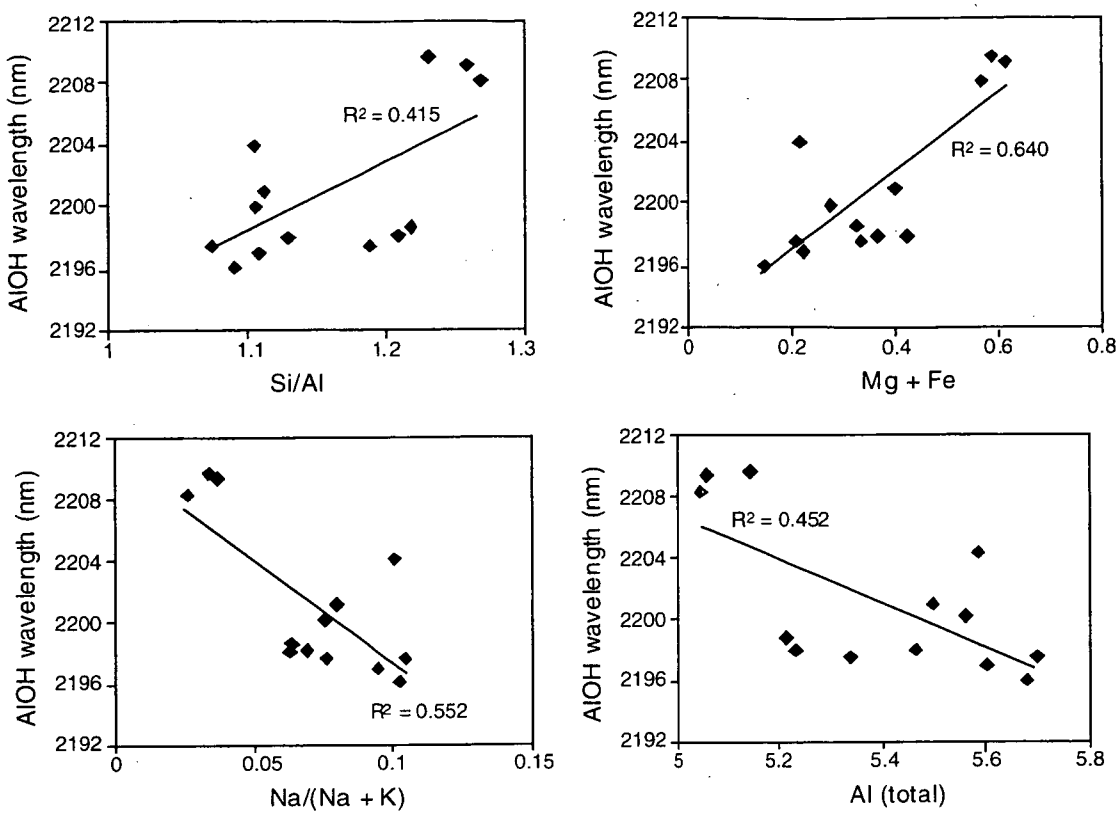

Figure 7.15: Scatter plots illustrating the general increase in Fe, Mg and Si with increasing AlOH wavelength, reflecting a shift from muscovite to phengitic white mica compositions. Phengitic micas also have lower Na and Al^{VI} contents, shown by the negative trends. Each data point represents an average of white mica compositions from electron microprobe data (see Appendix 6.2).

analyses do show minor changes in white mica compositions, which correlate with shifts in the AlOH wavelength feature (Table 7.2). The analyses indicate that the white micas are K-micas, and range from muscovite to phengitic compositions.

The scatter diagrams, in Figure 7.15, compare averaged white mica compositions with the AlOH wavelength for each sample. The diagrams indicate that there are significant correlations between AlOH wavelengths and the proportion of paragonite (measured by Na/(Na+K) values), and the phengitic content of white micas (measured by cationic Si/Al ratios and the Fe+Mg content). Generally, as AlOH wavelengths decrease, the Na/(Na+K) ratio increases slightly to a value of 0.1 atoms per formula unit, at AlOH wavelengths of <~2197nm. The Si/Al ratios increase from 1.0 in proximal samples to 1.3 atoms p.f.u. in background samples, with AlOH wavelengths >2205nm. The increase in Si in background white mica is accompanied by increasing Fe+Mg values. With increasing AlOH wavelengths, the Fe+Mg values increase from 0.2 (at AlOH wavelengths of 2195nm) to 0.6

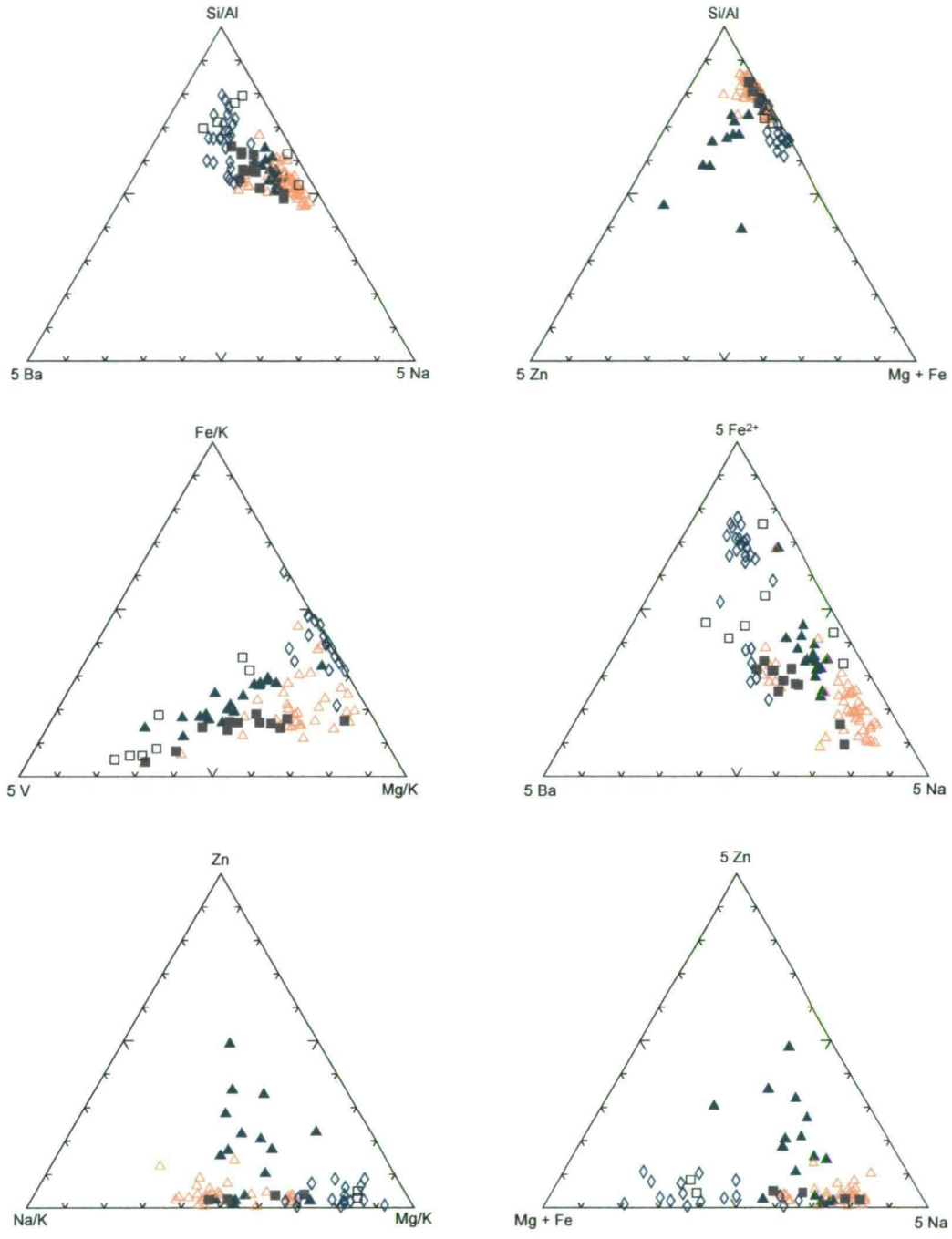

Figure 7.16: Triplots illustrate different white mica compositions based from microprobe analyses in hangingwall samples.

White micas in Battle chert from samples: SJ784, L14-681, 355.5m; SJ774, L14-683, 396.3m; SJ154, 18-1126, 71.4m; SJ161b, 18-1127, 39m; SJ151, 18-1126, 59.5m. White micas in Battle green siltstone above ore from samples SJ749, SJ754 and SJ758, G171XS. White micas in Battle basin argillite from sample: SJ765, L14-676, 231m. White micas in HW Horizon rhyolite (proximal) from samples: SJ639 and SJ650, S335C, HW mine. White micas in distal HW Horizon rhyolite from samples: SJ66, W202, 1050m; SJ600, 16-33, 25.3m; SJ558A, 20-675, 5.9m.

Legend

White micas in:

- △ Battle chert
- ▲ Battle green silt (near ore)
- □ Battle basin argillite (distal)
- ■ HW Horizon rhyolitic siltstone (proximal)
- ◊ HW Horizon rhyolitic siltstone (distal)

atoms p.f.u. (at AlOH wavelengths of 2210nm). This data is consistent with other studies which suggest that the AlOH absorption wavelength changes systematically with varying proportions of octohedral Al and Fe+Mg in white micas (Post & Noble, 1993; Herrmann et al., 2001).

The triplots in Figure 7.16, and the xy scatter plots in Figure 7.17, also illustrate white mica compositional variation from proximal and background hangingwall samples. White micas in strongly altered Battle mine samples have markedly higher V and Zn and lower Ba values than samples from the HW mine and regional areas. V and Zn substitutes for Mg and/or Fe in tetrahedral sites (Yang, 1998).

	Battle white chert (n = 59)	**Battle green silt/chert (n = 7)**	**HW Horizon rhyolite (proximal) (n = 12)**	**Battle basin argillite (n = 7)**	**HW Horizon rhyolite (distal) (n = 15)**	**Andesite (n = 10)**
AlOH	**2210nm**	**2197nm**	**2199nm**	**2207nm**	**2207nm**	**2210nm**
Si	6.19	6.14	6.31	6.36	6.32	6.33
Ti	0.01	0.01	0.06	0.02	0.02	<0.01
Al^{IV}	1.81	1.86	1.69	1.64	1.68	1.67
Al^{VI}	3.76	3.60	3.59	3.54	3.52	3.47
Cr	<0.01	<0.01	0.01	0.01	<0.01	<0.01
Fe^{2+}	0.07	0.13	0.07	0.11	0.17	0.27
V	0.01	0.03	0.02	0.07	<0.01	<0.01
Zn	0.01	0.07	<0.01	<0.01	<0.01	0.01
Mn^{2+}	<0.01	<0.01	<0.01	<0.01	<0.01	<0.01
Mg	0.18	0.27	0.24	0.29	0.34	0.32
Ca	<0.01	<0.01	0.03	<0.01	<0.01	<0.01
Na	0.16	0.14	0.13	0.08	0.07	0.06
K	1.70	1.72	1.70	1.77	1.80	1.83
Ba	0.03	0.04	0.06	0.04	0.06	0.06

Table 7.2: Average AlOH wavelengths and atomic % of the main elements in white micas from electron microprobe analyses (full results listed in Appendix 6.2). White mica compositions were calculated on the basis of 22 oxygens. White chert samples represent the siliceous caprocks above the Battle orebody and include: SJ784, SJ774, SJ154, SJ161b and SJ151. Green silt/chert samples are from G171XS, Battle mine and include: SJ749 and SJ758. HW Horizon rhyolite (proximal) represents rhyolitic volcaniclastics immediately above the HW orebody, drive S335C, HW mine and includes samples SJ650 and SJ639. Battle basin argillite, SJ765 from drillhole L14-676, about 300m south of the Battle orebody. HW Horizon rhyolite (distal) is from the Thelwood Valley, South Flank and HW north, including samples: SJ261, SJ066 and SJ600; Hangingwall andesite sample SJ558A from the 43 Block area, HW mine.

White micas intimately associated with VHMS ore, consistently have higher AlOH wavelengths, up to 2203-2204nm (e.g., Figure 7.10). These samples commonly have an unusual green tone, and microprobe analyses indicate that these white micas have higher Fe, Mg, V and Zn contents, than white micas in white cherts and adjacent rhyolitic

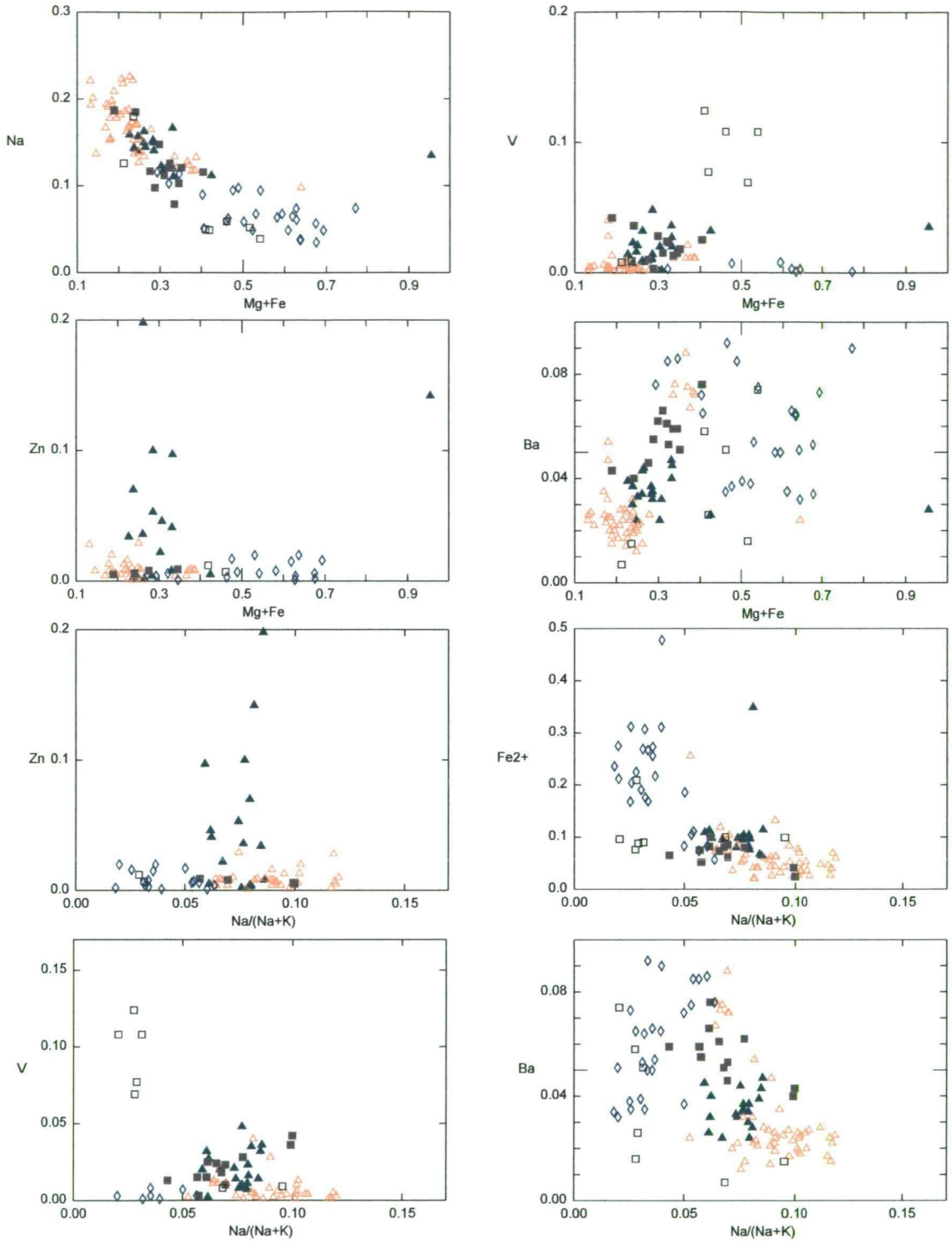

Figure 7.17: Scatter plots illustrate white mica compositional variation, based on microprobe analyses in hangingwall samples across the property (see text for discussion). Sample numbers and locations given in Figure 7.16.

volcaniclastics. Fe contents are up to 0.35 wt.%, Mg up to 0.60 wt.%, with lower V and Zn contents, up to 0.05 and 0.20 respectively. However, as Fe+Mg and V contents are well below 1 wt.%, with the exception of one analysis, the micas cannot be classified as celadonite or roscoelite respectively (Wells and Brannock, 1946; Ernst, 1963; Velde, 1965; Miyashiro and Shido, 1985). Similar white mica compositional variation in Fe contents was observed in rocks associated with massive sulphides in the Iberian Pyrite Belt (IPB) by Plimer and de Carvalho (1982). They found a common association of green celadonitic mica with massive sulphides in the Salgadinho copper deposit, Portugal. The greenish colour of the celadonitic white mica, was caused by a high Fe^{2+} content.

In general, at Myra Falls the property-scale alteration pattern appears to be muscovite in proximal zones (within 100m of ore), grading out into muscovite-phengite in regional zones, >100m from ore. This is similar to compositional variation reported from the Rio Tinto deposit in the IPB, with muscovite in proximal zones and phengite in distal zones (Leistel et al., 1998). Herrmann et al. (2001) report similar white mica compositional variations in Western Tharsis, which is part of the Mt Lyell system in Western Tasmania. Regional samples or the least altered rocks had AlOH wavelengths from 2200-2210nm, with a systematic decrease in AlOH wavelengths towards ore, with values between 2196-2200nm, decreasing to 2194-2198nm in proximal zones. The decreasing AlOH wavelengths corresponded with an increase in the paragonite component in white micas proximal to ore (Na/(Na+K) up to 0.1 atoms p.f.u.), and a marked decrease in the Fe-Mg content (<0.1 Fe-Mg atoms p.f.u. in proximal samples).

7.7 Summary and conclusions

- In summary, white mica and quartz are the most common alteration minerals throughout the sequence. Chlorite is only a minor component of the rhyolitic HW horizon, but is more common in the dacitic and andesitic lithologies.

- SWIR analyses indicate that variation in white mica and chlorite spectral characteristics at Myra Falls reflect the bulk rock composition and the intensity of hydrothermal alteration. Proximal rhyolitic samples have average white mica AlOH wavelengths of 2198nm (paragonite-muscovite) and background HW horizon rhyolite samples have average AlOH wavelengths of 2206nm (muscovite-phengite). Footwall andesites in proximal zones have average AlOH wavelengths of 2201nm (muscovite) and 2204nm (muscovite-phengite) in background samples. Hangingwall andesites show much less variation with average AlOH wavelengths in proximal zones, 2207nm, and in background zones, 2210nm. White micas intimately associated with VHMS ore, appear

to have a higher Zn-V-Fe-Mg content than white micas from strongly altered samples, not intimately associated with ore.

- The average FeOH wavelengths for chlorites in proximal rhyolitic samples, is 2241nm (Mg-Intermediate chlorite) and 2247nm (Intermediate-Fe rich chlorite) in background samples. FeOH wavelengths are much less variable in the footwall and hangingwall andesite. An average FeOH wavelength of 2246nm was measured in proximal and background footwall samples, while an average of 2250nm was measured in hangingwall andesite from across the property. However, these figures are based on limited chlorite spectra, and future studies, which concentrate on the more mafic lithologies may establish more systematic compositional variations in the chlorite.

- The changing mineral compositions most likely reflect different water/rock ratios, with the background or regional samples being rock buffered (i.e., low water/rock ratios) and proximal or strongly altered samples being fluid buffered (i.e., high water/rock ratios).

- The relatively flat-lying sequence at Myra Falls is ideal for the construction of hangingwall spectral parameter maps. Maps are constructed using only rhyolitic samples from the HW horizon to eliminate the bulk rock effect on white mica compositions. The white mica AlOH map provides the best results, as it is based on a larger data set, and shows a marked difference in the AlOH values between proximal and distal samples. Two distinct zones of hydrothermal alteration (low AlOH values, <2197nm) occur above the Battle and HW deposits. Small anomalous low AlOH zones are also located in the Thelwood Valley area, where minor mineralised zones are present.

- The alteration halo over the Battle mine is much better developed than the one over the HW mine and this may reflect the timing of ore formation and deposition of the hangingwall rocks. Field mapping and petrological studies (Chapter 6), indicate that the HW orebody formed directly on the seafloor, with sediment deposition occurring during and after ore formation. Localised alteration zones in the hangingwall rocks in the HW mine, most likely represent the feeder zones for the upper mineralised layers which occur near the top of the HW Horizon. In comparison, the hangingwall of the Battle orebody is more strongly altered than the hangingwall of the HW orebody. The Battle orebody displays distinct replacement textures, indicating ore formation occurred within the sediment pile (subseafloor replacement). During Battle ore formation, hot

fluids percolated through the overlying sediments, resulting in a much greater degree of hydrothermal alteration than is present in the HW mine. The formation of the upper mineralised lenses, which occur near the top of the HW Horizon, added to the intensity of hydrothermal alteration in the Battle mine.

- This study indicates that SWIR analysis is an effective exploration tool for locating alteration halos associated with VHMS orebodies in the Myra Falls district. The systematic trends in mineral compositions, identified by SWIR analysis, can be used as mine-scale vectors to ore.

Chapter 8
Caprock geochemistry

8.1 Introduction

Fine-grained siliceous horizons are spatially and temporally associated with a number of VHMS deposits. Examples include, the Main Contact Tuff of the Millenbach deposit in the Noranda camp (Kalogeropoulous and Scott, 1989); tetsusukei above Kuroko deposits (Kalogeropoulous and Scott, 1983); the Key Tuffite at the Matagami deposit in Quebec (Liaghat and MacLean, 1992); the Brunswick Horizon, Bathurst mining camp, New Brunswick (Peter and Goodfellow, 1996); silica iron exhalites in the Mount Windsor volcanic belt (Duhig et al., 1992). Major and trace element geochemical signatures indicate that many of these siliceous horizons are chemical sediments, 'exhalites', deposited from hydrothermal vents on the seafloor. The broad lateral extent of these horizons and their distinct trace element chemistry, makes them useful marker horizons for exploration.

At Myra Falls the Battle chert does not form discrete silica horizons, such as the Main Contact Tuff (Kalogeropoulous and Scott, 1989), but instead forms a 3-5m thick zone of fine grained siliceous rocks with fine laminations to diffuse cm scale beds. Petrological features indicate that the Battle chert is a replacement product, rather than a true 'exhalative' deposit, and this chapter examines the major and trace element chemistry of the siliceous caprocks to further evaluate it's origin. These rocks may consist of several different physical components that can be distinguished geochemically and the percentage of each has genetic implications. The Battle chert and adjacent Battle basin argillite are characterised by 53 geochemical samples selected from composite section 1260-1420E.

In addition to documentation of the siliceous caprocks, the geochemical study in this chapter is extended to a property-scale study of the fine-grained caprock horizon, which forms a semi-continuous unit at the base of the HW Horizon and includes chert, argillite and siltstone. The fine-grained caprock horizon can be mapped across the property, and paleoseafloor reconstructions (Chapter 5) indicate the presence of three main depocentres (topographic lows). These areas include, the Battle and HW basins, which lie along a NW-

trending ridge, and the South Flank-Thelwood Valley areas, which have thick argillite-siltstone deposits. The geochemical data in this chapter is divided into three groups, representing the fine-grained facies from the three main zones. All samples from thick argillite-siltstone deposits in the Thelwood Valley and South Flank areas were collected close to the base of the HW Horizon, at a stratigraphically equivalent position to the caprock horizon in the Battle and HW basins.

Major and trace element variation in the caprock horizon is examined to determine whether there is a discernible hydrothermal signature in the fine-grained sediments, which would provide useful vectors for exploration in the Myra Falls area. A paleoenvironmental analysis of the argillaceous caprocks, based on geochemical parameters, is also undertaken, to constrain the environment of deposition.

The chapter is divided into seven main sections:

1. Geochemistry of the siliceous caprocks above the Battle orebody;
2. Chemostratigraphy of the caprocks above the Battle and HW orebodies;
3. Mass balance calculations between the argillite and siliceous caprocks;
4. Rare earth element analysis of siliceous and argillaceous caprocks.
5. Argillite geochemistry, with particular emphasis on metal enrichment and metal sources;
6. Paleoenvironmental analysis of Battle and HW basins and the South Flank area; and
7. Sulphur isotope analysis of argillaceous caprocks

8.2 Methods

Drillcore samples were collected from the Battle and HW mine (AQ core, sample lengths 10-30cm), and from exploration drillholes across the property (NQ2 core, sample lengths 5-15cm). Underground samples were also collected throughout the Battle and HW mines. All lithologies of the HW Horizon were sampled, with particular emphasis on the fine-grained caprock horizon.

A total of 148 samples were selected for XRF analysis of whole rock major and trace elements (full results listed in Appendix 3). To accurately characterise the geochemistry of the Battle chert and argillite, care was taken to analyse samples, which were texturally uniform, without clastic laminae.

Samples were crushed, pulverised (tungsten-carbide mill) and made into pressed powder pills using the method of Norrish and Chappell (1977), and fused discs by the method of Norrish and Hutton (1969). They were then analysed for major and trace elements by XRF

at the University of Tasmania. XRF analyses were conducted by Phil Robinson on the Phillips PW1480 X-ray flourescence spectrometer (analytical details and full results listed in Appendix 3). Price Andesite and quartz-feldspar porphyry (QFP) data used for comparison with the caprocks is from Robinson (1996). These samples were analysed at X-Ray Assay Laboratories, Earth and Planetary Sciences, McGill University, Montreal, Canada. Rare earth elements (REE) were measured in 15 argillite, and 8 chert samples from the base of the HW Horizon. Samples were analysed by Z. Yu on the ICP-MS at the Geology Department, University of Tasmania, using the method of Yu et al. (2001). REE were normalised to chondrite values from Boynton (1984).

Total organic carbon was measured in 61 argillite and black chert samples across the property. Organic carbon was determined by the author at the Geology Department, University of Tasmania, using the 'ashing' method of Krom and Berner (1983). Total carbon and sulphur analyses were collected by Graeme Rowbottom, on a Karlo Erber Elemental Analyser at the Central Science Laboratory, University of Tasmania (results in appendix 5.1).

Sulphide sulphur contents were measured on 42 samples by the author in the Geology Department, University of Tasmania, using the chromium reduction method of Canfield et al. (1986). A total of 21 $\delta^{34}S$ analyses were carried out on sulphide sulphur samples and the precipitated Ag.S (including mono-sulphide and di-sulphide) was analysed conventionly at the Central Science Laboratory, University of Tasmania, using the analytical techniques of Robinson and Kusakabe (1975). Results are listed in Appendix 5.1. Identification of all mono and di-sulphide phases present was difficult, due to the fine-grained nature of the argillite. However, pyrite is most likely the dominant di-sulphide phase present in the argillite and black chert. Mono-sulphides were found in regional and Battle basin argillite samples (none was present in HW basin argillite). Mono-sulphide phases include rare fine pyrrhotite in regional argillite, and fine galena and sphalerite in black chert.

Degree of pyritisation was calculated for 42 argillite samples from Myra Falls, by the method of Berner (1970). The HCl-soluble Fe was obtained by the author at the Geology Department, University of Tasmania, using the 1 N HCl 24-hour extraction method, recommonded by Leventhal and Taylor (1990). The HCl-soluble Fe was measured by Ashley Townsend on the ICP-OES at a wavelength of 259.9 nm, at the Central Science Laboratory, University of Tasmania (results listed in Appendix 5.1).

The concentration of carbon, sulphur and total Fe is often reported on a $CaCO_3$-free basis (e.g., Raiswell and Berner, 1985). $CaCO_3$ contents generally increase as organic carbon increases, resulting in a slight negative correlation between Fe and organic carbon. However, the low calcic nature of argillite samples from Myra Falls (< 4 wt.%) indicates that this adjustment is not necessary, and samples can be assumed to be $CaCO_3$-free (e.g., Quinby-Hunt and Wilde, 1994).

8.3 Geochemistry of siliceous caprocks above the Battle orebody

Petrological features, described in Chapter 6, suggest that the chert above the Battle deposit, formed by silicification of pre-existing fine-grained sediments (argillite), rather than as a primary 'exhalative' deposit. White to pale grey chert is well developed immediately above the Battle orebody, but grades laterally into black chert at a distance of about 100m from the ore zone, and out into black finely laminated argillite at distances of 120 to 160m from ore. This section examines the major and trace element chemistry of the siliceous caprocks to characterise them and determine their likely origin. If the chert did form as a replacment of pre-existing sediments, lithogeochemistry can be used to determine it's original composition/provenance.

8.3.1 Rationale of geochemical analysis for affinity and precursor determination

Trace element concentrations in sediments reflect a combination of provenance, weathering, diagenesis, sediment sorting and the aqueous chemistry of individual elements (Rollinson, 1993). Lentz (1996) groups these processes and suggests that the composition of sedimentary rocks generally reflects two geochemical components: 1) immobile element variations reflecting the provenance of the terrigenous (allochemical) material; 2) mobile hydrothermal-hydrogenous elements (orthochemical) variations reflecting the depositional and environmental setting (including the effect of diagenetic processes).

Selected trace elements can be used to identify the sedimentary provenance. Provenance analysis in seafloor volcanogenic terrains relies upon elements which remain immobile during seafloor alteration, diagenesis, and low-grade metamorphism. Immobile elements can include Al, Ga, Ti, Sc, Zr, Hf, Y, Th, HREE, and possibly Nb and Ta, (e.g., Pearce and Cann, 1973; Floyd and Winchester, 1978; MacLean and Barrett, 1993). Other elements, such as Si, Fe, Mn, Pb and sometimes Cr are mobile during diagenesis, while Sr is leached during weathering (Rollinson, 1993). These elements are not useful for provenance analysis.

If immobile, elements such as Zr, Ti, Al, Ga, would be transported exclusively in the terrigenous component of a sediment and reflect the chemistry of their source (Lentz, 1996). However, immobile elements such as Zr, Hf and Sn, may also be mechanically distributed according to grain size and therefore, may be controlled by the concentration of heavy minerals (Rollinson, 1993). In finely laminated mudstones and chert, mechanical sorting is not a dominant depositional process and the concentration of elements, such as Zr, in the siliceous and argillaceous caprocks, most likely reflects the chemistry of their source. Care was also taken to sample homogenous mudstone-chert horizons and clastic laminae were removed during sample preparation for XRF analysis.

A now standard approach for provenance analysis is to first plot element pairs, such as Ti-Zr or Al-Zr, of sample populations on x-y scatter plots to test their immobility. If immobile, but mass has been lost or gained, they will form positively correlated linear trends which pass through the origin (MacLean and Kranidiotis, 1987; MacLean and Barrett, 1993). These must still be examined carefully as some igneous fractionation processes can produce similar trends. Primary (pre-alteration) variation within each population can result in a narrow fan of lines, rather than a discrete line. In volcaniclastic and sedimentary sequences these primary variations could be the result of mechanical mixing of mafic and felsic components (Barrett and Sherlock, 1996).

8.3.2 Siliceous caprocks geochemical features

This section examines geochemical features of the siliceous caprocks in order to characterise them and determine their origin. The average major and trace element content of the siliceous caprocks and the adjacent Battle basin argillites are compared with chemical and clastic tetsusukei layers (Kalogeropoulous and Scott, 1983); haematite-ironstone from the Brunswick Horizon (Peter and Goodfellow, 1996); and the average shale standard, SDO-1 (Huyck, 1990) in Table 8.1.

The most noticeable feature of the siliceous caprocks is the high silica contents, with SiO_2 ranging from 78.6 to 97.57 wt.% in white-pale grey chert (most have greater than 90 wt.% SiO_2) and 89.23 to 96.11 wt.% in black chert. Fe_2O_3 contents are low in the chert, ranging from 0.2 to 2.34 wt.% in white chert, and 0.36 to 1.81 wt.% and in the black chert. Low Mn values are also observed, ranging from 0 to 0.06 in the white and black chert. Al_2O_3 ranges from 0.81 to 11.86 wt.% in the white chert, and from 1.14 to 3.39 wt.% in the black chert. The silica contents of the siliceous caprocks are higher than many tetsusukei and chemical sediments of the Brunswick Horizon, whereas the Fe and Mn contents of the caprocks are generally much lower.

	Myra Falls						Kuroko		New Brunswick	
	Average White Chert (n=32)	St.dev.	Average Black Chert (n=14)	St. dev.	Average Battle argillite (n=8)	St.dev.	Tetsusukei chemical layer	Tetsusukei clastic layer	hem IF Brunswick Horizon	Average shale SDO-1
Wt. %										
SiO_2	91.21	± 4.33	93.38	±2.21	70.31	±11.79	47.05	59.22	91.00	49.28
Al_2O_3	3.96	± 2.50	2.04	±0.75	9.89	± 2.85	5.45	10.67	0.08	12.27
CaO	0.2	± 0.22	0.18	±0.37	3.87	± 6.16	0.70	0.32	0.01	1.05
MgO	0.22	± 0.20	0.15	±0.17	1.81	± 1.62	2.94	4.89	0.75	1.54
Na_2O	0.09	± 0.06	0.01	±0.02	1.11	± 1.59	b.d.	b.d.	0.04	0.38
K_2O	1.08	± 0.68	0.60	±0.22	2.11	± 1.01	0.80	1.65	0.01	3.35
FeO^{Tot}	0.82	± 0.59	0.95	±0.59	3.28	± 1.52	25.31	13.35	5.45	8.40
MnO	0.03	± 0.02	0.01	±0.02	0.04	± 0.04	0.09	0.14	2.43	0.04
TiO_2	0.14	± 0.10	0.08	±0.03	0.30	± 0.09	0.23	0.57	0.05	0.71
P_2O_5	0.07	± 0.10	0.05	±0.08	0.45	± 1.01	0.41	0.14	2.22	0.11
S	0.90	± 0.50	0.98	±0.60	1.56	± 0.84	14.48	6.01	0.18	5.35
LOI	1.36		1.44		5.72		0.65	2.5	0.05	21.7
Total	100.08		100.00		99.62		98.11	99.46	-	-
ppm										
Ba	712.6	-	887.3	-	2498.4	-	684.0	1824.0	38	397.0
Rb	14.4	± 9.1	7.8	± 2.6	28.4	± 14.5	19.0	52.0	5	126.0
Sr	8.4	± 65.7	4.7	± 4.6	84.4	± 76.2	12.0	15.0	3.2	75.1
Th	2.5	± 0.7	3.5	± 1.4	2.5	± 0.8	1.2	4.6	-	10.5
U	3.9	± 2.3	4.0	± 1.9	8.4	± 5.2	1.2	1.4	-	48.8
Nb	2.0	± 1.2	1.2	± 0.4	4.2	± 0.8	-	-	23	11.4
Y	8.2	± 7.3	4.1	± 1.8	18.2	± 8.0	13.0	12.0	1.8	40.6
Zr	34.2	± 23.8	15.3	± 7.6	87.1	± 18.4	64.1	129.0	1.5	165.0
Ni	6.5	± 4.1	23.5	± 21.6	49.2	± 31.4	5.7	11.5	3	99.5
V	179.8	-	206.3	-	714.0	-	-	-	9	160.0
Cr	24.7	± 24.2	23.2	± 7.6	53.6	± 32.3	-	-	12	66.4
Sc	5.1	± 2.5	2.9	± 0.8	12.3	± 5.2	6.2	12.5	0.3	13.2
Ga	5.0	± 3.1	2.2	± 0.9	10.5	± 2.4	-	-	-	9.0
Zn	5454.0	-	3564.0	-	1579.0	-	181.0	191.0	1.2	64.1
Cu	667.6	-	455.8	-	108.6	± 57.3	76.4	58.5	2.5	60.2
Pb	108.9	-	1229.0	-	110.1	± 84.9	282.0	99.0	7	27.9
Cd	26.9	± 19.0	16.3	± 13.0	18.6	± 15.6	-	-	0.1	5.0
As	38.4	± 90.4	81.5	± 84.7	99.3	± 86.7	159.0	44.2	1.5	68.5
Sb	5.1	± 4.9	104.6	-	5.2	± 3.2	14.7	6.7	5	4.5
Ag	3.4	± 2.4	59.1	± 62.4	4.7	± 2.0	2.1	0.6	0.1	0.1

Table 8.1: Average major and trace elements for the siliceous caprock horizon and adjacent Battle Basin argillite, compared with average clastic and chemical tetsusukei from the Kuroko deposits (data from Kalogeropoulous and Scott, 1983), hem IF=haematite iron formation, Brunswick Horizon (data from Peter and Goodfellow, 1996), and the average shale standard, SDO-1 (Huyck, 1990).

b.d.=below detection; Standard deviations for trace elements greater than 100ppm are not shown.

The siliceous caprocks are generally metal rich, but metal contents are highly variable. For example, Zn values range from 25 to 38106ppm in white chert, and 21 to 9900ppm in the black chert. Pb and Cu values in the white chert range from 2 to 713ppm and 3 to 3100ppm respectively, and in the black chert Pb and Cu range from 3 to 4000ppm and 37 to 1809ppm respectively.

To determine the origin of the siliceous caprocks, geochemical features of the chert are compared to metalliferous seafloor sediments, on the basis of their volcanogenic seafloor setting. A standard representation of metalliferous sediment affinity is the Fe-Al-Mn Bostrom plot (Bostrom, 1973b). The chert and argillite plot together in the non-hydrothermal or terrigenous field (Figure 8.1a), close to pelagic sediments from the Pacific Ocean (Spry et al., 2000), and the average shale standard, SDO-1 (Huyck, 1990). The caprocks plot well away from the hydrothermal (orthochemical) field, which includes 'exhalative' sediments, e.g., the Brunswick Horizon (Peter and Goodfellow, 1993); and EPR metalliferous sediments (Adachi et al., 1986). On this basis they are interpreted to lack affinity with typical Fe-Mn rich metalliferous sediments. The chert and argillite also plot together on the Fe-Al-Mg plot (Figure 8.1b), close to the fields for clastic tetsusukei and tuff horizons, and the average shale standard, SDO-1 (Huyck, 1990), well away from the chemical tetsusukei (Kalogeropoulous and Scott, 1983).

The Bostrom plot (Figure 8.2), shows the relative contributions of terrigenous clastic and hydrothermal components in the chert and argillite (Bostrom, 1973b). Fe and Mn are used to measure the hydrothermal component in marine sediments, because these elements are derived mainly from hydrothermal sources, whereas Al and Ti represent elements of clastic origin. The chert and argillite from Myra Falls again plot together in the non-hydrothermal or terrigenous field (with the exception of one white chert sample), indicating that the chert contains a large detrital component, similar, for instance, to some other proposed chemical sediments, such as the Key Tuffite (Liaghat and MacLean, 1992).

The very low Fe and Mn content of the Battle chert results in their classification as non-hydrothermal or terrigenous sediments. However, the high metal contents of the chert, shown in Table 8.1, indicate a significant hydrothermal component. Figure 8.3 illustrates the high Zn, Ba and Cu values of Battle chert in comparison to the adjacent Battle basin argillite, the average shale standard, SDO-1 (Huyck, 1990), and tetsusukei from the Kuroko deposits (Kalogeropoulous and Scott, 1983).

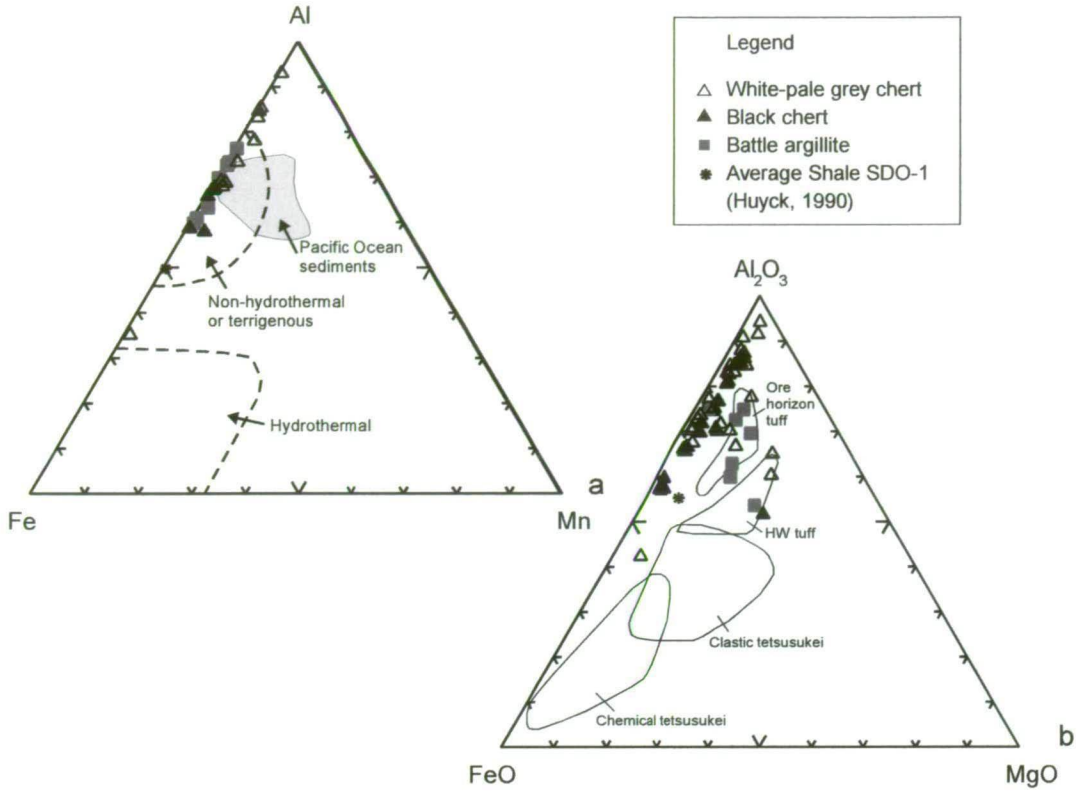

Figure 8.1: a) The Fe-Al-Mn plot (Bostrom, 1973a) indicates that the argillite and chert plot within the non-hydrothermal or terrigenous field, suggesting that the sediments do not have a significant hydrothermal component. Pacific Ocean sediment data from Spry et al. (2000); **b)** The Fe-Al-Mg plot compares the Battle Basin caprock data with chemical and clastic tetsusukei and tuff horizons from the Kuroko Deposits (data from Kalogeropoulous and Scott, 1983).

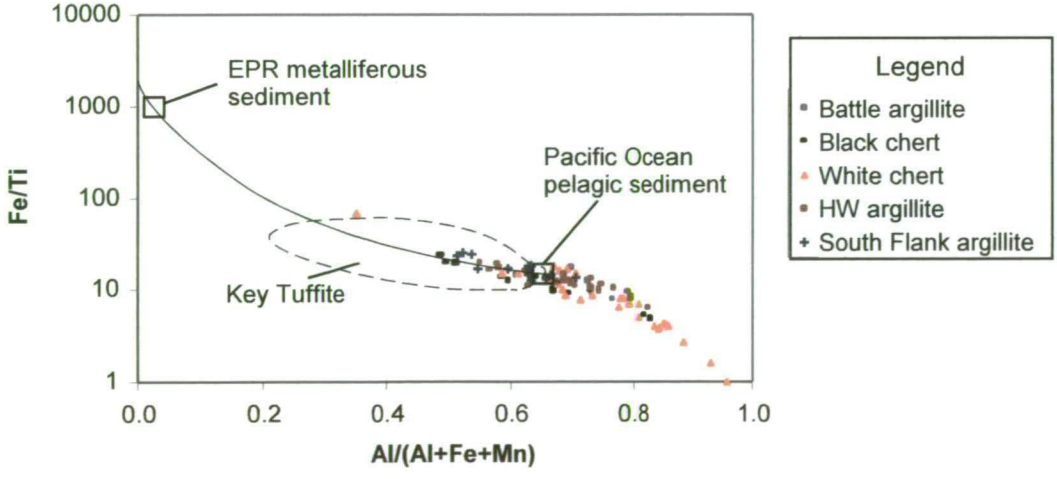

Figure 8.2: Fe/Ti vs Al/(Al+Fe+Mn) Bostrom plot (Bostrom, 1973b) of argillite and chert samples from the caprock horizon. Also shown for reference are fields for Pacific Ocean pelagic sediment and EPR metalliferous sediment and Key Tuffite (Spry et al. 2000).

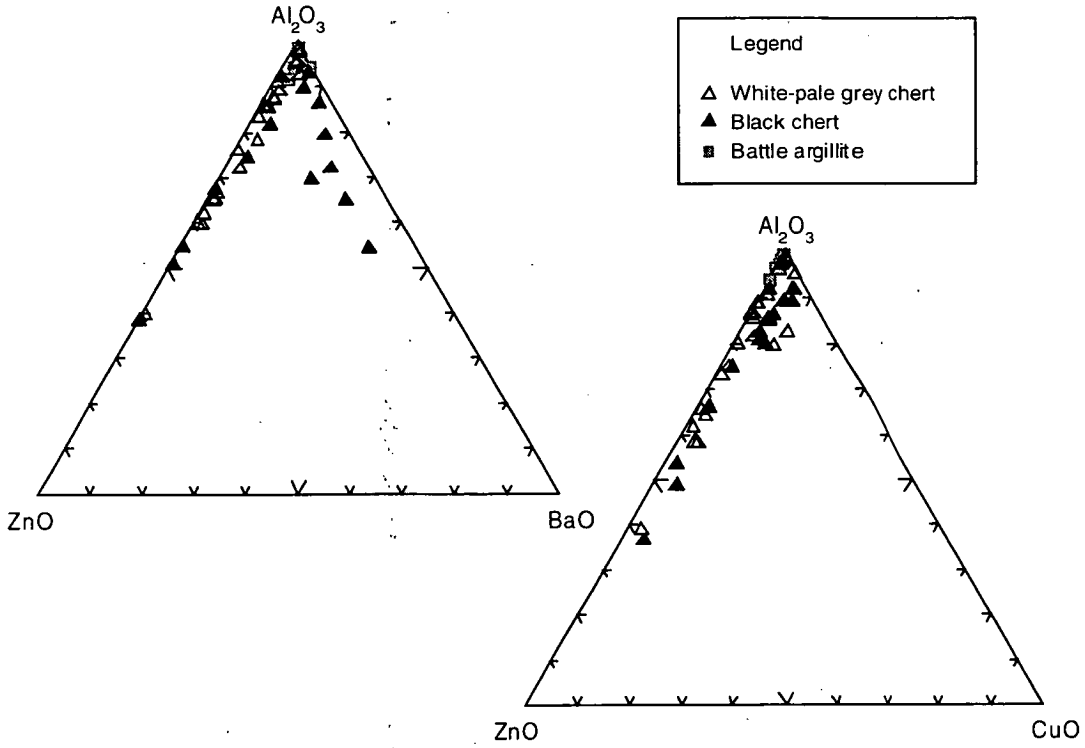

Figure 8.3: Ternary diagrams illustrate the metal-rich nature of the siliceous caprocks above the Battle orebody, compared with the Battle basin argillite to the south.

8.3.3 Siliceous caprocks source

In this section, the siliceous caprocks and argillites from the caprock horizon, are compared with Price Andesite (A) and the quartz-feldspar porphyry (QFP). Data for Price Andesite and QFP data is from Robinson et al. (1996). The complete data set is plotted on selected xy scatter plots in Figure 8.4, and falls into three distinct lithological groups. Narrow positive linear trends shown by element pairs, such as Ti-Zr, Al-Zr and Al-Ti, are consistent with their immobility, but show marked differences between the caprocks and the adjacent Price Andesite and QFP. The fine-grained facies (chert and argillite) appear to form a separate trend from Price Andesite and QFP in terms of TiO_2-Zr and Al_2O_3-TiO_2 variation. In comparison, the pale siltstone, which is interbedded with the chert and argillite, clearly has a rhyolitic composition, plotting within the QFP field. Immobile element ratios, such as Ti/Zr, can also be used to highlight differences between lithological units. The andesite and QFP form distinct fields in Al_2O_3-Ti/Zr, SiO_2-Ti/Zr, Fe_2O_3-Ti/Zr and Cr-Ti/Zr plots, quite separate from the argillite and chert. Ti/Zr ratios are generally greater than 18 for the quartz-feldspar porphyry and greater than 35 for the Price Andesite. In comparison, chert and argillite Ti/Zr values are usually between 15 to 45, similar to the Ti/Zr value, 25.8, of the average shale standard, SDO-1 (Huyck, 1990).

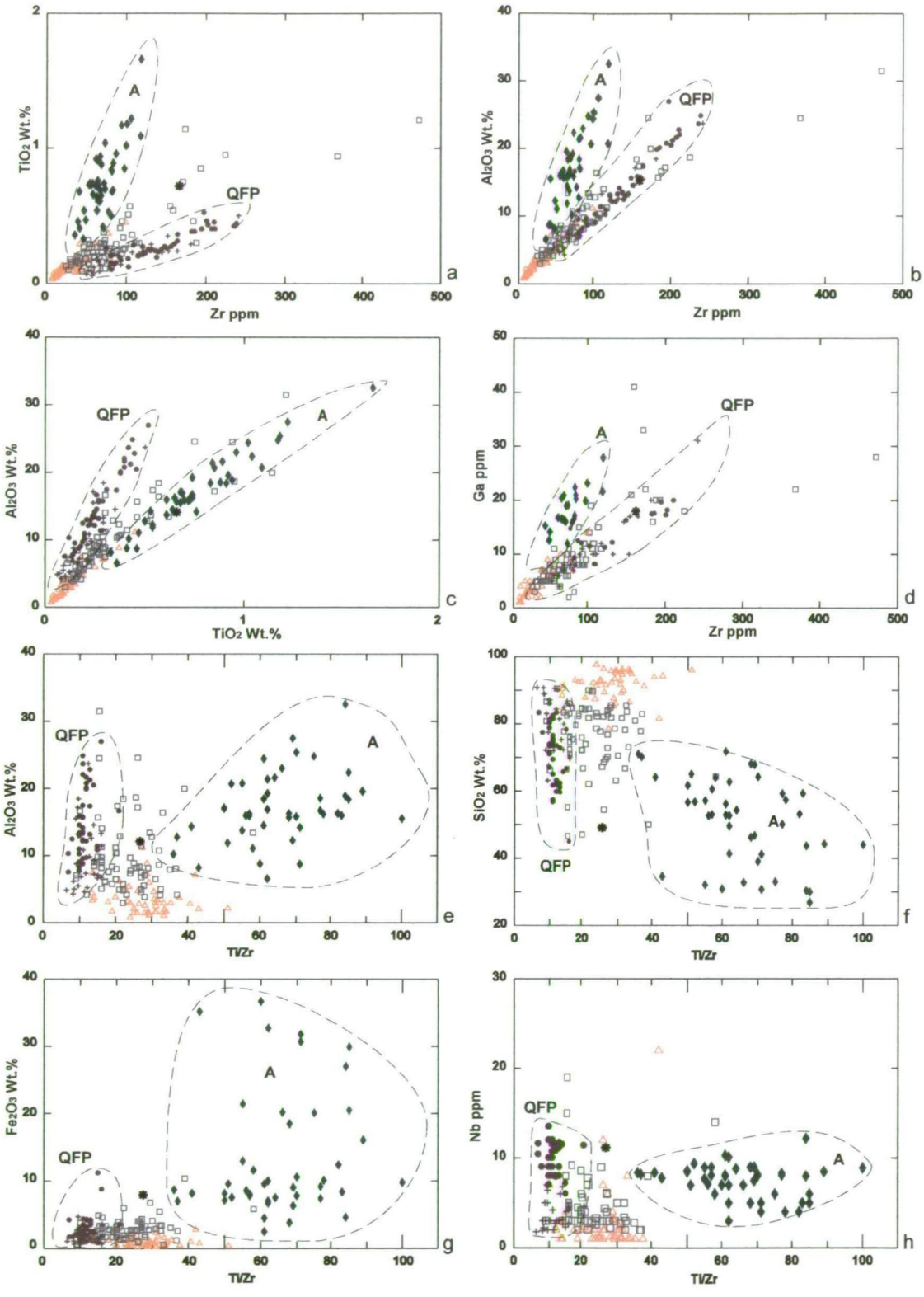

Figure 8.4: Immobile element plots illustrating the typical range of values for the fine-grained facies at the base of the HW Horizon (including chert and argillite), Price Andesite (A) and quartz-feldspar porphyry (QFP). The argillite and chert have very similar immobile element values and ratios of immobile element pairs, such as Ti/Zr clearly illustrate the differences between the various lithologies.

The very similar nature of Ti/Zr, Ti/Al and Zr/Al ratios of the argillite and chert is evidence supporting the view that these lithologies share a similar sediment source or provenance, distinct from the Price Andesite and the rhyolitic quartz-feldspar porphyry. A likely sediment source for the fine-grained facies would be pelagic sedimentation, quite distinct from the local andesite and rhyolite derived sediments. However, the spread of Ti/Zr values for the fine-grained facies, indicates a likely wide range of sediment sources, such as pelagic sediments, mixed with andesitic and rhyolitic detritus from local sources.

The similarity of Ti/Zr ratios and Fe-Mn-Al values for the argillite and chert suggests that the chert does not represent a true 'exhalative' deposit, but instead represents silicification of pre-existing fine-grained sediments. This is consistent with the petrological features described in Chapter 6.

8.4 Caprock chemostratigraphy

Siliceous caprocks are best developed above the Battle orebody, and this section examines the major and trace element geochemical variation throughout the siliceous rocks. The white to pale grey chert located above the orebody is compared with the black chert, which is found at the edge of the siliceous alteration (~100m distance from ore), and the unaltered Battle basin argillite (120-200m south of the orebody). In the HW mine, major and trace element variations in localised bleached and silicified argillite above the HW orebody are also examined.

Al is used to highlight the siliceous zones in the HW Horizon by mass correction, because of the relative immobility of Al over a range of hydrothermal alteration conditions, and minimal variation of Al in a range of crystal-matrix ratios in volcaniclastic and sedimentary rocks (Lentz, 1996). Fractionation in felsic rocks also produces only minimal variations in Al contents. Al decreases with increasing dilution by hydrothermal components, such as silica, and ratioing with respect to Al, corrects for the mass changes and can enhance the data (Pearce, 1963). Al ratios are commonly used in the Bathurst Camp for mass corrections, for example (Fe+Mg/Al) values consistently increase toward the ore horizon at Bathurst (Lentz and Goodfellow, 1993; Leitch and Lentz, 1994).

Battle basin siliceous caprocks

Selected major and trace elements are plotted against a graphic log, Figure 8.5, to illustrate the geochemical variation through the siliceous caprocks and the HW Horizon (composite log 18-1003-1003, from section 1420E, Battle mine). The Si/Al plot highlights the siliceous zones, with the main white-grey chert horizon located immediately above the ore horizon, and minor fine-grained siliceous zones above (shown in Figure 8.5). Ti/Zr values

are similar throughout the HW Horizon, although the siliceous caprock horizon has slightly higher values (Ti/Zr = 10-30), compared to massive rhyolite (QFP) (Ti/Zr values <15). There is a distinct rise in Ti/Zr to values of 30 to 50 in the andesitic footwall, and in a mixed andesite-rhyolite volcaniclastic layer within the HW Horizon, at about 49-56m. The siliceous zones, highlighted by the Si/Al values, coincide with some high metal values, including Zn, Cu, Pb, V, Cd, and Cr, but low Al_2O_3, Fe and Ba values.

A second graphic log, Figure 8.6, shows the geochemical variation in the black chert/argillite at the edge of the siliceous alteration, about 120m south of the Battle orebody. In general, the geochemical variation is very similar to the previous diagram, with the siliceous zone highlighted by the Si/Al plot. The Ti/Zr values are similar throughout the rhyolitic units of the HW Horizon (<15-20), and are much lower than the hangingwall and footwall andesites (>30). The fine-grained caprock horizon (black chert-argillite) has slightly higher Ti/Zr values of 15 to 30, similar to values for the siliceous caprock horizon in Figure 8.4. The black chert/argillite horizon is enriched in metals, particularly Pb, Ag and Sb, but also Zn, Cu, As, Cd, U, Cr and Ni. However, in contrast to Figure 8.4, Fe is distinctly enriched in the siliceous zones.

The variation in metal contents from the white chert immediately above the orebody, to the black chert at the edge of the siliceous zone, and out into the Battle basin argillites is best shown by the plots in Figure 8.7. The metal content of the chert horizon changes dramatically with distance from ore. The white-pale grey chert, immediately above the orebody, has high Zn, Cu, As, Ni, V, U, and Cd values. At the edge of the siliceous zone, in the black chert, there is a marked increase in Pb, Sb, As and Ag, and a sharp drop in Si/Al, Zn, Cu and Cd values. In the Pb-rich black chert, SEM images (see Chapter 6) show galena growing on fine pyrite framboids, suggesting that this metal enrichment was late diagenetic. Fine (<1μm) Ag inclusions were observed in the galena during microprobe analysis, and this is consistent with the accompanying high Ag values in the black chert.

The average zinc ratio, 100 Zn/(Zn+Pb) (Huston and Large, 1987) of white chert is 93, which is very similar to the Battle basin argillites (average zinc ratio = 91), whereas the average black chert has a much lower zinc ratio of 68. The zinc ratio throughout the Battle orebody is similar to the overlying chert, and ranges from 92 to 100, with the highest ratios in the Gopher lens, and the lowest values in the upper lenses (Sinclair, 2000). Ag values are also highest in the upper lenses. Ba is moderately enriched in the Battle basin, compared with regional argillite, but shows no change in value from the chert to the Battle basin argillite. Other elements, such as S, U, V, As, Ni and Cr remain high throughout the Battle basin, but show a marked decrease in the South Flank region.

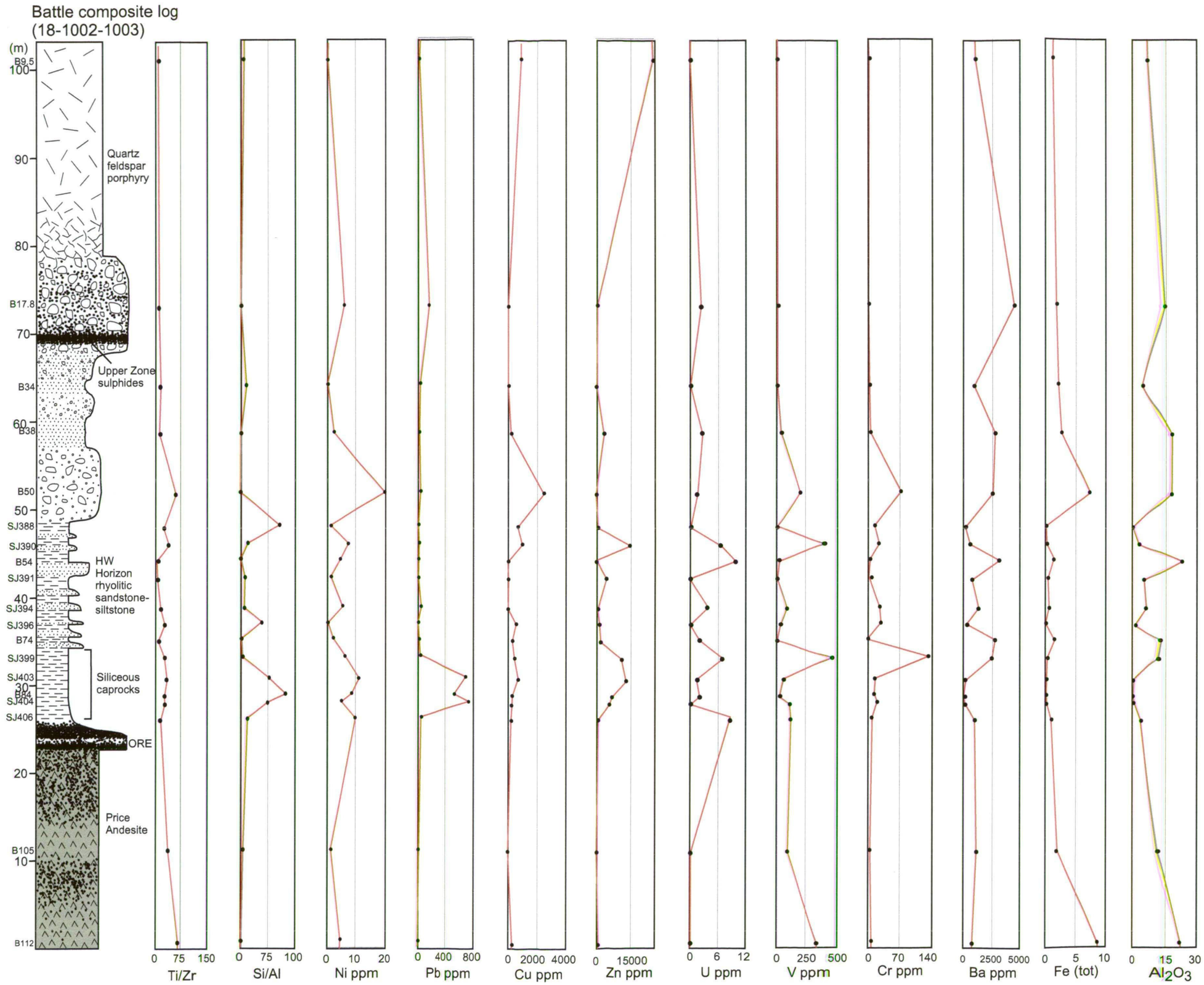

Figure 8.5: Graphic log and geochemistry plots illustrate the chemostratigraphy of the HW Horizon, above the Battle orebody. 1420E. Ti/Zr values are similar throughout the HW Horizon, with slightly higher values in the chert horizon. The high silica content of this horizon is clearly visible on the Si/Al plot. Although this horizon is metal-rich with greater contents of Pb, Ni Zn, Cr, V and U, it is not as well defined as in drillhole L14-680 (Figure 8.4). A decrease in Al_2O_3, Fe and Ba is associated with the siliceous caprocks.

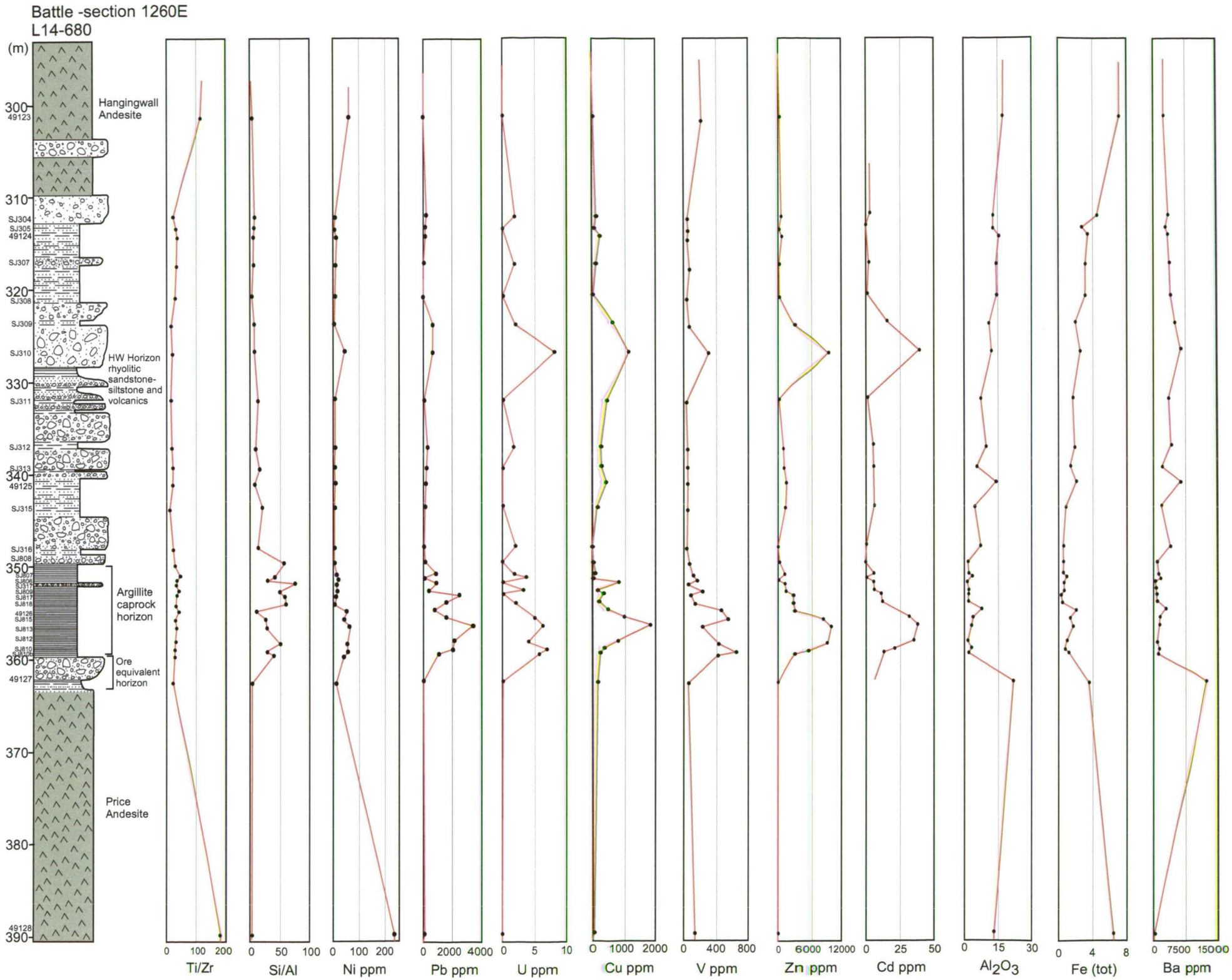

Figure 8.6: Graphic log and geochemistry plots illustrate the chemostratigraphy of the HW Horizon, south of Battle orebody. Ti/Zr values are similar throughout the HW Horizon, with slightly higher values in the argillite/black chert horizon. The silica content of this horizon is clearly visible on the Si/Al plot. This horizon forms a distinct metal-rich horizon with good correlation between Ni, Pb, U, Cu, V, Zn and Cd. Other elements such as Ba and Fe display a good correlation with Al_2O_3 suggesting that they could be associated with the detrital component.

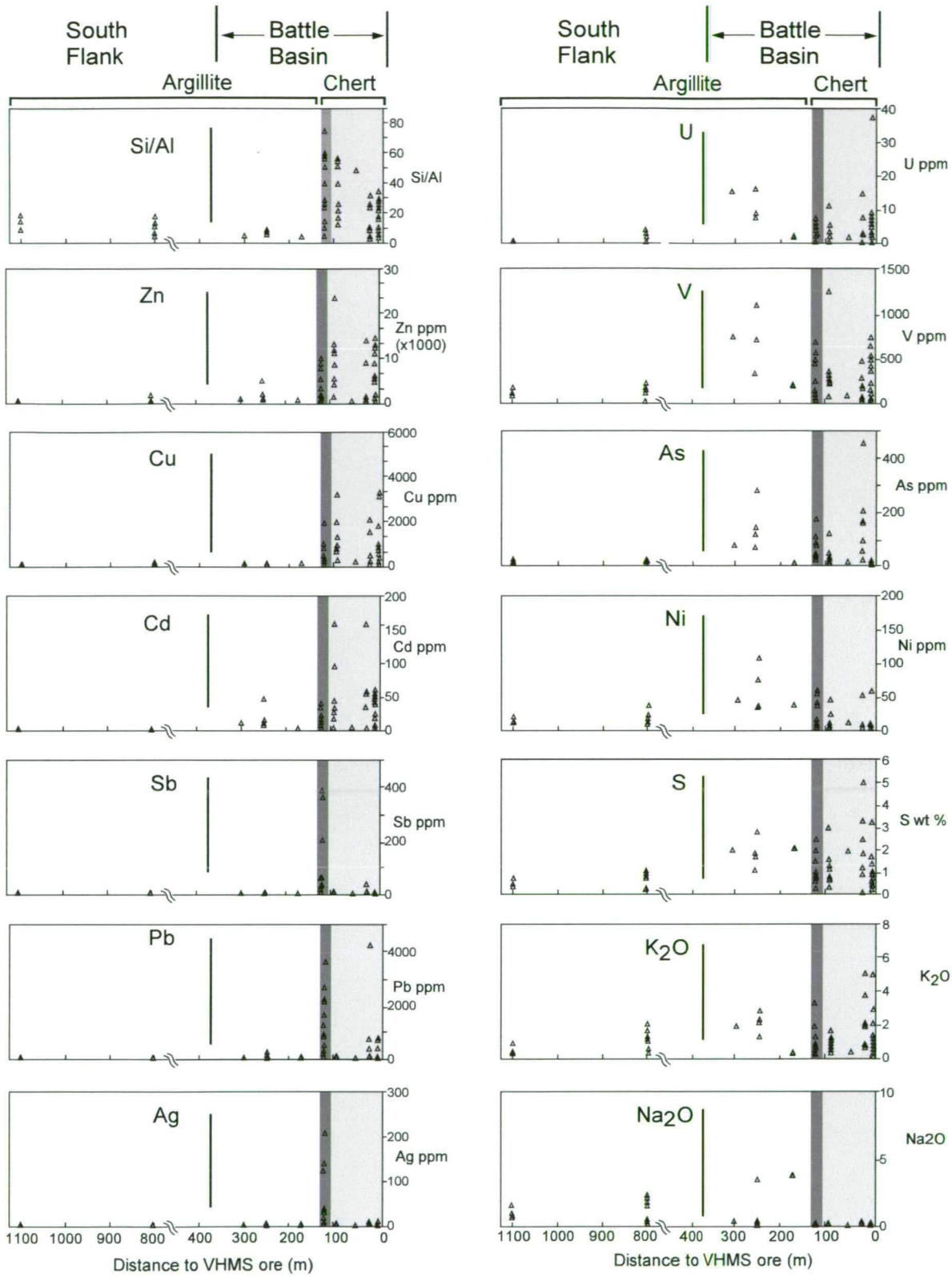

Figure 8.7: Plots illustrate major and trace element variation in the fine-grained facies (caprocks) with distance from the Battle orebody. A sharp decrease in Si/Al values marks the edge of the chert (black chert zone). This boundary is also defined by a sharp decrease in metal contents such as Zn, Cu, and Cd and a localised high in Ag, Sb and Pb. Other elements remain relatively high throughout the Battle Basin and include S, V, U, Ni and As. An increase in K_2O in the area proximal to ore is accompanied by low Na_2O levels.

Selected major and trace elements shown in Figures 8.8 and 8.9, illustrate the geochemical variation between the argillite, black chert and white chert. Strong positive correlations are displayed between immobile elements, such as Al, Zr, Ti, Ga and Sc, but also with Fe and Ba. Metals, such as Zn, Cu, Pb and Cd, show strong positive inter-element correlations, particularly Cd and Zn. Positive correlations are also displayed by transition metals such as V, Ni, Cr and As (particularly in the 'unaltered' Battle basin argillite). However, only weak correlations are observed between Cu-Zn-Pb-Cd and Ni-V-Cr-U pairs in the Battle cherts. Weak positive correlations between Pb, Ag and Sb occur in the Battle basin argillites, but no significant interelement correlations between these elements were observed in the black cherts, even though the black cherts are enriched in Pb, Ag and Sb.

The high metal values in the chert, and the close spatial association between the chert and the Battle orebody favour a hydrothermal source for the metal-rich silica bearing fluids. However, the high metal values in the unaltered Battle basin argillite indicate metal transport by an alternate process, such as a hydrothermal plume, and/or scavenging of metals from the seawater by inorganic and organic particles (e.g., Piper, 1994; Peter and Goodfellow, 1996). Metal sources in the unaltered Battle basin and argillite are examined, along with argillite from the HW basin and South Flank area, in Section 8.5.

The very strong positive correlations between Zn and Cd in the white and black chert ($n = 46$, $r^2 = 0.996$) and in the unaltered Battle argillite ($n = 8$, $r^2 = 0.98$), suggests that most or all the Cd resides in sphalerite. Microprobe analyses confirm this, with an average of 0.35wt.% Cd measured in fine sphalerites in Battle chert (Appendix 6.3). Studies of Cd:Zn ratios in sphalerites of various deposits, such as Rosebery and Hercules, NW Tasmania, indicate that Cd:Zn ratios are usually consistent throughout the deposit (e.g., Groves and Loftus-Hills, 1968). Smith and Huston (1992) suggest that the consistent correlation of Zn and Cd reflects saturation of the hydrothermal fluids in these elements. The chemical behaviour of these elements is similar and both are readily transported as chloride complexes (Mookherjee, 1962; Seward and Barnes, 1997). If so, the Zn:Cd ratio of a saturated fluid would depend only on pH and $a\mathrm{Cl}^-$, and the ratio for a given hydrothermal system would be relatively constant (Mookherjee, 1962; Smith and Huston, 1992). However, at Myra Falls, the Cd:Zn ratio for the Battle cherts is quite different to that of the unaltered Battle basin argillite. The metal content of this distal region is most likely sourced from a hydrothermal plume, and it is possible that pH and/or $a\mathrm{Cl}^-$ conditions of the buoyant pluming hydrothermal fluids, differed from subsequent silica-bearing fluids, which formed the Battle cherts. Similar variations in Zn:Cd ratios have been noted in vent fluids and sulphides from the TAG area, and were attributed to the complex interplay among

various metals and the suites of mineral being deposited in vent mounds and chimneys (Metz and Trefry, 2000).

HW argillaceous and siliceous caprocks

Finely laminated argillite is the dominant facies above the HW orebody, with only minor bleached and/or siliceous zones (Figure 6.9). Selected major and trace element variation in the argillite is shown in Figure 8.10 (drillhole 23-503, HW mine). The shaded zone at the base represents the altered horizon immediately above the massive sulphides. The Ti/Zr ratios are similar throughout, suggesting little compositional variation in the argillite with stratigraphic depth. However, the altered zone above the massive sulphides, has lower Si, Ca and Fe values, and higher values of Al_2O_3, Na_2O and Ba. Microprobe data, presented in Chapter 7, indicates that Ba resides in white micas, which may account for the correlation between Ba and Al_2O_3 in Figure 8.10.

A more detailed view of the argillite and chert immediately above the massive sulphides is shown in Figure 8.11 (sequence from drive S335C, HW mine). The Si/Al plot highlights the siliceous zones, with $SiO_2 > 80\%$ in samples SJ644, SJ642 and SJ638. These siliceous zones coincide with a decrease in Ba, Al_2O_3, Na_2O, CaO, V, Cu and Fe, and may reflect silica dilution from hydrothermal alteration.

The xy scatter plots in Figure 8.12, compare major and trace element variation in the unaltered argillite and the 'altered' zone immediately above the massive sulphides. The argillite and 'altered' argillite form linear trends on the TiO_2-Al_2O_3 and Ga-Al_2O_3 plots, suggesting mass loss and mass gain from a common precursor (e.g., MacLean and Kranidiotis, 1987; Herrmann, 1998). However, the Al-Zr and Ti-Al relationships indicate that the 'altered' argillite from drive S335C, may have a slightly different precursor to 'unaltered' argillite sampled elsewhere. These relationships suggest that mass balance calculations between the 'unaltered' argillite and the 'altered' argillite would not be appropriate.

The majority of black argillite samples are strongly siliceous (>75% SiO_2). Silica deposition most likely occurred during early diagenesis, as early sedimentary features are preserved and non-compacted (e.g., the circular form of radiolarian tests is commonly preserved, Figure 6.22). The 'altered' argillite appears to be less siliceous than the typical black argillite and has a greater content of Zr, TiO_2, Al_2O_3 and Ga. This increase in 'immobile' elements could be partly due to mass loss (e.g., MacLean and Kranidiotis, 1987; Herrmann, 1998).

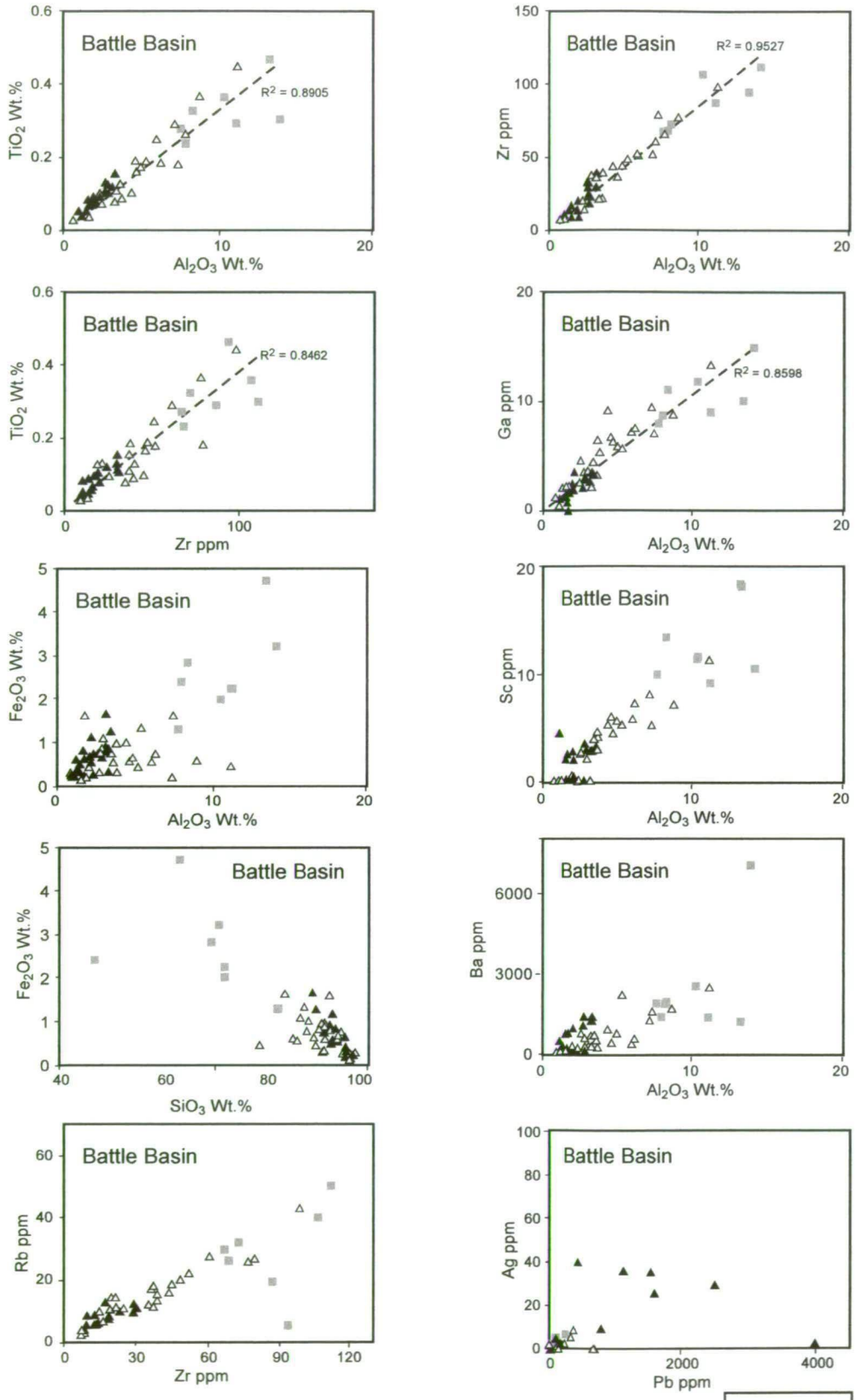

Figure 8.8: Scatter plots illustrate selected major and trace element variation between the Battle Basin argillite, black chert, and white-pale grey chert above the Battle orebody (see discussion in text).

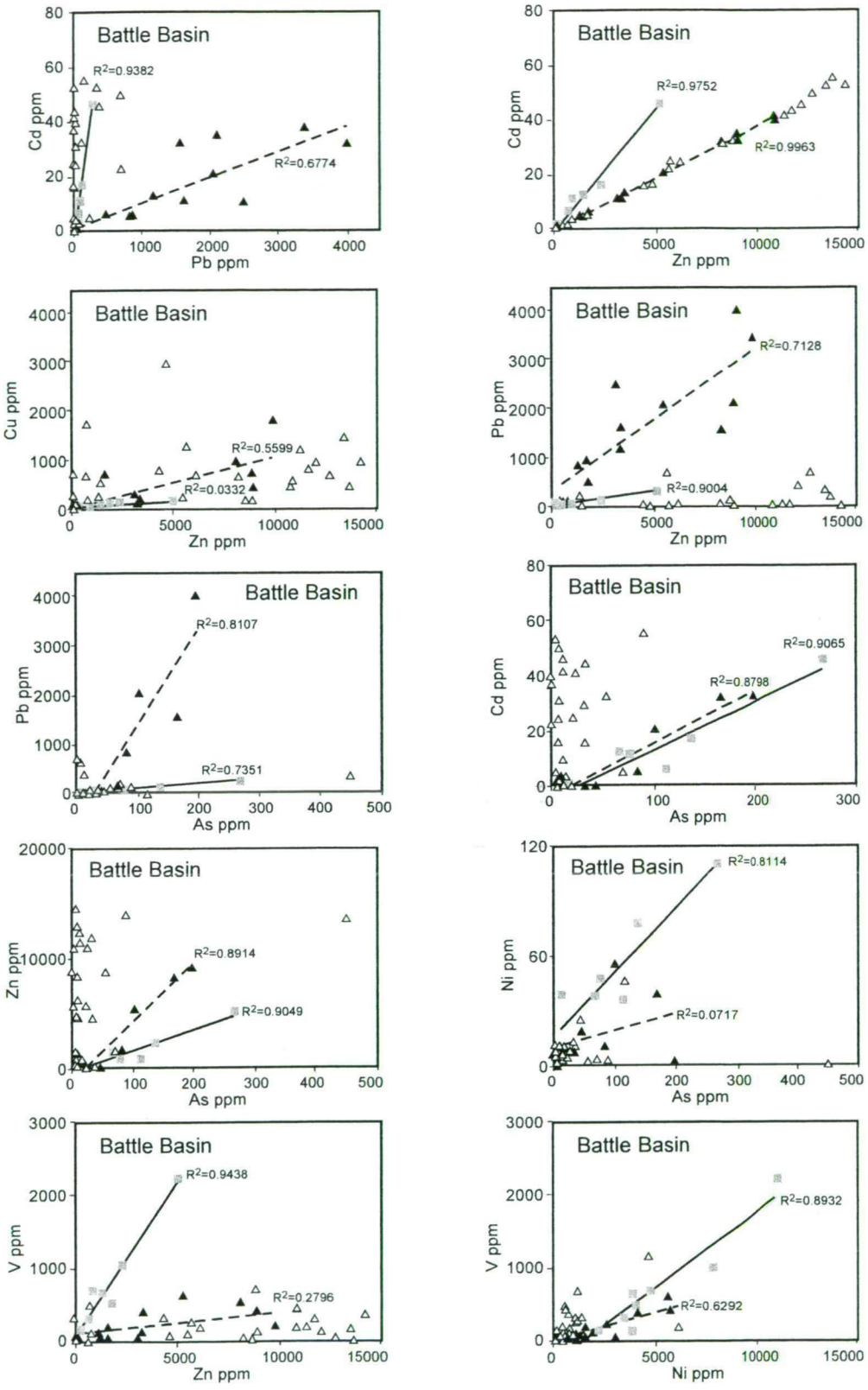

Figure 8.9: Scatter plots illustrate selected major and trace element variation between the Battle Basin argillite, black chert, and white-pale grey chert above the Battle orebody (see discussion in text).

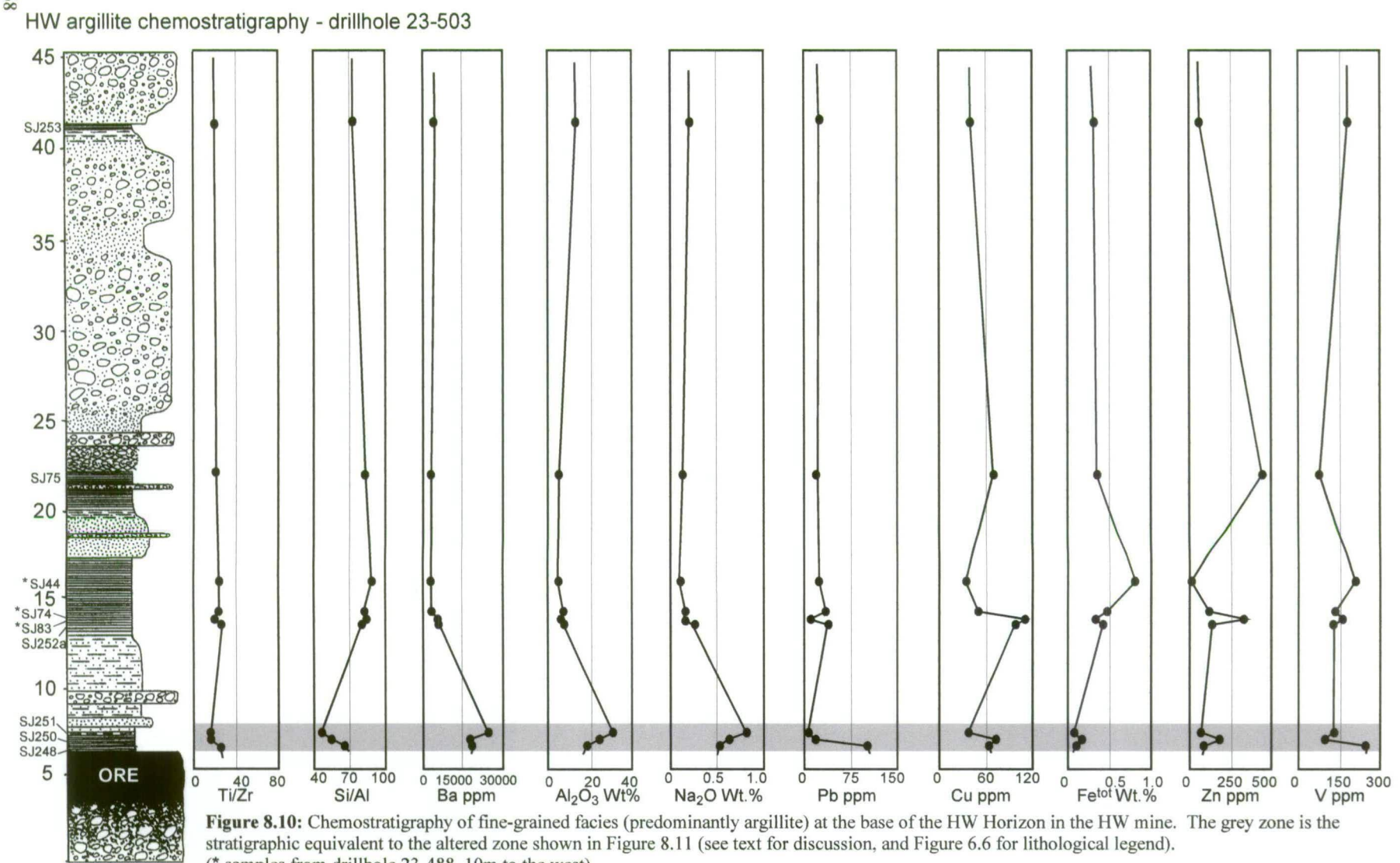

Figure 8.10: Chemostratigraphy of fine-grained facies (predominantly argillite) at the base of the HW Horizon in the HW mine. The grey zone is the stratigraphic equivalent to the altered zone shown in Figure 8.11 (see text for discussion, and Figure 6.6 for lithological legend). (* samples from drillhole 23-488, 10m to the west).

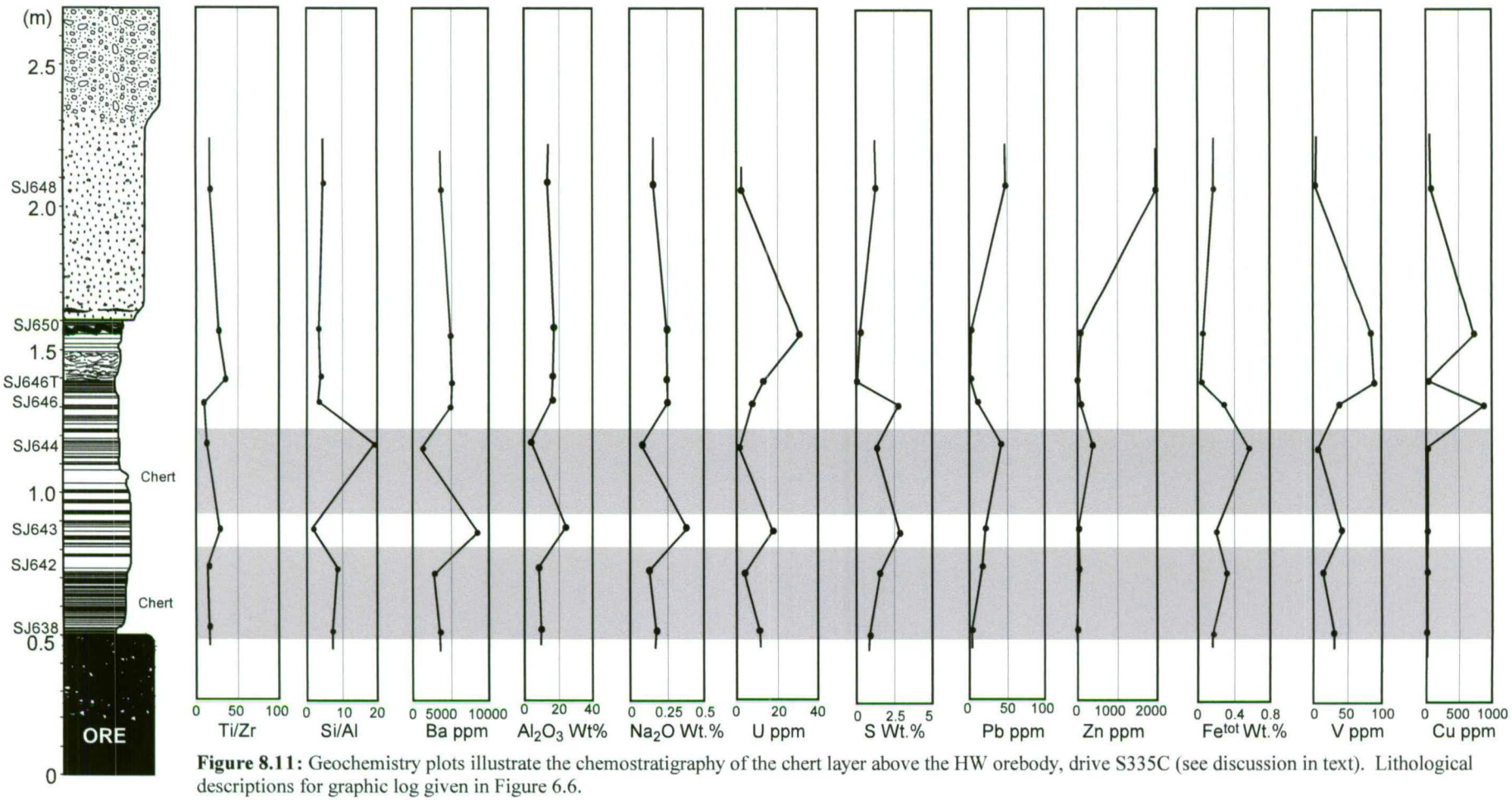

Figure 8.11: Geochemistry plots illustrate the chemostratigraphy of the chert layer above the HW orebody, drive S335C (see discussion in text). Lithological descriptions for graphic log given in Figure 6.6.

Comparison of Battle and HW caprocks chemostratigraphy

Major and trace element geochemistry of the Battle caprocks, differ markedly from the HW orebody caprocks. Above the Battle orebody, the fine-grained caprock horizon predominantly consists of pale silicified argillite grading out to black silicified argillite (black chert) at the edge of the siliceous zone, with SiO_2 contents generally >90 wt.%. In comparison, the caprock horizon above the HW orebody is dominated by black graphitic argillite with only localised siliceous and/or bleached zones, and an absence of black chert.

Immobile element plots of the Battle caprocks and adjacent Battle basin argillite clearly show the chert to be the altered equivalent of the argillite (mass balance calculations between these units are presented in the following section). However, in the caprock horizon above the HW orebody, Al-Zr-Ga relationships suggest that the 'altered' argillite zones may have a different precursor to the 'unaltered' argillite sampled elsewhere. The alteration in these localised zones may be too complex to undertake simple mass balance calculations, instead, a more detailed study would be necessary.

The difference in style and intensity of alteration above the Battle and HW orebodies most likely reflects the timing of ore formation and deposition of the caprock horizon. Petrological evidence, such as radiolarian tests infilled by quartz, apatite, rutile and minor sulphides, indicates that the Battle orebody formed during and after deposition of the caprock horizon. Hydrothermal alteration associated with ore formation resulted in the silicification of the overlying porous seafloor muds. Petrological and sedimentological evidence, such as the abundance of ore clasts in mass flow units overlying the HW orebody, indicate that the HW orebody formed on the seafloor, prior to deposition of the caprock horizon. Therefore, only minor hydrothermal alteration, associated with the waning stages of ore formation, would affect the overlying fine-grained sediments. The localised 'altered' argillite zones may have formed close to a late-stage vent and could an exhalative component. Alternatively, these zones may represent feeder zones for the minor upper ore lenses, which are located at the top of the HW Horizon.

The difference in style and intensity of hydrothermal alteration of hangingwall rocks above the Battle and HW orebodies is also shown by SWIR spectral mapping of white mica and chlorite (Chapter 7). A large alteration halo is developed in hangingwall rocks above the Battle orebody. In comparison, only patchy alteration zones are present in HW hangingwall rocks.

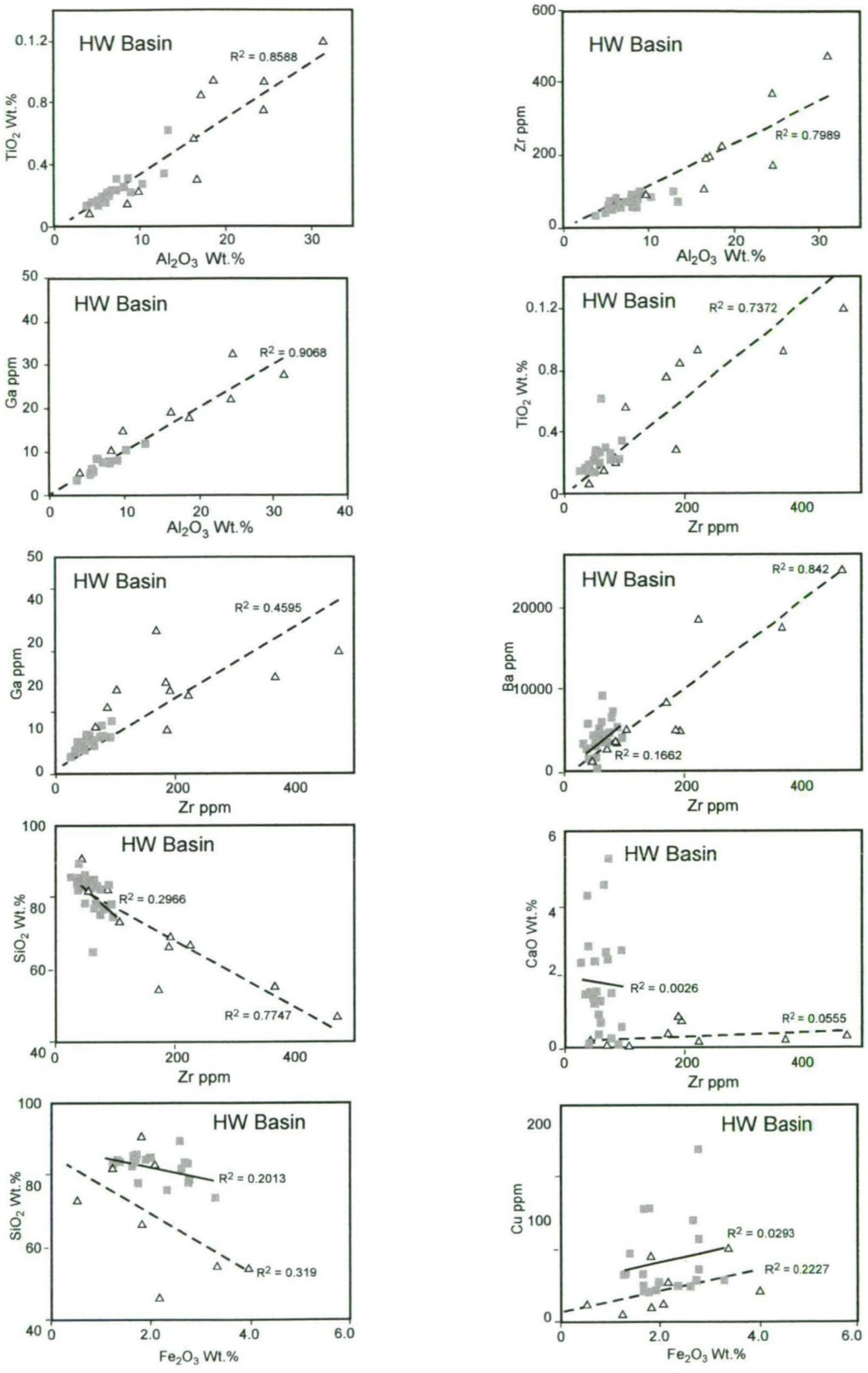

Figure 8.12: Scatter plots illustrate selected major and trace element variation in HW Basin argillite and 'altered' argillite (see discussion in text).

8.5 Mass balance of siliceous caprocks above the Battle orebody

8.5.1 Mass balance equations

Immobile element plots (Figure 8.4), indicate that the chert above the Battle orebody is the silicified equivalent of the adjacent argillite in the Battle basin. Mass balance calculations can be used to estimate the gains and losses in major and trace elements associated with silica deposition above the Battle mine. The fact that the unaltered argillite has the same sedimentary composition to the adjacent chert, reduces the effect of lithological variation on the mass balance equations.

Gresens (1967) defined a set of composition-volume relations between altered and unaltered rocks to describe the effects of metasomatic alteration. Mass balance equations involve the correction of an analysis by using a correction factor (CF) for mass change, and subtraction of the original protolith composition for each element to give net mass change. The correction factor, CF = immobile component (unaltered)/immobile component (altered), e.g., CF = $Al_2O_{3fresh}/Al_2O_{3altered}$ (Lentz, 1996). Mass gains and losses of the mobile components causes changes in the concentration of immobile elements, but the inter-element ratios of immobile elements will not vary (Herrmann, 1998).

To test the immobility of an element, immobile element pairs, such as Zr-Ti, Al-Ti, are plotted on xy scatter plots. If immobile, they should form narrow linear trends, which pass through the origin (MacLean and Kranidiotis, 1987; MacLean and Barrett, 1993). Mass gains and losses will cause a spread of data along the linear trend. Net mass gains, move the rocks toward the origin, whereas net mass losses move data in the opposite direction (Finlow-Bates and Stumpfl, 1981).

Grant (1986) and subsequently Huston (1988, 1993) modified these mass balance equations to provide a graphical method, the isocon diagram, to show gains and losses associated with hydrothermal alteration. The isocon diagram is a plot of scaled major and trace elements of altered rocks against unaltered rocks to illustrate changes in composition. Immobile elements, such as Al, Ti, P, Zr, Nb and Y, should plot along a straight line (the isocon) which passes through the origin (Grant, 1986). The slope of this line depends on addition (or subtraction) of net mass without gain or loss of the immobile elements, and can be estimated from a best-fit line through the immobile elements. Deviation of data away from the isocon defines the change in concentration for the corresponding component. Elements that plot above the isocon have been relatively enriched, while elements plotting below the isocon have been relatively depleted. The graphical technique of Huston (1988; 1993) requires that for graphical presentation, elements are sequenced such that, 1) elements that underwent large mass gains are early in the sequence; and 2) elements that underwent mass

losses are late in the sequence; and 3) immobile elements are interspersed evenly throughout.

Huston (1988) suggests that there are several limitations to calculating mass changes in this way: 1) mass changes are calibrated against a least-altered equivalent, which may or may not be the protolith to the altered rock, depending on the available geological control; and 2) the least altered equivalent could contain internal variation in composition, such as igneous fractionation, independent of alteration. For these reasons, the careful selection of the least altered sample is a critical part of the mass balance equation. In this study, the selection of the least altered sample was based on petrographic and sedimentological similarities, and the immobile element ratios. To minimise the effect of internal compositional variation in the unaltered sample, an average of 8 unaltered Battle basin argillites was used (see Table 8.1, full results listed in Appendix 3). Average values of the altered samples were also chosen, to reduce the effect of variable alteration in the silicified argillite.

8.5.2 Battle chert/argillite mass balance

The isocon diagram, Figure 8.13a, illustrates major and trace element gains and losses between the least-altered Battle basin argillite and the white-grey chert immediately above the Battle orebody, and the black chert at the edge of the siliceous caprock horizon. The 'unaltered equivalent', used in the mass balance equations, is an average of 8 unaltered Battle basin argillites (REE are based on an average of 4 samples). The white chert mass balance equations are based on an average of 32 white chert samples (REE are based on an average of 5 samples). above the Battle orebody, and the black chert is based on an average of 14 black chert samples (REE are based on an average of 3 samples) (see Table 8.1, full results listed in Appendix 3).

In general, most elements, including the 'immobile' elements, display a net loss in both the white and black cherts, due to dilution by mass addition of silica. The isocon slopes for the white and black cherts in Figure 8.13a are based on the position of immobile elements, Zr, Ti, Ga, Nb and Al. The isocon slope for the white chert is 0.391, with $r^2 = 0.964$ (n = 32), and 0.286 with $r^2 = 0.783$ (n = 14) for the black chert. Net mass gain in the white and black cherts are indicated by the low value of the isocon slopes (<1) (e.g., Huston, 1987, 1993).

In the white chert, large relative gains are shown by Si, Cu, Cd and Zn, moderate relative gains by As, Sb, Ag and Pb and moderate relative losses are shown by Sr, Mg, Ca, P, Na and REE (discussed in next section). In the black chert, large relative gains are shown by Si, Sb, Ag, S, Pb, Cu, Cd and Zn, and moderate relative losses are displayed by Sr, Mn, Na,

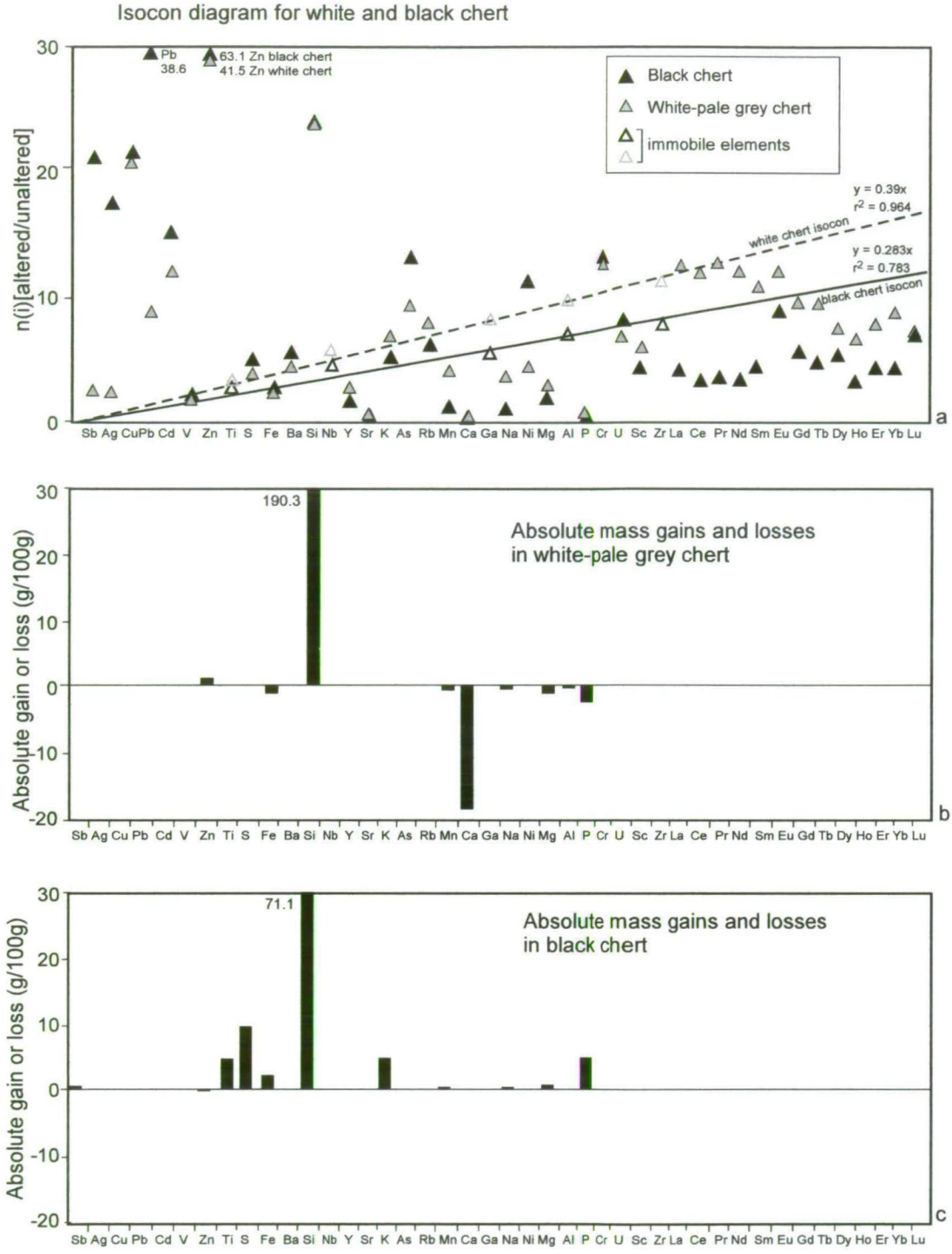

Figure 8.13: Mass balance diagrams for the siliceous caprocks above the Battle orebody (white chert) and the black chert at the edge of the siliceous horizon. Mass balance equations are based on unaltered Battle Basin argillite (average of 8 samples), and averages of 32 white chert samples and 14 black chert samples. **a)** Isochon diagram illustrates the relative gains and losses. Isocon slopes are based on the following immobile elements, Zr, Ti, Ga, Nb and Al, and as both slopes are <1, mass gains are indicated for the chert. Most major and trace elements in the white and black chert plot below the isocon slopes, indicating depletion in these elements accompanied the addition of silica in the fine sediments above the Battle orebody. The marked increase in SiO_2 is accompanied by addition of Zn, Pb, Cu, Sb, Cd and Ag; **b)** absolute gains and losses of major and trace elements in white-pale grey chert; **c)** absolute gains and losses of major and trace elements in black chert.

Mg, Ca, P, and REE (discussed in next section). However, the errors associated with the isocon for the black chert ($r^2 = 0.783$, n = 14), are much greater than for the white chert, and the accuracy of this mass balance calculation is reduced.

The histograms in Figures 8.13b and 8.13c illustrate the absolute gains and losses in the white and black cherts. The dominant effect of the alteration is the mass addition of silica, reflecting the intense silicification of the seafloor mudstones. Mass balance calculations indicate that SiO_2 increases by nearly 200% (190g/100g) in the white chert above the Battle orebody and about 70% (71g/100g) in the black chert at the edge of the siliceous alteration zone. In comparison, most other elements show very small absolute mass changes of less than about 6g/100g, apart from CaO, which records an absolute mass loss of –18g/100g. Absolute mass gains were observed for most metals in the chert, relative to the adjacent unaltered argillite. In the white chert, absolute mass gains included Cu (0.2g/100g), Pb (0.06g/100g), Ba (0.03g/100g) and Zn (1.5g/100g). In the black chert, absolute mass gains included Sb (0.19g/100g), Ag (0.06/100g), and Pb (0.1g/100g).

8.6 Rare Earth Elements

Fractionation of rare earth elements (REE) due to subtle differences in ionic size and behaviour, makes them useful as tracers of many physical and chemical processes. REE all form stable 3+ ions of similar size, but Ce and Eu are particularly useful, as these elements exist in additional oxidation states, Ce^{4+} and Eu^{2+}. These form a smaller and larger ion respectively, relative to the 3+ oxidation state (Rollinson, 1993).

REE were measured in 15 argillite, 5 white chert and 3 black chert samples from the base of the HW Horizon. REE were normalised to chondrite values from Boynton (1984), to enable wide comparison with the literature, and were also normalised to the average shale SDO-1 (Huyck, 1990), to enhance differences between Myra Falls argillite and chert from the different depocentres, including the Battle and HW basins, and the South Flank.

8.6.1 REE results

Chrondite-normalized rare earth element (REE) patterns for argillite and chert samples from the basal part of the HW Horizon (caprock horizon) are shown in Figure 8.14, with average values for each area listed in Table 8.2. The REE patterns for the argillite and chert are similar, with most samples displaying weak to moderate enrichment in LREE. However, subtle differences do exist between the argillite and chert and these are examined in detail. REE values for average shale standards, NASC (Gromet et al., 1984), PAAS (Taylor and McLennan, 1988), and SDO-1 (Huyck, 1990), are shown in Figure 8.14f.

	Average Battle white chert (n = 5)	Average Battle black chert (n = 3)	Average Battle basin argillite (n = 4)	Average HW basin argillite (n = 5)	Average regional argillite (n = 6)	Average Shale SDO-1
La	4.0	2.0	14.4	14.2	15.6	38.5
Ce	7.0	3.0	26.8	26.6	27.3	79.3
Pr	0.9	0.4	3.5	3.5	3.6	8.9
Nd	3.7	1.6	14.7	14.2	14.8	36.6
Sm	0.8	0.5	3.4	3.4	3.5	7.7
Eu	0.3	0.3	1.2	0.7	1.0	1.6
Gd	0.8	0.7	3.6	3.9	3.6	6.5
Tb	0.1	0.1	0.6	0.7	0.6	1.2
Dy	0.8	0.7	3.7	4.6	3.6	6.0
Ho	0.2	0.1	0.8	1.0	0.8	1.2
Er	0.5	0.4	2.5	3.1	2.2	3.6
Yb	0.6	0.4	2.6	3.0	2.1	3.4
Lu	0.1	0.1	0.4	0.5	0.3	0.5
La/Yb	6.7	5.0	5.5	4.7	7.4	11.3
Eu/Eu*	1.6	0.7	1.5	0.8	1.2	1.0
Ce/Ce*	0.8	0.6	0.8	0.8	0.7	0.9

Table 8.2: Average rare earth element values for Myra Falls chert and argillite and the average shale SDO-1 (Huyck, 1990). Eu/Eu* and Ce/Ce* values are normalised to NASC (Gromet et al, 1984).

Myra Falls argillite and chert data are normalised against the SDO-1 shale standard, and these plots are shown in Figure 8.15.

The degree of LREE enrichment is described by the use of La/Yb ratios, and Eu anomalies are defined by the expression of McLennan (1989):

$$\frac{Eu}{Eu^*} = \frac{Eu_n}{(Sm_n \times Gd_n)^{0.5}}$$

Where n is the NASC normalising value, the average of composite shales from North America (Gromet et al., 1984). Ce anomalies are defined by the expression of Toyoda and Masuda (1991):

$$\frac{Ce}{Ce^*} = \frac{5Ce_n}{(4La_n + Sm_n)}$$

Argillite REE patterns

On chondrite-normalised plots (Figure 8.14a) the regional argillites display weak LREE enrichment, resulting in consistent gently sloping REE patterns, with La/Yb ratios ranging

from 5.6 to 8.7, slightly lower than the average shale (Table 8.2). Although the regional argillites show a large spread in REE contents, the patterns are consistent. They are generally much smoother than HW and Battle basin argillite and chert, as Eu and Ce anomalies are very weak or absent. The Eu/Eu* values range from 0.8 to 1.2, which are very similar to the average shale. The similar Eu/Eu* values and La/Yb ratios result in very flat patterns on the shale-normalised plots (Figure 8.15a).

HW basin argillites display similar patterns to the regional argillites on chondrite-normalised plots, with no Ce anomaly, but with slightly less LREE enrichment, and pronounced negative Eu anomalies (Figure 8.14b). La/Yb ratios are predominantly lower,

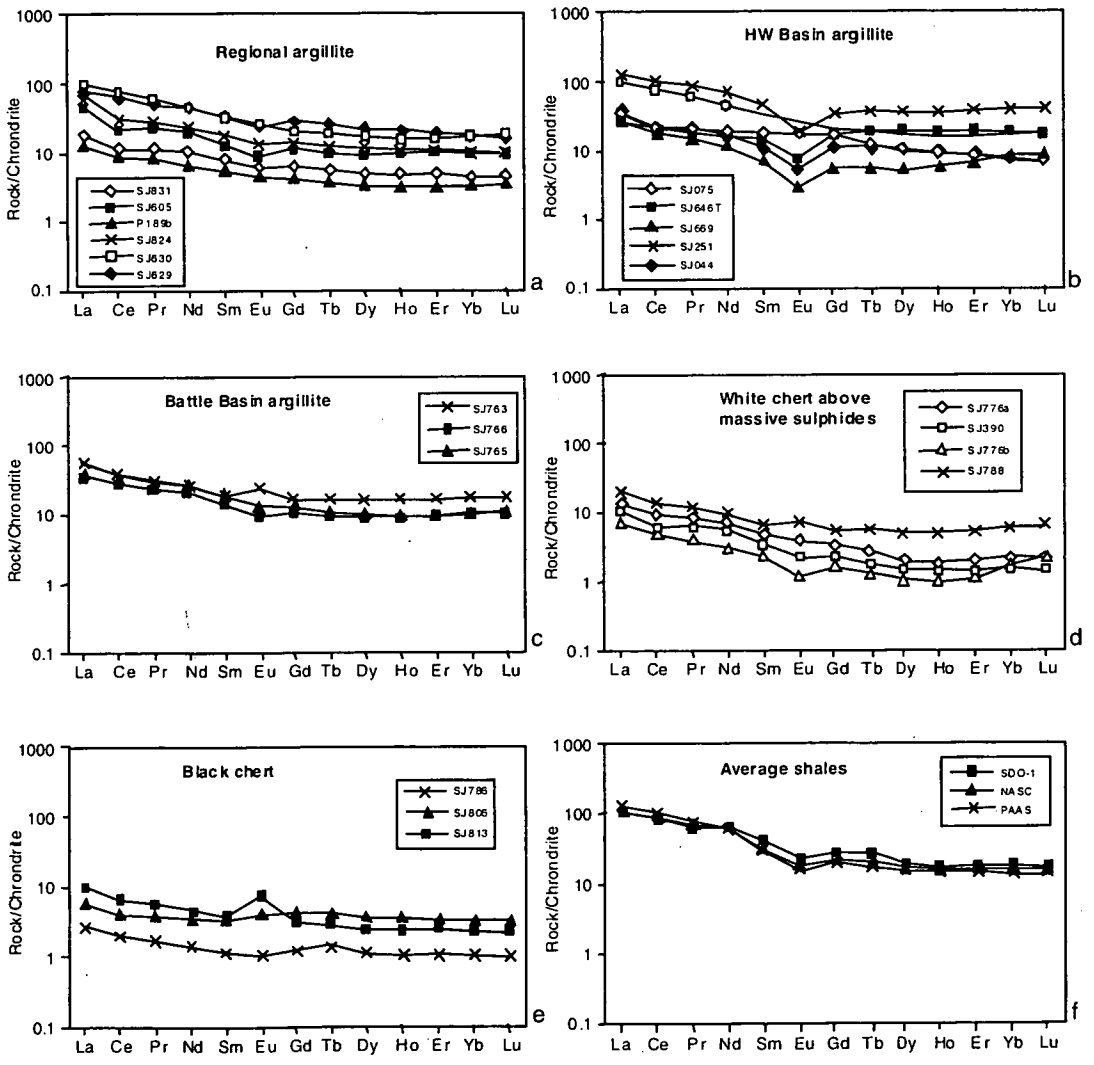

Figure 8.14: Chondrite-normalised rare earth element plots for Myra Falls argillite and chert (samples from the base of the HW Horizon). Chondrite values from Boynton (1984); average shale values from SDO-1 (Huyck, 1990); North American Shale Composite (NASC) from Gromet et al. (1984); and Post Archaean Average Shale (PAAS) from Taylor and McLennan (1988).

ranging from 2.1 to 7.7 (average = 4.7), with most significantly lower than the average shale, SDO-1 (Huyck, 1990) (Table 8.2). The HW basin argillites also have low Eu/Eu* values, ranging from 0.5 to 1.2, resulting in strong negative Eu anomalies on chondrite-normalised plots, and weak negative Eu anomalies on shale-normalised plots (Figure 8.15b). The HW basin argillites can be clearly distinguished from the regional argillites on the shale-normalised plots (except SJ251), by the depletion in LREE relative to the average shale.

Battle basin argillites also display weak LREE enrichment on chondrite-normalised plots, and weak LREE depletion on shale-normalised plots, with La/Yb ratios ranging from 2.3 to 7.3 (Figure 8.14c). Weak positive Eu anomalies are present on chondrite-normalised plots with Eu/Eu* values ranging from 0.6 to 1.5 (sample SJ763, about 300m from the

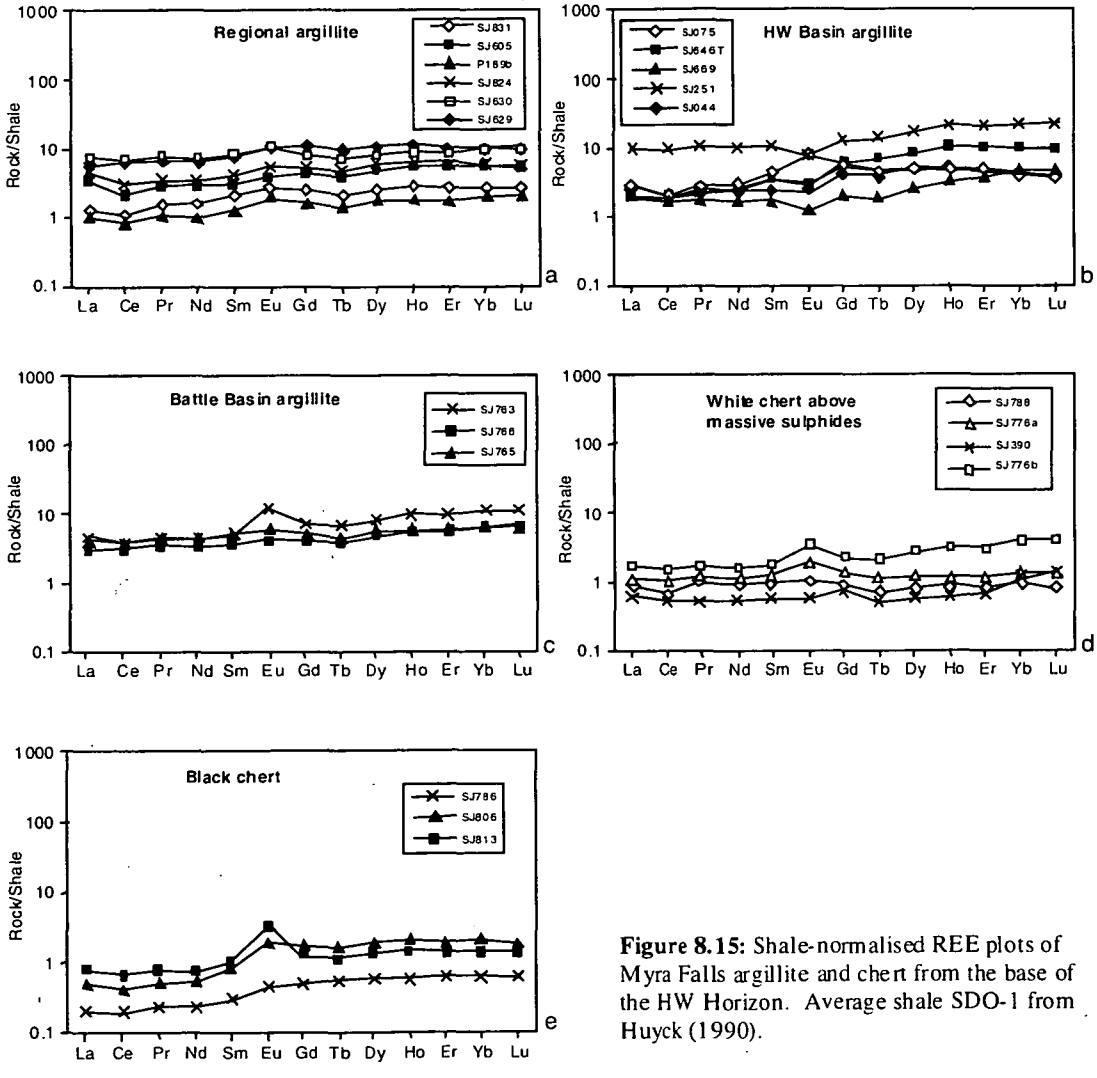

Figure 8.15: Shale-normalised REE plots of Myra Falls argillite and chert from the base of the HW Horizon. Average shale SDO-1 from Huyck (1990).

orebody, has the largest positive Eu anomaly). The positive Eu anomalies are slightly more pronounced on the shale-normalised plots, and there is no discernable Ce anomaly.

White chert REE patterns

The white chert above the Battle orebody has a similar REE pattern to the regional argillites on chondrite-normalised plots (Figure 8.14d), but with much lower REE contents, and weak positive Eu anomalies (Eu/Eu* values range from 0.7 to 1.3). LREE enrichment is indicated by La/Yb ratios ranging from 5.0 to 10.5. The positive Eu anomalies are slightly more pronounced on the shale-normalised plots, particulary sample SJ776b (Figure 8.15d). No appreciable Ce anomaly is present.

Black chert REE patterns

The black chert, which is located at the edge of the siliceous alteration, displays similar REE patterns to the white chert on chondrite-normalised plots, but with a more pronounced positive Eu anomaly in sample SJ813 (Figure 8.14e). Weak LREE enrichment is shown by La/Yb ratios ranging from 3.7 to 6.3, distinctly lower than the white chert. Eu/Eu* values range from 0.9 to 2.3, resulting in pronounced positive Eu anomalies on the shale-normalised plots (Figure 8.15e).

8.6.2 Interpretation of REE results

Interpretation of argillite REE patterns

The regional argillites have REE patterns very similar to the average shales (NASC, PAAS and SDO-1), resulting in very flat trends on shale-normalised plots. The large spread in REE contents of the regional argillites may reflect varying degrees of silicification and dilution of REE contents. Most argillites at Myra Falls have SiO_2 contents greater than 50 wt.% (Table 8.3), and the silicification may reflect early diagenetic processes and/or the effects of greenschist metamorphism (discussed in section 8.7.2).

The strong negative Eu anomaly of HW basin argillites and the LREE depletion relative to the average shale (SDO-1), result in marked differences between HW basin argillites and regional argillites on shale-normalised plots (Figure 8.15a-b). Most HW basin argillites have negative Eu anomalies, but a positive Eu anomaly has been reported in a mudstone sample above the HW orebody by Barrett and Sherlock (1996), and was reported to be indicative of a hydrothermal input (see discussion below). The strong negative Eu anomalies, displayed by most HW basin argillites, may reflect loss of Eu due to alteration of volcanic glass (and/or plagioclase?) to sericite, due to the anomalously high Eu contents of plagioclase and volcanic glass (e.g., Graf, 1977; Campbell et al., 1988; Michard et al.,

1983; Michard and Albarede, 1986; Peter and Goodfellow, 1996). The distinct Eu anomaly could also reflect differences in the sedimentary source of the HW basin argillites, with a greater input of rhyolite-rhyodactite into these sediments. Negative Eu anomalies are common in rhyolite, and Figure 8.16f shows REE element patterns from rhyolite in the HW basin, which has moderate negative Eu anomalies (Barrett and Sherlock, 1996). Alternatively, regional argillite from the South Flank and Thelwood Valley may have had greater seawater interaction and contain a greater proportion of hydrogenous Eu.

The HW basin argillites also display relative LREE depletion on shale-normalised plots, making them distinct from the regional argillite (Figure 8.15c). This feature is also displayed by the Battle basin argillite and the black chert (Figure 8.15d-e), and suggests slight mobility of the LREE, relative to the HREE. LREE mobility is reported by Barrett and Sherlock (1996) in sericitized rocks above the HW orebody and has also been reported from altered volcanic rocks near the Phelps Dodge and Ansil VHMS deposits in the Abitibi Greenstone belt (MacLean, 1988; Barrett et al., 1981).

The Battle basin argillites have similar REE patterns to the HW basin argillite, but Eu anomalies are positive in Battle basin argillite. Positive Eu anomalies are thought to result from the preferential incorporation of Eu^{+2} into the hydrothermal fluids, during fluid-rock interactions at high temperatures under reducing, slightly acid conditions (e.g., Michard et al., 1983; Michard and Albarede, 1986; Lentz and Goodfellow, 1996). In general, reduced fluids favour Eu^{2+}, therefore preserving Eu anomalies (Peter and Goodfellow, 1996). Figure 8.16b illustrates typical positive Eu anomalies in hydrothermal vent fluids from the East Pacific Rise (Peter and Goodfellow, 1996). A hydrothermal origin for the positive Eu anomalies in the Battle basin argillite and Battle chert, is consistent with the greater degree of metal enrichment in these sediments (see discussion in Sections 8.7.3 and 8.7.4).

The absence of a strong Ce anomaly in Myra Falls argillite and chert may reflect the redox conditions of the basins, during deposition of the mudstones and formation of the Battle chert. Ce/Ce* values less than 0.9 are considered to be negative and all Myra Falls samples have Ce/Ce* values close to or < 0.9 (Table 8.2). In 'normal' oxidised seawater, Ce^{3+} is oxidised to Ce^{4+}, which is highly insoluble and is preferentially incorporated into precipitates. Therefore, Ce becomes depleted relative to other REE under oxidising conditions (Hogdahl et al., 1968; Masuda and Ikeachi, 1979; Peter and Goodfellow, 1996). Figure 8.16a shows the typical negative Ce anomaly in seawater from the Atlantic and Pacific (De Baar et al., 1985; Hogdahl et al., 1968), while Figure 8.16d, shows the strong negative Ce anomaly in Cyprus umbers and ochres (Robertson and Fleet, 1976). In

comparison, the deep anoxic ocean waters of the Cariaco Trench have no Ce anomaly, probably due to the dissolution of Ce under reducing conditions (De Baar et al., 1988).

Interpretation of Battle chert REE patterns

The dominant feature of the black and white chert above the Battle deposit is the much lower REE contents, compared to the average shale and Myra argillite. This is most likely a result of dilution by the addition of silica (e.g., Skirrow and Franklin, 1994; Barrett and Sherlock, 1996; Peter and Goodfellow, 1996). Mass balance calculations between the unaltered Battle basin argillite and Battle chert (Section 8.5.2, Figure 8.13), indicate mass addition of up to 70% SiO_2 in the black chert, and close to 200% SiO_2 in the white chert. Gresens analysis, indicate mass losses in REE, with most plotting well below the chert isocons. However, LREE in the white chert, plot on or very close to the white chert isocon, which could suggest immobility in these elements (La, Ce, Pr and Nd). However, the white

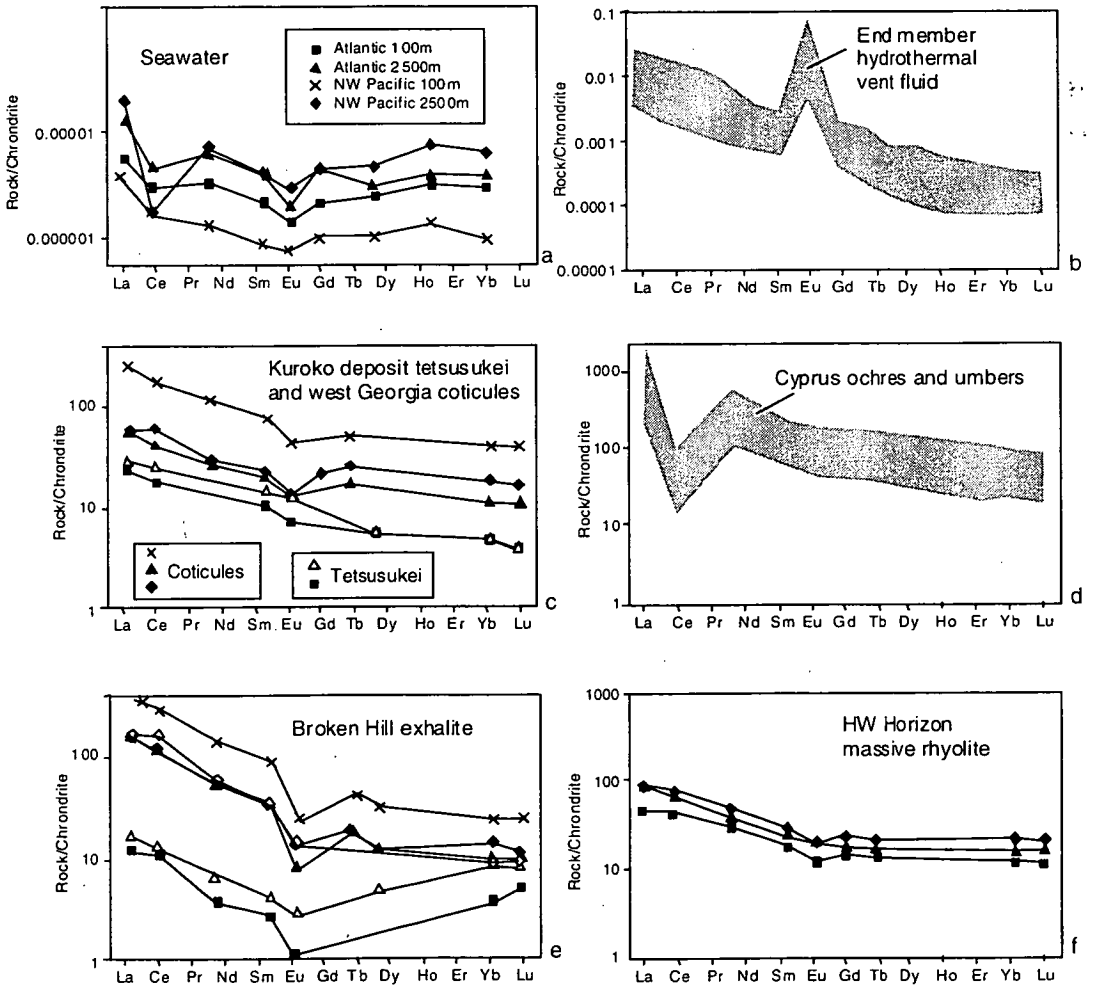

Figure 8.16: Chondrite-normalised REE plots for seawater, endmember hydrothermal vent fluids, chemical sediments and HW Horizon rhyolite. REE data and references for seawater, hydrothermal fluids, Kuroko tetsusukei, Cyprus ochres and umbers, and Broken Hill exhalite in Peter and Goodfellow (1996); HW Horizon massive rhyolite REE data from Barrett and Sherlock (1996).

cherts on chondrite-normalised plots (Figure 8.14) clearly show LREE enrichment, relative to the black chert and Battle basin argillites. Metal-bearing hydrothermal fluids mobilised metals through the cherts and introduced external reduced silica, and it is probable that LREE were introduced too. LREE enrichment in intensely silicified zones has been described by Peter and Goodfellow (1996), for the silicified stockwork zone beneath the Brunswick No. 12 deposit.

Positive Eu anomalies are displayed by many chert samples, with Eu/Eu* values ranging from 0.7 to 2.3. However, these are still relatively low when compared with hydrothermal sediments, such as the iron formations of the Brunswick Horizon, which have Eu/Eu* values ranging from 0.29 to 11.80 (Peter and Goodfellow, 1996). Although in other hydrothermal sediments, such as the Kuroko tetsusukei, Cyprus umbers and ochres and Broken Hill exhalites, positive Eu anomalies are absent (e.g., Figures 8.16c-e). Peter and Goodfellow (1996) suggest that the Eu anomaly is not present in modern and ancient sediments of oxidised oceans, because of the rapid oxidation of hydrothermal Eu^{2+} to Eu^{3+} in the water column. The preservation of Eu anomalies in the Battle and HW basin argillites may partly reflect the bottom water redox conditions of these basins (see paleoenvironmental analysis, Section 8.8).

8.7 Argillite geochemistry

8.7.1 Introduction

This section examines geochemical variation, in particular, metal enrichment, in the argillite near the base of the HW Horizon. Battle and HW basin argillite appears to be enriched in metals, relative to argillites from regional areas, which include the Thelwood Valley and South Flank, and average shale standards such as NASC (Gromet et al., 1984) and SDO-1 (Huyck, 1990). This section examines the variation in metal enrichment throughout the mine property and determines the likely source of the metals.

8.7.2 Argillite characteristics

Average major and trace element characteristics of the argillite from the caprock horizon are listed and compared to the average shale SDO-1 (Huyck, 1990) in Table 8.3. Myra Falls argillite has much greater SiO_2 contents than the average shale, which may in part reflect early diagenetic processes or the effects of greenschist metamorphism. Preserved features such as spherical radiolarians (e.g., Figure 6.22), suggest that at least some silicification occurred prior to compaction.

Myra Falls argillite is Fe and Mn-poor, relative to SDO-1, and predominantly has low CaO contents, < 2.00 wt.%, and low P_2O_5, < 0.60 wt.%. The trace element content of argillite

	Average Battle Basin argillite n = 7	Average HW Basin argillite n = 16	Average Thelwood-Price argillite n = 11	Average South Flank argillite n = 13	Average shale standard SDO-1
Wt.%					
SiO_2	73.64	82.88	75.03	76.29	49.28
TiO_2	0.31	0.20	0.35	0.27	0.71
Al_2O_3	10.16	6.96	9.95	8.02	12.27
Fe_2O_3	3.68	2.07	3.50	3.69	9.34
MnO	0.03	0.02	0.05	0.05	0.04
MgO	1.83	0.96	1.51	1.55	1.54
CaO	1.75	1.25	2.01	3.56	1.05
Na_2O	1.20	0.26	1.50	1.43	0.38
K_2O	2.12	1.49	2.12	1.00	3.35
P_2O_5	0.09	0.40	0.35	0.56	0.11
LOI	4.43	2.98	3.18	3.26	21.7
Total	99.63	99.98	99.81	99.75	
S	1.51	1.17	0.75	0.72	5.35
TOC	0.29	0.32	0.14	0.20	9.68
ppm					
Ba	2675.3	4294.8	1773.7	1231.8	397.0
Rb	28.8	21.5	34.1	12.5	126.0
Sr	62.1	29.4	97.6	70.4	75.1
Th	2.7	2.9	3.5	2.5	10.5
U	7.4	3.5	3.1	2.6	48.8
Nb	4.3	3.3	4.5	5.4	11.4
Y	15.5	12.6	18.4	52.6	40.6
Zr	90.2	59.9	92.7	47.6	165.0
Ni	49.5	26.5	23.4	41.4	99.5
V	715.3	149.5	151.5	110.2	160.0
Cr	53.9	58.0	59.9	50.7	66.4
Sc	11.0	6.8	11.0	27.4	13.2
Ga	10.8	6.8	9.7	5.8	16.8
Zn	1679.6	189.0	193.7	90.2	64.1
Cu	108.7	53.4	68.2	66.2	60.2
Pb	112.4	31.6	28.4	16.3	27.9
Cd	20.4	2.0	1.7	1.6	5.0
As	103.0	50.8	39.2	15.5	68.5
Sb	5.6	3.6	3.7	3.9	4.5
Ag	4.3	2.6	2.8	2.8	0.1

Table 8.3: Average major and trace elements of Myra Falls argillite and the average shale, SDO-1 (Huyck, 1990).

from the three main depocentres (Battle and HW basins, and South Flank), is highly variable, and the next section examines this variation, with emphasis on the metal enrichment of argillite from the Battle and HW basins.

8.7.3 Metal enrichment

Finely laminated argillites are commonly associated with very low sedimentation rates, and typically contain high contents of hydrothermal and hydrogenous trace metals (Vine and Tourtelot, 1970). Although organic carbon contents are low, most Battle basin argillites and many HW basin argillites contain enough metals to be classified as metalliferous black shales, based on the definition by Huyck (1990). Huyck (1990) modified the earlier definition by Vine and Tourtelot (1970), and defined a metalliferous black shale as, "a black shale that is enriched in any given metal by a factor of 2x (except Be, Co, Mo and U, for which 1x is sufficient)". This definition is based on comparison to the USGS Devonian Ohio Shale standard (SDO-1). This standard is preferable to other standards such as the NASC (Gromet et al., 1984), as it is a well characterised shale, with a full range of trace elements and good analytical statistics (Huyck, 1990). Table 8.3 shows the SDO-1 major and trace element values beside typical argillite and black chert samples from the Battle and HW basins and regional argillite samples. The Battle basin argillite and black chert are highly enriched in metals, compared to the SDO-1 standard and the regional argillite. For example, Battle Argillite typically has Zn values >1200ppm, and Pb values >100ppm, compared with 64.1ppm and 27.9ppm for the shale standard, SDO-1, and ~75ppm and ~15ppm for the regional argillites, respectively.

Argillite from the caprock horizon are normalised to the SDO-1 standard and plotted to illustrate the variable metal enrichment across the property (Figure 8.17). In general, argillite from the Battle and HW basins, show the greatest degree of metal enrichment. The Battle basin argillite shows a significant metal enrichment in Zn, Pb, As, Ag, Cu, Cd, Sb, Ba and V, quite different to the HW basin argillites. The trace element pattern displayed by the Battle basin argillite is similar to the adjacent black chert, although the degree of enrichment is lower in the argillite.

The HW basin argillite displays a much lesser degree of metal enrichment compared with the Battle argillite, but does show a significant enrichment in Ba, Zn and Ag. Argillite from the HW north and Price areas display a similar pattern to the HW basin argillite, but with lower Ba values. The HW north-Price argillite is more similar to the regional argillite, which predominantly has metal values close to the average shale. However, a slight enrichment in Zn, Cu, Ag, As and Ba is displayed by a few regional argillite samples, which are located in the Thelwood Valley area.

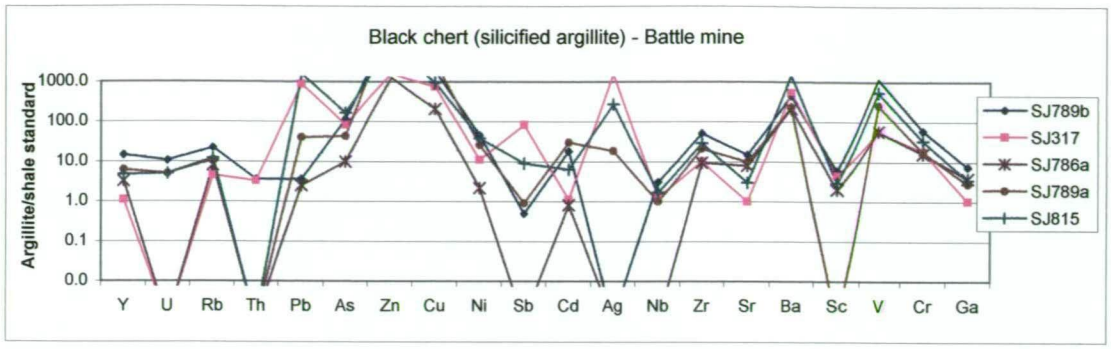

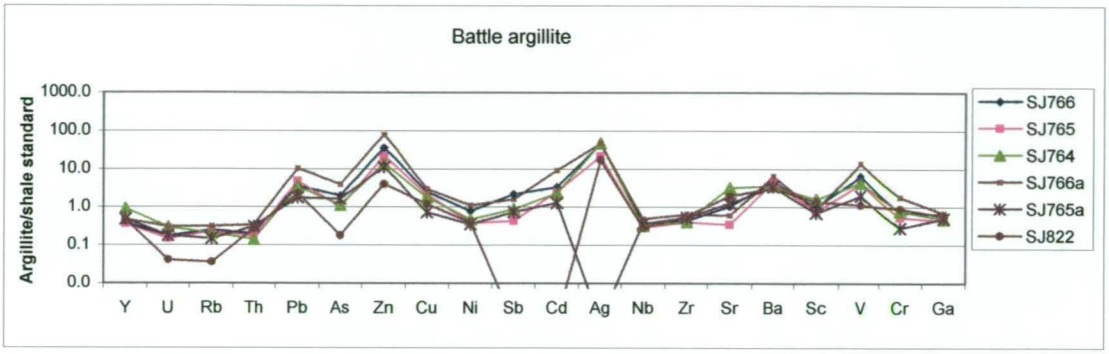

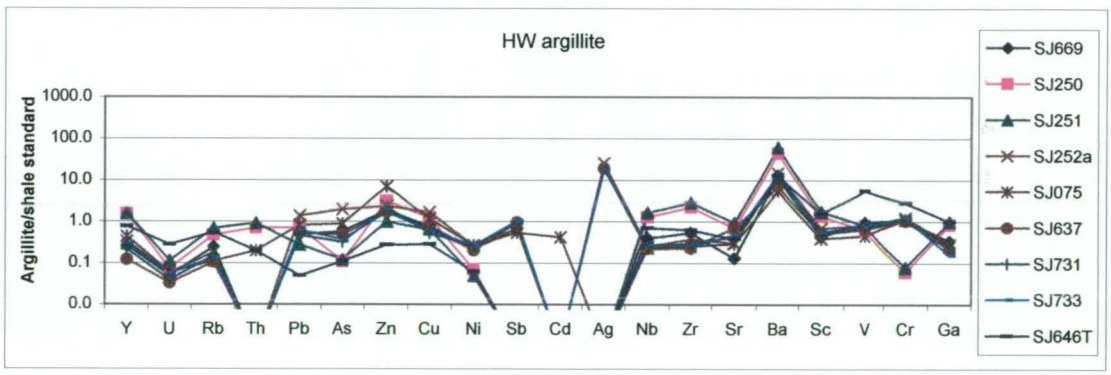

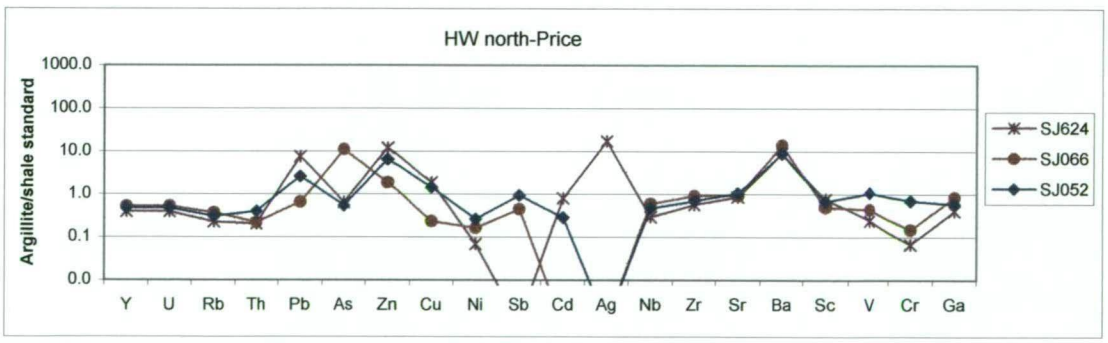

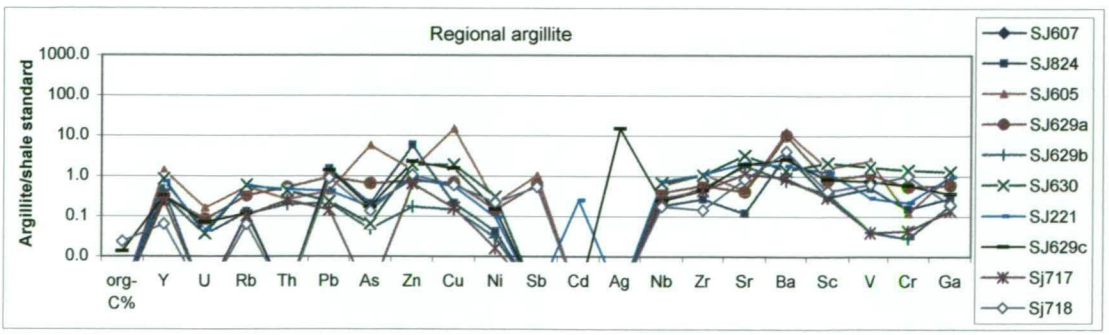

Figure 8.17: Trace element variation in argillite samples from proximal and distal zones to the VHMS orebodies. Argillite values are normalised to the USGS Devonian Ohio Shale standard, SDO-1 (Huyck, 1990). Note the metal enrichments displayed by the Battle and HW basin argillite samples in comparison to regional argillite samples (see discussion in text).

The xy scatter plots in Figure 8.18 illustrate some of the major and trace element variation in argillite from the three main areas, Battle basin, HW basin and regional areas, which include the Thelwood Valley and South Flank. Generally, the Battle basin argillites are much more enriched in metals such as Zn, Cu, Pb and V. The Battle and HW basin argillite has higher S, and lower Na_2O, than the South Flank argillite, and the HW argillites are best distinguished from other argillites by high Ba and low Fe and Mn values.

8.7.4 Metal sources – detrital, hydrothermal or hydrogenous

The metal-rich Battle and HW basin argillites are spatially associated with hydrothermal vents and the most likely metal source is therefore, from a hydrothermal plume. However, metals such as Ni, Cr, U and Th are not enriched in the Battle and HW deposits and are commonly assigned a seawater or hydrogenous source, as their abundances in many mudstones (ppm) match those in seawater (ppb) (Holland, 1979; Piper, 1994). Another source for metals, such as Ni and Cr, is in ferromagnesian minerals in the detrital component of the fine-grained sediment.

Inter-element correlations can be used to distinguish between the detrital, hydrothermal and hydrogenous component of the sediment. In studies of iron formations, elements such as Fe, Mn, Cu and Zn are commonly assigned a hydrothermal origin, based on comparison with modern sea floor hydrothermal vent fluids (e.g., Von Damm, 1990; Spry et al., 2000). Whereas, strong positive correlations between a major component such as Al_2O_3 and trace elements such as Cr, Zr, Nb, Y, Ga, Th and REE suggest that these trace elements may reside in clay-rich detrital clastic material of sedimentary or volcanic origin (e.g., Peter and Goodfellow, 1996).

In this study, xy scatter plots were created for significant element pairs to determine the different sample populations. For example, Battle basin argillite was separated from strongly silicified argillite (black chert), from the edge of the siliceous zone. HW basin argillites were also separated into two populations, consisting of altered argillite and unaltered argillite, to aid interelement correlation. Only the unaltered argillites were used for interelement correlations, and a correlation matrix was created for each population to measure the covariance of the data sets.

Battle basin argillite

Selected element pairs of Battle basin argillites and the adjacent black chert are shown on the xy scatter plots in Figures 8.8, 8.9 and 8.19, illustrating some of the interelement

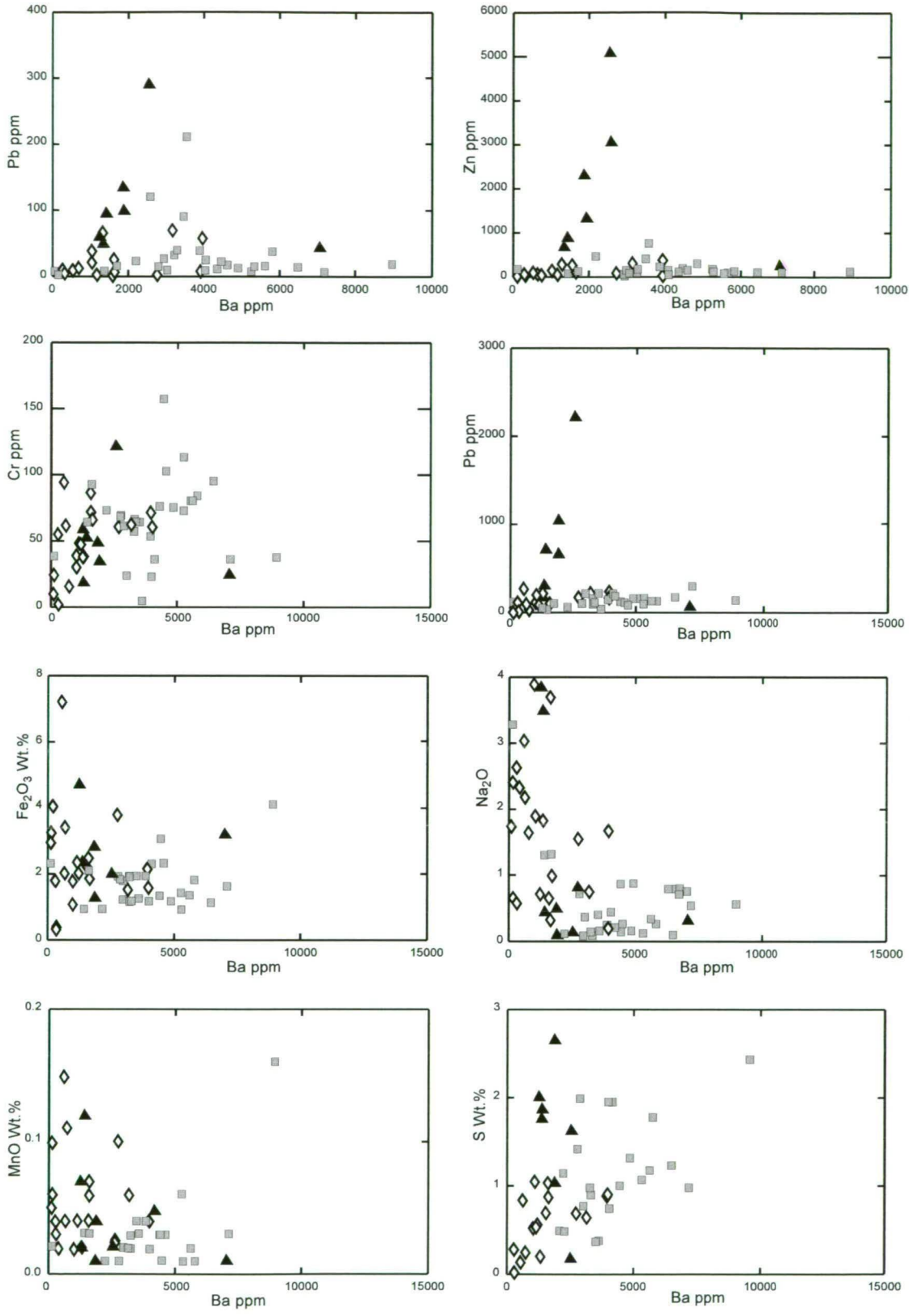

Figure 8.15: Scatter plots illustrate major and trace element variation in argillites from the Battle and HW basins and the South Flank area.

correlations. Significant positive interelement correlations occur between two groups of elements, which are as follows:

1) Ti, Al, Zr, Mg, K, Mn, Ga, Sc, Y, Rb, Fe and Ba. These elements show significant positive interelement correlations and are common in aluminosilicate minerals, such as clays, chlorite and micas – minerals most likely associated with the detrital component of the sediment (e.g., Peter and Goodfellow, 1996).
2) Zn, Cu, Ag, As, S, Cd, U, Pb, V, Sb, Nb, Cr and Ni. These elements also show significant positive interelement correlations. These elements most likely reside in carbonate and sulphide minerals, attributed to hydrothermal and/or hydrogenous sources (e.g., Piper, 1994; Peter and Goodfellow, 1996).

Aluminium is usually assigned a detrital origin, and the strong positive correlation of Al_2O_3 with TiO_2 ($r = 0.9007$, $n = 8$) (Figure 8.16) is consistent with the Al residing in clay minerals (Bostrom, 1973a; Peter and Goodfellow, 1996). The strong positive correlation between Al_2O_3 and Zr ($r = 0.9607$, $n = 8$) and Fe_2O_3 ($r = 0.700$, $n = 8$), and the weak positive correlation with MgO ($r = 0.314$, $n = 8$) suggests an association with detrital ferromagnesian minerals. Fe is usually assigned a hydrothermal origin (e.g., Peter and Goodfellow, 1996; Spry et al., 2000), however, in these sediments, Fe shows positive correlations with Al, Ti, Zr, Na and Ga. Fe is therefore more likely associated with the detrital component of the sediment. Metals such as Zn, Cu, Pb which are clearly associated with the hydrothermal component, display significant negative correlations with Fe, which provides further evidence for the association of Fe with the detrital component.

Cu, Ni, Th, Sb, and Ag display moderate positive correlations with sulphur (> 0.4910), and Zn, As, Pb and Cd show weak positive correlations with sulphur (< 0.40). In comparison, Ba displays a strong negative correlation with S ($r = -0.822$, $n = 8$) and metals such as Zn, Pb and Cu. Ba also shows positive correlations with Al_2O_3 ($r = 0.547$, $n = 8$), Zr ($r = 0.652$, $n = 8$), K ($r = 0.795$, $n = 8$) and Rb ($r = 0.773$, $n = 8$). The positive correlation between Ba and, and the strong negative correlation with S and metals such as Zn, Pb and Cu, indicate that Ba resides in K-micas, with little or no barite present. Electron microprobe data also indicates the presence of Ba in white micas (Appendix 6.2).

Strong positive interelement correlations exist between numerous metal pairs such as, Zn and Cu ($r = 0.951$, $n = 8$), Zn and Pb ($r = 0.945$, $n = 8$), Zn and Cd ($r = 0.988$, $n = 8$), Pb and As ($r = 0.857$, $n = 8$), Pb and Cd ($r = 0.969$, $n = 8$), Pb and V ($r = 0.957$, $n = 8$) Cd and V ($r = 0.994$, $n = 8$), Cd and As ($r = 0.952$, $n = 8$), As and V ($r = 0.940$, $n = 8$), V and Zn ($r = 0.987$, $n = 8$), V and Sb ($r = 0.735$, $n = 8$). These elements also display negative correlations or a lack of correlation with Al_2O_3, TiO_2, Zr, Ga, Ba, Ca, Na, K, Mg and Fe.

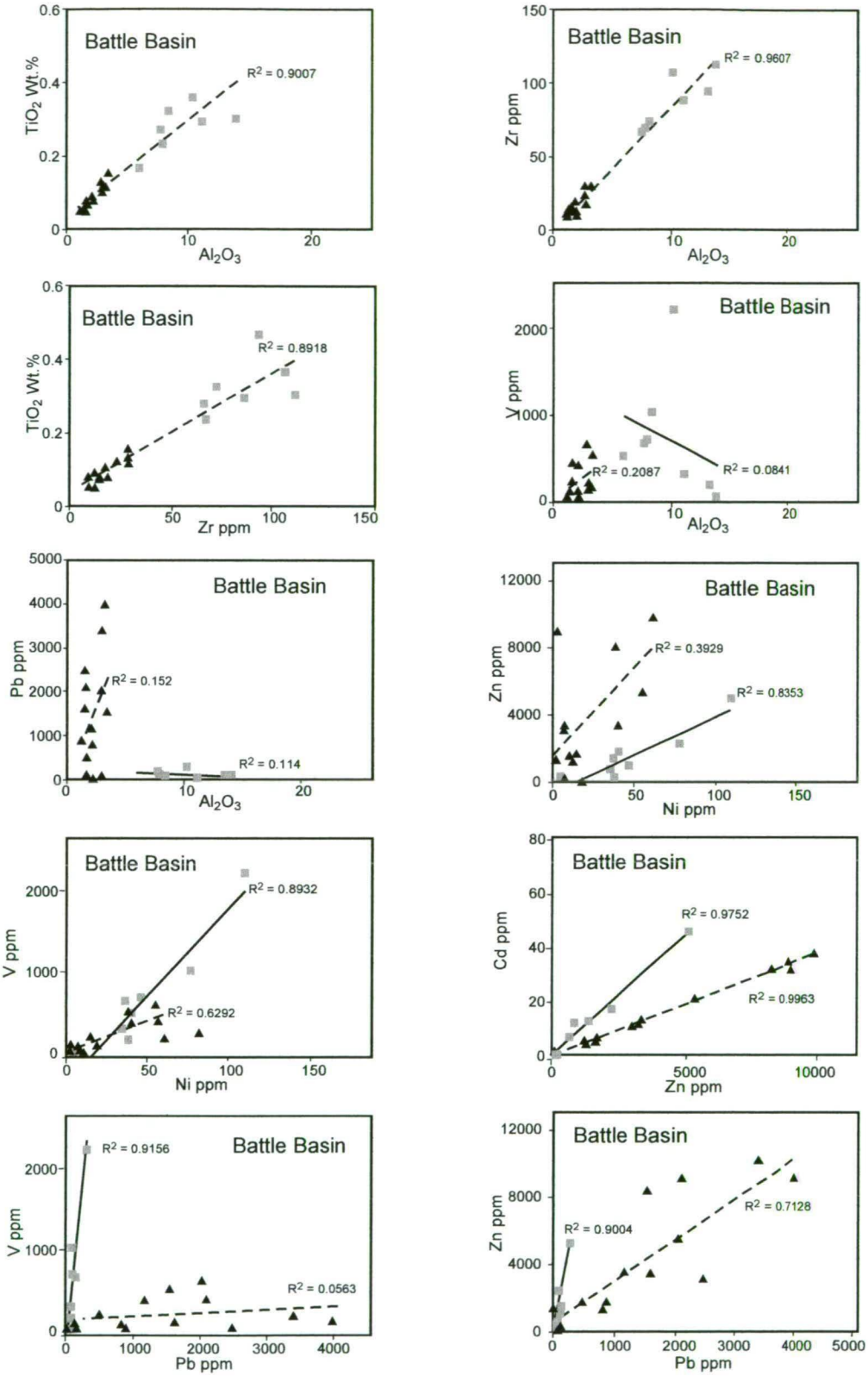

Figure 8.19: Scatter plots illustrate selected major and trace element variation in Battle Basin argillite and adjacent black chert. Strong positive correlations are shown between Al_2O_3, TiO_2 and Zr, while negative or poor correlations exist between Al_2O_3 and metals such as Zn and V. Strong positive inter-element correlations are shown by metals such as Zn, Pb, V, Ni and Cd (see discussion in text).

The strong positive interelement correlations between the metals, and their lack of correlation with detrital elements, indicates a common source and/or similar enrichment mechanisms for these metals. The negative correlation or lack of correlation with elements such as Ca, Na, K and Mg, which are usually associated with hydrothermal alteration (Kalogeropoulous and Scott, 1983), indicate that the high metal values are not associated with hydrothermal alteration. The negative correlation of metals with elements such as Al, most likely reflects the dilution effect of an increasing detrital component.

Trace element enrichments, such as As and V, are reported in hydrothermal plume particulates and in ridge-crest sediments proximal to vents (e.g., Birolleua et al., 1988; Metz and Trefry, 1988). The increase in trace metals such as As and Cd, with proximity to the Battle orebody (Figure 8.7) suggest that they have a hydrothermal source, rather than a hydrogenous source. Spry et al. (2000) suggests that the hydrogenous component is very minor in Fe-Si deposits proximal to massive sulphide deposits, due to the short residence time of plume particles which precipitate close to the ore deposit (reducing the potential to scavenge elements from the seawater). However, the Battle basin argillite, which is located up to 300m away from the orebody, has a large pelagic sediment component and could contain significant hydrogenous elements.

Possible hydrogenous elements include Ni, Cr and U ± Co? (Co was not analysed due to possible contamination from use of the tungsten-carbide mill during sample preparation). Although concentrations of these elements are relatively low in the Battle basin argillites, they display strong positive correlations with metals, such as Zn, Cu, Cd, As, Pb, Ni, V and Sb, which have been assigned a hydrothermal origin. For example, Ni and Sb ($r = 0.827$, $n = 8$), Ni and V ($r = 0.944$, $n = 8$), Cr and Cd ($r = 0.853$, $n = 8$), U and As ($r = 0.767$, $n = 8$), U and Cd ($r = 0.763$, $n = 8$). Peter and Goodfellow (1996) and Spry et al. (2000), assign Ni, Cr, U and Th to a detrital origin due to significant correlations with Al_2O_3. However, these metals in the Battle basin argillites, show negative correlations with Al, Ti, Zr, Ga and Fe, therefore, a hydrothermal and/or hydrogenous source is more likely.

The strong positive correlation between V and Ni ($r = 0.944$, $n = 8$) suggests that they precipitated at a near constant proportion, and this relationship has been noted in crude oils (Lewan, 1984; Briet and Wanty, 1991). The abundance of V in these sediments is much greater than Ni, and Wedepohl (1970) and Brumsack (1980) suggest that this is a commonly observed relationship in most shales. However, in the Battle basin argillites, the proportion of V:Ni is about 16:1, much greater than the average abundance observed in normal seawater, 1.9ppm V to 0.5ppm Ni, with a V:Ni ratio of 5:1 (Brumsack, 1980). The much higher V:Ni ratio in the Battle basin argillite most likely reflects the greater

abundance of V available for complexing in the depositional environment, supplied from venting hydrothermal fluids. The spatial association of V enrichment with the Battle orebody and the presence of V-rich minerals, such as colusite, in the upper zone of the orebody (Sinclair, 2000), is consistent with a hydrothermal origin for the vanadium. The much lower abundance of Ni (also Cr and U) may suggest a hydrogenous source for these elements, with adsorption of these metals from seawater, onto inorganic and organic particles that have a surface charge (Holland, 1979; Piper, 1994).

The majority of Battle basin argillites display significant positive correlations between the metals mentioned above and organic carbon ($r^2 \leq 1.0$). Beier and Hayes (1989) suggest that the most important mechanism controlling the concentration of most metals in the marine environment is adsorption onto particulate organic matter. Metals removed from surface waters by this mechanism are released within the water column via decomposition of the organic matter, in the same way that phosphate is recycled in the ocean. The distribution of trace metals in the modern ocean commonly correlates with the distribtution of nutrients (Beier and Hayes 1989). Piper (1994) also suggests that the organic matter drives the redox reactions in the bottom water and sediments, which determine the suite of elements that precipitates. The accummulation of metals such as Ag, Cu, Pb, Zn, Cd, Sb and As are controlled by their fixation as sulphides, which can precipitate directly from seawater in anoxic conditions. Precipitation is controlled by the availability of H_2S, derived by bacterial reduction of seawater sulphate within stratified water columns or below the sediment surface (Leventhal, 1983; Schultz, 1991). Sulphate reduction and preservation of resultant sulphide phases is a function of the amount of organic matter present, and occurs in the deepest, most anoxic levels, of stratified ocean basins (Maynard, 1983; Ripley et al., 1990; Leventhal, 1998).

HW basin argillite

The HW basin argillites also show a degree of metal enrichment compared to the SDO-1 shale standard (Huyck, 1990) with higher levels of Zn, Cu, Ba, V and As. Although the metal contents are much lower in the HW argillites (with the exception of Ba), they are still much greater than argillites from regional areas such as the South Flank and Thelwood Valley. Selected element pairs of HW basin argillites and altered HW basin argillite are shown on the xy scatter plots (Figures 8.12 and 8.20), which illustrate some of the interelement correlations.

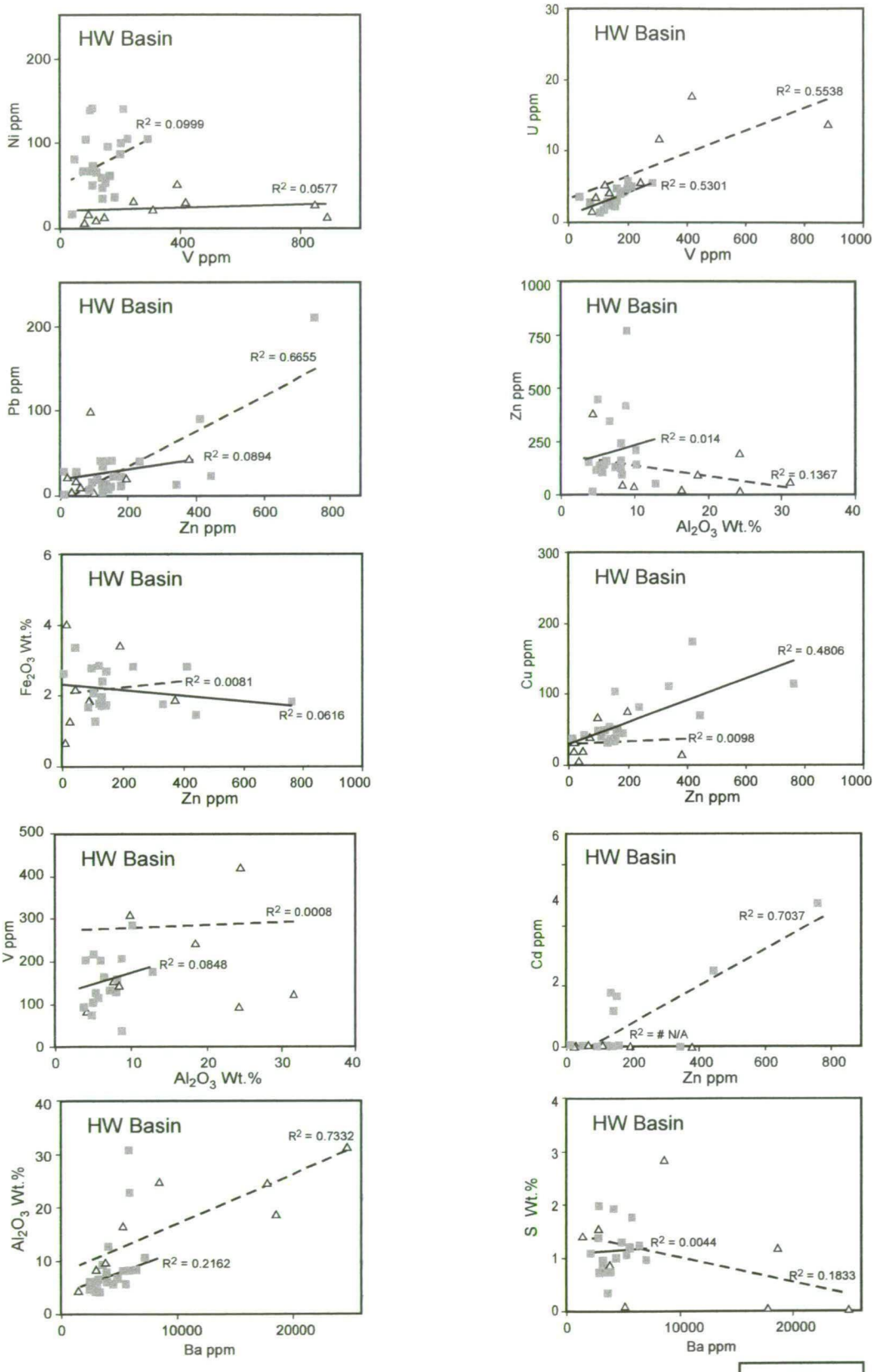

Figure 8.20: Scatter plots illustrate selected major and trace element variation in HW Basin argillite and 'altered' argillite (see discussion in text).

Significant interelement correlations exist between two groups of elements.

3) Ti, Al, Zr, K, Ga, Sc, Y, Rb, Nb and Ba show significant positive interelement correlations.
4) Zn, Pb and Cd, display good positve interelement correlations. These elements are most likely present in various carbonate and sulphide minerals that can be attributed to hydrothermal and/or hydrogenous sources (e.g., Piper, 1994; Peter and Goodfellow, 1996).

HW basin argillite displays strong positive correlations between Al_2O_3, TiO_2 and Zr, K, Ga, Nb, Sc, and Y. These elements most likely reside in the aluminosilicate detrital fraction (e.g., Peter and Goodfellow, 1996). Ba also displays strong positive correlations with Al, Ti, Zr, K, Rb, Nb, Y and Th, and a negative correlation with S ($r = -0.314$, $n = 16$), indicating that Ba resides in K-micas or feldspar in the detrital component rather than sulphates. Electron microprobe data of white micas in the HW argillite and chert also indicate high Ba levels (Chapter 7, Appendix 6.2). The absence of mound or chimney structures in the HW orebody (pers. comm., Mark Hannington, 2000) may also reflect the lack of sulphates such as barite and early anhydrite(?).

HW basin argillite shows significant positive correlations between Zn and Pb ($r = 0.726$, $n = 16$), and Zn and Cd ($r = 0.780$, $n = 16$), Pb and Cd ($r = 0.656$, $n = 16$) and Cu and As ($r = 0.967$, $n = 16$), Cu and V ($r = 0.469$, $n = 16$), and As and V ($r = 0.450$, $n = 16$). However, no correlations exist between the Pb-Cd-Zn and Cu-As-V sets. Cu, As and V also display weak positive correlations with Al, Ti, Ga, Rb, Th and Zr. In comparison, Pb, Cd and Zn show negative correlations with these elements. The Cu, As and V, may reside in the detrital fraction, while the Pb, Cd and Zn may be associated with a hydrothermal source. Zn levels in the HW basin argillite are enriched over the average shale standard (SDO-1, Huyck, 1990) (Figure 8.14), whereas Cu, As and V values are equal or lower than the shale standard. The low values for Cu, As and V in the HW basin argillite are consistent with an association with the detrital fraction.

The lack of correlation between Cu, Pb, Cd and Zn and elements such as K, Ca, Na, Mg and Fe, which are usually associated with hydrothermal alteration (Kalogeropoulous and Scott, 1983), indicate that the relatively high metal values are most likely not associated with hydrothermal alteration of the sediments.

Regional argillite

Only minor metal enrichment, relative to the SDO-1 shale standard was noted in the regional argillites, with a few samples showing slightly anomalous levels in Ag, Ba, As, Zn

and Cu, especially in areas closer to the HW basin, such as the Price and HW north areas. For this reason only samples from the South Flank area were used for interelement correlation.

Interelement correlations show strong positive correlations between Al, Ti, Fe, Mg, Rb, Nb, Zr and Ga. These elements most likely reside in aluminosilicate and ferromagnesian minerals of the detrital fraction. Cu also displays positive correlations with Nb, Ni, U, Y, Al, Ti, Fe and Mg and is most likely associated with the detrital fraction. Metals such as Zn, Pb, Sb, Cd, Ag and V display good positive interelement correlations but only weak correlations with Cu and negative correlations with S. Pb, Zn, Cd, Sb and V show good positive correlations with elements such as Zr and Th, and as the metal values in the regional argillite are close to the average shale values, this suggests that they are associated with the detrital fraction, perhaps with rhyolitic material. Therefore a hydrothermal signature is not recognised in the regional argillite.

8.7.5 Summary and comparison of major and trace element behaviour in argillite from the Battle basin, HW basin and regional areas

Major and trace element behaviour in the caprock horizon argillite varies markedly in the three main depocentres (Battle basin, HW basin and the South Flank). The most noticeable geochemical feature of the argillite is the degree of metal enrichment in the Battle basin with much higher levels of Zn, Cu, Cd, As, Pb, Ni, V and Sb, compared to the HW basin argillite, South Flank argillite and the average shale SDO-1 (Huyck, 1990). The strong positive interelement correlations between the metals, and negative correlations with elements associated with detrital minerals, such as Al, Ti and Zr, suggest a hydrothermal origin. The metals were most likely precipitated from a local hydrothermal plume from vents associated with Battle ore formation. Ba is also slightly enriched in the Battle basin argillite, and negative correlations between Ba and S, and positive correlations with Al and K suggest that the Ba resides in white mica rather than barite, which is consistent with petrological studies.

In comparison, the HW basin argillite has much lower levels of metals such as Cu, Cd, As, Pb, Ni, V and Sb, but still has moderate amounts of Zn and is Ba rich. The Ba in the HW basin argillite behaves in a similar manner to Ba in the Battle basin argillite, with a negative correlation with S, and a positive correlation with Al and K, which also suggests that Ba resides in white mica rather than barite. Zn shows good positive correlations with Cd and Pb, and negative correlations with elements associated with detrital minerals, such as Al, Zr, and Ti, which may indicate a hydrothermal source. However, other metals such as Cu, As and V, do not correlate with Zn, Cd and Pb. Instead they correlate with elements such

as Al, Zr and Ti, which are more likely associated with the detrital component. The lower metal values, the lack of strong correlations between Zn and Cu-As-V, and the positive correlation between Cu-As-V with Al-Zr-Ti suggests that the HW basin argillite has a much weaker hydrothermal signature than the Battle basin argillite.

The marked differences in element behaviour in argillite from these proximal zones could reflect the timing of ore formation in the Battle and HW basins with respect to the deposition of the argillite caprock horizon. For example, there is good evidence that the HW orebody formed on the seafloor, prior to deposition of seafloor mudstones (e.g., Figure 6.29). In comparison, the Battle orebody most likely formed during and after deposition of the seafloor mudstones (e.g., Figures 6.28 and 6.31). Seafloor muds deposited during venting of hydrothermal fluids in the Battle basin would have a much stronger hydrothermal signature than muds deposited after formation of the massive sulphide deposit in the HW basin.

Only minor metal enrichment, relative to the SDO-1 shale standard (Huyck, 1990), was noted in the regional argillites. A few samples have anomalous levels of Ag, Ba, As, Zn and Cu, especially in areas close to the HW basin, such as the Price and HW north areas. The regional argillites display strong positive interelement correlations between Al, Ti, Fe, Mg, Rb, Nb, Zr, Ga and Cu, which suggest that these elements reside in aluminosilicate and ferromagnesian minerals of the detrital fraction. Metals such as Zn, Pb, Sb, Cd, Ag and V display good positive interelement correlations but only weak correlations with Cu and negative correlations with S. These metals also show good positive correlations with elements such as Zr and Th, and as the metal values in the regional argillite are close to the average shale values, this suggests that they are associated with the detrital fraction, perhaps with rhyolitic material. Therefore a hydrothermal signature is not recognised in the regional argillite.

The argillite deposits are useful for locating depocentres, but can also provide a record of hydrothermal activity in a basin. The higher metal contents and the hydrothermal signature of argillite from the Battle and HW basins, compared with argillite from the South Flank indicate their proximity to hydrothermal activity. The implications of argillite geochemistry for exploration in the Myra Falls area is discussed in Chapter 11, Section 11.3.

8.8 Paleoenvironmental analysis of sediment basins

8.8.1 Introduction

The chemical composition of mudstone deposits associated with hydrothermal vents depends on the physicochemical conditions of the venting hydrothermal fluid (e.g., pH, T, ionic strength, fS_2), the redox conditions of the basin or water column into which venting occurs (water depth may partly control this also), the degree of basin isolation from clastic sedimentation, the amount of hydrothermal fluid input via venting, and bottom current drift (e.g., Leventhal, 1983; Schultz 1991).

The depositional environment of Phanerozoic argillaceous rocks is best determined by faunal and sedimentological classifications. For example, a normal oxygenated environment is indicated by homogeneous bioturbated sediments, trace fossils, and abundant benthic fossils. Restricted conditions are indicated by poorly laminated sediments, calcareous concretions, and sparse bioturbation, while a bituminous (or euxinic) environment is suggested by very finely laminated sediments with little or no bioturbation (Raiswell and Berner, 1985).

In the HW Horizon argillites, the only fossil fauna observed are radiolarians, and as they are pelagic fauna, they give few clues to the seafloor conditions at the time of deposition. No benthic, burrowing fauna are observed, and there is a marked lack of bioturbation, with very fine laminations well preserved, indicating a restricted to possibly euxinic environment.

In addition to faunal and sedimentological classifications, chemical and isotopic parameters can be used to constrain the depositional environment, and these include:

- ratio of organic carbon to sulphide sulphur
- Degree of Pyritization (DOP)
- conventional sulphur isotope analyses of pyrite
- metal ratios such as Fe/Mn, Mn/Al, V/(V+Ni)

8.8.2 Organic carbon and sulphide sulphur

Organic carbon is the most widely used parameter to determine paleoenvironmental conditions and is part of the IGCP definition of metal-rich black shales (Huyck, 1990). However, a number of factors affect the organic carbon content. The dominant factors are the rate of biomass production in surface waters and the degree of oxygenation of bottom waters. To determine the degree of oxygenation of bottom waters, organic carbon can be plotted against sulphide sulphur.

Total organic carbon (TOC) was measured in 61 argillite and argillaceous chert samples from the caprock horizon above the Battle and HW orebodies, and argillite from the base of the HW Horizon in the South Flank and Thelwood Valley areas (Table 8.4). Organic carbon contents were low, <0.6 wt.% throughout the area, with the highest organic carbon contents in Battle and HW basin argillite, with lower values in regional argillite.

Low organic carbon contents are common in many ancient shales that have undergone low grade metamorphism, with temperatures up to 200-250°C. Although these shales are still black, they commonly contain only 0.5-1.0 % TOC, which is now in the form of crypto-crystalline graphite (Leventhal and Hofstra, 1990; Leventhal, 1998). Much of the original organic matter in these shales was probably removed during metamorphism. Baker and Claypool (1970), and Raiswell and Berner (1987), describe significant loss of organic carbon (as much as 40-60%) in normal marine shales with increasing vitrinite reflectance.

In modern environments, three types of pattern are displayed on organic carbon-sulphide sulphur plots. Normal marine environments give a positive linear correlation, which passes through the origin. This trend reflects that the amount of sulphur converted from sulphate to sulphide by bacteria, and is controlled by the amount of carbon available as food. Freshwater environments display a very flat trend, with points plotting close to the organic carbon axis. This trend is controlled by the very low amount of sulphate available for conversion to sulphide. In comparison, in euxinic marine basins, with little or no oxygen and free H_2S in the water, sulphate reduction can occur in the water column. As a result, there is usually a poor correlation between organic carbon and sulphide sulphur, and a positive intercept on the sulphide sulphur axis (Leventhal, 1983). Myra Falls organic carbon and sulphide sulphur data is plotted in Figure 8.21; all samples plot in the shaded field above the normal seawater line. This field is defined by Leventhal (1998), as sulphide-rich samples typical of diagenetic and epigenetic addition of sulphides in a marine environment. Analyses from each area are examined in greater detail in section 8.8.4.

Di-sulphide vs mono-sulphide

Di-sulphide and mono-sulphide contents were determined as part of the sulphide sulphur analytical method and abundant mono-sulphide was found in regional argillite samples and in Battle basin argillites, but was rare in samples overlying the HW orebody (see Appendix 5.1 for full results). As this area has undergone greenschist metamorphism, the mono-sulphide in argillite samples is most likely pyrrhotite. However, it was not observed in petrographic analysis, probably due to the fine-grained nature of these rocks.

8.8.3 Degree of Pyritization (DOP)

To further evaluate the degree of anoxia in marine basins, Berner (1970) defined the Degree of Pyritization (DOP) as a measure of the fraction of the reactive iron (HCl-soluble) in the sediment, which is transformed to pyrite during diagenesis. This parameter removes the effect of changing iron contents in different sediments, and is defined as:

$$DOP_R = \text{Pyrite iron}/(\text{Pyrite iron} + \text{HCl-soluble iron})$$

The DOP parameter is commonly calculated using total Fe, instead of HCl-soluble Fe, giving rise to DOP_T and DOP_R respectively (Raiswell and Berner, 1985). The DOP_T values tend to be much lower than DOP_R, and Raiswell and Berner (1985) recommend the use of DOP_R values. The DOP_R index was intially calibrated as a paleoenvironmental indicator of bottom water oxygenation for Devonian and younger rocks (Raiswell et al., 1988), but has now been extended to early Paleozoic rocks. Raiswell et al. (1988) define three separate categories: non-euxinic ($DOP_R < 0.42$); semi-euxinic ($DOP_R = 0.46$-0.80) and fully euxinic or inhospitable ($DOP_R > 0.55$-0.93). There is some overlap in the restricted and inhospitable categories, reflecting fluctuating redox conditions in the bottom water.

Non-euxinic or normal conditions

Pyrite formation in normal marine sediments, deposited from an oxygenated water column, is only possible beneath the sediment-water interface, where anoxic conditions can occur. Under anoxic conditions, seawater sulphate is reduced to H_2S via microbiological sulphate reduction coupled with oxidation of organic carbon:

$$2CH_2O + SO_4^{(2-)} \Leftrightarrow 2HCO_3^{(-)} + H_2S \qquad (1)$$

The resultant H_2S reacts with detrital iron minerals to form pyrite (Raiswell et al., 1988). The amount of reactive organic matter that can be metabolised by sulphate reducing bacteria will limit the degree of pyrite formation (Raiswell et al., 1988). Bioturbation, which adds dissolved oxygen to the sediments, results in the oxidation and poor preservation of pyrite and organic matter in normal marine sediments. Therefore, these sediments are characterised by low DOP_R values.

Euxinic or anoxic conditions

In euxinic environments, free H_2S is present in the bottom water, and reaction with iron minerals to form pyrite can occur in the water column and in the sediments, for long periods after deposition. In this environment, preservation of sulphides and organic carbon is very good, and a much greater proportion of detrital iron minerals in the sediment are converted to pyrite. As a result, these sediments have much higher DOP_R values, and the

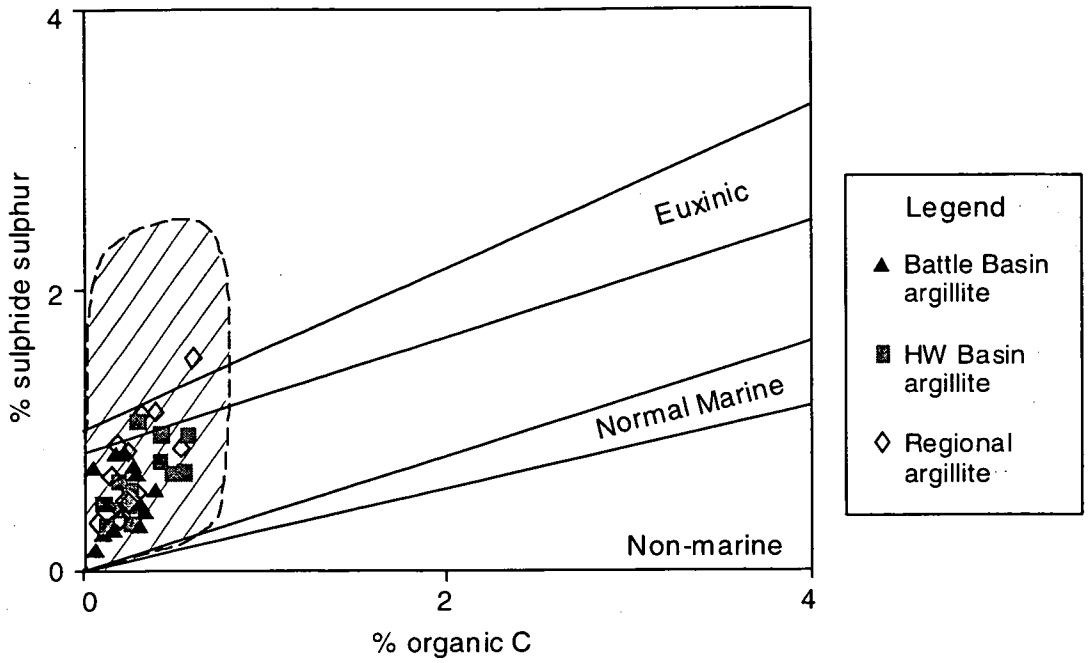

Figure 8.21: Scatter plot illustrates the sulphide sulphur-organic carbon relations of Myra Falls argillite. The cross-hatched area represents sulphur-rich samples, typical of diagenetic and epigenetic addition of sulphur (Leventhal, 1998).

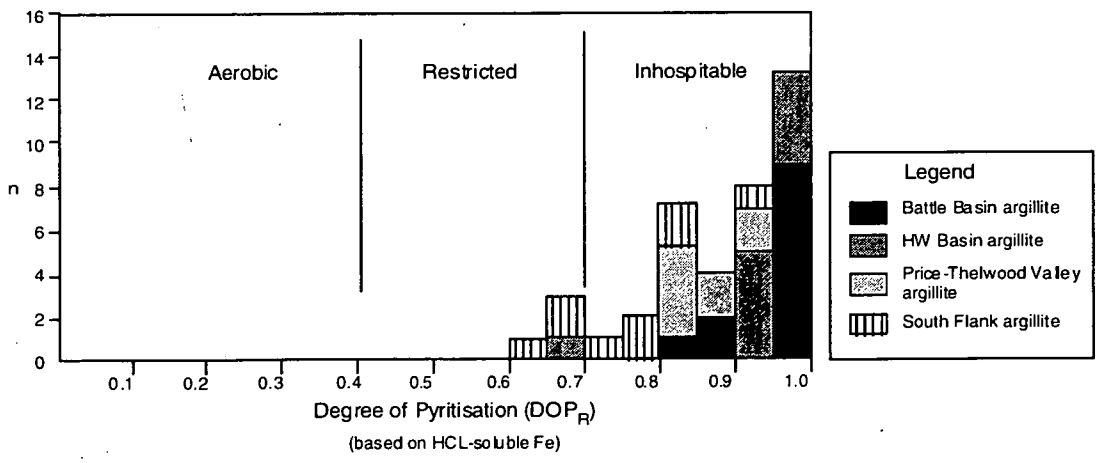

Figure 8.22: Histogram shows the range of DOP_R values for the argillaceous caprock horizon. The Battle and HW basin argillites have higher DOP_R values than the regional argillites (Price, Thelwood Valley and South Flank argillites) and indicate inhospitable or euxinic conditions. The lower DOP_R values of the regional argillite indicate restricted to inhospitable conditions, but slightly more oxygenated than the Battle and HW basin argillites.

extent of pyrite formation is mainly limited by the reactive iron content (Raiswell et al., 1988).

8.8.4 Degree of pyritisation results

Degree of pyritisation was calculated for 42 argillite samples from Myra Falls and the results are plotted in Figure 8.22. The HCl-soluble iron was measured using the 1 N HCl 24 hour extraction method recommended by Leventhal and Taylor (1990). To test for problems with dissolution by this method, the 12 N HCl boiling method of Berner (1970) was also used for 4 repeat samples (see Appendix 5.1). Although HCl-soluble iron contents were slightly higher in the 4 repeats, the DOP_R parameter was only affected by ± 0.01. Therefore the HCl-soluble iron values from the 1 N HCl 24 hour extraction method were used throughout.

The greatest DOP_R values, >0.90, are displayed predominantly by argillite samples from the Battle and HW basins (Figure 8.22). Argillite from the Thelwood Valley and Price areas have DOP_R values from 0.83 to 0.93, while the South Flank samples have the lowest DOP_R values with most below 0.85. Average DOP values, S, C and Fe data from the four main areas, are listed and compared with the average shale standard, SDO-1 (Huyck, 1990) in Table 8.4. The high DOP_R values displayed by the Battle and HW argillite samples, indicate inhospitable or euxinic conditions. The lower DOP_R values for the South Flank

	Battle basin argillite (av.) (n = 11)	HW basin argillite (av.) (n = 13)	Thelwood-Price argillite (av.) (n = 8)	South Flank argillite (av.) (n = 9)	SDO-1 Shale standard
Wt.%					
mono S	0.12	0	0.07	0.21	
di S	0.56	0.64	0.52	0.37	
TOC	0.25	0.32	0.19	0.20	9.68
C_{CARB}	0.10	0.30	0.52	0.55	
S	1.26	1.13	0.82	0.72	5.35
Fe^{TOT}	1.04	1.36	1.80	2.23	6.53
Py Fe	0.28	0.33	0.26	0.19	
HCl-sol Fe	0.01	0.03	0.03	0.05	
DOP_R	0.98	0.92	0.88	0.76	0.71

Table 8.4: Average organic carbon, Fe, sulphur, and DOP values for Myra Falls argillite compared with the average shale standard, SDO-1 (Huyck, 1990).

and Thelwood Valley argillite samples indicate restricted to inhospitable conditions, but slightly more oxygenated than the Battle and HW basin. Although the DOP_T values are much lower, they also show a similar trend, with the Battle and HW basin argillites having higher DOP_T values than the South Flank and Thelwood Valley samples.

8.8.5 Organic carbon-sulphur-iron relations

Raiswell and Berner (1985) defined organic carbon-pyrite sulphur-iron relationships, based on work on Black Sea sediments. Figure 8.23 illustrates the various combinations of the parameters and describes the environments associated with these patterns. Iron commonly shows a positive correlation with organic carbon (TOC), which is partly due to the association of fine clays with both colloidal organic matter and colloidal iron-oxide particles. An increase in deposition of clay, results in an increase in deposition of organic matter and iron. This also results in a positive correlation of pyrite sulphur and organic

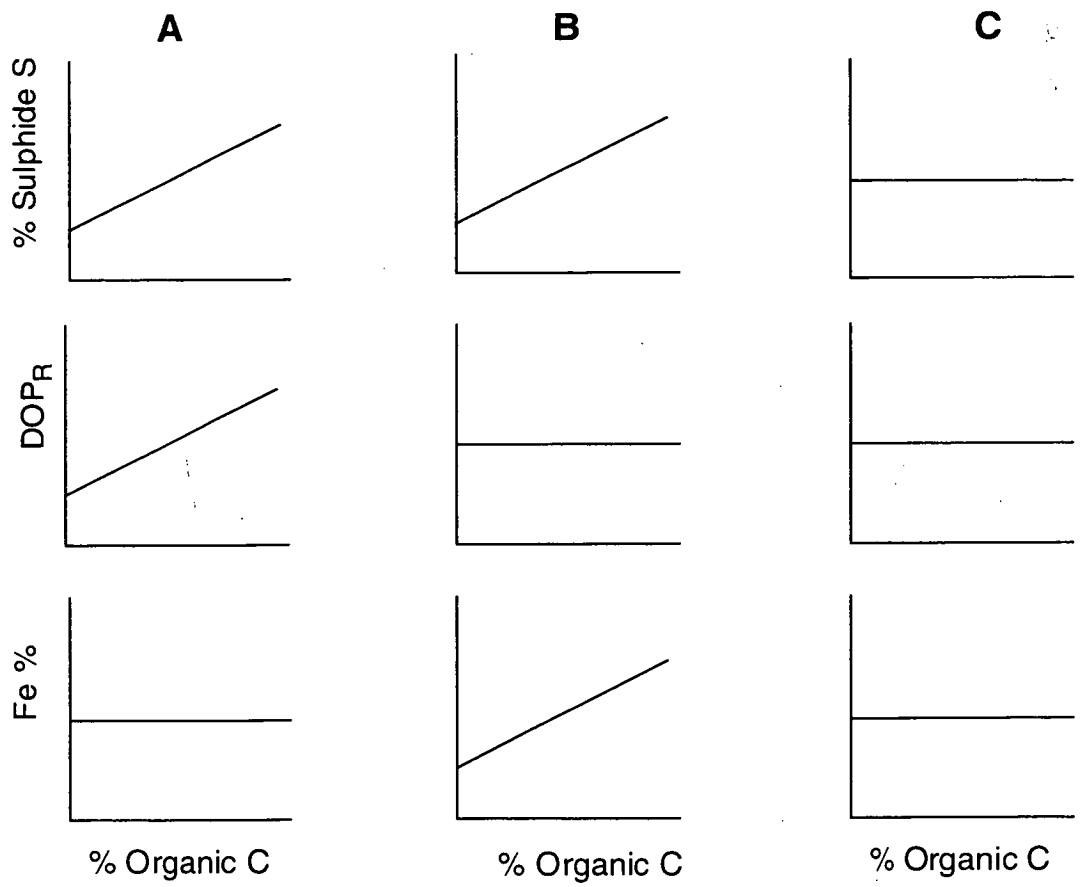

Figure 8.23: Organic carbon-pyrite sulphur-iron relationships as defined by Raiswell and Berner (1985). The set of vertical figures indicate (A) a system with syngenetic and diagenetic formation of FeS_2, organic C limitation, and no coupling of Fe and organic C; (B) a system with only syngenetic formation of FeS_2, Fe limitation, and coupling of Fe with organic C; and (C) a system with only syngenetic formation of FeS_2, Fe limitation, and no coupling of Fe with organic C.

carbon, as iron is the limiting factor and reactive Fe correlates with organic carbon (Raiswell et al., 1988). Therefore, the organic carbon-sulphide sulphur plot has two alternate interpretations: 1) all pyrite is syngenetic with Fe and C coupled and 2) syngenetic pyrite plus additional diagenetic, C-limited pyrite formation. The DOP_R parameter distinguishes between the two types.

The scatter plots in Figures 8.24, 8.25 and 8.26, illustrate the organic carbon-sulphur-Fe relations for argillite samples from the caprock horizon at Myra Falls. Although the organic carbon contents are low, the data still displays good correlations between Fe and sulphide sulphur.

Battle argillite

Argillite samples from Battle basin display a weak positive correlation between sulphide sulphur wt.% and organic carbon wt.% ($n = 11$, $r^2 = 0.4942$) and a positive intercept on the sulphide sulphur axis of 0.4 (Figure 8.24a). No correlation exists between DOP_R and organic carbon wt.% (Figure 8.24b), while a weak positive correlation occurs between total

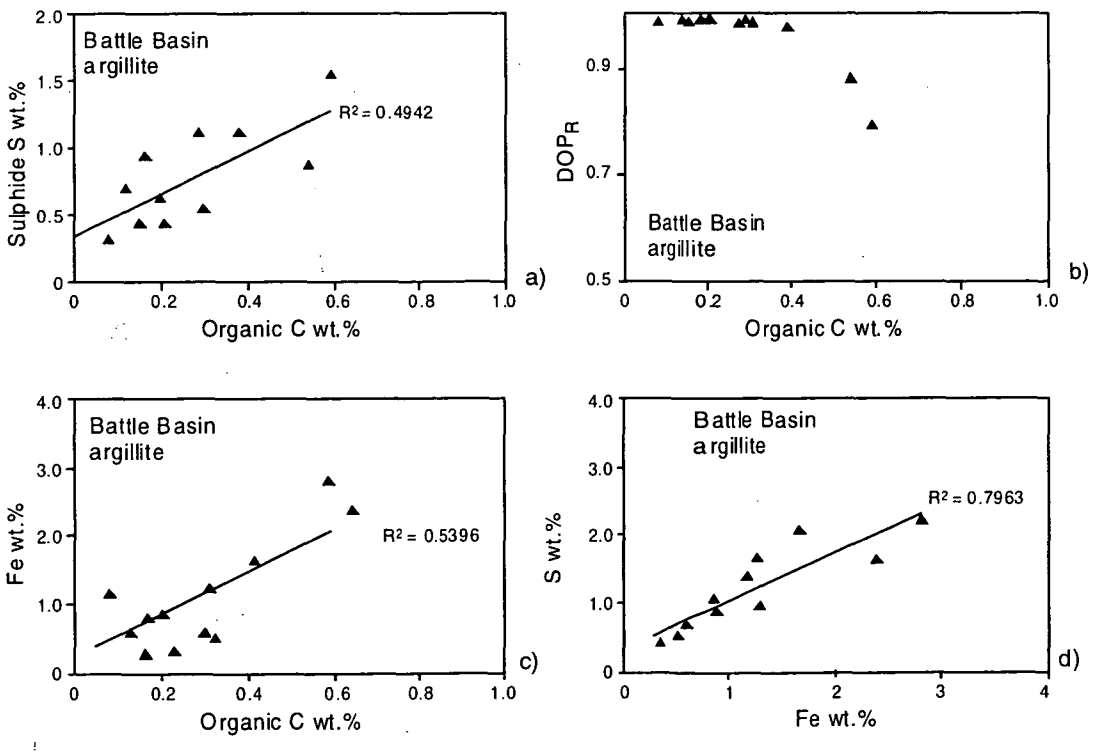

Figure 8.24: Scatter plots illustrate the sulphur-iron-carbon relations of Battle basin argillite.

Fe wt.% and organic carbon wt.% (n = 11, r^2 = 0.5396) in Figure 8.24c. A good positive correlation is displayed by Fe wt.% and sulphur wt.% (n = 11, r^2 = 0.7963) in Figure 8.24d. These relationships suggest a system with only syngenetic pyrite formation, Fe limitation, and coupling of Fe with organic carbon (Raiswell et al., 1988).

HW argillite

Argillite samples from HW basin display a weak positive correlation between organic carbon wt.% and sulphide sulphur wt.% (n = 13, r^2 = 0.408) in Figure 8.25a, with a small positive intercept on the sulphide sulphur axis (0.3). There is no correlation between DOP_R and organic carbon wt.% (Figure 8.25b), and total Fe wt.% and organic carbon wt.% (Figure 8.25c). A weak positive correlation is displayed by sulphur wt.% and total Fe wt.% (n = 18, r^2 = 0.6642) (Figure 8.25d). These plots suggest a normal to slightly restricted environment, and the positive DOP_R-organic carbon and flat Fe-organic carbon trends suggest a system with syngenetic and diagenetic pyrite formation, organic carbon limitation and no coupling between Fe and organic carbon. In this environment, there was enough reactive detrital Fe for some to survive reaction with H_2S in the bottom water, and be converted to pyrite diagenetically, after burial. Because of the abundant Fe, formation of pyrite was therefore limited by the local deposition of organic matter.

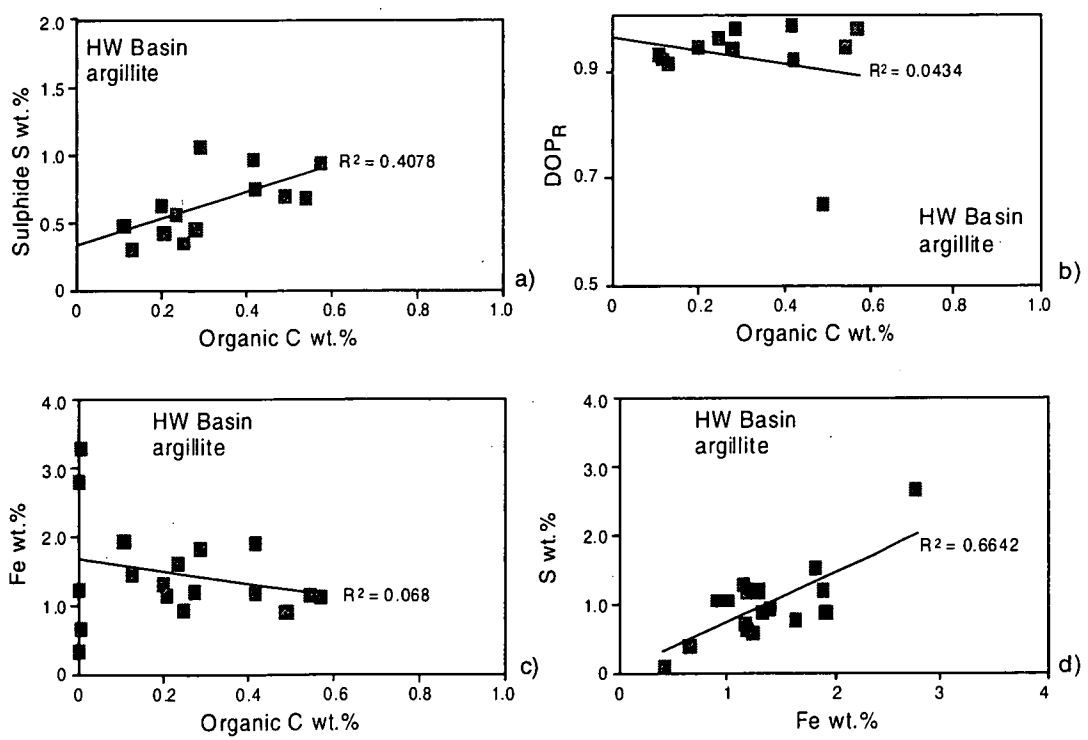

Figure 8.25: Scatter plots illustrate the sulphur-iron-carbon relations for HW basin argillite.

Regional argillite

The very low organic carbon values of argillite samples from regional areas, make correlations between the various parameters difficult (Figure 8.26). There appears to be little correlation between organic carbon wt.% and DOP_R or total Fe wt.%. However, there may be a very weak positive correlation between organic carbon wt.% and sulphide sulphur wt.%, with an intercept close to zero on the sulphide sulphur axis. The lack of positive trends suggests a system with only syngenetic pyrite formation, Fe limitation and no coupling between Fe and organic carbon. However, this interpretation is hindered by the very low organic carbon contents.

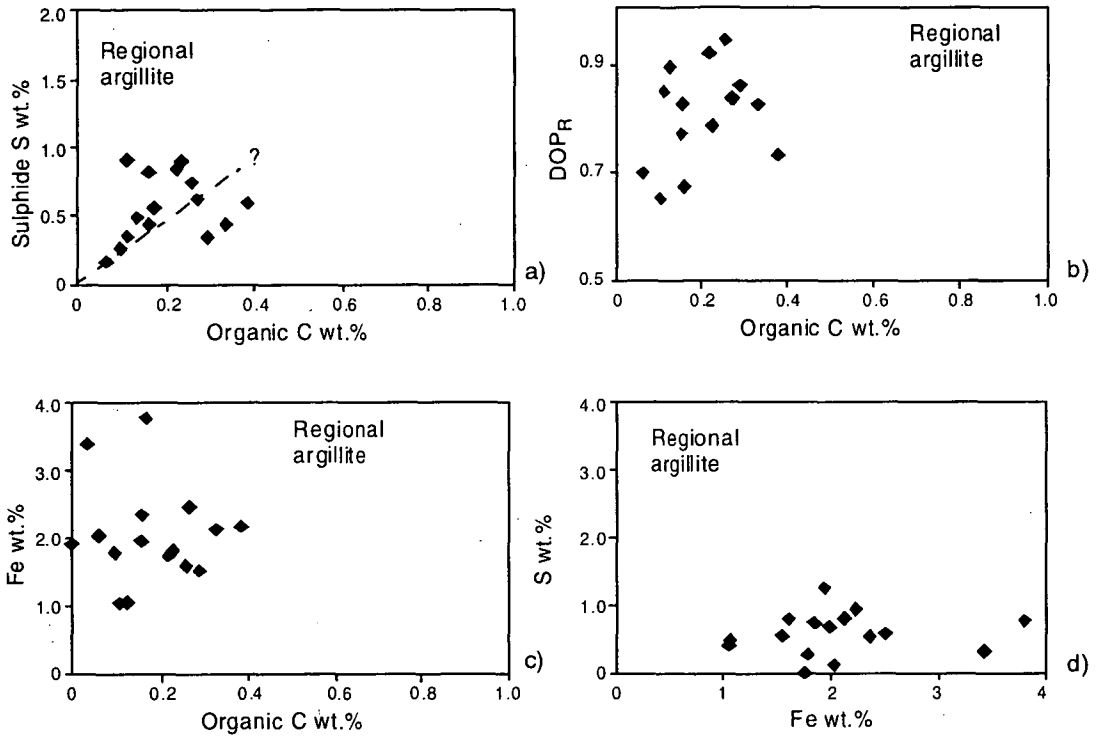

Figure 8.26: Scatter plots illustrate the sulphur-iron-carbon relations for regional argillite from the South Flank, Thelwood Valley and HW north areas.

8.8.6 Metal ratios – paleoenvironmental indicators

Vine and Tourtelot (1970) and other authors have used the presence of carbon/graphite, and metal enrichment in black shales to indicate anoxic sedimentary environments. However, the presence of carbon reflects the degree of production and preservation, and these processes can be affected by a number of factors, only one of which is the basin redox conditions (Quinby-Hunt and Wilde, 1994). For example, Calvert et al. (1996) describes the preservation of organic carbon in anoxic and oxic conditions. Quinby-Hunt and Wilde

(1994) also suggest that metal-carbon fixation can occur in both oxic and anoxic conditions, although the solubility-saturation behaviour of individual metals will vary.

The trace metal content of shales formed under oxic conditions differs markedly from unbioturbated black shales formed in anoxic conditions (Quinby-Hunt and Wilde, 1994). The bulk chemical composition of shales reflects, 1) the detrital or allochemical component; and 2) the chemistry of the depositional environment, controlled by early diagenetic processes and post-lithification processes such as hydrothermal alteration and metamorphism. In general, seawater redox reactions control the distribution of the various hydrothermal components, particularly Fe and Mn and other metals such as U, V, Cr and Mo (Whitehead, 1973; Force and Cannon, 1988). For this reason metal ratios, in combination with carbon and sulphur data, provide a good indication of the paleoredox conditions.

Table 8.5 shows the average metal contents, metal ratios and DOP_R values for the three main argillite depo-centres, for comparison with the shale standard, SDO-1 (Huyck, 1990). The DOP_R value for SDO-1 (0.71), is similar to the South Flank argillite (DOP_R = 0.76), and suggests deposition under restricted bottom water conditions. The similarity of the SDO-1 shale standard to the South Flank argillite makes it a useful example for comparison with Myra Falls argillite.

	SDO-1 Shale standard $DOP_R = 0.71$	**Battle basin Argillite (av.)** (n = 7) $DOP_R = 0.98$	**HW basin Argillite (av.)** (n = 16) $DOP_R = 0.92$	**South Flank Argillite (av.)** (n = 13) $DOP_R = 0.76$
ppm				
Fe	65300	25493	16359	25807
Mn	300	318.3	203.8	409.1
V	160	715	150	110
Ni	100	50	27	41
Zn	64	1680	189	90
Cr	66	54	58	51
Fe/Mn	217.7	80.1	80.3	63.1
Mn/Al	0.005	0.003	0.003	0.01
V/Cr	2.4	13.3	3.7	2.2
V/Ni	1.6	14.5	5.7	2.7
V/(V+Ni)	0.62	0.94	0.84	0.73

Table 8.5: Average metal values and metal ratios for argillites from the Battle basin, HW basin and the South Flank area. The shale standard, SDO-1, is from Huyck (1990).

Other shale types, representing shales deposited under a range of O_2 bottom water conditions are shown in Table 8.6, and include a metalliferous black shale (the Stark Shale Member, Kansas, Hatch and Leventhal, 1992); and two Pennsylvanian shales, including the Mecca-type shale, deposited under restricted conditions with moderate to high Zn and Mo values; and the organic-poor Shanghai-type shale, deposited in relatively oxic bottom water conditions, with much lower metal values (data from Schultz and Coveney, 1992).

The Fe content of Myra Falls argillite is lower than the average shale (SDO-1) and other shales in Table 8.6, while Mn values are similar in Myra Falls argillite. Metal values in the Battle basin argillite, including Zn, Cu, V, Pb, As and Cd, are much higher than the average shale (SDO-1), and the Pennsylvanian shales, and are most similar to the Stark Shale Member, which is classified as a metalliferous black shale. The DOP_R value of the Stark Shale Member (0.88) is the closest to the Battle argillite ($DOP_R = 0.98$).

The South Flank argillite, with $DOP_R = 0.76$, has much lower Zn, Cu and Pb, than the Battle argillite, and is more similar to the average shale standard (SDO-1), with $DOP_R = 0.71$, and metal values generally <100 ppm. However, the South Flank argillite does have high Ba values, 1598 ppm. Other metals, such as Ni, Cr and U, are low in Myra Falls argillite, compared with the Mecca-type Pennsylvanian shale and the Stark Shale Member, and are more similar to the SDO-1 average shale and the Shanghai-type Pennsylvanian shale. The Battle basin argillite has lower P_2O_5 values (average = 0.09, n = 7), than the South Flank average, 0.56 wt.%, and is similar to the Mecca-type shales (< 0.3 wt.%), while the South Flank P_2O_5 content is similar to the Shanghai-type shale, > 0.5 wt.% P_2O_5 (Schultz and Coveney, 1992).

Mn/Al = 0.003 in Battle basin argillite, which is significantly lower than the South Flank argillite, which has Mn/Al = 0.01. The South Flank argillite has similar Mn/Al values to carbon-poor marine shales, Mn/Al = 0.01 (Solomon, 1999), and average shales, NASC, Mn/Al = 0.01 (Gromet et al., 1984); and PAAS, Mn/Al = 0.016 (Taylor and McLennan, 1988). However, Mn/Al values are uniformly low (<0.005) for the other shale types listed in Table 8.6, with no clear difference between Mecca-type and Shanghai-type shales.

Fe/Mn values can be used to estimate the relative oxygen levels in a stratified basin (e.g., Whitehead, 1973; Maynard, 1983; Force and Cannon, 1988; Spry and Wonder, 1989). Changes in the Fe/Mn ratios reflect the fact that Mn is more soluble than Fe over a larger range of Eh and pH conditions, allowing chemical separation to occur (Krauskopf, 1957; Maynard, 1983; Spry and Wonder, 1989). Force and Cannon (1988) examined Fe/Mn values of oxic and euxinic facies in the Black Sea, and found that high Fe/Mn values (e.g.,

	Battle basin argillite (n = 7) $DOP_R = 0.98$	South Flank Argillite (av.) (n = 13) $DOP_R = 0.76$	Organic-rich Mecca-type Pennsylvanian Shale (73) $DOP_R = 0.65$	Organic-poor Shanghai-type Pennsylvanian Shale (SH1) $DOP_R = 0.21$	Metalliferous Black Shale Stark Shale Member (S-2-1) $DOP_R = 0.88$	SDO-1 shale standard $DOP_R = 0.71$
Wt.%						
Al_2O_3	10.16	9.95	8.80	35.89	9.07	12.27
Na_2O	1.20	1.50	0.32	0.92	-	0.38
CaO	1.75	2.01	0.77	2.81	3.92	1.05
K_2O	2.12	2.12	2.06	4.39	-	3.35
P_2O_5	0.09	0.35	<0.03	>0.05	0.27	0.11
S	1.51	0.75	4.19	1.44	3.3	5.35
TOC	0.29	0.14	25.15	4.74	29.5	9.68
ppm						
Mn	318	409	130	400	100	300
Fe	25493	25808	33800	55400	38000	65300
Ba	2675	1232	300	400	-	397
Sc	11	27	12	18	-	13
V	715	110	2850	180	3900	160
Ni	50	41	530	190	600	100
Cr	54	51	610	360	730	66
U	7	3	165	14	180	49
Zn	1680	90	3350	84	5500	64
Cu	109	66	-	-	170	60
Pb	112	16	-	-	34	28
As	103	16	35	26	-	69
Fe/Mn	139.1	63.1	260.0	138.5	380	217.7
Mn/Al	0.003	0.01	0.003	0.002	0.002	0.005
V/Cr	13.3	2.2	4.7	0.5	5.3	2.4
V/Ni	14.5	1.7	5.4	1.0	6.5	2.7
V/(V+Ni)	0.94	0.70	0.84	0.49	0.87	0.73

Table 8.6: Comparison of selected major and trace elements of Myra Falls argillite and other shale types. Pennsylvanian shale data from Schultz and Coveney, (1992) (73) and (SH1) = sample numbers of Pennsylvanian shales; metalliferous black shale from the Stark Shale Member of the Dennis Limestone, Kansas (Hatch and Leventhal, 1992) (S-2-1) = field number; average shale standard, SDO-1from Huyck (1990).

>100) were associated with anoxic to euxinic facies, while low Fe/Mn values (e.g., < ~50) were associated with oxic facies. Intermediate Fe/Mn values were indicative of a transitional environment with fluctuating redox conditions, typical in stratified, stagnant oceans with restrictied circulation. The Battle basin argillite has an average Fe/Mn value of 139, similar to the euxinic Black Sea facies of Force and Cannon (1988), while the South Flank argillite has Fe/Mn = 63.1, similar to the transitional Black Sea facies. The lower DOP_R values for the South Flank argillite (0.76) are also consistent with a transitional environment with fluctuating redox conditions.

Quinby-Hunt and Wilde (1994) suggest that black shales with low Mn and Fe values indicate that the Mn and Fe are reduced and relatively soluble, reflecting anoxic but non-

sulphate reducing conditions. High V levels, such as those observed in Battle basin argillites, with V >300ppm, combined with the low Fe and Mn values, suggest deposition under conditions of high organic preservation, with low pH and possible methanogenesis (Quinby-Hunt and Wilde, 1994).

Lewan (1984) suggest that V accumulates at a greater proportion, relative to Ni (high V/Ni) in strongly reducing, H_2S rich environments. Consistent with this analysis, Wenger and Baker (1986) determined that greater levels of anoxia favoured large V/Ni ratios (> 5) as well as larger contents of both metals. Hoffman et al. (1998) suggests V/(V+Ni) values of 0.6-0.9 and V/Cr values of 1.0-5.0, in finely laminated, non-bioturbated Upper Pennsylvanian shales, represent deposition in the anoxic zone. In comparison, weakly bioturbated shales with V/(V+Ni) values < 0.6 and V/Cr < 1.0 represent deposition in the dysoxic zone.

Hatch and Leventhal (1992) suggest that high Cd, Mo, U, V, Zn and S contents, combined with a high DOP_R > 0.75, and high V/(V+Ni) (> 0.8) indicate the presence of H_2S in a strongly stratified water column. Intermediate contents of metals and S, intermediate DOP_R (0.67-0.75) and intermediate V/(V+Ni) (0.54-0.82) indicate a less strongly stratified anoxic water column, whereas low metal contents and low V/(V+Ni) indicate a weakly stratified, dysoxic water column.

The Battle argillites have high metal contents, including V, Cu, Zn, Cd, Sb, As, Ag, Pb and Ba, moderate to high S contents, high DOP_R values (>0.75), V/Cr (>5.0), and high V/(V+Ni) (>0.8), which suggests strongly reducing conditions with free H_2S in a strongly stratified water column. The similar metal ratios and DOP_R values for the HW basin argillites, suggest similar bottom water conditions in this basin. Although Ba levels are high in both the Battle and HW basin argillites, barite is not observed; instead Ba resides in aluminosilicates. The absence of sulphate is also consistent with low O_2 bottom water conditions. The much lower DOP_R and metal ratios in the South Flank area suggest a slightly more oxygenated depositional environment. A similar variation in metal ratios is observed between the organic-poor Shanghai-type shales deposited under oxic conditions, and the organic-rich Mecca-type shales and metalliferous Stark Shale Member deposited under anoxic bottom water conditions (Table 8.6).

Elevated metal ratios, such as V/Cr, V/Ni and V/(V+Ni), in the Battle basin argillites most likely reflect a combination of hydrothermal and hydrogenous sources. Excess V would be derived from hydrothermal vents associated with Battle ore formation, but could also reflect the strongly reducing conditions in the basin. For example, argillites in the HW basin have

much lower V levels and no clear correlation between V and hydrothermally derived elements, such as Zn and Pb, but still have high V/Ni (5.7) and V/Cr (3.7) values, indicative of deposition under anoxic conditions (Wenger and Baker, 1986).

8.8.7 Phosphate nodules

Phosphate nodules are found in a number of discrete horizons in the upper part of the caprock horizon in the Battle and HW basins (see descriptions, Chapter 6), but appear to be more common in the regional argillites, such as the South Flank and Thelwood Valley areas.

Hatch and Leventhal (1992) report that phosphate nodules in shales are best developed at the top of black shale units, indicating that nodule formation was enhanced near the boundary between anoxic and dysoxic conditions. This is similar to observations of Holocene phosphorites from the East Australian continental margin (O'Brien et al., 1990; Heggie et al., 1990).

Phosphate nodules are thought to form by a process of Fe and P cycling. P is scavenged from the seawater by iron oxyhydroxides at the sediment surface and in the oxidised burial zone, and following burial to depths at which porewaters become anoxic, dissolution of the iron oxyhydroxides releases both Fe and adsorbed P. Both components diffuse upward to be reprecipitated at depths about 10-18cm beneath the sediment-seawater interface (O'Brien et al., 1990). The redox related Fe cycling, retains the P within the shallow subsurface allowing sufficient time for slow growth of phosphate nodules. Therefore, the most favourable conditions for phosphate precipitation entails bottom waters which are oxygen depleted but not fully anoxic (O'Brien et al., 1990; Heggie et al., 1990).

The restricted distribution of phosphate nodules, with most occurring in a discrete horizon near the top of the caprock horizon, suggests that conditions during deposition of the caprocks were not favourable for phosphate precipitation and nodule formation. Rapid sedimentation or low O_2 bottom water conditions may have inhibited the formation of phosphate nodules at this time.

8.8.8 Paleoenvironmental summary

The paleoseafloor reconstruction in Chapter 5 indicates that the Battle and HW orebodies formed in small basins along a NW-trending ridge. The reconstructed paleoseafloor appears to deepen to the south, with much thicker argillite deposits in this area (South Flank and Thelwood Valley). Sedimentological features in the argillite and chert, such as the very fine parallel laminations, lack of bioturbation and turbidite facies, indicates deep quiet

depositional environments, at least below storm wave base (>80-100m depth). The lack of benthic fauna, and the presence of graphite and phosphate nodules, indicates low O_2 to fluctuating O_2 bottom water conditions.

The geochemical parameters described in this section are also consistent with low O_2 bottom water conditions in the more restricted Battle and HW basins. Battle basin argillites contain the highest organic carbon contents, high DOP_R values (>0.8), high metal contents, including Zn, Pb, Cu, Cd, As, Sb, Ag, Ba and V, low Fe and Mn, and high metal ratios such as V/(V+Ni) >0.8. These geochemical parameters suggest strongly reducing conditions with free H_2S in a strongly stratified water column. Elevated metal ratios, such as V/Cr, V/Ni and V/(V+Ni), in the Battle basin argillites most likely reflect a combination of hydrothermal and hydrogenous sources. Excess V would be derived from hydrothermal vents associated with Battle ore formation, but could also reflect the strongly reducing conditions in the basin. For example, argillites in the HW basin have much lower V levels and no clear correlation between V and hydrothermally derived elements, such as Zn and Pb, but still have high V/Ni (5.7) and V/Cr (3.7) values, indicative of deposition under anoxic conditions (Wenger and Baker, 1986). The DOP_R values for HW basin argillite (>0.8) are also consistent with anoxic conditions, similar to the Battle basin. The lower DOP_R and V-Ni metal ratios in the South Flank area indicate a slightly more oxygenated depositional environment.

The low O_2 bottom water conditions indicated by the geochemistry of the Battle and HW basin argillites, is consistent with areas of more restricted circulation, such as small deep basins, as shown by the paleoseafloor reconstruction (Chapter 5). The restricted seawater circulation would have allowed the formation of a stratified water column, either in terms of temperature or salinity, which would have greatly slowed any mixing of atmospheric O_2 into the bottow water and helped maintain euxinic or anoxic conditions (Leventhal, 1998). In comparison, the geochemistry of the South Flank argillites indicates a slightly more oxygenated environment, consistent with deposition in more open seafloor conditions, exposed to open seafloor circulation, as shown by the paleoseafloor reconstruction in Chapter 5.

8.9 Sulphur isotopes

Sulphur isotope data was collected from 21 argillite and black chert samples from the Myra Falls property to determine the source of the sulphur in the fine-grained caprock horizon. Sinclair (2000) described sulphur isotope variation throughout the Battle orebody, and the aim of this study was to compare the sulphur isotopic signature of the basin sediments with those of the orebody.

	di-sulphide $\delta^{34}S$	mono-sulphide $\delta^{34}S$	Average metal values (ppm)
Battle basin black chert	−9.0 to −18.4 ‰ (av. −10.9 ‰) (n = 3)	−5.4 to −7.4 ‰ (av. −6.4 ‰) (n = 2)	Pb = 1229 Zn = 3564 Cu = 456 (n = 14)
Battle basin argillite	−15.1 to −26.0 ‰ (av. −20.6 ‰) (n = 2)	−18.2 ‰ (only one sample with mono-sulphide)	Pb = 110 Zn = 1579 Cu = 109 (n = 8)
HW basin Argillite	−14.1 to −35.2 ‰ (av. −27.7 ‰) (n = 4)		Pb = 32 Zn = 189 Cu = 53 (n = 16)
Regional Argillite	−10.3 to −31.7 ‰ (av. −21.0 ‰) (n = 6)	−24.9 to −32.3 ‰ (av. −27.7 ‰) (n = 3)	Pb = 16 Zn = 90 Cu = 66 (n = 13)
Battle Orebody (sulphide) (Sinclair, 2000)	−1.1 to +4.1 ‰ (av. +2.1 ‰) (with 2 exceptions: −3.2 and −7.9 ‰)		Massive Sulphides (Zn-Pb-Cu)
Battle Upper Lenses (sulphate) (Sinclair, 2000)	+18.4 to +28.7 ‰ (av. +22.1 ‰)		Massive sulphide + sulphate Zn-Pb-Cu

Table 8.7: Summary of $\delta^{34}S$ analyses and average metal values of argillite and black chert samples from the HW Horizon, and the Battle orebody. Battle orebody and upper lens sulphur isotope data from Seccombe et al. (1990) and Sinclair (2000).

8.9.1 Results

Negative $\delta^{34}S$ values were recorded in all argillite and black chert samples, with a range of $\delta^{34}S$ from −5.4 to −35.2 ‰ (Figure 8.27). The range of sulphur isotope values for each area is shown in Table 8.7. The regional argillite, which includes argillite from the South Flank and Thelwood Valley, has $\delta^{34}S$ values ranging from −10.3 to −32.3 ‰, and is similar to the range for HW basin argillite, with $\delta^{34}S$ from −14.1 to −35.2 ‰. The Battle basin argillite has a range of $\delta^{34}S$ from −15.1 to −26.0 ‰, while the black chert has distinctly heavier $\delta^{34}S$

values, from –5.4 to –18.4 ‰. No sulphide sulphur was collected from white chert samples, but Sinclair (2000) obtained a $\delta^{34}S$ value of +1.6 ‰ in pyrite in white chert above the Battle orebody, although the pyrite was most likely from crosscutting ore veins, with a different origin to disseminated sulphides in black chert and argillite.

The regional argillite $\delta^{34}S$ values include mono- and di-sulphide samples, and as the mono-sulphide ^{34}S values were similar to the di-sulphides, no discernable isotopic difference was noted between the mono and di-sulphide samples. Only minor mono-sulphide was observed in Battle and HW basin argillites. However, mono-sulphides in the black chert are distinctly heavier than the di-sulphides. The mono-sulphides have $\delta^{34}S$ values ranging from –5.4 to –7.4 ‰, while the di-sulphides range from –9.0 to –18.4 ‰. The black chert is Pb-rich and galena overgrowths on pyrite framboids were observed in SEM images, and the mono-sulphide phase is most likely galena.

A tight cluster of $\delta^{34}S$ values were reported for sulphides in the Battle orebody, ranging from –1.1 to +4.1 ‰, with two exceptions, –7.9 and –3.2 ‰ (Seccombe et al., 1990; Sinclair, 2000). Sulphate $\delta^{34}S$ values from the Battle upper lenses, ranged from +18.4 to +28.7 ‰, (average = +22.1 ‰). A general increase in $\delta^{34}S$ values was observed with increasing stratigraphic height, from an average of +2.1 ‰ in the Battle main lens, to +2.6 ‰ in the upper lenses and +3.0 ‰ in the Gap lens (Seccombe et al., 1990; Sinclair, 2000).

The histogram, Figure 8.27, illustrates the variation in $\delta^{34}S$ values from the argillite and massive sulphides, and shows the much lighter sulphur isotope signature of the argillites, in comparison to the massive sulphides. Sulphur isotope values for sulphides in the black chert are intermediate between argillite and Battle orebody $\delta^{34}S$ values. Figure 8.28 illustrates the lateral change in $\delta^{34}S$ values of the caprock horizon in the Battle basin. The heaviest values are found in pyrite in the white chert above the massive sulphides ($\delta^{34}S$ = +1.6 ‰, Sinclair, 2000), with a shift to intermediate values in the black chert at the edge of the siliceous alteration ($\delta^{34}S$ = –10.9 ‰), and lighter values in the unaltered Battle basin argillite to the south ($\delta^{34}S$ = –19.7 ‰).

8.9.2 Sulphur sources

The three principal sources of sulphur in seafloor VHMS systems are considered to be from, 1) the reduction of seawater sulphate; 2) magmatic sulphur; and 3) sulphur derived from the leaching of hostrocks, which may or may not be igneous rocks (Ohmoto and Rye, 1979; Goodfellow and Jonasson, 1984; Ueda and Sakai, 1984).

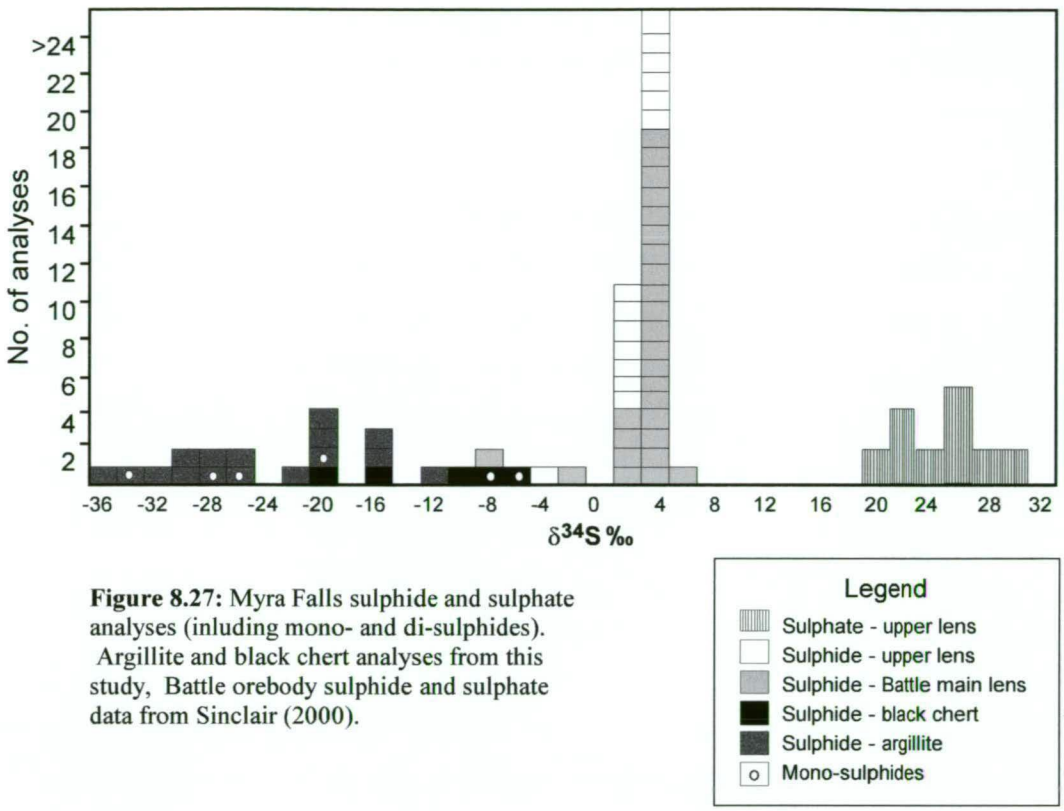

Figure 8.27: Myra Falls sulphide and sulphate analyses (inluding mono- and di-sulphides). Argillite and black chert analyses from this study, Battle orebody sulphide and sulphate data from Sinclair (2000).

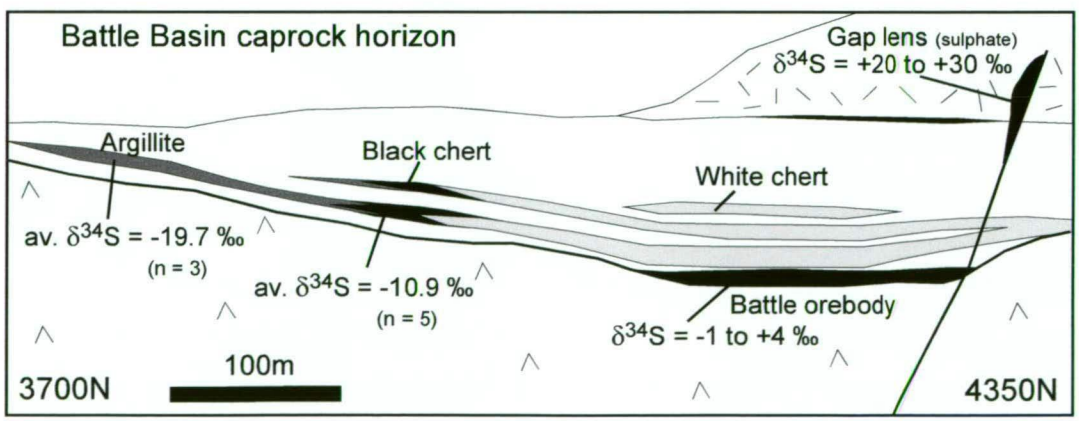

Figure 8.28: Spatial variation of $\delta^{34}S$ of sulphides in the caprock horizon and Battle orebody and sulphate values in the Battle Upper lenses. Battle orebody $\delta^{34}S$ values from Sinclair (2000).

Sangster (1968) observed that the $\delta^{34}S$ values of VHMS deposits and that of contemporaneous seawater (based on evaporite deposits) varied with time in a parallel manner. Sangster (1968) demonstrated that, on average, the $\delta^{34}S$ values of seawater sulphate is 17.5 to ± 2.5 ‰ greater than that of contemporaneous sulphide minerals in VHMS deposits through time. The consistent shift between ambient seawater sulphate and the $\delta^{34}S$ values of the sulphide minerals in VHMS deposits is attributed to reduction of seawater sulphate. Both inorganic and organic reduction (via bacterial reduction) of seawater sulphate is possible, and fractionation effects during reduction result in markedly different $\delta^{34}S$ values, where reduction is incomplete. Inorganic reduction of seawater sulphate can result from the oxidation of ferrous iron or reduced carbon in the host volcanics or intercalated sediments (Ohmoto et al., 1983; Solomon et al., 1988).

In general, $\delta^{34}S$ values resulting from bacterial reduction of seawater sulphate are much lighter and far more variable than those from inorganic reduction processes; bacterial reduction is a non-equilibrium process strongly favouring ^{32}S (Ohmoto and Goldhaber, 1997). The products of low degrees of bacterial sulphur reduction are very depleted in ^{34}S, producing a very large difference between coeval seawater sulphate and sulphides (up to 60 ‰) (McKibben, 1993). As VHMS sulphides do not generally contain values with this range, biogenic reduction of seawater sulphate is not considered a major source of sulphur (Ohmoto and Rye, 1979). Additionally, the typical hydrothermal fluid temperatures of VHMS systems (250-350°C), are far too high to allow bacterial activity. Although in the Guaymas Basin, bacterial sulphate reduction has been recorded in hydrothermal vent sediments at temperatures greater than 100°C (Jorgensen et al., 1992). Light isotopic signatures in VHMS systems, could be attained by the leaching of sedimentary sulphides (formed from bacterially reduced seawater sulphate), near the seafloor (Ohmoto and Rye, 1979).

Fractionation of sulphur isotopes results from the mass dependency of the chemical reaction rates and the differing reaction rates of isotopic species. Generally, molecules containing the lighter isotope species have the fastest reaction rates and therefore, the initial products will be more enriched in the lighter isotope. If all the seawater sulphate was reduced the resulting sulphides would have an average $\delta^{34}S$ value approximately equal to the ambient seawater sulphate. In VHMS systems, the gap between coeval sulphate and sulphide values was thought to be the result of incomplete reduction of seawater sulphate (e.g., Ohmoto and Rye, 1979). However, measured H_2S/SO_4 in exiting vent fluids is very high, suggesting complete reduction (Shanks and Seyfried, 1987). The sulphate-sulphide gap in VHMS systems is more likely to be due to the venting fluids containing up to 70-

80% rock sulphur (leached from host rocks) and 20-30% reduced seawater sulphate, which is completely reduced (Shanks and Seyfried, 1987).

Magmatic sulphur in hydrothermal fluids could be sourced directly from magmatic emanations, or by the leaching of magmatic sulphur from the host rocks (Ohmoto and Rye, 1979; Solomon et al., 1988). Magmatic sulphur generally has $\delta^{34}S$ values of 0 ± 5 ‰ in intracontinental settings, and 0 ± 4 ‰ in arc settings (Ueda and Sakai, 1984). Sulphides formed from magmatic sulphur will have $\delta^{34}S$ values ranging from –5 to +5 ‰, while sulphides forming from combined sulphur sources will show a much wider range of values.

8.9.3 Interpretation of Myra Falls sulphur isotopes

The light sulphur isotope values of Myra Falls argillite, most likely indicate a sulphur source originating from bacterial reduction of seawater sulphate, which would have $\delta^{34}S$ values of 20-25 ‰ in mid-Upper Devonian times (Figure 8.29) (Claypool et al., 1982). The presence of organic carbon in the argillite is consistent with a biogenic source of sulphur. In comparison, the black chert has $\delta^{34}S$ values intermediate between the argillite and sulphides in the Battle orebody, consistent with a mixture of sulphur from different sources. Alternatively, light $\delta^{34}S$ values could be attained by sulphide precipitation under oxidised conditions at low H_2S/SO_4 ratios. However, this is not likely, given the abundant organic carbon and lack of oxidised phases in the black cherts. Sinclair (2000) suggested that the tight cluster of the Battle orebody $\delta^{34}S$ values indicated a very homogeneous source, which could be from 1) inorganic reduction of seawater sulphate; 2) leached magmatic sulphur; or 3) direct input of magmatic sulphur. However, the source of the sulphur was not conclusively identified due to the similar values of inorganically reduced seawater sulphate during the mid-Upper Devonian and values of magmatic sulphur.

The intermediate $\delta^{34}S$ values in the black chert provide further evidence of a replacement origin for the siliceous caprocks above the Battle orebody. The distinct shift to heavier $\delta^{34}S$ values in the black chert (–10.9 ‰), from the light values in the unaltered Battle basin argillite (–19.7 ‰), reflects input of hydrothermal sulphur into the sediments during alteration. The black chert also contains significant mono-sulphide with heavier $\delta^{34}S$ values (–6.4 ‰). The high Pb content of the black chert suggests that the dominant mono-sulphide phase is most likely galena, which was also observed as overgrowths on pyrite framboids in SEM images, and is associated with the hydrothermal alteration.

As black chert represents a replacement of argillite, initial $\delta^{34}S$ values can be assumed to be similar to the Battle basin argillite (–19.7 ‰), reflecting bacterial reduction of seawater

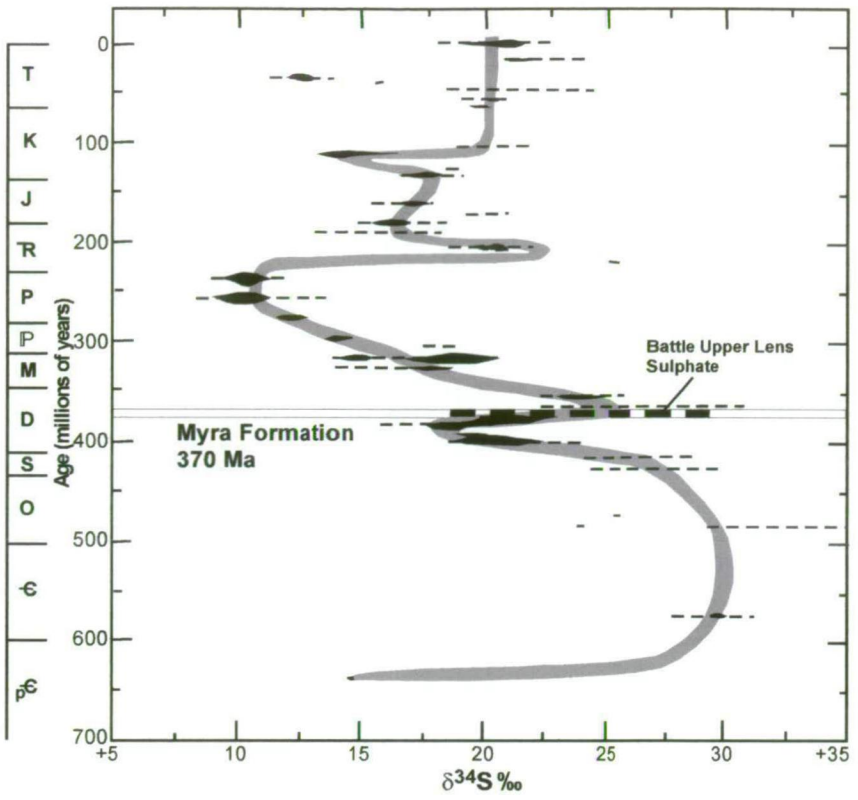

Figure 8.29: Variation of the isotopic composition of marine sulphate during Phanerozoic time with sulphate from the Battle Upper Lens (from Claypool et al., 1980). The sulphate data is from Sinclair (2000) and the 370 Ma date for the Myra Formation is from U-Pb dating in Juras (1987).

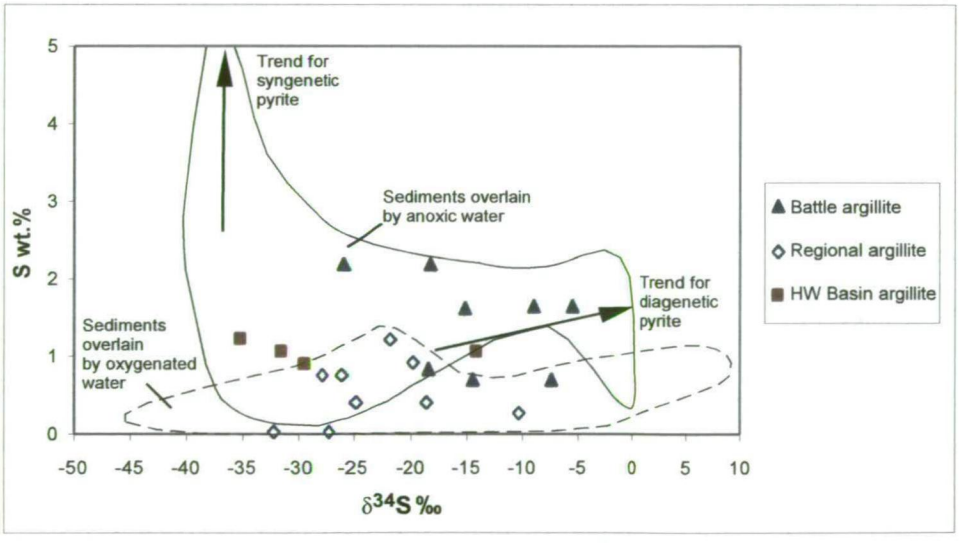

Figure 8.30: Scatter plot comparing the variations in sulphur concentration and $\delta^{34}S$ in argillite samples from the Battle Basin, HW Basin and regional areas such as the South Flank, with modern Black Sea sulphide. The upper dashed field represents Black Sea sediments overlain by an anoxic water column; the lower dashed field represents sediments overlain by an oxygenated water column. Black Sea fields from Ohmoto et al. (1990); diagram modified from Ohmoto and Goldhaber (1997).

sulphate in the seafloor sediments. The hydrothermal fluids have $\delta^{34}S$ values in the range, 0 to +4 ‰, reflecting magmatic sulphur and/or magmatic sulphur leached from the host rocks, with some inorganically reduced seawater sulphate. Mass balance calculations between the unaltered argillite and the black chert indicate mass gains of 70% SiO_2 (Figure 8.13). A simple mass balance between hydrothermal $\delta^{34}S$ values (0 to +4 ‰), and $\delta^{34}S$ values in the unaltered argillite (–19.7 ‰), results in a shift from –19.7 ‰, to about –8 to –10 ‰, for 70-80% mass gain in the black chert.

The xy scatter plot, Figure 8.30, compares the $\delta^{34}S$ values with the sulphur content of the sediments to indicate the bottom water O_2 levels. The two fields illustrate the range of sulphur-$\delta^{34}S$ values for modern sediment samples from the Black Sea (Ohmoto et al., 1990). The lower field indicates sediments, which have formed under an oxygenated water column, while the top field shows the field for sediments overlain by an anoxic water column. The seawater curve from Claypool et al. (1980) (Figure 8.29) indicates that the bulk $\delta^{34}S_{seawater}$ values for the modern Black Sea and Mid to Upper Devonian seawater may have been similar (~20 ‰ for the modern Black Sea, and ~20-25 ‰ for Devonian seawater). For this reason, Myra Falls $\delta^{34}S$-sulphur wt.% values in argillite are compared to the anoxic and oxic sedimentary facies of the modern Black Sea. Although there are only a few Myra Falls sulphur isotope analyses shown, the regional argillite plots well within the more oxygenated field, compared to the Battle and HW basin argillites. This is consistent with other geochemical paleoenvironmental indicators, such as DOP_R, organic carbon-sulphur relations and metal ratios, which indicate that the Battle and HW basins were euxinic or inhospitable, with slightly more oxidised conditions in the South Flank.

Sinclair (2000) suggested that the increasing $\delta^{34}S$ values with stratigraphic height through the Battle orebody could reflect either: 1) a gradual increase in the $\delta^{34}S$ values of the ambient seawater during the Frasnian Stage (Claypool et al., 1980), (but this is unlikely to have occurred in the time frame of ore formation); or 2) an increase in the amount of oxygenated seawater mixing with the hydrothermal fluids, which formed the upper lenses; a similar effect has been observed at Roseberry (Solomon et al., 1988). The greater amount of seawater mixing could be due to the greater porosity of the coarse-grained rhyolitic sediments, which form the footwall to the upper ore lenses. A marked change in the ore mineralogy also occurs with stratigraphic height. Barite is rare or absent in the main Battle lenses, but becomes common in the upper ore zones. The absence of barite in the lower lenses is consistent with ore formation in low O_2 bottom water conditions, whereas ubiquitous barite in the upper lenses could reflect changes in the redox conditions of the Battle basin, with more oxygenated seawater mixing with the hydrothermal fluids, and/or

changes in the fO_2 of the hydrothermal fluid. However, Ohmoto and Goldhaber (1997) suggest that in an open system, if the ratio of oxidised to reduced sulphur isotope species increases (i.e., due to oxidation), the $\delta^{34}S$ values of the individual fluid species will decrease if they remain in equilibrium.

8.9.4 Comparison with other VHMS systems

Typical average sulphur isotope values for a large number of Phanerozoic VHMS deposits range from –4.8 to +13.6 ‰ (Huston, 1999), overlapping the range reported for the Battle orebody, –7.9 to +4.1 ‰ (Sinclair, 2000). However, the hydrothermally altered black chert has much lighter $\delta^{34}S$ values (–18.4 to –5.4 ‰), which fall outside the typical range of $\delta^{34}S$ values for VHMS deposits and reflect a mixture of sulphur sources. Light $\delta^{34}S$ values (–10 to –20 ‰) are recorded at a number of Devonian VHMS deposits, for example, the minimum $\delta^{34}S$ values of sulphides in the Iberian Pyrite Belt, is –20.3 ‰, and in the Hodgkinson Province is –10.0 ‰, (references for each district, in Huston, 1999). These light values may partly represent a biogenic contribution from the host sediments.

8.10 Summary and conclusions

- Immobile element pairs indicate that the siliceous caprocks above the Battle deposit, have a similar sedimentary signature to the adjacent Battle basin argillites. The chert most likely formed by silicification of pre-existing argillite, rather than as a primary 'exhalite', and this is consistent with similar petrological and sedimentological features in the chert and argillite. Battle cherts plot in the non-hydrothermal or terrigenous field on the Al-Fe-Mn, and Fe/Ti-Al/(Al+Fe+Mn) Bostrom plots, largely due to their very low Fe and Mn contents. However, the high metal values of the chert suggest a significant hydrothermal component.

- The siliceous caprocks above the Battle orebody are enriched in metals such as, Zn, Cu, Pb, Cd, As, S, U and V. The highest Zn, Cu and Cd levels are in the white-grey chert above the Battle orebody, and these metals decrease toward the outer edge of the siliceous zone. In the black chert, which forms the outer fringe of siliceous alteration, there is a marked increase in Pb, Ag and Sb.

- Mass balance relationships between the Battle chert and unaltered Battle basin argillite indicate that with the addition of silica, most major and trace elements, including immobiles, display a net loss from dilution by the mass addition of silica. A mass gain of 200% and 70% Si is estimated for the white chert and black chert respectively.

- REE patterns of argillite and chert are similar across the property, most likely reflecting common sediment sources. However, Eu anomalies are only observed in Battle and HW basin argillites and chert, which most likely reflects the proximity to hydrothermal vents in these areas. This is consistent with the greater degree of metal enrichment in argillite from these areas, in comparison with the regional argillite samples.

- Battle basin argillites are strongly enriched in Zn, Pb, As, Ag, Cu, Cd, Sb, Ba and V, whereas, the HW basin argillites are moderately enriched only in Ba, As, Zn, Cu and V. South Flank and Thelwood Valley argillites display little or no metal enrichment.

- In the Battle basin argillite, Zn, Cu, Ag, As, S, Cd, U, Pb, V and Sb, are assigned a hydrothermal origin, due to the strong positive interelement correlations and negative correlations with detrital elements, such as Ti, Al, Zr, Mg, K, Mn, Ga, Sc, Y, Rb, Fe and Ba. Positive correlations of Ba with Al, K, and Rb, and negative correlations with S, indicate that Ba resides in white micas, rather than sulphate.

- HW basin argillite also shows a degree of metal enrichment, with higher Zn, Cu, Ba, V and As, than regional argillites. Metals such as Zn, Pb and Cd are assigned a hydrothermal origin due to the negative correlation with detrital elements, such as Ti, Al, Zr, K, Ga, Sc, Y, Rb, Nb and Ba.

- Geochemical parameters indicate much lower O_2 bottom water conditions in the Battle and HW basins, compared to argillites from the South Flank area. Battle basin argillites contain the highest organic carbon contents, high DOP values (>0.8), high metal contents, including Zn, Pb, Cu, Cd, As, Sb, Ag, Ba and V, low Fe and Mn, and high metal ratios such as V/(V+Ni), >0.8. These geochemical parameters indicate strongly reducing conditions with free H_2S in a strongly stratified water column. HW basin argillites, although not as enriched in metal contents, still have high V/(V+Ni), and relatively high DOP values (>0.8) indicating similar bottom water conditions in the HW basin. The lower DOP and V-Ni metal ratios in the South Flank area indicate a slightly more oxygenated depositional environment.

- Sulphur isotope values in argillites from the caprock horizon (300-320m from the orebody) are very light, with a range from –35.2 to –10.3 ‰, whereas $\delta^{34}S$ values for sulphides in black chert (100m from the orebody) range from –18.4 to –5.3 ‰. The black chert $\delta^{34}S$ values are intermediate between the unaltered argillite and Battle orebody values (–1.1 to +4.1 ‰). The light sulphur isotope values in the argillite reflect bacterial reduction of seawater sulphate, whereas, the heavier sulphur isotopes

of the Battle orebody reflect magmatic sulphur and/or inorganic reduction of seawater sulphate.

- The distinct shift from light $\delta^{34}S$ values in the unaltered argillite, to heavier $\delta^{34}S$ values in the black chert reflect input of hydrothermal sulphur ($\delta^{34}S = -1.1$ to $+4$ ‰) into the seafloor sediments during hydrothermal alteration, and provide further evidence for a replacement origin for the Battle chert.

Chapter 9
Fluid inclusion study of siliceous caprocks and Battle and HW orebodies

9.1 Introduction

Fluid inclusions are not commonly observed in siliceous caprocks or chert, due to their fine grained nature. However, at Myra Falls abundant fine inclusions were observed in spherical megaquartz patches in the siliceous caprocks above the Battle orebody. These megaquartz patches represent early infilling and replacement of radiolarian tests, prior to compaction. Most inclusions in the megaquartz were less than 1μm in size, but some ranged in size from 3-10μm, and were large enough to be studied. Although spherical megaquartz patches after radiolarians and/or algal cysts are described in cherts elsewhere (e.g., Adachi et al. 1986; Pollack, 1987; Schieber, 1996), fluid inclusions in these megaquartz patches are not reported.

The presence of fine inclusions in spherical megaquartz patches in the chert or siliceous caprock above the Battle orebody, provides a unique opportunity to determine the trapping temperature and salinity of the hydrothermal fluids associated with near-seafloor silica deposition above the VHMS deposit. Although trace element geochemistry and stable isotopes have been used to show genetic links between the massive sulphides and overlying caprocks or 'exhalites' (e.g., Kalgeropoulous and Scott, 1983, 1989; Liaghat and MacLean, 1992; Peter and Goodfellow 1996), direct measurement of fluid inclusions have not been possible, due to the fine grained nature of these siliceous deposits.

At Myra Falls, fine euhedral apatite and rutile are also common within the spherical megaquartz patches, displaying good open space growth textures. Electron microprobe analyses of the euhedral apatite grains indicate elevated sulphur and barium levels, suggesting a hydrothermal, rather than diagenetic origin. Geothermal studies suggest that apatite and rutile growth is associated with hydrothermal fluids with temperatures of apatite

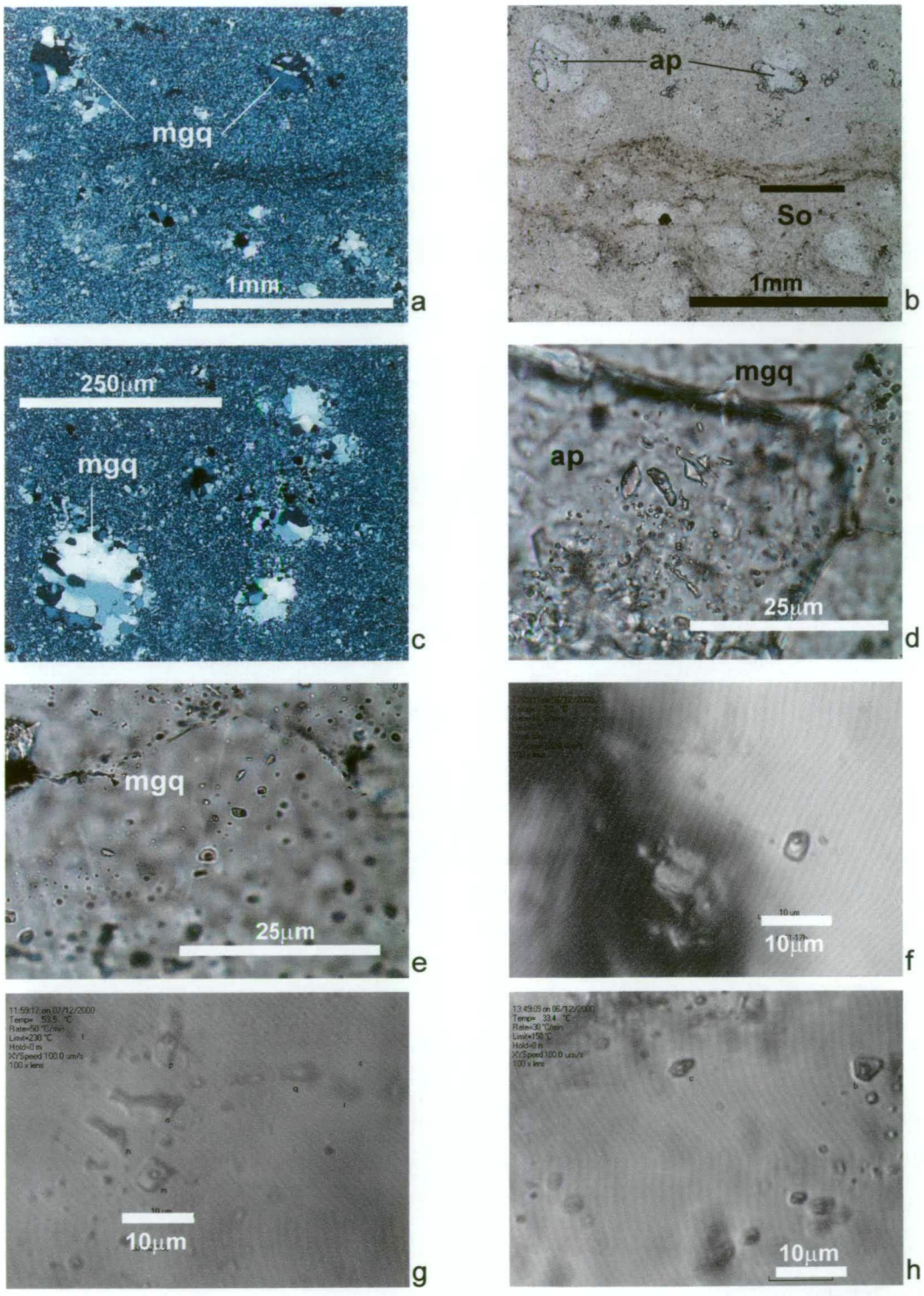

Figure 9.1: a) Spherical megaquartz (mgq) patches after radiolarian tests in chert above the Battle orebody, XPL (SJ161a, 18-1127, 39m); **b)** same view but PPL, bedding is defined by wispy carbonaceous layers and euhedral apatite (ap) grows within the megaquartz (mgq) patches, PPL (SJ161a, 18-1127, 39m); **c)** spherical megaquartz (mgq) patches randomly scattered in the microcrystalline groundmass, XPL (SJ161a, 18-1127, 39m); **d)** fluid inclusions in euhedral apatite (ap), PPL (SJ161a, 18-1127, 39m); **e)** fluid inclusions in megaquartz, interstitial to apatite, PPL (SJ161a, 18-1127, 39m); **f-h)** fluid inclusions measured in this study, from the spherical megaquartz patches in chert above the Battle orebody (SJ161a, 18-1127, 39m and SJ152, 18-1126, 61.4m).

formation ranging from 90 to 210°C, and rutile formation, greater than 200°C (Reyes, 1990). Fluid inclusions in the quartz interstitial to the euhedral rutile and apatite were examined to determine the nature of the hydrothermal fluid associated with the early precipitation of rutile, quartz and apatite in the semi-consolidated fine-grained sediments above the Battle ore horizon.

Fluid inclusions were also examined in quartz interstitial to sphalerite-chalcopyrite-galena ore in samples from various levels in the Battle orebody, and compared with data from the overlying caprocks. Inclusion data was also collected from various levels in the HW orebody for comparison with the Battle orebody data, and previous data published by Barrett and Sherlock (1996). Crosscutting quartz veins, probably associated with a later metamorphic event, contain variable carbonate, chlorite, chalcopyrite and tetrahedrite. Fluid inclusions in these veins were examined to determine whether they could be distinguished from inclusions in quartz interstitial to ore and in the siliceous caprocks.

The aims of this chapter are to:

1) Describe the fluid inclusions in the siliceous caprocks and compare with inclusion data from the underlying ore lenses;
2) Describe the fluid inclusion data from the HW orebody and compare with previously collected data from this orebody (Barrett and Sherlock, 1996), and fluid inclusion data from the Battle orebody;
3) Describe fluid inclusions in quartz in crosscutting metamorphic veins and determine whether they can be distinguished from primary fluid inclusions; and,
4) Compare fluid inclusion data from Myra Falls with other VHMS systems and active seafloor vent fluids.

9.2 Methods

Thirteen doubly polished thin sections (100μm thick) were made from drillhole and underground samples. These were collected from various positions in the massive sulphide orebodies, the overlying caprocks, and late crosscutting quartz-chlorite-carbonate-chalcopyrite-tetrahedrite veins and patches. All inclusions studied (about 350) were in quartz.

Microthermometric analysis was carried out on a Linkam MDS-600 heating freezing stage at CODES, University of Tasmania. The data reported here was reproducible to ± 2.0°C for heating and ± 0.3°C for freezing runs.

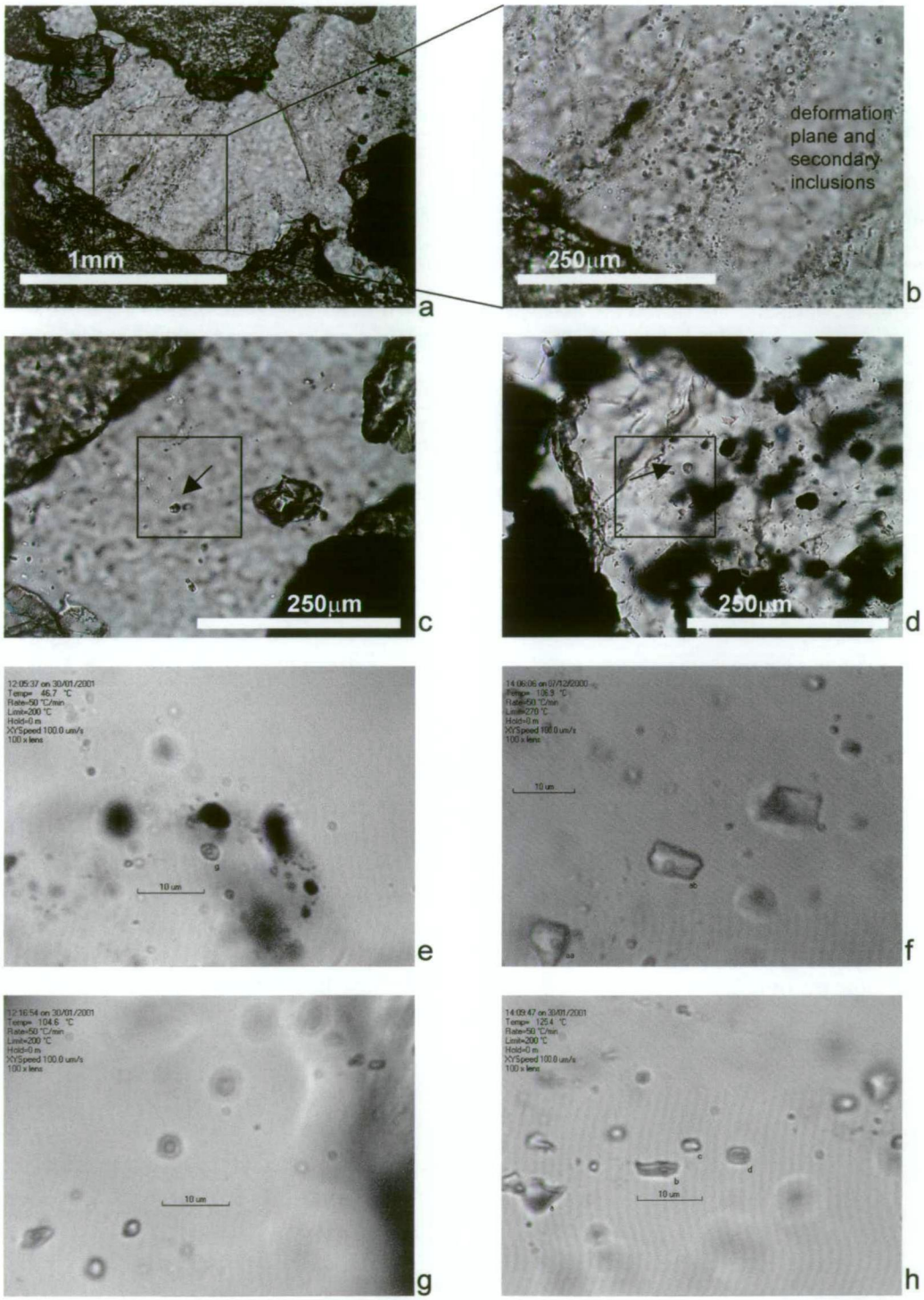

Figure 9.2: a) Interstitial quartz with sphalerite-chalcopyrite-galena-pyrite ore in the Battle orebody, PPL (18-979. 93.1m); **b)** close-up of same quartz patch with secondary inclusions defining deformation planes in the quartz, PPL (18-979. 93.1m); **c)** interstitial quartz with fine inclusions in sphalerite-chalcopyrite ore in the Battle orebody, PPL (18-979. 93.1m); **d)** interstitial quartz in sphalerite-chalcopyrite ore with fine ore inclusions, PPL (SJ639, drive S335C, HW mine); **e-h)** typical inclusions measured in interstitial quartz to ore from samples 18-979, 93.1m, SJ152, 18-1126, 61.4m, Battle mine and SJ85, 23 Shop, HW mine.

9.3 Fluid inclusion characteristics

Primary fluid inclusions were examined in quartz interstitial to euhedral apatite and rutile in spherical megaquartz patches in chert immediately above the Battle orebody (Figure 9.1a-c). The fluid inclusions were generally irregularly shaped and occurred in clusters, with individual inclusions, ranging from 3-8μm (Figure 9.1d-h). Fine inclusions were also observed in apatite, but as they were generally less than 1-2 μm, measurements were not possible.

Abundant inclusions were also examined in quartz, interstitial to sphalerite-chalcopyrite-galena ore in samples from the Battle and HW mines (Figure 9.2a-h). Inclusions in samples from different areas of the orebodies were examined, and compared with inclusions in late crosscutting quartz-chlorite-carbonate±chalcopyrite±tetrahedrite veins and patches (Figure 9.3a-c and 9.4a-f).

Primary, pseudosecondary and secondary inclusions were recognised in all types of quartz and were distinguished by the criteria summarised by Roedder (1984). Generally, the inclusions used in this study were of either primary or pseudosecondary origin, although in many cases it was difficult to distinguish the different types. Fluid inclusions that were most easily verified as primary, occupied quartz containing fine inclusions of the surrounding ore minerals (Figure 9.2d). However, secondary inclusions were common throughout, and often defined healed fracture planes developed during deformation events, especially during the D_1 folding event (eg. Figure 9.2a-b and 9.4c). Care was taken to identify and avoid these secondary inclusions.

Fluid inclusions observed in this study were liquid-vapour type-2a (liquid > vapour) and usually contained about 80% liquid and 20% vapour. Barrett and Sherlock (1996) recognised CO_2 and CH_4 gas rich inclusions in ore samples from the HW orebody, but these inclusion types were not observed in this study. Daughter minerals were not seen in any inclusions.

9.4 Results

A broad range of homogenisation temperatures and melting temperatures were observed in fluid inclusions from Myra Falls, and the full results are listed in Appendix 7.

a

b

Figure 9.3: a) Crosscutting quartz-chalcopyrite-carbonate vein at the upper contact of the massive sulphides and the overlying coarse-grained rhyolitic volcaniclastic unit (43 Block area, HW mine); **b)** crosscutting quartz-carbonate-chlorite-chalcopyrite vein in banded ore in the HW mine (23 level); **c)** crosscutting quartz-chlorite-carbonate-tetrahedrite veins in the HW mine (drive B390).

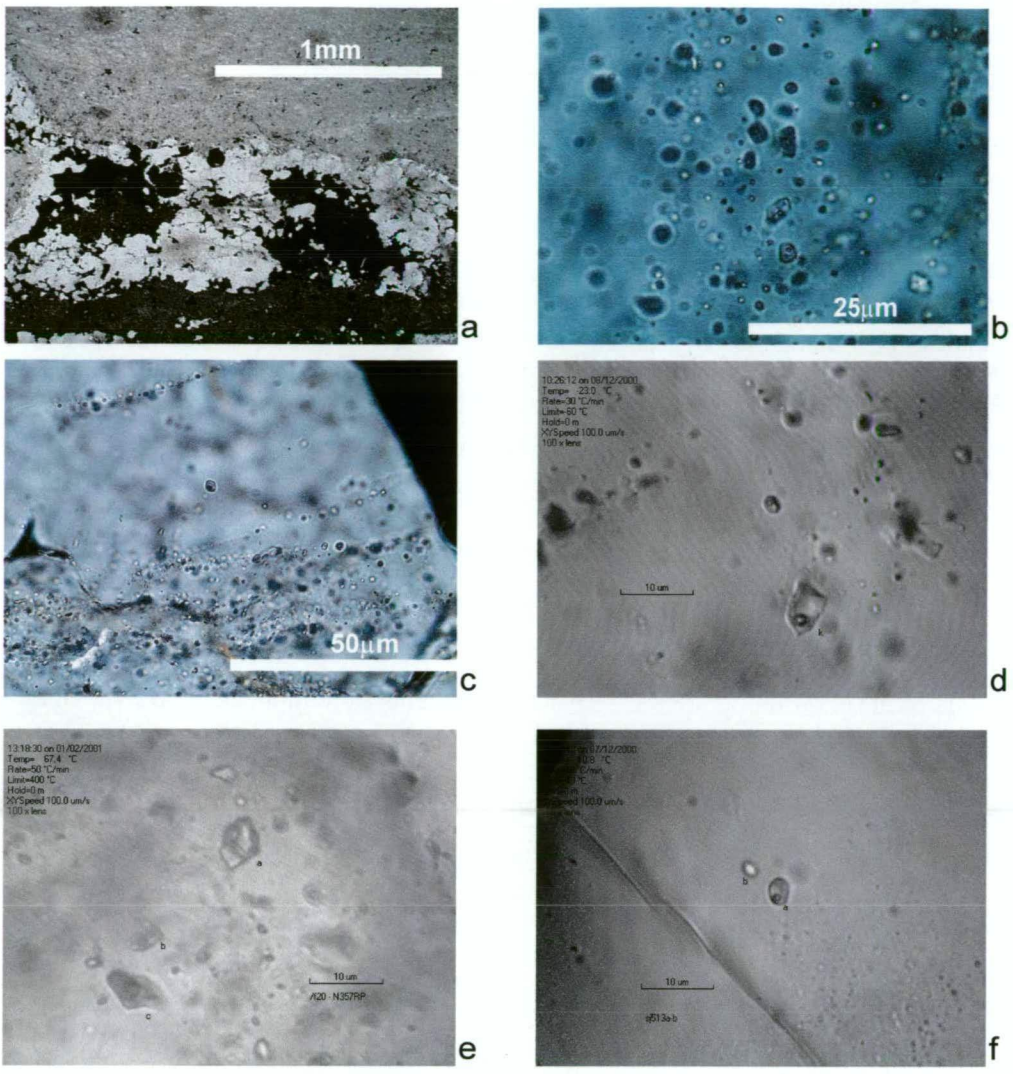

Figure 9.4: a) Crosscutting quartz-carbonate-pyrite vein in the contact zone between sphalerite-chalcopyrite ore and the overlying chert, PPL, SJ513, drive ST183A, Battle mine; **b)** fluid inclusions from the previous quartz vein in previous photomicrograph, PPL (SJ513, drive ST183A, Battle mine); **c)** secondary fluid inclusions in a late quartz vein crosscutting chalcopyrite-rich ore in drive N357RP, HW mine, PPL; **d-e)** typical inclusions measured in late quartz veins from sample SJ513, drive ST183A, Battle mine and F20, N357RP, HW mine.

9.4.1 Temperature of homogenisation (Th)

Siliceous caprocks above Battle orebody

The results from heating experiments indicate that hydrothermal solutions ranged from 102 to 250° C, in fluid inclusions from quartz in the siliceous caprocks above the Battle orebody. Homogenisation temperatures are shown in Figure 9.5a.

Battle orebody

Hydrothermal solutions ranged from 100-215° C in fluid inclusions from quartz interstitial to sulphides in the main lens of the Battle orebody (Figure 9.5b-c). Homogenisation temperatures measured in quartz in the Upper Zone massive sulphide lenses also display a similar range, from 101 to 210° C, and are shown in Figure 9.5d.

There appears to be a slight shift in homogenisation temperatures with increasing depth in the main Battle ore lens. Fluid inclusions from samples at the upper ore contact display slightly lower homogenisation temperatures than the majority of inclusions from samples in the middle of the main Battle ore lens. However, in general, homogenisation temperatures from inclusions in quartz from the Battle orebody, are very similar to those measured in the overlying siliceous caprocks, indicating that the temperature of the hydrothermal fluids in the Battle orebody was similar to hydrothermal fluids flowing through the overlying caprocks.

Inclusions in crosscutting quartz-carbonate-chlorite-chalcopyrite veins and patches display a wide range of homogenisation temperatures, 95 to 175°C, but in general, appear to be slightly lower than the majority of primary inclusions in quartz interstitial to ore and in the siliceous caprocks (Figure 9.5e).

HW orebody

Homogenisation temperatures in quartz interstitial to ore in the HW mine range from 120 to 215°C (Figure 9.6a-c), and are similar to Th measurements (145 to 210°C) recorded by Barrett and Sherlock (1996). This range of Th data is similar to Th data from the Battle orebody, and the HW orebody also displays a slight increase in Th with depth in the orebody, similar to the Battle deposit. In the HW mine, the majority of inclusions are less than 180°C at the upper ore contact, and greater than 160-180°C in samples from the basal part of the orebody and the stockwork feeder zone (stockwork samples from Barrett and Sherlock, 1996).

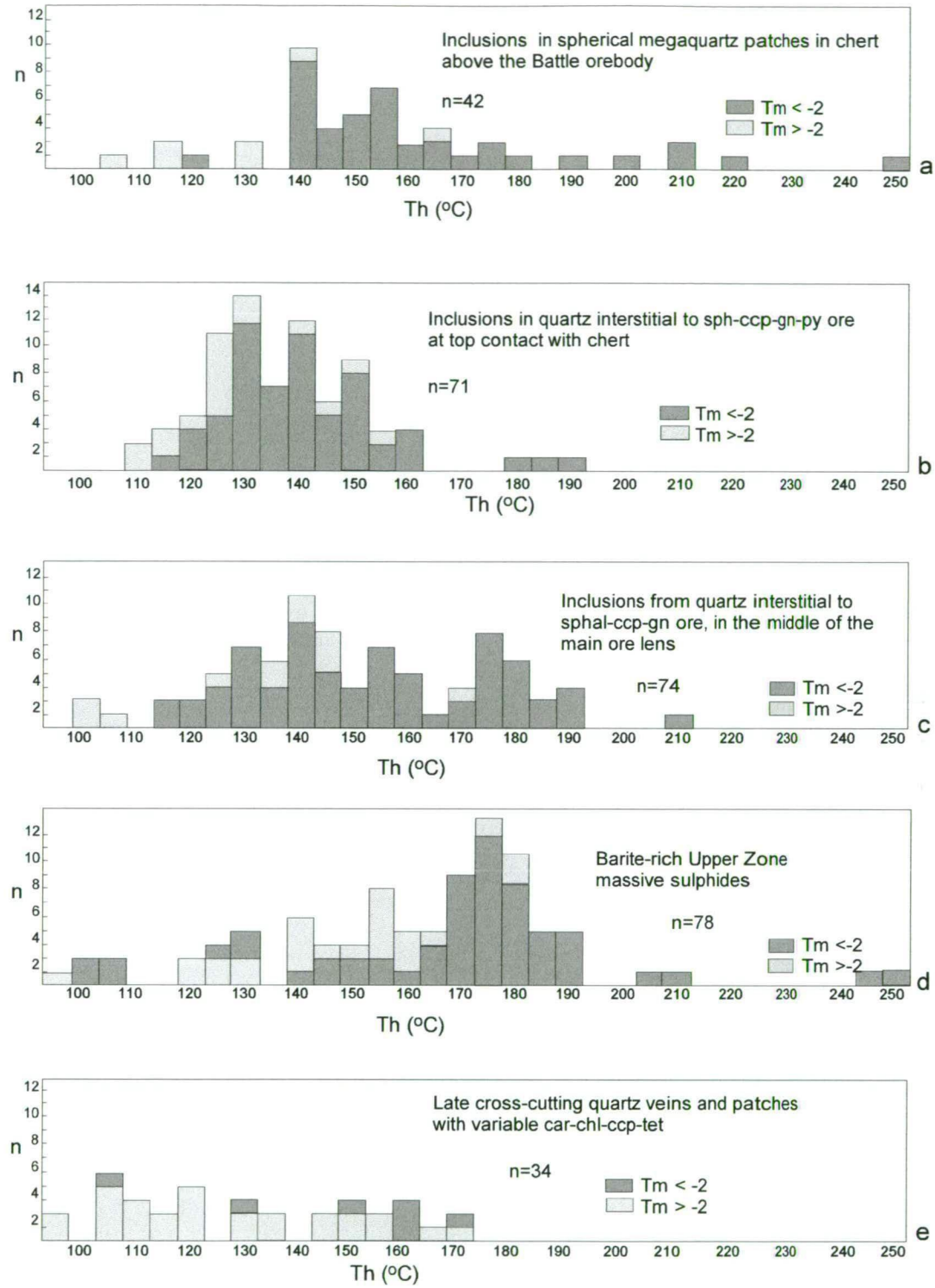

Figure 9.5: Histograms of fluid inclusions from selected samples from various locations in the Battle mine: **a)** inclusions in spherical megaquartz patches, after radiolarian tests (samples: SJ161a, 18-1127, 39.5m; SJ152, 18-1126, 61.4m); **b)** inclusions in quartz interstitial to sphalerite-chalcopyrite-galena ore at upper ore contact with chert (sample: SJ160, 18-1127, 39m); **c)** inclusions from quartz interstitial to sphalerite-chalcopyrite-galena ore in the middle of the main ore lens (samples: F18, 18-979, 93.1m; F22, 18-1006, 101.7m); d) inclusions in quartz interstitial to barite-rich ore in the Upper Zone, Battle Mine (sample F16, section 1420E, drillhole 18-975, 77.5m); **e)** inclusions in late crosscutting quartz veins with variable carbonate, chlorite, chalcopyrite and tetrahedrite (samples F15, 18-1003, 93.4m; SJ513, drive ST183A). Mineral abbreviations: car = carbonate; tet = tetrahedrite; q = quartz; chl = chlorite; ccp = chalcopyrite; gn = galena; sph = sphalerite.

Fluid inclusions in crosscutting quartz-carbonate-chlorite-chalcopyrite veins and patches display a wide range of homogenisation temperatures, 95 to 195°C, but overall, appear to be slightly lower than the majority of primary inclusions in quartz interstitial to ore (Figure 9.6d).

9.4.2 Temperature of melting (Tm) and salinity

Successful freezing runs were performed on over 350 inclusions and yielded melting temperatures (Tm), ranging from +2.3 to -8.6°C. Salinity determinations based on Tm, indicate that the quartz hosted inclusion fluids are dilute to saline, ranging from 0 to 12.4 eq. wt % NaCl. However, salinity estimates determined from Tm in relatively dilute fluids, can be significantly in error (up to –1.5°C) when CO_2 or other volatiles are present (Hedenquist and Henley, 1985). Preferential loss of CO_2 to the gas phase on effervescence can result in an increase in the ice melting temperature for the residual liquid and therefore give an apparent salinity decrease. Therefore, the salinities described above represent maximum values and could be up to 2.5 eq. wt % NaCl lower (-1.5°C = 2.5 eq. wt % NaCl). However, as gas hydrates were not observed in any freezing runs, the gas content in the inclusion fluids must be less than 4 wt.% CO_2 (Hedenquist and Henley, 1985). No clathrates (Collins, 1979) were observed in any freezing runs.

Siliceous caprocks above the Battle orebody

The majority of inclusions from the siliceous caprocks have salinities ranging from 2.5 to 12.1 eq. wt % NaCl, with most greater than 4 eq. wt % NaCl (Figure 9.7a). A few inclusions display low salinities (<2 eq. wt % NaCl) and generally have lower homogenisation temperatures than the more saline inclusions. These lower salinity inclusions most likely represent secondary inclusions.

Battle orebody

Salinities, based on Tm, for inclusions throughout the Battle orebody are shown in Figure 9.7b-c, and range from 0 to 12.4 eq. wt % NaCl. Salinities for inclusions in quartz from the Upper Zone sulphides also display a similar range, from 0 to 9.6 eq. wt % NaCl (Figure 9.7d). Fluid inclusions with very low salinities, less than 2-3 eq. wt % NaCl, are similar to the lower salinities measured in the crosscutting quartz veins (Figure 9.7e) and most likely represent secondary inclusions.

There appears to be a slight increase in salinity with depth in the Battle orebody, with the majority of inclusions from the upper ore contact ranging from 3 to 9 eq. wt % NaCl; whereas, inclusions from the middle of the ore lens have salinities ranging from 2.5 to 12.4

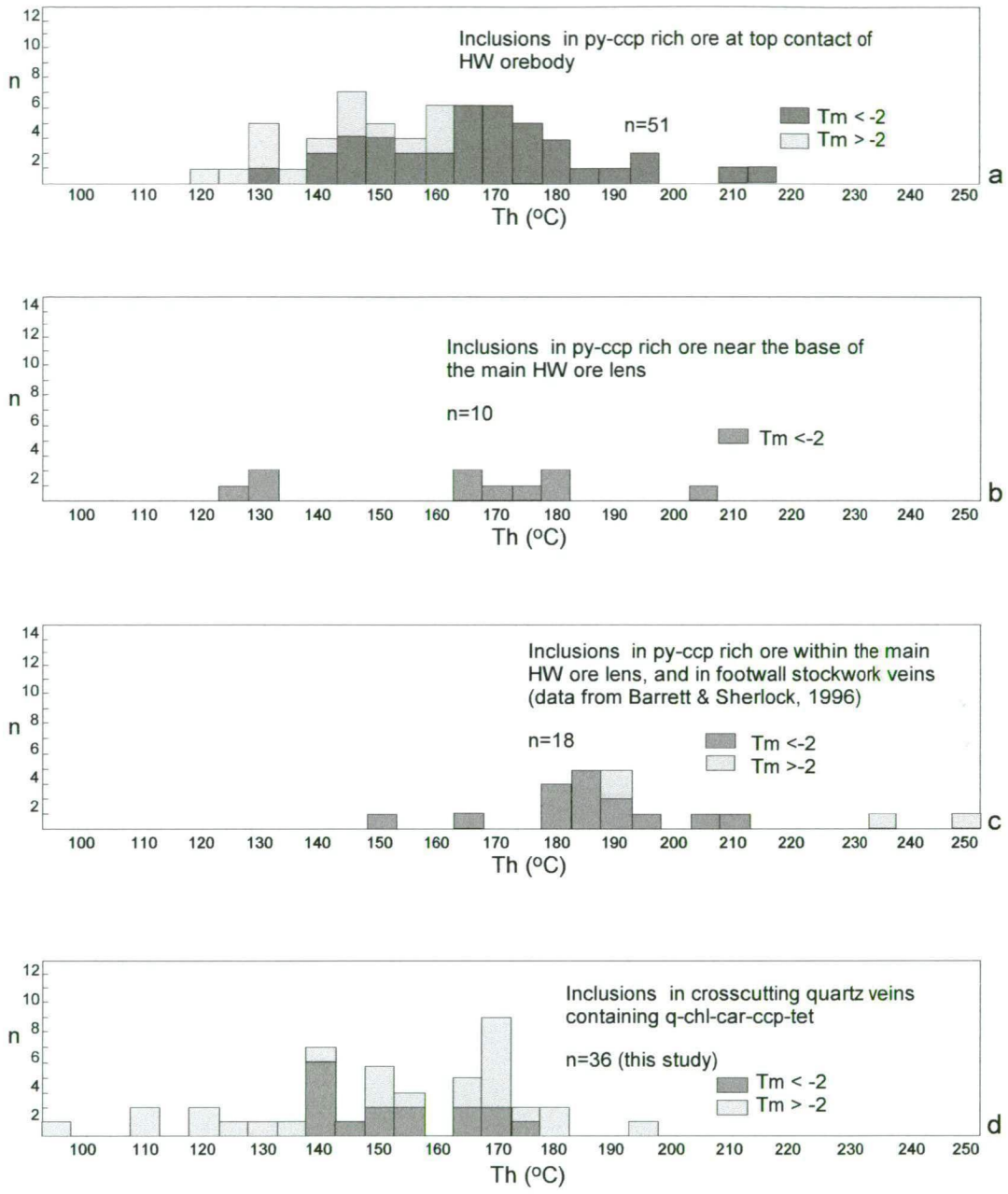

Figure 9.6: Histograms illustrating the variation in homogenization temperatures of inclusions from different areas of the HW orebody: **a)** data from inclusions in quartz interstitial to chalcopyrite-pyrite ore at the upper ore contact (samples: SJ638, drive S335C; SJ80, 23-488, 1.2m; SJ85, 23-488, 14.3m); **b)** inclusions in pyrite-chalcopyrite ore in basal zone of the main ore lens (sample F20, drive N357RP); **c)** inclusions in pyrite-chalcopyrite ore at base of the main ore lens and in footwall stockwork veins (data from Barrett and Sherlock, 1996); **d)** inclusions in crosscutting quartz-carbonate-chlorite-chalcopyrite veins (sample: F20, N357RP; data from Barrett and Sherlock, 1996). Mineral abbreviations: car = carbonate; tet = tetrahedrite; q = quartz; chl = chlorite; ccp = chalcopyrite; gn = galena; sph = sphalerite.

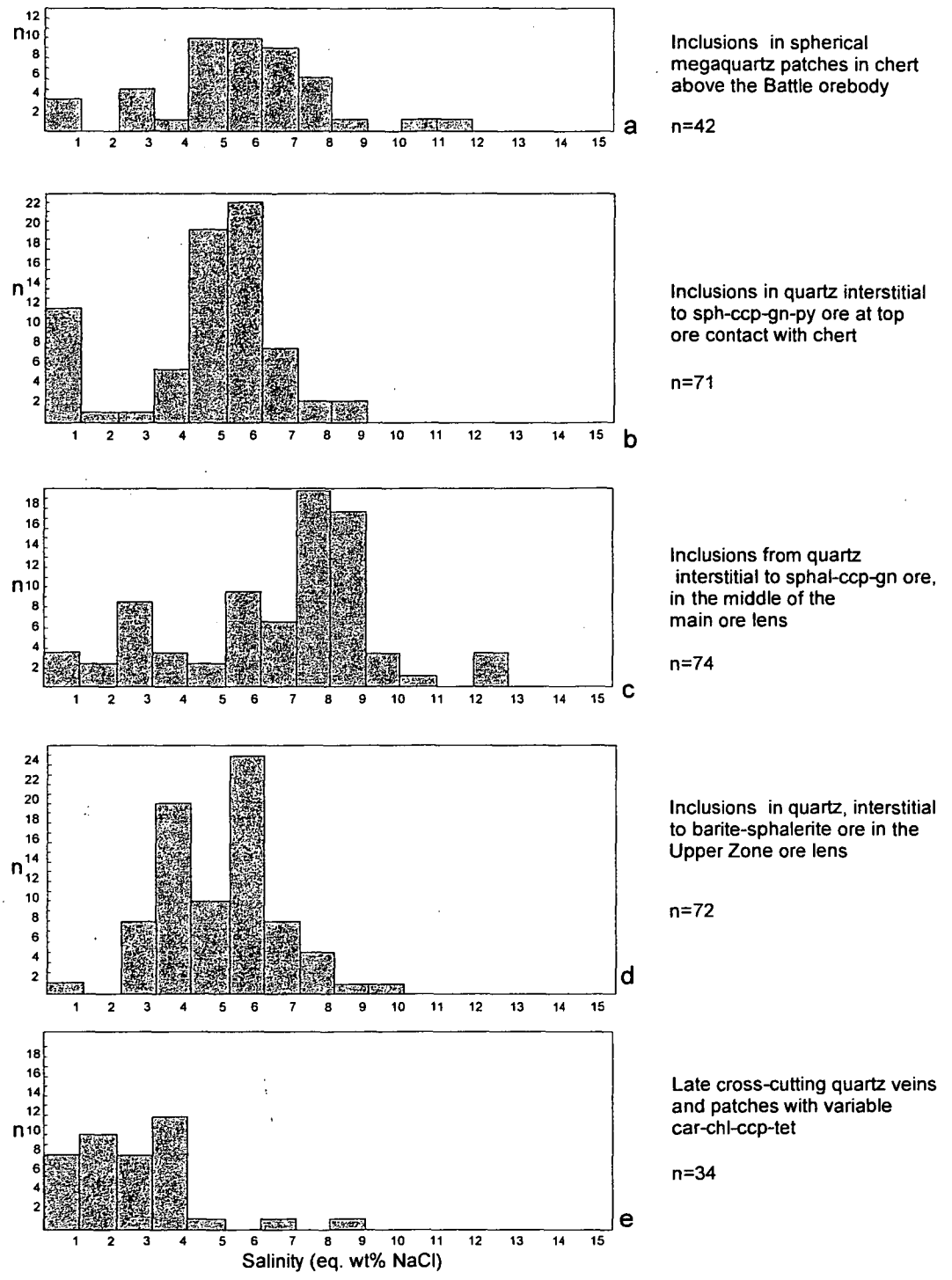

Figure 9.7: Histograms illustrating the variation in salinity of fluid inclusions from selected samples from various locations in the Battle mine: **a)** inclusions in spherical megaquartz patches, after radiolarian tests (samples: SJ161a, 18-1127, 39.5m; SJ152, 18-1126, 61.4m); **b)** inclusions in quartz interstitial to sphalerite-chalcopyrite-galena ore at upper ore contact with chert (sample: SJ160, 18-1127, 39m); **c)** inclusions from quartz interstitial to sphalerite-chalcopyrite-galena ore in the middle of the main ore lens (samples: F18, 18-979, 93.1m; F22, 18-1006, 101.7m); **d)** inclusions in quartz interstitial to barite-sphalerite ore in upper lens, Battle mine, (sample: F16, 18-975, 77.5m); **e)** inclusions in late crosscutting quartz veins with variable carbonate, chlorite, chalcopyrite and tetrahedrite (samples F15, 18-1003, 93.4m; SJ513, drive ST183A). Mineral abbreviations: car = carbonate; tet = tetrahedrite; q = quartz; chl = chlorite; ccp = chalcopyrite; gn = galena; sph = sphalerite.

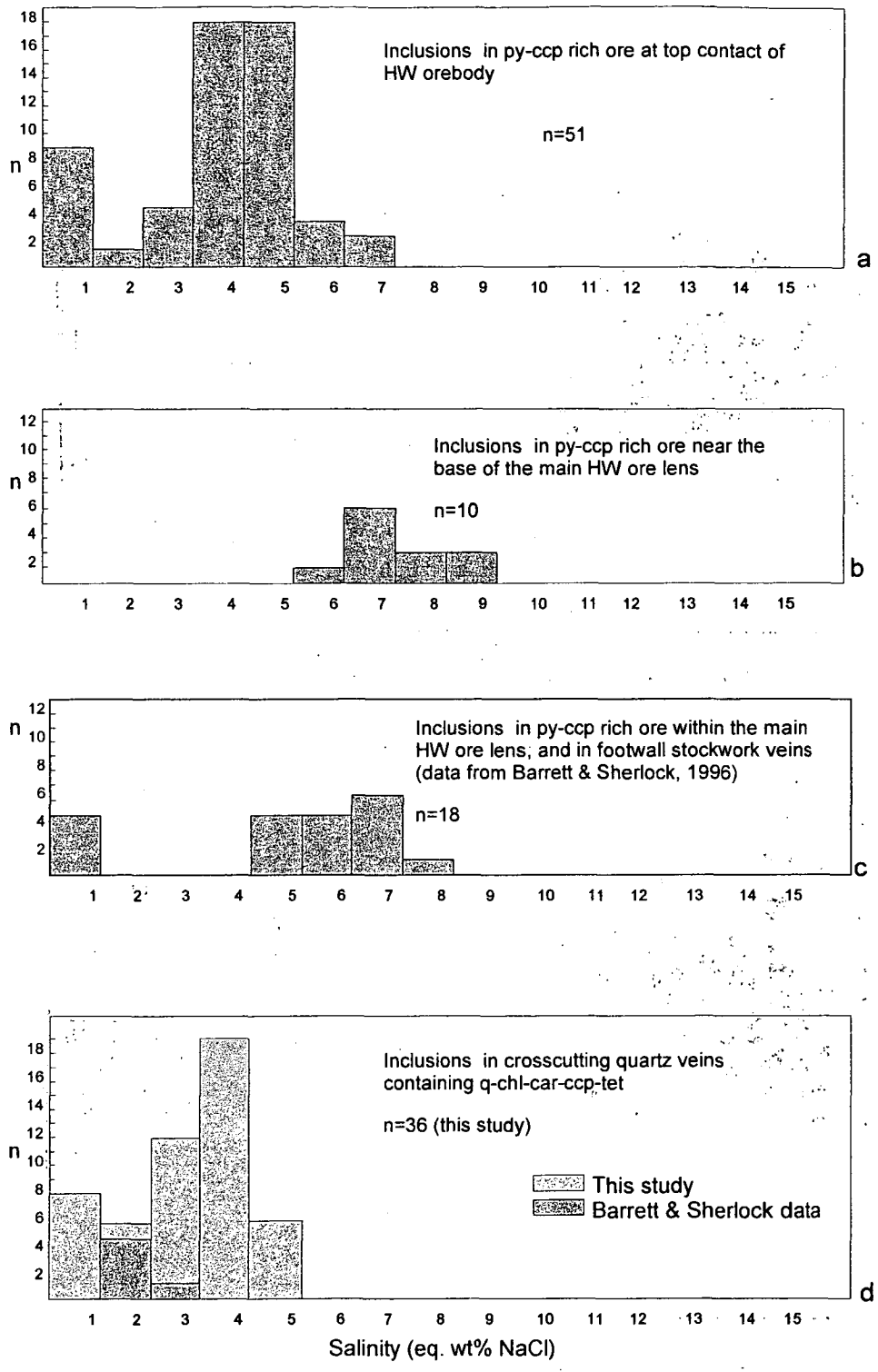

Figure 9.8: Histograms illustrating the variation in salinity of inclusions from different areas of the HW orebody: **a)** data from inclusions in quartz interstitial to chalcopyrite-pyrite ore at the upper ore contact (samples: SJ638, drive S335C; SJ80, 23-488, 1.2m; SJ85, 23-488, 14.3m); **b)** inclusions in pyrite-chalcopyrite ore in basal zone of the main ore lens (sample F20, drive N357RP); **c)** inclusions in pyrite-chalcopyrite ore at base of the main ore lens and in footwall stockwork veins (data from Barrett and Sherlock, 1996); **d)** inclusions in crosscutting quartz-carbonate-chlorite-chalcopyrite veins (sample: F20, N357RP; data from Barrett and Sherlock, 1996). Mineral abbreviations: car = carbonate; tet = tetrahedrite; q = quartz; chl = chlorite; ccp = chalcopyrite; gn = galena; sph = sphalerite.

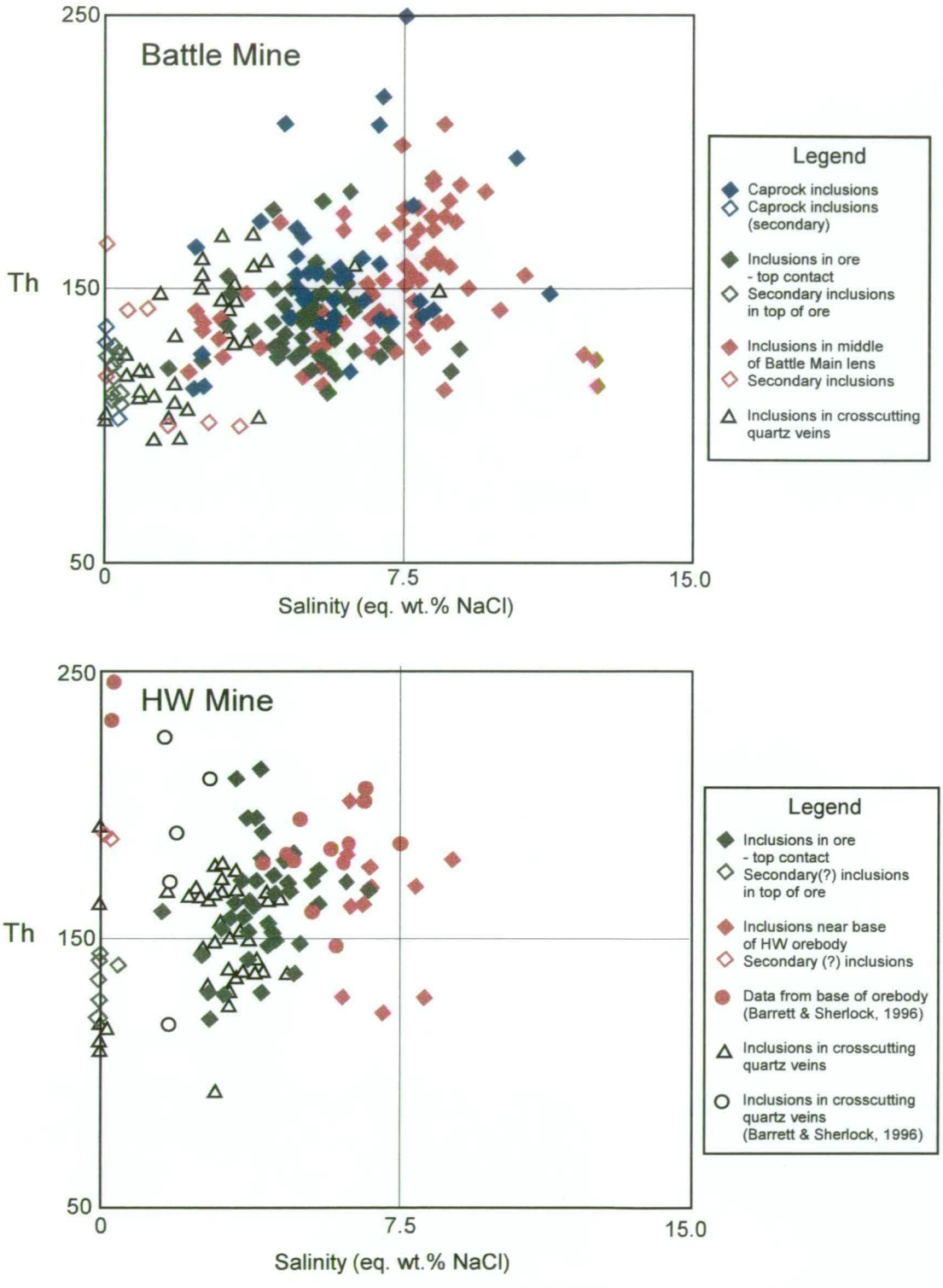

Figure 9.9: Th-salinity diagrams illustrating the variation in fluid inclusions from different parts of the Battle and HW orebodies (including the siliceous caprocks above the Battle orebody).

eq. wt % NaCl. The range of salinities observed in the Battle orebody, is very similar to those measured in the overlying siliceous caprocks.

HW orebody

The range of salinities, based on Tm, for inclusions from quartz interstitial to massive sulphides in the HW orebody are shown in Figure 9.8. The majority of inclusions have salinities greater than 2 eq. wt % NaCl, and range from 2 to 8.8 eq. wt % NaCl. Salinities measured in samples from the upper ore contact appear to be slightly lower than the inclusion data from the middle and base of the orebody. At the upper ore contact salinities range from 2 to 7 wt.% equiv., whereas, the samples from greater depths in the orebody display a range from 4-9 eq. wt % NaCl. The very low salinity inclusions (<2 eq. wt % NaCl) most likely represent secondary inclusions.

Salinites measured in inclusions from crosscutting quartz veins are generally lower than 5 wt.% NaCl equiv, with most less than 2 wt.% NaCl (Figure 9.8d). These values are similar to those recorded by Barrett and Sherlock (1996), shown in Figure 9.8d.

Salinity and homogenisation temperature data for the siliceous caprocks, and the Battle and HW orebodies are shown in Figure 9.9. These plots illustrate the similar homogenisation temperatures of inclusions in the two orebodies. Inclusions in the siliceous caprocks and the Battle orebody display a broader range of salinities than the HW orebody. The plots also show the slight shift to lower salinities and homogenisation temperatures in samples at the upper ore contact. Fluid inclusion data from the crosscutting quartz veins form broad fields in both plots, but generally display lower salinities than the majority of fluid inclusions in the caprocks and ore, with the exception of probable secondary inclusions in these samples.

9.4.3 Fluid densities

The density of hydrothermal fluids can be estimated from the homogenisation temperatures and salinities of fluid inclusions (Roedder and Bodnar, 1980; Brown, 1989). Figure 9.10a shows the total Battle and HW orebody inclusion data, with density contours in g/cm^3. A wide range of fluid densities is indicated by the inclusion data, ranging from 0.88 to 1.04 g/cm^3. The highest density fluids occur in quartz interstitial to sulphides in the Battle orebody. Inclusion fluids in the overlying siliceous caprocks have a similar density to the majority of inclusions from the Battle orebody and are generally <1.0 g/cm^3. The lowest density inclusion fluids occur in quartz interstitial to sulphides in the stockwork zone of the HW orebody, 0.81g/cm^3. The effect of changing densities on the behaviour of the hydrothermal fluids is discussed in section 9.6.4.

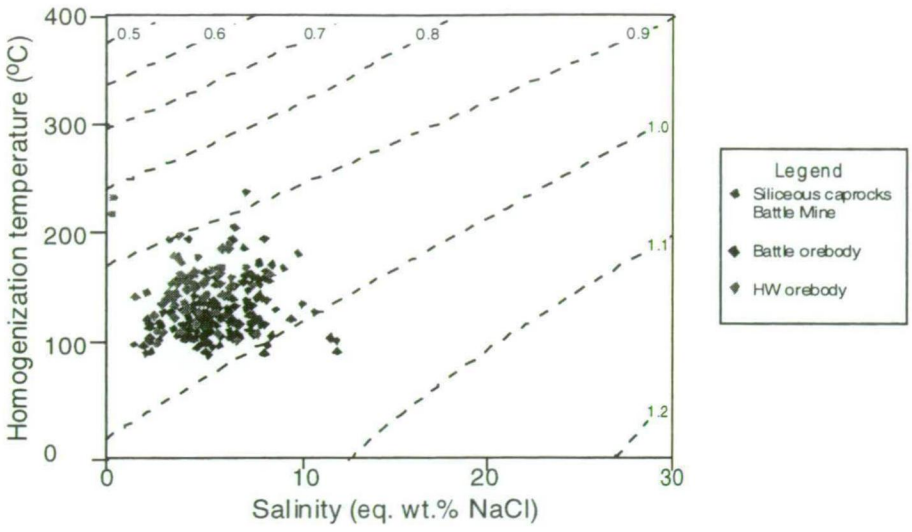

Figure 9.10: Temperature-salinity plot showing densities (g/cm^3) of vapour-saturated NaCl-H_2O solutions (modified from Wilkinson, 2001).

A comparison of fluid densities from inclusions in the caprocks and massive sulphides at Myra Falls with other VHMS deposits, including recent seafloor deposits, is shown in Figure 9.11. In general, inclusion data from Myra Falls, particularly from the Battle deposit and the overlying siliceous caprocks, appear to be more dense than many other VHMS deposits and are most similar to the range of fluid densities displayed by the Silvermines and Sullivan Pb-Zn deposits. Fluid densities of inclusion data from Myra Falls are close to the density of ambient bottom water at 2000m depth and 2° C, which is 1.03 g/cm^3 (Scott, 1997). The low density contrast of the hydrothermal fluids and the ambient bottom water will affect the behaviour of the hydrothermal fluid and is discussed in Section 10.3.9.

9.4.4 Eutectic temperature (Te)

The composition of the fluids can be estimated from the eutectic temperature (Te), or temperature of first melt. However, eutectic temperatures were only clearly observed in a few inclusions, due to their small size. The eutectic temperatures observed, ranged from –21 to –24°C. This is slightly lower than those observed by Barrett and Sherlock (1996), who measured eutectic temperatures ranging from –21.3 to –38.9°C (average –34.3°C). The results from this study suggest that the first melting temperature approximates the eutectic temperature of the salt-water system and is consistent with melting of salt hydrates in the H_2O-NaCl system (Davis et al., 1990).

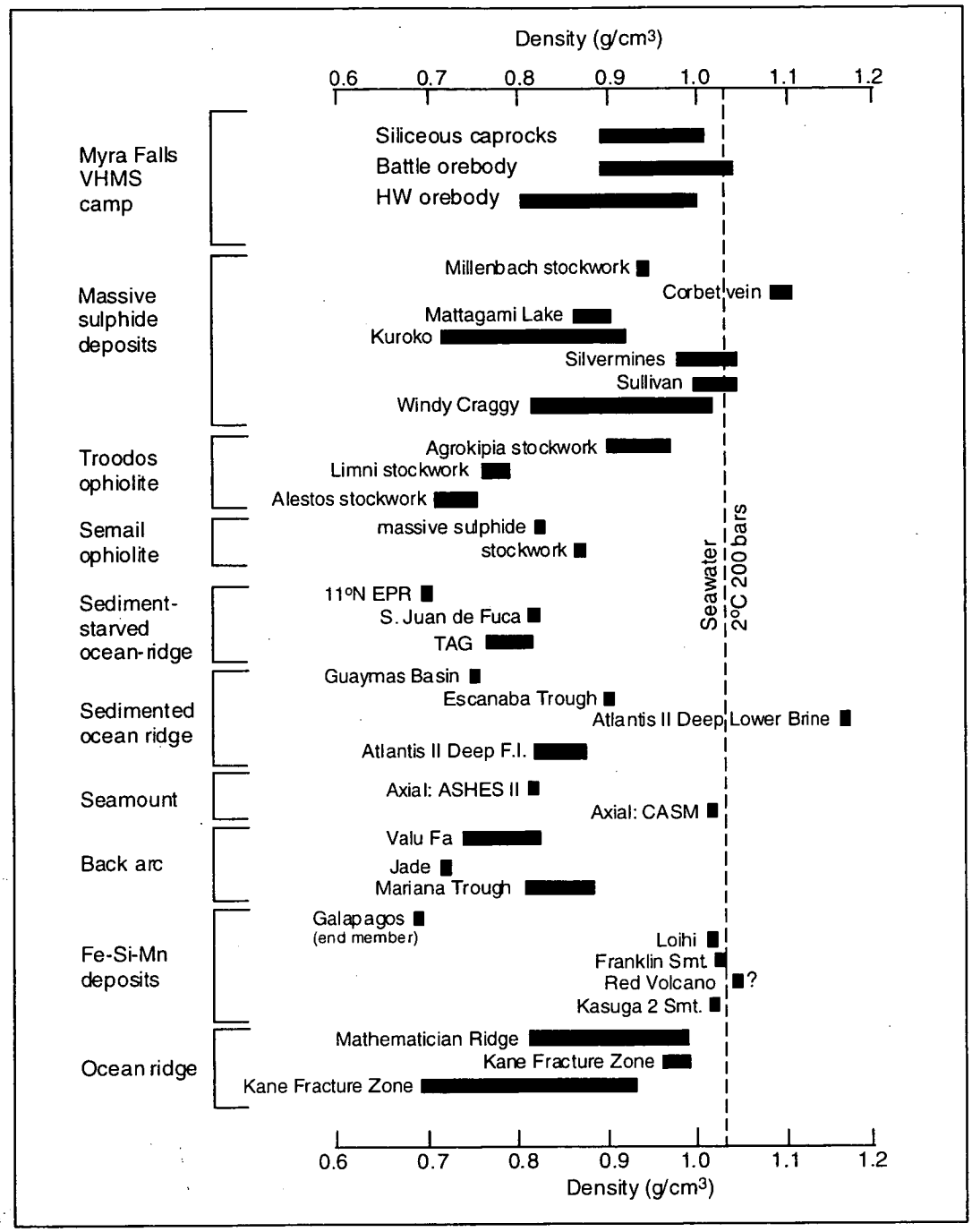

Figure 9.11: Densities of ancient and modern hydrothermal fluids, relative to seawater at 2°C and 2000m water depth (200 bars Pf), modified from Scott (1997). Density estimates from fluid inclusion data from Myra Falls are also included.

9.5 Metamorphic effects

The sequence at Myra Falls has been affected by lower to mid greenschist facies metamorphism and multiple deformation episodes. Ore textures have been described in detail by Sinclair (2000), and display evidence of widespread recrystallization. However, many primary textures are still preserved including features such as, pyrite framboids, early

open-space filling by euhedral apatite and rutile in spherical megaquartz patches in chert (Figure 9.1a-c), and fine intergrowths of galena and pyrite (e.g., Figure 6.20e). The abundant crosscutting quartz-carbonate-chlorite±chalcopyrite±tetrahedrite veins are most likely related to the metamorphic event. The lower salinities and low to moderate homogenisation temperatures of fluid inclusions from these veins makes them clearly distinguishable from primary fluid inclusions in quartz interstitial to ore. This suggests that the primary inclusions in quartz interstitial to ore and in the siliceous caprocks, represent trapped fluids related to ore formation and do not reflect the late metamorphic event.

Primary fluid inclusions have been recognised in other deformed VHMS deposits such as the Raul Mine, in Peru. Ripley and Ohmoto (1977) recorded homogenisation temperatures of 350±10°C in many primary inclusions, even though the host rocks had been metamorphosed to upper greenschist-lower amphibolite facies, with temperatures up to 400-500°C. Khin Zaw and Large (1992) recognized two major fluid systems in a fluid inclusion study of the South Hercules deposit in Western Tasmania. The first fluid type was associated with the Cambrian ore formation event, and was composed of low salinity, low temperature fluids (Th 125-210°C, <4.2 eq. wt % NaCl). The second fluid type, observed in inclusions in crosscutting veins, was associated with Devonian metamorphic fluids and/or granite related fluids. This fluid type had more variable temperatures, higher salinity and contained CO_2 (Th 125-300°C, up to 15 eq. wt % NaCl).

9.6 Discussion

9.6.1 Caprock fluid inclusions

The presence of fine inclusions in spherical megaquartz patches in the chert or siliceous caprocks above the Battle orebody, provides a unique opportunity to determine the trapping temperature and salinity of the hydrothermal fluids associated with near-seafloor silica deposition above a VHMS deposit. However, as the megaquartz patches represent early infilling of primary pore space, predating the main silicification event, they only provide an approximate guide to temperature and salinities of silica-bearing fluids associated with the formation of the siliceous caprocks.

Fluid inclusions in the caprocks at Myra Falls range from 2.1 to 12.1 eq. wt % NaCl, with Th ranging from 100 to 250°C. The salinities and Th values are very similar to those measured in quartz interstitial to sulphides near the top of the Battle orebody (2 to 12.4 eq. wt % NaCl, Th 100 to 215°C). The similar salinity and Th values indicate that the caprock silica and sulphides in the upper part of the Battle orebody were deposited from hydrothermal fluids with similar properties.

Caprock fluid inclusion data plots together with data from the Battle and HW orebodies on a Th-salinity plot (Figure 9.12) and lies in the Kuroko field, illustrating the similarity between these deposits. Fluid inclusion studies of the Kuroko deposits indicate that aqueous, two-phase liquid-vapour inclusions with relatively low to moderate salinities, 1-8.4 eq. wt % NaCl, and low to moderate homogenisation temperatures, 80-340°C are dominant (Pisutha-Arnond and Ohmoto, 1983; Bryndzia et al., 1983; Foley, 1986). Fluid inclusion data from Myra Falls shows a slightly wider range of salinities and generally lower homogenisation temperatures than the Kuroko deposits. The relatively low temperatures may indicate significant mixing with seawater and/or conductive cooling of the hydrothermal fluids in the near seafloor environment.

Table 9.1 provides a more detailed comparison between Myra Falls inclusion data (including the caprock inclusions) and other VHMS deposits and active seafloor hydrothermal fields. Th and salinity data from Myra Falls is most similar to the Eskay Creek deposit, which has Th ranging from 82 to 179°C, and salinity from 2.9 to 10.5 eq. wt % NaCl (Sherlock et al. 1999). Most other VHMS deposits and active seafloor hydrothermal fields appear to have formed from higher temperature fluids.

9.6.2 Salinity

Salinity measurements in the siliceous caprocks (2 to 12.1 eq. wt % NaCl) and in quartz interstitial to massive sulphides in the Battle and HW orebodies (2 to 12.4 eq. wt % NaCl) are generally much higher than normal seawater, which is thought to be approximately 3.0 eq. wt % NaCl, with a Tm of about −1.8°C (Roedder, 1984).

Salinities, both above and below normal seawater, have been reported from other VHMS deposits. For example, 3.1 to 21 eq. wt % NaCl in quartz from the Hellyer deposit, western Tasmania (Khin Zaw, 1996; Solomon et al. in press); 2 to 15 eq. wt % NaCl in quartz in the active Jade hydrothermal field, Central Okinawa Trough, Japan (Petersen et al. 2001); 3 to 9 eq. wt % NaCl in the ophiolite-hosted copper deposit in Guatemala (Wilson and Petersen, 1989); up to 45 eq. wt % NaCl in vein quartz on Mathematician Ridge on the Mid Atlantic Ridge (Vanko, 1988); and 3.8 to 4.1 eq. wt % NaCl in active seafloor vent fluids in the Guaymas Basin (Peter and Scott, 1988). Further examples are listed in Table 9.1.

Large salinity variations in active seafloor vent fluids have been used as evidence for two-phase separation at depth. For example, the Mid Atlantic Ridge (Vanko et al.1992); Mathematician Ridge, EPR, (Stakes and Vanko, 1986; Bischoff and Rosenbauer, 1987);

TAG hdyrothermal field, Mid-Atlantic Ridge (Petersen et al. 2000); and the Jade hydrothermal field in the Central Okinawa Trough, Japan (Lueders et al. 2001).

Boiling in geothermal systems is recognised as an effective process for increasing the salinity of the hydrothermal fluids, by producing residual, more saline liquids (e.g., Cathles, 1993). Boiling is also an important process for metal deposition, such as in epithermal vein systems (e.g., Buchanan, 1981; Seward, 1989). Evidence for boiling is provided by mineralogical textures, such as bladed calcite (e.g., Simmons and Christenson, 1994) and the presence of coexisting vapour-rich and liquid-rich inclusions in the same healed fracture. However, these textures are not common in VHMS deposits, but two-phase separation is still inferred in seafloor geothermal systems where hydrothermal fluid temperatures are above the critical point of water, in water depths between 1-3km (Bischoff and Rosenbauer, 1987). At depths of 2500-3000 m, the two-phase boundary of water is between 385-405°C (Herzig and Hannington, 2000). Lueders et al. (2001) suggest that the wide range of salinities measured in the Jade hydrothermal system is the result of two-phase separation at depth. The resultant brine favoured the transportation of other metals besides Pb, Zn, Fe and Cu, and lead to a complex tetrahedrite/tennantite and enargite-bearing sulfide orebody in the stockwork region. They also show that the fluid inclusions in the enargite have salinities more than three times higher than seawater.

Wilkinson (2001) lists a number of processes, excluding boiling, which could also affect the salinity of a hydrothermal fluid and these include, 1) mixing of seawater with more saline liquids; 2) water loss/gain during rock hydration/dehydration reactions; and 3) buffering by a soluble Cl-bearing phase. The effects of these different processes on the salinity of the fluid are summarised in Figure 9.13. Cathles (1993) also suggests that narrow upflow zones in a hydrothermal system could make the physical system vulnerable to rapid chemical changes, especially fluctuations of discharge salinity, which could vary from 0.5 to 2x seawater salinity.

No direct evidence of boiling was found at Myra Falls (co-existing pairs of vapour-rich and liquid-rich inclusions were not observed). However, the very wide range of salinities and the lack of a local brine source (e.g., evaporites), indicates that two-phase separation may have occurred at depth, resulting in a more saline fluid. However, the higher salinities could also reflect input of magmatic fluids.

The slight increase in homogenisation temperatures and salinity with depth in the Battle and HW orebodies is similar to temperature shifts in inclusion data from the Kuroko deposits (Roedder, 1984). At Kuroko, in deposits such as the Fukazawa mine, Th and salinity values

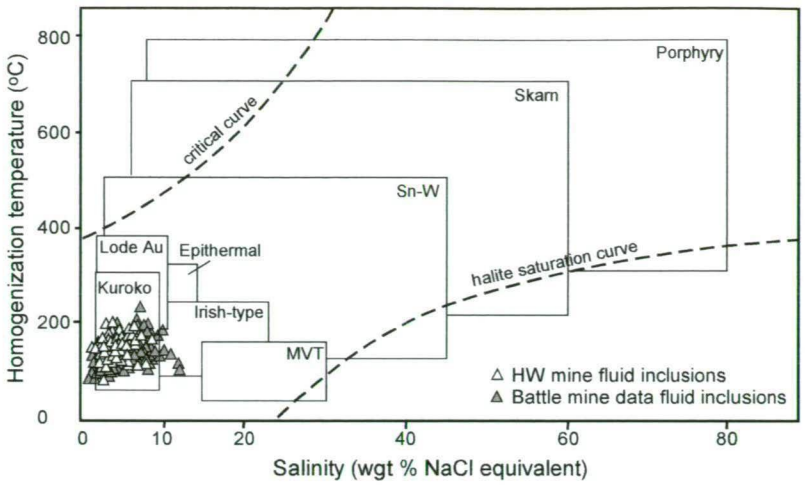

Figure 9.12: Homogenisation temperature-salinity diagram illustrating the typical ranges for inclusions from different deposit types (modified from Wilkinson, 2001). Note that the HW and Battle mine data fall into the Kuroko field, although with slightly higher salinities in several samples from the Battle mine.

DEPOSIT	TYPE	Th (°C)	Tm (°C)	REFERENCE
Myra Falls (Canada)				
Siliceous caprocks	felsic volc.	102-250	-1.0 to -8.1	This study
Battle orebody		100-215	-1.0 to -8.4	
HW orebody		120-215	-0.9 to -5.7	
Eskay Creek (Canada)	felsic volc. mudstone-hosted	82-179	-1.7 to -7.0	Sherlock et al. 1999
Cyprus	ophiolite	288-380	-1.4 to -2.8	Spooner and Bray, 1977; Spooner 1981
Uwamuki 2 (Japan)	Kuroko	243-347	-2.3 to -4.2	Bryndzia et al. 1983
Kuroko District (Japan)	Kuroko	200-330	-2.1 to -3.7	Pisutha-Arnoud and Ohmoto, 1983
Hellyer (Tasmania)	felsic volc.	170-322	-1.8 to -17.7	Khin Zaw et al, 1996; Solomon et al. in press
Oxec (Guatemala)	ophiolite	250-357	-1.8 to -5.8	Wilson and Petersen, 1989
MODERN SEAFLOOR DEPOSITS				
East Pacific Rise (14°N)	ophiolite	160-350	-2.4 av.	Vanko et al. 1991
Mid Atlantic Ridge	young volc. seamount	290-362	-43.0 max.	Vanko et al. 1992
Lau Back Arc (SW Pacific)	felsic-mafic volcanics	225-280	-2.5 to -4.0	Herzig et al.1993
Jade hydrothermal field	Kuroko-type	270-360	-1.1 to -11	Lueders et al. 2001
TAG hydrothermal field	felsic-mafic volcanics	191-364	-1.1 to -3.8	Petersen et al. 2000
SEAWATER			-1.7 to -2.2	Barrett and Sherlock, 1996

Table 9.1: Comparison of fluid inclusion data from Myra Falls VHMS camp and other VHMS deposits and active seafloor hydrothermal fields.

tend to be higher in the basal stockwork zones, and decrease slightly in the upper parts of the ore system (e.g., Bryndzia et al. 1983). Similar increases in homogenisation temperatures with increasing depth are also reported from the TAG mound (Petersen et al. 2000). The spatial variation in salinity and temperature with depth in the Battle and HW orebodies, could in part reflect the overprinting of earlier high temperature stages by cooler fluids as the hydrothermal system waned; or varying degrees of fluid mixing. The lower salinity-lower temperature zones may have had a greater component of cooler, more dilute seawater than the higher salinity-temperature zones in the middle of the ore lens.

9.6.3 Water depth estimates

Haas (1971) suggested that water depths, greater than 1000-1500m, are needed to prevent subseafloor boiling. A number of studies have used the lack of evidence of boiling to estimate the depth of the water above the deposits during ore formation, and estimates range from 50 to 1500m water depth, e.g., Marutani and Takenouchi (1978); Yoshida (1979) and Pisuth-Arnond and Ohmoto (1980). Figure 9.14 shows the boiling point curves for H_2O liquid (0 wt. %) and for brine of constant composition, given in wt. % NaCl. The temperature at 0 metres for each curve is the boiling point for the liquid at 1.013 bars (1atm) load pressure which is equivalent to the atmospheric pressure at sea level (Haas, 1971).

At Myra Falls, based on the boiling point curves, fluids with an average temperature of 200°C, and salinity of 5-10 eq. wt % NaCl, imply minimum water depths greater than 180-200m. This is consistent with sedimentological evidence, such as the fine parallel laminations and interbedded turbidites in argillite and chert overlying the deposits, which suggest water depths at least greater than storm-wave base, which is estimated to be about 100m depth (Jones and Desrochers, 1992).

9.6.4 Fluid source

There is still debate on the source of ore fluids in VHMS systems, and the most common models presented are a magmatic origin vs recycled seawater origin, or a combination of both. These models present two alternative sources for the metals in VHMS systems, 1) metals leached from footwall volcanics and basement rocks by the convective circulation of heated seawater above a magmatic intrusion (e.g., Ohmoto and Rye, 1974; Solomon, 1976; Gemmell and Large, 1992, 1993), and 2) direct input of a magmatic volatile phase from the magma chamber (e.g., Henley and Thornley, 1979; Stanton, 1990). The source of the ore fluids has not been conclusively determined by either isotopic and geochemical studies as both have been presented to support the alternate models (e.g., Gulson and Porritt, 1987; Stanton, 1990).

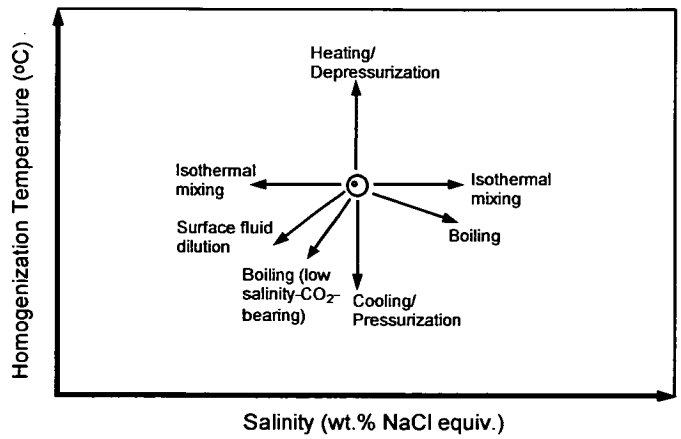

Figure 9.13: Schematic diagram showing typical trends in Th-salinity space due to various fluid evolution processes (from Wilkinson, 2001).

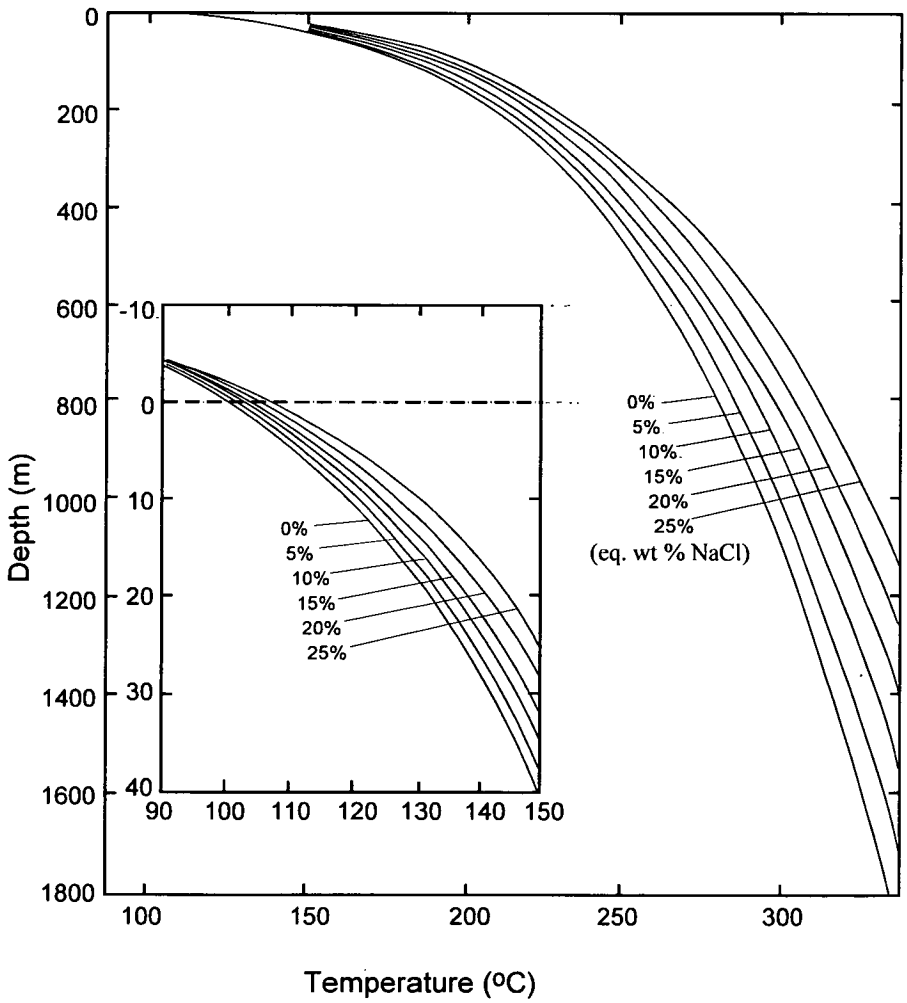

Figure 9.14: Boiling point curves for H_2O liquid (0 wt %) and for brine of constant composition given in eq. wt % NaCl. The insert gives a detailed view of the relations between 100-150°C. The temperature at 0 metres for each curve is the boiling point for the liquid at 1.013 bars (1 atm) pressure, which is equivalent to atmospheric pressure at sea level (from Haas, 1971).

The origin of hydrothermal fluids is best determined by direct measurement of active venting fluids and comparison with present-day seawater (e.g., Hannington and Scott, 1988; Von Damm, 1990). Hydrothermal fluids differ markedly from seawater, often being depleted in Mg and enriched in K and Ca, relative to present-day seawater (Khin Zaw et al. 1996). These differences, in combination with the higher salinities of the ore fluids, suggest that the hydrothermal fluids are not just seawater. Instead, they most likely represent recycled seawater, modified by leaching of elements from the volcanic pile and underlying basement rocks (Khin Zaw et al. 1996).

There is also evidence for the direct input of magmatic fluid and gas contributions to seafloor hydrothermal systems in back-arc vent fluids and precipitates (Gamo et al. 1997; Herzig et al. 1998). However, most magmatic components are difficult to identify as they are usually masked by the large amount of seawater in the circulation systems (Herzig and Hannington, 2000). Stuart et al. (1995) found that vent fluids are highly enriched in Ch_4 and ^3He over seawater, and that the $^3He/^4He$ ratios (7-9) are more typical of mantle values. These ratios indicate that the ^3He originates from MORB magma which is degassing into the hydrothermal system (Baker and Lupton, 1990). A magmatic component is important as magmatic fluids and gases can be responsible for a significant input of metals into the hydrothermal system, as they are known to be highly concentrated (Herzig and Hannington, 2000). At the Hellyer deposit in Tasmania, Solomon et al. (in press) suggest the circulation of modified seawater, together with the presence of an additional fluid, of probable magmatic origin, could account for the very high salinities of some inclusion fluids and their porphyry copper-like K/Na and K/Ca compositions. Varying degrees of mixing are thought to have occurred between the fluids to account for the range in salinities and element compositions.

At Myra Falls the hydrothermal fluids may have a magmatic component, to account for the relatively high salinities. However, the wide range of salinities could also be the result of two-phase separation at depth and subsequent mixing between the fluids.

9.7 Summary and conclusions

- Fluid inclusions ranging from 3 to 10 μm are measured in spherical megaquartz patches in chert above the Battle orebody. The megaquartz patches most likely represent an early infill and replacement of radiolarian tests, prior to compaction;

- Primary fluid inclusions in the spherical megaquartz patches in the chert have homogenisation temperatures (Th) ranging from 135 to 250°C, and salinities based on

melting temperatures (Tm) from 3 to 12.1 eq. wt % NaCl. These values are very similar to salinities and temperatures measured in inclusions in the underlying orebody and provide evidence of a genetic link between the chert and the massive sulphides;

- In the Battle orebody, fluid inclusion homogenisation temperatures range from 140-250°C in quartz interstitial to ore and salinities range from 3-12.4 eq. wt % NaCl. Inclusion data from the HW orebody shows a similar range of salinities and temperatures (2.5-9.0 eq. wt % NaCl, and Th 145-210°C) and closely matches data collected by Barrett and Sherlock (1996);

- Salinities and homogenisation temperatures from quartz in the siliceous caprocks have a similar range to data from the underlying orebody. Homogenisation temperatures measured in the caprocks are consistent with the temperature of formation of apatite and rutile (>200°C) estimated from geothermal systems (Reyes, 1990);

- The Battle and HW orebodies display a slight increase in salinity and homogenisation temperatures with depth in the ore horizons. This could in part, reflect the overprinting of earlier high temperature stages by cooler fluids as the hydrothermal system waned; or varying degrees of fluid mixing. The lower salinity-lower temperature zones may have had a greater component of cooler, more dilute seawater;

- Although the sequence has undergone lower to mid greenschist facies metamorphism, primary textures are observed, suggesting primary fluid inclusions may still be preserved. The abundant crosscutting quartz-carbonate-chlorite±chalcopyrite±tetrahedrite veins are may be associated with the metamorphic event. The distinctly lower salinities and low to moderate homogenisation temperatures of inclusions in the crosscutting quartz veins (generally <2 eq. wt % NaCl and <170-180°C), suggest that the fluids associated with later metamorphism can be distinguished from Devonian ore fluids;

- The range of salinities displayed by primary inclusions in the Battle and HW deposits (2-12.4 eq. wt % NaCl) is generally much higher than normal seawater (about 3.0 eq. wt % NaCl);

- Fluid densities, estimated from Th and salinity, of inclusion fluids in the siliceous caprocks and in quartz interstitial to ore at Myra Falls, range from 0.88 to 1.05 g/cm^3.

These values are higher than many other VHMS deposits and are close to that of ambient seawater at 2000m depth and 2°C (1.03 g/cm^3);

- A minimum water depth of 180-200m is estimated from the lack of evidence of boiling in fluid inclusions, and boiling point curves; and

- The source of the ore fluids is most likely modified seawater, possibly with some two-phase separation at depth to account for the wide range of salinities, or a possible magmatic component.

Chapter 10
Geological and geochemical model for the caprocks

10.1 Introduction

Fine-grained siliceous deposits are commonly documented from the VHMS environment, e.g., tetsusukei above the Kuroko deposits (Kalogeropoulous and Scott, 1983); ironstones associated with the Brunswick Horizon, Bathurst District (Peter and Goodfellow, 1996); or the silica-barite cap above the Hellyer Deposit, Tasmania (Sharpe, 1991; Gemmell and Large, 1992). However, few papers discuss their mechanisms of formation. This chapter provides a geological and geochemical model for the origin of the siliceous caprocks at Myra Falls.

The structural and depositional setting of the caprock horizon is summarised to provide a framework, essential for the genetic model. This summary is followed by a description of the geochemical environment of siliceous caprock formation, the mechanisms of silica dissolution and deposition, metal zoning, metal transport and deposition, and the behaviour of the silica-bearing fluid. A genetic model is then presented for the formation of the Battle orebody and associated siliceous caprocks.

10.2 Structural and depositional setting of Myra Falls caprock horizon

The caprock horizon forms a semi-continuous layer at the base of the HW Horizon, and consists of argillite, siltstone, chert and black chert. Siliceous caprocks are best developed above the Battle orebody, but are also observed in the Ridge and Extension zones. Minor chert and bleached argillite zones are also found above the HW orebody. Elsewhere the caprock horizon is composed of black argillite and interlayered siltstone.

10.2.1 Structural setting

The volcanic sequence at Myra Falls, has been affected by numerous deformation episodes, which have folded and dissected the caprock horizon. Deformation events include D_1 folding, resulting in a predominantly E-W striking, N-dipping foliation; localised WNW oriented D_2 shear zones; D_3 strike-slip faulting; D_4 normal faults and D_5 thrust faults and steep NE-oriented sinistral strike-slip faults. In order to determine the structural and depositional setting of the caprocks, the effects of deformation were removed and the paleoseafloor reconstructed (Chapter 5).

The footwall, Price Andesite, represented the paleoseafloor close to the time of ore formation. The contoured top surface of the Price Andesite is shown with the major structures, which affected the present-day elevation of the footwall surface (Figure 10.1a). The block model below (Figure 10.1b) illustrates the reconstructed paleoseafloor, after the removal of the effects of the D_1-D_5 events. The Battle and HW orebodies were located in small paleo-basins along a NW trending ridge, and the seafloor progressively deepened to the south. Growth structures have been identified by rapid changes in the footwall elevation, facies changes and thickness variation in isopach maps. The location of the orebodies appears to coincide with a change in orientation of the major growth structures, from dominantly NW-oriented to E-NE oriented (Figure 10.1b).

10.2.2 Depositional environment

Facies maps of the caprock horizon indicate that the distribution of the fine-grained facies including argillite, siltstone and chert, coincides with the topographic lows on the reconstructed paleoseafloor, and most likely represent the major depocentres (Figure 10.2). The fine-grained horizon marks a time of tectonic and/or volcanic quiescence. Sedimentological features of the argillite and chert, such as the fine parallel laminations and turbidites, indicate that water depths were at least below storm wave base (>80-100m depth).

A much greater water depth of 1000-1500m is indicated by the lack of evidence of boiling in fluid inclusion data from the Battle and HW orebodies (Chapter 9). Haas (1971) suggested that the water depth and associated fluid pressure determines whether boiling takes place in the ascending hydrothermal fluid before it reaches the seafloor. To prevent subseafloor boiling of fluids with low to moderate salinity, water depths of 1000m or greater are necessary. If subseafloor boiling did occur, footwall brecciation and extensive sulphide precipitation in the stockwork zone should be evident. At Myra Falls, the stockwork zones, although well developed, are not brecciated and only contain minor sulphides.

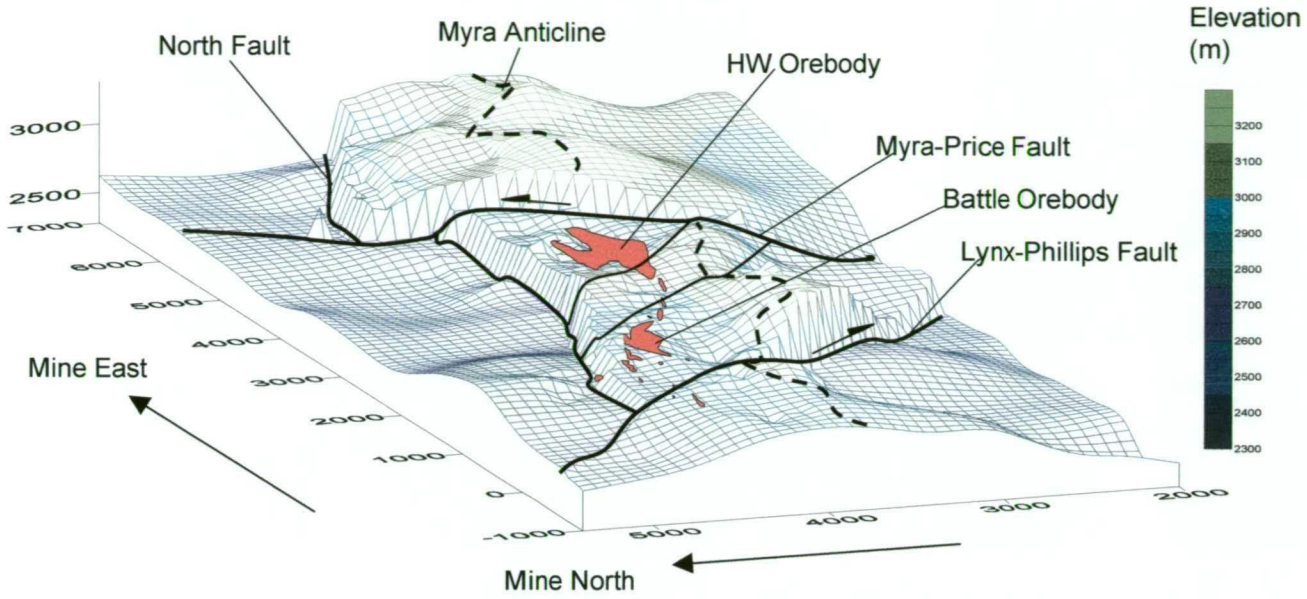

Figure 10.1: a) Present day surface contours of Price Andesite (or paleoseafloor) showing the effects of deformation. The large topographic high in the centre of the block diagram is largely a result of D_1 folding (Myra Anticline), and the large topographic low to the north is due to large down throw on the North Fault. Uplift and lateral displacements also occur along the Myra-Price and Lynx-Phillips Faults.

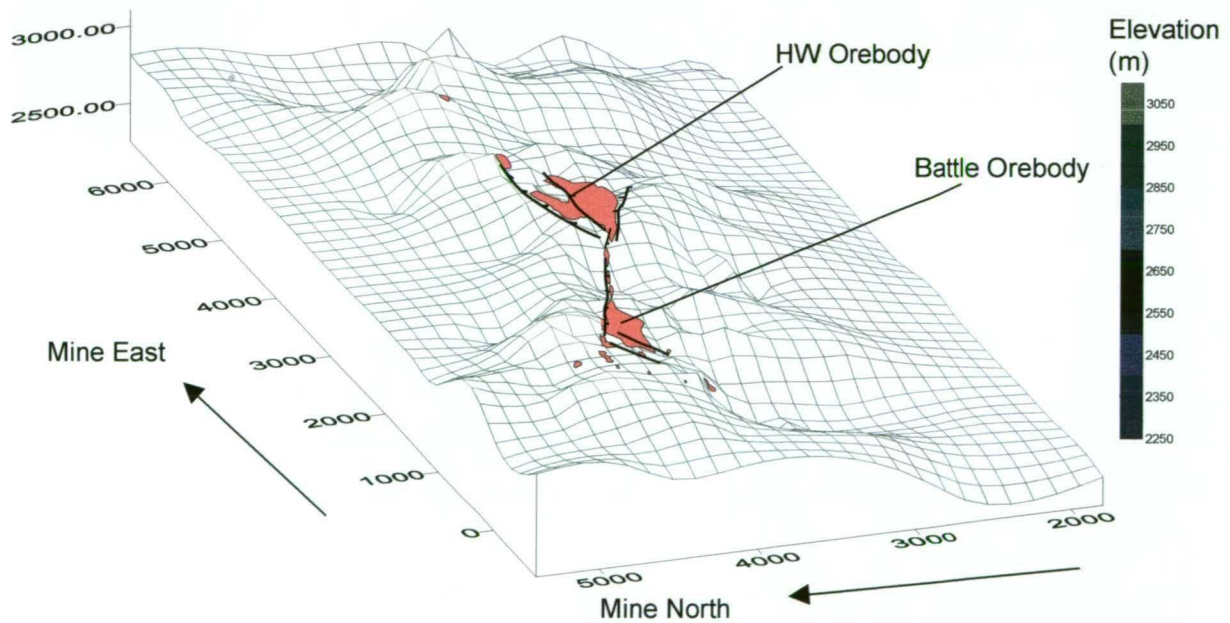

Figure 10.1: b) Restored paleoseafloor (at time of deposition of the Thelwood Formation) showing the location of growth faults and VHMS orebodies. The orebodies are spatially associated with the growth faults and these structures most likely acted as ore fluid conduits. The HW orebody is located within a small basin, separated from the large topographic low to the south. The Battle orebody is also associated with a small basin, but appears to be located on the steep northern edge of the basin. Isopach maps indicate that the location of the orebody (on a slope) is most likely a result of subsequent uplift on younger growth faults at the edge of the basin.

The lack of benthic fauna, the common presence of graphite, and phosphate nodules suggests low O_2 to fluctuating O_2 bottom water conditions. Geochemical parameters measured in argillites from the Battle basin are also consistent with low O_2 bottom water conditions. Battle basin argillites contain the highest organic carbon contents, high DOP values (> 0.90), high metal contents, including Zn, Pb, Cu, Cd, As, Sb, Ag, Ba and V, low Fe and Mn, and high metal ratios such as V/(V+Ni) > 0.8. These geochemical parameters indicate strongly reducing conditions with free H_2S in a strongly stratified water column. HW basin argillites, although not as enriched in metal contents, still have high V/(V+Ni), and relatively high DOP values (>0.8) suggesting similar bottom water conditions in the HW basin. The lower DOP and V-Ni metal ratios in the South Flank area indicate a slightly more oxygenated depositional environment.

The low O_2 bottom water conditions indicated by the geochemistry of the Battle basin argillites, is consistent with areas of more restricted circulation, such as small deep basins, as indicated by the paleoseafloor reconstruction. In comparison, the South Flank argillites were deposited on a broad deepening zone of seafloor, which may have been more exposed to open ocean circulation. Therefore, bottom water conditions would most likely be slightly more oxygenated than the more restricted Battle and HW basins. A similar change from localised anoxic zones to broader oxic zones is observed in the distribution of anoxic and oxic facies in the present-day Black Sea Basin, and reflects changes in the bottom water O_2 conditions (e.g., Force and Cannon, 1988).

10.2.3 Metal distribution in the caprock horizon

The caprock horizon, which predominantly consists of argillite, shows marked variation in metal contents across the property (Figure 10.3). The Battle basin argillites are strongly enriched in Zn, Pb, As, Ag, Cu, Cd, Sb, Ba and V (Chapter 8). The HW basin argillites are moderately enriched in Ba, As, Zn, Cu and V, whereas argillites from regional areas, such as the South Flank and Thelwood Valley areas, contain very low metal contents.

In the Battle basin argillite, elements such as Zn, Cu, Ag, As, S, Cd, U, Pb, V, Sb, and Nb, are assigned a hydrothermal origin, due to the strong positive interelement correlations and negative correlations with detrital elements, such as Ti, Al, Zr, Mg, K, Mn, Ga, Sc, Y, Rb, Fe and Ba (Chapter 8). Positive correlations of Ba with Al, K, and Rb, and negative correlations with S, indicate that Ba resides in white micas, rather than sulphate. HW basin argillite also shows a degree of metal enrichment, with higher Zn, Cu, Ba and As, than regional argillites. Metals such as Zn, Pb and Cd are assigned a hydrothermal origin due to the negative correlation with detrital elements, such as Ti, Al, Zr, K, Ga, Sc, Y, Rb, Nb and Ba.

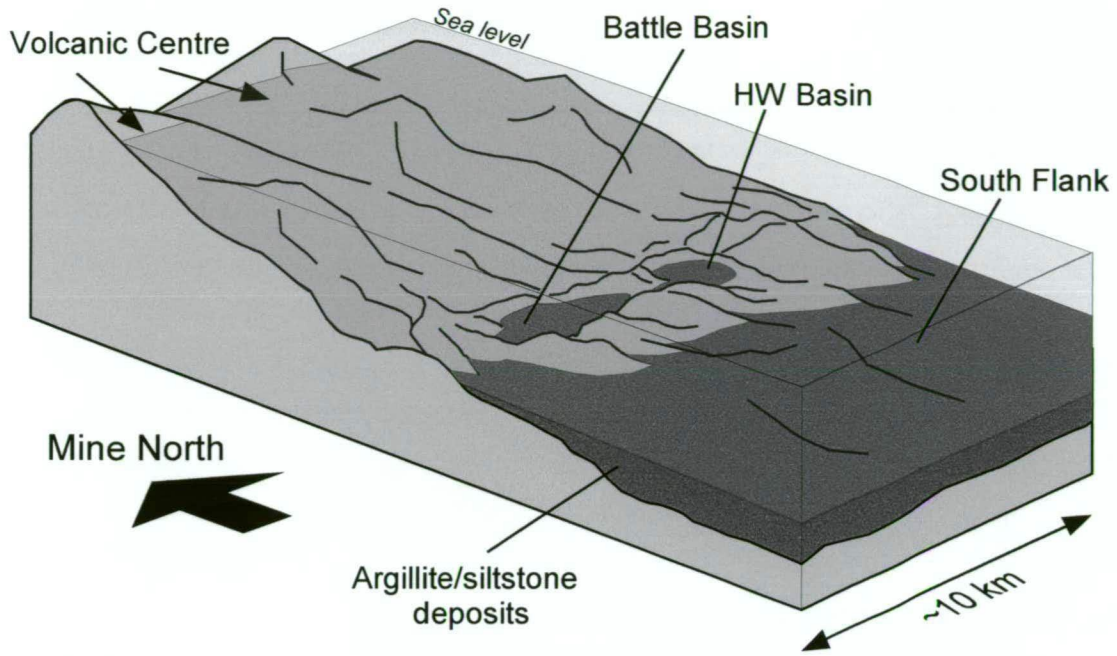

Figure 10.2: Interpreted paleogeography of the Myra Falls area, based on paleoseafloor reconstruction and facies mapping (Chapter 5).

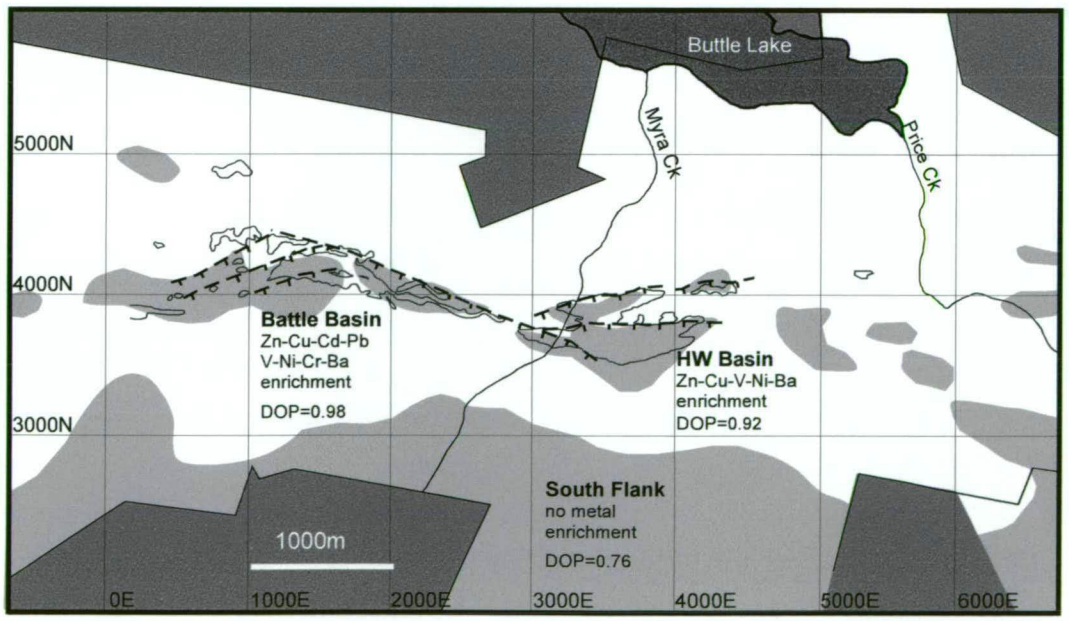

Figure 10.3: Distribution of the argillaceous caprock horizon (chert excluded), and property-scale variation in metal contents and geochemical paleoenvironmental indicators measured from argillite. Argillite at the base of the HW horizon (caprock horizon) is only present in the grey zones indicated, other areas are dominated by coarse-grained rhyolitic volcaniclastics.

The metal enrichment of argillites in the Battle and HW basins most likely represents deposition from hydrothermal plumes. The low metal values in argillites from regional areas, such as the South Flank, indicate that the hydrothermal plumes were not extensive; instead they were localised within the smaller basins.

Elevated metal ratios, such as V/Cr, V/Ni and V/(V+Ni), in the Battle basin argillites most likely reflect a combination of hydrothermal and hydrogenous sources. Excess V would be derived from hydrothermal vents associated with Battle ore formation, but could also reflect the strongly reducing conditions in the basin. For example, argillites in the HW basin have much lower V levels and no clear correlation between V and hydrothermally derived elements, such as Zn and Pb, but still have high V/Ni (5.7) and V/Cr (3.7) values, indicative of deposition under anoxic conditions (Wenger and Baker, 1986).

10.3 Formation of siliceous caprocks

The Battle chert is best developed above the Battle orebody where it usually forms a 3-5m thick zone of strongly laminated chert. It forms a siliceous 'cap' to the underlying ore horizon, and is predominantly white to pale grey immediately above the orebody, grading latererally into dark grey to black chert about 120m from the Battle orebody (Figure 10.4). The black chert forms a narrow transitional zone, 10-15m wide, at the edge of the siliceous zone and then grades southward into the unaltered Battle basin argillite. Similar zones of chert are also developed above massive sulphides in the Ridge zone, the Extension zone and in localised zones above the HW orebody (HW caprock alteration is discussed in section 10.5).

10.3.1 Siliceous caprock origin

The Battle chert is spatially and temporally associated with the underlying massive Cu-Zn-Pb sulphides. The gradual transition of the chert into the adjacent unaltered Battle basin argillite, their similar immobile element signature and similar petrological and sedimentological features, indicate that the chert formed by silicification of finely laminated argillite, overlying the Battle orebody. No chimney structures, resedimented chert, or slump features were identified in the cherts. The chert does not represent a 'true' exhalative silica deposit, precipitated from a hydrothermal plume, e.g., exhalites of the Brunswick Belt (Peter and Goodfellow, 1996), or white smoker deposits (Hannington et al., 1998). The lack of discrete silica horizons, and the high detrital component of the Battle chert, indicated by Al-Mn-Fe and Fe/Ti – A/(Al+Fe+Mn) plots, is also consistent with a replacement origin (Chapter 8). However, the very low Fe contents of the cherts, shown on these plots, may also partly reflect the low O_2 bottom water conditions of the Battle basin (Section 10.3.7).

The relatively high base metal content of the cherts reflects a large hydrothermal component.

The Battle chert typically contains >90% SiO_2, very low Fe and Mn, but moderate to high trace metal contents, including Cu, Zn, Pb, Cd, Ag, As and Sb. These elements usually occur as fine anhedral sulphides disseminated throughout the microcrystalline quartz groundmass. Although metal contents are not high enough in the chert to be classified as ore grade, distinct metal zonation is observed in the chert, indicating that metals were transported and deposited from the silica-bearing fluids. The very fine-grained nature of metallic minerals in chert, such as sphalerite and chalcopyrite, support coprecipitation, rather than later precipitation (post silicification). Metal contents vary with increasing distance from ore, with high Cu and Zn contents in the white-pale grey chert immediately above the orebody, grading out into Pb-Ag-Sb-rich black chert, in a 10-20m wide zone, at the edge of the siliceous horizon (Figure 10.4b). This zone typically has galena overgrowths on fine pyrite framboids, often with very fine sub-micron Ag inclusions in the galena (Chapter 6). The lower metal contents of the chert, relative to the underlying ore horizon, most likely reflects lower temperatures of formation (<200° C) and prior deposition of sulphides in the underlying coarse-grained rhyolitic volcaniclastic layer.

Sulphur isotope values in Battle basin argillite, 300-320m from the Battle orebody, are very light, ranging from –35.2 to –10.3 ‰; whereas $\delta^{34}S$ values for sulphides in black chert (100m from the orebody) range from –18.4 to –5.3 ‰. The black chert $\delta^{34}S$ values are intermediate between the unaltered argillite and Battle orebody values (–1.1 to +4.1 ‰). The light sulphur isotope values in the argillite most likely reflect bacterial reduction of seawater sulphate; whereas, the heavier sulphur isotopes of the Battle orebody reflect magmatic sulphur and/or inorganic reduction of seawater sulphate. The distinct shift from light $\delta^{34}S$ values in the unaltered argillite, to heavier $\delta^{34}S$ values in the black chert reflect input of hydrothermal sulphur ($\delta^{34}S$ = –1.1 to +4 ‰) into the seafloor sediments during hydrothermal alteration, and provide further evidence for a replacement origin for the Battle chert.

10.3.2 Timing of silicification

The timing of formation of the siliceous caprocks is most likely early in the depositional/diagenetic history of the fine-grained sediments. Silicification clearly postdates deposition of the fine sediments and occurred during ore formation. There is good evidence of hydrothermal fluid flow through the uncompacted fine-grained sediments overlying the massive sulphides, with deposition of hydrothermal rutile, apatite and minor sulphides, in

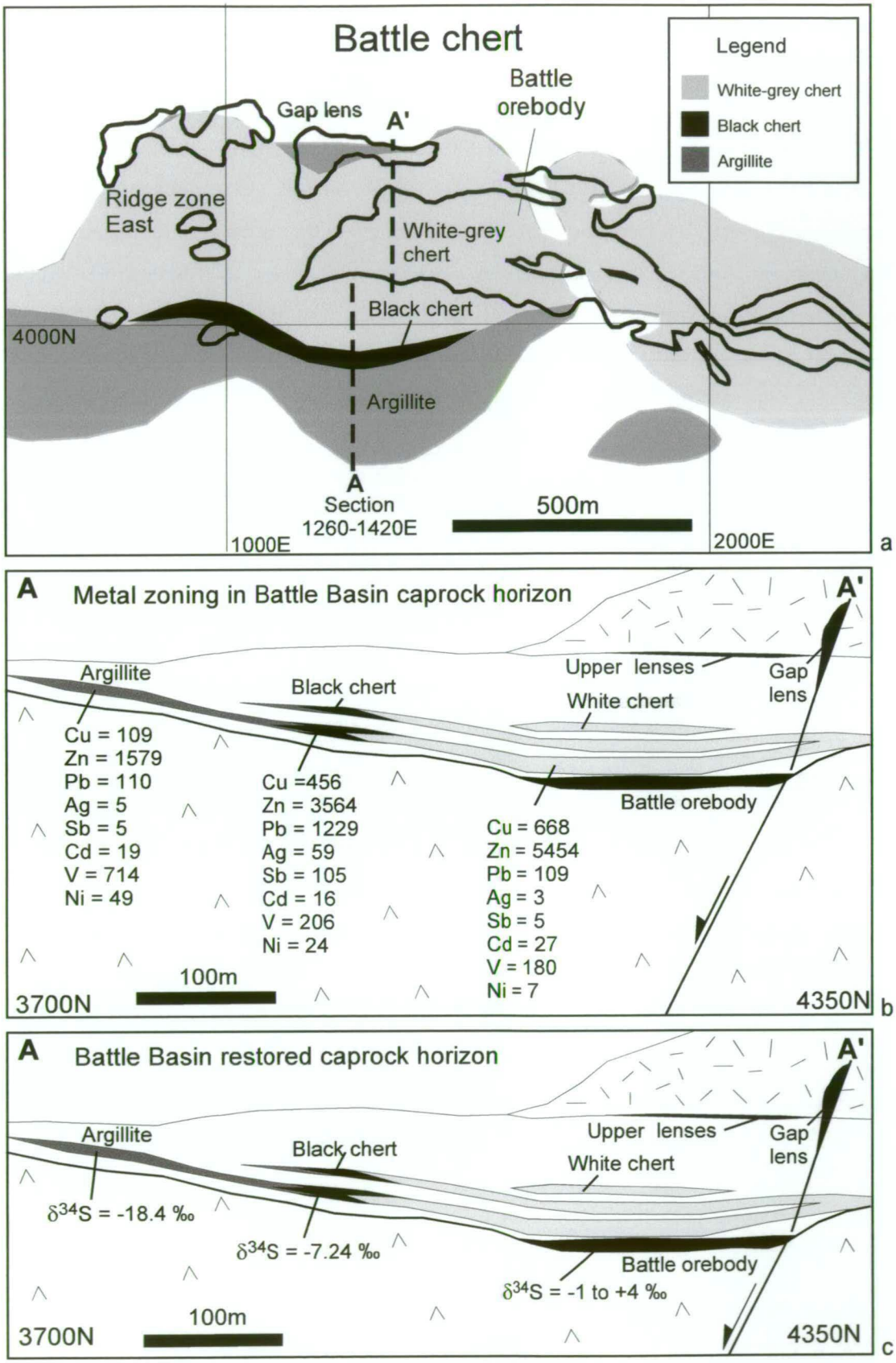

Figure 10.4: Battle basin caprock horizon; **a)** distribution map of the Battle chert, with the pale grey-white chert located immediately above the Battle orebody and the black chert forming a transitional zone into the unaltered Battle basin argillite; **b)** Metal zoning in the caprock horizon along composite section 1260-1420E. Note the gradual decrease in metals such as Zn, Cu and Cd with distance from ore, but metals such as V and Ni show a marked increase. The black chert has much higher Pb, Ag and Sb than the adjacent white-grey chert (metal values are averages for each unit, in ppm); **c)** $\delta^{34}S$ values for the Battle caprock horizon and the underlying Battle orebody (Battle orebody $\delta^{34}S$ values from Sinclair, 2000).

primary pore spaces, such as radiolarian tests. In other geothermal systems, estimated temperatures of formation of apatite range from 90 to 210°C, and rutile greater than 200°C (Reyes, 1990). Evidence that these textures formed prior to silicification, and were overprinted by the silicification event, is presented in Chapter 6. The incorporation of 1-30cm diameter chert clasts into the overlying mass flow units, is perhaps the most compelling evidence for the early silicification of the seafloor muds. The ubiquitous presence of bedding-parallel micro-stylolites also indicates that silicification occurred prior to compaction.

Mass balance calculations between the Battle basin argillite and chert indicate mass gains in the chert of up to 200%. This degree of mass gain is observed in intensely silicified footwall sedimentary rocks at the Brunswick No. 12 deposit, and is thought to be consistent with formation near the paleoseafloor at or near hydrostatic pressures (Lentz and Goodfellow, 1996).

10.3.3 Physicochemical conditions of Battle chert formation

The physicochemical conditions at the site of chert formation can be determined by the mineral assemblages, fluid inclusion microthermometry, and comparisons with fluid chemistry measured from active seafloor vent systems. The mineral assemblage of the Battle chert is relatively simple, consisting predominantly of silica, muscovite, pyrite and minor sphalerite, chalcopyrite and galena.

Fluid inclusion microthermometry provides estimates of the temperature and salinity of the silica-bearing hydrothermal fluids. Although direct measurement of fluid inclusions was not possible in the microcrystalline chert, inclusions in associated quartz were measured throughout the Battle orebody, and in early infills of primary pore space in the fine-grained host sediments (Chapter 9). Evidence for the early precipitation of silica, rutile and apatite in primary pore space, followed by the overprinting silicification event is presented in Chapter 6. Temperatures ranged from 140-250°C, with a wide range of salinities from 2 to 12.4 eq. wt % NaCl. A slight decrease in homogenisation temperature and salinity was noted in inclusions from the centre of the sheet-like orebody to inclusions measured near the top contact and in the overlying fine sediments. These fluids appear to be more saline than other VHMS deposits, such as the Kuroko district, which has salinities ranging from 3.5 to 6.7 eq. wt % NaCl (Pisutha-Arnoud and Ohmoto, 1983).

The muscovite stability field provides an estimate of the pH conditions, between about 3 to 5.8, assuming the maximum fluid temperature of 250°C. An estimate of the oxidation-state

during ore and caprock formation can be made from the sulphide mineralogy, with the dominance of pyrite and the absence of pyrrhotite and magnetite indicating moderately reducing fO_2 conditions. The log fO_2-pH diagrams in Figure 10.5, from Cooke et al. (2000), illustrate the stability fields for muscovite, and other minerals, such as pyrite, pyrrhotite, magnetite, siderite, hematite for two different sets of conditions. The first diagram (Figure 10.5a) is for a temperature of 150°C and salinity of 25 eq. wt % NaCl; the second diagram (Figure 10.5b) is at 250°C and 10 eq. wt % NaCl. The temperature and salinity of Myra Falls ore fluids are probably closest to conditions in the second diagram. However, the first diagram, with lower temperature conditions and higher salinity, is still useful, as it illustrates the broader redox field of pyrite stability at lower temperatures. Myra Falls hydrothermal fluids, with lower salinities, would have lower concentrations of Pb-Zn chloride species (Pb-Zn transport, is discussed in Section 10.3.6).

Minor pyrrhotite is found in unaltered argillite adjacent to the Battle chert, indicating more strongly reducing fO_2 conditions. At the edge of the siliceous alteration zone, fS_2 might also increase as very little S was deposited in the chert; instead S was leached from the argillite precursor during hydrothermal alteration, as indicated by the S isotope data (Chapter 8).

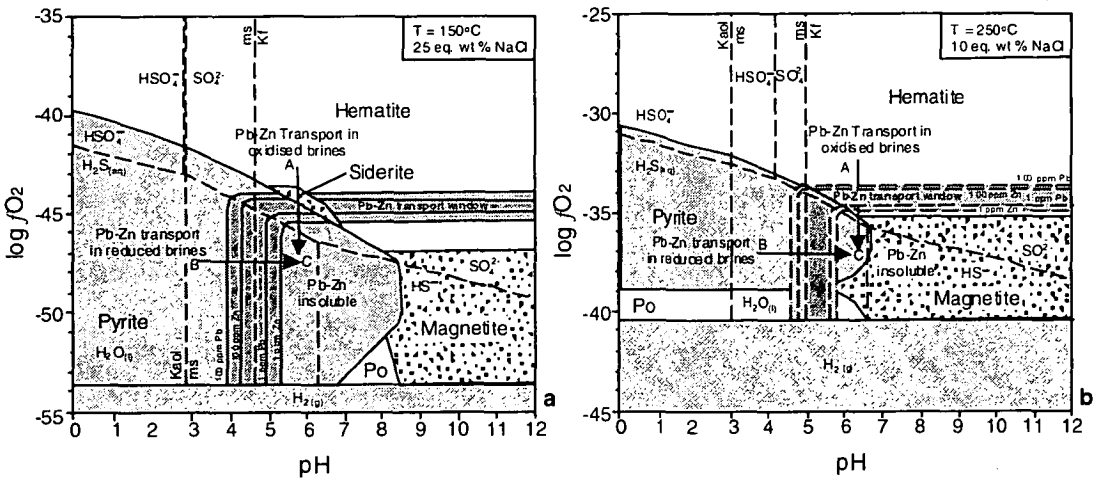

Figure 10.5: Log fO_2-pH diagrams illustrating the stability field for sulphides, Fe oxides, siderite, kaolinite, muscovite and orthoclase, solubility contours and the metal transport window for galena and sphalerite (from Cooke et al., 2000). The diagrams also show the predominance fields for the main aqueous sulphur-bearing species, and the stability fields for water and $H_{2(g)}$ (P_{H_2} = 1 bar); **a)** Conditions for this diagram are 150° C, *m* (Na^+) = 4.76; *m* (K^+) = 0.46; *m* (Ca^{2+}) = 0.31; *m* (Cl^-) = 5.83 (≈25 wt % NaCl equiv); **b)** conditions for this plot are 250° C, *m* (Na^+) = 1.58; *m* (K^+) = 0.15; *m* (Ca^{2+}) = 0.10; *m* (Cl^-) = 1.94 (≈ 10 wt % NaCl equiv). Diagrams calculated for ΣS = 0.001 *m* and ΣC = 0.256 *m*. Abreviations: kaol = kaolinite, Kf = K feldspar, ms = muscovite, po = pyrrhotite.

10.3.4 Silica deposition

The dominantly microcrystalline to cryptocrystalline nature of the Battle chert may indicate that it formed from precipitation of amorphous silica, rather than quartz (e.g., Lentz and Goodfellow, 1996). Within the microcrystalline groundmass, rare relict patches containing 'gel-like' features are present, and may represent preserved amorphous silica textures. As amorphous silica (opal-A) is thermodynamically unstable, it eventually recrystallizes to the more stable silica forms (chalcedony and quartz), through the transformation sequence; opal-A → opal-CT → quartz (Williams et al., 1985).

The silica polymorphs, opal-A, opal-CT, and chalcedony have significantly higher solubilities than quartz (Figure 10.6), but all display similar solubility trends with temperature, pressure, pH and salinity (Fournier, 1985). Quartz solubility is virtually independent of pH below about 8 (Figure 10.7), and is only affected by increasing salinity at temperatures greater than about 350°C (Figure 10.8a). Increasing salinity at higher temperatures has the effect of slightly increasing the peak temperature of retrograde solubility (Figure 10.8b), which could result in the fluid containing a greater amount of dissolved silica from the source area (Fournier, 1983; Rimstidt, 1997).

If the Battle chert formed by the precipitation of amorphous silica, rather than quartz, the fluids may have been much cooler than those precipitating quartz. Generally, higher temperature solutions (>150°C) precipitate silica almost exclusively as quartz (Rimstidt, 1997). The precipitation of amorphous silica from low temperature fluids (15-100°C) has been observed in modern seafloor settings (e.g., Janecky and Seyfried, 1984; Alt et al., 1987; Hannington and Scott, 1988) and epithermal deposits, where it is much better documented (e.g., Ohaki-Broadlands hydrothermal area, New Zealand, Browne and Ellis, 1970; Browne, 1978). These low temperature fluids represent mixtures of relatively high temperature (>150°C) quartz-saturated hydrothermal fluids and cold seawater. For example, silica chimneys at the Galapagos spreading centre, form by precipitation of large volumes of non-sulphidic silica from very low temperature fluids fluids (32 to 42° C), whereas silica intimately associated with sulphides, precipitates from hotter fluids, around 100° C (Herzig et al., 1988).

Vent fluids from a range of tectonic settings, typically contain a major silica component, with values ranging from about 17 to 22.9 mmol/kg silica, at typical hydrothermal temperatures of about 350° C (Scott, 1997). The relatively consistent silica component most

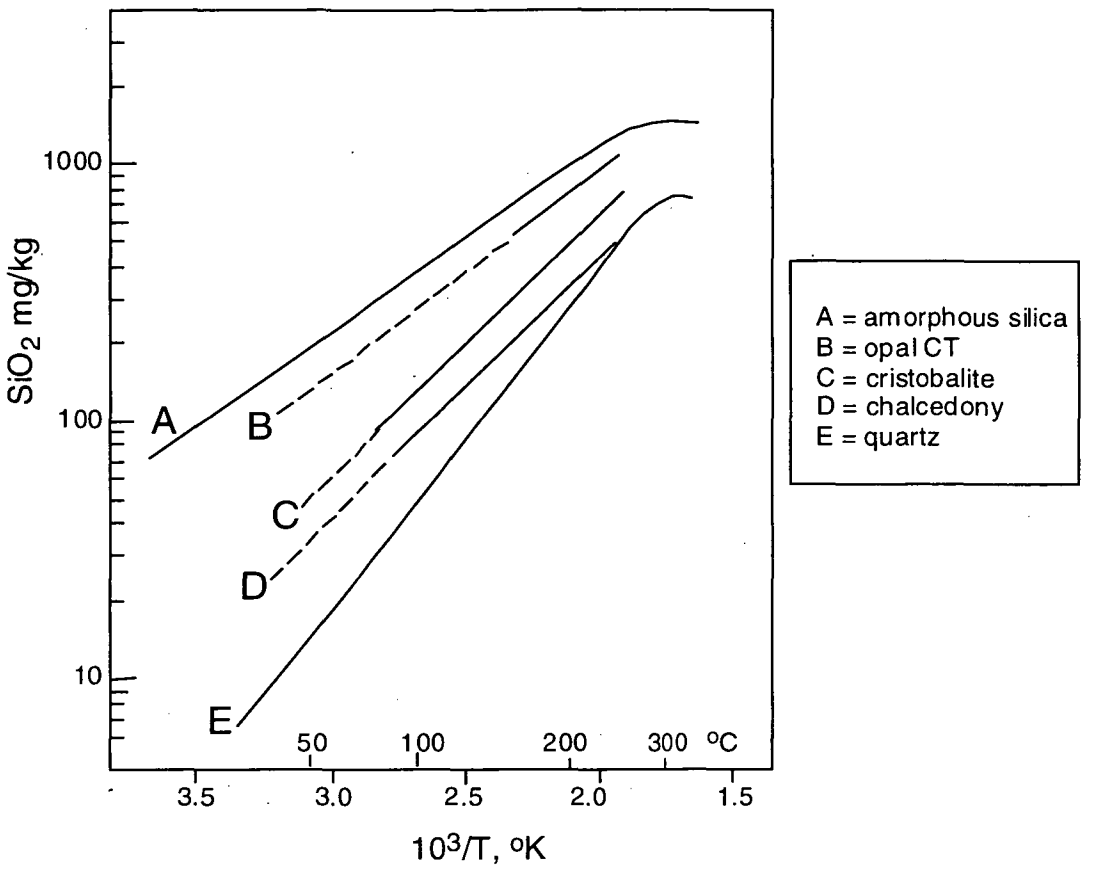

Figure 10.6: Calculated silica solubilites of the various silica polymorphs, from Fournier (1985).

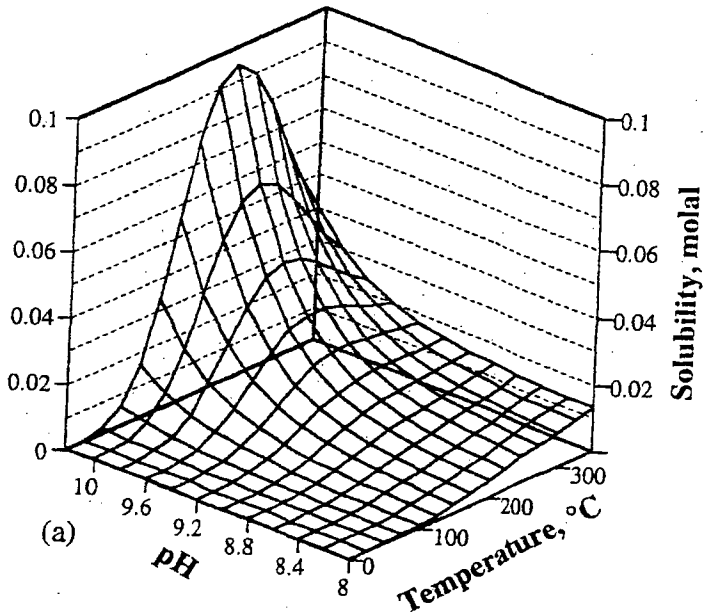

Figure 10.7: The solubility of quartz as a function of pH and temperature along the three-phase curve (quartz + solution + vapour), from Fleming and Crerar (1982) and Rimstidt (1997). The diagram shows a solubility maximum at about 225°C and pH > 8.5, and that at values < 8.5, pH is not an important control on the solubility of silica.

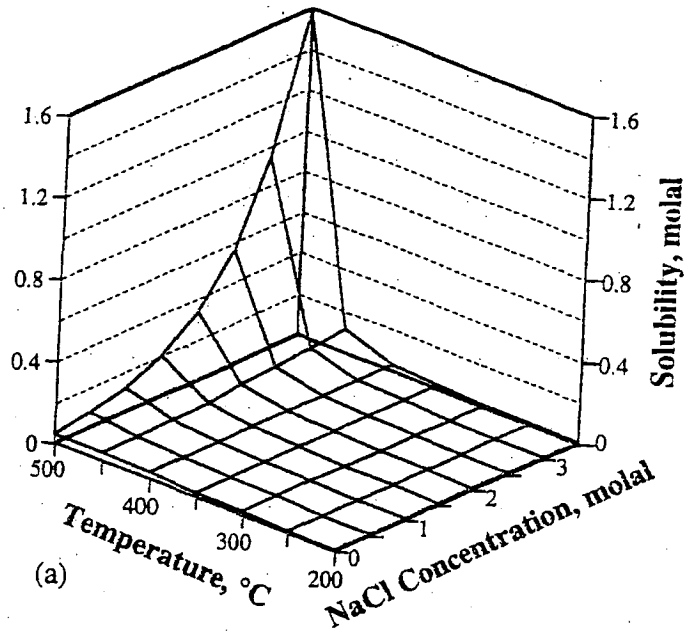

Figure 10.8: a) The solubility of quartz as a function of sodium chloride concentration and temperature at 1 kbar, from Rimstidt (1997). The diagram shows that the solubility of quartz increases with increasing temperature and sodium chloride concentration.

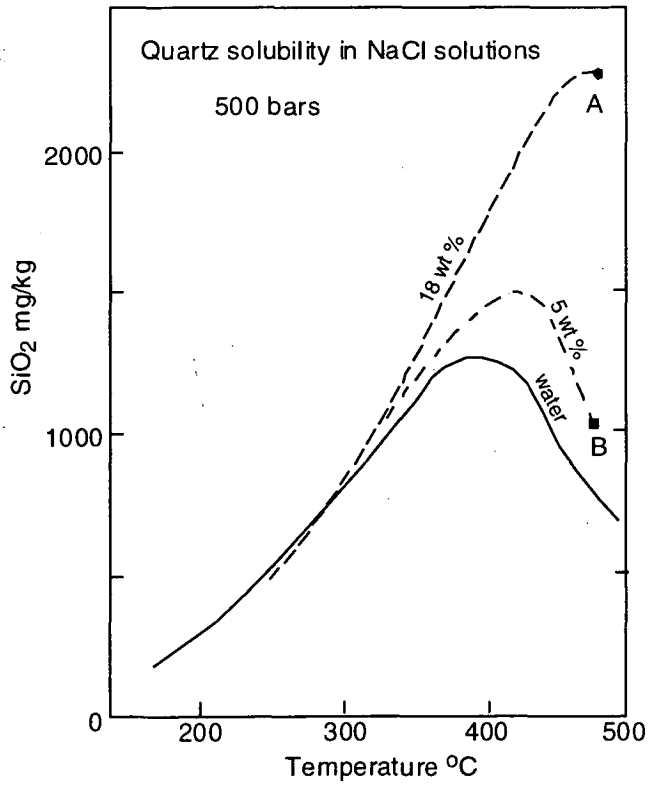

Figure 10.8: b) The solubility of quartz as a function of sodium chloride concentration and temperature at 1 kbar, from Rimstidt (1997). The diagram shows that the solubility of quartz increases with increasing temperature and sodium chloride concentration.

likely reflects silica saturation with respect to quartz, as most hydrothermal fluids become saturated with respect to quartz in the high temperature (>350°C) reaction zones. Silica dissolution in the source region is controlled by quartz solubility and the quartz is most likely mobilised as H_4SiO_4 and alkali silica hydroxide complexes (Fournier, 1983; Rimstidt, 1997). The common reaction for silica mineral dissolution is:

$$SiO_2(s) + 2H_2O = H_4SiO_4 \qquad (1)$$

Although silica dissolution in the source region is controlled by quartz solubility, precipitation on or near the seafloor can be controlled by the much higher solubility of amorphous silica. Rimstidt (1997) suggests that as the hydrothermal fluids cool below 350°C, the fluids become supersaturated with respect to quartz, but for kinetic reasons, quartz commonly does not precipitate. Instead, once the silica solution becomes supersaturated enough to reach the amorphous silica saturation curve, that phase nucleates and grows instead of quartz. Generally, considerable conductive cooling as well as mixing with seawater is necessary before the amorphous silica saturation curve is reached (Figure 10.9). Large supersaturations with respect to quartz usually occur in fluids with temperatures less than 200°C, due to the increased quartz precipitation rates in higher temperature fluids (Rimstidt, 1997).

Lentz and Goodfellow (1996) suggest that high degrees of silica supersaturation may be achieved by three main mechanisms:

1) Thermal quenching of a silica-bearing fluid by conductive cooling or mixing with seawater (Figure 10.9);
2) Rapid drop in geostatic pressure as the fluid ascends adiabatically toward the seafloor;
3) Boiling/effervescence of the fluid due to depressurization that reduces the liquid water volume and induces chemical changes in the buoyant stockwork fluid in the upper levels of the stockwork zone.

The precipitation of amorphous silica is greatly affected by kinetic effects. Amorphous silica forms first as colloidal particles, which then accumulate as amorphous masses in low flow rates. Rimstidt and Barnes (1980) show that during simple cooling, silica precipitation increases in proportion to the available nucleation surface area, expressed as the ratio of surface area to the mass of SiO_2-bearing water. For example, large volumes of silica will precipitate from slow cooling fluids in areas with large available surface areas, such as fine unconsolidated muds (e.g., clastic layers of tetsusukei, Kuroko deposits, Kalogeropoulous and Scott, 1983), or the fractured stockworks below some VHMS ores (e.g., cherty footwall alteration beneath the Brunswick No. 12 deposit, Bathurst, Lentz and Goodfellow, 1996). In

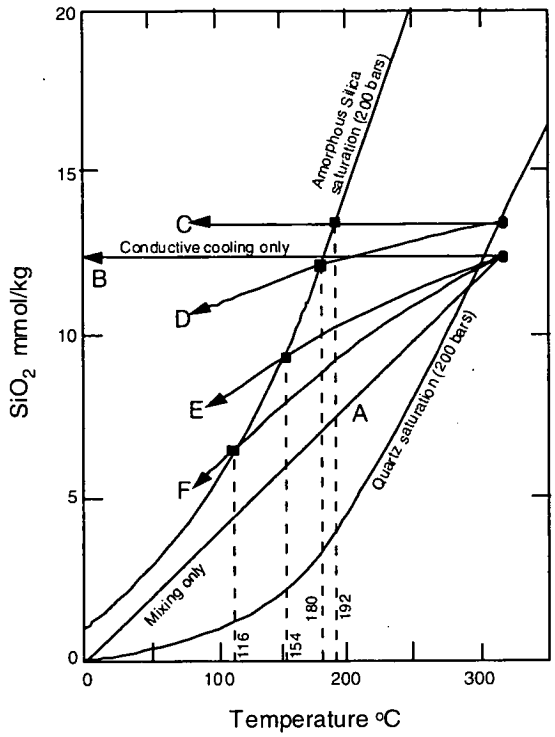

Figure 10.9: Diagram illustrating the various cooling paths of two different fluids at Guaymas Basin. Variable cooling paths result from differing amounts of conductive cooling combined with mixing, and lead to the precipitation of amorphous silica in chimneys (from Peter and Scott, 1988; Scott, 1997). Quartz does not precipitate due to kinetic reasons, and amorphous silica does not precipitate from mixing alone (e.g., line A); instead amorphous silica precipitates from fluids cooled conductively and by mixing with seawater (Scott, 1997).

comparison, in systems where the ratio of the available surface area to the mass of SiO_2-bearing fluid is low, silica precipitation is minimal. For example, in a hot buoyant hydrothermal plume (e.g., black smoker), mixing and dilution with cold seawater will greatly reduce the available nucleation surfaces, resulting in only minor silica precipitation. The typically thin nature of 'true' exhalites, most likely reflects this process (Davidson, 1992).

The microcrystalline to cryptocrystalline nature of the Battle chert, the relict 'gel-like' textures, and the low homogenization temperatures from fluid inclusions (most <200°C) indicate that the Battle chert may have formed by the precipitation of amorphous silica. The silica most likely precipitated from relatively low temperature hydrothermal fluids with low flow rates. The temperature of formation is estimated to be between 80-150°C, based on typical silica concentrations of 15-20 mmol/kg in hydrothermal fluids (Scott, 1997), a starting temperature of 200-250°C, and a mix of conductive cooling and mixing with cold seawater.

The silica replaced highly porous muds on the seafloor, similar in many aspects to formation of the clastic tetsusukei of the Kuroko deposits (Kalogeropoulous and Scott, 1983). Intercalated sandstone layers within the chert are only weakly silicified, reflecting the kinetic effects of silica precipitation. In the slightly more permeable sandstone layers precipitation would be slower than in the muds, because of the lower surface areas of the large grains. Rapid flushing by pore fluids in sandy domains would have inhibited the development of silica-supersaturated pore fluids. In the adjacent muds, the much higher surface area and lower permeability, likely decreased flow rates and enhanced the development of silica-supersaturated pore waters and silica precipitation.

10.3.5 Metal zoning in Battle chert

Metal zoning observed in the Battle chert, can be used to estimate changing physicochemical conditions during chert formation. Figure 10.10 illustrates the lateral changes in metal contents in the basal metre of the Battle chert. In the white-pale grey chert above the Battle orebody, Zn, Pb, Cd, Ag, Sb, V and Ni contents are low, whereas Cu values are highest in this zone. After a small decrease in the Cu content, Zn, Cd and Cu increase steadily and peak at about 340m from the orebody, whereas Pb, Sb and Ag remain at very low levels until a sharp increase at 380m from the orebody, at the edge of the siliceous horizon. V, Ni and to some extent As and Cr, show a steady increase away from the orebody, out into the unaltered Battle basin argillite. The very different trend of V, Ni and As, most likely reflects their precipitation from a hydrothermal plume. As residence time in the water column increases with distance from the vent, plume particulates have a greater opportunity to scavenge metals such as V, Ni and Cr, from the seawater.

The Cu-Zn-Cd-Pb-Sb-Ag zoning pattern in the cherts is most readily interpreted as the result of precipitation of metals, transported as chloride complexes, from a cooling hydrothermal fluid. Chloride complexes are very temperature dependent, and are considered to be the most important transport mechanism for these elements in hydrothermal fluids, especially above about 250° C (Ruaya and Seward, 1986; Seward and Barnes, 1997; Hanor, 1994; 1998; Cooke, 2000). The steep temperature dependence of the stabilities of metal-chloride complexes results in the efficient deposition of metals from chloride complexes, with decreasing temperature (in neutral to weakly acid solutions with low H_2S and HS^- concentrations) (Seward and Barnes, 1997).

$$\text{e.g., } ZnCl_n^{2-n} + H_2S_{(aq)} \Leftrightarrow ZnS_{(s)} + 2\,H^+ + n\,Cl^- \qquad (2)$$

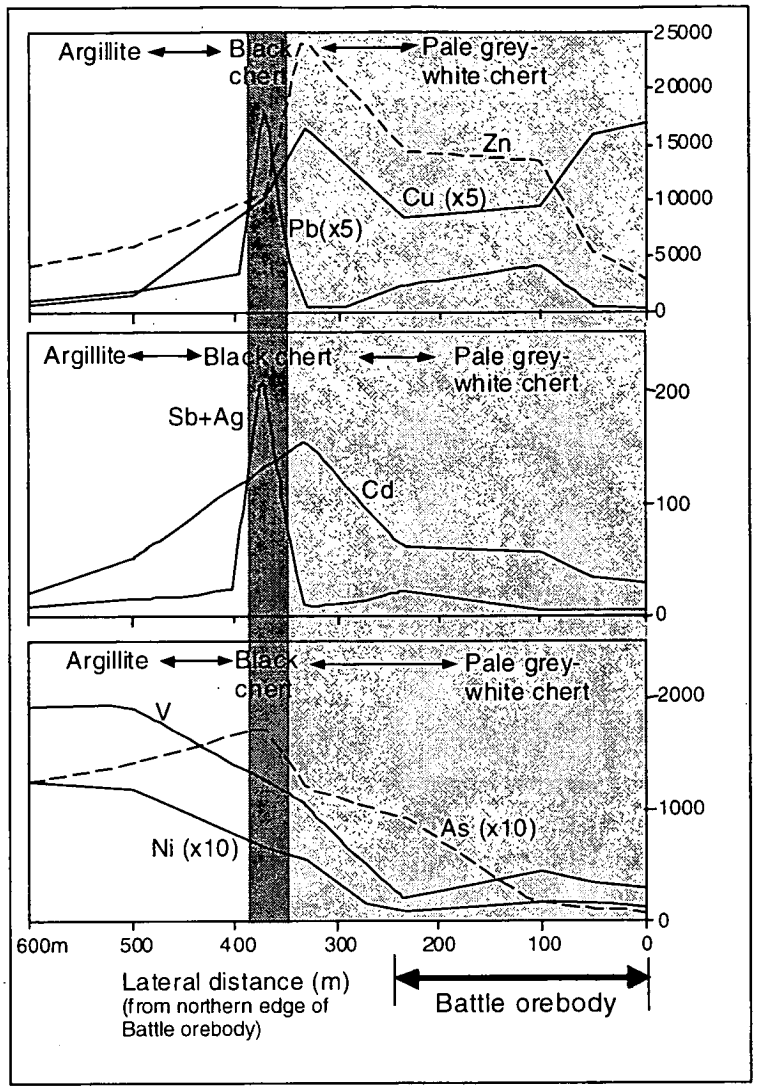

Figure 10.10: Plots showing the lateral variation in metal concentrations (ppm) along the basal lens of the Battle chert (based on samples from composite section 1260-1420E). The white pale grey chert is located immediately above the ore lens, and grades out to the black chert, at the edge of the siliceous alteration, and out to the unaltered argillite to the south of the Battle orebody.

A distinct spike in Pb, Ag and Sb values occurs in the black chert, adjacent to a Zn, Cu, Cd high. The highest Cu values occur in the proximal zone, which has much lower Zn, Cd and Pb values. As shows a similar trend to Cd and Zn. In comparison, V and Ni display a steady increase away from the orebody (see discussion in text).

It is unlikely that the metal zoning in the Battle chert is the result of deposition from bisulphide complexes, as metals transported as bisulphide complexes are not readily deposited via a temperature gradient. Giordano and Barnes (1981) suggest that ore forming solutions at temperatures <200°C with dissolved S <1molal (about 32000 mg/l) cannot transport significant Pb and Zn as bisulphide complexes, and that high pH levels are necessary for extensive complexing by bisulphides. Studies of geothermal systems, such as Broadlands in New Zealand also indicate the importance of chloride complexes for the transport and deposition of metals such as Ag and Sb. For example, amorphous antimony-sulphide rich siliceous precipitate, containing up to 500ppm Ag, deposits from dilute sodium chloride waters, and chloride-silver complexes probably account for much of the Ag (Seward, 1976).

Metal zoning in base metal deposits is thought to result from differences in the solubilities of metal-chloride complexes (Ruaya and Seward 1986; Scott, 1997). Hemley and Hunt (1992) predict outward zoning of Cu-Zn-Pb-Fe, based on the fluid temperature and solubilities of chloride complexes. Figure 10.11 (redrawn from Hemley and Hunt, 1992) shows a composite of metal-chloride complexes based on 1 kbar saturation curves on the KMQ buffer, 1m total chloride concentration. They suggest that this diagram can be used as a general illustration of metal solubilities with changing temperature. As chloride concentrations increase, the mutual relations are constant, but the curves rise appropriately, provided the same metal chloride species distribution applies. In general, a higher pH buffer control and increased fS_2 conditions will lower the curves and vice versa. However, the relative positions of the saturation curves could be significantly different with some changes in the pH-fS_2-fO_2 buffer assemblage and chloride concentrations, and at lower temperatures, there is much greater uncertainty about choride speciation and equilibrium conditions. The field for Pb-Zn transport under conditions ranging from 150-250°C and 10 to 25 eq. wt % NaCl are also shown in Figure 10.5. The diagrams indicate that under pyrite-stable conditions, such as those in the Battle chert, Pb-Zn transport as chloride species, would be virtually independent of redox variation, and precipitation would be more likely due to decreasing temperature and/or changes in the pH conditions.

In Figure 10.11, the fluid transport paths are horizontal, and the fluids are undersaturated in the various metals until they intersect their respective saturation surfaces. In general, Fe precipitates first, then Cu, then Fe plus Cu and Zn (although Fe becomes progressively depleted with less Fe coprecipitated with Zn than with Cu), and Zn and Pb (Hemley and Hunt, 1992). Reasonable Pb-Zn transport paths would intersect their saturation surfaces at about 150°C. Hemley and Hunt (1992) describe Pb-Zn zonation in the outermost zones of Butte-type orebodies in Utah, with the Butte Main Stage veins having a sphalerite zone followed by a galena zone. The width of the sphalerite zone, produced before the start of galena precipitation, would have been dependent on the relative concentrations, but after the fluid reached the Pb saturation surface, coprecipitation of Pb and Zn resulted. Cu-Zn-Pb zoning has also been described in many VHMS deposits, such as the Rosebery deposit in Western Tasmania (Smith and Huston, 1992), which has a stratigraphically lower high temperature Cu-Bi-Fe zone and an upper, lower temperature Zn-Pb-Ag-Sb rich zone. Smith and Huston (1992) suggest that the Cu-Bi-Fe precipitated during slow cooling of hotter fluids ~300°C, while Pb-Zn-Cd and Ag deposited from rapid cooling of warm (~250° C) fluids caused by seawater mixing.

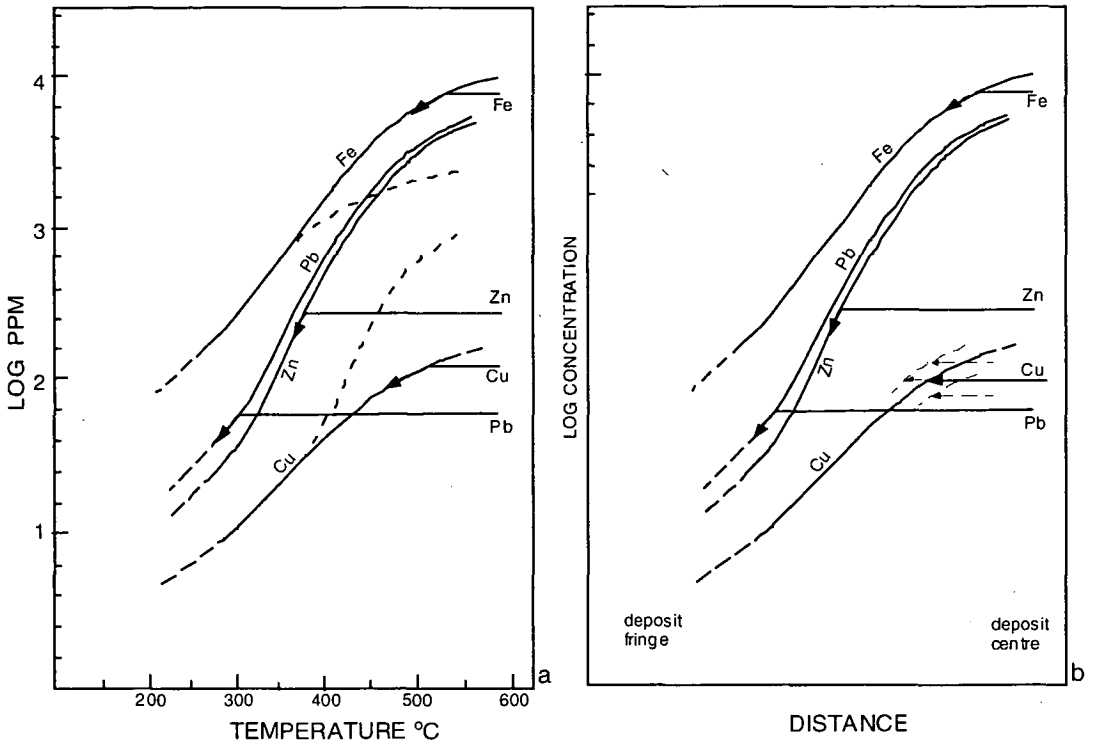

Figure 10.11: a) Solubility diagram using the K feldspar-muscovite-quartz buffer in the mixed sulphide system, at1 kbar, 1 *m* total chloride, modified from Hemley and Hunt (1992). The diagram illustrates the implied transport, deposition and zoning relationships for Zn, Cu, Pb and Fe as a function of temperature. The horizontal arrows are undersaturated transport paths for the metals in an increment of migrating, cooling solution, with precipitation occurring down the saturation curves once the curves are intersected. The dotted curves are hypothetical saturation curves for Fe and Cu under different buffering conditions, as discussed in text. **b)** This diagram shows the same relationships for Zn, Cu, Pb and Fe as Figure 10.14a, but is instead plotted as a cross section of a hypothetical Butte-type orebody at a given point in time, with the curves representing solubility fronts (from Hemley and Hunt, 1992).

At Myra Falls the Cu-Zn-Cd-Pb-Ag-Sb zonation in the Battle chert, can be described by a temperature-solubility model (Figure 10.12), modified from Hannington et al. (1999). The model provides a thermal profile along the chert and is based on chloride complex solubilities (data from Hannington et al. (1999), and references within), physicochemical conditions indicated by the observed mineral assemblage, and estimates of fluid compositions, based on measurements of active vents from the Lau Basin. Metal concentrations are 100ppm Fe, 50ppm Cu, 50ppm Zn, 1ppm Pb, 1 ppm As, 10 ppb Ag, and the physicochemical conditions are estimated at: pH=4, 1m NaCl. H_2S activity and fO_2 are buffered by the assemblage py-po-mt and fluid temperatures around 300°C, reflecting conditions close to that of modern vent fluids. These fluids were slightly more reducing than those that formed the Battle chert, as pyrite dominates, with no pyrrhotite observed. Although differences exist in the fO_2 and H_2S activity of the Battle chert, the order of mineral precipitation in the model matches the metal zonation observed in the chert. Fluid

inclusion data from the caprock horizon also suggest a similar range of temperatures for the Battle chert, and indicates that the model is a good approximation to account for the metal zonation.

The model indicates that at the low metal concentrations predicted for the silica-bearing fluids, most of the sphalerite would be precipitated below about 170°C, with the galena and Ag precipitated at lower temperatures <100°C. Hannington et al. (1999) suggest that Ag is transported as $AgCl_2^-$ over a wide range of temperatures, pH and fO_2. The low metal content of the chert is consistent with relatively low temperatures (<200°C) of the silica-bearing fluid. Metal zoning, combined with metal solubility data, indicates that the lower temperature metal assemblage (Pb-Ag-Sb) is located further from the vent than the higher temperature metal assemblage (Cu-Zn-Cd). The lack of separation of a Zn and Cu zone, indicates a very steep thermal gradient in this zone. The changing metal assemblages most

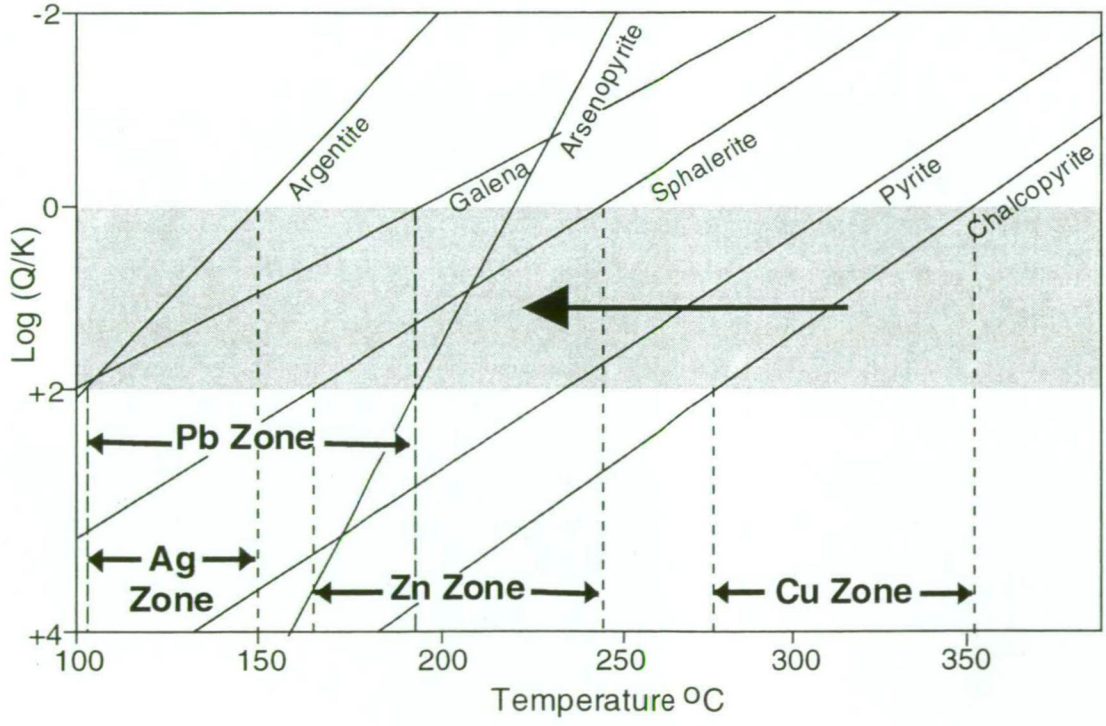

Figure 10.12: Temperature-solubility model for sulphide minerals in the Battle chert, with mineral solubilities based on chloride complexes of the major metals (modified from Hannington et al., 1999). The composition of the fluid is based on the composition of modern vent fluids from the Lau Basin (Von Damm, 1990). The shaded region shows the likely temperatures of deposition for the main ore minerals, based on their solubilities. The dashed lines indicate the range of temperatures for ore formation within the Cu-rich and Zn-rich zones. A thermal profile for the different zones can be constructed according to the mineral solubilities. Note that Pb and Ag are precipitated at much lower temperatures than sphalerite and chalcopyrite.

likely represent precipitation from the same end-member fluid during progressive cooling. Lateral and vertical metal zonation is also observed in the underlying Battle orebody (Sinclair, 2000). Vertical zonation in the Battle main lens consists of a high Cu-Fe zone, overlain by a high Zn zone, which is in turn overlain by an area enriched in Pb-As-Ag±Bi. Lateral zonation consists of a central Zn-Cu rich core flanked by zones of higher Pb and As. Lateral flow of the silica-bearing fluid through the porous seafloor muds above the massive sulphides, would have resulted in the migration of a thermal front. In studies based on fluid modelling, Cathles (1997) indicated that significant deposition of silica and metals can be expected only where thermal anomalies are immobilised. This could be achieved by mixing of hot hydrothermal fluids and cold seawater. It is also likely that the thermal front was accompanied by a chemical front, such as a marked pH gradient into the more acid hydrothermal fluid. In the Battle chert, the migration of a chemical and thermal front is indicated by a rapid decrease in organic carbon, from the unaltered Battle basin argillite to the Battle chert (Figure 6.32).

10.3.6 Organic carbon degradation and metal complexes

Organic carbon contents (TOC) are much lower in the Battle chert above the massive sulphides, than the adjacent black chert and Battle basin argillite. The Battle basin argillite has TOC values up to 0.60 wt.%, while the black chert at the edge of the siliceous alteration zone has TOC values up to 0.16 wt.%, and the white chert, proximal to ore, contains very low TOC values; maximum 0.07 wt.% (Chapter 8, Appendix 5.1). Sedimentological, petrological and geochemical evidence indicates that that the Battle chert is the altered equivalent of the adjacent argillite (Chapters 6 and 8). Therefore, original TOC contents in the chert would have been similar to the adjacent argillite. This section examines the processes, which resulted in the destruction and removal of the organic carbon in the Battle chert. The sequence has undergone greenschist facies metamorphism and the organic carbon in the argillite and chert is now predominantly graphite. However, at the time of chert formation, the organic carbon was relatively immature, as diagenesis was incomplete. Therefore the solubility of immature organic ligands must be examined rather than graphite.

A number of experimental investigations have determined the dominant processes which degrade organic ligands (e.g., Price et al., 1983; Sanders, 1986; Bell and Palmer, 1994; Hofmann and Bernasconi, 1998; Simoneit, 2000; McCollom et al., 2001). Three dominant processes have been identified and include oxidation, thermal degradation and bacterial digestion, generally at temperatures less than 80° C (Seward and Barnes, 1997). However, in the reduced hydrothermal ore-transporting environment, thermal degradation dominates.

Bell and Palmer (1994) presented experiments on the kinetics of decarboxylation of the acetate ligand as a function of temperature, and representative reactions for this process include;

the decarboxylation of acetic acid

$$CH_3COOH_{(aq)} \Leftrightarrow CH_{4(g)} + CO_{2(aq)} \quad (3)$$

or degradation of the acetate anion

$$CH_3COO^- + H_2O_{(l)} \Leftrightarrow CH_{4(g)} + HCO_3^- \quad (4)$$

High concentrations of CH_4 and CO_2 have been recorded in some hydrothermal fluids (e.g., Sakai et al., 1990; Simoneit et al., 1988). At Myra Falls, fluid inclusions from quartz interstitial to Battle ore and in the siliceous caprocks were generally CO_2 poor. However, CO_2 and CH_4 gas-rich inclusions were observed in quartz interstitial to sulphides in the HW orebody (Barrett and Sherlock, 1996).

The alteration and degredation of organic matter in hydrothermal systems is thought to occur over a temperature range from 60 to > 400°C (Simoneit, 2000). Experiments have shown H_2O to be an effective organic solvent and the aqueous solubility of organic compounds increased as the temperature approached the critical point to essentially complete miscibility (Simoneit, 2000). For example, at 300° C, the solvent properties of H_2O approached those of acetone (Siskin and Katritzky, 1991; Landais and Gize, 1997). Hydrothermal products migrate with the fluids as they are formed, and have been observed in venting fluids. For example, oil globules were collected under in situ conditions (200 bars, 2-3° C) in Guaymas Basin vent fluids (Simoneit et al., 1988). Peter et al. (1991) suggest that formation and migration of the hydrothermal products of organic matter is a rapid process, taking place over time scales ranging from days to years.

Giordano and Barnes (1981) suggested that organic complexes in hydrothermal systems, especially below 250° C, may have had a significant role in the transport of metals, particularly zinc and lead. However, the role of organic acids as potential ligands for metal complexation and transportation in low temperature hydrothermal fluids is still debated (Giordano and Kharaka, 1994). Most experiments have been concentrated on carboxylic ligands such as acetate, which is the most abundant organic acid species; constituting 80-90% of total dissolved organic acid anions in formation waters (Hofmann and Bernasconi, 1998). Seward and Barnes (1997) suggest that a general sequence of stabilities is observed in carboxylate complexes, $Al>Pb>Zn>Fe^{2+}$, and that the dicarboxylate complexes are more stable (ie stronger and relatively more soluble) than monocarboxylate complexes. However,

the decreased persistence of dicarboxylate complexes at higher temperatures diminish their hydrothermal importance (Seward and Barnes, 1997). Hofmann and Bernasconi (1998), also indicate that organic acid complexes such as oxalates are not stable over temperatures of about 140° C.

The much lower TOC contents of the chert, reflect thermal degradation of organic matter by lateral flow of hot hydrothermal fluids. The rapid change from white-grey chert to black chert at the edge of the siliceous alteration zone most likely reflects a steep thermal gradient, rather than a redox front, due to the low O_2 bottom water conditions in the Battle basin at the time of chert formation (Chapter 8). The development of organic ligand-metal complexes may have occurred during chert formation, but most likely did not result in significant metal transport, due to the instability of many organic complexes in hydrothermal fluids with temperatures >150 to 240° C (e.g., Seward and Barnes; Hofmann and Bernasconi, 1998; Simoneit, 2000). Instead, metal transport by chloride complexes was more likely in the reduced siliceous fluids above the Battle orebody. The metal zonation observed at the edge of the chert is also better explained by transport of Zn-Pb as chloride complexes, which are independent of redox conditions (e.g., Figure 10.5), but strongly affected by a rapid decrease in temperature.

10.3.7 Effects of low O_2 bottom water conditions

The marked absence of sulphate and oxides in the Battle orebody and overlying chert may reflect the low O_2 bottom water conditions in the Battle basin during ore formation. The Battle chert has very low Fe and Mn levels and highly variable Cu-Zn-Pb-Cd-Ag-Sb-Ba contents (up to several 1000 ppm Zn, Cu and Pb in places). Although Ba levels are relatively high in the Battle chert and adjacent argillite, no barite is observed. Instead, Ba resides in white mica, with positive correlations with Al, K, Rb and Zr, and negative correlations with S. However, fine rectangular megaquartz patches (after anhydrite or barite?) do occur in a single fine layer in the laminated chert above the orebody (e.g., Figures 6.13d-f). If the rectangular megaquartz patches were originally sulphate, they may represent precipitation during a period of fluctuating O_2 conditions.

The paucity of sulphates in the Battle Main lens and overlying caprock horizon reflects the low O_2 bottom water conditions, as relatively oxidised conditions are necessary for the stability of sulphates, such as anhydrite and barite (e.g., Cooke and Simmons, 2000). The lack of sulphates may have enhanced the sheet-like morphology of the orebody, due to the absence of chimney or mound structures, which are formed predominantly by the precipitation of early anhydrite, barite, sulphides and silica. Mounds, chimney structures

and breccias are also absent in the HW orebody (pers. comm., M. Hannington, 2000). This orebody has a lack of sulphate and also formed in a deep anoxic basin, similar to the Battle orebody (Section 10.5). In the Battle basin, barite becomes common in the Battle upper lenses, which are located near the top of the HW Horizon (Figure 10.4). The presence of barite most likely reflects more oxidised bottom water conditions during formation of the upper lenses.

In normal, oxidised seawater, Fe-Si-barite deposits commonly form above VHMS orebodies and active seafloor vents. For example, the Fe-rich tetsusukei above the Kuroko deposits (Kalogeropoulous and Scott, 1983), Fe-Si-barite caps above many Australian VHMS deposits such as Rosebery, Hellyer, Scuddles (e.g., Sharpe, 1991; Gemmell and Large, 1992; Large, 1992) or Fe-Si deposits active seafloor vents such as the silica chimneys at the Galapagos spreading centre (Herzig et al., 1988). End-member, high temperature seafloor vent fluids are reduced, acidic and predominantly Fe-rich (Von Damm, 1990). Fe is very soluble in hydrothermal fluids and very high Fe values are measured in some saline hydrothermal systems, especially >250°C, e.g., Fe = 21-1710 μmol/kg in back arc vent fluids (Fouquet et al., 1993; Campbell et al., 1994; Ishibashi and Urabe, 1995) or Fe = 600 to 2400 μmol/kg in fluids from seafloor Fe-Si-Mn oxide deposits, (e.g., Von Damm, 1990; Binns et al., 1993; McMurtry et al., 1993). At typical vent fluid temperatures of 50-200° C, Fe^{2+} dominates; at temperatures <50° C, iron is soluble as Fe^{2+} and as $Fe(OH)^{+}$ at alkaline pH (Barnes, 1979).

In normal, oxidised seawater, fO_2 is too high, and P_{CO_2} too low to permit significant transport of Fe^{2+}, and very little Fe remains in solution (Garrels, 1987). Typical Fe contents of normal seawater are <0.001 μmol/kg (Von Damm, 1990). However, the low O_2 conditions of the bottom water in the Battle basin could have allowed significant transport of Fe^{2+}, and most likely accounted for the lack of Fe in the siliceous caprocks above the Battle orebody. Although there is little or no Fe in the Battle chert, finely laminated angular jasper clasts (up to 10-30cm size) are relatively common in the mass flow units overlying the siliceous caprocks. The finely laminated jasper clasts also contain radiolarians in some layers and most likely formed by pelagic sedimentation. Bedded jasper deposits have not been observed in situ, anywhere within the Battle basin. The ubiquitous presence of laminated jasper clasts in the units immediately overlying the Battle cherts, indicates that there was a significant Fe component in the seawater, close to the time of ore formation. However, deposition of these Fe-deposits was distal to the ore body and did not occur within the Battle basin.

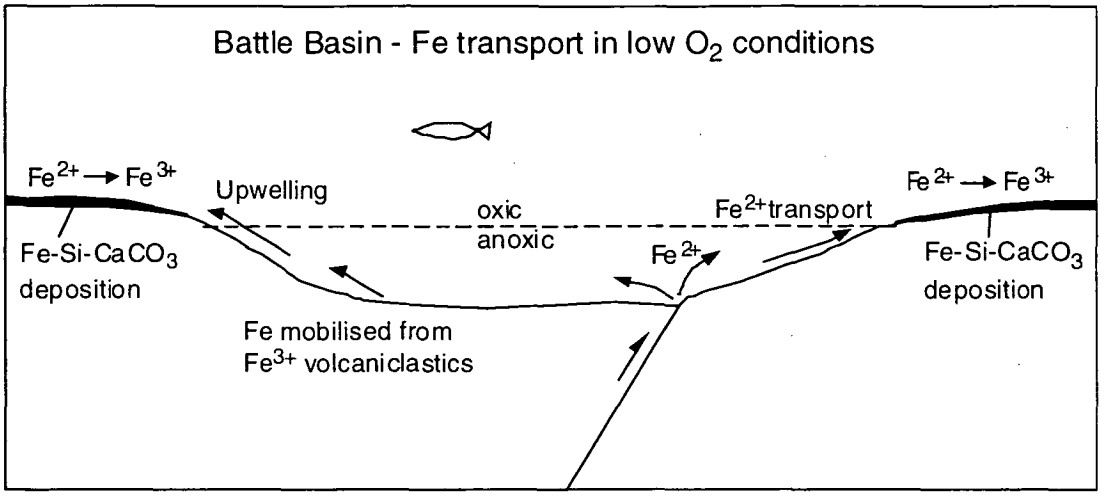

Figure 10.13: Model for the formation of bedded Fe-Si deposits on clastic-free shelves at the edge of the Battle basin. Deeper water, enriched in Fe^{2+} from volcanic and diagenetic sources, migrates out of the anoxic basin and precipitates Fe, Si and carbonate as a result of oxidation.

A model for the formation of distal Fe-Si deposits (finely bedded jasper) at the edges of the Battle basin is illustrated in Figure 10.13. Upwelling of the relatively Fe-Si(?) rich water into more oxidised conditions, above the oxic-anoxic boundary, may have resulted in the deposition of Fe and Si ± carbonate by oxidation (Maynard, 1983). This model has similarities to the Fe-oxide deposits observed at the edge of the reduced Atlantis II Deep (Zierenberg, 1990). Within the Battle basin the dominant source of the iron would most likely be from the release of Fe^{2+} from venting fluids, but also from remobilisation of the ferric iron adsorbed on the surface of clastic particles (Maynard, 1983). However, in the present-day anoxic environment of the Black Sea, most of the Fe is precipitated in the deep water as Fe-sulphides. In other anoxic environments, Fe could still be transported if, 1) all or most of the S in the deep water was precipitated as Fe-sulphides, but excess Fe^{2+} (added to seawater by rivers) was available for transportation to shallower environments, and/or, 2) the deeper zones had an oxidation potential low enough to convert Fe^{3+} to Fe^{2+}, but was not low enough to allow the reduction of SO_4^{2-} to H_2S (Drever, 1974). The preservation potential of finely bedded Fe-Si deposits at the edges of the Battle basin would most likely be low as this is a tectonically/volcanic active area. Instead, these deposits would be easily eroded and redistributed within the basin by mass flow deposits.

In summary, anoxic bottom water conditions affected the form and mineralogical character of the upper parts of the Battle main lens and overlying siliceous caprocks. The absence of sulphate in the reduced conditions may have enhanced the sheet-like morphology of the orebody, with a lack of sulphate-sulphide chimney or mound-like features. The siliceous caprocks have very low Fe contents, most likely reflecting the low O_2 bottom water

conditions. Laminated jasper deposits do occur, but are only seen as clasts in mass flow units above the caprock horizon. The anoxic water column also served to protect freshly precipitated sulphides on the seafloor and just below the sediment-seawater interface from oxidation, enhancing the base metal signature of the Battle basin argillites.

10.3.8 Fluid behaviour

Several authors have suggested that the morphology of a VHMS system reflects the behaviour of the hydrothermal fluid (e.g., Sato, 1972; Solomon and Walshe, 1979; and Turner and Campbell, 1987). The behaviour of the hydrothermal fluid is dependent on fluid properties, such as temperature, density, flow velocity and phase behaviour, and the physical properties of the host rock (e.g., porosity, permeability).

Sato (1972) outlined three main types of fluid behaviour (type I, II and III), based on fluid densities (Figure 10.14a).

Type I fluid: a very saline, dense, bottom-hugging fluid, which remains denser than seawater, forming density currents and brine pools. This fluid forms thin (low aspect ratio), well layered, tabular base metal deposits, such as those forming in the Red Sea. Although, an alternative model for the thin tabular deposits is by dispersed hydrothermal discharge from many small vents as suggested for the Rosebery deposit, Tasmania (Huston, 1988).

Type II fluid: a hot saline fluid, initially more buoyant than seawater, but on mixing with seawater, displays a buoyancy reversal. Fluid modelling by Turner and Campbell (1987), shows that all fluids >300°C will at first be more buoyant than seawater, but if the temperature is <~300°C, the fluids display buoyancy reversal when mixing with seawater.

Type III fluid: a hot buoyant plume, which is less dense than seawater. For example, a black smoker, which undergoes turbulent mixing with seawater results in mineral precipitation high in the plume, and dispersal over a wide area.

The density of ambient bottom water at 2000m depth and 2° C is 1.03 g/cm^3 (Scott, 1997). The majority of most measured vent fluids are lower than this value, although some approach this density (e.g., Figure 9.14). However, even the most saline fluids, such as the hydrothermal fluids of the Atlantis II Deep, vent as buoyant plumes due to their high temperatures (type II to III behaviour of Sato, 1972). The lower density of most active vent fluids results in the dominance of type III behaviour at active vents. For example, black smoker vent fluids have a density contrast with the ambient seawater of about 0.2-0.3 g/cm^3, and therefore form high velocity buoyant plumes. However, fluids from Fe-Si-Mn oxide deposits have a much lower density contrast, only 0.01 g/cm^3 and flow velocities are much lower, only a few cm/sec (Binns et al., 1993). Type I or II fluid behaviour (Sato, 1972) is

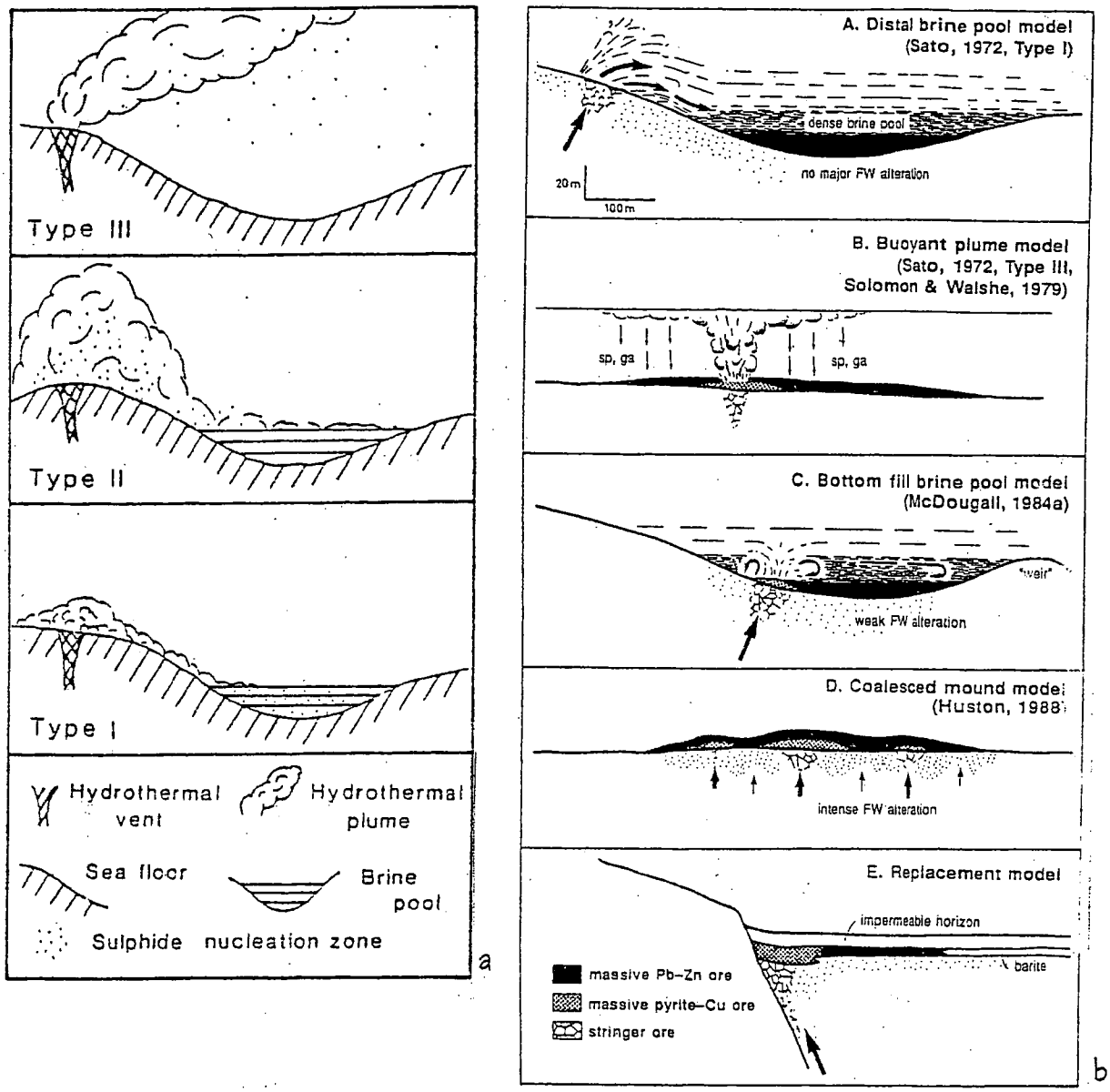

Figure 10.14: a) Schematic diagram of three fluid types, modified from Sato (1972). Type I fluids are dense bottom-hugging brines; type II fluids are have intermediate salinities and exhibit buoyancy reversal on mixing with seawater; type III fluids are less dense than seawater and form buoyant plumes. **b)** Diagram illustrating the various models used to explain the genesis of sheet- or blanket-style VHMS deposits (from Large, 1992).

likely for the formation of the Fe-Si-Mn deposits. Figure 10.14b, from Large (1992), summarises a number of models used to describe the morphology and formation of VHMS systems. These models are based on fluid behaviour and diffuse or focussed flow through the footwall rocks.

Although the majority of measured vent fluids appear to exhibit type II or III behaviour, bottom-seeking hydrothermal fluids have been observed. For example, Lonsdale et al.

(1982) describe an unanalysed 10-15°C bottom-seeking fluid emitted from an iron oxide deposit in a submarine caldera. Fluid inclusion data from the Pb-Zn Silvermines and Sullivan deposits also suggest that the ore-forming fluids barely exceeded the density of seawater, and may have behaved as a type I to II fluid (Figure 9.14). Myra Falls data also plots close to ambient seawater on this diagram (Figure 9.14), suggesting a relatively low density contrast between the ore-forming fluids and the ambient seawater.

Fluid behaviour can be estimated from a comparison of fluid densities from Battle and HW orebody inclusions and the ambient seawater at 2° C ($\rho = 2.08 g/cm^3$), on a diagram modified from Sangster (*in press*) (Figure 10.15). Myra Falls data predominantly lies in the 'intermediate brine' and 'buoyant brine' fields, with a few plotting in the 'dense brine' field, indicating that the hydrothermal fluids may have behaved in a number of ways. For example, there is evidence of buoyant hydrothermal plumes (type III behaviour of Sato, 1972), including 1) the elevated base metal signature of the Battle basin argillites, indicating wide dispersal of plume particulates; 2) fine sulphide-rich mud entrained into the base of an overlying turbidite. However, there is much evidence for the formation of the Battle orebody and associated siliceous caprocks to be the result of diffuse lateral flow through the porous substrate at or near the seafloor. This evidence includes, the sheet-like morphology

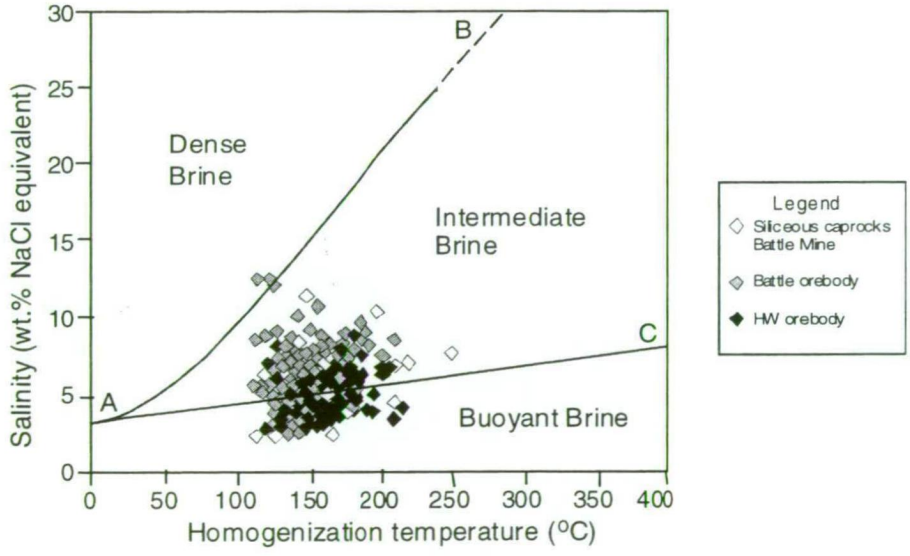

Figure 10.15: Temperature versus salinity plot modified from Sangster (in press). Point A is the position of seawater at 2° C. Line AB is the seawater isodensity line; points on this line have the same density of seawater at 2°C (ρ = 1.208 g/cm3). Ore fluids plotting in the field below this line are less dense than seawater; fluids plotting above the line are denser than seawater. Line AC defines the lower limit of the field of buoyancy reversal. The field between AB and AC represents fluids which are initially less dense than seawater and form a buoyant plume. Upon mixing with cold dense seawater, the plume collapses, with the fluid sinking down and collecting on the seafloor as a dense brine.

of the Battle orebody and associated siliceous caprocks; replacement textures in ore and chert; lateral metal zonation in the chert and Battle orebody (Sinclair, 2000); relatively high salinity (and density) of ore fluids; and the porous nature of the seafloor muds overlying the Battle orebody, prior to silicification. Hydrothermal fluid flow through the porous seafloor sediments would most likely have been diffuse and unfocussed, resulting in lower flow velocities, as diffuse flow does not reach the velocities of channelised flow. The lower flow velocity combined with relatively high salinities (3 to 12.4 eq. wt % NaCl) and moderate temperatures (150-250°C) may have enhanced lateral fluid flow rather than buoyant venting, and resulted in the sheet-like morphology of the Battle orebody.

Evidence has been suggested for type III buoyant behaviour (Sato, 1972), but some buoyant hydrothermal fluids, after venting and mixing with seawater may have experienced buoyancy reversal and sunk back down to the seafloor (type II behaviour, Sato, 1972), and formed a brine pool (e.g., McDougall, 1984), or percolated back down into the porous seafloor muds (e.g., Sangster, *in press*). If the rising hydrothermal fluids mixed with seawater within the porous seafloor sediments, venting may not have occurred, instead fluids would flow laterally through the porous seafloor sediments. Mixing between the rising hydrothermal fluids and seawater, within the sediments, is suggested by a progressive decrease in homogenisation temperatures and salinities of fluid inclusions from the centre of the Battle main lens to the upper ore contact and siliceous caprocks (Chapter 9).

10.4 Genetic model for Battle orebody and associated siliceous caprocks

A genetic model for the formation of the Battle orebody and overlying caprocks is shown in a series of illustrations in Figure 10.16.

Stage 1: Basin development

A basin began to form by normal movement on growth structures located at the northern edge of the basin. The onset of rhyolitic volcanism resulted in early basin infill of coarse-grained rhyolitic volcaniclastics. A period of tectonic and/or volcanic quiescence began, with the deposition of several metres of finely laminated muds, silts, and minor interbedded turbidites. Within the deep basin, restricted from open-ocean circulation, a stratified water column began to develop with low to fluctuating O_2 bottom water conditions.

Stage 2: Onset of hydrothermal activity

During deposition of the seafloor muds, hot hydrothermal fluids began to percolate through the sediments from a vent at the northern edge of the basin. The sheet-like form of the Battle orebody, the relatively weak footwall alteration and good ore-replacement textures indicate that the orebody formed by diffuse lateral flow of ore-forming fluids through a coarse-

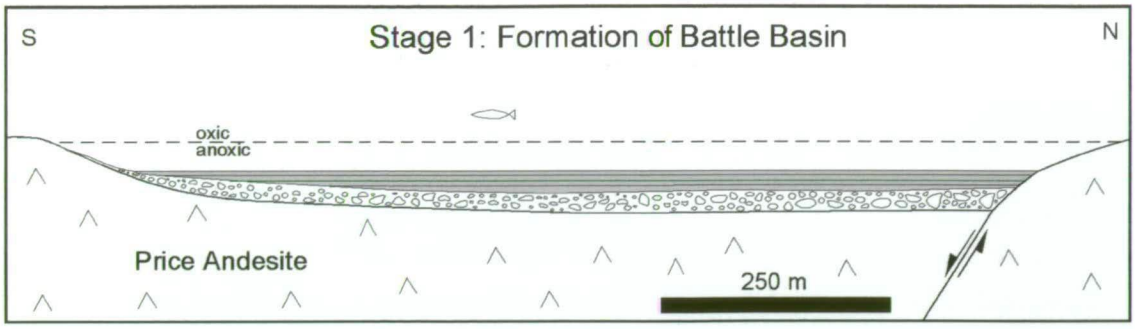

Figure 10.16a: Stage 1: A basin began to form by normal movement on growth faults located at the northern edge of the basin. The onset of rhyolitic volcanism resulted in early basin infill of coarse-grained rhyolitic volcaniclastics. A period of tectonic and/or volcanic quiessence began, with the deposition of several metres of finely laminated muds, silts and minor interbedded turbidites. Within the deep basin, restricted from open ocean circulation, a stratified water column developed, with low to fluctuating O_2 bottom water conditions.

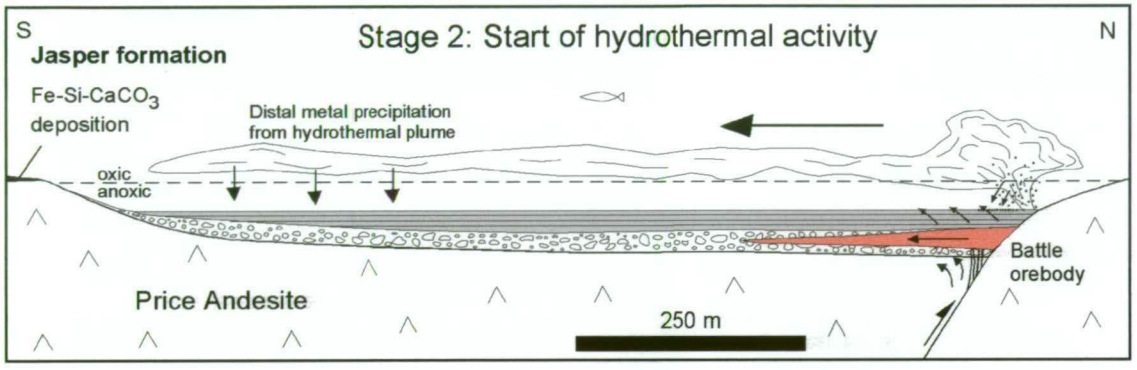

Figure 10.16b: Stage 2: During deposition of the seafloor muds, hot hydrothermal fluids began to percolate through the sediments from vents at the northern edge of the basin. The sheet-like form of the Battle orebody, the relatively weak footwall alteration and good ore-replacement textures indicate the dominance of diffuse lateral fluid flow, rather than channelised flow through a coarse-grained layer of rhyolitic detritus. The hydrothermal fluids also percolated through the overlying muds, depositing rutile, apatite and minor sulphides in primary pore space. Buoyant venting into the overlying water column also occurred and is indicated by the spatial distribution of metals in the Battle Basin and the presence of fine sulphide-rich layers in the mudstone. The buoyant plumes may have collapsed on mixing with cold seawater, and sunk back onto the seafloor, possibly forming a brine pool. Fe-Si-$CaCO_3$ deposition occurred at the margins of the Battle Basin, above the oxic/anoxic boundary to form laminated jasper beds.

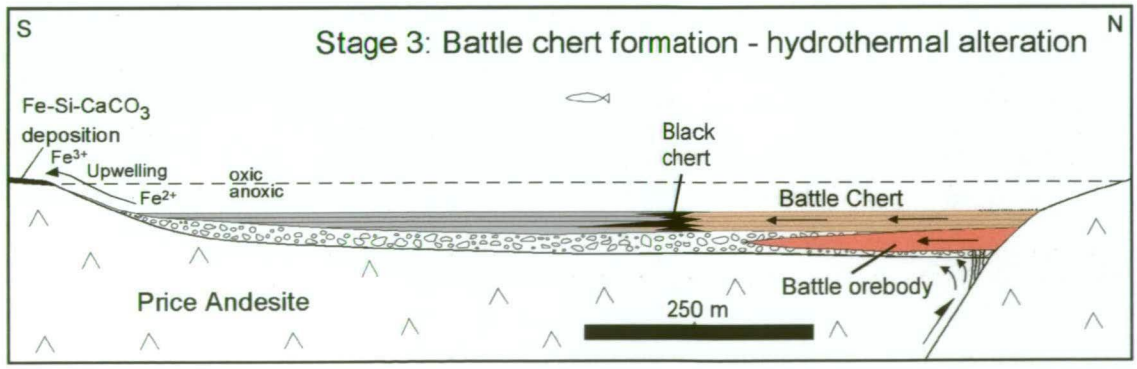

Figure 10.16c: Stage 3: Subsequent low to moderate temperature, saline silica-bearing fluids flowed laterally through the unconsolidated seafloor muds to form the Battle chert. The timing of silicification is constrained by the presence of chert rip-up clasts in overlying mass flow units. Silicification overprints early hydrothermal mineral textures in the fine-grained caprocks and it is likely that the silica-bearing fluids had a similar origin to the ore fluids. The low metal contents of the chert reflects relatively low temperatures (<200°C) and prior deposition of sulphides in the underlying coarse-grained rhyolitic layer.

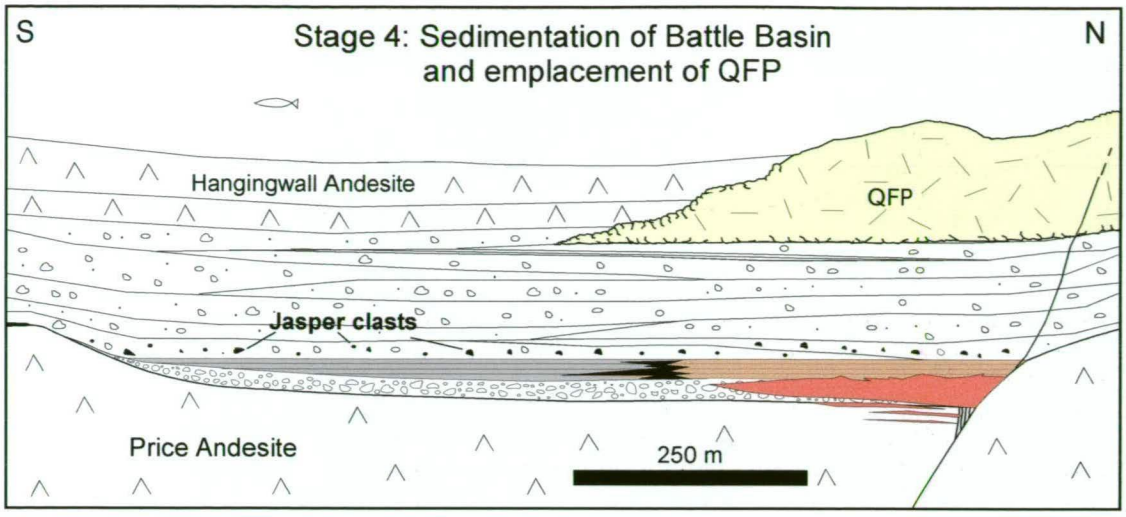

Figure 10.16d: Stage 4: Formation of the siliceous caprocks on the seafloor was followed by renewed tectonism and volcanism with the rapid deposition of thick rhyolitic mass flow units, interlayered rhyolitic sandstones, siltstones and volcaniclastics. Finely laminated jasper clasts are relatively common in mass flow units just above the caprocks and most likely originate from Fe-Si deposits forming on the margins of the Battle Basin. Following the deposition of the thick rhyolitic volcaniclastic pile, a large quartz-feldspar porphyry body was emplaced at the top of the HW Horizon.

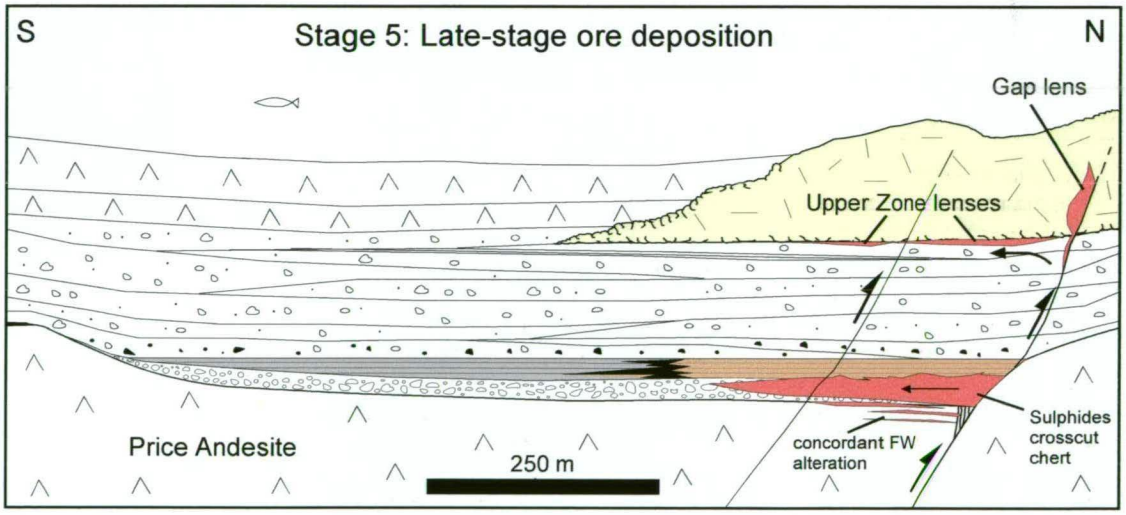

Figure 10.16e: Stage 5: Ore deposition continued throughout the deposition of the HW Horizon rhyolitic volcaniclastic rocks and after the intrusion of the quartz-feldspar porphyry. The more focussed fluid flow resulting from the formation of the silica cap is shown by the markedly different style of the Gap Lens at the northern edge of the basin. The barite-rich Gap Lens formed during the last stage of ore formation, from fluid flow along a large growth structure at the northern edge of the basin. Upper ore lenses, beneath the massive QFP body, were also forming at this time from diffuse fluid flow through the coarse-grained rhyolitic sediments and ponding beneath the less permeable massive porphyry. The abundant barite in the upper lenses (barite is rare in the main Battle lens) suggests a change to more oxic bottom water conditions.

grained layer of rhyolitic detritus. Diffuse lateral flow rather than buoyant venting may have been enhanced by the relatively high salinities and low to moderate temperatures of the hydrothermal fluids, which ranged from 3-12.4 eq. wt % NaCl and 120-250° C. At the time of ore formation the coarse-grained rhyolitic detritus was overlain by 1-3m of fine-grained muds. The hydrothermal fluids percolated upwards, depositing rutile, apatite and minor sulphides in primary pore spaces in the overlying fine-grained pelagic sediments. Some venting onto the seafloor also occurred, resulting in the development of fine sulphide-rich mud layers. In places, these sulphide-rich muds were entrained into overlying sandstone turbidite layers. Buoyant plumes are also indicated by the metal-rich signature of the Battle basin argillites, up to 300-350m away from the source vents.

The percolation of hydrothermal fluids through the seafloor muds, indicate that the muds were relatively porous and did not act as an impermeable cap. Hydrothermal fluid flow through the sediments would have been diffuse and unfocussed, resulting in lower flow velocities, as diffuse flow does not reach the velocities of channelised flow. The lower flow velocity combined with relatively high salinities (3 to 12.4 eq. wt % NaCl) and moderate temperatures (150-250°C) may have enhanced lateral fluid flow rather than buoyant venting, and resulted in the sheet-like morphology of the Battle orebody. The lateral flow of hydrothermal fluids during ore formation resulted in only weak footwall alteration away from the main vent zone. There is no intense footwall alteration pipe, like that described at the Hellyer deposit, Tasmania (Gemmell and Large, 1992), or the very intense footwall alteration observed in zones beneath the Rosebery deposit, from coalescing mounds (Huston, 1988). Instead, concordant weakly to moderately altered zones are observed in the footwall beneath the Battle orebody. A moderately developed stringer zone, about 20-50m wide, is observed 100-200m beneath the northern part of the Battle orebody in the Battle mine (24 level). The stringer zone consists of steep quartz veins and moderately to strongly chlorite-silica-sericite altered andesite.

Stage 3: Formation of siliceous caprocks

Subsequent low to moderate temperature, saline silica-bearing fluids flowed laterally through the unconsolidated seafloor muds to form the Battle chert. Silicification occurred close to the paleo-seafloor, early in the diagenetic history, as chert rip-up clasts are incorporated into the overlying mass flow units. Mass gains of up to 200% (190g/100g) SiO_2 in the Battle chert are also consistent with formation near the paleoseafloor at or near hydrostatic pressures (e.g., Lentz and Goodfellow, 1996). Silicification overprinted early hydrothermal mineral textures in the fine-grained caprocks and it is likely that the silica-bearing fluids had a similar origin to the ore fluids. The low metal contents of the chert,

reflect relatively low fluid temperatures (<200° C) and prior deposition of sulphides in the underlying coarse-grained rhyolitic volcaniclastic layer. Silicification took place by lateral fluid flow through the fine sediments, rather than buoyant venting onto the seafloor. Lateral fluid flow is indicated by the metal zoning in the chert, with a (higher temperature Cu-Zn-Cd zone grading out to a lower temperature Pb-Ag-Sb zone at the edge of the chert), the gradual transition from chert to argillite, and their similar immobile element signatures. Lateral fluid flow through the porous seafloor muds would be enhanced by the lower velocities of diffuse flow, rather than channelised flow, and the low density contrast between the silica-bearing fluid and the ambient seawater, similar to those of modern Fe-Si-Mn seafloor deposits (e.g., Binns et al., 1993). The diffuse lateral flow resulted in the sheet-like morphology of the Battle orebody and the overlying siliceous caprocks. The sheet-like morphology of the orebody could also partly reflect the lack of mound and chimney structures due to the paucity of sulphate (e.g., anhydrite and barite) in the low O_2 bottom water conditions.

Plugging of the porous seafloor sediments by precipitation of silica, changed the hydrothermal flow regime from diffuse to more focussed flow, leading to enhanced lateral flow of subsequent ore-bearing fluids beneath the silica cap. Massive sulphides crosscut the basal contact of the chert in places.

Stage 4: Sedimentation of Battle basin

Formation of the siliceous caprocks on the seafloor was followed by renewal of tectonism and volcanism, with the rapid deposition of thick rhyolitic mass flow units, interlayered with rhyolitic sandstones, siltstones and volcaniclastics. Finely laminated jasper clasts are relatively common in the overlying mass flow units and most likely originated from Fe-Si deposits forming on the margins of Battle basin, above the anoxic-oxic boundary. The end of rhyolitic volcanism is marked by the intrusion of a massive quartz-feldspar porphyry body at the top of the rhyolitic volcanic sequence.

Stage 5: Late-stage hydrothermal activity

Ore deposition continued throughout the deposition of the HW Horizon rhyolitic volcaniclastics and intrusion of the quartz-feldspar porphyry. The more focussed fluid flow resulting from the formation of the silica cap above the Battle orebody, lead to the development of the Gap lens at the northern edge of the basin. This lens displays a markedly different style to the Battle main lens and appears to be structurally controlled. The barite-rich Gap lens formed during the last stage of ore formation, from the upflow of a more focussed hydrothermal fluid along the main growth structure at the northern edge of the basin. Upper ore lenses, beneath the massive quartz-feldspar porphyry, were most likely

also forming at this time. Their formation appears to be a result of diffuse fluid flow through the coarse-grained rhyolitic sediments and ponding beneath the less permeable massive quartz-feldspar porphyry. Diffuse fluid flow through the volcaniclastic pile, is indicated by silicification of fine-grained layers throughout the HW Horizon, and the alteration of jasper clasts, with patchy haematite destruction. The continued flow of hydrothermal fluids resulted in a distinct alteration halo in the HW Horizon above the Battle orebody. This alteration halo is shown by white mica and chlorite compositions, and is easily mapped using SWIR spectral characteristics.

Barite is common in the upper lenses and most likely indicates 1) changing bottom water conditions in the Battle basin, with the development of a more oxygenated environment during deposition of the upper zone sulphides, and/or 2) a change in fO_2 of the hydrothermal fluids, as suggested by Sinclair (2000).

10.5 Comparison with the HW basin

The HW orebody also formed within a basin and is overlain by fine-grained sediments, predominantly composed of argillite and fine siltstone interbeds. However, the timing of ore formation, relative to the deposition of the fine-grained caprock horizon differs markedly to the Battle deposit. Massive sulphides were deposited in the coarse-grained rhyolitic detritus in the shallow subseafloor, and directly on the seafloor, prior to deposition of the fine caprock horizon. The top surface of the HW orebody is eroded in places, and ore clasts are commonly entrained into the overlying mass flow units. Elsewhere, the sharp contact between the massive sulphides and the finely laminated argillite is preserved, presumably in zones protected from mass flows.

Geochemical parameters measured in the HW basin argillite, indicate low O_2 bottom water conditions during deposition of the argillite. The lack of sulphate and oxides in the overlying sediments, and in the upper part of the orebody, suggest reducing conditions in the HW basin at the time of ore formation. No chimney and mound structures or chimney breccias were observed in the massive sulphides (pers. comm., M. Hannington, 2000), which may reflect the lack of sulphate (pers. comm., M. Solomon, 2001). Ba appears to reside in white micas (microprobe data, Appendix 5.2), with good positive correlations with Al, K, Rb and Zr, and a negative correlation with S.

Fluid inclusion data shows the similar nature of ore-bearing fluids in the HW orebody to the Battle orebody, with a similar range of homogenization temperatures and slightly lower

salinities (Figure 10.15). The sheet-like morphology of this orebody suggests that it may have also formed from type I to type II fluids (Sato, 1972), with a large component of lateral fluid flow. As the orebody formed at or very close to the seafloor, there was no impermeable cap to enhance lateral fluid flow. Instead, the initially buoyant hydrothermal fluids may have vented into the water column and after mixing with cold dense seawater, sunk back onto the seafloor, possibly forming a brine pool or sinking back down into the porous seafloor sediments (e.g., McDougall, 1984; Solomon et al., *in press;* Sangster, *in press*). The rising hydrothermal fluids may also have mixed with seawater within the porous seafloor sediments, with only minor venting, and lateral fluid flow dominating. Footwall alteration is relatively minor beneath the orebody, but a well-developed stockwork zone occurs in an 80-100m wide zone beneath the southern edge of the orebody, close to a large growth structure. The stockwork zone consists of numerous steep quartz veins and moderate to strong chlorite-sericite-quartz alteration of the footwall andesite.

There is evidence for late hydrothermal fluid flow through the argillaceous caprocks. However, this was more limited than the fluid flow above the Battle orebody, with silicification and bleached argillite forming in a few localised zones, close to growth structures. These altered caprock zones most likely represent the final stages of the hydrothermal system and may have acted as feeder zones for the smaller upper mineralised lenses. Other evidence for minor hydrothermal fluid flow through the overlying argillite is the infilling of primary voids (e.g., radiolarian tests) with pyrite.

Finely laminated jasper clasts are also common in the mass flow units immediately above the orebody and overlying argillite layers. A similar origin to the Battle basin jasper clasts, is suggested, due to the reduced nature of the HW basin.

10.6 Comparison with other VHMS deposits

Silica caps are a common feature of many VHMS deposits such as Hellyer (Sharpe, 1991; Gemmell and Large, 1992), Rosebery (Huston, 1988), Scuddles (Barley, 1992) and Kuroko deposits (Kalogeropoulous and Scott, 1983; Tsutsumi and Ohmoto, 1983). However, they are usually associated with barite and iron. In comparison, the Battle chert has a very low Fe content and little or no sulphate, instead Ba resides in white micas.

Hydrothermal fluids associated with the Battle and HW deposits have similar and higher salinities (and densities) than other VHMS deposits. The higher densities, the sheet-like morphology of the Battle and HW orebodies, and the fact that they formed on the seafloor, suggests type I to II fluid behaviour (Sato, 1972), with lateral flow dominant over buoyant hydrothermal pluming. Although the Battle cherts have much lower Fe and barite contents

than the Kuroko tetsusukei, they may have formed in a similar manner, with formation by lateral fluid flow through highly porous seafloor muds. The major difference between the Kuroko tetsusukei and the Battle chert, is the lack of Fe and barite in the Battle chert, reflecting formation under strongly reducing conditions. Fe^{2+} is transported away from the vent zone, with Fe^{3+} deposition above the anoxic-oxic boundary at the edge of the Battle basin, rather than close to the vents, e.g., Kuroko tetsusukei (Kalogeropoulous and Scott, 1983).

Chapter 11
Conclusions

11.1 Conclusions

The following conclusions were made from the caprock study at Myra Falls:

1) Paleoseafloor reconstructions indicate that the Battle and HW orebodies formed in small basins along a NW-trending ridge. Argillite deposits above the orebodies coincide with paleo-topographic lows and represent depocentres. The thick argillite deposits in the South Flank and Thelwood Valley areas represent much larger depocentres and coincide with an area of progressively deepening paleoseafloor, away from the NW-trending ridge.

2) Paleoseafloor reconstructions and recognition of major growth faults was possible after the removal of the effects of multiple deformation. Five separate deformation events were recognised:

   Early extension and formation of growth faults;
   D_1 folding and variable development of E-W oriented foliation;
   D_2 localised shear zones;
   D_{3a} and D_{3b} compression resulting in steep strike-slip faults and shallow N-S dipping thrust faults;
   D_4 extension with abundant steep planar normal faults; and
   D_5 compression resulting in large gouge-rich, shallow N-S dipping thrusts and steep NE-oriented strike-slip faults.

3) The 'caprocks' form a distinct fine-grained horizon across the property and the horizon commonly occurs immediately above, or within 1-2m above the ore horizons, and close to the contact with the Price Andesite in areas distal to ore. Chert (siliceous caprock) is best developed above the Battle deposit, but is also present in the Ridge and Extension ore zones. Only minor chert occurs above the HW deposit, instead, the orebody is overlain by a thick sequence of argillite.

4) Siliceous caprocks above the Battle deposit are replacement cherts (after mudstone), rather than true 'exhalative' deposits or biogenic cherts. The Battle basin argillites and Battle chert share similar sedimentological and petrological features, such as abundant parallel laminations, interbedded turbidites, radiolarian-rich layers, soft-sediment deformation, scours, flame structures and small phosphatic concretions.

5) Immobile elements indicate a similar provenance for the argillite and chert, which is significantly different from the Price Andesite, rhyolitic volcaniclastics and the quartz-feldspar porphyry bodies.

6) Trace element geochemistry and the spatial association of the Battle cherts with the underlying Battle orebody indicate that the chert represents hydrothermal alteration of seafloor muds.

7) The timing of silicification was early in the depositional/diagenetic history of the fine-grained sediments, indicated by the incorporation of chert into the overlying mass flow units. Silicification postdated deposition of the fine sediments and occurred during ore formation. Mass gains in SiO_2 of up to 200% in the chert, is also consistent with silicification on or very close to the seafloor at hydrostatic pressure. Ubiquitous bedding-parallel micro-stylolites indicate that silicification occurred prior to compaction.

8) The gradational change from white chert above the Battle orebody; to black chert, 80-100m south of the orebody; and to argillite in the Battle basin, reflects the lateral flow of hydrothermal fluids through the seafloor muds. Lateral fluid flow is also indicated by the lateral metal zonation in the Battle chert, reflecting precipitation from a cooling hydrothermal fluid. A higher temperature Cu-Zn-Cd zone is present in the white chert, and a lower temperature Pb-Ag-Sb zone is observed in the black chert at the edge of the siliceous alteration.

9) At the time of ore formation and caprock deposition, bottom water conditions in the Battle basin were moderately anoxic to euxinic. These conditions are indicated by paleoenvironmental parameters including DOP values (average = 0.98), Fe-sulphur-carbon relations, low Fe and Mn values, and high V/Cr, V/Ni and V/(Ni+V) ratios. Barite and haematite, which are common in VHMS caprocks, are absent in the Battle cherts, most likely reflecting the low O_2 bottom water conditions.

10) Sulphur isotope values in Battle basin argillite, 300-320m from the Battle orebody, are very light, ranging from –35.2 to –10.3 ‰; whereas $\delta^{34}S$ values for sulphides in black chert (100m from the orebody) range from –18.4 to –5.3 ‰. The black chert $\delta^{34}S$

values are intermediate between the unaltered argillite and Battle orebody values (−1.1 to +4.1 ‰). The light sulphur isotope values in the argillite most likely reflect bacterial reduction of seawater sulphate; whereas, the heavier sulphur isotopes of the Battle orebody reflect magmatic sulphur and/or inorganic reduction of seawater sulphate. The distinct shift from light $\delta^{34}S$ values in the unaltered argillite, to heavier $\delta^{34}S$ values in the black chert reflect input of hydrothermal sulphur ($\delta^{34}S$ = −1.1 to +4 ‰) into the seafloor sediments during hydrothermal alteration, and provide further evidence for a replacement origin for the Battle chert.

11) Fluid inclusions in spherical megaquartz patches in the siliceous caprocks above the Battle orebody indicate that hydrothermal fluids had temperatures between 135 to 250°C and salinities ranging from 3 to 12.1 eq. wt % NaCl. This is similar to inclusion fluids measured in quartz interstitial to sulphides in the underlying Battle orebody with homogenisation temperatures ranging from 140 to 250°C and salinities from 3 to 12.4 eq. wt % NaCl. Therefore the temperature and salinity of the hydrothermal fluids which formed the siliceous caprocks was very similar to the ore-forming fluids.

12) Inclusions in quartz within the HW orebody also showed a similar range of homogenisation temperatures, ranging from 145 to 210°C, but with slightly lower salinities, ranging from 2.5 to 9.0 eq. wt % NaCl. Inclusions in late stage metamorphic quartz, are distinguished from the hydrothermal fluids, by their low salinities, generally less than 3 eq. wt % NaCl.

13) Homogenisation temperatures and salinities indicated by the fluid inclusions in the siliceous caprocks and the Battle and HW orebodies, suggest fluid densities ranging from 0.88 to 1.05 g/cm^3. This is very close to, or above the density of ambient seawater at 2°C at 2000m depth (1.03 g/cm^3).

14) The wide range of densities indicated by fluid inclusions, suggests that the hydrothermal fluids displayed a range of behaviour types, from buoyant plumes to type II lateral fluid flow. However, the sheet-like morphology of the Battle orebody, replacement textures, and lateral metal zonation in the massive sulphides and overlying siliceous caprocks, suggest that diffuse lateral fluid flow through the sediments dominated over buoyant venting. Most hydrothermal fluids at Myra Falls can be described as 'intermediate brines' (from Sangster, *in press*). These fluids are initially less dense than seawater, but upon mixing, experience buoyancy reversal, and sink back onto the seafloor to form a dense brine pool, or percolate back into the porous seafloor sediments. Mixing between the rising hydrothermal fluids and seawater also occurred within the sediments, and may have enhanced lateral flow over buoyant plumes.

15) The HW orebody also formed within an anoxic basin, similar to the Battle orebody, with average DOP values = 0.92, low Fe and Mn values and high V/Cr, V/Ni ratios. However, the timing of ore formation, relative to the deposition of the fine-grained caprock horizon differs markedly to the Battle deposit. Massive sulphides were deposited in the coarse-grained rhyolitic detritus in the shallow subseafloor, and directly on the seafloor, prior to deposition of the fine caprock horizon. The top surface of the HW orebody is eroded in places, and ore clasts are commonly entrained into the overlying mass flow units. Elsewhere, the sharp contact between the massive sulphides and the finely laminated argillite is preserved, presumably in zones protected from mass flows. Hangingwall alteration is restricted to small zones consisting of bleached and silicified argillite, most likely representing the final stages of hydrothermal activity. The alteration halo over the HW deposit is patchy and more localised than alteration above the Battle deposit, reflecting the more limited alteration above the HW deposit.

16) The Battle basin argillites are enriched in Zn, Pb, Cu, As, Ag, V, and Cd, and the HW basin argillites are enriched in Cu, Zn and Ba, and these elements have been assigned a hydrothermal origin. Argillites from the South Flank show no metal enrichment, reflecting a lack of hydrothermal activity in this area.

17) SWIR spectral mapping, based on AlOH and FeOH wavelength variation in white mica and chlorite, indicates two distinct zones of hydrothermal alteration in the HW Horizon above the Battle and HW deposits. The altered hangingwall zones are indicated by AlOH values <2197nm, and FeOH values <2243nm. The alteration halo over the Battle mine is much better developed than the one over the HW mine, reflecting the relative timing of ore formation and deposition of hangingwall rocks.

18) A genetic model for the formation of the Battle orebody and overlying caprocks is described in five stages, listed below:

Stage 1: Basin development

A basin began to form by normal movement on growth structures located at the northern edge of the basin. The onset of rhyolitic volcanism resulted in early basin infill of coarse-grained rhyolitic volcaniclastic rocks. A period of tectonic and/or volcanic quiescence began, with the deposition of several metres of finely laminated muds, silts, and minor interbedded turbidites. Within the deep basin, restricted from open-ocean circulation, a stratified water column began to develop with low to fluctuating O_2 bottom water conditions.

Stage 2: Onset of hydrothermal activity

During deposition of the seafloor muds, hot hydrothermal fluids began to percolate through the sediments, via diffuse lateral flow, from a vent at the northern edge of the basin. At the time of ore formation the coarse-grained rhyolitic detritus was overlain by 1-3m of fine-grained muds. The hydrothermal fluids percolated upwards, depositing rutile, apatite and minor sulphides in primary pore spaces in the overlying fine-grained pelagic sediments. Some venting onto the seafloor also occurred, resulting in the development of fine sulphide-rich mud layers. In places, these sulphide-rich muds were entrained into overlying sandstone turbidite layers. Buoyant plumes are also indicated by the metal-rich signature of the Battle basin argillites, up to 300-350m away from the source vents.

The lower flow velocity combined with relatively high salinities (3 to 12.4 eq. wt % NaCl) and moderate temperatures (150-250°C) may have enhanced lateral fluid flow rather than buoyant venting, producing the sheet-like morphology of the Battle orebody. The lateral flow of hydrothermal fluids during ore formation resulted in only weak footwall alteration away from the main vent zone.

Stage 3: Formation of siliceous caprocks

Subsequent low to moderate temperature, saline silica-bearing fluids flowed laterally through the unconsolidated seafloor muds to form the Battle chert. Silicification occurred close to the paleo-seafloor, early in the diagenetic history, as chert rip-up clasts are incorporated into the overlying mass flow units. Silicification overprinted early hydrothermal mineral textures in the fine-grained caprocks and it is likely that the silica-bearing fluids had a similar origin to the ore fluids. The low metal contents of the chert, reflect relatively low fluid temperatures (<200° C) and prior deposition of sulphides in the underlying coarse-grained rhyolitic volcaniclastic layer.

The gradual transition from chert to argillite, their similar immobile element signatures, and lateral metal zoning in the chert indicate that silicification took place by lateral fluid flow through the fine seafloor muds. Plugging of the porous seafloor sediments by precipitation of silica, changed the hydrothermal flow regime from diffuse to more focussed flow, leading to enhanced lateral flow of subsequent ore-bearing fluids beneath the silica cap. Massive sulphides crosscut the basal contact of the chert in places.

Stage 4: Sedimentation of Battle basin

Formation of the siliceous caprocks on the seafloor was followed by renewal of tectonism and volcanism, with the rapid deposition of rhyolitic mass flow units, interlayered with rhyolitic sandstones and volcaniclastics. Finely bedded jasper clasts are common in the overlying mass flow units and most likely originated from Fe-Si deposits forming on the margins of Battle basin, above the anoxic-oxic boundary. The end of rhyolitic volcanism is marked by the intrusion of a massive quartz-feldspar porphyry body at the top of the rhyolitic volcanic sequence.

Stage 5: Late-stage hydrothermal activity

Ore deposition continued throughout the deposition of the HW Horizon rhyolitic volcaniclastics and intrusion of the quartz-feldspar porphyry. The more focussed fluid flow resulting from the formation of the silica cap above the Battle orebody, lead to the development of the Gap lens at the northern edge of the basin. The barite-rich Gap lens formed during the last stage of ore formation, from the upflow of a more focussed hydrothermal fluid along the main growth structure at the northern edge of the basin. Upper ore lenses, beneath the massive quartz-feldspar porphyry, formed by diffuse fluid flow through the coarse-grained rhyolitic sediments and ponding beneath the less permeable massive quartz-feldspar porphyry. The continued flow of hydrothermal fluids resulted in a distinct alteration halo in the HW Horizon above the Battle orebody. This alteration halo is shown by white mica and chlorite compositions, and is easily mapped using SWIR spectral characteristics.

Barite is common in the upper lenses and most likely indicates 1) changing bottom water conditions in the Battle basin, with the development of a more oxygenated environment during deposition of the upper zone sulphides; and/or 2) a change in fO_2 of the hydrothermal fluids, as suggested by Sinclair (2000).

11.2 Implications for exploration at Myra Falls

Facies mapping of the HW Horizon, reconstruction of the paleoseafloor, and recognition of major growth structures in the Myra Falls area, will increase the general understanding of this VHMS district. Knowledge of the main growth fault trends, and the structural and depositional setting of the VHMS orebodies at Myra Falls, will aid in the location of prospective drilling sites. For example, basins with significant argillite deposits along the NW-trending ridge, are clearly the most prospective zones for future exploration. The anoxic nature of bottom water conditions in these basins would enhance the preservation

potential of sulphide deposits. Other areas are less prospective, such as the area of elevated topography to the north, which has no significant depocentres in the HW Horizon, or to the south, where the topography progressively deepens away from the NW-trending ridge.

The argillite deposits are useful for locating depocentres, but can also provide a record of hydrothermal activity in a basin. The higher metal contents in argillites of the Battle and HW basins compared with argillite from the South Flank indicate their proximity to hydrothermal activity. Metals such as Zn, Pb, Cu, Sb, As, Ag, V, and Cd were found to be useful indicators. Argillites in other areas of the Myra Falls property could also be analysed for trace elements to test for a possible hydrothermal input. For example, in the Marshall Zone, argillite was found in drillhole L10-2023 (4950mN, 350mE), at the base of the HW Horizon, close to a reconstructed paleoseafloor low. The argillite may indicate a depocentre to the west, and the trace element geochemistry of the mudstone could be used to identify possible hydrothermal activity in this area.

An understanding of the deformation history and the different fault styles at Myra Falls is also useful for mine-scale and property-scale exploration and mining. Although the fault maps presented in this study are not applicable for mine-scale work, the separation and description of individual fault styles and kinematics, should aid in the mapping of underground fault movements and the interpretation of drillhole sections.

SWIR analysis is an effective exploration tool for mapping alteration halos associated with VHMS orebodies in the Myra Falls district. The systematic trends in mineral compositions, identified by SWIR analysis, can be used as mine-scale vectors to ore. At Myra Falls, compositional variation in white mica and chlorite can be mapped in felsic and mafic lithologies, in the hangingwall and footwall. The most prospective area highlighted by the SWIR mapping, would be the Price-Thelwood area, which lies on the NW trend of the Battle and HW orebodies and has many low AlOH wavelength zones in the HW Horizon.

11.3 Future work

The success of SWIR mapping of alteration halos above VHMS deposits at Myra Falls, suggests that a follow-up study looking at footwall alteration would be a useful exercise. White mica and chlorite compositional variation in the Price Andesite could be used to identify hydrothermally altered zones. One of the main disadvantages of mapping alteration in hangingwall rocks (HW Horizon), was that the size and intensity of the alteration halo was dependent on the timing of ore formation in relation to deposition of the hangingwall sediments. An alteration study of the footwall andesite would avoid this problem.

Further study on the trace element geochemistry and carbon-sulphur-iron contents of the argillites at Myra Falls would also be useful. The argillites provide a record of basin conditions and in future studies, the variation in trace element geochemistry with stratigraphic height, could also be examined. For example, in the South Flank area, argillite samples were selected close to the base of the HW Horizon, in a similar stratigraphic position to argillite samples in the Battle and HW basins. However, a more detailed study of the entire argillite sequence in the South Flank area would be useful to determine how the bottom water conditions varied over time. A similar chemostratigraphic study of the thick HW basin argillite sequence could also be undertaken for comparison with the South Flank area.

References

Adachi, M., Yamamoto, K., and Sugisaki, R., 1986. Hydrothermal chert and associated siliceous rocks from the Northern Pacific. Their geological significance as indication of ocean ridge activity. Sedimentary Geology, V.47, p125-148.

Alt, J.C., Lonsdale, P., Haymon, R. and Muehlenbachs, K., 1987. Hydrothermal sulfide and oxide deposits on seamounts near 21°N, East Pacific Rise. Geological Society of America Bulletin, Vol. 98, p157-168.

Baker, D.R. and Claypool, G.E., 1970. Effects of incipient metamorphism on organic matter in mudrock. American Association of Petroleum Geologists Bulletin, Vol. 54, p456-468.

Baker, E.T. and Lupton, J.E., 1990. Changes in submarine hydrothermal 3He/ heat ratios as an indicator of magmatic/tectonic activity. Nature, Vol. 346, p556-558.

Barley, M.E., 1992. A review of Archean volcanic-hosted massive sulfide and sulfate mineralization in Western Australia. Economic Geology, Vol. 87, p855-872.

Barnes, H.L., 1979. Solubilities of ore minerals. *In* Barnes H.L. (ed) Geochemistry of hydrothermal ore deposits, 2nd edition, Wiley-Interscience, New York, p404-460.

Barrett, T.J., MacLean, W.H., Cattalani, S., Hoy, L. and Riverin, G., 1991. Massive sulfide deposits of the Noranda area, Quebec. III. The Ansil Mine. Canadian Journal of Earth Sciences, Vol. 28, p1699-1730.

Barrett, T.J., and Sherlock, R.L., 1996. Volcanic stratigraphy, lithogeochemistry, and seafloor setting of the H-W massive sulfide deposit, Myra Falls, Vancouver Island, British Columbia. Exploration and Mining Geology, Vol. 5, p421-458.

Baskov, E.A., 1987. The fundamentals of paleohydrogeology of ore deposits. Springer and Verlag, 253p.

Beier, J.A. and Hayes, J.M., 1989. Geochemical and isotopic evidence for paleoredox conditions during deposition of the Devonian-Mississipian New Albany Shale, southern Indiana. Geological Society of America Bulletin, Vol. 101, p774-782.

Bell, J.L.S. and Palmer, D.A., 1994. Experimental studies of organic acid decomposition. *In* E.D. Pittman and M.D. Lewan (eds.), The Role of Organic Acids in Geological Processes, Springer-Verlag, New York, Chapter 9, p226-269.

Bendel, V., Fouquet, Y., Auzende, J.M., Lagabrielle, Y., Grimaud, D. and Urabe, T., 1993. The White Lady hydrothermal field, North Fiji back-arc basin, Southwest Pacific. Economic Geology, Vol. 88, No. 8, p 2237-2249.

Benvenuto, G., 1986. Structural study of the H-W orebody. Internal Westmin Company Report, 10p.

Berner, R.A., 1970. Sedimentary pyrite formation. American Journal of Science, Vol. 268, p1-23.

Berry, R., 1995. Report on activities, June 1995. Structure of the Westmin Mine at Myra Falls. Internal company report, 11p.

Berry, R., 1996. Report on activities, August 1996 – Structure of the Myra Falls Operation. Internal Westmin Company Report, 9p.

Berry, R., 1998. Structural geology of the Myra Falls Operation. Centre for Ore Deposit Research, University of Tasmania. Internal company report, 15p.

Berry, R., 2000. Structural geology of the Myra Falls Operation. Centre for Ore Deposit Research, University of Tasmania. Internal company report, 18p.

Binns, R.A., Parr, J.M., Scott, S.D., Gemmell, J.B., and Herzig, P.M., 1995. Pacmanus. An active seafloor hydrothermal field on siliceous volcanic rocks in the eastern Manus Basin, Papua New Guinea. Proceedings of the 1995 PACRIM Congress, Exploring the Rim, AUSIMM, p49-54.

Binns, R.A., Scott, S.D., Bogdanov, Y.A., Lisitzin, A.P., Gordeev, V.V., Gurvich, E.G., Finlayson, E.J., Boyd, T., Dotter L.E., Wheller, G.E., and Muravyev, K.G., 1993. Hydrothermal oxide and gold-rich sulfate deposts of Franklin Seamount, western Woodlark Basin, Papua New Guinea, Economic Geology, Vol. 88, p2122-2153.

Birolleua, A., Charlou, J.L., and Bougault, H., 1988. Hydrothermal tracers. As and As/Fe in sediments. Chemical Geology, Vol. 70, p132.

Bischoff, J.L. and Rosenbauer, R.J., 1987. Phase separation in seafloor geothermal systems. An experimental study of the effects on metal transport. American Journal of Science, Vol. 287, p953-978.

Bostrom, K., 1973a. The origin and fate of ferromanganoan active ridge sediments. Stockholm Contributions to Geology, Vol. 27, p147-243.

Bostrom, K., 1973b. Submarine volcanism as a source for iron. Earth and Planetary Science Letters, Vol. 9, p348-354.

Bramlette, M.N., 1946. The Monterey Formation of California and the origin of its siliceous rocks. United States Geological Survey, Professional Paper, 212, 55p.

Brandon, M.T., 1985. Mesozoic melange of the Pacific Rim Complex, western Vancouver Island. Geological Society of America, Cordilleran Section Meeting, Vancouver B.C., Guidebook, 28p.

Brandon, M.T., Orchard, M.J., Parrish, R.R., Sutherland Brown, A. and Yorath, C.J., 1986. Fossil ages and iotopic dates from the Paleozoic Sicker Group and associated intrusive rocks, Vancouver Island, British Columbia. *In* Current Research, Part A, Geological Survey of Canada, Paper 86-1A, p683-696.

Breit, G.N. and Wanty, R.B., 1991. Vanadium accumulation in carbonaceous rocks. A review of geochemical controls during deposition and diagenesis. Chemical Geology, Vol. 91, p83-97.

Brown, P.E., 1989. FLINCOR. A microcomputer program for the reduction and investigation of fluid inclusion data. America Mineralogy, Vol. 74, p1390-1393.

Browne, P.R.L. and Ellis, A.J., 1970. The Ohaki-Broadlands hydrothermal area, New Zealand: mineralogy and related geochemistry. American Journal of Science, Vol. 269, p97-131.

Browne, P.R.L., 1978. Hydrothermal alteration in active geothermal fields. Annual Review Earth Planet Science Letters, Vol. 6, p229-250.

Brumsack, H.J., 1980. Geochemistry of Cretaceous black shales from the Atlantic Ocean (DSDP legs 11, 14, 36, and 41). Chemical Geology, Vol. 31, p1-25.

Bryndzia, L.T., Scott, S.D., and Farr, J.E., 1983. Mineralogy, geochemistry, and mineral chemistry of siliceous ore and related footwall rocks in the Uwamuki 2 and 4 deposits, Kosaka Mine, Hokuroku District, Japan. *In* H. Ohmoto and B.J. Skinner (eds.). The Kuroko and Related Volcanogenic Massive Sulphide Deposits. Economic Geology Monograph 5, p507-522.

Buchanan, L.J., 1981. Precious metal deposits associated with volcanic environments in the southwest. Geological Society of Arizona Digest, Vol. 14, p237-262.

Calvert, S.E., Bustin, R. and Ingall, E., 1996. Influence of water column anoxia and sediment supply on the burial and preservation of organic carbon in marine shales. Geochimica et Cosmochimica Acta, Vol. 60, p1577-1593.

Campbell, A.C., Palmer, M.R. and Klinkhammer, G.P., 1988. Chemistry of hot springs on the Mid-Atlantic Ridge. Nature, Vol. 335, p514-519.

Campbell, A.C., German, C.R., Palmer, M.R. and Edmond, J.M., 1994. Geochemistry of hydrothermal fluids from the Escanaba Trough, Gorda Ridge. U.S. Geological Survey Bulletin, 2202, p201-221.

Canfield, D.E., Raiswell, R., Westrich, J.T., Reaves, C.M., and Berner, R.A., 1986. The use of chromium reduction in the analysis of reduced inorganic sulfur in sediments and shales. Chemical Geology, Vol. 54, p149-155.

Carlisle, D., and Susuki, T., 1974. Emergent basalt and submergent carbonate-clastic sequences including the Upper Triassic Delleri and Welleri zones on Vancouver Island. Canadian Journal of Earth Sciences, Vol. 11, p254-279.

Cathelineau, M., 1988. Cation site occupancy in chlorites and illites as a function of termperature. Clay Minerals, Vol. 23, p471-485.

Cathelineau, M., and Izquierdo, G., 1988. Temperature-composition relationships of authigenic micaceous minerals in the Los Azufres geothermal system. Contributions to Mineral Petrology, Vol. 100, p418-428.

Cathles, L.M., 1986. Discussion. Review of modern stratiform analogues *In* R.J.W. Turner and M.T. Einaudi (eds) The Genesis of Stratiform Sediment-Hosted Lead and Zinc deposits. Conference Proceedings. Stanford University Publications, Geological Sciences, Vol. 20, p213-218.

Cathles, L.M., 1993. A capless 350°C flow zone model to explain megaplumes, salinity variations, and high temperature veins in ridge axis hydrothermal systems. Economic Geology, Vol. 88, p1977-1988.

Cathles, L.M., 1997. Thermal aspects of ore formation. *In* Barnes H.L. (ed) Geochemistry of hydrothermal ore deposits, Third Edition, p191-227.

Caulfield, J.G.D., LeHuray, A.P., Dixon, P.R. and Rye, D.M., 1986. Lead and sulfur isotope studies of Zn-Pb-Ba deposits in Central Ireland and their constraints on models ofr the genesis of the Irish stratabound and stratiform ores. *In* R.J.W. Turner and M.T. Einaudi (eds) The Genesis of Stratiform Sediment-Hosted Lead and Zinc deposits. Conference Proceedings. Stanford University Publications, Geological Sciences, Vol. 20, p73-82.

Clague, J.J., 1991. Quaternary glaciation and sedimentation. Chapter 12 in Geology of the Cordilleran Orogen in Canada, Gabrielse, H. and Yorath, C.J., (eds). Geological Survey of Canada, Geology of Canada, no. 4, p419-434.

Clapp, C.H., 1912. Southern Vancouver Island. Geological Survey of Canada, Memoir 13, 208p.

Clark, R.N., Vance, S., and Green, R.O., 1998. Mineral mapping with imaging spectroscopy. the Ray Mine, AZ. In Proceedings of the 7th Annual JPL Earth Sensing Workshop.

Claypool, G.E., Holser, W.T., Kaplan, I.R., Sakai, H. and Zak, I., 1980. The age curves of sulfur and oxygen isotopes in marine sulfate and their mutual interpretation. Chemical Geology, Vol. 28, p199-260.

Collins, P.L.F., 1979. Gas hydrates in CO_2-bearing fluid inclusions and the use of freezing data for estimation of salinity. Economic Geology, Vol. 74, p1435-1444.

Cooke, D.R., Bull, S.W., Large, R.R. and McGoldrick, J.M., 2000. The importance of oxidised brines for the formation of Australian Proterozoic stratiform sediment-hosted Pb-Zn (Sedex) deposits. Economic Geology, Vol. 95, p1-18.

Cooke, D.R. and Simmons, S.F., 2000. Characteristics and genesis of epithermal gold deposits. Chapter 6, SEG Reviews, Vol. 13, p221-244.

Cresswell, S.D., 1997. A study of the Upper Zone mineralization of the H-Zone of Westmin Resources Ltd., Myra Falls Operations, Vancouver Island, British Columbia, Canada. Unpublished M.Sc. thesis, University of Exeter, 112p.

Davidson, G.J., 1992. Hydrothermal geochemistry and ore genesis of sea-floor volcanogenic copper-bearing oxide ores. Economic Geology, Vol. 87, p889-912.

Davis, D.W., Lowenstein, T.K., and Spencer, R.J., 1990. The melting behaviour of fluid inclusions in laboratory-grown halite crystals in the systems NaCl-H2O, NaCl-KCl-H2O, NaCl-MgCl2-H2O and NaCl-CaCl2-H2O. Geochimica et Cosmochimica Acta, Vol. 54, p591-601.

Dawson, K.M., Panteleyev, A., Sutherland Brown, A., and Woodsworth, G.J., 1991. Regional metallogeny, Chapter 19. *In* Geology of the Cordilleran Orogen in Canada, Gabrielse, H. and Yorath, C.J., (eds). Geological Survey of Canada, Geology of Canada, no. 4, p707-768.

Deer, W.A., Howie, R.A., Zussman, J., 1996. An introduction to the rock-forming minerals, second edition. Addison Wesley Longman Ltd., 696p.

De Baar, H.J.W., Bacon, M.P., and Brewer, P.G., 1985. Rare earth elements in the Pacific and Atlantic oceans. Geochimica et Cosmochimica Acta, Vol. 49, p1943-1959.

De Baar, H.J.W., German, C.R., Elderfield, H. and Van Gaans, P., 1988. Rare earth element distributions in anoxic waters of the Cariaco Trench. Geochimica et Cosmochimica Acta, Vol. 52, p1203-1219.

Dishaw, G., 1998. Price Orebody. Unpublished Honours Thesis.

Drever, J.I., 1974. Geochemical model for the origin of Precambrian banded iron formations. Geological Society of America Bulletin, Vol. 85, p1099-1106.

Duhig, N.C., Stolz, J., Davidson, G.J. and Large, R.R., 1992. Cambrian microbial and silica gel textures in silica iron exhalites from the Mount Windsor Volcanic Belt, Australia. Their petrography, chemistry and origin. Economic Geology, Vol. 87, p764-784.

Einsele, G., 2000. Sedimentary Basins, Evolution, Facies, and Sediment Budget, 2nd Edition, Springer, p94-107.

England, T.D.J., and Calon, T.J., 1991. The Cowichan fold and thrust systme, Vancouver Island, southwestern British Columbia. Geological Society of America Bulletin, Vol. 103, p336-362.

Ernst, W.G., 1963. Significance of phengitic micas from low-grade schists. Americal Mineralogist, Vol. 48, p1357-1373.

Etchecopar, A., Vasseur, G., and Daignieres, M., 1981. An inverse problem in microtectonics for the determination of stress tensors from fault striation analysis. Journal of Structural Geology, Vol.3, No.1, p51-65.

Eugster H.P., and Yoder, H.S., 1955. The join muscovite – paragonite. Yb. Carnegie Institution Washington, 54, p124-126.

Finlow-Bates, T. and Stumpfl, E.F., 1981. The behaviour of so-called immobile elements in hydrothermally altered rocks associated with volcanogenic submarine-exhalative ore deposits. Mineralium Deposita, Vol. 16, p319-328.

Fleming, B.A. and Crerar, D.A., 1982. Silicic acid ionization and calculation of silica solubility at elevated temperature and pH. Geothermics, Vol. 11, p15-29.

Flinn, D., 1965. On the symmetry principle and the deformation ellipsoid. Geological Magazine, Vol.102, p32-45.

Floyd, P.A. and Winchester, J.A., 1978. Identification and discrimination of altered and metamorphosed volcanic rocks using immobile elements. Chemical Geology, Vol. 21, p291-306.

Foley, N.K., 1986. Fluid inclusion study of ores from the Fukazawa mine, Hokuroko District, Akita Prefecture, Japan. Mining Geology, Vol. 36, p11-20.

Folk, R.L., 1950. Petrology of authigenic silica in the Beekmantown group of central Pennsylvania. M.S. Thesis, Pennsylvanian State College, P.A., 114p.

Folk, R.L., and McBride, E.F., 1978. Radiolarites and their relation to subjacent "oceanic crust" in Liguria, Italy. Journal of Sedimentary Petrology, Vol. 48, p1069-1102.

Folk, R.L., and Weaver, C.E., 1952. A study of the texture and composition of chert. American Journal of Science, Vol. 250, p498-510.

Force, E.R. and Cannon, W.F., 1988. Depositional model for shallow manganese deposits around black shale basins. Economic Geology, Vol. 83, p93-117.

Fouquet, Y., Von Stackelberg, U., Charlou, J.L., Erzinger, J., Herzig, P.M., Muhe, R. And Wiedicke, M., 1993. Metallogenesis in back-arc environments. The Lau Basin example. Economic Geology, Vol. 88, p2154-2181.

Fournier, R.O., 1983. A method of calculating quartz solubilities in aqueous sodium chloride solutions. Geochimica et Cosmochimica Acta, Vol. 47, p579-586.

Fournier, R.O., 1985. The behaviour of silica in hydrothermal systems. In Berger, B.R. and Bethke, P.M. (eds), Geology and Geochemistry of Epithermal Systems. Reviews in Economic Geology, Vol. 2, p45-61.

Gabrielse, H., 1991. Structural styles. Chapter 17. *In* Geology of the Cordilleran Orogen in Canada, Gabrielse, H. and Yorath, C.J., (eds). Geological Survey of Canada, Geology of Canada, no. 4, p571-675.

Gabrielse, H., and Yorath, C.J., 1991. Tectonic synthesis, Chapter 18. *In* Geology of the Cordilleran Orogen in Canada, Gabrielse, H. and Yorath, C.J., (eds). Geological Survey of Canada, Geology of Canada, no. 4, p677-705.

Galley, A.G., Watkinson, D.H., Jonasson, I.R., and Riverin, G., 1995. The subsea-floor formation of volcanic-hosted massive sulfide. evidence from the Ansil Deposit, Rouyn-Noranda, Canada. Economic Geology, Vol. 90, p2006-2017.

Gamble, J.A., Wright, I.C., Woodhead, J.D., and McCulloch, M.T., 1995. Arc and back-arc geochemistry in the southern Kermadec arc – Ngatoro Basin and offshore Taupo Volcanic Zone, SW Pacific. *In* Volcanism Associated with Extension at Consuming Plate Margins. Smellie, J.L. (ed.), Geological Society of London, Special Publication 81, p193-212.

Gamo, T., Okamura, K., Charlou, J.L., Urabe, T., Auzende, J.M., Ishibashi, J., Shitashima, K., Chiba, H., ManusFlux Shipboard Scientific Party, 1997. Acidic and sulfate-rich hydrothermal fluids from the Manus back-arc basin, Papua New Guinea. Geology, Vol. 25, p139-142.

Garrels, R.M., 1987. A model for the deposition of the micro-banded Precambrian iron formations. American Journal of Science, Vol. 287, p81-106.

Gemmell, J.B., 1998. District-scale metal zoning, Myra Falls VHMS Deposits, B.C., Canada. Internal Boliden-Westmin Company Report, 31p.

Gemmell, J.B.G. and Large, R.R., 1992. Geological and geochemical evolution of the footwall alteration pipe to the Hellyer deposits. Special Issue on Australian VHMS Deposits, Economic Geology, Vol. 87, p620-649.

Gemmell, J.G.B. and Large, R.R., 1992. Stringer system and alteration zones underlying the Hellyer volcanogenic massive sulfide deposit, Tasmania. Economic Geology, Vol. 87, p620-649.

Gemmell, J.B.G. and Large, R.R., 1993. Evolution of a VHMS hydrothermal system, Hellyer Deposit, Tasmania, Australia. Sulfur isotope evidence. Resource Geology Special Issue 17, p108-119.

Giordano, T.H. and Barnes, H.L., 1981. Lead transport in Mississippi Valley-type ore solutions. Economic Geology and the Bulletin of the Society of Economic Geologists, Vol. 76, No. 8, p2200-2211.

Giordano, T.H. and Kharaka, Y.K., 1994. Organic ligand distribution and speciation in sedimentary basin brines, diagenetic fluids and related ore solutions. *In* J. Parnell (ed.), Geofluids: Origin, Migration and Evolution of Fluids in Sedimentary Basins, Geological Society Special Publication, Vol. 78, p75-202.

Glover, J.K., 1990. Structural study. H-W Deposit. Internal Westmin Company Report, 13p.

Godwin, C.I., Robinson, M. and Juras, S.J., 1996. Galena lead isotopes, Buttle Lake mining camp, Vancouver Island, British Columbia, Canada. Economic Geology, Vol. 91, p549-562.

Goodfellow, W.D. and Jonasson, I.R., 1984. Ocean stagnation and ventilation defined by delta S secular trends in pyrite and barite, Selwyn Basin, Yukon. Geology, Vol. 12, p583-586.

Gordey, S.P., Geldsetzer, H.H.J., Morrow, D.W., Bamber, E.W., Henderson, C.M., Richards, B.C., McGugan, A., Gibson, D.W., and Poulton, T.P., 1991. Upper Devonian to Middle Jurassic assemblages, Chapter 8. *In* Geology of the Cordilleran Orogen in Canada, Gabrielse, H. and Yorath, C.J., (eds). Geological Survey of Canada, Geology of Canada, no. 4, p219-327.

Graf, J.L., Jr., 1977. Rare earth elements as hydrothermal tracers during the formation of massive sulfide deposits in volcanic rocks. Economic Geology, Vol. 72, p527-548.

Grant, J.A., 1986. The isocon diagram – a simple solution to Gresens' equation for metasomatic alteration. Economic Geology, Vol. 81, 1976-1982.

Greenwood, H.J., Woodsworth, G.J., Read, P.B., Ghent, E.D., and Evenchick, C.A., 1991. Metamorphism. Chapter 16 *in* Geology of the Cordilleran Orogen in Canada, Gabrielse, H. and Yorath, C.J., (eds). Geological Survey of Canada, Geology of Canada, no. 4, p533-570.

Gresens, R.L., 1967. Composition-volume relationships of metasomatism. Chemical Geology, Vol. 2, p47-65.

Gromet, L.P., Dymek, R.F., Haskin, L.A. and Korotev, R.L., 1984. The "North American Shale Composite". Its compilation, major and trace element characteristics. Geochimica et Cosmochimica Acta, Vol. 48, p2469-2482.

Groves, D.I. and Loftus-Hills, G., 1968. Cadmium in Tasmanian sphalerites. Proceedings of the Australian Institute of Mining and Metallurgy, Vol. 228, p43-51.

Guidotti, C.V., Sassi, F.P., and Blencoe, J.G., 1994. The effects of ferromagnesian components on the paragonite-muscovite solvus. a semiquantitative analysis based on chemical data for natural paragonite-muscovite pairs. Journal of Metamorphic Geology, Vol. 12, p779-788.

Gulson, B.L. and Porritt, P.H., 1987. Base metal exploration of the Mount Read Volcanics, western Tasmania. Part II, Lead isotope signatures and genetic implications. Economic Geology, Vol. 82, p291-307.

Gunning, H.C., 1931. Buttle Lake Map Area, Vancouver Island, B.C. *In* Geological Survey of Canada, Summary Report, 1930, Part A, p56A-78A.

Gunning, H.C., 1932. Preliminary report on the Nimpkish Quadrangle, Vancouver Island, British Columbia; Geological Survey of Canada, Summary Report, 1931, Part A, p22-35.

Haas, Jr., J.L., 1971. The effect of salinity on the maximum thermal gradient of a hydrothermal system at hydrostatic pressure. Economic Geology, Vol. 66, p940-946.

Halbach, P, and Pracejus, B., 1993. Geology and mineralogy of massive sulfide ores from the Central Okinawa Trough, Japan. Economic Geology, Vol. 88, No. 8, p2210-2225.

Hannington, M.D., and Scott, S.D., 1988. Mineralogy and geochemistry of a hydrothermal silica-sulfide-sulfate spire in the caldera of Axial Seamount, Juan de Fuca Ridge. Canadian Mineralogist, Vol. 26, p603-627.

Hannington, M.D., Bleeker, W. and Kjarsgaard, I., 1999. Sulfide mineralogy, geochemistry, and ore genesis of the Kidd Creek deposit. Part I. North, Central, and South orebodies. Economic Geology, Monograph 10, p163-224.

Hannington, M.D., Galley, A.G., Herzig, P.M., and Petersen, S., 1998. Comparison of the tag mound and stockwork complex with Cyprus-type massive sulphide deposits. Proceedings of the Ocean Drilling Program, Scientific Results, Vol. 158, p 389-415.

Hanor, J.S., 1994. Origin of saline fluids in sedimentary basins. Geological Society of London Special Publication 78, p151-174.

Hanor, J.S., 1998. Geochemistry and origin of metal-rich brines in sedimentary basin. Hobart, Tasmania, University of Tasmania, Centre for Ore Deposit Research Special Publication 2, p129-146.

Hatch, J.R. and Leventhal, J.S., 1992. Relationship between inferred redox potential of the depositional environment and geochemistry of the Upper Pennsylvanian (Missourian) Stark Shale Member of the Dennis Limestone, Wabaunsee County, Kansas, U.S.A. Chemical Geology, Vol. 99, p65-82.

Hedenquist, J.W., and Henley, R.W., 1985. The importance of CO2 on freezing point measurements. evidence from active geothermal systems and implication for epithermal ore deposition. Economic Geology, Vol. 80, p1379-1406.

Heggie, D.T., Skyring, G.W., O'Brien, G.W., Reimers, C., Herczeg, A., Moriarty, D.J.W., Burnett, W.C. and Milnes, A.R., 1990. Organic carbon cycling and modern phosphorite formation on the East Australian continental margin. an overview. *In* Notholt, A.J. and Jarvis, I. (eds), Phosphorite Research and Development, Geological Society Special Publication, No. 52, p87-117.

Hemley, J.J. and Hunt, J.P., 1992. Hydrothermal ore-forming processes in light of studies in rock buffered systems. II. Some general geologic applications. Economic Geology, Vol. 87, p23-43.

Henley, R.W. and Thornley, P., 1979. Some geothermal aspects of polymetallic massive sulphide formation. Economic Geology, Vol. 74, p1600-1612.

Herrmann, W., 1998. Use of immobile elements and chemostratigraphy t determine precursor volcanics. Centre for Ore Deposit Research, University of Tasmania, Internal Publication.

Herrmann, W., Blake, M., Doyle, M., Huston, D., Kamprad, J., Merry, N. and Pontual, S., 2001. Short-wavelength infra red spectral analysis of hydrothermal alteration zones associated with base metal sulfide deposits at Roseberry and Western Tharsis, Tasmania, and Highway-Reward, Queensland. Economic Geology (*in press*).

Herzig, P.M. and Hannington, M.D., 2000. Input from the deep. Hot vents and cold seeps. *In* Schulz, H.D. and Zabel, M. (eds), Marine Geochemistry. Chapter 13, p398-416.

Herzig, P.M., Becker, K.P., Stoffers, P., Backer, H., and Blum, N., 1988. Hydrothermal silica chimney fields in the Galapagos spreading centre. Earth and Planetary Science Letters, Vol. 89, p261-272.

Herzig, P.M., Hannington, M.D. and Arribas, A. (jr.), 1998. Sulfur isotopic composition of hydrothermal precipitates from the Lau back-arc. implications for magmatic contributions to seafloor hydrothermal systems. Mineralium Deposita, Vol. 33, p226-237.

Herzig, P.M., Hannington, M.D., Fouquet, Y., von Stackelberg, U., and Petersen, S., 1993. Gold-rich polymetallic sulfides from the Lau Back Arc and implications for the geochemistry of gold in sea-floor hydrothermal systems of the Southwest Pacific. Economic Geology, Vol. 88, p2182-2209.

Hesse, R., 1990a. Origin of chert. Diagenesis of biogenic siliceous sediments. *In* McIlreath, I.A., Morrow, D.W., (eds), Diagenesis. Geological Association of Canada, Geoscience Canada Reprint Series 4, p227-252.

Hesse, R., 1990b. Origin of chert. Diagenesis of inorganic and replacement cherts. *In* McIlreath, I.A., Morrow, D.W., (eds), Diagenesis. Geological Association of Canada, Geoscience Canada Reprint Series 4, p253-275.

Hinman, N.W., 1998. Sequences of silica phase transitions effects of Na, Mg, K, Al and Fe ions. Marine Geology, Vol. 147, p13-24.

Hoffman, D.L., Algeo, T.J., Maynard, J.B., Joachimski, M.M., Hower, J.C. and Jaminski, J., 1998. Regional and stratigraphic variation in bottomwater anoxia in offshore core shales of Upper Pennsylvanian cyclothems from the Eastern Midcontinent Shelf (Kansas), U.S.A. *In* J. Schieber, W. Zimmerle, and P. Sethi (eds), Shales and Mudstones II, Petrography, Petrophysics, Geochemistry, and Economic Geology, p243-269.

Hofmann, B.A. and Bernasconi, S.M., 1998. Review of occurrences and carbon isotope geochemistry of oxalate minerals: implications for the origin and fate of oxalate in diagenetic and hydrothermal fluids. Chemical Geology, Vol. 149, p127-146.

Hogdahl, O.T., Melson, S. and Bowen, V., 1968. Neutron activation analysis of lanthanides elements in seawater. Advances in Chemistry Series, Vol. 73, p308-325.

Holland, H.D., 1979. Metals in black shales. a reassessment. Economic Geology, Vol. 74, p1676-1680.

Holser, W.T. and Kaplan, I.R., 1966. Isotope geochemistry of sedimentary sulfates. Chemical Geology, Vol. 1, No. 2, p93-135.

Homberg, C., Lacombe, O., Angelier, J., and Bergerat, F., 1999. New constraints for indentation mechanisms in arcuate belts from the Jura Mountains, France. Geology, Vol. 27, p827-830.

Huston, D.L. and Large, R.R., 1987. Genetic and exploration significance of the Zinc Ratio (100 Zn/(Zn+Pb)) in massive sulfide systems. Economic Geology, Vol. 82, p1521-1539.

Huston, D.L., 1988. Aspects of the geology of massive sulfide deposits form the Balcooma district, northern Queensland and Rosebery, Tasmania. Implications for ore genesis. Unpublished PhD thesis, University of Tasmania.

Huston, D.L., 1988. The distribution, mineralogy and geochemistry of gold and silver in the north end orebody, Rosebery mine, Tasmania. Economic Geology, Vol. 83, p1181-1192.

Huston, D.L., 1993. The effect of alteration and metamorphism on wall rocks to the Balcooma and Driy River South volcanic hosted massive sulfide deposits, Queensland, Australia. Journal of Geochemical Exploration, Vol. 48, p277-307.

Huston, D.L., 1999. Stable isotopes and their significance for understanding the genesis of volcanic-hosted massive sulfide deposits. A review. *In* Barrie, C.T. and Hannington, M.D., (eds), Volcanic-associated massive sulfide deposits processes and examples in modern and ancient settings. Chapter 7, p157-179.

Huston, D.L., Kamprad, J., and Brauhart, C., 1999. Definition of high-temperature alteration zones with PIMA. an example from the Panorama VHMS district, central Pilbara Craton. AGSO Research Newsletter, No. 30, p10-12.

Huyck, H.L.O., 1990. When is a metalliferous black shale not a black shale? *In* Grauch, R and Leventhal, J. (eds) USGS Circular 1058. p42-56.

Hyndman, R.D., Yorath, C.J., Clowes, R.M., and Davis, E.E., 1990. The northern Cascadia subduction zone at Vancouver Island. seismic structure and tectonic history. Canadian Journal of Earth Sciences, Vol. 27, p313-329.

Irving, E., and Wynne, P.J., 1991. Paleomagnetism. review and tectonic implications, Chapter 3. *In* Geology of the Cordilleran Orogen in Canada, Gabrielse, H. and Yorath, C.J., (eds). Geological Survey of Canada, Geology of Canada, no. 4, p61-86.

Irving, E., and Yole, R.W., 1987. Tectonic rotations and translations in Western Canada; new evidence from Jurassic rocks of Vancouver Island. Geophysical Journal of the Royal Astronomical Society, Vol. 91, p1025-1048.

Ishibashi, J. and Urabe, T., 1995. Hydrothermal activity related to arc-backarc magmatism in the western Pacific. *In* Taylor, B. (ed) Tectonics and Magmatism, New York, Plenum press, p451-495.

Ishizuka, H., Kawanobe, Y. and Sakai, H., 1990. Petrology and geochemistry of volcanic rocks dredged from the Okinawa trough, an active back-arc basin. Geochemical Journal, Vol. 24, p75-92.

Janecky, D.R. and Seyfired, W.E., Jr., 1984. Formation of massive sulfide deposits on oceanic ridge crests. Incremental reaction models for mixing between hydrothermal solutions and seawater. Geochimica et Cosmochimica Acta, Vol. 48, p2723-2738.

Jeffery, W.G., 1967. Buttle Lake. British Columbia Ministry of Energy. Mines and Petroleum Resources, Geological Branch, Open File Report, June 21-67.

Jeffery, W.G., 1970. Buttle Lake. British Columbia Ministry of Energy, Mines and Petroleum Resources Miscellaneous Open File Report, map with notes.

Jones, B. and Desrochers, A., 1992. Shallow platform carbonates. In Walker, R.G. and James, N.P. (eds), Facies Models, Response to Sea Level Change, GEO Text 1, Geological Association of Canada, p277-302.

Jones, D.L., Silberling, N.J., and Hillhouse, J., 1977. Wrangellia – A displaced terrane in northwestern North America. Canadian Journal of Earth Science, Vol. 14, p2565-2577.

Jones, S.A. and Berry, R., 2001. Recognition of early growth structures after multiple deformation episodes at Myra Falls VHMS camp, Vancouver Island, B.C., Canada. Abstract in Geological Society of Australia, Specialist Group in Tectonics and Structural Geology, 2001. A structural Odessey, p101-102.

Jorgensen, B.B., Isaksen, M.F. and Jannasch, H.W., 1992. Bacterial sulfate reduction above 100 degrees C in deep-sea hydrothermal vent sediments. Science, Vol. 258, No. 5089, p1756-1757.

Journeay, J.M. and Csontos, L., 1989. Preliminary Report on the structural setting along the Southeast Flank of the Coast Belt, British Columbia. *In* Current Research, Part E, Geological Survey of Canada, Paper 89-1E, p177-187.

Juras, S.J.; 1987. Geology of the polymetallic volcanogenic Buttle Lake camp, with emphasis on the Price hillside, Central Vancouver Island, British Columbia, Canada. Unpublished PhD thesis, University of British Columbia, 278p.

Juras, S.J., and Pearson, C.A., 1990. Mineral deposits of the southern Canadian Cordillera. *In* Guidebook for Field Trip B2, Vancouver 90, Geological Association of Canada – Mineralogical Association of Canada, p1-21.

Kalogeropoulos, S.I. and Scott, S.D., 1983. Mineralogy and geochemistry of tuffaceous exhalites (tetsusekiei) of the Fukazawa Mine, Hokuroko District, Japan. Economic Geology, Monograph 5, p 412-432.

Kalogeropoulos, S.I. and Scott, S.D., 1989. Mineralogy and geochemistry of an Archean tuffaceous exhalite; the Main Contact Tuff, Millenbach Mine area, Noranda, Quebec. Canadian Journal of Earth Sciences, Vol. 26, p88-105.

Khin Zaw, and Large, R.R., 1992. The precious metal-rich South Hercules mineralisation, western Tasmania. A possible subsea-floor replacement volcanic-hosted massive sulphide deposit. Special Issue on Australian VHMS deposits. Economic Geology, Vol. 87, p931-952.

Khin Zaw, Gemmell, J.B., Large, R.R., Mernagh, T.P., and Ryan, C.G., 1996. Evolution and source of ore fluids in the stringer system, Hellyer VHMS deposit, Tasmania, Australia. evidence from fluid inclusion microthermometry and geochemisty. Ore Geology Reviews, Vol. 10, p251-278.

Knauth, L.P., 1994. Petrogenesis of chert. *In* Heaney, P.J., Prewitt, C.T., and Gibbs, G.V., (eds), Silica. Physical behaviour, geochemistry, and materials applications. Mineralogical Society of America, Reviews in Mineralogy, V. 29, p231-258.

Kneller, W.A., Kriege, H.F., Saxer, E.L., Wilband, J.T., and Rohrbacher, T.J., 1968. The properties and recognition of deleterious cherts which occur in aggregate used by Ohio Concrete Producers. Research Foundation, University of Toledo, Ohio, Report 1014, 201p.

Krauskopf, K.B., 1957. Separation of manganese from iron in sedimentary processes. Geochimica et Cosmochimica Acta, Vol. 12, p61-84.

Krom, M.D. and Berner, R.A., 1983. A rapid method for the determination of organic and carbonate carbon in geological samples. Journal of Sedimentary Petrology, Vol. 53, p660-663.

Krom, M.D. and Berner, R.A., 1983. A rapid method for the determination of organic and carbonate carbon in geological samples. Journal of Sedimentary Petrology, Vol. 53, p660-663.

Large, R.R., 1992. Australian volcanic-hosted massive sulfide deposits. features, styles, and genetic models. Economic Geology, Vol. 87, p471-510.

Leistel, J.M., Marcoux, E., Thieblemont, D., Quesada C., Sanchez, A., Alomdovar, G.R., Pascual, E., and Saez, R., 1998. The volcanic hosted massive sulfide deposits of the Iberian Pyrite Belt. Mineralium Deposita, Vol. 33, p2-30.

Leitch, C.H.B. and Lentz, D.R., 1994. The Gresens approach to mass balance constraints of alteration systems: methods, pitfalls, examples. *In* Lentz, D.R. (ed.) Alteration and Alteration Processes Associated with Ore-Forming Systems. Geological Association of Canada, Short Course Notes, Vol. 11, p161-192.

Lentz, D.R., 1996. Recent advances in lithogeochemical exploration for massive-sulphide deposits in volcano-sedimentary environments. Petrogenetic, chemostratigraphic, and alteration aspects with examples from the Bathurst Camp, New Brunswick. *In* Trends, Technologies, and Case Histories for the Modern Explorationist. Proceedings of a Short Course by Prospectors and Developers Association, Toronto, p145-217.

Lentz, D.R. and Goodfellow, W.D., 1993. Petrology and mass-balance constraints on the origin of quartz augen schist associated with the Brunswick massive sulfide deposits, Bathurst, New Brunswick. Canadian Mineralogist, Vol. 31, p877-903.

Lentz, D.R. and Goodfellow, W.D., 1996. Intense silicification of footwall sedimentary rocks in the stockwork alteration zone beneath the Brunswick No. 12 massive sulphide deposit, Bathurst, New Brunswick. Canadian Journal of Earth Science, Vol. 33, p284-302.

Leventhal, J. and Taylor, C., 1990. Comparison of methods to determine degree of pyritization. Geochimica Cosmochimica Acta, Vol. 54, p2621-2625.

Leventhal, J.S. and Hofstra, A., 1990. Characterization of carbon in sediment-hosted disseminated gold deposits, north central Nevada. In Hausen, D., et al. (eds), Gold, '90 Salt Lake City. – Society of Mineralogy and metal Exploration, Denver, p365-368.

Leventhal, J.S., 1983. An interpretation of carbon and sulfur relationships in Black Sea sedimentas as indicators of environments of deposition. Geochimica Cosmochimica Acta, Vol. 47, p133-137.

Leventhal, J.S., 1998. Metal-rich black shales. Formation, economic geology and environmental considerations. *In* J. Schieber, W. Zimmerle, and P. Sethi (eds), Shales and Mudstones II, Petrography, Petrophysics, Geochemistry, and Economic Geology, p255-282.

Lewan, M.D., 1984. Factors controlling the proportionality of vanadium to nickel; ratios in crude oils. Geochimica Cosmochimica Acta, Vol. 48, p2231-2238.

Liaghat, S., and MacLean, W.H., 1992. The Key Tuffite, Matagami mining district. Origin of the tuff components and mass changes. Exploration and Mining Geology, Vol. 1, p197-207.

Lonsdale, P., Batiza, R. and Simkin, T., 1982. Metallogenesis at seamounts on the East Pacific Rise. Marine Technology Society Journal, Vol. 16, p54-60.

Lowe, D.R., 1999. Petrology and sedimentology of cherts and related silicified sedimentary rocks in the Swaziland Supergroup. *In* Lowe, D.R., and Byerly, G.R., (eds) Geologic Evolution of the Barberton Greenstone Belt, South Africa. Boulder, Colorado, Geological Society of America Special Paper 329, p83-114.

Lueders, V., Pracejus, B. and Halbach, P., 2001. Fluid inclusion and sulfur isotope studies in probable modern analogue Kuroko-type ores from the Jade hydrothermal field (Central Okinawa Trough, Japan). Chemical Geology, Vol. 173, 1-3, p45-58.

Mackenzie, F.T., and Gees, R., 1971. Quartz. synthesis at earth-surface conditions. Science, Vol. 173, p533-535.

MacLean, W.H., 1988. Rare earth element mobility at constant inter-REE ratios in the alteration zone at the Phelps Dodge massive sulfide deposit, Matagami, Quebec. Mineralium Deposita, Vol. 23, p231-238.

MacLean, W.H. and Barrett, T.J., 1993. Lithogeochemical techniques using immobile elements. Journal of Geochemical Exploration, Vol. 48, p109-133.

MacLean, W.H., and Kranidiotis, P., 1987. Immobile elements as monitors of mass transfer in hydrothermal alteration. Phelps Dodge massive sulfide deposit, Matagami, Quebec. Economic Geology, Vol. 82, p951-962.

Marutani, M. and Takenouchi, S., 1978. Fluid inclusion study of stockwork siliceous orebodies of Kuroko deposits at the kosaka mine, Akita, Japan. Mining Geology, Vol. 28, p349-360.

Massey, N.W.D., 1992. Geology and mineral resources of the Duncan sheet, Vancouver Island, Geological Survey of Canada Report 92B/13, 57p.

Massey, N.W.D., and Friday, S.J., 1989. Geology of the Alberni-Nanaimo Lakes area, Vancouver Island (92C/ 1W, 92F/ 2E and part o f92F/ 7). *In* Geological Fieldwork 1988, B.C. Ministry of Energy, Mines and Petroleum Resources, Paper 1989-1, p61-74.

Masuda, A., and Ikeachi, Y., 1979. Lanthanide tretrad effect observed in marine environment. Geochemical Journal, Vol. 13, p19-22.

Mathias, G.K., Simmons, S.F. and Fleming, J., 1985. High sulfidation alteration at the Island Porphyry Copper deposit, Vancouver Island, Canada. *In* PACRIM 1995 abstract volume. Auckland, New Zealand: Australian Institute of Mining and Metallurgy.

Maynard, J.B., 1983. Geochemistry of sedimentary ore deposits, Springer-Verlag New York, 305p.

McCollom, T.M., Seewald, J.S. and Simoneit, B.R.T., 2001. Reactivity of monocyclic aromatic compounds under hydrothermal conditions. Geochimica et Cosmochimica Acta.65; 3, Pages 455-468

McDougall, T.J., 1984. Fluid dynamic implications for massive sulphide deposits of hot saline fluid flowing into a submarine depression from below. Deep-Sea Research, Vol 31, p145-170.

McKibben, M.A., 1993. Shrimp study of extreme bacteriogenic sulfur isotope enrichments in the Moat sediments of the Creede Caldera. Abstracts with Programs, Geological Society of America, Annual Meeting, p316.

McKinley, S.D., Pearson, C.A., Juras, S.J., 1997. Paleotopography and ore zonation of the Battle Zn-Cu-Au-Ag VMS deposit, Vancouver Island, British Columbia. In 50th Anniversary GAC/MAC Annual Meeting, Ottawa.

McLennan, S.M., 1989. Rare earth elements in sedimentary rocks: influence of provenance and sedimentary processes. In Reviews in Mineralogy. B.R. Lipin and G.A. McKay (eds), Mineralogical Society of America, Washington D.C., Vol. 21, p169-200.

McLeod, R.L., & Stanton, R.L., 1984. Phyllosilicates and associated minerals in some Paleozoic stratiform sulfide deposits of southeastern Australia, Economic Geology, Vol. 79, 1-21.

McMurtry, G.M., Sedwick, P.N., Fryer, P., VonderHaar, D.L. and Yeh, H.W., 1993. Unusual geochemistry of hydrothermal vents on submarine arc volcanoes. Kasuga Seamounts, Northern Mariana Arc. Earth and Planetary Science Letters, Vol.114, p517-528.

Merry, N.J., Pontual, S., 1998. The Spectral Geologist, Vol. 1.1, User Manual. Ausspec International Pty. Ltd., PO Box 2235, Kew, Victoria 3101, Australia.

Metz, S. and Trefry, J.H., 1988. Scavenging of V by iron oxides in hydrothermal plumes. EOS, Vol. 69, p1489.

Metz, S. and Trefry, J.H., 2000. Chemical and mineralogical influences on concentrations of trace metals in hydrothermal fluids. Geochimica et Cosmochimica Acta, Vol. 64, No. 13, p2267-2279.

Michard, A., Albarede, F., Michard, G., Minster, J.F. and Charlou, J.L., 1983. Rare earth elements and uranium in high temperature solutions from East Pacific Rise hydrothermal vent field (13°C). Nature, Vol. 303, p43-65.

Michard, A. and Albarede, F., 1986. The REE content of some hydrothermal fluids. Chemical Geology, Vol. 55, p51-60.

Miyashiro, A. and Shido, F., 1985. Tschermak substitution in low- and middle grade pelitic schists. Journal of Petrology, Vol. 26, p449-487.

Monger, J.W.H., Price, R.A., and Tempelman-Kluit, D.J., 1982. Tectonic accretion and the origin of the two major metamorphic and plutonic welts in the Canadian Cordillera. Geology, Vol. 10, p70-75.

Mookherjee, A., 1962. Certain aspects of the geochemistry of cadmium. Geochimica et Cosmochimica Acta, Vol. 26, p351-360.

Muller, J.E., 1980. The Paleozoic Sicker Group of Vancouver Island, British Columbia. Geological Survey of Canada, Paper 79-30, 22p.

Muller, J.E., Cameron, B.E.B., and Northcote, K.E., 1981. Geology and mineral deposits of Nootka sound map-area, Vancouver Island, British Columbia. Geological Survey of Canada, Paper 80-16, 53p.

Muller, J.E., Northcote, K.E., and Carlisle, D., 1974. Geology and mineral deposits of Alert-Cape Scott map-area, Vancouver Island, British Columbia. Geological Survey of Canada, Paper 74-8, 77p.

Nixon, G.T., Hammack, J.L., Koyanagi, V.M., Payie, G.J., Panteleyev, A., Massey, N.W.D., and Hamilton, J.V., 1994. Preliminary geology of the Quatsino-Port McNeill map areas, northern Vancouver Island (92L/12, 11). *In* Geological Fieldwork 1993, Paper 1994-1, Geological Survey of Canada, p63-85.

Nixon, G.T., Hammack, J.L., Payie, G.J., and Snyder, L.D., 1995. Quatsino-San Josef map area, northern Vancouver Island. Geological overview (92L/12W, 102I/8, 9). *In* Geological Fieldwork 1994, Paper 1995-1, Geological Survey of Canada, p9-21.

Norrish, K. and Chappel, B.W., 1977. X-ray flourescence spectrometry. *In*, Hawkesworth, C.J. and Norry M.J. (eds) Continental Basalts and Mantle Xenoliths, Shiva, Orpington, London, and Birkhauser Boston, p230-249.

Norrish, K. and Hutton, J.T., 1969. An accurate X-ray spectrographic method for the analysis of a wide range of geological samples. Geochemica et Cosmochimica Acta, Vol. 33, p431-453.

O'Brien, G.W., Milnes, A.R., Veeh, H.H., Heggie, D.T., Riggs, S.R., Cullen, D.J., Marshall, J.F., and Cook, P.J., 1990. Sedimentation dynamics and redox iron-cycling. controlling factors for the apatite-glauconite association on the East Australian continental margin. *In* Notholt, A.J. and Jarvis, I. (eds), Phosphorite Research and Development, Geological Society Special Publication, No. 52, p61-86.

Ohmoto, H. and Goldhaber, M.B., 1997. Sulfur and carbon isotopes. *In* Barnes, H.L. (ed), Geochemistry of hydrothermal ore deposits, Chapter 11, Third Edition, Wiley, New York, p517-611.

Ohmoto, H., and Rye, R.O., 1974. Hydrogen and oxygen isotopic compositions of fluid inclusions in the Kuroko deposits, Japan. Economic Geology, Vol. 69, p947-953.

Ohmoto, H. and Rye, R.O., 1979. Isotopes of sulfur and carbon. *In* Barnes, H.L. (ed), Geochemistry of hydrothermal ore deposits, Second Edition, Wiley, New York, p509-567.

Ohmoto, H., Kaiser, C.J. and Geer, K.A., 1990. Systematics of sulphur isotopes in recent marine sediments and ancient sediment-hosted basemetal deposits. *In* Herbert, H.K. and Ho, S.E. (eds), Stable Isotopes and Fluid Processes in Mineralization, Vol. 23, Perth, University of Western Australia Publication, p70-120.

Ohmoto, H., Mizukami, M., Drummond, S.E., Eldridge, C.S., Pisutha-Arnond, V. and Lenagh, T.C., 1983. Chemical processes of Kuroko formation. Economic Geology, Monograph 5, p570-604.

Pearce, T.H., 1963. The petrochemistry and petrology of the quartz-feldspar porphyry, Bathurst, New Brunswick. Unpublished M.Sc. Thesis, University of Western Ontario, London, Ontario.

Pearce, T.H. and Cann, J.R., 1973. Tectonic setting of basic volcanic rocks determined using trace element analysis. Earth and Planetary Science Letters, Vol. 19, p290-300.

Peter, J.M., Peltonen, P., Scott, S.D., Simoneit, B.R.T. and Kawka, O.E., 1991. Carbon-14 ages of hydrothermal petroleum and carbonate in Guaymas Basin, Gulf of California – implications for oil generation, expulsion and migration. Geology, Vol. 19, p253-256.

Peter, J.M., and Goodfellow, W.D., 1993. Bulk and stable sulphur and carbon isotope geochemistry of hydrothermal sediments associated with the Brunswick No. 12 deposit, northern New Brunswick. *In* S.A. Abbot (ed), Current Research, New Brunswick Department of Natural Resources and Energy, Mineral Resources, Information Circular 93-1, p154-169.

Peter, J.M. and Goodfellow, W.D., 1996. Genesis of massive sulphide-associated hydrothermal sediments along the Brunswick Belt, Bathurst Camp, New Brunswick. Canadian Journal of Earth Sciences, Vol. 33, p252-283.

Peter, J.M. and Goodfellow, W.D., 1996. Mineralogy, bulk and rare earth element geochemistry of massive sulphide-associated hydrothermal sediments of the Brunswick Horizon, Bathurst Mining Camp, New Brunswick. Canadian Journal of Earth Sciences, Vol. 33, p252-283.

Peter, J.M. and Scott, S.D., 1988. Mineralogy, composition, and fluid-inclusion microthermometry of seafloor hydrothermal deposits in the Southern trough of Guaymas Basin, Gulf of California. Canadian Mineralogist, Vol. 26, p567-587.

Petersen, S., Herzig, P.M. and Hannington, M.D., 2000. Third dimension of a presently forming VMS deposit. TAG hydrothermal mound, Mid-Atlantic Ridge, 26°N. Mineralium Deposita, Vol. 35, p233-259.

Petit, J.-P., 1987. Criteria for the sense of movement on fault surfaces in brittle rocks. Journal of Structural Geology, Vol. 9, p597-608.

Piper, D.Z., 1994. Seawater as the source of minor elements in black shales, phosphorites and other sedimentary rocks. Chemical Geology, Vol. 114, p95-114.

Pisutha-Arnond, V. and Ohmoto, H., 1983. Thermal history, and chemical and isotopic compositions of the ore-forming fluids responsible for the Kuroko massive sulphide deposits in the Hokuroku district of Japan. *In* H. Ohmoto and B.J. Skinner (eds.). The Kuroko and Related Volcanogenic Massive Sulphide Deposits. Economic Geology Monograph 5, p523-558.

Plimer, I.R. and de Carvalho, D., 1982. The geochemistry of hydrothermal alteration at the Salgadinho copper deposit, Portugal. Mineralium Deposita, Vol. 17, p193-211.

Pollock, S.G., 1987. Chert formation in an Ordovician volcanic arc. Journal of Sedimentary Petrology, Vol. 57, No. 1, p75-87.

Pontual, S., Merry, N., Gamson, P., 1997a. G-Mex Vol. 1, Spectral Interpretation Field Manual. Ausspec International Pty. Ltd.

Pontual, S., Merry, N., Gamson, P., 1997b. G-Mex Vol. 7, Volcanic-hosted massive sulphide systems. Ausspec International Pty. Ltd.

Post, J.L., and Noble, P.L., 1993. The near-infrared combination band frequencies of dioctohedral smectites, micas and illites. Clays and Clay Minerals, Vol. 41, No. 6, p639-644.

Potter, P.E., 1998. Shale-rich basins. Controls and origin. *In* Schieber, J., Zimmerle, W., and Sethi, P.S., (eds), Shales and mudstones I. Basin studies, sedimentology, and paleontology. Stuttgart, p21-32.

Price, L.C., Wenger, L.M., Ging, T. and Blount, C.W., 1983. Solubility of crude oil in methane as a function of pressure and temperature. Organic geochemistry, Vol. 4, p201-221.

Quinby-Hunt, M.S. and Wilde, P., 1994. Thermodynamic zonation in the black shale facies based on iron-manganese-vanadium content. Chemical Geology, Vol. 113, p297-317.

Raiswell, R. and Berner, R.A., 1985. Pyrite formation in euxinic and semi-euxinic sediments. American Journal of Science, Vol. 287, p33-49.

Raiswell, R. and Berner, R.A., 1987. Organic carbon losses during burial and thermal maturation of normal marine shales. Geology, Vol. 15, p853-856.

Raiswell, R., Buckley, F., Berner, R.A., and Anderson, T.F., 1988. Degree of pyritization of iron as a paleoenvironmental indicator of bottom-water oxygenation. Journal of Sedimentary Petrology, Vol. 58, p812-819.

Ramsay, J.G., 1967. Folding and fracturing of Rocks. McGraw-Hill Book Company, New York, 568p.

Reid, R.R., 1993. Westmin structure, 18 and 20 level data. Internal Westmin Company Report, 48p.

Reyes, A.G., 1990. Petrology of Philippine geothermal systems and the application of alteration mineralogy to their assessment. Journal of Volcanology and Geothermal Research, Vol. 43, p279-309.

Riddihough, R.R., and Hyndman, R.D., 1991. Modern plate tectonic regime of the continental margin of western Canada. Chapter 13, *in* Geology of the Cordilleran Orogen in Canada, Gabrielse, H. and Yorath, C.J., (eds), Geological Survey of Canada, Geology of Canada, no. 4, p435-455.

Rimstidt, J.D. and Barnes, H.L., 1980. The kinetics of silica-water reactions. Geochimica et Cosmochima Acta, Vol. 44, p1683-1699.

Rimstidt, J.D., 1997. Gangue mineral transport and deposition. *In* Barnes H.L. (ed) Geochemistry of hydrothermal ore deposits, Third Edition, p487-513.

Ripley, E., Shaffer, N. and Gilstrap, M., 1990. Distribution and geochemical characterization of the New Albany Shale, Indiana. Economic Geology, Vol. 85, p1790-1807.

Ripley, E.M., and Ohmoto, H., 1977. Mineralogic, sulphur isotope, and fluid inclusion studies of the stratabound copper deposits at the Raul Mine, Peru. Economic Geology, Vol. 72, p1017-1041.

Robertson, A.H.F. and Fleet, A.J., 1976. The origins of rare earths in metalliferous sediments of the Troodos Massif, Cyprus. Earth and Planetary Sciences, Vol. 28, p385-394.

Robinson, B.W. and Kusakabe, M., 1975. Quantitative preparation of sulphur dioxide, for $^{34}S/^{32}S$ analyses, from sulphides by combustion with cuprous oxide. Analytical Chemistry, Vol. 47, p1179-1181.

Robinson, M., 1992. Geology, mineralization and alteration of the Battle Zone, Buttle Lake camp, Central Vancouver Island, Southwestern British Columbia. Unpublished M.Sc. thesis, University of British Columbia, 268p.

Robinson, M., Godwin, C.I., Stanley, C.R., 1996. Geology, lithogeochemisty, and alteration of the Battle volcanogenic massive sulfide zone, Buttle Lake Mining Camp, Vancouver Island, British Columbia. Economic Geology, Vol. 91, p527-548.

Roedder, E. and Bodnar, R.J., 1980. Geologic pressure determinations from fluid inclusion studies. Annual Reviews of Earth and Planetary Sciences, Vol. 18, p263-301.

Roedder, E., 1968. The non-colloidal origin of 'colloform' textures in sphalerite ores. Economic Geology, Vol. 63, p451-471.

Roedder, E., 1984. Fluid inclusions. Reviews in Mineralogy, Vol. 12, Mineralogical Society of America, 646p.

Rollinson, H.R., 1993. Using geochemical data. evaluation, presentation, interpretation. Addison Wesley Longman Ltd, England, 352p.

Ruaya, J.R. and Seward, T.M., 1986. The stability of chlorozinc (II) complexes in hydrothermal solutions up to 350°C. Geochimica et Cosmochimica Acta, Vol. 50, p651-661.

Sakai, H., Gamo, T. and Kim, E.S., 1990. Venting of carbon dioxide-rich fluid and hydrate formation in mid-Okinawa Trough backarc basin. Science, Vol. 248, p1093-1096.

Sanders, N.D., 1986. Visual observation of the solubility of heavy hydrocarbons in near-critical water. Industrial Engineering and Chemical Fundamentals, Vol. 25, p169-171.

Sangster, D.F., 1968. Relative sulfur isotope abundance of ancient seas and stratabound sulphide deposits. Proceedings of the Geological Association of Canada, Vol. 19, p79-86.

Sangster, D.F., *in press*. The role of dense brines in the formation of vent-distal sedimentary-exhalative (SEDEX) lead-zinc deposits: Field and laboratory evidence. Mineralium Deposita.

Sato, T., 1972. Behaviours of ore-forming solutions in seawater. Mining Geology, Vol. 22, p31-42.

Schieber, J., 1996. Early diagenetic silica deposition in algal cysts and spores. A source of sand in black shales? Journal of Sedimentary Research, Vol. 66, No.1, p175-183.

Schieber, J., 1998. Sedimentary features indicating erosion, condensation, and hiatuses in the Chattanooga Shale of Central Tennessee. Relevance for sedimentary and stratigraphic evolution. *In* Schieber, J., Zimmerle, W., and Sethi, P.S., (eds), Shales and mudstones I. Basin studies, sedimentology, and paleontology. Stuttgart, p187-215.

Schultz, R.B., 1991. Metalliferous black shales. Accumulation of carbon and metals in cratonic basins. In Force, E.R., Eidel, J.J. and Maynard, J.B. (eds), Sedimentary and Diagenetic Mineral Deposits. A Basin Analysis Approach to Exploration. Reviews in Economic Geology, Vol. 5, p171-185.

Schultz, R.B. and Coveney, R. M. Jr., 1992. Time-dependent changes for Midcontinent Pennsylvanian black shales, U.S.A. Chemical Geology, Vol. 99, p83-100.

Schutter, S.R., 1998. Characteristics of shale deposition. . *In* Schieber, J., Zimmerle, W., and Sethi, P.S., (eds), Shales and mudstones I. Basin studies, sedimentology, and paleontology. Stuttgart, p79-108.

Scott, S.D., 1997. Submarine hydrothermal systems and deposits. *In* Barnes H.L. (ed) Geochemistry of hydrothermal ore deposits, Third Edition, p797-860.

Seccombe, P.K., Godwin, C.I., Krouse, H.R. and Juras, S.J., 1990. Sulphur and lead isotopic studies of the Buttle Lake Massive Sulphide deposit, Vancouver Island, B.C., Canada: Sources of ore constituents in a submarine exhalative environment. *In* Pacific Rim 90 congress. Gold Coast, Queensland, Australia: The Australian Institute of Mining and Metallurgy.

Seward, T.M. and Barnes, H.L., 1997. Metal transport by hydrothermal ore fluids. *In* Barnes, H.L. (ed.), Geochemistry of Hydrothermal Ore Deposits, 3rd Edition, p435-486.

Seward, T.M., 1976. The stability of chloride complexes of silver in hydrothermal solutions up to 350°C. Geochimica et Cosmochimica Acta, Vol. 40, p1329-1341.

Seward, T.M., 1989. The hydrothermal chemisty of gold and its implications for ore formation. Boiling and conduction cooling as examples. Economic Geology Monograph 6, p398-404.

Shanks, W.C. and Seyfried, W.E. Jr., 1987. Stable isotope studies of vent fluids and chimney minerals, southern Juan de Fuca Ridge; sodium metasomatism and seawater sulfate reduction. Journal of Geophysical Research, B, Solid Earth and Planets, Vol. 92, p11387-11399.

Sharpe, R., 1991. The distribution, mineralogy and paragenesis of the Hellyer baritic and siliceous caps. Unpublished Honours Thesis, University of Tasmania, 114p.

Sheppard, S.M.F., 1977. Identification of the origin of ore-forming solutions by the use of stable isotopes. Volcanic Processes in Ore Genesis. Geological Society, London, Special Publication, Vol. 7, p25-41.

Sherlock, R.L., Roth, T., Spooner, E.T.C. and Bray, C.J., 1999. Origin of the Eskay Creek Precious metal-rich volcanogenic massive sulfide deposit. fluid inclusion and stable isotope evidence. Economic Geology, Vol. 94, p803-824.

Simmons, S.F., and Christenson, B.W., 1994. Origins of calcite in a boiling geothermal system. American Journal of Science, Vol. 294, p361-400.

Simoneit, B.R.T., Kawka, O.E. and Brault, M., 1988. Origin of gases and condensates in the Guaymas Basin hydrothermal system. Chemical Geology, Vol. 71, p169-182.

Simoneit, B.R.T., 2000. Alteration and migration process of organic matter in hydrothermal systems and implications for metallogenesis. *In* M.Glikson and M. Mastalerz (eds.), Organic matter and mineralisation, Kluwer Academic Publishers, Great Britain, p13-37.

Simonson, B.M., 1985. Sedimentology of cherts in the Early Proterozoic Wishart Formation, Quebec-Newfoundland, Canada. Sedimentology, Vol. 32, p23-40.

Sinclair, B., 2000. Geology and genesis of the Battle Zone VHMS deposits, Myra Falls district, British Columbia, Canada. Unpublished PhD thesis, University of Tasmania, 321p.

Siskin, M. and Katritzky, A.R., 1991. Reactivity of organic compounds in hot water. Geochemical and technological implications. Science, Vol. 254, p231-237.

Skirrow, R.G. and Franklin, J.M., 1994. Silicification and metal leaching in semiconformable alteration beneath the Chisel Lake massive sulfide deposit, Snow Lake, Manitoba. Economic Geology, Vol. 89, p31-50.

Smith, R.N. and Huston, D.L., 1992. Distribution and association of selected trace elements at the Rosebery Deposit, Tasmania. Economic Geology, Vol. 87, p706-719.

Solomon, M. and Walshe, J.L., 1979. The formation of massive sulfide deposits on the sea floors. Economic Geology, Vol. 74, p797-813.

Solomon, M., 1976. "Volcanic" massive sulphide deposits and their host rocks – a review and explanation. *In* K.H. Wolf (ed.) Handbook of Stratabound and Stratiform Ore Deposits, II. Regional Studies and Specific Deposits, 6, p21-50.

Solomon, M., 1999. Discussion. Sulpur isotope composition of the Brunswick No. 12 massive sulphide deposit, Bathurst Mining Camp, New Brunswick. implications for ambient environment, sulphur source, and ore genesis. Canadian Journal of Earth Sciences, Vol. 36, p121-125.

Solomon, M., Eastoe, C.J. and Walshe, J.L., 1988. Mineral deposits and sulfur isotope abundances in the Mount Read Volcanics between Que River and Mount Darwin, Tasmania. Economic Geology, Vol. 83, p1307-1328.

Solomon, M., Gemmell, B.J. and Khin Zaw, *in press*. The nature and origin of the fluids responsible for forming the Hellyer volcanic-hosted massive sulfide deposit, Tasmania, as indicated by fluid inclusions, and stable and radiogenic isotopes of sulfides, sulfates, silicates and carbonates. Economic Geology.

Spooner, E.T.C. and Bray, C.J., 1977. Hydrothermal fluids of seawater salinity in ophiolitic sulfide ore deposits in Cyprus. Nature, Vol. 26, p808-812.

Spooner, E.T.C., 1981. Fluid inclusion studies of hydrothermal ore deposits. Mineralogical Association of Canada., Short Course Handbook 6, p232-240.

Spry, P.G. and Wonder, J.D., 1989. Manganese-rich rocks associated with the Broken Hill lead-zinc-silver deposit, New South Wales, Australia. Canadian Mineralogist, Vol. 27, p275-292.

Spry, P.G., Peter, J.M., Slack, J.F., 2000. Meta-exhalites as exploration guides to ore. *In* P. Spry, B., Marshall, and F.M., Vokes (eds), Metamorphosed and Metamorphogenic Ore Deposits. Reviews in Economic Geology Vol. 11, p163-201.

Stakes, D.S. and Vanko, D.A., 1986. Multistage hydrothermal alteration of gabbroic rocks from the failed Mathematician Ridge. Earth and Planetary Science Letters, Vol. 79, p75-92.

Stanton, R.L., 1990. Magmatic evolution and the ore type-lava type affiliations of volcanic exhalative ores. Australasion Institute of Mining and Metallogeny Monograph 15, p101-107.

Stuart, F.M., Harrop, P.J., Knott, R., Fallick, A.E., Turner, G., Fouquet, Y. and Richard, D., 1995. Noble gas isotopes in 25,000 years of hydrothermal fluids from 13°N on the East Pacific Rise. *In*, Pason, L.M., Walker, C.L. and Dixon, D.R. (eds), Hydrothermal Vents and Processes, Geological Society Special Publication, 87, p133-143.

Sugitani, K., Horiuchi, Y., Adachi, M., and Sugisaki, R., 1996. Anomalously low Al2O3/TiO2 values for Archean cherts from the Pilbara Block, Western Australia – possible evidence for extensive chemical weathering on the early earth. Precambrian Research, Vol. 80, p49-76.

Talbot, C.J., 1970. The minimum strain ellipsoid using deformed quartz veins. Tectonophysics, Vol.9, p47-76.

Taylor, S.R. and McLennan, S.M., 1985. The continental crust. its composition and evolution. Blackwell Scientific Publications, Boston, Massachusetts, 312p.

Taylor, S.R. and McLennan, S.M., 1988. The significance of the rare earths in geochemistry and cosmochemistry. In Gschneidner, K.A., Jr. and Eyring, L., (eds), Handbook on the physics and chemistry of rare earths, Vol. 11, New York, Elsevier, p485-578.

Thompson, A.J.B., Hauff, P.L., Robitaille, A.J., 1999. Alteration mapping in exploration. Application of short-wave infrared (SWIR) spectroscopy. Society of Economic Geologists Newsletter, No. 39, p15-27.

Toyoda, K. and Masuda, A., 1991. Chemical leaching of pelagic sediments: identification of the carrier of Ce anomaly. Geochemical Journal, Vol. 25, p95-119.

Tsutsumi, M. and Ohmoto, H., 1983. A preliminary oxygen isotope study of tetsusekiei ores associated with the Kuroko Deposits in the Hokuroko District, Japan. *In* Skinner, B.J. (ed.), The Kuroko and Related Volcanogenic Massive Sulfide Deposits, Economic Geology, Monograph 5, p433-438.

Turner, J.S. and Campbell, I.H., 1987. Temperature, density and buoyancy fluxes in "black smoker" plumes, and the criterion for buoyancy reversal. Earth and Planetary Science Letters, Vol. 73, p85-92.

Ueda, A. and Sakai, H., 1984. Sulfur isotope study of Quaternary volcanic rocks from the Japanese Islands arc. Geochimica et Cosmochimica Acta, Vol. 48, 1837-1848.

Vanko, D.A., 1988. Temperature, pressure and composition of hydrothermal fluids, with their bearing on the magnitude of tectonic uplift at mid-ocean ridges, inferred from fluid inclusions in oceanic layer 3 rocks. Journal of Geophysical Research, Vol. 93, p4595-4611.

Vanko, D.A., Griffith, J.D., and Erickson, C.L., 1992. Calcium-rich brines and other hydrothermal fluid inclusions from plutonic rocks, Oceanographer Transform, Mid-Atlantic Ridge. Geochimica Cosmochimica Acta, Vol. 56, p35-47.

Vanko, D.A., Milby, B.J., and Heinzquith, S.W., 1991. Massive sulphides with fluid-inclusion-bearing quartz from a young seamont on the East Pacific Rise. Canadian Mineralogy, Vol. 29, p453-460.

Velde, B., 1965. Phengite micas: synthesis, stability, and natural occurrence. American Journal of Science, Vol. 263, p886-913.

Vine, J.D., and Tourtelot, E.B., 1970. Geochemical investigation of some black shales and associated rocks. U.S. Geological Survey Bulletin, 1314-A. Contributions to Geochemistry, 43p.

Von Damm, K.L., 1990. Seafloor hydrothermal activity. black smoker chemistry and chimneys. Annual Review of Earth and Planetary Sciences, Vol. 18, p173-204.

Walker, R.R., 1985. Westmin Resources' massive sulphide deposits, Vancouver Island; trip 1. *In* Tempelman-Kluit, D., (ed.), Field guides to geology and mineral deposits in the southern Canadian cordillera, p1-13.

Weaver, F.M., and Wise, S.W., 1972. Ultramorphology of deep sea cristobalitic chert. Nature, Vol. 237, p56-57.

Wedepohl, K.H., 1970. Environmental influence of the chemical composition of shales and clays. *In* Ahrens, L.H., Press, F., Runcorn, S.K., and Urey, H.C. (eds), Physics and Chemistry of the Earth, Vol. 8, p305-333.

Wells, R.C. and Brannock, W.W., 1946. Composition of roscoelite. U.S. Geological Survey Bulletin, p121-127.

Wenger, L.M., and Baker, D.R., 1986. Variations in organic geochemistry of anoxic-oxic black shale-carbonate sequences in the Pennsylvanian of the Midcontinent, U.S.A. Organic Geochemistry, Vol. 10, p85-92.

White, D.E., 1986. Environments favorable for generating stratiform sediment-hosted Pb-Zn deposits. *In* R.J.W. Turner and M.T. Einaudi (eds) The Genesis of Stratiform Sediment-

Hosted Lead and Zinc deposits. Conference Proceedings. Stanford University Publications, Geological Sciences, Vol. 20, p177-179.

Whitehead, R.E.S., 1973. Environment of stratiform sulphide deposition; variation in Mn.Fe ratio in host rocks at Heath Steele Mine, New Brunswick, Canada. Mineralium Deposita, Vol. 8, p148-160.

Wilkinson, J.J., 2001. Fluid inclusions in hydrothermal ore deposits. Lithos, Vol. 55, p229-272.

Williams, L.A., Parks, G.A., and Crerar, D.A., 1985. Silica diagenesis, I. Solubility controls. Journal of Sedimentary Petrology, Vol. 55, No. 3, p301-311.

Wilson, P.N. and Petersen, E.U., 1989. Fluid inclusion evidence for fluid mixing in the Oxec Cyprus-type copper deposit, Guatemala. Economic Geology, Vol. 84, p44-49.

Yang, K., 1998. Compositional variations of white micas, a literature review. Exploration and Mining Report 469F, CSIRO Australia, 24p.

Yole, R.W., 1969. Upper Paleozoic stratigraphy of Vancouver Island, British Columbia. Proceedings of the Geological Association of Canada, Vol. 20, p30-40.

Yorath, C.J., 1991. Upper Jurassic to Paleogene assemblages. *In* Geology of the Cordilleran Orogen in Canada, Gabrielse, H. and Yorath, C.J., (eds), Geological Survey of Canada, Geology of Canada, no. 4, p329-371.

Yorath, C.J., and Nasmith, H.W., 1995. The geology of Southern Vancouver Island – a field guide. Orca Book Publishers.

Yorath, C.J., Sutherland Brown, A, and Massey, N.W.D., 1999. Lithoprobe, southern Vancouver Island, British Columbia. Geology. Geological Survey of Canada Bulletin 498, 145p.

Yoshida, T., 1979. Fluid inclusion study and ore forming process of the Iwami deposit, Shimane prefecture, Japan. Mining Gology (Japan), Vol. 29, p21-31.

Yu, Z., Robinson, P. and McGoldrick, P., 2001. An evaluation of methods for the chemical decomposition of geological materials for trace element determination using ICP-MS. The Journal of Geostandards and Geoanalysis, Geoanalysis 2000 Conference Volume. Vol. 25, No. 2.

Zierenberg, R.A., 1990. Deposition of metalliferous sediment beneath a brine pool in the Atlantis II Deep, Red Sea. *In* McMurray, G.R., (ed), Gorda Ridge. a seafloor spreading centre in the United States' exclusive economic zone, Springer-Verlag, New York, p131-142.

Appendix 1:
Drill logs and underground maps

This section gives a list of the drill holes logged and the metres logged in each drillhole (logging was concentrated on the HW Horizon). Examples of typical drill logs and underground maps are also given. The complete set of drill logs and underground maps are with the author and can be accessed by request.

APPENDIX 1

List of drillholes logged

(In the deeper exploration holes, only the HW horizon was logged)

HOLE #	Area	E	N	elevation	azimuth	dip	m logged
BG18 1032	Battle mine	1420	4240	3032	180	-86	0-123.5
BG18 1033	Battle mine	1420	4240	3032	0	-87	0-158.5
BG18-1256	Battle mine	1885	4210	3026	0	-24	0-152.4
BG18 1101	Battle mine	1870	4105	2990	180	-24	30-56
BG18 1126	Battle mine	1855	4222	3025	180	-40	55-97
BG18 1127	Battle mine	1855	4222	3025	180	-62	0-48
BG18 480	Battle mine	1600	4122	3030	0	-74	0-77.7
BG18 483	Battle mine	1600	4120	3030	180	-56	0-60
BG18 541	Battle mine	1561	4141	3040	214	-59	0-94.5
18-980	Battle mine	1420	4165	3044	179	-63	0-134.6
18-981	Battle mine	1420	4165	3044	179	-71	0-124.4
18-982	Battle mine	1420	4165	3044	179	-80	0-99.9
18-983	Battle mine	1420	4165	3044	0	-90	0-102.2
18-1000	Battle mine	1423	4167	3044	0	-86	0-103.6
18-1001	Battle mine	1423	4167	3044	0	-79	0-112.8
18-1002	Battle mine	1423	4168	3044	0	-72	0-113.8
18-1003	Battle mine	1423	4168	3044	0	-66	0-112.8
18-1004	Battle mine	1423	4168	3044	0	-61	0-118.9
18-976	Battle mine	1420	4164	3044	179	-40	0-153.3
18-1035	Battle mine	1420	4240	3032	0	-72	0-123
18-1034	Battle mine	1420	4240	3032	0	-80	0-126.5
L14 680	Battle south	1260	4393	3247	0	-74	298-382
L14-681	Battle south	1263	3842	3247	353	-67	314-408
L14-682	Battle south	1263	3842	3247	0	-59	300-396
L14-683	Battle south	1263	3842	3247	356	-48	308-428
L14-676	Battle south	1263	3842	3247	180	-78	219-276
L14-677	Battle south	1263	3842	3247	185	-62	207-232
L14-675	Battle south	1263	3842	3249	0	-90	220-291.5
L14-678	Battle south	1263	3842	3249	180	-43	185-240
L14-679	Battle south	1263	3842	3249	0	-83	235-331
BG18 1082	Extension	2530	3847	3077	178	16.5	0-114.3
BG18 1085	Extension	2530	3847	3077	182	6	0-79.2
BG18 1086	Extension	2530	3847	3077	182	-8	0-76.2
BG18 1087	Extension	2530	3847	3077	184	-19.5	0-70
BG18 1088	Extension	2530	3848	3077	183	-41	0-70.1
BG18 1089	Extension	2530	3849	3077	185	-62	0-70.1
BG18 1090	Extension	2530	3850	3077	173	-78	0-79.2
BG18 1091	Extension	2530	3850	3077	180	-90	0-91.4
W148	Extension	2365	3750	3520	360	-60	505-538

HOLE #	Area	E	N	elevation	azimuth	dip	m logged
HW23 488	HW mine	3568	3669	2835	45	30	0-60
HW23 489	HW mine	3563	3664	2837	225	45	0-38
HW23 493	HW mine	3565	3666	2837	0	-90	0-35
HW23 494	HW mine	3565	3666	2837	270	56	0-36
HW23 496	HW mine	3565	3660	2836	90	23	0-48.2
HW23 503	HW mine	3565	3666	2836	315	30	0-61
HW23 533	HW mine	3577	3640	2832	180	30	0-45.5
HW23-553	HW mine	3655	3660	2835	90	50	0-56.4
HW23-554	HW mine	3655	3660	2835	0	90	0-39.6
HW23-560	HW mine	3655	3660	2845	35	30	0-44
HW23-561	HW mine	3655	3660	2845	35	60	0-39.9
HW23-514	HW mine	3485	3815	2910	0	30	0-108.1
21-2072	HW mine	3416	3865	2930	52	-50	0-107.6
P13 309	HW mine	3932	3718	3292	180	-88	390-500
P13 315	HW mine	4085	3717	3293	180	-69	375-396
P13 320	HW mine	3932	3719	3292	360	-82	303-431
P13-310	HW mine	3796	3565	3292	180	-71	360-452
W132	HW mine	3635	3959	3396	0	-90	522-618
HW23-562	HW mine	3654	3658	2837	215	30	0-49.4
W113	HW mine	3010	3648	3356	0	-90	293-375
W117	HW mine	3191	3651	3356	0	-90	362-408
20-845	43 Block	4405	3975	2995	0	-81	0-111.25
20-675	43 Block	4390	3971	2995	0	-84	0-109.7
HW23-679	43 Block	4282	3920	2895	20	-50	0-61
HW23-684	43 Block	4282	3920	2895	20	0	0-100.6
HW23-683	43 Block	4282	3920	2895	20	-10	0-85.3
HW23-681	43 Block	4282	3920	2895	20	-30	0-68.6
HW23-680	43 Block	4282	3920	2895	20	-40	0-61
HW23-685	43 Block	4282	3920	2895	20	20	0-123.4
HW23-682	43 Block	4282	3920	2895	20	-20	0-91.5
PR111	Thelwood V.	5573	4366	3270	280	-86	314-510.5
PR13-68	Price Hillside	5244	3828	3291	180	-80	0-94.5
CR88-4	Thelwood V.	6696	2441	3368	195	-82	514-608
PR109	Thelwood V.	6455	4472	3277	0	-90	511-651
PR101	Thelwood V.	5575	4364	3271	0	-90	390-488
PR107	Thelwood V.	6069	4233	3271	160	-71.5	254-311
PR124	Thelwood V.	5876	3717	3286	102	-88	70-159
PR126	Thelwood V.	6924	3489	3283	235	-87.5	75-170
16-33	South Flank	2195	3176	3151	0	-90	0-221.3
W151	South Flank	2660	3108	3364	360	-65	370-397
W202	HW North	4540	4372	3723	228	-82.5	995-1061
W143	HW North	3979	4716	3360	0	-90	680-856
L10 2001	Ridge Zone	519	3910	3436	67	-50.5	570-655
L10 2011	Ridge Zone	363	4483	3430	40	-50	756-814
L14 633	Ridge Zone	182	4086	3250	43	-72	193-312
L15 431	Ridge Zone	823	4359	3203	180	-73	246-256
L15-501	Marshall Zone	1010	4492	3204	356	-52	344-557
L14-631	Ridge Zone	181	4084	3250	340	-62	242-362
L12-2023	Ridge Zone	-549	3921	3345	0	-45	275-315.2
L14-625	Sth Fk-Ridge	181.4	4081	3250	182	-58	225-306.9
L14-641	Sth Fk-Ridge	156.4	3338	3248	180	-75	705-852.8
L14-624	Sth Fk-Ridge	181.4	4079	3250	181	-33	343-458

DIAMOND DRILL LOG

project:
location:
coords: E N

DDH No. L14-675
page 1 of 3

AZ: Dip: Scale: 1:200
Logged by: Date:

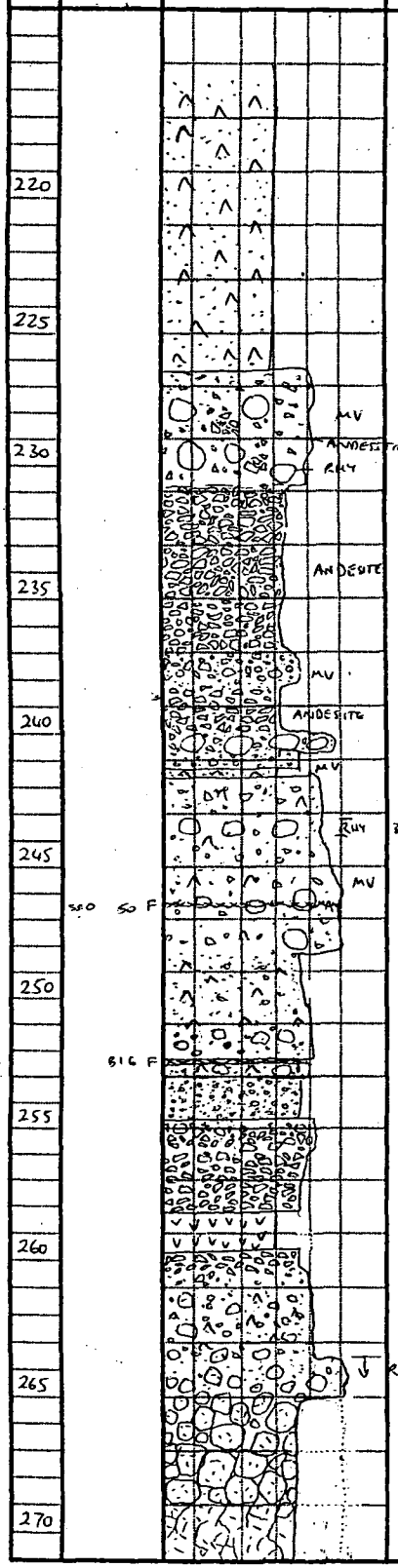

Description

220 → 226.5
med gn gy msv andesite w 1-2cm v uniform txt th.
bcon is sharp + 30 dca - pt fl

226.5 - 230.95
vcg mixed volc w mod 90°6
rhy upto 10°6 - large rounded cobbles
v poorly sorted w large ang and frag' in an andesitic matrix - w ple' the and frag' are tightly packed almost in a flow bx txt.
The bcon is sharp - sy shal (soft sed) at 40 dca (fl = 30 dca)

230.95 - 236.95
med gn ang and frag' tightly packed in a p gn matrix - good flow bx txt' scattered wn copper? within matrix
* sy sharp sy shal (soft sed) bcon at 55-60 dca
foliation still ~30 dca

236.95 - 237.9
p gy + gn, ang to cg mixed andesite + rhyolitic sst w alt f grn' th - scattered rhy clasts up to 1-2cm th.
the bcon is sy sharp inc change into andesite frag' (looks pepertic)

237.9 - 240.6
tightly packed d gn and frag' in a pale gn matrix often w f grn' - andesite looks msv in ple' but mostly clastic to jigsaw txt
240 at 240.5 - coarse rhy (qfp) clasts in this zone 2-4cm
bcon is sharp, 40 dca - sly oblique to fl at ~30 dca

240.6 - 241.2
p gy + gn mixed volc w 50-80% rhyolite + 20-40°6 and becomes more rhyolitic towards base.
The bcon is sharp and wavy 10-15 dca = steeper than flow at ~30 dca

241.2 - 241.7
mod to d gn ang andesitic sst, sy fl at 30 dca
sharp bcon 50-60 dca no rhyolite

241.7 - 248.1
mixed conglomerate w 20-30% rhy. 50-70% andesite clasts in an andesitic matrix
rhy clasts = subrounded to subangular (mostly subrnd) and = mostly in matrix but ang frag' do occur 1-2% the dk py th.
good bcon
243.2 - 243.6 - rhy contact inc to 30°6 below ~246cm to 3cm clasts calc
246.3 - 246.4 - gouge y faults ~50 dca ss planes.
246.4 - 247.1 steep fr' = common at base broken core steep fl 10-20 dca

248.1 - 252.4
mod to d gn andesitic sst - w gsz 1-3mm gradg + occ clasts up to 2cm - wnn rhyolitic clasts
below ~249m - start getting occ large rhy clasts + occ clasts scattered in the and matrix
round rhy clasts up to 5cm occ up to 12cm

DIAMOND DRILL LOG

project:
location:
coords: E N

DDH No. LI4-675
page 2 of 3

AZ: Dip: Scale: 1:200
Logged by: Date:

m | structure | Grain size (log scale, mm: 0.06 0.5 2 8 32 Max) | Samples

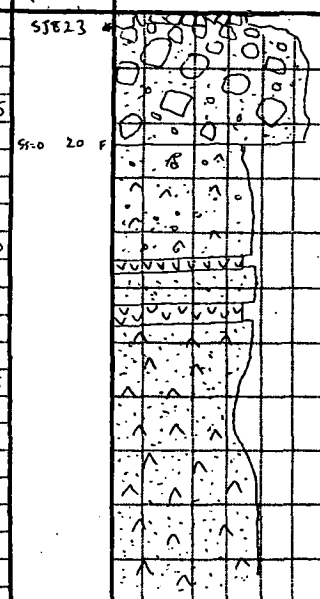

Description

252.4 - 252.5
large gouge zone + qz mg - possibly fairly flat-lying although all = gouge
mod unit is stable for ~ 20cm + fe-oxide stnd

2525 - 253
fe oxide stained med to cg andesitic sst w scattered rhy clasts - sly altd & wnd ser altd + stained.
gsz 2 - 10mm, poorly sorted.
bcon is sharp + ~25 dca sly steeper than fol

253 - 254.8
p to med gy, med to cg 2-5mm tightly packed.
p gy sil rhy frag - sly ser altd clast boundaries are indistinct
sharp irr bcon at 30 dca (pk fol)
mod andesitic appears to be intrbedded w the rhy at the contact (or is this pegmatite?

254.8 - 255.6
mixed, mingled zone of dl gn andesitic - ang frag + pale + rhyolitic frag - fairly coarse rhy frag.
grad bcon

255.6 - 261.15
tightly packed ang dl gn and frag in a pale gn matrix
good flow bx txt

258.3 - 259.7 med gn altn
sharp contacts
vcon = 50 dca - same dip as fol but fol = 30 dca
bcon = 25 dca

This bcon is good over 2cm into a coarse mixed zone w a rhy component.

261.15 - 263.5
p gy gn + gy, andesitic sst w up to 20% rhy frag + fine diss py. gsz 2-10mm v poorly sorted.
grad bcon

263.5 - 264.4
p - med gy, med to cg (bec cg dk) rhyolitic wke rounded to subangular rhy frag up to 1-2cm in a fine p gy matrix (no andesite)
basal 10cm has round rhy clasts up to 5cm — sharp clast boundaries
grad bcon — no or very little ser altn

good sharp contact of qfp

* no ser or silic alteration

264.4 - 269
basically same units as above but qfp clasts now very coarse - almost clast supported in pk' - clasts up to 20cm - more angular but shell zones where mafics dom'
grad bcon — no ser altn, sharp clast boundary

269 - 271.55
p gy glassy vy porphyritic qfp - sly jigsaw fit in pk' but bec more mfc dk.
v good jigsaw txt near bcon
bcon = grad

DIAMOND DRILL LOG

project:
location:
coords: E N

DDH No. L14-675
page 3 of 3

AZ: Dip: Scale: 1:200
Logged by: Date:

m	structure	Grain size (log scale, mm: 0.06 0.5 2 8 32 Max)	Samples	Description

271.55 - 275.8

v cg dty volc w v sharp clast boundaries, v poorly sorted, ang dty frag' predy 1-10mm but w lots of scattered dty frag' ggs to 20cm — start to see an andestic component in the groms
matrix dom' ht
beom =gouge zone (10cm wide)
20dca 555dca
new pt fl

275.8 - 291.3

blk + lem coarse altd and fw w scattered round to sub angular dty frag' (ry cg 2-10cm) - slightly less blk than L14-676
andesite is sy blk - bullseye txt in large frag'

280 - 280.5 mfc sharp planar contact 40 dca -nt fn

281.6 - 282.1 mfc sharp planar contact -40dca

gets sly finer grained below 285.4m

286.8 → below here gsz inc to 2-20mm still sy blk + fract

291.3 - 291.9

shd gougey zone at 10-20 dca
alt gouge

291.5 →

more sy blk andesitic - cg volc

DIAMOND DRILL LOG

project: RIDGE
location: LYNX
coords: 1263.1 E 3842 N 3247.3 elev

DDH No. L14-683
page 1 of 6

AZ: 356 | Dip: -48 | Scale: 1:200
Logged by: SAJ | Date: 3-8

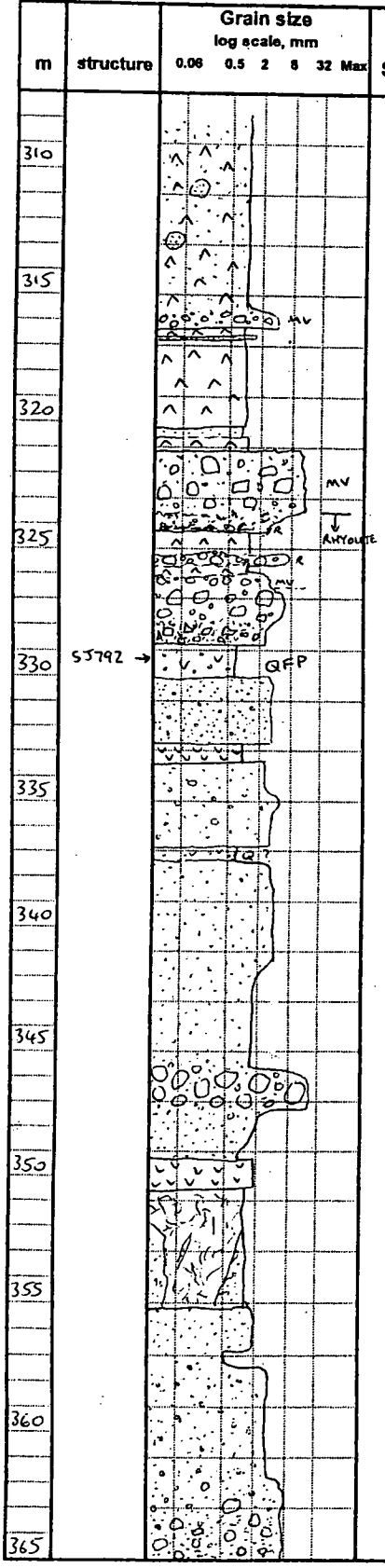

Description

→ 315.6

med gy gn, fmg (predy 1mm) msv andesitic sst? w scattered large subrounded clasts? or sty blk and clasts up to 5cm + fine p gn gy clasts + dl gn clasts 1-4mm
- also mn fine 2-5mm py clasts (or py blebs?)
a v wk fol at ~30 dca

The bcon is v gradl w mixed clastic unit approx ~50 dca = bedding?

315.6 - 316.2

p to med gy + gn gy, med to cg (gsz is predy 2-5mm clasts in a fine matrix), poorly sorted mixed volcaniclastic matrix dom ff but w alt p gy rhy fsg + p gn gy fg dac? or rhy clasts + mn ore clasts. + alt dl gn cl in matrix + mn f gn mod fsg. The clasts are predy subrounded and v distinct gn boundaries. (to py ff and in clasts)
rhyolite = 60-70%
dacite - 10-20%
andesite - 10-20% → mostly as matrix material.

The bcon is v sharp and 45-50 dca alt 2-5% fine ds py in 3cm wide zone at bcon.
a mod fol occurs that 35-60 dca.

316.2 - 321.1

mod to dl gy gn, fmg (predy 1-1.5mm) v msv + uniform andesitic flow, f p gn lt ff and tr fine py

316.65 - 316.75 py r zone of rhy sst ± carb up to 10-15% ff
v sharp + wavy upper bcon at 35-40 dca.

320.3 - 320.55 - p gy rhy (fg) msv w alt fine to cg py ff - esp at base - up to 30-40%
upper contact = v sharp + planar at 35 dca
bcon = more ir and steep 15-20 dca and overprinted by alt cg py

The bcon is v sharp and 40 dca

321.1 - 323.7

p to med gy predy + mod to dl gy gn, mod to cg, mixed volcaniclastic w mn ore clasts ff. poorly sorted matrix dom fgl ff w subrounded clasts 1-10cm mod fol ff at ~35-40 dca
p gy rhyolite 60%
gn andesite 10-40% - inc dn after first 50cm
ore clasts ff - up to 1-2cm
below 322cm andesite is more dominant
andesite 50-60%
rhyolite 30-40-50%
andesite as large subrounded clasts and fine gn in matrix - still matrix dom
grad bcon w rhyolitic volcaniclastic

DIAMOND DRILL LOG

project:
location:
coords: E N

DDH No. L14-683
page 2 of 6

AZ: Dip: Scale: 1:200
Logged by: Date:

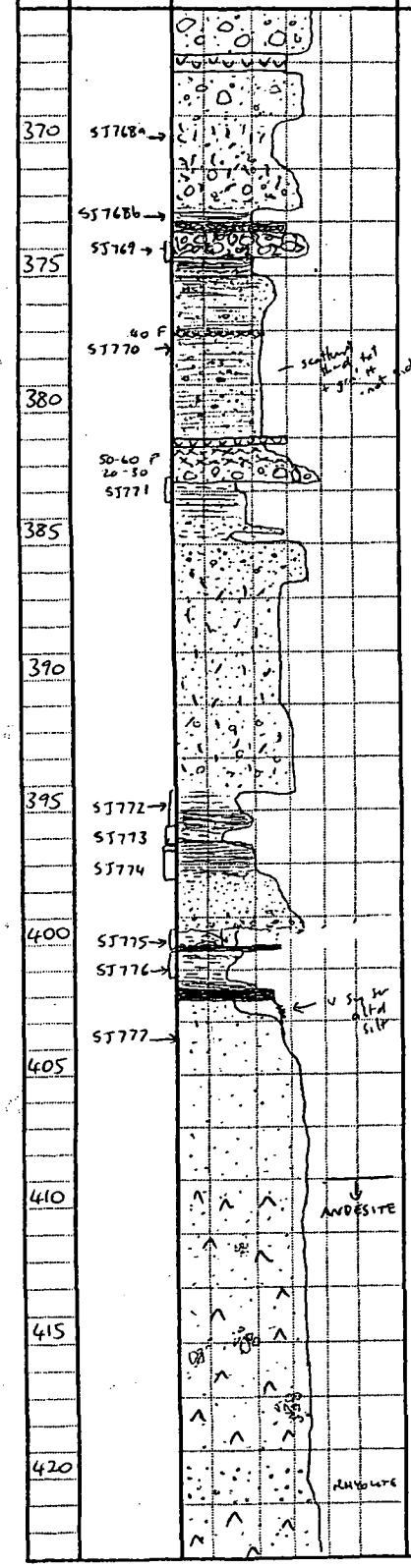

Description

323.7 – 324.1

p gy predy, mg to cg, poorly sorted rhyolitic volcaniclastic w cg subrounded to subangular p gy glassy rhy frag' up to 3cm in a mg (1-3mm) matrix of subrounded fe grn' alt py + esp st' + semi msv patr occur th esp in basal 10cm (up to 20-30% th)

The bcon is sy sharp at 40 dca

324.1 – 325.75

med to d gy gn, msv v unifm andesite flow? w fw p gy to wh amygdales in t/p 20cm (1-3mm) (gsz is predy 1-2mm th) well fol at 35-40 dca th.

325.25 – 325.40 large fe + dac clasts (subrounded) 1-5cm occur in this zone – in an andesitic matrix. q in matrix too

sy sharp chge at upper t bcon' (but not knife sharp = diffuse)

1-2% ds py th this zone.

The bcon is v sharp + planar at 45-50 dca.

325.75 – 326.4

p to med gy, + med gy gn, med to cg poorly sorted rhyolitic dominated mixed volcaniclastic w about 50-60% andesite dec to ~10% andesite near grad bcon. alt q eyes' + 1-2mm rhy grn' th matrix. p gy rhy subrounded clasts th at 1-2cm predy ore clasts up to bcon = sy common in upper ½ which is andesite rich.

The bcon is v grad.

326.4 – 328.8

p to med gy, cg poorly sorted rhyolitic volcaniclastic w abt qfp clasts + alt ds py + st' th locally up to 10% especially in upper ½ of unit. gsz is predy 2-4cm matrix dom (1-2mm) th. sy fol th at ~60 dca.

The basal metre has a diffrnt txt w large l-shdly ir subangular qfp clasts + wavy ir fag' 'shard-like' in matrix – sy ser altd w much less py = only tr py 'shard-like' p gy fag' in c dh to bcon.

v sharp bcon at 45 dca

328.8 – 330.15

p gy msv q-fr qfp w mod flow banding in upper 20cm pla contact. sy pla txt th in a glassy vfg gmass. (classic qfp appearance)

v sharp sy planar bcon at 40 dca.

330.15 – 332.8

p to med gy, sg (1-3mm) w abt p gy to wh q eye' + grn' 1-3mm + rounded in a med to d gy sy ser altd + fractured (sharp wavy fn' th) matrix, sy sorted txt th.

tr to v rare py dss th.

The bcon is sharp + ir at 30-35 dca

SJ778 at 427.6m – altered andesite

DIAMOND DRILL LOG

project:
location:
coords: E N

DDH No. L14-683
page 3 of 6

AZ: Dip: Scale: 1:200
Logged by: Date:

m	structure	Grain size (log scale, mm: 0.06 0.5 2 8 32 Max)	Samples	Description
425				332.8-333.4 med gn gy, fg -1mm msv v uniform mfv -andesite? non fol w sharp planar bcon at 30 dca. (not pbo upon)
				333.4-349.25 p to med gy, med grained predy (but coarser than msv + uniform unit above dyke - but still same composition = just slightly coarser zone). chloritic wilcoxclastic w a ... wy to wy sorted tht. matrix dominated 1-2mm w abt p subangular to subrounded dom p gy fc clasts up to 2-4mm abt 2 eyes th matrix (332 inc dk to 2-5mm clasts (336.7-345.2) ↗ grad dom 334.8-335 gouge + fg zone upper one = 50 dca alt gouge then steep fol 5-15 dca w alt gouge w ss at 80-85 dca 335.2 → 336.95 gsz predy 1-3mm w occ fc clasts subrounded up to 5mm sy fol th at 30-35 dca. v msv + uniform tht th 336.95-337.25 p gy phc gfp chlor ? msv but basal 5-10cm = sy fragmental-autoclastic (2 eyes th) tht 337.25-341.2 - sy fol 2-5mm gsz + wy fragmental 341.2 → 345.5 gsz dec to 1-2mm predy and core is less sy fol + fragmented v msv and wy bounded at ~40 dca bcon is v good. 345.5-346.3 p gy glassy 2 eyes + gfp large clasts dom vcg w diffuse clast boundary clast dominated th v good bcon 346.3-349.25 - p gy wy msv matrix dom (1-2mm) but w abt p clasts rounded (2-20mm) thin basal 30cm = v msv + prophyritic The bcon is v sharp + wy planar at 30 dca
430				349.25-350.65 med gn gy, fg (1mm) v msv + uniform mfv (non fol) The bcon is sharp + cntct at 35-40 dca
				350.65-355.1 mil wh to clear 2 cav-ser vn w mm cub py 1-2mm + disp'nt of py v steep in 0-10 dca - v selvedge (sy ser altn) parts th. mostly = barren. The bcon is v ir and steep at 5-10 dca. below 352.2 = more of host rock selvedge which = next to py fc vnlc The wng exists the fc in the surrounding host rocks. generally v steep + highly ir
435				355.1-361.8 p gy fmg (?) diff to tell, msv fc wilcoxclastic in plc' lost wy 1-2mm, elsewhere it is vfg, 0.5mm or just sid? 356.8-357.3 vfg 0.5mm 357.3m → 361.8 gsz inc to 1-3mm predy sy fol th at 30 dca v good bcon

DIAMOND DRILL LOG

project:
location:
coords: E N

DDH No. L14-683
page 4 of 6

AZ: Dip: Scale: 1:200
Logged by: Date:

m	structure	Grain size (log scale, mm: 0.06 0.5 2 8 32 Max)	Samples	Description

361.8 - 374.2

p to med gy, rly cg (2-5mm predy) poorly sorted rly volcaniclastic w up to 5% p honey coloured sphal ± py (+gn or tennantite) p gy rly clasts are up to 2cm but v diffuse clast boundaries - matrix = v sy ser altd - mainly down hh sy fol hh at ~30 dca

366.8 - 367.3 med gy gy, msv mfw fol hh w sharp ir contacts at 40 dca (locally rotated 70 dca)

369 → 370.6 st' now = only py (no sphal or gn) and gsz now predy 1-1.5mm v msv + uniform v mm py (locally +sph)

370.6 - 372.5 - grad bcon < 1-2% med to cg (clasts up to 2cm) w p honey sphal + gn up to 2-3% (locally up to 5-10%)

372.5 - 373. fg med gy silty + v sy ser altd v mm sulphides in parts sy sharp base

373 - 373.45 semi msv sphal-gn-py ± ccp

373.45 - 374.2 p gy glassy rly - clt? clastic? dom w alt sphal-gn-py st' hh either cg or msv rly - clt? probably = cg (diff to tell) The bcon is sy sharp and ~40 dca.

374.2 - 374.9

predy med to rl gy, fg silty matrix dom' mg fol hh at ~60 dca w pat' of sphal-py-gn (semi msv zones 5-6cm wide) in between = no sulphides just silty unit.

v grad bcon

374.9 - 376

p to med gy, mg msv mg sorted ft volcaniclastic gsz is predy 1-2mm. tr fine dissem py hh. silty matrix

v grad bcon

376 - 382.7

med gy silty matrix dom' but w a speckled tex of fine (1mm) fr grn' th The unit is sy fol (+fr) at ~15 dca hh. - core is mg fragmented at this ang hh.

377 - 377.2 several gouge z fm zones at ~40 dca

381 - 381.25 med gn gy mfw sharp ir con' at 50 dca

381.25 - 381.75 abt gouge fm zones sy bxd at ~50-60 dca + 20-30 dca shallow F dom mak gsz inc to 1-2cm loc

381.75 - 382.7 - gsz inc' to 2-5mm predy w coarser clasts up to 5cm

Sharp sly wavy bcon at 35-40 dca

DIAMOND DRILL LOG

project:
location:
coords: E N

DDH No. L14-683
page 5 of 6

AZ: Dip: Scale: 1:200
Logged by: Date:

m	structure	Grain size (log scale, mm: 0.06 0.5 2 8 32 Max)	Samples	Description

382.7 - 383

p to med gy, vfg <0.5mm, mg to sy laminated clst-s.lt laminations are 40 dca
v grad bcon w fn sst

383 - 386.4

p to med gy, mg predy 1-3mm, v slt clst fag' msv rby-clst sst well sorted txt ft.

383 - 384.2 mg fg 1mm - 0.5mm ft mod v mic to mg banded

384.2 - 384.5 mg 1-2mm msv sst v grad bcon

384.5 - 384.7 fg <0.5mm mg banded grad bcon

384.7 - 386.4 msv well sorted sst gsz 2-4mm predy subrounded to subang

The bcon = grad.

386.4 - 394.2

p to med gy, mg fg volc-sst v up to 1-2% py-sphal st' ft. v well sorted txt ft, gsz 1-2mm predy msv + uniform ft. st' dec out below 386.5m approx

gsz inc below ~ 391m to ~2-3mm matrix + slt well rounded fg clasts up to 2cm still matrix dom.

392.2 - 394.2 1-2% p sphal - py st' ft (dec dn) gsz still 1-2mm mg msv + uniform grad bcon

394.2 - 399.6

mixed unit of clst, s.lt + fn sst, wh, p gy + med gy ft. interbedded at ~50 dca.

394.2 - 395 - wh-lt s.l zone interbedded w fg silty pats - s.l zones = v fg to glassy looks sy sil rather than clst

mx up to 1%, v fn p sphal st' + tr fn dis py

395 - 395.65 - p to med gy s.lt v fg <0.5mm gradg dom wh v wh clst

395.65 - 396.05 - wh glassy msv clst - sharp highly irr bcon sly fragmented

396.05 - 397.3 p to med gy fn s.lt <0.5 - 0.5mm gsz ft wk banding ft at ~40-50 dca. v grad bcon.

397.3 - 398 p to med gy, fg (0.5-1mm) msv well sorted fn fg sst grad bcon

398 - 399.6 - still p gy, but gsz inc to 1-3mm w scattered larger fg clasts up to 1cm still a v silty matrix. basal 10cm = mi wh & msv w sphal-ft + py blebs ft v con' ~ 30 dca

399.6 - 400

p gy vfg sy sil wh-msv clst - basal 10cm = more fragmental w slt py st' & str ser alts probably grading oth wh & sst - sy overprinted by py mz

DIAMOND DRILL LOG

project:
location:
coords: E N

DDH No. L14-683
page 6 of 6

AZ: Dip: Scale: 1:200
Logged by: Date:

m	structure	Grain size (log scale, mm: 0.06 0.5 2 8 32 Max)	Samples	Description
				400 - 400.2 ~sv py ± cgp ~2 v a grad top and v sharp bcon at 50 dcn. 400.2 - 401.3 wk msv clt - top 50cm - not so wk + msv as basal ½ (looks more fragmental + rsd occ sphal-gn-py st' (flat pb laminations) wy laminated ft at ~60 dcn. v grad bcon into p pkle br-gy laminated s.lt (just laminated in top 2cm) 401.3 - 401.88 p to mod gy br, fmg silky v sy ser altd unit The str ser alth overprints orig text - diff to see orig lithology but can still see scattered fe clasts (subrounded up to 5-6mm) v sharp bcon w wk ~2 at ~20-25 dcn 401.88 - 402.3 msv sphal ~2 + gn + py v sharp v ir bcon at ~20 dcn (highly ir) 402.3 - → >430 approx p to mod br + gy, fg silky v sy ser altd unit w gn sphal-py st' ft (down to ~404m) top 20-30cm = v fg s.lt zone sy ser altd gsz inc below ~404m to 1-3mm m sh (on fg edges) v sy ser altd w ds fine + cg py ft up to 5% in pkl' fg unit difficult to tell what original lithology was some fe looky clasts still present. 409 andesite? below here? → below ~409m - still v sy ser altd but unit really looks like sy altd and w autobxd tst + cg py ft (sy bkle andesite) coarse autbxtd tst w ang frag' 1-2cm fe unit here? 409.7 - 421 → approx here start seeing fine fe grn' within the sy ser unit - don't see autbxd tst maybe back in to a fe unit. - still sy bkle unit + v sy ser altd w cg py ft up to 5-10% 421 → 426 no fe grn' visible ang 2-4mm pr'ly v ast cg py ft, v sy ser altd but ast of gn gy ang mod frag' sy ser altd mod bkle ft. 426 - gsz inc start seeing 'shard' like tst in v sy bkle + ser altd andesite, still v sy altd ft * this andesite unit down to ~426m stays transitional - diff to tell if there isn't a fe component v sy ser altd and still ast cg py ft (up to 20-30% in pkl') = FW altn - just may be a bit fe? (see SJ 778)

DIAMOND DRILL LOG

project: BATTLE
location: 18-149 RP elev. 3044.6
coords: 1423.1 E 4168.2 N

DDH No. 18-1004
page 1 of 8

AZ: 000 | Dip: -61 | Scale: 1:200
Logged by: SAJ | Date:

Grain size, log scale, mm: 0.06 0.5 2 8 32 Max

m | structure | Samples

Description

0 - 0.2
spkal st' (10-20%) stockwork pattern with gy f porphyry (grad lcon)

0.2 - 14.8
p gy, msv, sy sil g f porphyry w a msv fe gneiss fr. They eyes are up to 2-3cm and randomly scattered th mn st mz (spkal) occurs fr:
4.5-6.4 - 5-20% spk ± gn ± cpy ± py (surface st in basal 30cm)
a wk fabric + dev in ple' (probably = f) at ~40 dca.
The bcon is v sharp + std against mod unit at about 25 dca - narrow gouge seam along contact.
The mod unit is darker-med gy matrix + more clastic appearance (see SJ427)
The basal 20cm of the qfp - looks a bit fragmented and contains ~5% cpy spkal py st'

4.8 - 17.0
p to med gy, med to cg (altho predy matrix = 2-3mm?) altd unit but definitely less + clastic fab (auto br or volcaniclastic? sharp boundary w overlying qfp bo
st spkal, occ gn + py 5-20% occurs th w a grad lcon. A wk to mod fr occurs in ple' at ~40-50 dca.
The unit appears to grade down into a coarse grained zone (without st mz)

17.0 - 18.5
p to med gy, vy cg bcc finer grained with and more sy ser altd than st zone. The unit has a coarse clastic appearance th but is ser altd w a mod fr th at ~ 50 dca. The fr clasts are up to 2 cm w dist q grn (smoky q, ~5%) in the matrix - p gn v sy ser altd in this zone + fol 50 dca
17.5 - 17.9 - unit looks bedded w sly finer looking material - or is this just large clasts elongated by fr? - (looks more silty + darker gy = bedding)
The bcon is v grad w st mz

18.5 - 20.15
15-20% p honey spkal ± cpy ± gn ± py st stockwork in a dk gy br sy ser altd unit.
18.9 - 19.18 = no st only mn th py
dk gy br sy ser altd + fg ? in this zone
18.7 - 18.9 - steep w fr w mn gouge
core is quite fragmented in this zone
fault = 20-25 dca - couldn't find slickensides (possibly ph ec?)
The bcon is (actually = vy sharp + v wavy w darker fg zone below)
a vy melanged zone

20.15 - 24.3
p to med gy, predy vg (1-2mm) msv fe volcaniclastic w a wk fr dev th at ~ 50 dca
20.15 - 20.8 - vy dk gy br - looks finer grained than mod unit
= bedding + grades down in to slightly coarse zone
20.3 - 20.5 - p gn bk matrix contact 45 dca - sharp + wavy
20.8 - 22.8 - variable gsz - sy ser altd so diff to see any lithology but looks fairly cg (cm size clasts) in a darker matrix - 1-2 mm
22.8 - 23 - dk gy br fg zone w sharp wavy contact w underlying fe unit
23 - 23.5 - p gy mg (1-3mm) sy sil msv fe volcaniclastic unit w fragmental (fol or bedding? at ~ 50 dca) (mn st th)
23.5 - 24.3 - darker gy br, msv - lam or < mm sy fol at 50 dca (v planar fabric)
The bcon good (bedding disappears) w lower unit. - mn st in ple' The basal 20cm has p gy fr (mm to cm scale clasts)

DIAMOND DRILL LOG

project:
location:
coords: E N

DDH No. 18-1004
page 2 of 8

AZ: Dip: Scale: 1:200
Logged by: Date:

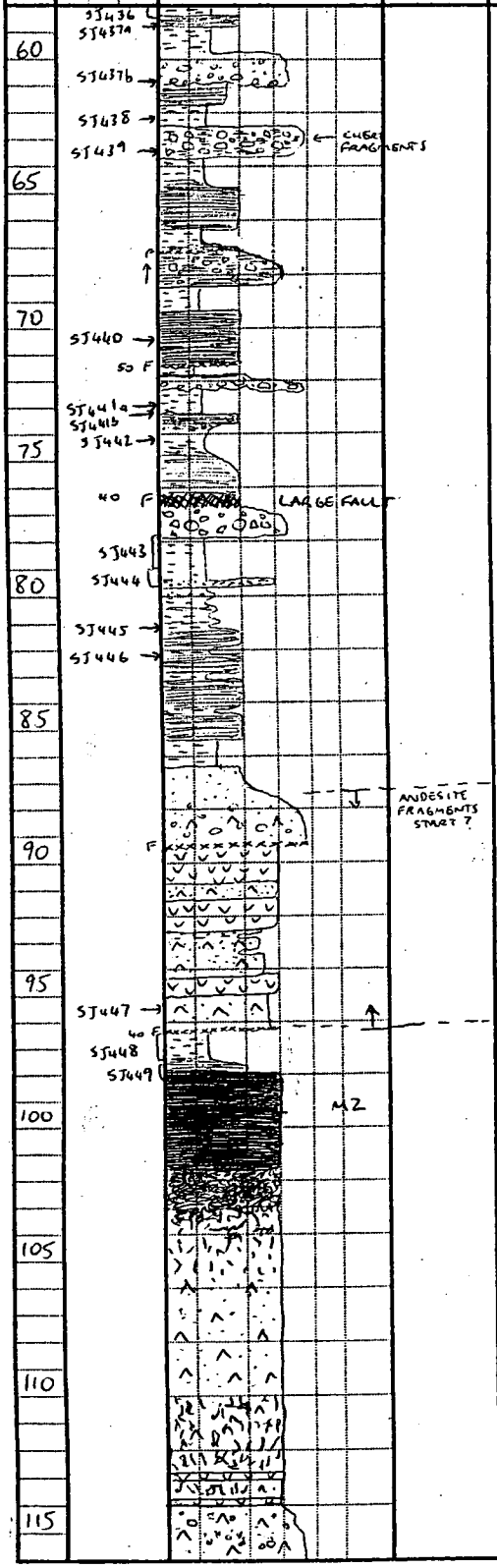

Description

24.3 - 26.1
dl gy bn, fg (<0.5mm, silty unit predy) but v occ 1mm size grn scattered th). msv txt th although fe laminations are visible in pl'. A wk fe is obsv at ~50 dca (wavy)

25.35 - 25.45 -
p gy mg sil sandy unit has a v sharp upper contact w dl gy bn silty unit & is msv wavy (disrupted by fe) unit = msv

25.45 - 26.1 dl gy bn fine silty matrix obsv but v alt p gy fe bands + clasts (?) disrupted & irregularly by fl at 40-50 dca

25.9 - 26.1 - steep fe zone w narrow gouge seams on steep fes at ~25-30 dca (slickensides = ~20 dca on fault plane)
mn sulphides occ in the fault

The bcon = gradl w underlying unit as you can still see the fine silty unit within the faulted zone.

26.1 - 27
md to dl gy + bn gy, fg (predy a dl silty matrix w pats of more coarser grnd material).

26.1 - 26.3 - gsz is 2-4mm, fe grn'd ang in a dl silty matrix gradl dk to next unit

26.3 - 27 - darker gy, fine grnd silt st w st sulphides (up to 20%)
py ± v mn cpy

The basal 15cm = v dark = argillic has a v sharp lcon w cg sst, ort at 50 dca ry planar

The sulphides extend in a planar zone (dark) 15cm into the next unit. (see SJ429)

27 - 30.2 (predy 2-3mm)
p gy, sg (2-5mm) egg fe sst w a v uniform (& the matrix-p gy) appearance th. The clasts looked tightly packed and relatively well sorted. The fe is only vy visible at ~40-45 dca. The fe grn' = ry rounded to subrounded.

The basal 2cm = sy sc altd - looks much finer grained and the contact = v sharp + steep 30 dca + wavy.

30.2 - 30.7
semi msv py m2 + st m2 in basal 20cm
The py is ry cg at the bo (up to 3-4mm in pl') w it q pat in upper 5cm. The host rx are still mg sst
The bcon = gradl w st m2 dying out dk.

30.7 - 31.5
p to md gy w dl gy pats, ry fg - s.silty looking matrix but w coarser sil pats - highly v. These sil pats coated by sly cg - (up to 0.5-1mm) - look more like a fine sst

30.7 - 31 - fine p sil zones dominate w only mn darker gy fg zones highly v contacts

31 - 31.5 - dark gy - bcc now sy ser altd dk w p gn pats (to original bedding (?). The unit becs ry sy fl at ~35-40 dca and the core begins to fragment.

The bcon = in broken core (fault zone) and ry cg py blebs occ in basal 10cm.

DIAMOND DRILL LOG

project:
location:
coords: E N

DDH No. 18-1004
page 3 of 8

AZ: Dip: Scale: 1:200
Logged by: Date:

m	structure	Grain size (log scale, mm: 0.06 0.5 2 8 32 Max)	Samples	Description

31.6 - 32.5
fault zone w abt gouge zones th. Hostrock = sltl the fg unit from above but abt steep + v flatter fa zones occur th fa' orted at 10-20 dca + 50-70 dca
The core is pulverised in pl'. Slickensides are not well developed but in pl' appear on steep fa' to = ~20 dca

32.5 - 34
mixed zone of fg sst + fine cl siltstone - ezg + msv text - vg well sorted th. monomict rhyolitic composition
32.5 - 32.7 - cl. gy fg s.lth unit grades down into:
32.7 - 32.9 - p gy fg v sty ser altd zone?
32.9 - 33.65 - p to med gy, mg fc sst gsz is predy 2-3mm w p clasts subrounded in a darker fine matrix
The bcon is v sharp + wavy ~60 dca w med s.ttst.
33.65 - 33.85 - cl. gy fine s.lt a narrow gouge zone occurs at base of this zone ~ 60-70 dca (no slickensides)
33.85 - 34 - med gy, mg fc sst

34 - 36
p to med gn, ch altd + bleached, ser altd, msv ezg mfv. The dyke is fol at ~ 35-40 dca
34.23 - 34.7 - sty ser altd eg fc volcaniclastic w p gn ser pat'th gsz in this zone = 2-4 mm w q eyes visible in matrix. good fol at 35-40 dca. mn py occurs th.
- py cubes (1-2 m) are scattered in a 10-15 cm wide zone in the surrounding mfv either side of zone.
Upper + lower contacts of mfv = ~60-70 dca = sharp + wavy.

36 - 38.2
p to med gy, fmg dty volcaniclastic w variable gsz th. The unit is vg to vg fol at ~40-50 dca (steeper around small fault zones).
36 - 38 gsz = predy ~1mm good con'
38 - 38.2 - gsz = ~2-4mm
36.85 - 37 - v wispy grad zone w ser altd pats + mn fi & scattered py cubes #.
Faults { 37.9 - 38 - abt gouge zone fa' orted 35-40 dca - rel pte fm
36.4 - 36.65 - 90% gouge zone - no slickensides orted at ~65 dca.
The bcon is sharp + steep but highly irr, orted at 25 dca.

38.2 - 39.5
p gy, ble + ser altd mfv - a med fi occurs th at 30 dca.
38.3 - 38.4 - small med gy zone of dty volcaniclastic con' at ~ 40 dca (xenolith or wallrock ?)
The bcon is v sharp + irr - orted ~ 80 dca. looks same as overlying unit

39.5 - 49.4
p to med gy, predy cg (2-15mm - odd 50mm clasts) w p fc clasts randomly oriented + poorly sorted in a darker gy fine matrix w alt g gm'. clasts are subangular to subrounded. - matrix supported.
A wk to mod fa occurs th at ~40 dca
39.5 - 39.65 - cg w clasts up to 1-2cm
39.65 - 40 - p gn v sty fg altd zone w mn irr g mg planar steep irr vn' w cg py scattered in thm. The zone is sty fol at 35-40 dca. core is sty fragmented.

DIAMOND DRILL LOG

project:
location:
coords: E N

DDH No. 18-1004
page 4 of 8

AZ: Dip: Scale: 1:200
Logged by: Date:

m	structure	Grain size (log scale, mm: 0.06 0.5 2 8 32 Max)	Samples	Description

40 - 40.4 = fg 0.5mm
40.4 - 40.6 - gsz = ~1mm
40.6 - 41 - gsz = 0.5 or < grades ↓
41 - 42.35 cg gsz = 2-5mm ↓ occ clasts up to 20mm (subangular)
(tr py tt)
42.35 - 42.6 - narrow gouge zone 40 deg
42.4 - 43.2 fg zone 0.5mm grading down to 1mm (more py here ~2%)
43.2 - 43.3 - fg gouge zone on fg 60 deg (no slickensides)
43.3 - 43.5 - cg ↓ cherty clasts 1-2cm ↓ ir boundary
bedding? fg gouge zone at ~30 deg
43.5 - 44.5 - fine 0.5mm or less more like p siltst
F
43.8 - 43.9 - gouge fg zone at 40-45 deg (ie shallower than fg - no slickensides)
44.25 - 44.35 steep 30-35 fg pcl fg zones w mm gouge
44.4 - 45.3 - mg cg clasts are upto to 20mm in md matrix.
45.3 - fg inc dk - still cg but fg at 25-30 deg is occ v cly dkr + fragmenting the core (esp at 46.2 - 46.7) several gouge zones thro fg.
clast clasts
thick cm cg = disrupted beds in a fine d silty zone
48.55 - 48.7 - chert clast w rare v bedding/laminations another chert clast occurs at 49.2 - 49.3 - this clast has highly ir boundary sharp but fragmental - similar to upper clast.
46.7 - 49.4 - the unit is w a fine d matrix but is much less fol - still see a weak fg at ~ 40 - 50 deg. (Chert clasts or beds occur in this)
The base = sharp but ir against med chert - ch is sly shrd + fragmented

49.4 - 50.1
p + med gy s.l s.ltstone grades slowly dk into more msv wh chert. This unit is predy a p siltst ir py st'l + gshal veins occur tt (predy steep).
Fine laminations occur in pkl' ortet at 35-40 deg also 'jellybean'-like blebs in dkr'y zone
49.8 - 49.9 - p gn mfv - ir sharp ea'at about 60 deg.
The base is in smashed core (many sampling)

50.1 - 56.3
predy wh msv chert w interbed silty zones
Good sampling through here fr geochemistry see if chert diff from silt is petrologically + chemically
(mm py-spiral st' tt)
50.1 - 50.25 - white mste cm laminated chert at ~35 deg w 'jellybean-like' blebs
(approx depths many sampling)
50.20 - 50.55 p gy silty zone - see sample.
50.55 - 50.8 wh msv chert
50.8 - 51 - darker gy s.l.stone
51 - 51.4 wh msv chert
51.4 - 52.4 p silty zone s.l but w 0.5mm
52.4 - 53.7 wh msv chert

DIAMOND DRILL LOG

project:
location:
coords: E N

DDH No. 18-1004
page 5 of 8

AZ: Dip: Scale: 1:200
Logged by: Date:

m	structure	Grain size (log scale, mm: 0.06 0.5 2 8 32 Max)	Samples	Description

53.7 - 53.85 - med gy to silty zone my fol ~50 dca. (contacts = gone)
53.85 - 54.3 - wh msv clst

54.3 - 57
pred g fg to + dgn, fg silty material. my to sy fol ff at 50 + in pl' 30-40 dca. → These are probably lake fn related to faulting.
narrow zones of clst occur ff w 5cm or so and have sharp contacts w fine unit but are often quite fragmented.
whole zone looks sheared
56.85 - 56.9 - fault zone w 60-70% gouge - no slickensides fault = 30-50 dca

57 - 59.85
wh + p gy speckled to msv wh clst wh planar fabric at ~50 dca

57 - 2.25 → small gouge zone at ~60-70 dca
57.25 - 57.40 - p gy mg w/ rhy sst unit (can't see contacts)
57.4 - 58.1 - wh clst (no contact)
58.1 - 58.2 - bxd zone w intense py ± carb sl zone + clst frags + bornite (see SJ436)
58.2 - 58.5 - wht clst
58.5 - 58.8 - med gy fg silty zone
58.8 - 59.85 - white msv clst

59.85 - 60.8
p to med gy, cg (?) v diffuse grn bounding v sy sicl + with spkl blebs ff - sicl silt or a sicl cg unit? (see SJ437) (fm spkl st also occurs)
The bcon is gradl w unit. BUT the underlying unit = fg and the conn clastic unit at basal 5-10 cm contains clasts of underlying unit (ie erosive base).

60.8 - 61.7
p to med gy fg (~<0.5-0.5mm) wy bedded + laminated in pl' at 40 dca. The unit is sy fragmtd on steep (0-10) fa' but no gouge (not really faulted).
The bcon is v sharp + wavy ~ at 70-80 dca

good clst seq
61.7 - 62.5
white msv clst (see SJ438) overbroke seq sampled
The bcon is sharp + ~ at ~50 dca and is wy sh

62.5 - 63.8
predy dgy fn matrix w clst frs to coarse angular clst fragments (matrix supported).
The bedding has steepened up in this zone to about 10-15 dca and looks sly folded in pl'. Sy fol ff w/ bedding
The bcon is sharp against a clst lapse at ~20 dca.

63.8 - 76.2
mixed unit of clst + siltstone
bedding / fn still steep 25-30 dca
msv py esp sf' occ ff most steep + in-

DIAMOND DRILL LOG

project:
location:
coords: E N

DDH No. 18-1004
page 6 of 8

AZ: Dip: Scale: 1:200
Logged by: Date:

m	structure	Grain size (log scale, mm: 0.06 0.5 2 8 32 Max)	Samples	Description

63.8 - 64.7 - pr dy wk msv clst grading down into p bnded sdst

64.7 - 66.35 p gy s.lty unit gsz up to 0.5mm
mg + sg fl = 25-30 dca
sharp base at 30 dca

66.35 - 66.9 wk msv clst
sharp base but shd at base and ang clst frags incorporated into lower s.lt

67.2-67.25 - gouge zone at 50 dca

66.9 — 68.3 - dk gy bn s.lty matrix w clsty clasts + rng (sub angular) (up to 2cm gsz)
sharp base - shd sly at ~25 dca
This unit shows a fining up sequence upper 20cm = zone free. (apart from any clst clasts right at upper contact)

68.3 - 69.3 wk msv clst
sharp base with siltstone at ~30 dca

69.3 - 71.45
p to med gy msv to vy laminated in pl' s.lty unit (not particularly sil) fairly soft still
but sly sil bands within it in pale zones
But bizzare s. alth at

71.45 - 71.55 - fra zone w 40% gouge at ~50 dca (no slickensides)

71.55 - 71.8 wk msv clst - steep base at 25 dca w dbl shd s.lty zone

71.8 - 71.9 dk s.lty unit a- s.lty matrix w p fi gsn up to 5mm - sg shd at 10-25 dca

71.9 - 72 - p gy sy s.l msv? unit w gy & grn + g slds (probably = clasts) but gsn boundary extremely diffing w sy s.l grades down into clastic zone

72 - 72.35 cg slt clty frags in dk gy bn matrix, bcm = v sharp + highly irr + fragmental against msv clst.

73.0-73.2 clasts in clst →
72.35 - 73.2 - wk msv clst
sharp + fragmental contact w msv s.lty unit. more like diorite bounding through

73.2 - 73.7 - s.lty p gy finely laminated in a few pl' - fairly good lcm w interbedded clst

73.7 - 74.35
wk msv clst - 'jellybeans' in upper 20 cm of clst?
clst bec more gy dk grades into p s.lt

74.35 - 76.2
* p s.lt interbedded w clty zones v well bedded - steep ~25 dca
good bedding
bedding = mm + cm scale (mm py along some beds) - looks interesting

76.2 - 76.5
Big fault zone slt gouge fra all diff orth' core = really smashed up (basal fault = v 40 dca - slickensides ~ 20-30 dca on fault plane)

DIAMOND DRILL LOG

project:
location:
coords: E N

DDH No. 18-1004
page 7 of 8

AZ: Dip: Scale: 1:200
Logged by: Date:

m	structure	Grain size (log scale, mm: 0.06 0.5 2 8 32 Max)	Samples	Description

76.5 – 77.9
a dl gy fn matrix w fine 1-2mm fe grn' t abt mg clt frag' - some large up to 5-6 cm
The whole zone is quite sft fol/sh at 30 dca w steeper fa' ft at 10-15 dca. sharp bcon

77.9 – 86.3
whole chert grades down into interbedded silt (dark fn w wh sil bands - very good bedding + laminations (looks exhalative?)
- sulphides in silty horizons
(see SJ 443)
77.9 – 79.4 = chert w silty horizons described above
79.4 – 79.6 - dl gy fn matrix w p fine 1-2mm fe grn' sharp contact w mod clt at ~40 dca.
79.6 – 81.7
p bandedl(wy) silt and clt grade in and out (clt dominates) bedding now ~ 40-50 dca
bedding angle dec'
81.7 – 85.4
p siltstone dominates - still chty horizons. The silt is very banded at about 50-60 dca
The bcon = sharp at 60-50 dca + wavy
The basal 10 cm of siltstone = p gn v sy ser altd.
- looks like epiclastic altn in mod clt (only 5mm wide)
85.4 – 86.3
wh msv chert w a sharp low boundary at 70 dca wavy contact

86.3 – 89.4
dl fn gy, v sy ser altd dl unit - diff to tell orig lithology + gsz
Could even be altd andesite? - or siltstone?)
unit gets coarser dk - has clt fe grn' clasts in it up to 5-6 mm - sub angular (could be mixed unit) w andesitic matrix
The bcon is faulted.

89.4 – 89.6
Fault zone - v sy sheared core w alt gouge w steep fa' 10-20 dca, sy slcd along fa too which is 40-50 dca

89.6 – 95
p gn wy fol mfiv (p pk f pro'inple)
90.8 – 91.3 - dl gn gy wy cgg andesitic clastic unit v sy ser altd mod fol at ~50 dca
2 narrow gouge zones at top of zone altd at 50 dca (cliff orth to fa)
92.7 – 94.2 - more cgg and looks msv + plc' but fine zones interbedded def. andesite
bedding = 35-40 dca
v steep contacts with dykes 5 dca ucon, 25 dca lcon
The bcon = sharp + 25 dca.

95 – 96.1
v dl gn gy, sy ser + ch altd w pat py shds - looks like FV st zone. The bcon is faulted

DIAMOND DRILL LOG

project:
location:
coords: E N

DDH No. 18-1004
page 8 of 8

AZ: Dip: Scale: 1:200
Logged by: Date:

m	structure	Grain size (log scale, mm: 0.06 0.5 2 8 32 Max)	Samples	Description
				96.1-96.2 – faulted core in a fine d gy unit – v sy se alt w faults orted at 40 dcm – can't see slickensides on gouge on f planes.
				96.2-97.95 Wh msv cht w good interbedded silty zones Clasts v much like previous interbedded zone (at 82-82.5m) The cht is laminated at ~40dcm and below 97.6m grades down into a fine p gy silt (<0.5mm) (see SS448)
				97.95 → 101.7 massive spiral ccp py mZ, sy boudins at 50 dcm – can't see host lithology grad lcon
				101.7-103 semi-msv mZ host 20-30% py spiral ccp. 102.4-102.5 – gouge core at ~50 dca shall alt py
				103-105.7 st sulphidic pred py ± ccp in sy se altd + fol unit, fol is at 60dcm.
				105.7-109.8 – d gn gy + lt gy v sy se altd unit – looks like andesitic composition v chl alt grad lcon
				109.8-114 st sulphidic py domains v mn ccp 112.8-113.1 m fin steep contact 20 dca 113.8-114 – steep v fn'r gouge top of fault zone = 15 dca base = 40-50 dca v fn' + gouge
				114-118.9 d lt gy sy se altd andesitic msv granular text – see clasts up to 1-4mm patchy sp py occurs throughout in zones
				118.9 = EOH

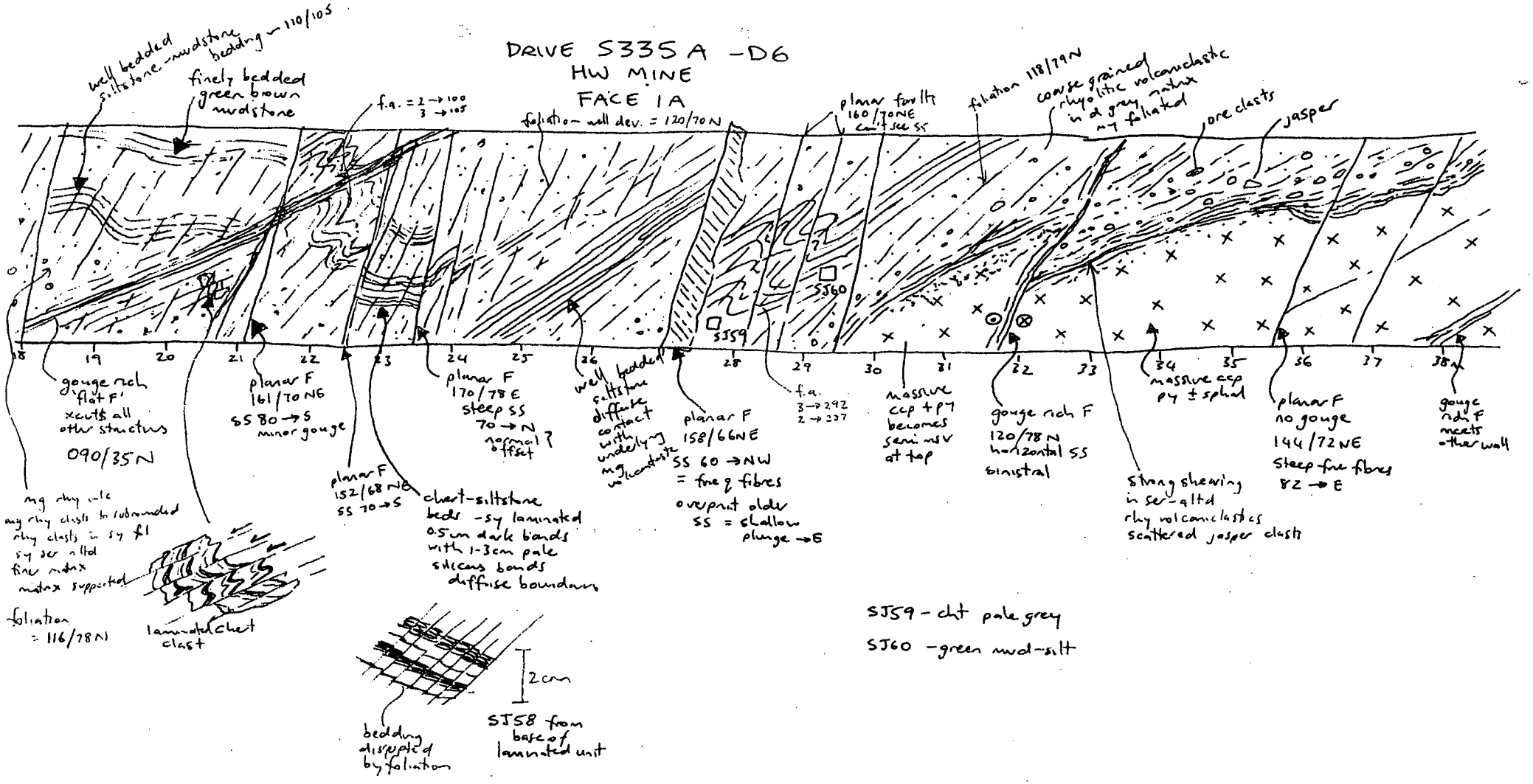
DRIVE S335A -D6
HW MINE
FACE 1A
well bedded siltstone-mudstone bedding ~ 110/10S
finely bedded green brown mudstone
f.a. = 2 → 100, 3 → 105
foliation - well dev. = 120/70N
planar fault 160/70NE cm-f sec SS
foliation 118/79N
coarse grained rhyolitic volcaniclastic in d grey matrix m-f foliated
ore clasts
jasper
SJ60
SJ59
gouge rich 'flat F' xcut$ all other structrs 090/35N
planar F 161/70NE SS 80 → S minor gouge
planar F 152/68NE SS 70 → S
planar F 170/78E steep SS 70 → N normal? offset
well bedded siltstone diffuse contact with underlying mg lithic wacke
planar F 158/66NE SS 60 → NW = fine g fibres overprint older SS = shallow plunge → E
f.a. 3 → 292, 2 → 237
massive ccp + py becomes semi msv at top
gouge rich F 120/78N horizontal SS sinistral
massive ccp py ± sphal
planar F no gouge 144/72NE steep fine fibres 82 → E
gouge rich F meets other wall
mg rhy wke mg rhy clasts to rounded rhy clasts in sy fl sy ser altd fine matrix matrix supported
foliation = 116/78N
laminated chert clast
chert-siltstone beds - sy laminated 0.5cm dark bands with 1-3cm pale silicous bands diffuse boundaries
2cm
bedding disrupted by foliation
SJ58 from base of laminated unit
strong shearing in ser-altd rhy volcaniclastics scattered jasper clasts
SJ59 - cht pale grey
SJ60 - green mud-silt

23 SHOP - HW MINE

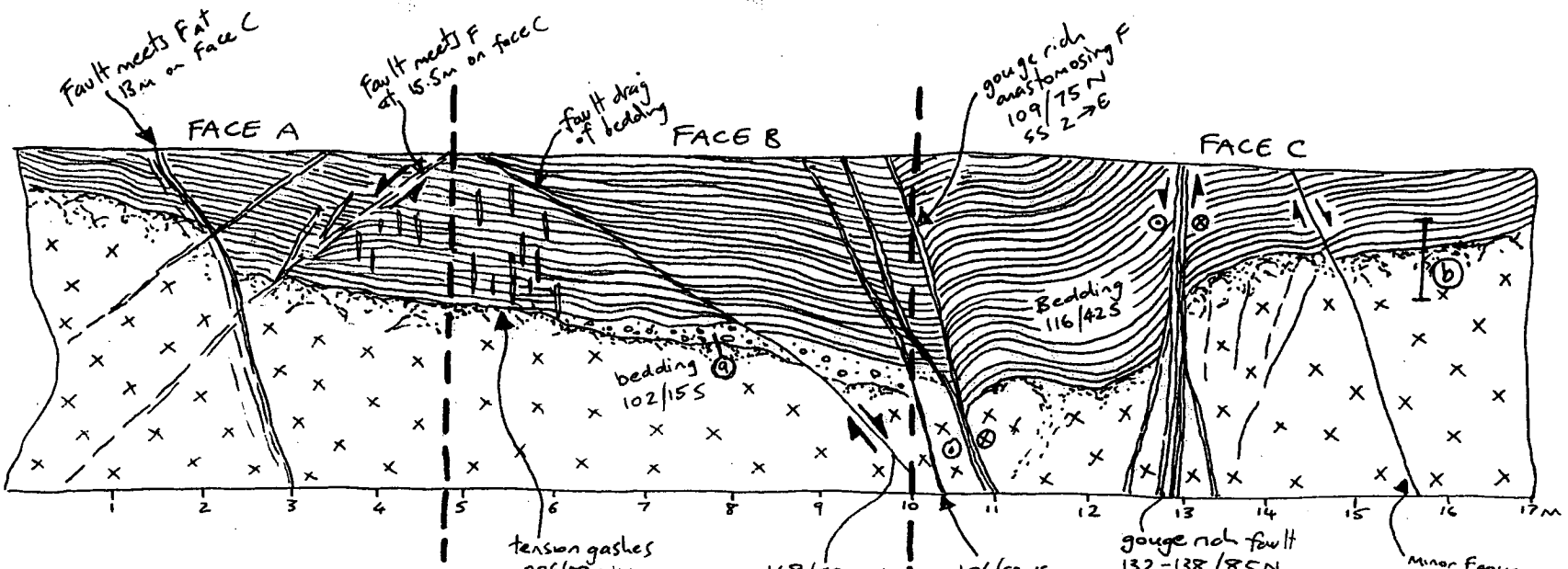

tension gashes
006/88 NW
018/75 E
022/80 E

168/52 SW
SS 70→SW
planar F
v. little gouge & fibres
~normal offset ~30cm
→this fault gets xcutt by large gouge rich F at 11m.

106/52 NE
gouge rich fault
horizontal SS

gouge rich fault
132-138/85N
horizontal SS
sinistral

Minor F gouge
116/64 NE
~planar
horizontal SS
5-10 → W

ⓐ pale to med. grey angular to subrounded rhyolitic clasts in a dk grey sericite altd matrix
-abundant angular argillite rip up clasts at base + minor ore clasts

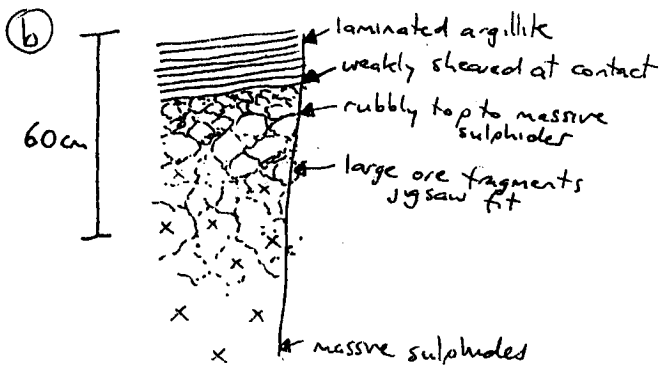

*FACE B faces mine south

Appendix 2:
Sample locations

Sample locations, catalogue numbers, field numbers and samples descriptions are given in the following table.

Catalog#	Field#	DDH	Northing	Easting	Depth (m)	Lithology	Unit	Area	Rock description
147867	F15	18-1003	4168	1420	93.4	sphalerite ore	HW Horizon	Battle main	massive sulphides-py-sphal-ccp
147868	F16	18-975	4160	1420	77.5	barite ore	HW Horizon	Battle main	Upper zone barite-rich massive sulphides
147869	F18	18-979	4162	4160	93.1	chalcopyrite	HW Horizon	Battle main	massive sulphides - ccp rich
147870	F20	N357RP	3640	3680	23 level	quartz vein	HW Horizon	HW main lens	q-tet vein in main HW ore lens
147871	F22	18-1006	4170	1420	101.7	chalcopyrite	HW Horizon	Battle main	ccp-rich massive sulphides, Battle main lens
147872	P189b-G111	L14-641	3338	152	772.97	argillite	HW Horizon	South Flank	black massive to laminated argillite
147873	SJ004b-G84	18-1032	4240	1420	43.6	siltstone	HW Horizon	Battle main	diffusely laminated white siliceous siltstone
147874	SJ009bc-G85	18-1032	4240	1420	62.3	chert	HW Horizon	Battle main	massive chert, weakly laminated, grainy texture
147875	SJ010b-G86	18-1032	4240	1420	66	chert	HW Horizon	Battle main	massive to weakly laminated white chert
147876	SJ017a-G82	18-1032	4240	1420	74	chert	HW Horizon	Battle main	strongly laminated white-pale grey chert
147877	SJ017c	18-1032	4240	1420	74.3	chert	HW Horizon	Battle main	strongly laminated white-pale grey chert
147878	SJ024-G81	18-1032	4240	1420	92.65	siltstone	HW Horizon	Battle main	massive white to pale grey siltstone
147879	SJ025-G29	18-1032	4240	1420	97	chert	HW Horizon	Battle main	white opaque chert, just above mz
147880	SJ026G83	18-1032	4240	1420	98	chert	HW Horizon	Battle main	white massive opaque chert
147881	SJ034	18-1101	4150	1870	40	chert	HW Horizon	Battle main	white massive opaque chert
147882	SJ044-G115	23-493	3666	3565	14.1	argillite	HW Horizon	HW mine	dark grey argillite, weakly laminated
147883	SJ048	W202	4372	4540	999.5	sandstone	HW Andesite	HW North	graded beds, green andesitic sandstone
147884	SJ052-G95	W202	4372	4540	1012.3	argillite	HW Horizon	HW North	black massive to laminated silicified argillite
147885	SJ066-G94	W202	4372	4540	1054	argillite	HW Horizon	HW North	black massive to laminated silicified argillite
147886	SJ074-G113	23-489	3664	3565	14	argillite	HW Horizon	HW mine	black massive to laminated silicified argillite
147887	SJ075-G93	23-489	3664	3565	19.9	argillite	HW Horizon	HW mine	weakly laminated argillite, just above sulphides
147888	SJ080	23-488	3669	3568	2	ore	HW Horizon	HW mine	massive sulphides, ccp rich
147889	SJ083-G116	23-488	3669	3568	11.2	argillite	HW Horizon	HW mine	black massive to weakly laminated argillite
147890	SJ085	23-488	3669	3568	14.3	argillite	HW Horizon	HW mine	black massive to weakly laminated argillite
147891	SJ090	S335A-D6	3620	3280	23 level	rhyolite	HW Horizon	HW mine	pale grey, medium to cg, poorly sorted rhyolite
147892	SJ092	S335A-D6	3620	3280	23 level	rhyolite	HW Horizon	HW mine	pale grey, medium to cg, poorly sorted rhyolite
147893	SJ093	S335A-D6	3620	3280	23 level	jasper	Mixed Volc	HW mine	dark red jasper clasts in rhyolitic volcaniclastic
147894	SJ113	18-1033	4240	1420	56.5	sandstone	HW Horizon	Battle mine	medium grey, medium grained rhyolitic sst
147895	SJ129	18-480	4122	1600	37	chert	HW Horizon	Battle mine	pale grey-white massive chert
147896	SJ134	18-483	4120	1600	36	chert	HW Horizon	Battle mine	pale grey-white massive chert
147897	SJ150	18-1086	3847	2530	40.5	chert	HW Horizon	Extension Zone	pale grey-white massive chert
147898	SJ151	18-1126	4222	1855	59.5	chert	HW Horizon	Battle mine	pale pink-grey to white chert, with siltstone
147899	SJ152	18-1126	4222	1855	61.4	chert	HW Horizon	Battle mine	white chert, strongly laminated, py-sphal stringers
147900	SJ158	18-1127	4222	1855	38	chert	HW Horizon	Battle mine	white massive chert
147901	SJ159	18-1127	4222	1855	38.5	chert	HW Horizon	Battle mine	white massive chert
147902	SJ160	18-1127	4222	1855	39	chert	HW Horizon	Battle mine	white massive chert
147903	SJ161	18-1127	4222	1855	39.4	chert	HW Horizon	Battle mine	white massive chert
147904	SJ161a	18-1127	4222	1855	39.5	chert	HW Horizon	Battle mine	white massive chert
147905	SJ179	18-1091	3850	2530	18	chert	HW Horizon	Extension Zone	white massive chert
147906	SJ221-G103	PR124	3717	5876	136.5	argillite	HW Horizon	Thelwood V.	black massive to weakly laminated argillite, silicified
147907	SJ223b-G120	PR124	3717	5876	126.2	argillite	HW Horizon	Thelwood V.	black massive to weakly laminated argillite, silicified
147908	SJ248-G96	23-503	3666	3565	7.6	siltstone	HW Horizon	HW mine	pale and dark brown banded silstone, just above mz
147909	SJ250-G97	23-503	3666	3565	8	chert/siltstone	HW Horizon	HW mine	pale grey chert/siltstone, laminated
147910	SJ251-G98	23-503	3666	3565	8.8	siltstone	HW Horizon	HW mine	tan to brown laminated siltstone
147911	SJ252a-G79	23-503	3666	3565	14.8	argillite	HW Horizon	HW mine	weakly bedded dark grey mudstone
147912	SJ253-G80	23-503	3666	3565	47	argillite	HW Horizon	HW mine	medium to dark gray weakly laminated argillite

Catalog#	Field#	DDH	Northing	Easting	Depth (m)	Lithology	Unit	Area	Rock description
147913	SJ254a-G76	23-503	3666	3565	55	argillite	HW Horizon	HW mine	dark grey siltstone, weakly laminated
147914	SJ254b-G88	23-503	3666	3565	57	Siltstone	HW Horizon	HW mine	dark grey weakly laminated siltstone
147915	SJ260	23-503	3666	3565	148	argillite	HW Horizon	HW mine	dark grey weakly laminated siltstone and sandstone
147916	SJ261	23-503	3666	3565	135	sandstone	HW Horizon	HW mine	medium grained sandstone, and argillite
147917	SJ287	15-431	4359	823	252.2	chert/siltstone	HW Horizon	Ridge Zone	interbedded chert, siltstone and sandstone
147918	SJ304-G128	L14-680	4393	1260	312.1	siltstone	HW Horizon	Battle south	pale grey weakly laminated siltstone (sst removed)
147919	SJ305-G58	L14-680	4393	1260	313.7	mudstone	HW Horizon	Battle south	Medium to dark grey siltstone bed above chert
147920	SJ307-G129	L14-680	4393	1260	318	siltstone	HW Horizon	Battle south	dark grey weakly laminated siltstone
147921	SJ308-G130	L14-680	4393	1260	320.6	siltstone	HW Horizon	Battle south	dark grey weakly laminated siltstone/sandstone
147922	SJ309-G131	L14-680	4393	1260	324	rhyolite	HW Horizon	Battle south	medium to pale grey rhyolitic volcaniclastic rock
147923	SJ310-G132	L14-680	4393	1260	327.3	siltstone	HW Horizon	Battle south	dark grey angular felsic clasts in argillaceous matrix
147924	SJ311-G133	L14-680	4393	1260	331.1	siltstone	HW Horizon	Battle south	pale to medium grey, med to cg sst-volcaniclastic
147925	SJ312-G134	L14-680	4393	1260	336.7	siltstone	HW Horizon	Battle south	pale to medium grey, med to cg sst-volcaniclastic
147926	SJ313-G46	L14-680	4393	1260	338.9	chert	HW Horizon	Battle south	massive to weakly laminated chert/siltstone
147927	SJ315-G20	L14-680	4393	1260	343.5	siltstone	HW Horizon	Battle south	pale to dark grey diffusely bedded siltstone
147928	SJ316-G31	L14-680	4393	1260	347.9	siltstone	HW Horizon	Battle south	pale grey weakly bedded siltstone, silicified
147929	SJ317-G11	L14-680	4393	1260	352	black chert	HW Horizon	Battle south	black siliceous argillite/chert, weakly laminated
147930	SJ319	23-N350B	3670	3575	23 level	siltstone	HW Horizon	HW mine	strongly laminated silt/sandstone (oriented sample)
147931	SJ327	14-633	4086	182	293	chert	HW Horizon	Ridge Zone	strongly laminated to cm bedded white chert
147932	SJ388-G70	18-1003	4168	1420	45.4	chert	HW Horizon	Battle main	white massive opaque chert, weakly laminated
147933	SJ390-G69	18-1003	4168	1420	47.6	chert	HW Horizon	Battle main	white massive opaque chert, weakly laminated
147934	SJ391-G64	18-1003	4168	1420	62.45	siltstone	HW Horizon	Battle main	white massive siltstone with a grainy texture
147935	SJ394-G63	18-1003	4168	1420	67.4	siltstone	HW Horizon	Battle main	weakly laminated fine-grained siltstone/chert
147936	SJ396-G68	18-1003	4168	1420	72.5	chert	HW Horizon	Battle main	white massive opaque chert
147937	SJ399-G67	18-1003	4168	1420	77.15	chert	HW Horizon	Battle main	pale grey and white chert, diffuse pale brown banding
147938	SJ403-G66	18-1003	4168	1420	83.45	chert	HW Horizon	Battle main	white massive opaque chert
147939	SJ404-G33	18-1003	4168	1420	84.4	chert	HW Horizon	Battle main	white opaque chert
147940	SJ406-G65	18-1003	4168	1420	88.1	chert	HW Horizon	Battle main	brecciated top of massive opaque chert
147941	SJ409	18-1003	4168	1420	103	andesite	Price Andesite	Battle main	pyrite altered andesite
147942	SJ427	18-1004	4168	1420	14.6	QFP	HW Horizon	Battle main	massive quartz-feldspar porphyry, silicified
147943	SJ432-G121	PR124	3717	5876	132	argillite	HW Horizon	Thelwood V.	v bk msv to wy lam arg - only wy sid
147944	SJ432-G122	PR124	3717	5876	132.1	argillite	HW Horizon	Thelwood V.	v bk msv to wy lam arg - only wy sid
147945	SJ434	18-1004	4168	1420	49.5	chert	HW Horizon	Battle main	white opaque chert
147946	SJ440	18-1004	4168	1420	70.6	chert	HW Horizon	Battle main	white opaque chert
147947	SJ441	18-1004	4168	1420	73	chert	HW Horizon	Battle main	white opaque chert - with argillite jellybeans
147948	SJ441b	18-1004	4168	1420	73.8	chert	HW Horizon	Battle main	white opaque chert - with argillite jellybeans
147949	SJ446	18-1004	4168	1420	82	siltstone	HW Horizon	Battle main	fine medium grey silstone
147950	SJ447	18-1004	4168	1420	95.6	andesite	Price Andesite	Battle main	medium-dark grey green, coarse-grained andesite
147951	SJ448b-G73	18-1004	4168	1420	96.2	chert/siltstone	HW Horizon	Battle main	white massive opaque chert, with fine sst removed
147952	SJ448a-G72	18-1004	4168	1420	96.4	siltstone	HW Horizon	Battle main	medium brown, tan and pale green siltstone
147953	SJ449	18-1004	4168	1420	98	siltstone	HW Horizon	Battle main	brown massive siltstone just above mz
147954	SJ454-G62	18-980	4165	1420	74.7	chert	HW Horizon	Battle main	massive to weakly laminated chert, grainy texture
147955	SJ458-G77	18-980	4165	1420	82.3	chert	HW Horizon	Battle main	white massive opaque chert
147956	SJ460-G78	18-980	4165	1420	85.2	siltstone	HW Horizon	Battle main	strongly laminated fine-grained siltstone/chert
147957	SJ469-G71	18-1000	4167	1420	58	chert	HW Horizon	Battle main	pale grey and white chert, diffuse pale brown banding
147958	SJ477	23-514	3815	3485	10.2	ore-clast bx	Mixed volc	HW mine	med grained to coarse grained ore clast breccia

Catalog#	Field#	DDH	Northing	Easting	Depth (m)	Lithology	Unit	Area	Rock description
147959	SJ491-G119	23-514	3815	3485	94.5	argillite	HW Horizon	HW mine	black massive to weakly laminated argillite
147960	SJ492a-G117	23-514	3815	3485	95	argillite	HW Horizon	HW mine	dark grey argillite, weakly laminated
147961	SJ492b-G118	23-514	3815	3485	95.1	argillite	HW Horizon	HW mine	dark grey argillite, weakly laminated
147962	SJ513	ST183A	4080	1830	18 level	siltstone/pyrite	HW Horizon	Battle mine	laminated dark grey siltstone and contact with mz
147963	SJ525	ST183A	4080	1830	18 level	chert	HW Horizon	Battle mine	strongly laminated to massive white-pale pink chert
147964	SJ526	ST183A	4080	1830	18 level	chert	HW Horizon	Battle mine	strongly laminated to massive white-pale pink chert
147965	SJ527	ST183A	4080	1830	18 level	chert	HW Horizon	Battle mine	strongly laminated to massive white-pale pink chert
147966	SJ528	ST183A	4080	1830	18 level	chert	HW Horizon	Battle mine	strongly laminated to massive white-pale pink chert
147967	SJ529	ST183A	4080	1830	18 level	chert	HW Horizon	Battle mine	strongly laminated to massive white-pale pink chert
147968	SJ530	ST183A	4080	1830	18 level	chert	HW Horizon	Battle mine	strongly laminated to massive white-pale pink chert
147969	SJ531	ST183A	4080	1830	18 level	chert	HW Horizon	Battle mine	strongly laminated to massive white-pale pink chert
147970	SJ534a	ST183A	4080	1830	18 level	rhyolite	HW Horizon	Battle mine	coarse-grained, poorly sorted rhyolitic volcaniclastic
147971	SJ534b	ST183A	4080	1830	18 level	rhyolite	HW Horizon	Battle mine	cg poorly sorted rhyolitic volcanics and chert contact
147972	SJ535	ST183A	4080	1830	18 level	rhyolite	HW Horizon	Battle mine	sulphide-rich mud and overlying felsic sandstone
147973	SJ539-G87	18-980	4165	1420	61	chert	HW Horizon	Battle main	white massive opaque chert
147974	SJ542-G135	20-845	3975	4405	3.7	andesite	HW Andesite	HW 43 Block	msv and sst (mud layers removed)
147975	SJ545	20-845	3975	4405	11.3	andesite	HW Andesite	HW 43 Block	cg, poorly sorted angular andesite clasts
147976	SJ550	20-845	3975	4405	21	dacite	HW Horizon	HW 43 Block	massive, medium grey green, chl-ep rich dacite
147977	SJ552-G139	20-845	3975	4405	42.9	FQP	HW Horizon	HW 43 Block	massive feldspar-quartz porphyry
147978	SJ553ab-G14	20-845	3975	4405	57.7	sandstone	HW Horizon	HW 43 Block	strongly foliated pale grey, sericitic altered rhy sst
147979	SJ555-G144	20-845	3975	4405	85.5	sandstone	HW Horizon	HW 43 Block	pale grey-green graded sandstone, rhy-dac
147980	SJ556-G145	20-845	3975	4405	89.4	sandstone	HW Horizon	HW 43 Block	pale grey-green graded sandstone, rhy-dac
147981	SJ558-G146	20-845	3975	4405	97.8	Price Andesite	Price Andesite	HW 43 Block	cg andesitic volcaniclastics, angular clasts
147982	SJ558A-G136	20-675	3971	4390	5.9	volcaniclastics	HW Horizon	HW 43 Block	rhyolitic clasts in a dacitic matrix
147983	SJ559-G148	20-845	3975	4405	110	Price Andesite	Price Andesite	HW 43 Block	cg and. volcs, angular clasts in gn matrix, bleached
147984	SJ561-G137	20-675	3971	4390	13.5	Dacite	HW Horizon	HW 43 Block	massive dactite, med green, minor haematite
147985	SJ565-G138	20-675	3971	4390	27	siltstone	HW Horizon	HW 43 Block	Dark-pale grey-green, laminated silt (andesitic?)
147986	SJ566	20-675	3971	4390	28	siltstone	HW Horizon	HW 43 Block	Dark-pale grey, laminated siltstone, arg jellybeans
147987	SJ568-G141	20-675	3971	4390	64.7	ore	HW Horizon	HW 43 Block	semi-massive sphalerite-rich sulphides
147988	SJ570-G142	20-675	3971	4390	71	ore	HW Horizon	HW 43 Block	top of sulphides, gradational contact into cg rhyolite
147989	SJ571-G143	20-675	3971	4390	81.5	ore	HW Horizon	HW 43 Block	basal contact of sulphides with cg rhy volcaniclastics
147990	SJ572-G147	20-675	3971	4390	103.7	Price Andesite	Price Andesite	HW 43 Block	cg andesitic volcaniclastics, angular clasts
147991	SJ588	L15-501	4492	1010	365	FQP	HW Horizon	Marshall Zone	massive, medium grey, feldspar phyric
147992	SJ601	16-33	3176	2195	26	conglomerate	HW Horizon	South Flank	basal contact rhyolite and dark green andesite
147993	SJ605-G101	16-33	3176	2195	117.1	argillite	HW Horizon	South Flank	black finely laminated argillite
147994	SJ607-G92	16-33	3176	2195	164.3	argillite	HW Horizon	South Flank	black finely laminated argillite
147995	SJ608-G17	L10-2024	5100	420	845	QFP	HW Horizon	Marshall Zone	p gy sy sil msv qfp with very fine q-f pno'
147996	SJ620	PR13-68	3828	5244	30.4	dacite	Upper dacite	Price Hillside	massive medium green weakly feldspar phyric dacite
147997	SJ621-G126	PR13-68	3828	5244	34.4	argillite	HW Horizon	Price Hillside	bk msv to wy lam arg - my to sy sid w mn py vng tt
147998	SJ621-G127	PR13-68	3828	5244	34.55	argillite	HW Horizon	Price Hillside	bk msv to wy lam arg - my to sy sid w mn py vng tt
147999	SJ624-G102	PR13-68	3828	5244	81.3	argillite	HW Horizon	Price Hillside	bk msv to wy lam arg - wy sid
148000	SJ629-G89	CR88-4	2441	6695	552.4	siltstone	HW Horizon	Thelwood V.	grey massive to weakly bedded silicified siltstone
148001	SJ629-G90	CR88-4	2441	6695	551.8	argillite	HW Horizon	Thelwood V.	black silicified argillite
148002	SJ629-G18	CR88-4	2441	6695	552.4	siltstone	HW Horizon	Thelwood V.	grey massive to weakly bedded silicified siltstone
148003	SJ630-G91	CR88-4	2441	6695	557.7	argillite	HW Horizon	Thelwood V.	black silicified argillite

Catalog#	Field#	DDH	Northing	Easting	Depth (m)	Lithology	Unit	Area	Rock description
148004	SJ634	Karst Creek				limestone	Karst Ck Fm	Karst Creek	pale grey, medium to coarse-grained, crinoid lst
148005	SJ635	Price Hillside				volcaniclastics	Upper mafics	Jim Mitchell Rd	medium and dark green, chl-ep rich, cg andesite
148006	SJ637-G36	21 L manway	3795	3400	21 level	argillite	HW Horizon	HW mine	black cm scale bedded graphitic argillite
148007	SJ638-G27	S335C	3680	3380	23 level	chert/siltstone	HW Horizon	HW mine	pale grey-brown siltstone-chert just above mz
148008	SJ639	S335C	3680	3380	23 level	mz/chert	HW Horizon	HW mine	top of massive sulphides with chert stringers
148009	SJ642-G22	S335C	3680	3380	23 level	chert/siltstone	HW Horizon	HW mine	pale grey chert/siltstone with a slightly grainy texture
148010	SJ643-G23	S335C	3680	3380	23 level	siltstone	HW Horizon	HW mine	pale grey siltstone with fine diffuse py bands
148011	SJ644-G21	S335C	3680	3380	23 level	chert/siltstone	HW Horizon	HW mine	Diffusely banded pale and dark grey siliceous zones
148012	SJ646-G19	S335C	3680	3380	23 level	chert/siltstone	HW Horizon	HW mine	banded silt/chert, tan to brown colour
148013	SJ646T-G25	S335C	3680	3380	23 level	chert/siltstone	HW Horizon	HW mine	green silt/chert
148014	SJ648-G24	S335C	3680	3380	23 level	Sandstone	HW Horizon	HW mine	medium grained pale grey sandstone
148015	SJ650-G26	S335C	3680	3380	23 level	chert/siltstone	HW Horizon	HW mine	tan-brown silt bands - very top of sequence below sst
148016	SJ658	S353DD	3620	3500	23 level	jasper clast	Mixed volc	HW mine	dark red and white, altered jasper clast in cg rhyolite
148017	SJ660-G114	23 SHOP	3795	3440	23 level	argillite	HW Horizon	HW mine	black massive to weakly laminated argillite
148018	SJ669-G28	23 SHOP	3795	3440	23 level	argillite	HW Horizon	HW mine	black cm scale bedded graphitic argillite
148019	SJ670	23 SHOP	3795	3440	23 level	argillite	HW Horizon	HW mine	black argillite interbedded with mg rhyolite
148020	SJ696	18-976	4164	1420	24	QFP	HW Horizon	Battle mine	pale grey, massive quartz-feldspar phyric, silicified
148021	SJ716	L14-641	3338	156	773.5	argillite	HW Horizon	South Flank	black massive to weakly laminated argillite
148022	SJ717-G74	L14-641	3338	156	779.5	argillite	HW Horizon	South Flank	black massive to weakly laminated argillite
148023	SJ718-G75	L14-641	3338	156	785.8	argillite	HW Horizon	South Flank	black massive to weakly laminated argillite
148024	SJ719	L14-641	3338	156	782.2	silt/argillite/mz	HW Horizon	South Flank	pale grey siltstone and interbedded argillite
148025	SJ722-G15	L14-682	3842	1260	342.8	sandstone	HW Horizon	Battle south	weakly bedded fine-grained sandstone
148026	SJ723a-G38	L14-682	3842	1260	350.8	chert	HW Horizon	Battle south	brecciated top of massive opaque chert
148027	SJ723b-G14	L14-682	3842	1260	351.3	siltstone	HW Horizon	Battle south	pale grey weakly bedded siltstone (sst removed)
148028	SJ731-G99	21-2072	3865	3416	44	argillite	HW Horizon	HW mine	black strongly laminated argillite
148029	SJ732-G112	21-2072	3865	3416	44.2	argillite	HW Horizon	HW mine	black massive to weakly laminated argillite
148030	SJ733-G100	21-2072	3865	3416	45.3	argillite	HW Horizon	HW mine	black strongly laminated argillite
148031	SJ740	21-2072	3865	3416	105.6	andesite	HW Horizon	HW mine	cg angular andesite clasts, matrix supported
148032	SJ749	G171XS	4070	1700	18 level	chert	HW Horizon	Gopher zone	fine pale grey-green chert/siltstone
148033	SJ751	G171XS	4070	1700	18 level	chert	HW Horizon	Gopher zone	fine pale grey-green chert/siltstone
148034	SJ752	G171XS	4070	1700	18 level	chert	HW Horizon	Gopher zone	fine pale grey-green chert/siltstone
148035	SJ753	G171XS	4070	1700	18 level	chert	HW Horizon	Gopher zone	fine pale grey-green chert/siltstone
148036	SJ754-G32	G171XS	4070	1700	18 level	chert	HW Horizon	Gopher zone	fine pale grey-green chert/siltstone
148037	SJ755	G171XS	4070	1700	18 level	chert	HW Horizon	Gopher zone	fine pale grey-green chert/siltstone
148038	SJ757	G171XS	4070	1700	18 level	chert	HW Horizon	Gopher zone	fine pale grey-green chert/siltstone
148039	SJ758	G171XS	4070	1700	18 level	chert	HW Horizon	Gopher zone	fine pale grey-green chert/siltstone
148040	SJ759	G171XS	4070	1700	18 level	chert	HW Horizon	Gopher zone	fine pale grey-green chert/siltstone
148041	SJ760	G171XS	4070	1700	18 level	chert	HW Horizon	Gopher zone	fine pale grey-green chert/siltstone
148042	SJ761-G30	G171XS	4070	1700	18 level	mudstone	HW Horizon	Gopher zone	pale-medium grey siliceous green siltstone
148043	SJ763-G37	L14-677	3842	1260	216.8	siltstone	HW Horizon	Battle south	pale grey weakly bedded siltstone, silicified
148044	SJ764a-G07	L14-677	3842	1260	220.7	argillite	HW Horizon	Battle south	medium to dark grey argillite-siltstone, silicified
148045	SJ764b-G45	L14-676	3842	1260	220.7	siltstone	HW Horizon	Battle south	pale grey siltstone, weakly bedded, silicified
148046	SJ765a-G34	L14-676	3842	1260	231.3	argillite	HW Horizon	Battle south	medium grey-black argillite/siltstone, weakly bedded
148047	SJ765b-G44	L14-676	3842	1260	231.3	argillite	HW Horizon	Battle south	medium grey-dark grey laminated argillite-siltstone
148048	SJ766a-G08	L14-676	3842	1260	233	argillite	HW Horizon	Battle south	black massive argillite
148049	SJ766b-G43	L14-676	3842	1260	233.3	argillite	HW Horizon	Battle south	black argillite, mm laminations

Catalog#	Field#	DDH	Northing	Easting	Depth (m)	Lithology	Unit	Area	Rock description
148050	SJ771-G01	L14-683	3842	1260	382.8	argillite	HW Horizon	Battle south	laminated medium grey siltstone-argillite
148051	SJ772a-G02	L14-683	3842	1260	394.8	chert	HW Horizon	Battle south	massive to weakly laminated chert, grainy texture
148052	SJ772b-G39	L14-683	3842	1260	395.4	siltstone	HW Horizon	Battle south	pale grey weakly bedded siltstone, silicified
148053	SJ773-G03	L14-683	3842	1260	395.6	chert	HW Horizon	Battle south	massive to weakly laminated chert, grainy texture
148054	SJ774-G04	L14-683	3842	1260	397.1	siltstone	HW Horizon	Battle south	pale grey weakly bedded siltstone, silicified
148055	SJ775-G05	L14-683	3842	1260	399.7	siltstone	HW Horizon	Battle south	pale grey weakly bedded siltstone, silicified
148056	SJ776a-G40	L14-683	3842	1260	400.7	black chert	HW Horizon	Battle south	medium-dark grey siliceous arg-chert, diffuse beds
148057	SJ776b-G06	L14-683	3842	1260	400.2	chert	HW Horizon	Battle south	white massive opaque chert, just below mz
148058	SJ776c-G42	L14-683	3842	1260	400.67	mudstone	HW Horizon	Battle south	tan mudstone with diffuse margins with white chert
148059	SJ776d-G41	L14-683	3842	1260	401.2	mudstone	HW Horizon	Battle south	Fine tan layers interbedded with white chert
148060	SJ778	L14-683	3842	1260	427.6	andesite	HW Horizon	Battle south	pale to medium grey green, ser-altered andesite
148061	SJ782	L14-681	3842	1260	345.2	jasper/rhyolite	HW Horizon	Battle south	cg rhyolite with jasper clasts, poorly sorted
148062	SJ783-G47	L14-681	3842	1260	352.9	siltstone	HW Horizon	Battle south	pale grey weakly bedded siltstone, silicified
148063	SJ783-G09	L14-681	3842	1260	355.2	siltstone	HW Horizon	Battle south	pale grey bedded siltstone, silicified, grainy texture
148064	SJ784a-G48	L14-681	3842	1260	355.55	siltstone	HW Horizon	Battle south	medium grey weakly bedded siltstone, silicified
148065	SJ784b-G12	L14-681	3842	1260	356.7	siltstone	HW Horizon	Battle south	pale grey weakly bedded siltstone
148066	SJ785a-G49	L14-681	3842	1260	363.5	chert	HW Horizon	Battle south	pale grey massive chert
148067	SJ785b-G16	L14-681	3842	1260	363.2	chert	HW Horizon	Battle south	diffuse bands pale-medium grey chert-argillite
148068	SJ786a-G50	L14-681	3842	1260	363.9	black chert	HW Horizon	Battle south	black to dark grey siliceous argillite
148069	SJ786b-G10	L14-681	3842	1260	364	chert	HW Horizon	Battle south	white and pale grey chert, diffuse banding
148070	SJ787-G51	L14-681	3842	1260	364.6	chert	HW Horizon	Battle south	pale grey and white chert, diffuse pale brown bands
148071	SJ788a-G35	L14-681	3842	1260	365.9	chert	HW Horizon	Battle south	pale grey laminated chert
148072	SJ788b-G52	L14-681	3842	1260	365.4	chert	HW Horizon	Battle south	medium grey weakly laminated chert (sst removed)
148073	SJ789a-G53	L14-681	3842	1260	366.35	chert	HW Horizon	Battle south	white and pale grey chert, diffuse banding
148074	SJ789b-G13	L14-681	3842	1260	378.7	chert	HW Horizon	Battle south	pale to dark grey diffusely banded chert
148075	SJ792	L14-683	3842	1260	329.5	QFP	HW Horizon	Battle south	pale grey, massive quartz-feldspar phyric, silicified
148076	SJ796	P13-304	3565	3796	407	FQP	HW Horizon	HW mine	massive pale grey, feldspar phyric, weakly silicified
148077	SJ806-G56	L14-680	4393	1260	350.6	black chert	HW Horizon	Battle south	black siliceous argillite/chert, weakly laminated
148078	SJ807-G105	L14-680	4393	1260	349.7	black chert	HW Horizon	Battle south	black weakly laminated siliceous argillite
148079	SJ808-G55	L14-680	4393	1260	348.1	black chert	HW Horizon	Battle south	black siliceous argillite/chert, weakly laminated
148080	SJ809-G107	L14-680	4393	1260	352.7	black chert	HW Horizon	Battle south	black weakly laminated siliceous argillite
148081	SJ810a-G106	L14-680	4393	1260	358.5	black chert	HW Horizon	Battle south	black weakly laminated siliceous argillite
148082	SJ810b-G57	L14-680	4393	1260	358.65	black chert	HW Horizon	Battle south	medium grey siliceous argillite-chert, diffuse banding
148083	SJ812-G109	L14-680	4393	1260	357.8	black chert	HW Horizon	Battle south	black weakly laminated siliceous argillite
148084	SJ813-G104	L14-680	4393	1260	357.2	black chert	HW Horizon	Battle south	black weakly laminated siliceous argillite
148085	SJ815-G54	L14-680	4393	1260	356.4	black chert	HW Horizon	Battle south	strongly siliceous black weakly laminated argillite
148086	SJ817-G110	L14-680	4393	1260	353.9	black chert	HW Horizon	Battle south	black weakly laminated siliceous argillite
148087	SJ818-G108	L14-680	4393	1260	353.7	black chert	HW Horizon	Battle south	black weakly laminated siliceous argillite
148088	SJ819-G60	L14-679	3842	1263	246.5	Siltstone	HW Horizon	Battle south	massive white to pale grey siltstone
148089	SJ822-G59	L14-679	3842	1263	300.9	argillite	HW Horizon	Battle south	medium grey laminated argillite
148090	SJ824-G61	16-43	3180	2180	481.6	argillite	HW Horizon	South Flank	argillite jellybeans in laminated argillite
148091	SJ830-G123	16-36	3180	2180	244.2	argillite	HW Horizon	South Flank	weakly laminated dark grey argillite (sst removed)
148092	SJ831-G124	16-45	3180	2300	123.4	argillite	HW Horizon	South Flank	black massive and laminated argillite, silicified
148093	SJ832-G125	16-61	3180	2400	364.2	argillite	HW Horizon	South Flank	black massive and laminated argillite, silicified
148094	SJ833	Westmin Rd	5020	5200		mudstone	Thelwood	Westmin Rd	laminated green mudstone interbedded sandstone
	49337*	16-642	4150	1260	282.2	argillite	HW Horizon	Battle south	black laminated mudstone

* sample from Myra Falls mine database

Appendix 3:
XRF analyses

Glass disks and pressed powder pellets were analysed by Phil Robinson on the Phillips PW1480 X-ray spectrometer at the Geology Department, University of Tasmania.

Instrument specifications

X-Ray Tubes 3kW max. ScMo anode side window
Elements analysed: Majors, S and Y, Rb, U, Th, Cu, Pb, Zn, Ni, As, Bi, Co, Ga, Tl, Se, W, Br
3kW max. Au anode side window.
Elements analysed: Nb, Zr, Sr, Ba, Cr, V, Sc, La, Ce, Nd, Sb, Sn
3kW max. Rh anode side window.
Elements analysed: Mo, occasionally Nb

Crystals: LiF 200, LiF 220, PX-1 (for Na and Mg), PE002, Ge111

Collimators: Coarse (0.7mm) and fine (0.3mm) with auxiliary (0.14mm)

Detectors: Gas flow proportional counter with P10 gas (10% methane in argon) and Scintillation Counter.

Sample Changer: Philips 30 position sample holder

Sample Preparation

Samples were crushed, pulverised (tungsten-carbide mill) and made into pressed powder pills using the method of Norrish and Chappell (1977), and fused discs by the method of Norrish and Hutton (1969). Co, W and Tl were not analysed because of the potential contamination from use of the tungsten-carbide mill during sample preparation.

Corrections

Corrections for mass absorption are calculated using Philips X40 software with De Jongh's calibration model and Philips (or CSIRO) alpha coefficients. Compton scattering is also used for many trace elements.

Calibration

Pure element oxide mixes in pure silica, along with international and Tasmanian standard rocks are used. Numerous checks of standard rocks and pure silica blanks are run with each program. On average, 2-3 standards, blanks, and one duplicate analysis was analysed for every 6-7 samples analysed.

Loss on Ignition (LOI)

Loss on ignition (L.O.I.) is the sum of H_2O^+, H_2O^-, and other gaseous phases measured on approximately 1 gm of powder held at 1000°C for 24 hours. The total iron content of analyses is expressed as Fe_2O_3 (unless otherwise specified).

Detection Limits

Major elements (wt. %)		Trace elements (ppm)			
SiO_2	0.02	Sb	2	Bi	2
TiO_2	0.006	Cd	1	Nb	1
Al_2O_3	0.008	Ag	2	Ba	4
Fe_2O_3	0.0041	Zn	1	Sr	1
MnO	0.0035	Cu	1	Rb	1
MgO	0.011	Ni	1	Tl	2
CaO	0.0009	Cr	1	Sc	2
Na_2O	0.024	V	1.5	Zr	1
K_2O	0.0004	U	1.5	Ga	1
P_2O_5	0.0026	Th	1.5	Y	1

Battle Basin Argillite XRF analyses

	Battle argillite	Battle argillite	Battle argillite	Battle argillite	Battle argillite	Battle argillite	Battle argillite	Battle argillite
Catalogue #								
field #	SJ766-G8	SJ765-G34	SJ764-G7	SJ766-G43	SJ765-G44	SJ822-G59	SJ771-G1	49337*
Drillhole/loc.	L14-676	L14-676	L14-677	L14-676	L14-676	L14-679	L14-683	16-642
wt.%								
SiO2	69.44	82.21	47.03	72.15	72.23	63.15	70.79	85.50
TiO2	0.32	0.27	0.23	0.36	0.29	0.46	0.30	0.17
Al2O3	8.36	7.78	8.02	10.37	11.18	13.39	14.04	5.97
Fe2O3	4.02	1.82	3.41	2.83	3.17	6.75	4.59	2.57
MnO	0.04	0.01	0.12	0.02	0.02	0.07	0.01	0.04
MgO	1.99	0.97	1.67	1.98	1.37	5.54	0.46	0.48
CaO	4.62	0.85	18.70	2.24	2.36	1.61	0.09	0.46
Na2O	0.10	0.50	0.45	0.13	3.50	3.85	0.31	0.05
K2O	2.38	2.21	2.02	2.89	1.37	0.42	3.81	1.74
P2O5	0.10	0.07	2.93	0.08	0.09	0.27	0.02	0.02
Loss inc. S	7.62	2.49	14.69	5.29	4.20	4.03	4.40	3.00
Total	99.51	99.58	99.55	99.31	100.03	99.73	99.63	
S	2.65	1.02	1.88	1.62	1.76	2.00	0.00	
ppm								
Y	15.7	14.7	36.8	19.1	19.4	18.5	16.7	4.5
U	8.6	7.2	14.6	15.2	8.7	2.0	2.6	
Rb	31.6	28.9	25.9	39.6	18.7	4.5	49.7	
Th	2.1	1.8	1.5	3.6	3.2	2.9	<1.5	
Pb	99	133	96	289	50	62	43	
As	136.2	67.5	76.9	267.9	113.0	12.2	21.4	
Tl	<1	<1	<1	<1	<1	1.13	5.96	
Bi	<2	<2	<2	<2	<2	<2	<2	
Zn	2300	1344	873	5100	715	258	210	1830
Cu	150	129	108	180	43	72	24	164
Ni	78.0	38.1	46.9	110.0	35.5	39.0	5.9	40.0
Sb	9.8	1.9	3.9	7.2	3.3	<2	<2	
Cd	16.7	12.8	11.5	45.7	6.4	<1	<1.5	
Ag	6.0	2.8	6.2	6.1	<2	2.3	<2	
Nb	4.4	3.3	3.7	5.6	4.2	3.3	4.7	
Zr	72.9	67.4	68.6	107.2	87.1	94.0	112.4	
Sr	79.0	26.0	240.0	46.0	93.0	145.0	33.0	12.9
Ba	1900	1900	1437	2550	1355	1271	7076	
Sc	13.40	9.90	21.10	11.47	9.12	18.05	10.50	4.90
V	1035.4	669.7	704.8	2216.5	318.4	182.3	66.0	519.0
Cr	47.8	35.1	52.0	120.5	18.6	59.2	23.8	72.0
Ga	11.2	7.9	8.6	11.8	8.9	10.1	14.8	

* sample from Myra Falls mine database

Battle Basin black chert XRF analyses

Battle black chert	Battle bk cht	Battle black cht	Battle black cht	Battle black cht
SJ317-G11	SJ786-G50	SJ815-G54	SJ808-G55	SJ806-G56
L14-680	L14-681	L14-680	L14-680	L14-680
95.85	95.96	89.94	92.64	92.58
0.05	0.08	0.15	0.05	0.10
1.14	2.16	3.39	1.47	2.92
0.88	0.36	1.81	0.74	1.24
<0.01	<0.01	<0.01	0.06	0.00
0.06	0.07	0.15	0.71	0.15
0.02	0.07	0.08	1.24	0.23
0.01	0.04	<0.03	0.04	0.04
0.33	0.58	1.02	0.40	0.89
0.00	0.04	0.06	0.07	0.17
1.13	0.62	2.12	2.38	1.51
99.91	100.19	100.20	99.93	100.01
0.80	0.29	1.85	0.25	0.98
1.1	3.3	4.7	6.2	7.9
<1.5	<1.5	5.0	<1.5	3.5
4.6	8.1	12.2	5.7	12.6
3.3	<2	<2	<2	<2
877	3	1554	135	93
83.6	9.9	167.4	34.3	44.2
<1	1.38	1.05	1.81	<1
<2	<2	2.21	<2	<2
1600	1274	8200	158	21
757	213	961	46	37
11.2	2.2	38.8	7.8	18.5
371.8	<2	40.4	3.6	8.2
5.6	4.1	32.2	<1	<1
204.9	<2	35.8	2.2	5.2
1.3	<1	1.7	1.0	1.3
10.2	9.4	29.1	12.0	17.7
1.0	8.0	3.0	10.0	16.0
536	215	1449	783	1437
4.70	1.97	2.91	<2	3.01
55.9	57.3	538.6	54.4	141.3
18.1	15.9	32.9	17.0	34.3
1.0	3.8	3.5	1.7	2.9

Battle Basin black chert XRF analyses

	Battle black cht	Battle black cht	Battle black cht	Battle black cht	Battle black cht	Battle black cht	Battle black cht	Battle black cht	Battle black cht
Catalogue #									
field #	SJ813-G104	SJ807-G105	SJ810-G106	SJ809-G107	SJ818-G108	SJ812-G109	SJ817-G110	SJ810-G57	SJ776-G40
Drillhole/loc.	L14-680	L14-680	L14-680	L14-680	L14-680	L14-680	L14-680	L14-680	L14-683
wt.%									
SiO2	89.23	94.21	93.01	94.81	95.77	93.39	96.11	91.55	92.20
TiO2	0.12	0.09	0.08	0.08	0.06	0.07	0.05	0.13	0.12
Al2O3	2.97	2.07	2.09	1.67	1.43	1.64	1.51	2.83	3.22
Fe2O3	2.37	0.76	1.66	0.86	0.47	1.18	0.43	1.04	0.47
MnO	0.00	0.01	0.00	0.00	0.00	0.00	0.00	0.01	0.02
MgO	0.10	0.18	0.09	0.07	0.07	0.05	0.07	0.27	0.14
CaO	0.13	0.31	0.05	0.04	-0.01	0.02	0.01	0.85	0.22
Na2O	0.00	0.00	-0.03	-0.02	0.01	0.01	0.01	0.04	<0.03
K2O	0.89	0.62	0.63	0.50	0.44	0.49	0.46	0.80	0.87
P2O5	0.10	0.01	0.05	0.04	0.00	0.02	0.01	0.30	0.01
Loss inc. S	2.33	1.40	1.49	1.18	0.92	1.39	0.85	1.53	1.23
Total	100.21	100.07	99.83	99.65	99.85	99.82	100.30	100.40	100.24
S	2.35	0.63	1.41	0.76	0.54	1.37	0.50	0.93	0.83
ppm									
Y	4.7	4.8	2.7	5.0	3.1	2.6	2.5	5.5	4.7
U	6.5	1.9	5.7	3.2	2.0	4.1	<1.5	7.2	2.4
Rb	10.0	8.5	7.2	6.8	5.9	6.5	5.7	9.5	10.9
Th	4.9	1.5	2.2	<1.5	2.7	5.0	4.7	<2	<2
Pb	3400	812	1166	483	1616	2107	2500	2043	4000
As	297.6	39.2	73.8	47.7	12.9	154.1	12.7	102.2	197.9
Tl	3.50	<2	<2	<2	<2	<2	<2	1.04	Pb, Ba interf.
Bi	<2	<2	<2	<2	<2	<2	<2	<2	<2
Zn	9900	1231	3400	1683	3300	8900	3100	5346	9000
Cu	1809	58	203	161	189	737	298	309	446
Ni	61.3	12.9	40.9	15.3	7.8	57.1	7.8	55.5	2.9
Sb	351.0	14.2	38.2	59.9	29.5	197.5	36.6	27.1	6.7
Cd	38.1	5.5	13.4	6.5	11.5	35.0	11.2	20.9	32.4
Ag	122.7	9.4	36.4	39.6	25.7	138.3	29.7	35.9	3.3
Nb	1.1	<1	1.2	1.1	<1	1.2	<1	2.4	1.3
Zr	23.4	12.6	19.0	14.3	12.8	14.3	9.2	29.2	29.7
Sr	2.0	6.0	2.0	2.0	1.0	<1	1.0	9.0	6.0
Ba	1217	1020	1050	785	694	738	724	1178	1295
Sc	3.50	2.90	<2	2.10	2.10	2.50	<2	<2	2.63
V	221.9	122.7	418.2	226.0	132.2	430.9	76.2	644.4	152.8
Cr	15.9	27.1	21.1	33.5	20.7	23.4	18.3	39.8	25.8
Ga	2.9	2.3	2.1	1.8	1.7	<1	1.0	2.3	2.9

Battle Mine white-pale grey chert XRF analyses

Battle white cht	Battle white cht	Battle white cht	Battle white cht	Battle white cht
SJ788-G35	SJ788-G52	SJ789-G53	SJ789-G13	SJ404-G33
L14-681	L14-681	L14-681	L14-681	18-1003
95.41	95.14	86.47	86.06	95.77
0.07	0.06	0.12	0.25	0.04
1.65	1.49	2.94	6.00	1.17
0.24	0.33	1.56	0.81	0.30
<0.01	<0.01	0.01	0.01	0.02
0.06	0.06	0.11	0.21	0.36
0.01	0.09	0.20	0.09	0.28
<0.05	0.05	<0.03	0.14	<0.05
0.45	0.44	0.83	1.71	0.26
0.01	0.07	0.16	0.08	0.01
0.75	0.80	2.02	1.61	0.90
100.10	100.11	99.57	100.11	99.94
0.64	0.73	2.86	1.51	0.32
3.5	3.3	6.3	14.6	2.8
1.7	2.6	5.0	10.7	<1.5
6.6	6.4	11.1	22.3	4.1
<1.5	<2	<2	3.6	3.9
4	10	41	4	713
24.1	11.6	43.9	117.1	<3
1.14	<1	1.26	1.35	<1
<2	<2	4.41	<2	<2
10925	11385	38016	22900	5623
624	1220	3100	1881	242
4.3	4.3	25.9	46.6	5.4
<2	2.0	4.1	2.2	<2
41.1	41.7	150.7	91.3	22.6
<2	<2	2.5	<2	<2
1.1	1.4	1.0	3.1	<1
13.5	12.2	21.4	51.5	8.2
5.0	4.0	10.0	15.0	3.0
139	137	228	453	173
<2	<2	<2	5.90	<2
208.7	226.8	256.8	1186.6	100.3
30.0	24.8	17.4	60.3	20.0
2.0	1.9	2.8	7.4	2.0

Battle Mine white-pale grey chert XRF analyses

	Battle white cht	Battle white cht	Battle white cht	Battle white cht	Battle white cht	Battle white cht	Battle white cht	Battle white cht	Battle white cht	Battle white cht	Battle white cht	Battle white cht	Battle white cht	Battle white cht
Catalogue #														
field #	SJ25-G29	SJ786-G10	SJ776-G6	SJ754-G32	SJ723-G38	SJ313-G46	SJ785-G49	SJ787-G51	SJ403-G66	SJ396-G68	SJ390-G69	SJ388-G70	SJ469-G71	SJ448-G73
Drillhole/loc.	18-1032	L14-681	L14-683	BAT G171-XS	L14-682	L14-680	L14-681	L14-681	18-1003	18-1003	18-1003	18-1003	18-1000	18-1004
wt.%														
SiO2	91.66	96.25	92.27	87.57	92.42	87.37	92.46	89.38	95.39	96.38	91.22	97.57	92.87	89.91
TiO2	0.19	0.05	0.07	0.29	0.04	0.19	0.13	0.16	0.04	0.06	0.13	0.03	0.11	0.17
Al2O3	4.63	1.57	2.59	7.25	1.70	5.36	3.81	4.74	1.06	1.48	3.71	0.81	3.51	5.04
Fe2O3	0.83	0.31	0.48	0.25	2.34	1.91	0.47	0.94	0.35	0.20	0.45	0.39	0.76	0.64
MnO	<0.01	<0.01	0.06	<0.01	0.03	0.03	<0.01	<0.01	0.02	<0.01	<0.01	<0.01	<0.01	0.01
MgO	0.19	0.05	0.32	0.23	0.22	0.96	0.10	0.12	0.39	0.09	0.14	0.04	0.14	0.23
CaO	0.09	0.07	0.37	0.07	0.25	0.47	0.15	0.08	0.09	0.43	0.02	0.02	0.10	0.19
Na2O	0.07	0.06	0.08	0.19	0.08	0.03	0.06	0.19	<0.03	0.05	0.05	<0.03	0.05	0.06
K2O	1.31	0.42	0.71	2.13	0.48	1.39	1.07	1.30	0.22	0.38	1.07	0.22	1.00	1.40
P2O5	0.08	0.03	0.01	0.06	0.01	0.06	0.10	0.07	0.01	0.26	0.02	<0.01	0.02	0.08
Loss inc. S	1.06	0.68	1.69	1.34	1.91	2.20	1.03	1.43	0.93	0.54	1.17	0.44	1.00	1.25
Total	100.19	100.63	100.66	100.65	99.52	100.45	100.30	100.02	100.25	100.15	99.94	99.71	99.96	99.93
S	0.57	0.58	1.09	0.49	1.82	1.01	0.58	1.20	0.70	0.19	0.98	0.32	0.61	0.63
ppm														
Y	11.4	2.4	2.6	12.7	4.0	13.6	11.4	15.1	3.9	4.5	2.3	1.7	3.6	33.4
U	4.9	<1.5	<1.5	7.5	1.5	<1.5	2.7	2.5	1.4	<1.5	6.6	<1.5	3.0	2.5
Rb	17.4	5.7	9.7	27.4	6.5	20.1	15.2	17.2	2.8	6.0	14.3	3.0	14.2	18.2
Th	2.5	<1.5	1.6	<1.5	<2	<2	<2	2.0	<2	<2	<2	<2	<2	<2
Pb	6	34	334	8	27	228	4	10	679	4	9	2	45	45
As	8.9	6.7	450.1	<3	14.8	70.8	21.6	33.9	7.3	5.2	4.5	7.1	15.3	6.1
Tl	<1	1.20	1.04	2.52	2.56	1.08	1.29	1.08	1.68	1.56	1.27	1.81	2.06	1.28
Bi	2.20	<2	<2	<2	<2	<2	<2	<2	<2	<2	<2	<2	<2	<2
Zn	28	8300	13500	8900	121	1375	5700	11781	12771	1438	14355	662	739	6200
Cu	280	690	1463	219	165	258	1263	862	670	569	955	697	1750	675
Ni	10.6	0.9	1.0	11.9	11.9	4.4	10.2	11.8	11.1	0.4	7.4	1.3	4.9	7.3
Sb	<2	<2	14.9	<2	<2	2.4	<2	3.4	<2	<2	<2	<2	<2	<2
Cd	<1.5	31.0	52.2	37.1	<1	5.1	24.7	43.8	49.7	5.3	53.0	3.0	2.6	24.5
Ag	<2	<2	5.8	<2	2.3	2.7	<2	<2	<2	<2	<2	2.2	2.2	<2
Nb	2.3	1.2	1.2	3.2	1.2	2.2	1.8	1.5	<1	1.3	1.1	<1	1.7	2.2
Zr	37.2	9.6	15.0	60.9	12.5	48.2	39.1	36.4	7.1	13.9	20.5	7.5	21.5	45.1
Sr	6.0	7.0	5.0	11.0	5.0	12.0	19.0	19.0	1.0	6.0	4.0	2.0	5.0	9.5
Ba	447	148	840	1322	179	2244	438	445	149	254	584	136	736	817
Sc	6.10	<2	2.50	8.30	<2	5.45	4.61	4.51	<2	<2	3.10	<2	3.95	5.78
V	334.7	70.2	182.0	706.8	82.5	33.0	276.2	307.5	57.1	31.4	392.6	17.1	504.0	209.1
Cr	48.6	15.0	26.6	58.1	24.2	2.8	32.3	17.8	14.8	28.1	24.1	15.3	29.6	19.8
Ga	6.8	1.4	4.7	9.6	2.4	5.6	5.5	6.6	0.7	2.3	3.3	1.4	4.5	6.0

Battle Mine white-pale grey chert XRF analyses

	Battle white cht	Battle white cht	Battle white cht	Battle white cht	Battle white cht	Battle white cht	Battle white cht	Battle white cht	Battle white cht	Battle white cht	Battle white cht	Battle white cht
Catalogue #												
field #	SJ458-G77	SJ17a-G82	SJ26G83	SJ9b-G85	SJ10b-G86	SJ539-G87	SJ785-G16	SJ772-G2	SJ773-G3	SJ406-G65	SJ454-G62	SJ399-G67
Drillhole/loc.	18-980	18-1032	18-1032	18-1032	18-1032	18-980	L14-681	L14-683	L14-683	18-1003	18-980	18-1003
wt.%												
SiO2	95.81	93.90	91.30	94.64	92.98	91.31	87.79	83.75	90.39	88.45	85.23	78.57
TiO2	0.09	0.13	0.09	0.10	0.11	0.10	0.18	0.18	0.08	0.10	0.37	0.45
Al2O3	1.96	2.84	3.76	2.46	3.10	2.93	6.18	7.40	3.38	4.42	8.81	11.16
Fe2O3	0.60	0.97	1.40	1.07	1.21	1.30	1.10	2.34	1.14	1.46	0.86	0.62
MnO	<0.01	<0.01	<0.01	<0.01	<0.01	<0.01	<0.01	<0.01	0.06	0.04	<0.01	0.02
MgO	0.04	0.10	0.09	0.06	0.07	0.08	0.14	0.35	0.31	0.57	0.13	0.48
CaO	0.01	0.03	0.18	0.02	0.02	<0.01	0.29	0.05	0.32	0.82	0.02	0.78
Na2O	0.05	0.08	0.04	0.07	0.04	0.04	0.15	0.18	0.10	0.09	0.22	0.17
K2O	0.48	0.80	1.05	0.67	0.87	0.82	1.76	2.05	0.93	1.25	2.14	2.98
P2O5	<0.01	0.01	0.15	0.01	0.01	<0.01	0.23	0.05	0.01	0.03	0.02	0.43
Loss inc. S	0.68	0.98	1.41	0.97	1.10	1.46	1.55	2.51	1.95	2.48	1.69	2.34
Total	99.86	99.89	100.47	100.12	99.60	99.78	100.08	100.14	100.52	99.94	99.69	99.69
S	0.44	0.71	1.29	0.81	0.90	1.61	1.03	2.35	1.68	0.96	0.62	0.81
ppm												
Y	2.0	2.6	9.0	1.5	3.5	3.2	14.1	20.7	10.3	8.9	9.1	12.0
U	<1.5	1.7	2.2	5.9	1.9	2.9	3.2	2.8	<1.5	8.8	4.7	6.8
Rb	6.3	10.7	13.4	8.3	11.3	10.6	21.5	26.7	12.2	16.0	26.0	43.5
Th	<2	<2	<2	<2	<2	<2	1.9	2.8	2.5	2.3	2.2	3.3
Pb	10	10	8	9	12	387	15	115	156	34	7	28
As	10.0	13.4	6.8	20.6	12.1	11.3	32.1	54.2	89.8	13.5	6.0	<3
Tl	1.84	1.26	<1	1.70	1.84	1.64	<1	2.24	2.33	2.31	2.35	4.58
Bi	<2	2.10	<2	<2	2.31	<2	<2	<2	<2	<2	<2	<2
Zn	91	25	4700	43	86	12177	4400	8700	13800	820	35	10900
Cu	741	67	3000	77	292	978	793	208	454	198	3	453
Ni	3.4	6.5	8.2	9.5	3.4	9.8	13.6	2.3	2.0	9.9	1.3	6.0
Sb	<2	<2	2.0	<2	<2	<2	3.0	<2	4.9	<2	<2	<2
Cd	<1	<1	16.6	<1	<1	45.7	16.0	32.7	55.4	4.1	0.0	39.9
Ag	2.0	<2	<2	<2	2.0	9.0	<2	<2	2.5	<2	<2	<2
Nb	<1	<1	1.1	1.2	1.5	1.0	2.3	2.9	1.0	1.4	4.1	5.6
Zr	16.1	19.2	38.6	19.2	37.0	24.7	51.6	79.4	35.3	43.9	77.4	98.9
Sr	1.0	3.0	4.0	3.0	5.0	5.0	26.0	11.0	6.0	16.0	12.0	20.0
Ba	337	313	322	264	354	625	644	1640	726	955	1701	2448
Sc	0.47	3.57	4.23	<2	2.26	<2	7.30	5.30	<2	5.31	7.05	11.28
V	105.3	89.9	83.7	78.8	37.6	143.0	340.0	32.0	29.1	116.9	34.4	459.8
Cr	17.6	20.7	10.9	20.4	22.1	16.8	16.9	7.9	17.7	6.9	2.0	129.4
Ga	2.5	3.6	6.5	2.6	3.7	3.7	7.6	7.1	2.3	9.3	8.9	13.5

Battle mine - green - tan mudstone XRF analyses

	Battle altd mud	Battle altd mud	Battle altd mud	Battle altd mud
Catalogue #				
field #	SJ776-G42	SJ305-G58	SJ761-G30	SJ776-G41
Drillhole/loc.	L14-683	L14-680	G171-XS	L14-683
wt.%				
SiO2	77.84	70.53	66.76	62.11
TiO2	0.32	0.51	0.54	0.57
Al2O3	8.08	12.81	17.38	18.42
Fe2O3	1.17	4.06	3.94	5.97
MnO	0.01	0.12	0.00	0.01
MgO	0.30	1.85	0.51	0.51
CaO	0.05	1.56	0.02	0.04
Na2O	0.12	0.15	0.30	0.42
K2O	2.21	3.37	5.01	5.13
P2O5	0.02	0.16	0.03	0.05
Loss inc. S	2.88	4.59	4.14	5.51
Total	99.98	100.08	99.60	99.70
S	3.11	1.45	3.02	4.78
ppm				
Y	13.7	28.2	26.2	20.5
U	7.3	<1.5	35.7	14.1
Rb	28.9	44.6	61.0	64.1
Th	<3	<2	3.0	3.3
Pb	15100	39	5	718
As	926.0	17.0	15.5	159.1
Tl	Pb, Ba interf.	<1	6.24	1.99
Bi	<2	<2	<2	<2
Zn	38800	200	1810	493
Cu	2000	59	3195	211
Ni	7.8	8.6	59.8	52.8
Sb	35.1	2.6	<2	7.1
Cd	150.7	<1	7.8	1.3
Ag	9.2	2.5	2.5	2.5
Nb	1.5	4.6	5.6	7.0
Zr	52.4	102.0	158.5	155.0
Sr	14.0	42.0	31.0	30.0
Ba	2448	2958	3000	7140
Sc	8.74	17.11	22.50	18.71
V	454.5	45.1	613.4	272.9
Cr	74.8	2.5	19.6	15.0
Ga	11.3	14.2	41.2	21.5

HW Mine - altered argillite XRF analyses

	HW mine altd arg	HW mine altd arg	HW mine altd arg	HW mine altd arg	HW mine altd arg	HW mine altd arg	HW mine altd arg	HW mine altd arg
Catalogue #								
field #	SJ644-G21	SJ642-G22	SJ638-G27	SJ646-G19	SJ643-G23	SJ646T-G25	SJ650-G26	SJ248-G96
Drillhole/loc.	HW S335C	HW S335C	HW S335C	HW S335C	HW S335C	HW S335C	HW S335C	23-503
wt.%								
SiO2	90.51	83.44	82.43	66.18	54.49	73.06	68.62	67.16
TiO2	0.09	0.16	0.22	0.30	0.75	0.57	0.85	0.95
Al2O3	4.18	8.43	9.83	16.65	24.56	16.41	17.20	18.68
Fe2O3	1.84	2.07	1.23	3.77	3.99	0.56	0.93	1.80
MnO	0.02	0.01	0.01	0.01	0.01	0.01	0.04	0.01
MgO	0.26	0.42	0.45	0.89	1.06	0.91	1.19	0.70
CaO	0.22	0.06	0.07	0.94	0.38	0.09	0.82	0.24
Na2O	0.08	0.13	0.18	0.25	0.39	0.25	0.25	0.53
K2O	1.21	2.46	2.97	4.94	7.41	4.86	5.08	4.19
P2O5	0.02	0.06	0.05	0.73	0.31	0.08	0.42	0.19
Loss inc. S	1.83	2.29	2.05	4.18	5.18	2.50	3.37	3.32
Total	100.47	99.86	99.90	99.53	99.48	99.88	99.44	99.87
S	1.43	1.54	0.88	2.77	2.87	0.11	0.39	1.18
ppm								
Y	13.2	11.6	14.7	56.4	32.7	31.3	56.7	30.3
U	1.7	4.4	11.8	7.9	17.7	13.6	31.0	5.6
Rb	16.3	34.3	40.1	68.1	97.3	69.1	72.1	54.1
Th	<1.5	1.7	1.6	2.7	2.0	2.1	4.7	5.4
Pb	42	18	3	12	21	1	3	100
As	14.1	14.0	10.4	396.5	57.7	7.6	338.3	104.4
Tl	9.23	19.83	26.44	32.66	53.05	32.92	34.99	Ba interfer.
Bi	<2	<2	<2	<2	2.70	<2	<2	<2
Zn	381	46	33	88	23	17	103	94
Cu	13	18	6	900	30	17	728	64
Ni	4.2	5.6	8.4	20.9	12.1	6.1	11.4	13.4
Sb	<2	<2	<2	4.6	2.8	<2	4.7	<2
Cd	<1.5	<1.5	<1.5	<1.5	<1.5	<1.5	<1.5	<1
Ag	<2	<2	<2	<2	<2	<2	2.5	<2
Nb	2.1	2.6	3.6	6.6	6.8	8.0	11.8	9.4
Zr	44.4	69.3	88.3	187.5	171.4	104.3	193.0	223.5
Sr	9.0	14.0	17.0	34.0	41.0	29.0	37.0	44.0
Ba	1429	2900	3700	5100	8500	5200	5100	18564
Sc	4.00	4.30	10.90	21.00	21.40	20.80	22.90	19.18
V	81.0	142.9	312.3	386.2	421.6	887.2	843.9	245.0
Cr	10.1	10.0	8.5	7.9	11.5	187.4	133.1	44.3
Ga	5.3	10.5	14.9	20.3	32.7	19.1	19.5	17.8

HW Mine - altered argillite

	HW mine altd arg	HW mine altd arg
Catalogue #		
field #	SJ250-G97	SJ251-G98
Drillhole/loc.	23-503	23-503
wt.%		
SiO2	55.19	46.61
TiO2	0.94	1.21
Al2O3	24.49	31.48
Fe2O3	3.35	2.14
MnO	0.04	0.04
MgO	3.61	2.59
CaO	0.28	0.35
Na2O	0.61	0.82
K2O	4.56	6.46
P2O5	0.21	0.26
Loss inc. S	4.37	4.84
Total	99.67	99.59
S	0.04	0.02
ppm		
Y	61.1	63.7
U	3.6	5.5
Rb	60.0	87.1
Th	7.3	9.6
Pb	20	8
As	7.4	8.2
Tl	Ba interfer.	Ba interfer.
Bi	<2	<2
Zn	196	64
Cu	75	39
Ni	6.9	4.9
Sb	<2	<2
Cd	<1	<1
Ag	<2	<2
Nb	14.6	18.7
Zr	367.7	472.3
Sr	53.0	71.0
Ba	17748	24888
Sc	17.95	22.94
V	95.8	124.5
Cr	4.0	5.2
Ga	22.0	27.8

HW Mine - argillite XRF analyses

	HW mine argillite	HW mine argillite	HW mine argillite	HW mine argillite	HW mine argillite	HW mine argillite	HW mine argillite	HW mine argillite	HW mine argillite	HW mine argillite
Catalogue #										
field #	SJ252a-G79	SJ253-G80	SJ75-G93	SJ254a-G76	SJ731-G99	SJ733-G100	SJ637-G36	SJ669-G28	SJ732-G112	SJ74-G113
Drillhole/loc.	23-503	23-503	23-489	23-503	21-2072	21-2072	21LEVEL	HW 23 SHOP	21-2072	23-489
wt.%									ARG	ARG
SiO2	82.17	73.94	84.22	77.70	84.54	84.80	83.75	83.09	85.57	83.23
TiO2	0.27	0.34	0.15	0.22	0.18	0.19	0.17	0.24	0.14	0.23
Al2O3	8.15	12.90	4.96	9.04	5.80	5.55	4.93	8.15	3.86	7.34
Fe2O3	2.64	3.29	1.39	1.79	1.91	2.00	2.72	1.28	1.67	2.75
MnO	0.01	0.02	0.01	0.03	0.03	0.02	0.01	0.01	0.03	0.02
MgO	0.61	1.19	0.13	1.17	1.11	0.86	1.18	0.68	0.89	2.08
CaO	0.74	0.57	2.83	2.75	1.39	1.56	1.54	0.16	2.39	0.40
Na2O	0.26	0.21	0.12	0.17	0.18	0.34	0.71	0.12	0.11	0.15
K2O	1.68	3.22	1.26	1.99	1.13	0.95	0.70	2.23	0.68	1.17
P2O5	0.56	0.23	2.12	0.55	0.09	0.22	0.07	0.11	0.71	0.30
Loss inc. S	2.55	3.53	2.10	3.51	3.28	3.23	3.50	2.91	3.27	2.60
Total	100.32	99.91	99.59	99.45	100.15	100.37	99.61	99.59	99.73	100.64
S	1.77	1.94	1.12	0.37	1.00	1.18	1.40	1.06	0.90	0.98
ppm										
Y	13.5	12.9	17.6	15.9	8.7	11.5	4.9	10.6	8.9	9.9
U	2.8	4.1	2.9	3.7	1.9	2.7	1.6	2.4	1.7	3.1
Rb	22.8	41.0	14.1	28.6	19.2	16.8	13.3	30.9	11.8	15.1
Th	<2	5.5	2.1	2.1	<2	<2	<1.5	<1.5	<1.5	<1.5
Pb	39	26	23	210	13	17	16	14	39	33
As	134.3	44.9	60.3	44.1	21.9	25.2	32.9	39.5	21.7	66.8
Tl	5.75	1.57	3.92	1.46	<1	<1	<1	11.12	<2	5.20
Bi	<2	<2	<2	<2	<2	<2	<2	<2	<2	<2
Zn	151	48	448	765	139	107	109	118	147	126
Cu	101	41	69	112	32	37	40	47	35	52
Ni	25.1	14.5	26.8	6.8	25.6	26.1	20.2	21.5	27.0	23.2
Sb	3.0	2.8	2.4	<2	4.0	4.6	4.2	3.0	5.4	1.7
Cd	<1	<1	2.1	4.0	<1	<1	<1.5	<1.5	<1	<1
Ag	3.3	<2	<2	2.3	<2	2.4	2.5	<2	2.7	<2
Nb	2.9	4.4	2.6	3.4	2.9	3.2	2.5	4.5	2.2	2.6
Zr	62.7	96.2	42.4	94.2	49.0	41.0	37.6	88.3	29.5	57.7
Sr	23.0	31.0	22.0	65.0	32.0	36.0	53.0	10.0	33.0	15.0
Ba	5814	4080	2203	3570	4386	5610	2800	5300	3277	3266
Sc	9.12	10.53	5.17	10.15	6.39	7.33	6.80	5.70	6.00	6.80
V	129.0	179.8	73.5	38.5	116.1	129.2	104.7	154.2	93.1	135.0
Cr	82.8	35.8	72.8	4.5	74.7	80.1	68.6	72.2	65.5	57.1
Ga	7.3	11.7	5.1	7.9	6.0	5.0	4.8	8.0	3.5	7.4

HW Mine - argillite XRF analyses

	HW mine argillite	HW mine argillite	HW mine argillite	HW mine argillite	HW mine argillite	HW mine argillite
Catalogue #						
field #	SJ660-G114	SJ44-G115	SJ83-G116	SJ492-G117	SJ492-G118	SJ491-G119
Drillhole/loc	23 SHOP	23-493	23-488	23-514	23-514	23-514
wt.%	ARG	ARG	ARG	ARG		
SiO2	82.34	89.60	84.47	86.09	84.72	75.89
TiO2	0.24	0.15	0.20	0.14	0.15	0.26
Al2O3	8.36	4.20	6.48	5.09	6.09	10.41
Fe2O3	1.64	2.59	1.69	1.73	1.68	2.33
MnO	0.00	0.00	0.00	0.02	0.02	0.03
MgO	0.70	0.08	0.12	1.38	1.36	1.84
CaO	0.30	0.09	1.30	1.27	1.23	1.52
Na2O	0.10	0.10	0.15	0.38	0.45	0.55
K2O	2.33	1.01	1.53	0.82	1.07	2.05
P2O5	0.22	0.08	0.98	0.07	0.07	0.09
Loss inc. S	3.12	2.33	2.20	2.92	2.88	3.78
Total	100.04	100.56	99.69	100.28	100.20	99.56
S	1.24	1.99	1.31	0.75	0.74	0.97
ppm						
Y	11.6	20.3	29.6	7.4	7.2	11.7
U	3.2	5.8	5.0	5.1	4.7	5.7
Rb	30.9	12.8	18.9	14.5	18.0	35.0
Th	<1.5	<1.5	1.7	<1.5	<1.5	<1.5
Pb	14	26	12	10	9	6
As	49.9	117.9	73.9	23.1	24.8	31.9
Tl	9.20	3.80	9.90	<2	<2	<2
Bi	<2	<2	<2	<2	<2	<2
Zn	92	10	343	131	148	141
Cu	48	35	112	29	31	36
Ni	24.1	35.2	24.9	41.7	39.6	41.7
Sb	4.6	2.8	2.1	4.2	3.3	5.5
Cd	<1	<1	<1	1.5	1.4	1.0
Ag	<2	2.5	<2	<2	<2	<2
Nb	4.5	2.8	3.2	3.1	3.0	4.2
Zr	77.7	38.9	59.4	52.8	52.1	79.1
Sr	12.0	8.0	20.0	29.0	33.0	49.0
Ba	6469	2907	4867	3002	4019	7147
Sc	6.90	4.50	5.30	5.10	4.70	8.30
V	161.1	202.6	164.5	217.3	203.9	289.0
Cr	94.5	60.8	75.2	23.5	22.9	36.4
Ga	8.3	4.5	8.3	5.1	5.3	10.4

South Flank argillite XRF analyses

	Sth Flank argillite	Sth Flank argillite	Sth Flank argillite	Sth Flank argillite	Sth Flank argillite	Sth Flank argillite	Sth Flank argillite
	SJ717-G74	SJ718-G75	SJ607-G92	SJ824-G61	SJ605-G101	P189b-G111	SJ830-G123
	L14-641	L14-641	16-33	16-43	16-33	L14-641	16-36
	85.55	83.67	83.11	72.85	82.95	80.95	74.58
	0.13	0.16	0.19	0.16	0.18	0.27	0.25
	4.12	5.02	5.80	4.53	4.17	7.91	9.30
	2.65	3.41	2.54	3.18	2.59	3.07	2.92
	0.04	0.04	0.02	0.06	0.03	0.04	0.02
	0.65	0.80	0.69	1.22	1.15	0.71	1.96
	2.09	2.12	2.17	8.01	3.51	1.37	3.28
	1.00	0.72	1.91	0.33	0.57	1.67	1.83
	0.41	0.56	0.42	0.72	0.49	0.95	1.07
	0.03	0.31	0.05	3.55	1.19	0.06	0.42
	2.77	2.92	3.16	4.83	2.74	2.73	3.57
	99.64	99.87	100.20	99.64	99.62	100.22	99.41
	0.88	0.55	1.05	1.04	0.28	0.90	0.20
	2.6	9.8	11.4	25.1	23.1	5.6	20.0
	<1.5	<1.5	<1.5	2.7	2.0	<1.5	3.8
	7.9	9.3	7.0	13.7	8.8	15.7	17.0
	<2	<2	<2	<2	<2	<1.5	2.5
	25	3	24	6	9	6	66
	9.3	25.7	12.3	11.1	18.6	23.4	28.5
	1.29	<1	<1	<1	<1	<2	<2
	<2	<2	<2	<2	<2	<2	<2
	69	61	158	104	78	61	287
	35	28	32	68	35	39	58
	21.9	13.0	17.9	23.6	12.8	21.6	21.9
	2.4	2.3	4.8	<2	<2	2.1	7.7
	<1	<1	1.9	1.0	<1	<1	2.0
	<2	<2	3.4	2.9	<2	<2	2.0
	2.0	2.5	1.9	2.6	2.3	2.8	3.8
	23.9	29.5	59.9	34.9	29.5	45.6	95.8
	62.0	45.0	85.0	97.0	54.0	71.0	75.0
	1653	1180	1044	1607	286	3934	1317
	5.64	6.49	6.96	10.06	8.18	9.40	11.70
	101.2	75.4	190.7	107.5	115.4	165.6	221.6
	66.4	47.9	29.5	72.1	56.3	71.3	37.6
	4.0	5.0	4.2	4.7	4.9	6.1	7.5

South Flank argillite XRF analyses

	Sth Flank argillite	Sth Flank argillite	Sth Flank argillite	Sth Flank argillite	Sth Flank argillite	Sth Flank argillite
Catalogue #						
field #	SJ831-G124	SJ832-G125	49329*	49251*	49252*	49257*
Drillhole/loc	16-45	16-61	14-641	16-45	16-45	16-46
wt.%						
SiO2	81.75	66.72	73.01	68.46	74.53	63.64
TiO2	0.20	0.38	0.37	0.37	0.27	0.53
Al2O3	6.52	10.75	10.60	12.32	9.56	13.66
Fe2O3	2.86	5.42	4.63	4.63	4.22	5.85
MnO	0.04	0.10	0.08	0.05	0.06	0.10
MgO	1.16	2.23	1.54	2.70	1.87	3.43
CaO	1.94	5.00	3.25	3.76	3.92	5.82
Na2O	2.18	1.56	2.02	1.74	0.66	2.40
K2O	0.47	1.27	1.35	2.17	1.77	1.39
P2O5	0.29	0.16	0.16	0.80	0.14	0.18
Loss inc. S	2.35	5.34	3.00	3.00	3.00	3.00
Total	99.86	99.26				
S	0.86	0.71				
ppm						
Y	9.6	16.1	8.1	110.0	156.0	287.0
U	<1.5	1.7				
Rb	8.0	25.3				
Th	<1.5	<1.5				
Pb	5	2				
As	5.6	5.4				
Tl	<2	<2				
Bi	<2	<2				
Zn	89	107	111	18	13	16
Cu	37	53	60	135	71	209
Ni	15.3	19.3	11.0	95.7	162.0	102.0
Sb	<2	<2				
Cd	<1	<1				
Ag	<2	<2				
Nb	2.7	3.4		12.8	11.1	17.4
Zr	38.4	71.2				
Sr	72.0	129.0	176.0	14.6	22.8	12.4
Ba	626	2738		111	137	148
Sc	7.90	15.80	11.60	76.00	121.00	66.00
V	100.7	174.1	143.0	12.0	10.0	16.0
Cr	62.4	59.6	111.0	10.0	25.0	10.0
Ga	5.4	10.2				

Thelwood Valley - Price Hillside argillite XRF analyses

	HW North argillite	HW North argillite	Thelwood argillite	Thelwood argillite	Thelwood argillite	Thelwood argillite	Thelwood argillite	Thelwood argillite
	SJ66-G94	SJ52-G95	SJ629-G89	SJ629-G90	SJ630-G91	SJ221-G103	SJ629-G18	SJ223b-G120
	W202	W202	CR88-4	CR88-4	CR88-4	PR124	CR88-4	PR124
	79.62	89.95	80.84	50.02	66.45	78.62	86.64	70.18
	0.20	0.10	0.12	1.14	0.46	0.29	0.11	0.41
	7.60	2.97	7.05	19.97	15.67	9.69	6.59	11.48
	2.78	1.54	0.50	10.34	4.87	1.54	0.55	3.57
	0.02	0.01	0.04	0.15	0.11	0.02	0.02	0.07
	1.04	0.43	0.21	4.06	1.40	0.76	0.26	1.99
	2.00	1.73	3.67	2.14	1.45	1.76	0.99	2.89
	0.06	0.84	2.62	3.05	1.65	3.88	2.34	3.69
	2.36	0.33	1.76	5.25	4.56	0.75	1.77	0.96
	1.36	0.43	0.41	0.40	0.12	0.12	0.04	0.12
	2.40	1.77	2.77	2.85	2.94	2.53	1.10	3.99
	99.68	100.15	100.03	99.46	99.77	100.11	100.45	99.59
	1.33	0.54	0.02	0.13	0.25	0.51	0.02	0.71
	19.7	10.7	17.9	34.5	29.3	13.0	9.9	17.4
	1.8	1.9	<1.5	1.8	2.2	3.4	<1.5	1.9
	38.1	7.2	14.2	74.7	69.1	14.9	13.1	17.9
	<2	<2	2.1	4.5	4.9	<2	2.6	2.8
	10	14	6	7	12	39	4	2
	28.1	21.1	3.3	4.5	11.8	11.6	<3	180.6
	3.37	1.20	1.17	<1	0.98	<1	<1	<2
	<2	<2	<2	<2	<2	<2	<2	<2
	84	131	11	122	56	145	42	249
	39	26	9	116	33	93	10	121
	22.4	20.5	3.0	30.6	9.4	14.9	1.6	18.4
	<2	2.0	<2	<2	<2	<2	<2	4.0
	<1	<1	<1	<1	1.2	<1.5	<1.5	<1
	<2	<2	<2	<2	<2	2.0	<2	2.8
	3.4	2.0	2.8	7.7	8.3	2.8	3.2	6.0
	65.6	27.2	81.4	174.4	184.4	72.3	73.4	92.2
	24.0	34.0	135.0	247.0	156.0	147.0	85.0	132.0
	2121	235	304	539	714	1021	353	1588
	6.39	3.95	4.79	28.20	16.45	10.90	3.90	12.70
	77.3	36.7	6.5	267.1	45.2	117.3	6.4	116.9
	67.0	52.7	1.9	94.0	14.5	38.5	2.9	85.5
	6.8	2.9	3.3	21.8	16.4	6.5	2.5	8.1

* sample from Myra Falls mine database

Thelwood Valley - Price Hillside argillite XRF analyses

	Thelwood argillite	Thelwood argillite	Price argillite	Price argillite	Price argillite
Catalogue #					
field #	SJ432-G121	SJ432-G122	SJ621-G126	SJ621-G127	SJ624-G102
Drillhole/loc	PR124	PR124	PR13-68	PR13-68	PR13-68
wt.%					
SiO2	75.93	76.23	84.04	81.84	72.46
TiO2	0.26	0.29	0.17	0.22	0.30
Al2O3	9.06	9.73	4.97	7.06	11.27
Fe2O3	2.25	2.31	3.04	3.29	3.02
MnO	0.06	0.04	0.03	0.02	0.04
MgO	1.14	1.20	1.21	1.72	1.63
CaO	3.20	2.32	1.91	0.72	2.01
Na2O	0.75	0.22	0.86	0.60	0.95
K2O	2.01	2.50	0.61	1.27	2.70
P2O5	0.31	0.35	0.11	0.14	0.41
Loss inc. S	4.34	3.94	3.06	2.87	4.34
Total	99.72	99.65	100.14	100.00	99.59
S	0.64	0.91	0.95	0.91	1.41
ppm					
Y	16.1	17.3	11.9	13.3	19.2
U	4.4	6.1	2.2	3.3	5.4
Rb	38.0	47.9	8.9	19.6	38.7
Th	2.5	2.2	<1.5	<1.5	4.2
Pb	69	58	22	9	72
As	12.8	26.8	41.2	55.5	37.1
Tl	<2	<2	<2	<2	<1
Bi	<2	<2	<2	<2	<2
Zn	329	384	110	109	412
Cu	77	82	38	39	86
Ni	36.0	34.7	20.8	23.9	26.3
Sb	4.5	5.2	2.1	<2	4.2
Cd	2.5	1.9	1.2	<1	1.4
Ag	2.7	3.7	<2	<2	<2
Nb	4.6	4.5	3.0	2.2	5.4
Zr	97.5	106.0	37.6	46.8	115.8
Sr	92.0	68.0	57.0	37.0	80.0
Ba	3169	3948	859	1849	3468
Sc	9.30	8.70	6.60	8.80	8.93
V	242.6	243.6	161.3	186.7	172.0
Cr	63.4	60.6	62.5	73.3	46.7
Ga	9.4	10.7	5.6	7.8	11.1

HW Horizon rhyolitic siltstone (interbedded with chert) - XRF analyses

	Battle siltstone	Battle siltstone	Battle siltstone	Battle siltstone	Battle siltstone	Battle siltstone	Battle siltstone	Battle siltstone
Catalogue #								
field #	SJ764b-G45	SJ772-G39	SJ783-G47	SJ784-G48	SJ775-G5	SJ315-G20	SJ784-G12	SJ763-G37
Drillhole/loc	L14-676	L14-683	L14-681	L14-681	L14-683	L14-680	L14-681	L14-677
wt.%								
SiO2	75.28	81.45	90.19	83.02	72.21	90.72	90.78	72.28
TiO2	0.29	0.23	0.12	0.14	0.24	0.08	0.06	0.35
Al2O3	12.59	9.85	5.24	8.76	15.51	4.29	4.87	14.55
Fe2O3	1.03	1.41	1.15	2.75	2.04	1.07	1.05	1.01
MnO	0.01	<0.01	<0.01	<0.01	<0.01	0.02	<0.01	0.01
MgO	0.12	0.31	0.11	0.20	0.43	0.27	0.12	0.14
CaO	1.42	0.06	0.02	<0.01	0.00	0.52	0.04	1.34
Na2O	6.79	0.23	0.12	0.22	0.38	0.06	0.12	7.93
K2O	0.36	2.78	1.45	2.31	4.23	1.23	1.33	0.36
P2O5	0.07	0.05	0.01	0.01	0.02	0.03	0.01	0.08
Loss inc. S	1.78	2.39	1.37	2.65	3.33	1.68	1.33	1.63
Total	99.77	99.69	99.87	100.28	99.50	100.41	99.84	99.72
S	0.72	1.35	0.85	2.05	1.89	0.82	0.80	0.75
ppm								
Y	19.2	20.6	10.0	22.1	17.0	12.3	14.5	22.4
U	8.2	<1.5	<1.5	1.8	5.1	<1.5	<1.5	11.9
Rb	4.9	35.0	18.2	29.5	52.1	17.7	17.0	4.4
Th	3.4	2.7	<2	2.3	4.4	<1.5	2.4	4.7
Pb	6	14	7	9	295	52	3	9
As	16.4	17.2	7.4	11.1	29.1	18.1	6.4	10.0
Tl	1.42	2.43	1.63	2.05	3.19	1.31	<1	<1
Bi	<2	<2	2.63	2.21	<2	<2	<2	<2
Zn	76	5544	11	25	5500	1473	13	16
Cu	3	147	108	657	302	156	452	2
Ni	17.5	4.9	1.0	1.4	2.6	4.6	0.9	13.1
Sb	<2	<2	<2	<2	<2	3.5	<2	2.1
Cd	<1	19.7	<1	<1	20.5	6.1	<1.5	<1.5
Ag	<2	<2	<2	<2	<2	2.8	<2	<2
Nb	5.9	3.3	2.6	2.8	5.0	1.9	1.8	6.8
Zr	131.4	107.5	59.4	93.0	164.0	59.1	57.1	152.0
Sr	133.0	14.0	14.0	24.0	24.0	8.0	17.0	165.0
Ba	171	2121	695	1198	3200	1800	624	269
Sc	7.24	8.18	3.76	5.73	7.50	4.70	2.80	7.20
V	34.7	49.9	9.0	7.5	78.5	41.0	4.7	44.5
Cr	1.5	12.2	2.6	1.1	3.4	4.5	1.1	2.2
Ga	9.8	10.5	6.3	10.5	17.1	4.1	5.7	10.3

HW Horizon rhyolitic siltstone (interbedded with chert) - XRF analyses

	Battle siltstone	Battle siltstone	Battle siltstone	Battle siltstone	Battle siltstone	Battle siltstone	Battle siltstone	Battle siltstone	Battle siltstone	Battle siltstone	Battle siltstone	Battle siltstone	Battle siltstone
Catalogue #													
field #	SJ316-G31	SJ783-G9	SJ774-G4	SJ723-G14	SJ722-G15	SJ394-G63	SJ460-G78	SJ4b-G84	SJ391-G64	SJ24-G81	SJ819-G60	SJ448-G72	SJ608-G24
Drillhole/loc	L14-680	L14-681	L14-683	L14-682	L14-682	18-1003	18-980	18-1032	18-1003	18-1032	L14-679	18-1004	L10-2024
wt.%													
SiO2	85.59	87.09	86.12	88.85	84.37	86.87	77.48	82.21	89.00	90.52	87.03	61.06	67.67
TiO2	0.17	0.13	0.16	0.07	0.13	0.21	0.23	0.14	0.09	0.10	0.09	0.50	0.29
Al2O3	6.77	7.58	6.66	5.02	7.36	7.08	13.19	6.85	6.19	4.60	5.50	23.71	18.45
Fe2O3	0.64	1.24	1.35	2.24	0.94	0.89	1.71	1.84	0.63	1.18	1.71	1.71	1.69
MnO	0.07	<0.01	<0.01	0.01	0.23	<0.01	<0.01	0.16	<0.01	<0.01	0.02	<0.01	0.03
MgO	0.84	0.18	0.22	0.18	0.87	0.24	0.24	1.08	0.17	0.13	0.52	0.65	1.08
CaO	1.10	<0.01	0.08	0.02	1.15	0.07	0.06	1.36	0.02	<0.01	0.82	0.19	0.28
Na2O	0.09	0.19	0.18	0.12	0.20	0.20	0.30	0.15	0.11	0.11	0.04	0.42	0.30
K2O	1.97	2.10	1.83	1.38	2.09	2.02	3.58	2.01	1.70	1.23	1.79	6.90	5.45
P2O5	0.06	0.01	0.08	0.01	0.03	0.04	0.06	0.02	0.02	0.01	0.03	0.14	0.07
Loss inc. S	2.55	1.73	2.01	1.93	3.08	1.56	2.72	3.67	1.36	1.47	2.11	3.92	3.50
Total	100.30	100.40	100.63	100.04	100.59	99.42	100.35	99.72	99.86	100.09	99.99	99.88	99.46
S	0.13	0.93	1.69	1.77	0.58	0.63	1.47	1.40	0.60	1.14	0.95	1.08	1.02
ppm													
Y	15.9	21.0	9.1	6.4	11.6	29.6	28.6	13.7	8.0	7.4	7.0	63.3	42.4
U	2.1	<1.5	3.5	1.7	2.3	3.6	1.6	<1.5	<1.5	<1.5	<1.5	7.6	9.6
Rb	27.3	26.5	23.3	17.0	28.8	26.3	39.3	23.6	19.4	14.6	27.8	80.6	73.3
Th	<1.5	2.9	25.0	2.5	2.7	3.2	4.0	2.4	2.8	<2	<2	5.0	3.5
Pb	23	8	6870	10	29	35	11	11	4	4	39	18	16
As	14.7	6.8	336.3	13.5	16.8	4.6	17.2	56.0	2.7	594.7	10.7	11.9	98.3
Tl	1.87	1.41	<2	<1	1.80	2.53	3.82	8.00	2.23	2.58	1.41	4.34	34.50
Bi	<2	<2	<2	<2	<2	<2	<2	<2	<2	<2	<2	<2	<2
Zn	56	22	7100	35	19	784	3900	25	3830	3861	136	1446	83
Cu	15	329	1074	1261	38	19	414	23	75	1334	501	483	219
Ni	6.0	0.8	8.2	3.2	4.4	5.3	3.3	2.2	1.1	0.2	1.0	15.1	12.6
Sb	<2	<2	22.3	<2	4.8	2.1	<2	<2	<2	32.3	<2	<2	1.9
Cd	<1.5	<1.5	27.1	<1.5	<1.5	2.8	14.2	<1	15.6	15.1	<1	7.0	<1.5
Ag	<2	<2	6.3	3.2	21.7	<2	<2	<2	<2	3.4	2.7	<2	<2
Nb	2.6	3.0	2.3	2.2	2.7	3.5	5.3	3.3	2.5	2.1	2.3	7.8	6.4
Zr	64.5	78.3	64.8	49.9	66.7	83.5	144.7	80.2	65.6	52.5	56.1	241.3	181.4
Sr	17.0	21.0	10.0	13.0	27.0	8.5	18.0	20.0	7.0	4.0	6.0	30.5	35.0
Ba	3900	1008	1543	537	1350	1265	2191	1952	772	937	2244	3876	5500
Sc	7.50	6.10	4.10	2.30	4.10	6.25	9.96	6.20	3.67	2.35	2.16	27.12	14.50
V	22.2	8.1	218.2	41.9	22.0	88.2	25.2	15.5	9.5	8.2	17.1	471.7	222.6
Cr	1.2	1.4	29.8	7.7	2.2	26.2	1.4	6.6	2.1	1.1	2.3	19.9	4.0
Ga	7.1	8.8	6.8	5.5	6.6	7.7	15.6	7.0	7.5	5.8	6.3	30.7	20.0

HW Horizon rhyolitic siltstone and volcaniclastic rocks (interbedded with chert)

43 Block and and rhy volc.

	Battle siltstone	Battle siltstone	Battle siltstone	Battle siltstone	Battle siltstone	Battle rhy sandst	Battle rhy sandst	Battle rhy sandst	Battle rhy sandst	43 Block HW andesite	43 Block HW MV	43 Block HW dacite
Catalogue #												
field #	SJ648-G17	SJ254b-G88	SJ304-G128	SJ307-G129	SJ308-G130	SJ309-G131	SJ310-G132	SJ311-G133	SJ312-G134	SJ542-G135	SJ558A-G136	SJ561-G137
Drillhole/loc	HW-S335C	23-503	L14-680	L14-680	L14-680	L14-680	L14-680	L14-680	L14-680	20-845	20-675	20-675
wt.%												
SiO2	70.51	63.15	73.95	68.00	68.10	72.11	69.58	84.93	79.95	54.18	83.20	61.69
TiO2	0.29	0.24	0.41	0.57	0.54	0.22	0.29	0.17	0.21	0.87	0.23	0.58
Al2O3	13.30	17.15	12.66	14.09	13.80	10.84	11.44	7.25	9.25	17.61	6.86	15.88
Fe2O3	1.83	4.72	2.24	4.54	4.54	2.88	3.57	2.26	2.77	9.41	2.82	4.86
MnO	0.01	0.04	0.06	0.11	0.12	0.13	0.05	0.00	0.05	0.15	0.02	0.08
MgO	1.02	4.07	1.43	2.21	2.28	2.01	1.98	0.39	0.99	4.12	0.88	1.43
CaO	0.58	1.04	1.35	1.53	1.24	2.66	1.82	0.12	0.56	6.03	1.34	5.59
Na2O	0.16	0.33	0.17	0.16	0.17	0.09	0.08	0.06	0.09	3.23	0.63	5.97
K2O	8.40	3.33	3.39	3.53	3.48	2.79	3.05	2.10	2.57	0.73	1.37	0.36
P2O5	0.24	0.06	0.13	0.18	0.17	0.06	0.23	0.02	0.04	0.17	0.07	0.24
Loss inc. S	2.49	4.74	3.13	4.05	4.63	4.20	4.96	2.15	2.93	3.33	2.20	2.93
Total	99.52	99.51	99.44	99.43	99.51	99.09	99.15	99.94	100.10	99.92	99.85	99.67
S	1.33	0.48	0.42	1.40	1.41	0.90	2.13	1.63	1.72	0.01	0.91	0.00
ppm												
Y	22.0	21.2	20.9	32.2	32.8	25.9	17.0	13.4	21.2	17.0	15.6	26.4
U	2.6	2.3	1.8	1.9	<1.5	2.0	8.1	<1.5	1.7	<1.5	1.6	<1.5
Rb	69.9	47.0	47.9	49.3	47.6	39.9	44.9	29.9	36.1	13.1	22.8	5.2
Th	1.5	2.3	2.3	1.5	<1.5	2.1	4.1	2.2	2.1	2.6	2.7	2.3
Pb	49	18	161	40	22	652	698	62	274	7	90	10
As	50.2	752.0	28.9	22.3	18.4	6.7	178.5	18.8	30.9	6.6	10.1	4.7
Tl	<1	<1	<2	<2	<2	<2	<2	<2	2.90	<2	<2	<2
Bi	<2	<2	<2	<2	<2	<2	<2	2.60	<2	<2	<2	<2
Zn	2000	120	537	280	188	3400	9400	321	1003	166	156	91
Cu	76	14	121	94	50	584	1124	423	208	64	299	12
Ni	1.9	16.1	9.3	9.3	7.2	5.1	43.4	2.5	5.7	5.7	2.2	3.2
Sb	<2	2.0	2.2	3.6	4.1	2.9	17.7	3.1	3.1	<2	<2	<2
Cd	7.1	<1	3.2	2.1	1.3	15.8	39.6	1.7	5.5	<1	<1	<1
Ag	3.3	<2	2.7	2.5	<2	5.9	20.6	6.5	2.8	<2	2.2	<2
Nb	4.5	6.9	4.6	4.4	4.3	4.2	4.3	3.1	2.6	2.6	2.8	2.9
Zr	109.9	153.4	116.6	114.2	109.8	116.2	110.3	74.8	89.0	59.4	64.5	87.5
Sr	76.0	69.0	35.0	40.0	34.0	48.0	49.0	11.0	21.0	485.8	83.8	363.6
Ba	3900	5610	3454	3820	3913	4911	6610	3843	4217	385	1323	333
Sc	7.10	6.58	13.40	19.70	18.80	14.30	9.10	6.80	10.90	23.90	8.50	18.00
V	23.8	70.3	45.5	65.5	37.3	60.1	295.1	23.0	37.9	191.7	60.0	66.3
Cr	1.9	9.9	2.9	3.9	2.1	5.7	28.4	4.3	3.6	8.7	7.2	4.9
Ga	9.8	16.6	13.4	15.2	14.5	11.8	9.9	8.0	10.2	17.4	6.9	15.9

43 Block andesite and rhyolitic volcaniclastics

	43 Block and. Silt	43 Block FQP	43 Block Rhy. Sst	43 Block rhy sst-mz	43 Block mz, rhy sst	43 Block mz, rhy sst	43 Block rhy sst	43 Block and. Sst	43 Block FW andesite	43 Block FW andesite	43 Block FW andesite
Catalogue #					G142	G143	G144	G145	G146	G147	G148
field #	SJ565-G138	SJ552-G139	SJ553ab-G140	SJ568-G141	SJ570-G142	SJ571-G143	SJ555-G144	SJ556-G145	SJ558-G146	SJ572-G147	SJ559-G148
Drillhole/loc	20-675	20-845	20-845	20-675	20-675	20-675	20-845	20-845	20-845	20-675	20-845
wt.%											
SiO2	59.88	71.65	73.83	51.05	52.97	59.82	64.78	53.17	52.41	54.22	63.12
TiO2	0.50	0.26	0.25	0.18	0.34	0.50	0.44	0.71	0.84	0.83	0.78
Al2O3	14.24	13.77	9.88	6.57	17.17	17.26	12.42	17.38	17.26	17.34	15.01
Fe2O3	5.95	2.57	2.74	4.99	10.52	5.38	4.79	8.34	10.16	8.67	4.76
MnO	0.08	0.03	0.04	0.06	0.02	0.03	0.09	0.10	0.14	0.11	0.10
MgO	2.79	1.16	1.07	0.77	1.03	1.71	2.73	4.30	4.52	4.17	1.41
CaO	6.44	1.80	2.80	3.76	1.04	1.74	4.61	6.21	8.05	6.89	7.63
Na2O	2.86	4.03	0.21	0.11	0.17	0.20	0.17	3.47	2.05	3.45	3.89
K2O	1.05	1.71	2.59	1.92	5.07	4.42	2.23	0.52	0.23	0.26	0.37
P2O5	0.22	0.08	0.07	0.04	0.05	0.27	0.10	0.23	0.18	0.23	0.31
Loss inc. S	5.21	2.66	5.24	11.43	8.12	5.30	5.83	5.31	3.87	3.77	2.76
Total	99.45	99.80	99.40	98.83	100.23	99.60	99.26	99.82	99.76	100.00	100.20
S	0.84	0.00	0.88	8.14	8.48	3.42	0.48	0.03	0.16	0.01	0.05
ppm											
Y	19.4	12.4	13.4	Pb interf.	18.3	28.2	23.8	15.7	17.7	17.9	21.2
U	2.3	1.5	<1.5	2.1	5.9	2.5	<1.5	<1.5	<1.5	<1.5	<1.5
Rb	19.4	33.1	48.2	38.0	80.3	68.9	36.8	7.6	3.9	4.1	5.7
Th	2.0	4.2	2.3	Ba, Th interf.	7.0	2.1	<1.5	<1.5	<1.5	<1.5	<1.5
Pb	5	5	86	13600	752	47	43	5	4	2	2
As	55.0	<3	7.8	1278.0	68.9	27.5	12.3	4.4	9.9	<3	5.3
Tl	<2	<2	<2	Ba, Pb int.	14.85	19.55	4.89	<2	<2	<2	<2
Bi	<2	<2	<2	<2	<2	<2	<2	<2	<2	<2	<2
Zn	74	36	566	45800	12200	10100	96	77	97	80	59
Cu	40	16	119	6400	4800	2100	68	79	86	94	43
Ni	12.0	1.8	5.7	10.2	11.8	7.9	17.4	13.8	17.0	12.5	5.0
Sb	2.4	<2	<2	137.1	6.4	<2	<2	<2	<2	<2	<2
Cd	<1	<1	3.2	194.0	44.8	45.2	<1	<1	<1	<1	<1
Ag	<2	<2	2.3	50.0	9.5	5.1	<2	<2	<2	<2	<2
Nb	3.5	3.3	3.5	2.0	4.8	3.1	3.0	2.0	2.7	2.7	3.1
Zr	84.0	123.0	89.0	74.8	152.6	132.3	71.9	39.0	54.1	47.5	53.9
Sr	200.0	203.0	92.9	1008.0	42.4	43.4	62.6	651.5	559.5	333.3	356.5
Ba	1900	687	5200	89400	13700	13000	9400	565	229	273	322
Sc	20.70	6.00	8.50	5.80	11.10	16.90	20.70	30.20	26.20	24.40	20.10
V	176.9	33.2	35.6	73.0	118.8	89.8	133.0	288.5	292.7	293.6	181.5
Cr	42.2	3.0	7.4	4.0	13.6	17.4	31.8	42.3	56.3	23.7	16.6
Ga	12.7	11.6	9.4	Pb, Ba interf.	24.9	19.2	10.5	12.9	16.6	14.5	13.0

Appendix 4:
REE analyses

Rare Earth Elements (REE) were measured in 15 argillite and 8 chert samples from the base of the HW Horizon. The samples were analysed by ICP-MS at the Geology Department, University of Tasmania, using the method of Yu et al. (2001).

Battle Mine - black chert

field #		drillhole	lithology	La	Ce	Pr	Nd	Sm	Eu	Gd	Tb	Dy	Ho	Er	Yb	Lu	La/Lu
SJ786	G50	L14-681	black chert	0.75	1.52	0.20	0.80	0.23	0.07	0.31	0.06	0.33	0.07	0.21	0.20	0.03	24.81
SJ806	G56	L14-680	black chert	2.55	2.51	0.35	1.52	0.54	0.24	0.91	0.17	0.98	0.21	0.61	0.55	0.09	29.59
SJ813	G104	L14-680	black chert	2.85	4.93	0.64	2.54	0.70	0.50	0.76	0.13	0.76	0.16	0.48	0.46	0.07	39.36

Battle Mine - chert/altered mudstone

SJ788	G35	L14-681	chert	3.28	4.92	0.80	3.25	0.69	0.16	0.57	0.08	0.47	0.10	0.29	0.31	0.05	72.43
SJ776	G6	L14-683	chert	4.05	7.68	0.97	3.97	0.91	0.29	0.83	0.13	0.66	0.13	0.39	0.45	0.07	60.47
SJ399	G67	18-1003	chert	13.75	24.66	3.11	13.14	2.86	0.78	2.84	0.38	2.00	0.46	1.44	1.77	0.32	43.35
SJ390	G69	18-1003	chert	2.27	3.96	0.48	1.86	0.42	0.09	0.41	0.06	0.32	0.07	0.23	0.38	0.07	33.16
SJ776	G42	L14-683	altd mud	6.30	11.39	1.40	5.59	1.32	0.54	1.38	0.25	1.53	0.34	1.07	1.27	0.20	30.92

Battle Basin -argillite

SJ763	G7	L14-677	argillite	16.64	27.55	3.66	15.64	3.65	1.86	4.61	0.81	5.06	1.20	3.59	3.62	0.57	29.00
SJ766	G8	L14-676	argillite	11.53	23.07	2.91	12.23	2.70	0.69	2.75	0.46	2.83	0.64	1.95	2.20	0.37	31.49
SJ765	G44	L14-676	argillite	15.13	29.75	3.90	16.13	3.74	0.92	3.28	0.50	3.05	0.66	2.02	2.07	0.33	45.48
SJ448	G72	18-1004	argillite/silt	16.87	34.01	4.36	19.10	5.59	1.14	8.29	1.57	10.03	2.33	7.11	7.43	1.17	14.46

HW Basin -argillite

SJ75	G93	23-489	argillite	9.89	15.50	2.39	10.60	3.19	1.18	3.70	0.54	3.03	0.59	1.54	1.28	0.20	50.72
SJ646T	G25	S335C	hw-arg	7.18	15.25	2.01	8.83	2.59	0.46	3.82	0.80	5.30	1.20	3.51	3.34	0.49	14.57
SJ669	G28	23 SHOP	hw-arg	7.71	12.77	1.60	6.12	1.26	0.20	1.30	0.23	1.55	0.39	1.28	1.57	0.25	30.76
SJ251	G98	23-503	argillite	36.34	73.67	9.24	36.94	8.05	1.22	8.07	1.54	10.38	2.38	7.43	7.49	1.18	30.75
SJ44	G115	23-493	argillite	10.09	15.57	2.26	8.71	1.88	0.38	2.59	0.48	2.97	0.61	1.68	1.38	0.20	49.56

Regional argillite

SJ831	G124	16-45	argillite	5.25	9.14	1.43	6.11	1.60	0.46	1.64	0.27	1.64	0.35	1.01	0.94	0.15	34.35
SJ605	G101	16-33	argillite	13.96	17.36	2.70	11.40	2.37	0.63	2.99	0.47	2.98	0.71	2.13	1.98	0.30	47.08
P189b	G111	L14-641	argillite	4.00	7.08	1.00	3.99	1.06	0.32	1.08	0.18	1.07	0.23	0.67	0.71	0.11	35.48
SJ824	G61	16-43	argillite	17.98	24.49	3.40	13.90	3.25	0.92	3.57	0.59	3.68	0.80	2.35	2.06	0.32	56.80
SJ630	G91	CR88-4	argillite	29.46	56.02	7.08	27.02	6.10	1.84	5.38	0.89	5.40	1.12	3.42	3.51	0.56	52.62
SJ629	G90	CR88-4	argillite	23.00	49.84	6.25	26.42	6.76	1.80	7.23	1.19	6.80	1.42	3.85	3.56	0.53	43.32

Appendix 5:
Sulphur-carbon-Fe analyses and sulphur isotopes

Appendix 5.1

Sulphide sulphur was determined by the chromium reduction method by Canfield et al. (1986), by the author at CODES, University of Tasmania.

Organic carbon was determined using the 'ashing' method of Krom and Berner (1983). Total carbon and sulphur analyses were collected on the Karlo Erber Elemental Analyser, Central Science Laboratory, University of Tasmania.

HCl-soluble Fe was obtained using the 1 N HCl 24-hour extraction method, recommended by Leventhal and Taylor (1990). HCl-soluble Fe was obtained on 4 repeat samples using the 12 N HCl boiling method of Berner (1970). The HCl-soluble Fe in solution was measured by Ashley Townsend using the ICP-OES (at a wavelength 259.9 nm, and detection limits of approximately 20 ppb) at the Central Science Laboratory, University of Tasmania.

Appendix 5.2

Sulphur isotope analyses were obtained from mono- and di-sulphides extracted from argillite and black chert samples, by the chromium reduction method of Canfield et al. (1986). Conventional $\delta^{34}S$ analyses were carried out at the Central Science Laboratory, University of Tasmania, using the analytical techniques of Robinson and Kusakabe (1975).

Appendix 5.1: Sulphur - Carbon - Fe analyses

Battle basin argillite/black chert

Field #	SJ764-G7	SJ766-G8	SJ317-G11	SJ807-G105	SJ765-G34	SJ815-G54	SJ806-G56	SJ813-G104	SJ810-G106	SJ809-G107
Drillhole	L14-677	L14-676	L14-680	L14-680	L14-676	L14-680	L14-680	L14-680	L14-680	L14-680
Lithology	Argillite	Argillite	Argillite	Argillite	Argillite	Black cht	Black cht	Black cht	Black cht	Black cht
Wt.%										
Carbonate C	2.90	0.75	0.03	0.07	0.10	0.05	0.08	0.04	0.03	0.01
Organic C	0.59	0.54	0.12	0.30	0.04	0.29	0.19	0.38	0.08	0.28
mono-S	0.004	0.020	0.047	0.040	0.000	0.173	0.000	0.316	0.056	0.054
di-S	1.53	0.85	0.65	0.50		0.95	0.62	0.81	0.27	0.37
Total S	1.53	0.87	0.70	0.54		1.12	0.62	1.12	0.32	0.42
S (XRF)	1.88	2.65	0.80	0.63		1.85	0.98	2.35	1.41	0.76
Fe_2O_3	3.41	4.02	0.88	0.76		1.81	1.24	2.37	1.66	0.86
Fe total	2.38	2.81	0.61	0.53		1.27	0.87	1.66	1.16	0.60
Py Fe	0.76	0.43	0.32	0.25		0.47	0.31	0.40	0.13	0.18
Fe_{TOT} - Py Fe	1.62	2.39	0.29	0.28		0.79	0.56	1.25	1.03	0.42
*HCl-sol Fe (1	0.19	0.06		0.00		0.00	0.00	0.01	0.00	0.00
*HCl-sol Fe (2)										
DOP_T	0.32	0.15	0.53	0.47		0.37	0.36	0.24	0.12	0.30
DOP_R	0.80	0.88		0.98		0.99	0.99	0.98	0.98	0.98

* HCl-sol Fe (1) refers to method 1, using 24 N HCL over 24 hours
* HCl-sol Fe (2) refers to method 2, using boiling HCl for 1 hour, then decanting (Leventhal and Taylor, 1990)

Battle basin black chert

Field #	SJ812-G109	SJ817-G110	SJ810-G57	SJ818-G108	SJ788-G35	SJ788a-G52	SJ789-G13	SJ789a-G53
Drillhole	L14-680	L14-680	L14-680	L14-680	L14-681	L14-681	L14-681	L14-681
Lithology	Black cht	Black cht	Black cht	Black cht	Black chert	Black chert	Black chert	Black chert
Wt.%								
Carbonate (	0.03	0.03	0.06	0.01	0.01	0.01	0.00	0.00
Organic C	0.16	0.15	0.07	0.21	0.07	0.06	0.00	0.00
mono-S	0.359	0.142	0.000	0.149	0.000	0.000	0.000	0.000
di-S	0.58	0.29		0.29				
Total S	0.94	0.43		0.44				
S (XRF)	1.37	0.50		0.54				
Fe_2O_3	1.18	0.43		0.47				
Fe total	0.83	0.30		0.33				
Py Fe	0.29	0.14		0.15				
Fe_{TOT} - Py F	0.54	0.16		0.18				
*HCl-sol Fe	0.00	0.00		0.00				
*HCl-sol Fe (2)								
DOP_T	0.35	0.48		0.44				
DOP_R	0.99	0.99		0.99				

Battle Mine white chert

SJ776-G06	SJ404-G33
L14-683	18-1003
Chert	Chert
0.08	0.07
0.06	0.02
0.000	

Battle Mine white chert

Field #	SJ25-G29	SJ786-G10	SJ776-G6	SJ810-G57	SJ785-G16	SJ404-G33
Drillhole	18-1032	L14-681	L14-683	L14-680	L14-681	18-1003
Lithology	Chert	Chert	Chert	Chert	Chert	Chert
Wt.%						
Carbonate C	0.00	0.00	0.08	0.06	0.00	0.07
Organic C	0.00	0.00	0.06	0.07	0.00	0.02
mono-S						
di-S						
Total S						
S (XRF)						
Fe_2O_3						
Fe total						
Py Fe						
Fe_{TOT} - Py Fe						
*HCl-sol Fe (1)						
*HCl-sol Fe (2)						
DOP_T						
DOP_R						

HW Mine Argillite

Field #	SJ733-G100	SJ637-G36	SJ669-G28	SJ75-G93
Drillhole	21-2072	21 LEVEL	23 SHOP	23-489
Lithology	Argillite	Argillite	Argillite	Argillite
Wt.%				
Carbonate C	0.69	0.47	0.03	0.11
Organic C	0.13	0.42	0.49	0.25
mono-S				
di-S	0.31	0.97	0.69	0.33
Total S	0.31	0.97	0.69	0.33
S (XRF)	1.18	1.40	1.06	1.12
Fe_2O_3	2.00	2.72	1.28	1.39
Fe total	1.40	1.90	0.90	0.97
Py Fe	0.15	0.48	0.34	0.16
Fe_{TOT} - Py Fe	1.25	1.42	0.55	0.80
*HCl-sol Fe (1)	0.01	0.04	0.19	0.01
*HCl-sol Fe (2)				
DOP_T	0.11	0.25	0.38	0.17
DOP_R	0.92	0.93	0.64	0.96

HW Mine Argillite

Field #	SJ731-G99	SJ732-G112	SJ74-G113	SJ660-G114	SJ44-G115	SJ83-G116	SJ492-G117	SJ492-G118	SJ491-G119
Drillhole	21-2072	21-2072	23-489	23 SHOP	23-493	23-488	23-514	23-514	23-514
Lithology	Argillite	Argillite	Argillite	Argillite	Argillite	Argillite	Argillite	Argillite	Argillite
Wt.%									
Carbonate C	0.59	0.47	0.11	0.02	0.02	0.02	0.44	0.43	0.50
Organic C	0.20	0.54	0.11	0.57	0.29	0.42	0.28	0.21	0.24
mono-S							0.003	0.0005	0.002
di-S	0.63	0.69	0.48	0.95	1.06	0.76	0.46	0.43	0.56
Total S	0.63	0.69	0.48	0.95	1.06	0.76	0.46	0.43	0.56
S (XRF)	1.00	0.90	0.98	1.24	1.99	1.31	0.75	0.74	0.97
Fe_2O_3	1.91	1.67	2.75	1.64	2.59	1.69	1.73	1.68	2.33
Fe total	1.34	1.17	1.92	1.15	1.81	1.18	1.21	1.17	1.63
Py Fe	0.31	0.34	0.24	0.48	0.53	0.38	0.23	0.21	0.28
Fe_{TOT} - Py Fe	1.02	0.82	1.68	0.67	1.28	0.80	0.98	0.96	1.35
*HCl-sol Fe (1)	0.02	0.02	0.02	0.01	0.01	0.00	0.01		
*HCl-sol Fe (2)									
DOP_T	0.23	0.29	0.13	0.42	0.29	0.32	0.19	0.18	0.17
DOP_R	0.95	0.94	0.93	0.98	0.98	0.99	0.95		

HW north-Price Argillite

Field #	SJ52-G95	SJ621-G126	SJ621-G127	SJ624-G102
Drillhole	W202	PR13-68	PR13-68	PR13-68
Lithology	Argillite	Argillite	Argillite	Argillite
Wt.%				
Carbonate C	0.14	0.60	0.31	0.65
Organic C	0.11	0.05	0.27	0.18
mono-S	0.002	0.002	0.000	0.003
di-S	0.34	0.72	0.61	0.85
Total S	0.34	0.72	0.61	0.85
S (XRF)	0.54	0.95	0.91	1.41
Fe_2O_3	1.54	3.04	3.29	3.02
Fe total	1.08	2.13	2.30	2.11
Py Fe	0.17	0.36	0.30	0.43
Fe_{TOT} - Py Fe	0.91	1.76	2.00	1.69
*HCl-sol Fe (1)	0.03	0.04	0.06	0.03
*HCl-sol Fe (2)				
DOP_T	0.16	0.17	0.13	0.20
DOP_R	0.85	0.90	0.85	0.93

Thelwood Valley Argillite

SJ221-G103	SJ630-G91	SJ629-G90	SJ223b-G120	SJ432-G121	SJ432-G122
PR124	CR88-4	CR88-4	PR124	PR124	PR124
Argillite	Chert	Chert	Argillite	Argillite	Argillite
0.37	0.19	0.05	0.54	0.83	0.72
0.13	0.03	0.00	0.27	0.29	0.26
0.085			0.297	0.050	0.084
0.41			0.32	0.28	0.66
0.49			0.62	0.33	0.74
0.51			0.71	0.64	0.91
1.54			3.57	2.25	2.31
1.08			2.50	1.57	1.62
0.20			0.16	0.14	0.33
0.87			2.34	1.43	1.29
0.02			0.03	0.02	0.02
0.19			0.06	0.09	0.20
0.89			0.84	0.85	0.94

South Flank Argillite

Field #	SJ605-G101	SJ824-G61	SJ607-G92	P189b-G111	SJ830-G123	SJ718-G75	SJ831-G124	SJ832-G125	SJ717-G74
Drillhole	16-33	16-43	16-33	L14-641	16-36	L14-641	16-45	16-61	L14-641
Lithology	Argillite	Argillite	Argillite	Argillite	Argillite	Argillite	Argillite	Argillite	Argillite
Wt.%									
Carbonate C	0.50	0.86	0.52	0.26	0.61	0.39	0.31	1.07	0.47
Organic C	0.10	0.38	0.22	0.33	0.06	0.16	0.16	0.17	0.23
mono-S	0.003		0.185	0.041	0.008	0.009	0.390	0.334	0.678
di-S	0.27	0.58	0.66	0.40	0.15	0.42	0.43	0.23	0.21
Total S	0.27	0.58	0.85	0.44	0.16	0.43	0.82	0.56	0.89
S (XRF)	0.27	1.04	1.05	0.90	0.20	0.55	0.86	0.71	0.88
Fe_2O_3	2.59	3.18	2.54	3.07	2.92	3.41	2.86	5.42	2.65
Fe total	1.81	2.22	1.78	2.15	2.04	2.38	2.00	3.79	1.86
Py Fe	0.13	0.29	0.33	0.20	0.07	0.21	0.21	0.11	0.11
Fe_{TOT} - Py Fe	1.68	1.93	1.45	1.95	1.97	2.17	1.79	3.68	1.75
*HCl-sol Fe (1)	0.07	0.11	0.03	0.04	0.03	0.06	0.04	0.05	0.03
*HCl-sol Fe (2)									
DOP_T	0.07	0.13	0.19	0.09	0.04	0.09	0.11	0.03	0.06
DOP_R	0.66	0.74	0.92	0.83	0.70	0.77	0.83	0.68	0.81

Appendix 5.2: Sulphur isotopes

SO_2 Analysis

CSL No.	Catalogue No.	Field No.	Chem. No.	Drillhole/ drive	Mineral	Weight (mg)	Yield (mmHg)	Delta S (wrt CDT)
6817		SJ764a	G7	L14-677	Pyrite (?)	26.6	14.0	-15.05
6818		SJ766	G8	L14-676	Pyrite (?)	28.1	14.6	-25.99
6819		SJ766	G8-monoS	L14-676	Pyrite (?)	8.5*	4.8	-18.19
6820		SJ317	G11	L14-680	Pyrite (?)	26.9	14.8	-14.49
6821		SJ317	G11 monoS	L14-680	Pyrite (?)	27.2*	15.0	-7.36
6822		SJ669	G28	23 shop	Pyrite (?)	31.6	18.4	-14.11
6832		SJ637	G36	21 level	Pyrite (?)	26.3	15.0	-35.21
6824		SJ815	G54	L14-680	Pyrite (?)	26.0	14.2	-8.96
6825		SJ815	G54 monoS	L14-680	Pyrite (?)	29.4	15.8	-5.39
6826		SJ806	G56	L14-680	Pyrite (?)	26.5	14.6	-18.37
6827		SJ824	G61	16-43	Pyrite (?)	38.8	21.8	-19.79
6828		SJ717	G74	L14-641	Pyrite (?)	32.9	17.5	-28.07
6829		SJ717	G74 monoS	L14-641	Pyrite (?)	23.8	13.2	-26.03
6830		SJ607	G92	16-33	Pyrite (?)	24.8	12.6	-27.33
6831		SJ607	G92 monoS	16-33	Pyrite (?)	26.8	14.2	-32.28
6833		SJ75	G93	23-489	Pyrite (?)	28.2	15.4	-31.67
6834		SJ731	G99	21-2072	Pyrite (?)	28.1	15.2	-29.51
6835		SJ605	G101	16-33	Pyrite (?)	30.5	17.2	-10.31
6836		SJ624	G102	PR13-68	Pyrite (?)	27.2	14.8	-21.76
6837		SJ221	G103	PR124	Pyrite (?)	25.2	12.0	-18.50
6838		SJ221	G103 monoS	PR124	Pyrite (?)	27.6	15.8	-24.86

Mono- and di-sulphur extracted from argillites by the chromium reduction method of Canfield et al. (1986).

Appendix 6:
Microprobe analyses

White mica, apatite and sphalerite were analysed by the Cameca SX-50 electron microprobe at the Central Science Laboratory, University of Tasmania.

Appendix 6.1 – Apatite microprobe analyses

Analytical conditions for the apatites were as follows:

Beam current 15 nA for F, Na, Cl, Ca, Mn
Beam current 60 nA for other elements
(F, Na and Cl run first to minimise alkali migration and halogen loss)
Acceleration voltage 20 kV
Take off angle 40°
Beam size 10 μm

Appendix 6.2 – White mica microprobe analyses

Analytical conditions for the white micas were as follows:

Beam current 25 nA
Acceleration voltage 15 kV
Take off angle 40°
Beam size 1 μm
Mineral formulae for the white mica were calculated on the basis of 22 oxygens

Appendix 6.3 – Sphalerite microprobe analyses

Analytical conditions for the sphalerite were as follows:

Beam current 60 nA
Acceleration voltage 20 kV
Take off angle 40°
Beam size 1 μm

Appendix 6.1
Microprobe analyses of apatite

Large type-2 apatites within spherical megaquartz patches in siliceous caprocks, Battle Mine

Catalogue #								
Field #	SJ161a-17	SJ161a-17	SJ161a-17	SJ161a-17	SJ161a-17	SJ161a-17	SJ161a-17	SJ161a-17
Drillhole	18-1127	18-1127	18-1127	18-1127	18-1127	18-1127	18-1127	18-1127
Point	apa1	apa2-1	apa2-2	apa2-3	apa2-4	apa3-1	apa3-2	apa3-3
SiO2	0.09	0.03	0.01	0.03	0.07	0.07	0.04	0.05
Fe2O3	0.00	0.00	0.02	0.06	0.00	0.05	0.02	0.03
MnO	0.03	0.04	0.00	0.04	0.03	0.03	0.02	0.04
MgO	0.00	0.00	0.00	0.00	0.00	0.00	0.00	0.00
CaO	54.17	55.06	54.36	54.14	53.80	53.27	54.55	53.95
Na2O	0.04	0.03	0.02	0.04	0.02	0.06	0.03	0.02
P2O5	40.95	41.42	39.74	40.42	40.55	40.35	40.55	40.63
SO3	0.08	0.03	0.03	0.1	0.17	0.22	0.03	0.14
La2O3	0.03	0	0	0.03	0	0.01	0.01	0.04
Ce2O3	0.04	0.01	0	0	0.05	0	0.01	0.02
Pr2O3	0	0	0	0.02	0	0	0	0.07
Nd2O3	0.11	0	0.01	0.01	0	0.02	0.07	0
Sm2O3	0	0.03	0	0	0	0.02	0	0
Y2O3	0.2	0.2	0	0.17	0.07	0.17	0.01	0.1
SrO	0.04	0.03	0.1	0.08	0.13	0.07	0.09	0.06
BaO	0	0.01	0	0.03	0.19	0	0	0.01
As2O3	0	0.02	0	0.02	0.02	0.02	0	0.02
F	4.56	4.53	4.36	4.19	4.41	4.47	4.87	4.32
Cl	0	0.01	0	0.01	0.02	0	0	0
H2O(c)	0	0	0	0	0	0	0	0
O=F	1.92	1.91	1.84	1.76	1.86	1.88	2.05	1.82
O=Cl	0	0	0	0	0	0	0	0
Sum Ox%	98.45	99.54	96.82	97.62	97.68	96.96	98.24	97.67
Si	0.016	0.006	0.001	0.005	0.012	0.011	0.007	0.009
Fe3+	0	0	0.003	0.007	0	0.007	0.002	0.004
Mn2+	0.005	0.005	0	0.006	0.004	0.005	0.003	0.006
Mg	0	0	0	0	0	0	0	0
Ca	9.976	10.028	10.215	10.054	9.987	9.945	10.106	10
Na	0.015	0.009	0.006	0.014	0.006	0.022	0.009	0.006
P	5.959	5.96	5.901	5.932	5.948	5.953	5.935	5.951
S	0.011	0.004	0.004	0.013	0.022	0.028	0.005	0.018
La	0.002	0	0	0.002	0	0.001	0.001	0.003
Ce	0.003	0.001	0	0	0.003	0	0.001	0.001
Pr	0	0	0	0.001	0	0	0	0.004
Nd	0.006	0	0.001	0.001	0	0.002	0.004	0
Sm	0	0.001	0	0	0	0.001	0	0
Y	0.019	0.019	0	0.016	0.006	0.016	0.001	0.009
Sr	0.004	0.003	0.01	0.008	0.014	0.007	0.009	0.006
Ba	0	0.001	0	0.002	0.013	0	0	0.001
As	0	0.002	0	0.002	0.002	0.002	0	0.002
F	2.478	2.436	2.42	2.297	2.414	2.461	2.662	2.364
Cl	0.001	0.002	0	0.003	0.004	0	0.001	0
OH	0	0	0	0	0	0	0	0
Sum Cat#	18.494	18.477	18.561	18.363	18.437	18.461	18.745	18.384
Me	10.023	10.065	10.231	10.101	10.034	9.996	10.129	10.032
X	5.975	5.966	5.905	5.944	5.961	5.971	5.944	5.963
Z	2.478	2.439	2.42	2.3	2.418	2.461	2.663	2.364

Appendix 6.1
Microprobe analyses of apatite

Large type-2 apatites within spherical megaquartz patches in siliceous caprocks, Battle Mine

Catalogue #								
Field #	SJ161a-17	SJ161a-17	SJ161a-17	SJ161a-17	SJ161a-17	SJ161a-17	SJ161a-17	SJ161a-17
Drillhole	18-1127	18-1127	18-1127	18-1127	18-1127	18-1127	18-1127	18-1127
Point	apa3-4	apa3-5	apa4-1	apa4-2	apa4-3	apa4-4	apa4-5	apa4-6
SiO2	0.06	0.17	0.03	0.01	0.12	0.04	0.02	0.02
Fe2O3	0.00	0.00	0.04	0.03	0.00	0.00	0.00	0.00
MnO	0.04	0.00	0.04	0.04	0.02	0.03	0.03	0.03
MgO	0.00	0.00	0.00	0.00	0.00	0.00	0.00	0.00
CaO	53.87	54.33	54.04	53.98	53.43	53.61	54.00	53.99
Na2O	0.12	0.07	0.27	0.14	0.05	0.07	0.06	0.06
P2O5	40.00	40.63	41.40	41.12	40.33	40.77	40.92	40.52
SO3	0.35	0.32	0.7	0.51	0.06	0.24	0.28	0.27
La2O3	0	0.01	0.02	0.01	0	0	0.02	0.01
Ce2O3	0.05	0	0	0.01	0.07	0.03	0.02	0
Pr2O3	0.03	0.04	0	0	0	0	0	0.14
Nd2O3	0.08	0.08	0.04	0	0.07	0.03	0.01	0.06
Sm2O3	0.04	0	0	0.02	0	0.04	0	0
Y2O3	0.16	0.1	0	0.04	0.12	0.08	0.07	0.01
SrO	0.14	0.06	0.09	0.11	0.03	0.11	0.17	0.16
BaO	0.03	0.03	0.01	0	0.01	0.03	0	0
As2O3	0.01	0	0.02	0	0.01	0.01	0.01	0
F	3.92	4.18	4.04	4.02	4.05	4.06	4.06	3.93
Cl	0	0.01	0	0.01	0.01	0.01	0	0
H2O(c)	0	0	0	0	0	0	0	0
O=F	1.65	1.76	1.7	1.69	1.71	1.71	1.71	1.66
O=Cl	0	0	0	0	0	0	0	0
Sum Ox%	97.24	98.27	99.04	98.37	96.67	97.45	97.97	97.55
Si	0.01	0.03	0.005	0.002	0.02	0.008	0.003	0.004
Fe3+	0	0	0.005	0.004	0	0	0	0
Mn2+	0.005	0	0.006	0.006	0.003	0.004	0.004	0.005
Mg	0	0	0	0	0	0	0	0
Ca	10.036	9.998	9.807	9.877	9.992	9.927	9.947	10.003
Na	0.042	0.025	0.09	0.045	0.016	0.024	0.02	0.021
P	5.889	5.909	5.936	5.946	5.959	5.966	5.956	5.932
S	0.046	0.041	0.089	0.065	0.007	0.031	0.036	0.035
La	0	0.001	0.001	0	0	0	0.001	0.001
Ce	0.003	0	0	0.001	0.005	0.002	0.001	0
Pr	0.002	0.002	0	0	0	0	0	0.009
Nd	0.005	0.005	0.003	0	0.004	0.002	0.001	0.004
Sm	0.003	0	0	0.001	0	0.002	0	0
Y	0.015	0.009	0	0.004	0.012	0.008	0.006	0.001
Sr	0.014	0.006	0.008	0.011	0.003	0.011	0.017	0.016
Ba	0.002	0.002	0.001	0	0.001	0.002	0	0
As	0.001	0	0.002	0	0.001	0.001	0.002	0
F	2.156	2.27	2.166	2.172	2.238	2.219	2.208	2.151
Cl	0	0.002	0	0.002	0.002	0.002	0	0
OH	0	0	0	0	0	0	0	0
Sum Cat#	18.228	18.3	18.118	18.14	18.263	18.208	18.203	18.181
Me	10.117	10.041	9.913	9.945	10.031	9.977	9.997	10.046
X	5.899	5.939	5.946	5.953	5.98	5.974	5.96	5.937
Z	2.156	2.272	2.166	2.174	2.24	2.221	2.208	2.151

Appendix 6.1
Microprobe analyses of apatite

Large type-2 apatites within spherical megaquartz patches in siliceous caprocks, Battle Mine

Catalogue #								
Field #	SJ161a-17	SJ161a-17	SJ161a-17	SJ161a-17	SJ161a-17	SJ161a-17	SJ161a-17	SJ161a-17
Drillhole	18-1127	18-1127	18-1127	18-1127	18-1127	18-1127	18-1127	18-1127
Point	apa4-7	apa5-1	apa5-2	apa5-3	apa6-1	apa6-2	apa6-3	apa7-1
SiO2	0.02	0.08	0.04	0.04	2.92	0.02	0.05	0.03
Fe2O3	0.00	0.01	0.00	0.03	0.00	0.00	0.03	0.00
MnO	0.01	0.05	0.02	0.00	0.01	0.03	0.05	0.03
MgO	0.00	0.00	0.00	0.00	0.00	0.00	0.00	0.00
CaO	54.16	54.31	53.21	54.18	53.73	53.35	53.75	53.76
Na2O	0.14	0.08	0.07	0.01	0.02	0.07	0.03	0.15
P2O5	40.68	41.10	40.44	40.04	39.46	40.81	40.35	39.53
SO3	0.56	0.34	0.08	0.05	0.1	0.18	0.26	0.51
La2O3	0	0	0.03	0.01	0	0.07	0.04	0.01
Ce2O3	0.02	0.02	0.08	0.04	0	0.01	0.04	0.01
Pr2O3	0	0	0.03	0.07	0	0	0	0
Nd2O3	0	0.08	0.1	0.12	0	0	0	0.03
Sm2O3	0.02	0	0.03	0	0.06	0	0.09	0.08
Y2O3	0.07	0	0.07	0.01	0.06	0.07	0.33	0.1
SrO	0.08	0.09	0.03	0.05	0.13	0.18	0.11	0.15
BaO	0	0	0.04	0.02	0.01	0.03	0	0.02
As2O3	0.02	0	0.02	0.02	0.02	0.03	0.01	0
F	3.94	4.42	4.06	4.02	5.03	4.7	4.74	4.14
Cl	0	0	0	0	0.01	0	0.01	0.01
H2O(c)	0	0	0	0	0	0	0	0
O=F	1.66	1.86	1.71	1.69	2.12	1.98	2	1.74
O=Cl	0	0	0	0	0	0	0	0
Sum Ox%	98.06	98.7	96.64	97.03	99.44	97.57	97.91	96.8
Si	0.004	0.014	0.007	0.008	0.495	0.003	0.009	0.005
Fe3+	0	0.001	0	0.003	0	0	0.003	0
Mn2+	0.002	0.007	0.003	0	0.002	0.005	0.008	0.005
Mg	0	0	0.001	0	0	0	0	0
Ca	9.955	9.941	9.953	10.131	9.768	9.902	9.982	10.08
Na	0.045	0.027	0.022	0.004	0.008	0.022	0.009	0.049
P	5.909	5.945	5.977	5.916	5.667	5.986	5.922	5.855
S	0.072	0.043	0.011	0.007	0.013	0.023	0.034	0.067
La	0	0	0.002	0.001	0	0.004	0.003	0.001
Ce	0.001	0.001	0.005	0.003	0	0.001	0.003	0.001
Pr	0	0	0.002	0.005	0	0	0	0
Nd	0	0.005	0.006	0.007	0	0	0	0.002
Sm	0.001	0	0.002	0	0.003	0	0.006	0.005
Y	0.007	0	0.006	0.001	0.006	0.007	0.031	0.009
Sr	0.008	0.009	0.003	0.006	0.013	0.018	0.011	0.015
Ba	0	0	0.003	0.002	0	0.002	0	0.001
As	0.002	0	0.002	0.002	0.002	0.003	0.001	0
F	2.139	2.386	2.24	2.22	2.699	2.575	2.598	2.291
Cl	0.001	0	0	0	0.002	0	0.003	0.004
OH	0	0	0	0	0	0	0	0
Sum Cat#	18.145	18.379	18.245	18.315	18.677	18.551	18.622	18.389
Me	10.018	9.985	9.999	10.147	9.797	9.961	10.047	10.161
X	5.913	5.96	5.983	5.928	6.162	5.988	5.934	5.86
Z	2.139	2.386	2.24	2.22	2.7	2.575	2.601	2.295

Appendix 6.1
Microprobe analyses of apatite

Large type-2 apatites within spherical megaquartz patches in siliceous caprocks, Battle Mine

Catalogue #								
Field #	SJ161a-17	SJ161a-17	SJ161a-17	SJ161a-17	SJ161a-17	SJ161a-17	SJ161a-17	SJ161a-17
Drillhole	18-1127	18-1127	18-1127	18-1127	18-1127	18-1127	18-1127	18-1127
Point	apa7-2	apa7-3	apa7-4	apa8-1	apa8-2	apa8-2	apa9	apa10-1
SiO2	0.12	0.02	0.41	0.06	0.10	0.04	0.07	0.07
Fe2O3	0.00	0.01	0.02	0.00	0.02	0.00	0.01	0.01
MnO	0.02	0.01	0.00	0.05	0.03	0.04	0.05	0.06
MgO	0.00	0.00	0.00	0.00	0.00	0.00	0.00	0.00
CaO	53.19	53.49	53.95	54.11	54.36	54.45	53.92	54.01
Na2O	0.11	0.15	0.03	0.07	0.13	0.08	0.04	0.06
P2O5	40.45	40.23	39.73	40.11	40.15	39.72	40.02	40.38
SO3	0.29	0.49	0.03	0.38	0.42	0.4	0.31	0.19
La2O3	0	0.02	0	0.04	0	0.03	0	0
Ce2O3	0	0	0.02	0.03	0.04	0	0	0.03
Pr2O3	0	0	0.06	0	0.07	0	0	0
Nd2O3	0	0.1	0.02	0.03	0.05	0	0.01	0.07
Sm2O3	0.03	0	0.01	0.01	0.01	0	0	0.02
Y2O3	0.13	0.11	0	0.03	0	0.07	0.36	0.05
SrO	0.13	0.11	0.03	0.08	0.11	0.11	0.16	0.15
BaO	0.01	0.02	0.01	0.04	0.06	0.03	0	0
As2O3	0.03	0.02	0	0.02	0.03	0.01	0.01	0.01
F	4	4.1	4.16	4.36	4.07	4.64	4.74	5.43
Cl	0.01	0.01	0.01	0.01	0	0	0	0
H2O(c)	0	0	0	0	0	0	0	0
O=F	1.69	1.73	1.75	1.84	1.72	1.95	1.99	2.29
O=Cl	0	0	0	0	0	0	0	0
Sum Ox%	96.83	97.16	96.72	97.59	97.95	97.66	97.72	98.26
Si	0.02	0.003	0.072	0.01	0.018	0.006	0.013	0.012
Fe3+	0	0.002	0.002	0	0.002	0	0.002	0.001
Mn2+	0.003	0.002	0	0.008	0.004	0.006	0.007	0.009
Mg	0	0	0	0	0	0	0	0
Ca	9.904	9.95	10.111	10.057	10.059	10.153	10.043	10.032
Na	0.036	0.05	0.01	0.025	0.045	0.028	0.014	0.019
P	5.952	5.913	5.884	5.891	5.87	5.852	5.89	5.926
S	0.038	0.064	0.005	0.049	0.054	0.052	0.04	0.024
La	0	0.001	0	0.002	0	0.002	0	0
Ce	0	0	0.001	0.002	0.003	0	0	0.002
Pr	0	0	0.004	0	0.005	0	0	0
Nd	0	0.006	0.001	0.002	0.003	0	0.001	0.004
Sm	0.002	0	0.001	0.001	0.001	0	0	0.001
Y	0.012	0.011	0	0.003	0	0.007	0.034	0.005
Sr	0.013	0.011	0.003	0.008	0.011	0.011	0.016	0.015
Ba	0	0.001	0	0.003	0.004	0.002	0	0
As	0.003	0.002	0	0.002	0.003	0.001	0.001	0.001
F	2.2	2.252	2.299	2.394	2.225	2.555	2.604	2.978
Cl	0.003	0.002	0.002	0.002	0	0	0	0
OH	0	0	0	0	0	0	0	0
Sum Cat#	18.187	18.268	18.395	18.458	18.308	18.676	18.666	19.031
Me	9.969	10.025	10.126	10.108	10.126	10.21	10.115	10.083
X	5.973	5.917	5.958	5.9	5.89	5.859	5.904	5.939
Z	2.203	2.254	2.301	2.395	2.225	2.555	2.605	2.978

Appendix 6.1
Microprobe analyses of apatite

Large type-2 apatites within spherical megaquartz patches in siliceous caprocks, Battle Mine

Catalogue #								
Field #	SJ161a-17	SJ161a-17	SJ161a-17	SJ161a-17	SJ161a-17	SJ161a-17	SJ161a-17	SJ161a-17
Drillhole	18-1127	18-1127	18-1127	18-1127	18-1127	18-1127	18-1127	18-1127
Point	apa10-2	apa10-3	apa11-1	apa11-2	apa11-3	apa12-1	apa12-2	apa12-3
SiO2	0.01	1.11	0.07	0.02	0.06	0.05	0.02	4.84
Fe2O3	0.00	0.04	0.00	0.01	0.02	0.02	0.00	0.03
MnO	0.10	0.02	0.02	0.03	0.06	0.05	0.05	0.02
MgO	0.00	0.01	0.00	0.00	0.00	0.00	0.00	0.01
CaO	54.90	53.30	54.14	54.45	54.64	54.13	53.71	53.63
Na2O	0.04	0.03	0.11	0.04	0.08	0.05	0.09	0.07
P2O5	39.99	39.02	39.99	40.20	39.91	39.54	39.77	38.20
SO3	0.09	0.04	0.4	0.18	0.2	0.24	0.19	0.13
La2O3	0	0	0.01	0.02	0	0.01	0.02	0.03
Ce2O3	0	0.02	0	0.02	0.02	0	0.01	0.02
Pr2O3	0.02	0.03	0	0	0	0.01	0	0
Nd2O3	0.03	0.01	0.09	0	0.07	0.02	0.04	0.11
Sm2O3	0	0	0	0.03	0.07	0	0	0
Y2O3	0.02	0.06	0.03	0.04	0.16	0.02	0.04	0.05
SrO	0.2	0.1	0.14	0.21	0.12	0.09	0.16	0.18
BaO	0.02	0.04	0	0	0.02	0.01	0.01	0
As2O3	0.02	0	0.01	0.02	0.03	0.01	0.01	0
F	5.29	5.36	4.99	4.72	4.82	4.93	5.15	5.33
Cl	0	0	0	0	0	0	0	0
H2O(c)	0	0	0	0	0	0	0	0
O=F	2.23	2.26	2.1	1.99	2.03	2.08	2.17	2.25
O=Cl	0	0	0	0	0	0	0	0
Sum Ox%	98.5	96.93	97.92	98	98.23	97.1	97.11	100.41
Si	0.001	0.196	0.012	0.003	0.011	0.008	0.003	0.814
Fe3+	0	0.006	0	0.002	0.002	0.003	0	0.003
Mn2+	0.014	0.003	0.003	0.005	0.008	0.007	0.008	0.003
Mg	0	0.003	0	0	0	0	0	0.004
Ca	10.212	10.035	10.072	10.118	10.161	10.173	10.096	9.664
Na	0.012	0.011	0.039	0.014	0.027	0.018	0.032	0.021
P	5.878	5.805	5.878	5.902	5.864	5.871	5.907	5.439
S	0.012	0.005	0.053	0.023	0.026	0.031	0.025	0.016
La	0	0	0	0.001	0	0	0.001	0.002
Ce	0	0.001	0	0.001	0.001	0	0.001	0.001
Pr	0.001	0.002	0	0	0	0.001	0	0
Nd	0.002	0	0.006	0	0.004	0.002	0.002	0.007
Sm	0	0	0	0.002	0.004	0	0	0
Y	0.002	0.006	0.003	0.003	0.015	0.002	0.004	0.005
Sr	0.02	0.01	0.015	0.021	0.012	0.009	0.017	0.017
Ba	0.001	0.002	0	0	0.001	0	0.001	0
As	0.003	0	0.001	0.002	0.003	0.001	0.001	0
F	2.906	2.98	2.743	2.588	2.644	2.736	2.859	2.836
Cl	0	0.001	0	0.001	0	0	0	0
OH	0	0	0	0	0	0	0	0
Sum Cat#	19.066	19.067	18.823	18.687	18.784	18.864	18.956	18.833
Me	10.262	10.072	10.132	10.165	10.226	10.211	10.158	9.717
X	5.88	6.006	5.889	5.907	5.877	5.882	5.91	6.257
Z	2.907	2.981	2.743	2.588	2.644	2.736	2.859	2.836

Appendix 6.1
Microprobe analyses of apatite

Large type-2 apatites within spherical megaquartz patches in siliceous caprocks, Battle Mine

Catalogue #								
Field #	SJ161a-17	SJ161a-17	SJ161a-17	SJ161a-17	SJ161a-17	SJ161a-17	SJ161a-17	SJ161a-17
Drillhole	18-1127	18-1127	18-1127	18-1127	18-1127	18-1127	18-1127	18-1127
Point	apa13-1	apa13-2	apa13-3	apa13-4	apa14-2	apa14-1	apa15-1	apa15-2
SiO2	0.04	2.52	0.06	0.09	0.19	0.04	0.01	0.04
Fe2O3	0.02	0.00	0.00	0.01	0.02	0.02	0.03	0.02
MnO	0.03	0.04	0.03	0.02	0.02	0.05	0.04	0.03
MgO	0.00	0.00	0.00	0.00	0.00	0.00	0.00	0.00
CaO	54.11	53.83	53.77	54.23	54.25	53.09	54.10	54.25
Na2O	0.12	0.07	0.13	0.14	0.10	0.03	0.04	0.16
P2O5	39.45	39.79	39.04	39.86	39.49	40.24	39.67	40.35
SO3	0.5	0.1	0.36	0.37	0.31	0.18	0.22	0.41
La2O3	0	0	0.01	0	0.02	0.00	0.00	0.01
Ce2O3	0	0.03	0.01	0	0.00	0.01	0.00	0.05
Pr2O3	0	0	0	0	0.00	0.00	0.01	0.00
Nd2O3	0	0.09	0	0	0.05	0.10	0.04	0.00
Sm2O3	0.07	0.02	0.03	0	0.00	0.07	0.00	0.00
Y2O3	0.07	0.1	0.19	0.09	0.04	0.26	0.03	0.02
SrO	0.11	0.12	0.14	0.08	0.11	0.12	0.13	0.11
BaO	0.03	0.03	0	0	0.02	0.00	0.00	0.00
As2O3	0.02	0	0.01	0	0.03	0.01	0.01	0.03
F	5.24	5.02	5.17	5.05	4.91	5.18	3.91	4.05
Cl	0	0	0	0.01	0.00	0.00	0.00	0.00
H2O(c)	0	0	0	0	0.00	0.00	0.00	0.00
O=F	2.2	2.11	2.18	2.13	2.07	2.18	1.64	1.70
O=Cl	0	0	0	0	0.00	0.00	0.00	0.00
Sum Ox%	97.6	99.64	96.77	97.83	97.48	97.23	96.58	97.81
Si	0.007	0.426	0.011	0.015	0.03	0.01	0.00	0.01
Fe3+	0.002	0	0	0.001	0.00	0.00	0.00	0.00
Mn2+	0.004	0.005	0.004	0.003	0.00	0.01	0.01	0.00
Mg	0	0	0	0	0.00	0.00	0.00	0.00
Ca	10.135	9.776	10.173	10.104	10.16	9.94	10.16	10.03
Na	0.042	0.023	0.044	0.049	0.03	0.01	0.01	0.05
P	5.837	5.71	5.836	5.868	5.84	5.96	5.89	5.90
S	0.066	0.013	0.047	0.048	0.04	0.02	0.03	0.05
La	0	0	0.001	0	0.00	0.00	0.00	0.00
Ce	0	0.002	0.001	0	0.00	0.00	0.00	0.00
Pr	0	0	0	0	0.00	0.00	0.00	0.00
Nd	0	0.005	0	0	0.00	0.01	0.00	0.00
Sm	0.004	0.001	0.002	0	0.00	0.00	0.00	0.00
Y	0.006	0.009	0.018	0.009	0.00	0.02	0.00	0.00
Sr	0.011	0.012	0.014	0.008	0.01	0.01	0.01	0.01
Ba	0.002	0.002	0	0	0.00	0.00	0.00	0.00
As	0.002	0	0.001	0	0.00	0.00	0.00	0.00
F	2.894	2.691	2.886	2.777	2.71	2.86	2.16	2.21
Cl	0	0.001	0.001	0.002	0.00	0.00	0.00	0.00
OH	0	0	0	0	0.00	0.00	0.00	0.00
Sum Cat#	19.013	18.676	19.039	18.883	18.85	18.86	18.28	18.27
Me	10.201	9.829	10.254	10.172	10.21	10.00	10.19	10.11
X	5.846	6.137	5.847	5.884	5.88	5.96	5.89	5.90
Z	2.894	2.691	2.887	2.778	2.71	2.86	2.16	2.21

Appendix 6.1
Microprobe analyses of apatite

	Large type-2 apatites within spherical megaquartz in siliceous caprocks, Ba				Type-2 apatite	Fine euhedral type-1 apatites in ovoid concretions, Battle mine		
Catalogue #								
Field #	**SJ161a-17**	**SJ161a-17**	**SJ161a-17**	**SJ161a-17**	**SJ161a-17**	**SJ441b-152**	**SJ441b-152**	**SJ441b-152**
Drillhole	**18-1127**	**18-1127**	**18-1127**	**18-1127**	**18-1127**	**18-1004**	**18-1004**	**18-1004**
Point	**apa16-1**	**apa16-2**	**apa16-3**	**apa16-4**	**apa16-5**	**apa1**	**apa2**	**apa3**
SiO2	0.02	0.41	0.02	8.12	14.98	3.95	2.79	3.30
Fe2O3	0.00	0.00	0.01	0.00	0.06	0.04	0.01	0.02
MnO	0.08	0.03	0.00	0.02	0.01	0.02	0.04	0.06
MgO	0.00	0.00	0.00	0.00	0.07	0.01	0.00	0.00
CaO	53.71	53.11	54.06	49.59	45.56	53.60	52.82	52.74
Na2O	0.28	0.06	0.06	0.06	0.11	0.01	0.00	0.02
P2O5	39.29	40.21	40.06	38.72	34.25	39.17	39.58	38.76
SO3	0.86	0.24	0.19	0.15	0.21	0.02	0.03	0.10
La2O3	0.00	0.01	0.00	0.00	0.01	0.01	0.00	0.03
Ce2O3	0.01	0.02	0.01	0.00	0.00	0.00	0.02	0.01
Pr2O3	0.00	0.04	0.01	0.00	0.07	0.00	0.00	0.00
Nd2O3	0.03	0.02	0.06	0.18	0.08	0.08	0.03	0.00
Sm2O3	0.03	0.00	0.00	0.03	0.02	0.00	0.06	0.00
Y2O3	0.16	0.15	0.01	0.05	0.06	0.04	0.03	0.05
SrO	0.17	0.12	0.10	0.17	0.13	0.05	0.06	0.06
BaO	0.00	0.00	0.01	0.05	0.10	0.00	0.00	0.00
As2O3	0.01	0.01	0.00	0.00	0.00	0.01	0.00	0.02
F	4.10	4.53	4.55	3.84	3.30	4.23	5.10	5.13
Cl	0.00	0.00	0.00	0.00	0.00	0.00	0.01	0.01
H2O(c)	0.00	0.00	0.00	0.00	0.26	0.00	0.00	0.00
O=F	1.72	1.91	1.91	1.62	1.39	1.78	2.15	2.16
O=Cl	0.00	0.00	0.00	0.00	0.00	0.00	0.00	0.00
Sum Ox%	97.03	97.05	97.25	99.38	97.88	99.46	98.40	98.15
Si	0.00	0.07	0.00	1.34	2.46	0.67	0.48	0.57
Fe3+	0.00	0.00	0.00	0.00	0.01	0.01	0.00	0.00
Mn2+	0.01	0.01	0.00	0.00	0.00	0.00	0.01	0.01
Mg	0.00	0.00	0.00	0.00	0.02	0.00	0.00	0.00
Ca	10.04	9.90	10.10	8.74	8.01	9.67	9.68	9.70
Na	0.10	0.02	0.02	0.02	0.03	0.00	0.00	0.01
P	5.80	5.92	5.91	5.39	4.76	5.58	5.73	5.64
S	0.11	0.03	0.03	0.02	0.03	0.00	0.00	0.01
La	0.00	0.00	0.00	0.00	0.00	0.00	0.00	0.00
Ce	0.00	0.00	0.00	0.00	0.00	0.00	0.00	0.00
Pr	0.00	0.00	0.00	0.00	0.00	0.00	0.00	0.00
Nd	0.00	0.00	0.00	0.01	0.01	0.01	0.00	0.00
Sm	0.00	0.00	0.00	0.00	0.00	0.00	0.00	0.00
Y	0.02	0.01	0.00	0.00	0.01	0.00	0.00	0.01
Sr	0.02	0.01	0.01	0.02	0.01	0.01	0.01	0.01
Ba	0.00	0.00	0.00	0.00	0.01	0.00	0.00	0.00
As	0.00	0.00	0.00	0.00	0.00	0.00	0.00	0.00
F	2.26	2.49	2.51	2.00	1.72	2.25	2.76	2.78
Cl	0.00	0.00	0.00	0.00	0.00	0.00	0.00	0.00
OH	0.00	0.00	0.00	0.00	0.28	0.00	0.00	0.00
Sum Cat#	18.36	18.47	18.59	17.54	17.35	18.20	18.67	18.74
Me	10.18	9.95	10.13	8.78	8.09	9.69	9.70	9.73
X	5.81	5.99	5.92	6.73	7.23	6.25	6.21	6.20
Z	2.26	2.49	2.51	2.00	2.00	2.25	2.76	2.79

Appendix 6.1
Microprobe analyses of apatite

Fine euhedral type-1 apatites
in ovoid concretions, Battle mine

Catalogue #								
Field #	SJ441b-152	SJ441b-152	SJ441b-152	SJ441b-152	SJ441b-152	SJ441b-152	SJ441b-152	SJ441b-152
Drillhole	18-1004	18-1004	18-1004	18-1004	18-1004	18-1004	18-1004	18-1004
Point	apa4	apa5	apa6	apa7	apa8	apa9	apa10	apa11
SiO2	0.13	17.05	0.07	0.35	4.66	4.12	0.32	0.08
Fe2O3	0.00	0.00	0.00	0.00	0.01	0.04	0.01	0.01
MnO	0.04	0.01	0.07	0.04	0.06	0.06	0.07	0.04
MgO	0.00	0.00	0.00	0.00	0.00	0.00	0.00	0.00
CaO	54.11	41.91	54.27	53.68	54.11	53.71	53.28	54.51
Na2O	0.02	0.00	0.02	0.01	0.03	0.04	0.00	0.04
P2O5	39.25	35.92	39.57	40.14	38.43	39.05	39.68	39.09
SO3	0.09	0.01	0.09	0.01	0.03	0.07	0.03	0.07
La2O3	0.02	0.00	0.01	0.00	0.00	0.00	0.00	0.00
Ce2O3	0.01	0.00	0.00	0.00	0.00	0.03	0.02	0.01
Pr2O3	0.02	0.00	0.00	0.01	0.00	0.01	0.00	0.00
Nd2O3	0.03	0.03	0.11	0.00	0.07	0.00	0.01	0.00
Sm2O3	0.05	0.02	0.00	0.07	0.00	0.03	0.00	0.00
Y2O3	0.07	0.06	0.08	0.00	0.02	0.03	0.00	0.04
SrO	0.05	0.11	0.04	0.05	0.06	0.06	0.05	0.04
BaO	0.01	0.00	0.00	0.00	0.00	0.00	0.00	0.01
As2O3	0.03	0.01	0.01	0.00	0.02	0.00	0.00	0.02
F	4.76	3.98	4.39	5.40	5.56	4.31	5.41	4.50
Cl	0.01	0.01	0.01	0.01	0.01	0.01	0.00	0.00
H2O(c)	0.00	0.00	0.00	0.00	0.00	0.00	0.00	0.00
O=F	2.01	1.68	1.85	2.28	2.34	1.81	2.28	1.89
O=Cl	0.00	0.00	0.00	0.00	0.00	0.00	0.00	0.00
Sum Ox%	96.70	97.45	96.89	97.51	100.73	99.76	96.61	96.56
Si	0.02	2.75	0.01	0.06	0.78	0.69	0.06	0.01
Fe3+	0.00	0.00	0.00	0.00	0.00	0.01	0.00	0.00
Mn2+	0.01	0.00	0.01	0.01	0.01	0.01	0.01	0.01
Mg	0.00	0.00	0.00	0.00	0.00	0.00	0.00	0.00
Ca	10.22	7.23	10.20	10.03	9.73	9.67	10.06	10.31
Na	0.01	0.00	0.01	0.00	0.01	0.01	0.00	0.01
P	5.86	4.90	5.88	5.93	5.46	5.55	5.92	5.84
S	0.01	0.00	0.01	0.00	0.00	0.01	0.00	0.01
La	0.00	0.00	0.00	0.00	0.00	0.00	0.00	0.00
Ce	0.00	0.00	0.00	0.00	0.00	0.00	0.00	0.00
Pr	0.00	0.00	0.00	0.00	0.00	0.00	0.00	0.00
Nd	0.00	0.00	0.01	0.00	0.00	0.00	0.00	0.00
Sm	0.00	0.00	0.00	0.00	0.00	0.00	0.00	0.00
Y	0.01	0.01	0.01	0.00	0.00	0.00	0.00	0.00
Sr	0.01	0.01	0.00	0.01	0.01	0.01	0.01	0.00
Ba	0.00	0.00	0.00	0.00	0.00	0.00	0.00	0.00
As	0.00	0.00	0.00	0.00	0.00	0.00	0.00	0.00
F	2.66	2.03	2.44	2.98	2.95	2.29	3.02	2.51
Cl	0.00	0.00	0.00	0.00	0.00	0.00	0.00	0.00
OH	0.00	0.00	0.00	0.00	0.00	0.00	0.00	0.00
Sum Cat#	18.82	16.93	18.58	19.03	18.97	18.25	19.07	18.72
Me	10.25	7.25	10.23	10.05	9.76	9.70	10.08	10.34
X	5.88	7.65	5.89	5.99	6.25	6.25	5.98	5.86
Z	2.66	2.03	2.44	2.98	2.95	2.29	3.02	2.51

Appendix 6.1
Microprobe analyses of apatite

Fine euhedral type-1 apatites
in ovoid concretions, Battle mine

Catalogue #								
Field #	SJ441b-152	SJ441b-152	SJ441b-152	SJ441b-152	SJ441b-152	SJ441b-152	SJ441b-152	SJ441b-152
Drillhole	18-1004	18-1004	18-1004	18-1004	18-1004	18-1004	18-1004	18-1004
Point	apa12	apa13	apa14	apa15	apa16	apa17	apa18	apa19
SiO2	4.54	0.05	0.33	0.43	1.22	0.02	0.10	4.37
Fe2O3	0.03	0.00	0.00	0.00	0.03	0.02	0.01	0.01
MnO	0.03	0.06	0.07	0.07	0.09	0.05	0.06	0.06
MgO	0.00	0.00	0.00	0.00	0.00	0.00	0.00	0.00
CaO	53.06	54.60	53.99	53.74	53.30	54.02	53.65	52.76
Na2O	0.03	0.02	0.00	0.02	0.02	0.01	0.04	0.01
P2O5	38.66	39.31	39.64	39.22	39.42	40.00	40.21	39.07
SO3	0.05	0.04	0.00	0.05	0.06	0.12	0.01	0.03
La2O3	0.00	0.04	0.02	0.00	0.06	0.00	0.00	0.02
Ce2O3	0.07	0.00	0.01	0.03	0.01	0.00	0.07	0.04
Pr2O3	0.01	0.00	0.01	0.00	0.00	0.00	0.00	0.06
Nd2O3	0.05	0.06	0.00	0.04	0.06	0.07	0.08	0.06
Sm2O3	0.00	0.00	0.01	0.04	0.00	0.00	0.03	0.00
Y2O3	0.06	0.00	0.07	0.01	0.00	0.07	0.00	0.02
SrO	0.06	0.02	0.04	0.04	0.03	0.03	0.04	0.07
BaO	0.00	0.00	0.00	0.03	0.00	0.02	0.01	0.00
As2O3	0.01	0.02	0.01	0.00	0.03	0.02	0.02	0.01
F	4.28	4.50	4.84	4.80	5.28	4.28	4.39	4.62
Cl	0.01	0.01	0.00	0.01	0.01	0.01	0.01	0.01
H2O(c)	0.00	0.00	0.00	0.00	0.00	0.00	0.00	0.00
O=F	1.80	1.90	2.04	2.02	2.22	1.80	1.85	1.95
O=Cl	0.00	0.00	0.00	0.00	0.00	0.00	0.00	0.00
Sum Ox%	99.13	96.84	97.00	96.52	97.40	96.94	96.88	99.29
Si	0.77	0.01	0.06	0.08	0.21	0.00	0.02	0.74
Fe3+	0.00	0.00	0.00	0.00	0.00	0.00	0.00	0.00
Mn2+	0.00	0.01	0.01	0.01	0.01	0.01	0.01	0.01
Mg	0.00	0.00	0.00	0.00	0.00	0.00	0.00	0.00
Ca	9.60	10.30	10.14	10.16	9.96	10.11	10.05	9.53
Na	0.01	0.01	0.00	0.01	0.01	0.01	0.01	0.01
P	5.53	5.86	5.88	5.86	5.82	5.92	5.95	5.58
S	0.01	0.01	0.00	0.01	0.01	0.02	0.00	0.00
La	0.00	0.00	0.00	0.00	0.00	0.00	0.00	0.00
Ce	0.00	0.00	0.00	0.00	0.00	0.00	0.01	0.00
Pr	0.00	0.00	0.00	0.00	0.00	0.00	0.00	0.00
Nd	0.00	0.00	0.00	0.00	0.00	0.00	0.01	0.00
Sm	0.00	0.00	0.00	0.00	0.00	0.00	0.00	0.00
Y	0.01	0.00	0.01	0.00	0.00	0.01	0.00	0.00
Sr	0.01	0.00	0.00	0.00	0.00	0.00	0.00	0.01
Ba	0.00	0.00	0.00	0.00	0.00	0.00	0.00	0.00
As	0.00	0.00	0.00	0.00	0.00	0.00	0.00	0.00
F	2.29	2.51	2.68	2.68	2.91	2.37	2.43	2.47
Cl	0.00	0.00	0.00	0.00	0.00	0.00	0.00	0.00
OH	0.00	0.00	0.00	0.00	0.00	0.00	0.00	0.00
Sum Cat#	18.22	18.70	18.79	18.81	18.95	18.45	18.49	18.35
Me	9.62	10.32	10.17	10.18	9.99	10.14	10.08	9.56
X	6.30	5.87	5.94	5.93	6.04	5.92	5.97	6.32
Z	2.29	2.51	2.68	2.68	2.91	2.37	2.43	2.47

Appendix 6.1
Microprobe analyses of apatite

Fine euhedral type-1 apatites
in ovoid concretions, Battle mine

Catalogue #					
Field #	SJ441b-152	SJ441b-152	SJ441b-152	SJ441b-152	SJ441b-152
Drillhole	18-1004	18-1004	18-1004	18-1004	18-1004
Point	apa20	apa21	apa22	apa23	apa24
SiO2	0.12	0.33	0.13	0.36	0.65
Fe2O3	0.02	0.04	0.04	0.02	0.00
MnO	0.04	0.05	0.03	0.07	0.07
MgO	0.00	0.01	0.00	0.01	0.00
CaO	54.09	54.04	55.02	54.68	53.96
Na2O	0.03	0.00	0.01	0.02	0.01
P2O5	39.91	39.23	40.11	39.74	39.18
SO3	0.03	0.09	0.09	0.06	0.09
La2O3	0.02	0.02	0.01	0.02	0.01
Ce2O3	0.02	0.01	0.05	0.00	0.01
Pr2O3	0.02	0.00	0.00	0.01	0.09
Nd2O3	0.13	0.01	0.09	0.00	0.05
Sm2O3	0.12	0.05	0.02	0.02	0.01
Y2O3	0.07	0.00	0.00	0.02	0.00
SrO	0.05	0.04	0.04	0.02	0.06
BaO	0.01	0.00	0.02	0.00	0.00
As2O3	0.01	0.00	0.02	0.01	0.01
F	4.28	5.14	4.18	4.75	4.58
Cl	0.01	0.00	0.00	0.00	0.00
H2O(c)	0.00	0.00	0.00	0.00	0.00
O=F	1.80	2.16	1.76	2.00	1.93
O=Cl	0.00	0.00	0.00	0.00	0.00
Sum Ox%	97.18	96.87	98.10	97.82	96.85
Si	0.02	0.06	0.02	0.06	0.11
Fe3+	0.00	0.01	0.01	0.00	0.00
Mn2+	0.01	0.01	0.00	0.01	0.01
Mg	0.00	0.00	0.00	0.00	0.00
Ca	10.13	10.20	10.20	10.19	10.15
Na	0.01	0.00	0.01	0.01	0.00
P	5.90	5.85	5.87	5.85	5.82
S	0.00	0.01	0.01	0.01	0.01
La	0.00	0.00	0.00	0.00	0.00
Ce	0.00	0.00	0.00	0.00	0.00
Pr	0.00	0.00	0.00	0.00	0.01
Nd	0.01	0.00	0.01	0.00	0.00
Sm	0.01	0.00	0.00	0.00	0.00
Y	0.01	0.00	0.00	0.00	0.00
Sr	0.01	0.00	0.00	0.00	0.01
Ba	0.00	0.00	0.00	0.00	0.00
As	0.00	0.00	0.00	0.00	0.00
F	2.37	2.86	2.29	2.61	2.54
Cl	0.00	0.00	0.00	0.00	0.00
OH	0.00	0.00	0.00	0.00	0.00
Sum Cat#	18.47	19.00	18.43	18.76	18.67
Me	10.16	10.21	10.22	10.22	10.17
X	5.93	5.91	5.90	5.92	5.94
Z	2.37	2.86	2.29	2.62	2.54

Appendix 6.2
White mica microprobe analyses

altered argillite above massive sulphides, Battle mine

Catalogue #								
Field #	SJ749-116	SJ749-116	SJ749-116	SJ749-116	SJ749-116	SJ749-116	SJ754-106	SJ758-109
Location	G171XS	G171XS	G171XS	G171XS	G171XS	G171XS	G171XS	G171XS
SiO2	44.06	46.17	46.59	46.43	45.22	47.87	47.76	45.63
TiO2	0.06	0.07	0.06	0.08	0.21	0.17	0.31	0.21
Al2O3	34.72	35.64	35.3	35.93	35.34	33.93	33.51	35.05
Cr2O3	0.04	0.01	0.04	0.06	0	0	0.01	0.05
FeO	3.13	1.03	0.89	0.95	0.57	0.68	1.02	0.87
V2O3	0.33	0.34	0.25	0.46	0.3	0.21	0.3	0.07
ZnO	1.45	0.08	0.43	1.04	2	0.03	0.05	0.02
MnO	0.09	0.03	0.01	0	0.01	0.01	0.06	0
MgO	3.05	1.1	1.19	0.93	0.99	0.82	1.58	0.83
CaO	0	0.03	0	0	0.03	0.06	0	0.01
Na2O	0.52	0.65	0.47	0.59	0.63	0.55	0.44	0.56
K2O	8.97	10.51	10.8	10.76	10.23	9.72	10.22	10.31
BaO	0.54	0.91	0.78	0.68	0.83	0.71	0.51	0.84
Rb2O	-	-	-	-	-	-	-	-
Cs2O	-	-	-	-	-	-	-	-
SrO	0	0	0	0	0	0	0	-
NiO	0.06	0.04	0.07	0	0	0	0	-
F	0.14	0.11	0.16	0.12	0.13	0.09	0.2	0.06
Cl	0.05	0.05	0.01	0	0.03	0	0.01	0.03
H2O(c)	4.42	4.47	4.46	4.52	4.41	4.46	4.43	4.41
O=F	0.06	0.05	0.07	0.05	0.06	0.04	0.09	0.02
O=Cl	0.01	0.01	0	0	0.01	0	0	0.01
Sum Ox%	101.56	101.19	101.44	102.48	100.87	99.28	100.32	98.92
Si	5.881	6.111	6.153	6.089	6.047	6.378	6.328	6.154
Ti	0.006	0.007	0.006	0.008	0.021	0.017	0.031	0.021
Al/Al IV	2.119	1.889	1.847	1.911	1.953	1.622	1.672	1.846
Al VI	3.343	3.67	3.649	3.641	3.617	3.705	3.561	3.725
Cr	0.004	0.002	0.005	0.006	0	0	0.001	0.006
Fe2+	0.349	0.114	0.098	0.104	0.064	0.076	0.113	0.098
V	0.035	0.036	0.027	0.048	0.032	0.023	0.032	0.008
Zn	0.142	0.008	0.041	0.1	0.198	0.003	0.005	0.002
Mn2+	0.011	0.003	0.001	0	0.002	0.001	0.007	0
Mg	0.606	0.217	0.234	0.181	0.197	0.162	0.311	0.166
Ca	0	0.004	0	0	0.004	0.009	0	0.002
Na	0.135	0.167	0.12	0.15	0.163	0.143	0.112	0.145
K	1.527	1.774	1.819	1.799	1.746	1.652	1.728	1.773
Ba	0.028	0.047	0.04	0.035	0.043	0.037	0.026	0.044
Rb	-	-	-	-	-	-	-	-
Cs	-	-	-	-	-	-	-	-
Sr	0	0	0	0	0	0	0	-
Ni	0.007	0.005	0.007	0	0	0	0	-
F	0.058	0.048	0.066	0.05	0.057	0.036	0.085	0.024
Cl	0.01	0.011	0.002	0	0.007	0	0.001	0.006
OH	3.931	3.942	3.931	3.95	3.936	3.963	3.914	3.97
Sum Cat#	18.194	18.054	18.047	18.074	18.086	17.828	17.928	17.991
XMg	0.635	0.656	0.705	0.636	0.755	0.68	0.735	0.629
Oct	4.468	4.026	4.041	4.041	4.098	3.964	4.029	4.019
Int	1.69	1.992	1.98	1.984	1.956	1.841	1.866	1.965

Appendix 6.2
White mica microprobe analyses

White mica in altered argillite
Battle Mine

Catalogue #								
Field #	SJ758-109	SJ758-109	SJ758-109	SJ758-109	SJ758-109	SJ758-109	SJ758-109	SJ758-109
Location	G171XS	G171XS	G171XS	G171XS	G171XS	G171XS	G171XS	G171XS
SiO2	46.34	46.44	46.19	46.98	46.2	46.03	46.02	46.08
TiO2	0.2	0.24	0.23	0.18	0.21	0.26	0.14	0.1
Al2O3	35.32	35.22	35.42	35.95	35.86	35.85	35.53	35.57
Cr2O3	0	0.12	0.08	0	0.04	0.04	0	0.08
FeO	0.93	0.96	0.86	0.75	0.6	0.89	0.72	0.91
V2O3	0.1	0.01	0.09	0.06	0.13	0.13	0.19	0.09
ZnO	0.04	0.47	0.37	0.72	0.35	0.55	0	0
MnO	0.02	0.05	0	0.1	0.02	0.05	0	0.05
MgO	0.9	1.01	0.83	0.79	0.8	0.95	0.85	0.91
CaO	0.02	0.02	0	0.01	0.02	0	0.01	0
Na2O	0.59	0.45	0.58	0.57	0.62	0.55	0.54	0.59
K2O	10.44	10.55	10.68	9.97	10.18	10.41	10.28	10.72
BaO	0.65	0.62	0.66	0.58	0.75	0.61	0.64	0.71
Rb2O	-	-	-	-	-	-	-	-
Cs2O	-	-	-	-	-	-	-	-
SrO	-	-	-	-	-	-	-	-
NiO	-	-	-	-	-	-	-	-
F	0.14	0.12	0.21	0.12	0.18	0.13	0.11	0.14
Cl	0.02	0.01	0	0	0.02	0.01	0.01	0.02
H2O(c)	4.43	4.46	4.41	4.51	4.43	4.46	4.43	4.43
O=F	0.06	0.05	0.09	0.05	0.07	0.06	0.05	0.06
O=Cl	0.01	0	0	0	0	0	0	0
Sum Ox%	100.1	100.71	100.52	101.25	100.33	100.87	99.4	100.34
Si	6.17	6.163	6.144	6.173	6.134	6.099	6.155	6.135
Ti	0.02	0.024	0.023	0.018	0.021	0.026	0.014	0.01
Al/Al IV	1.83	1.837	1.856	1.827	1.866	1.901	1.845	1.865
Al VI	3.713	3.671	3.696	3.74	3.745	3.697	3.756	3.716
Cr	0	0.012	0.008	0	0.004	0.004	0	0.008
Fe2+	0.104	0.107	0.095	0.082	0.067	0.098	0.08	0.101
V	0.011	0.002	0.009	0.007	0.014	0.014	0.021	0.01
Zn	0.004	0.046	0.036	0.07	0.034	0.053	0	0
Mn2+	0.002	0.005	0	0.011	0.002	0.006	0	0.005
Mg	0.179	0.2	0.165	0.155	0.159	0.187	0.169	0.181
Ca	0.003	0.003	0	0.001	0.003	0	0.001	0
Na	0.153	0.117	0.15	0.144	0.159	0.141	0.139	0.152
K	1.773	1.786	1.813	1.671	1.724	1.76	1.754	1.821
Ba	0.034	0.032	0.034	0.03	0.039	0.032	0.033	0.037
Rb	-	-	-	-	-	-	-	-
Cs	-	-	-	-	-	-	-	-
Sr	-	-	-	-	-	-	-	-
Ni	-	-	-	-	-	-	-	-
F	0.06	0.051	0.09	0.051	0.075	0.056	0.046	0.058
Cl	0.005	0.002	0	0	0.005	0.002	0.003	0.004
OH	3.935	3.947	3.91	3.949	3.92	3.942	3.951	3.938
Sum Cat#	17.996	18.004	18.03	17.93	17.971	18.018	17.967	18.042
XMg	0.634	0.652	0.635	0.654	0.704	0.655	0.678	0.642
Oct	4.022	4.064	4.024	4.077	4.033	4.072	4.019	4.022
Int	1.963	1.938	1.997	1.846	1.925	1.933	1.927	2.01

Appendix 6.2
White mica microprobe analyses

	White mica in altered argillite Battle Mine			White mica in chert Battle South				
Catalogue #								
Field #	SJ758-109	SJ758-109	SJ758-109	SJ784-160	SJ784-160	SJ784-160	SJ784-160	SJ774-158
Location	G171XS	G171XS	G171XS	L14-681	L14-681	L14-681	L14-681	L14-683
SiO2	46.81	45.61	47.02	47.15	46.42	46.96	46.45	46.38
TiO2	0.2	0.16	0.12	0.11	0.05	0.09	0.04	0.36
Al2O3	35.08	35.75	34.91	36.95	36.76	36.54	37.25	35.23
Cr2O3	0	0	0	0	0.04	0	0	0.06
FeO	0.99	0.86	0.85	0.47	0.4	0.42	0.44	0.95
V2O3	0.19	0.15	0.18	0	0	0	0	0.1
ZnO	0.99	0.04	0.22	0	0.06	0.02	0	0.08
MnO	0	0.04	0	0.1	0.05	0	0	0
MgO	1.14	0.74	1.05	0.78	0.77	0.92	0.83	1.44
CaO	0.03	0.03	0.05	0	0.01	0	0	0.03
Na2O	0.44	0.6	0.48	0.72	0.7	0.89	0.86	0.52
K2O	10.54	10.58	10.12	10.12	10.53	10.27	10.27	10.49
BaO	0.86	0.46	0.46	0.33	0.44	0.33	0.55	1.39
Rb2O	-	-	-	-	-	-	-	-
Cs2O	-	-	-	-	-	-	-	-
SrO	-	-	-	-	-	-	-	0
NiO	-	-	-	-	-	-	-	0
F	0.14	0.12	0.12	0.25	0.28	0.29	0.2	0.41
Cl	0	0	0	0	0.01	0.01	0.01	0.02
H2O(c)	4.48	4.42	4.46	4.48	4.42	4.44	4.48	4.34
O=F	0.06	0.05	0.05	0.1	0.12	0.12	0.08	0.17
O=Cl	0	0	0	0	0	0	0	0
Sum Ox%	101.84	99.52	99.99	101.35	100.81	101.06	101.29	101.61
Si	6.169	6.108	6.241	6.149	6.112	6.152	6.082	6.127
Ti	0.02	0.016	0.012	0.011	0.005	0.009	0.004	0.036
Al/Al IV	1.831	1.892	1.759	1.851	1.888	1.848	1.918	1.873
Al VI	3.617	3.75	3.702	3.828	3.816	3.793	3.831	3.612
Cr	0	0	0	0	0.004	0	0	0.006
Fe2+	0.109	0.097	0.095	0.052	0.044	0.046	0.048	0.104
V	0.02	0.016	0.02	0	0	0.001	0	0.011
Zn	0.097	0.004	0.022	0	0.006	0.002	0	0.008
Mn2+	0	0.005	0	0.011	0.005	0	0	0
Mg	0.224	0.149	0.208	0.152	0.151	0.18	0.162	0.284
Ca	0.005	0.004	0.007	0	0.001	0	0	0.004
Na	0.111	0.157	0.123	0.182	0.178	0.226	0.218	0.133
K	1.772	1.807	1.713	1.683	1.769	1.717	1.715	1.767
Ba	0.045	0.024	0.024	0.017	0.022	0.017	0.028	0.072
Rb	-	-	-	-	-	-	-	-
Cs	-	-	-	-	-	-	-	-
Sr	-	-	-	-	-	-	-	0
Ni	-	-	-	-	-	-	-	0
F	0.06	0.05	0.052	0.101	0.119	0.121	0.082	0.171
Cl	0	0	0	0	0.002	0.003	0.002	0.004
OH	3.94	3.95	3.948	3.899	3.879	3.876	3.916	3.825
Sum Cat#	18.018	18.029	17.925	17.934	18.002	17.99	18.006	18.037
XMg	0.673	0.605	0.688	0.746	0.775	0.797	0.772	0.731
Oct	4.066	4.02	4.038	4.052	4.032	4.029	4.045	4.05
Int	1.932	1.992	1.867	1.881	1.97	1.96	1.961	1.976

Appendix 6.2
White mica microprobe analyses

	White mica in chert Battle South						White mica in chert in Battle Mine	
Catalogue #								
Field #	SJ774-158	SJ774-158	SJ774-158	SJ774-158	SJ774-158	SJ774-158	SJ154-42	SJ154-42
Location	L14-683	L14-683	L14-683	L14-683	L14-683	L14-683	18-1126	18-1126
SiO2	47.31	46.63	47	46.76	46.16	47.22	46.61	48.61
TiO2	0.19	0.24	0.22	0.3	0.21	0.37	0.06	0.08
Al2O3	35.08	34.9	35.21	35.04	34.82	35.65	36.66	36.01
Cr2O3	0.07	0	0.04	0	0.04	0.02	0.05	0
FeO	0.66	0.89	1.08	0.67	0.69	0.85	0.31	0.61
V2O3	0.11	0.2	0.1	0.1	0.12	0.1	0	0.01
ZnO	0.1	0.08	0.09	0	0.04	0.04	0.21	0.01
MnO	0	0	0	0	0.01	0	0.05	0
MgO	1.56	1.38	1.36	1.33	1.32	1.41	0.77	1.01
CaO	0.04	0.1	0.08	0	0	0	0	0.04
Na2O	0.46	0.48	0.46	0.52	0.47	0.5	0.75	0.53
K2O	10.25	10.24	9.96	10.64	10.34	10.34	10	9.62
BaO	1.31	1.44	1.43	1.39	1.45	1.72	0.49	0.3
Rb2O	-	-	-	-	-	-	-	-
Cs2O	-	-	-	-	-	-	-	-
SrO	0	0	0	0	0	0	0	0
NiO	0	0	0	0	0	0	0	0.03
F	0.4	0.37	0.33	0.37	0.32	0.42	0.11	0.19
Cl	0	0	0.02	0	0	0.02	0	0
H2O(c)	4.38	4.35	4.39	4.36	4.33	4.4	4.5	4.54
O=F	0.17	0.16	0.14	0.16	0.13	0.18	0.05	0.08
O=Cl	0	0	0	0	0	0	0	0
Sum Ox%	101.73	101.15	101.63	101.34	100.18	102.88	100.54	101.53
Si	6.21	6.177	6.185	6.181	6.17	6.155	6.137	6.295
Ti	0.019	0.024	0.022	0.03	0.021	0.036	0.006	0.008
Al/Al IV	1.79	1.823	1.815	1.819	1.83	1.845	1.863	1.705
Al VI	3.637	3.625	3.646	3.64	3.656	3.632	3.826	3.791
Cr	0.007	0	0.004	0	0.004	0.002	0.006	0
Fe2+	0.072	0.098	0.119	0.074	0.077	0.093	0.034	0.066
V	0.011	0.021	0.011	0.011	0.013	0.011	0	0.001
Zn	0.009	0.008	0.009	0	0.004	0.004	0.02	0.001
Mn2+	0	0	0	0	0.002	0	0.006	0
Mg	0.305	0.273	0.266	0.262	0.263	0.274	0.152	0.195
Ca	0.005	0.014	0.012	0.001	0	0	0	0.005
Na	0.117	0.124	0.118	0.134	0.121	0.128	0.192	0.134
K	1.717	1.73	1.672	1.795	1.764	1.72	1.679	1.589
Ba	0.067	0.075	0.073	0.072	0.076	0.088	0.025	0.015
Rb	-	-	-	-	-	-	-	-
Cs	-	-	-	-	-	-	-	-
Sr	0	0	0	0	0	0	0	0
Ni	0	0	0	0	0	0	0	0.004
F	0.165	0.156	0.139	0.154	0.135	0.173	0.046	0.077
Cl	0	0	0.004	0	0.001	0.004	0.001	0
OH	3.835	3.844	3.857	3.846	3.864	3.823	3.953	3.923
Sum Cat#	17.966	17.991	17.951	18.019	18	17.987	17.946	17.81
XMg	0.809	0.735	0.692	0.78	0.773	0.747	0.816	0.748
Oct	4.049	4.028	4.065	4.006	4.027	4.041	4.049	4.065
Int	1.906	1.942	1.875	2.001	1.961	1.935	1.896	1.744

Appendix 6.2
White mica microprobe analyses

White mica in chert
in Battle Mine

Catalogue #								
Field #	SJ154-42	SJ154-42	SJ154-42	SJ154-42	SJ154-42	SJ154-42	SJ154-42	SJ154-42
Location	18-1126	18-1126	18-1126	18-1126	18-1126	18-1126	18-1126	18-1126
SiO2	46.11	46.72	46.87	46.61	46.57	46.87	48	47.25
TiO2	0.01	0.05	0.08	0.06	0.08	0.08	0.07	0.15
Al2O3	35.54	36.55	36.01	36.84	34.97	36.56	34.71	35.45
Cr2O3	0	0.04	0	0	0	0.01	0	0
FeO	0.53	0.51	0.45	0.33	1.18	0.37	0.51	0.47
V2O3	0.03	0	0.05	0.04	0.02	0.05	0	0
ZnO	0.1	0.08	0.14	0	0.07	0	0	0
MnO	0	0.05	0	0.05	0.06	0	0.03	0.01
MgO	0.87	0.86	0.84	0.75	0.73	0.7	0.92	0.99
CaO	0.05	0.01	0.06	0	0.09	0.02	0.07	0
Na2O	0.85	0.66	0.73	0.78	0.64	0.6	0.53	0.54
K2O	9.53	10.35	9.71	9.98	9.6	10.31	9.72	10.1
BaO	0.47	0.52	0.47	0.39	0.49	0.63	0.62	0.24
Rb2O	-	-	-	-	-	-	-	-
Cs2O	-	-	-	-	-	-	-	-
SrO	0	0	0	0	0	0	0	0
NiO	0.03	0	0	0.15	0	0.1	0.05	0.01
F	0.14	0.15	0.18	0.13	0.14	0.15	0.32	0.16
Cl	0.02	0.02	0.02	0.01	0.01	0.05	0.04	0.03
H2O(c)	4.4	4.49	4.45	4.5	4.41	4.48	4.37	4.45
O=F	0.06	0.06	0.07	0.05	0.06	0.07	0.13	0.07
O=Cl	0	0	0	0	0	0.01	0.01	0.01
Sum Ox%	98.65	100.99	99.97	100.57	99	100.88	99.82	99.77
Si	6.182	6.138	6.195	6.128	6.236	6.16	6.347	6.249
Ti	0.001	0.005	0.008	0.006	0.008	0.008	0.007	0.015
Al/Al IV	1.818	1.862	1.805	1.872	1.764	1.84	1.653	1.751
Al VI	3.797	3.798	3.804	3.837	3.753	3.822	3.757	3.775
Cr	0	0.005	0	0	0	0.001	0	0
Fe2+	0.06	0.056	0.05	0.036	0.132	0.041	0.056	0.052
V	0.003	0	0.006	0.004	0.002	0.005	0	0
Zn	0.01	0.008	0.013	0	0.007	0	0	0
Mn2+	0	0.005	0	0.006	0.007	0	0.003	0.001
Mg	0.174	0.168	0.165	0.148	0.146	0.137	0.181	0.195
Ca	0.008	0.002	0.008	0	0.013	0.004	0.01	0
Na	0.222	0.169	0.186	0.198	0.165	0.153	0.137	0.14
K	1.63	1.734	1.637	1.674	1.64	1.728	1.64	1.704
Ba	0.025	0.027	0.024	0.02	0.026	0.032	0.032	0.012
Rb	-	-	-	-	-	-	-	-
Cs	-	-	-	-	-	-	-	-
Sr	0	0	0	0	0	0	0	0
Ni	0.004	0	0	0.016	0	0.01	0.005	0.001
F	0.058	0.061	0.074	0.053	0.06	0.064	0.134	0.065
Cl	0.005	0.003	0.004	0.002	0.002	0.01	0.008	0.006
OH	3.937	3.936	3.922	3.945	3.938	3.926	3.858	3.929
Sum Cat#	17.934	17.976	17.902	17.946	17.899	17.939	17.829	17.895
XMg	0.745	0.751	0.769	0.803	0.524	0.769	0.764	0.79
Oct	4.046	4.044	4.04	4.049	4.054	4.018	4.01	4.039
Int	1.885	1.932	1.855	1.892	1.844	1.916	1.819	1.856

Appendix 6.2
White mica microprobe analyses

White mica in chert in Battle Mine

Catalogue #								
Field #	SJ154-42	SJ154-42	SJ154-42	SJ154-42	SJ154-42	SJ154-42	SJ154-42	SJ154-42
Location	18-1126	18-1126	18-1126	18-1126	18-1126	18-1126	18-1126	18-1126
SiO2	46.7	47.53	47.02	47.32	46.67	46.62	46.23	46.45
TiO2	0.08	0.05	0.04	0.05	0.05	0.05	0.04	0.09
Al2O3	36.72	35.67	35.97	35.28	37.03	36.18	36.7	36.23
Cr2O3	0	0	0.07	0	0	0.02	0.03	0
FeO	0.32	0.32	0.39	0.56	0.63	0.77	0.75	0.54
V2O3	0.12	0	0.08	0	0.05	0.03	0.04	0.01
ZnO	0	0.11	0.17	0.04	0.05	0.29	0.01	0.09
MnO	0.07	0	0.05	0.01	0.01	0	0	0
MgO	0.78	1.08	0.92	0.92	0.71	0.84	0.79	0.8
CaO	0.03	0.01	0.03	0	0.05	0.02	0	0
Na2O	0.74	0.5	0.65	0.67	0.88	0.54	0.72	0.63
K2O	9.8	9.78	10.04	10.32	9.93	10.28	10.19	10.17
BaO	0.36	0.4	0.27	0.41	0.42	0.43	0.52	0.54
Rb2O	-	-	-	-	-	-	-	-
Cs2O	-	-	-	-	-	-	-	-
SrO	0	0	0	0	0	0	0	0
NiO	0.03	0	0.01	0	0.1	0	0	0
F	0.11	0.16	0.15	0.16	0.08	0.13	0.14	0.13
Cl	0	0	0	0	0.02	0.02	0	0.01
H2O(c)	4.51	4.48	4.48	4.46	4.54	4.48	4.48	4.47
O=F	0.05	0.07	0.06	0.07	0.03	0.06	0.06	0.05
O=Cl	0	0	0	0	0	0	0	0
Sum Ox%	100.34	100.01	100.28	100.15	101.18	100.64	100.6	100.11
Si	6.142	6.26	6.197	6.257	6.109	6.152	6.101	6.151
Ti	0.008	0.005	0.004	0.005	0.005	0.005	0.004	0.009
Al/Al IV	1.858	1.74	1.803	1.743	1.891	1.848	1.899	1.849
Al VI	3.835	3.797	3.785	3.756	3.823	3.778	3.808	3.806
Cr	0	0	0.007	0	0	0.002	0.003	0
Fe2+	0.036	0.036	0.043	0.062	0.069	0.085	0.083	0.06
V	0.013	0	0.008	0	0.005	0.003	0.004	0.001
Zn	0	0.01	0.016	0.004	0.005	0.029	0.001	0.009
Mn2+	0.008	0	0.005	0.002	0.002	0	0	0
Mg	0.153	0.212	0.18	0.182	0.138	0.165	0.156	0.159
Ca	0.005	0.001	0.005	0	0.007	0.003	0	0
Na	0.188	0.127	0.166	0.171	0.223	0.139	0.185	0.163
K	1.644	1.644	1.689	1.74	1.658	1.731	1.716	1.719
Ba	0.018	0.02	0.014	0.021	0.022	0.022	0.027	0.028
Rb	-	-	-	-	-	-	-	-
Cs	-	-	-	-	-	-	-	-
Sr	0	0	0	0	0	0	0	0
Ni	0.003	0	0.001	0	0.011	0	0	0
F	0.046	0.068	0.061	0.067	0.033	0.055	0.06	0.054
Cl	0	0	0	0	0.004	0.003	0	0.001
OH	3.954	3.932	3.939	3.933	3.963	3.942	3.94	3.944
Sum Cat#	17.913	17.852	17.924	17.944	17.967	17.962	17.988	17.953
XMg	0.812	0.856	0.806	0.745	0.668	0.661	0.652	0.725
Oct	4.044	4.06	4.043	4.011	4.052	4.064	4.056	4.043
Int	1.856	1.792	1.873	1.933	1.91	1.896	1.928	1.909

Appendix 6.2
White mica microprobe analyses

White mica in chert in Battle Mine

Catalogue #								
Field #	SJ154-42	SJ154-42	SJ154-42	SJ154-42	SJ154-42	SJ154-42	SJ154-42	SJ154-42
Location	18-1126	18-1126	18-1126	18-1126	18-1126	18-1126	18-1126	18-1126
SiO2	47.3	47.32	46.87	46.83	48.8	49.22	47.19	46.59
TiO2	0.08	0.09	0.06	0.04	0.09	0.09	0.12	0
Al2O3	35.96	35.92	37.21	36.53	37.11	34.04	36.46	36.46
Cr2O3	0	0.02	0	0.03	0.11	0.06	0.01	0.01
FeO	0.37	0.38	0.64	0.57	0.37	0.7	0.56	0.23
V2O3	0.04	0.03	0.09	0	0	0.01	0	0
ZnO	0.09	0.14	0	0	0.07	0.06	0	0
MnO	0	0.05	0.01	0	0.08	0	0.03	0.03
MgO	1.1	0.7	0.79	0.86	0.78	0.6	0.91	0.76
CaO	0.03	0.04	0.06	0.02	0.03	0.07	0.02	0.02
Na2O	0.6	0.7	0.74	0.68	0.84	0.73	0.67	0.75
K2O	10.1	10.09	9.97	10.24	9.59	9.81	10.11	10.28
BaO	0.44	0.48	0.37	0.47	0.31	0.39	0.36	0.45
Rb2O	-	-	-	-	-	-	-	-
Cs2O	-	-	-	-	-	-	-	-
SrO	0	0	0	0	0	0	0	0
NiO	0	0	0	0.03	0.01	0.01	0	0
F	0.14	0.13	0.12	0.11	0.17	0.2	0.12	0.13
Cl	0.02	0.01	0.01	0.02	0	0.02	0	0
H2O(c)	4.5	4.49	4.54	4.51	4.61	4.47	4.53	4.48
O=F	0.06	0.05	0.05	0.05	0.07	0.08	0.05	0.05
O=Cl	0	0	0	0	0	0	0	0
Sum Ox%	100.7	100.52	101.43	100.88	102.9	100.4	101.05	100.12
Si	6.21	6.227	6.111	6.151	6.236	6.462	6.174	6.157
Ti	0.008	0.009	0.006	0.004	0.009	0.009	0.012	0
Al/Al IV	1.79	1.773	1.889	1.849	1.764	1.538	1.826	1.843
Al VI	3.774	3.798	3.829	3.805	3.825	3.729	3.795	3.835
Cr	0	0.002	0	0.003	0.011	0.006	0.001	0.001
Fe2+	0.041	0.042	0.07	0.063	0.04	0.077	0.062	0.025
V	0.004	0.003	0.01	0	0	0.001	0	0
Zn	0.009	0.013	0	0	0.007	0.006	0	0
Mn2+	0	0.006	0.001	0	0.008	0	0.004	0.004
Mg	0.214	0.137	0.154	0.168	0.149	0.118	0.178	0.15
Ca	0.004	0.006	0.008	0.003	0.004	0.009	0.003	0.003
Na	0.153	0.178	0.188	0.173	0.209	0.185	0.17	0.191
K	1.691	1.694	1.658	1.715	1.563	1.643	1.687	1.734
Ba	0.023	0.025	0.019	0.024	0.015	0.02	0.019	0.023
Rb	-	-	-	-	-	-	-	-
Cs	-	-	-	-	-	-	-	-
Sr	0	0	0	0	0	0	0	0
Ni	0	0	0	0.003	0.001	0.001	0	0
F	0.057	0.053	0.048	0.047	0.069	0.082	0.051	0.053
Cl	0.004	0.002	0.003	0.003	0.001	0.004	0	0
OH	3.939	3.946	3.949	3.949	3.931	3.914	3.949	3.947
Sum Cat#	17.921	17.912	17.942	17.96	17.842	17.806	17.932	17.966
XMg	0.839	0.765	0.688	0.728	0.789	0.605	0.743	0.856
Oct	4.046	4.007	4.06	4.045	4.05	3.947	4.053	4.015
Int	1.871	1.902	1.873	1.915	1.792	1.858	1.879	1.951

Appendix 6.2
White mica microprobe analyses

White mica in chert in Battle Mine

Catalogue #								
Field #	SJ154-42	SJ161b-32	SJ161b-32	SJ161b-32	SJ151-1	SJ151-1	SJ151-1	SJ151-1
Location	18-1126	18-1127	18-1127	18-1127	18-1126	18-1126	18-1126	18-1126
SiO2	47.12	47.88	45.36	49.12	46.73	48.36	45.91	47.99
TiO2	0.11	0.16	0.21	0.11	0.04	0.08	0.16	0.09
Al2O3	35.89	32.05	36.25	33.71	37.36	35.47	36.63	36.56
Cr2O3	0	0.11	0.15	0.01	0	0.01	0	0.04
FeO	0.37	2.29	0.17	0.23	0.24	0.48	0.24	0.19
V2O3	0.01	0.02	0.37	0.27	0.04	0	0.04	0.04
ZnO	0	0	0	0.08	0	0	0	0.08
MnO	0	0.01	0	0.01	0	0.04	0	0
MgO	0.98	1.93	0.8	0.78	0.54	0.61	0.56	0.64
CaO	0.02	0	0	0.01	0.02	0.01	0.04	0
Na2O	0.6	0.38	0.6	0.6	0.76	0.76	0.78	0.54
K2O	9.96	10.36	10.16	9.26	10.25	9.9	9.88	9.27
BaO	0.41	0.46	1.03	0.91	0.51	0.5	0.52	0.44
Rb2O	-	-	-	-	-	-	-	-
Cs2O	-	-	-	-	-	-	-	-
SrO	0	-	-	-	-	-	-	-
NiO	0.02	-	-	-	-	-	-	-
F	0.16	0.39	0.22	0.13	0.17	0.21	0.16	0.1
Cl	0.01	0	0.01	0.01	0	0.02	0	0.02
H2O(c)	4.47	4.31	4.38	4.47	4.5	4.48	4.43	4.54
O=F	0.07	0.16	0.09	0.06	0.07	0.09	0.07	0.04
O=Cl	0	0	0	0	0	0.01	0	0.01
Sum Ox%	100.09	100.18	99.61	99.66	101.09	100.85	99.27	100.51
Si	6.215	6.393	6.065	6.486	6.115	6.326	6.114	6.261
Ti	0.011	0.016	0.021	0.011	0.004	0.008	0.016	0.009
Al/Al IV	1.785	1.607	1.935	1.514	1.885	1.674	1.886	1.739
Al VI	3.794	3.437	3.777	3.732	3.877	3.796	3.863	3.882
Cr	0	0.011	0.016	0.001	0	0.001	0	0.004
Fe2+	0.041	0.256	0.02	0.026	0.027	0.053	0.026	0.021
V	0.002	0.002	0.04	0.028	0.004	0	0.004	0.005
Zn	0	0	0	0.008	0	0	0	0.008
Mn2+	0	0.002	0	0.001	0	0.005	0	0
Mg	0.194	0.384	0.16	0.154	0.106	0.118	0.112	0.125
Ca	0.003	0	0	0.001	0.003	0.002	0.006	0
Na	0.153	0.098	0.155	0.154	0.193	0.194	0.201	0.137
K	1.676	1.764	1.733	1.559	1.71	1.651	1.678	1.542
Ba	0.021	0.024	0.054	0.047	0.026	0.026	0.027	0.022
Rb	-	-	-	-	-	-	-	-
Cs	-	-	-	-	-	-	-	-
Sr	0	-	-	-	-	-	-	-
Ni	0.002	-	-	-	-	-	-	-
F	0.065	0.164	0.094	0.056	0.071	0.087	0.067	0.04
Cl	0.003	0.001	0.003	0.002	0	0.005	0	0.005
OH	3.932	3.835	3.903	3.941	3.929	3.907	3.933	3.955
Sum Cat#	17.898	17.994	17.974	17.723	17.95	17.853	17.933	17.755
XMg	0.824	0.6	0.891	0.858	0.798	0.692	0.809	0.856
Oct	4.043	4.106	3.993	3.933	4.013	3.98	4.017	4.049
Int	1.854	1.886	1.941	1.762	1.932	1.873	1.912	1.702

Appendix 6.2
White mica microprobe analyses

	White mica in chert in Battle Mine		White mica in altered argillite HW Mine					
Catalogue #								
Field #	SJ151-1	SJ151-1	SJ639-T03	SJ639-T03	SJ650-98	SJ650-98	SJ650-98	SJ650-98
Location	18-1126	18-1126	S335C	S335C	S335C	S335C	S335C	S335C
SiO2	46.07	47.85	46.82	47.9	47.51	47.58	45.85	46.84
TiO2	0.1	0.15	0.09	0.05	0.29	0.21	0.25	0.16
Al2O3	37.13	37.13	36.59	36.08	33.63	33.76	34.61	32.14
Cr2O3	0	0.02	0.02	0.07	0.01	0.13	0.06	0.06
FeO	0.24	0.3	0.22	0.38	0.66	0.74	0.72	0.57
V2O3	0.01	0.06	0.4	0.34	0.23	0.14	0.26	0.12
ZnO	0.28	0.04	0.05	0.07	0	0	0	0
MnO	0	0	0	0.08	0.04	0	0.02	0.02
MgO	0.53	0.71	0.85	1.03	1.24	1.15	1.09	1.32
CaO	0.03	0.09	0.01	0.02	0.03	0.02	0.02	0
Na2O	0.86	0.67	0.74	0.73	0.47	0.44	0.57	0.3
K2O	9.85	9.83	10.09	10.16	10.18	10.18	10.29	10.06
BaO	0.46	0.7	0.83	0.78	1.16	1.26	1.17	1.1
Rb2O	-	-	-	-	-	-	-	-
Cs2O	-	-	-	-	-	-	-	-
SrO	-	-	0	0	0	0	0	0
NiO	-	-	0	0	0	0	0	0.02
F	0.16	0.08	0.36	0.33	0.3	0.27	0.3	0.4
Cl	0	0	0.02	0.04	0.01	0.01	0.01	0.02
H2O(c)	4.46	4.61	4.4	4.45	4.35	4.37	4.31	4.18
O=F	0.07	0.03	0.15	0.14	0.13	0.12	0.13	0.17
O=Cl	0	0	0.01	0.01	0	0	0	0
Sum Ox%	100.13	102.2	101.32	102.37	99.98	100.15	99.4	97.13
Si	6.089	6.182	6.134	6.212	6.332	6.334	6.171	6.418
Ti	0.01	0.015	0.009	0.005	0.029	0.021	0.025	0.016
Al/Al IV	1.911	1.818	1.866	1.788	1.668	1.666	1.829	1.582
Al VI	3.871	3.835	3.783	3.726	3.614	3.631	3.66	3.608
Cr	0	0.002	0.002	0.007	0.001	0.014	0.007	0.006
Fe2+	0.027	0.032	0.024	0.041	0.073	0.082	0.08	0.065
V	0.001	0.006	0.042	0.036	0.024	0.015	0.028	0.013
Zn	0.028	0.004	0.005	0.006	0	0	0	0
Mn2+	0	0	0	0.008	0.005	0	0.002	0.002
Mg	0.105	0.137	0.165	0.199	0.247	0.228	0.218	0.27
Ca	0.005	0.012	0.002	0.003	0.004	0.003	0.002	0
Na	0.221	0.167	0.187	0.185	0.121	0.112	0.148	0.079
K	1.66	1.619	1.686	1.681	1.73	1.729	1.767	1.757
Ba	0.024	0.035	0.043	0.04	0.061	0.066	0.062	0.059
Rb	-	-	-	-	-	-	-	-
Cs	-	-	-	-	-	-	-	-
Sr	-	-	0	0	0	0	0	0
Ni	-	-	0	0	0	0	0	0.002
F	0.066	0.031	0.149	0.137	0.127	0.116	0.128	0.173
Cl	0	0	0.005	0.01	0.002	0.002	0.003	0.003
OH	3.934	3.969	3.845	3.853	3.871	3.882	3.868	3.824
Sum Cat#	17.951	17.866	17.947	17.937	17.91	17.902	17.999	17.879
XMg	0.797	0.809	0.872	0.828	0.771	0.735	0.73	0.805
Oct	4.04	4.026	3.988	3.994	3.97	3.977	3.993	3.97
Int	1.91	1.834	1.917	1.907	1.916	1.91	1.978	1.896

Appendix 6.2
White mica microprobe analyses

	White mica in altered argillite HW Mine						White mica in rhy-sst South Flank	
Catalogue #								
Field #	SJ650-98	SJ650-98	SJ650-98	SJ650-98	SJ650-98	SJ650-98	SJ600-T6	SJ600-T6
Location	S335C	S335C	S335C	S335C	S335C	S335C	16-33	16-33
SiO2	47.86	47.53	48.29	48.62	46.49	47.81	49.47	49.04
TiO2	0.37	0.18	3.61	0.29	0.34	0.99	0	0.01
Al2O3	33.69	34.58	31.1	31.26	34.36	31.76	32.01	30.76
Cr2O3	0.05	0	0.01	0.11	0.03	0.04	0.03	0.04
FeO	0.73	0.77	0.55	0.67	0.91	0.46	1.86	2.12
V2O3	0.17	0.21	0.1	0.14	0.23	0.03	0	0
ZnO	0	0	0.08	0.09	0	0	0	0.02
MnO	0.03	0	0.02	0	0	0	0.05	0.08
MgO	1.37	1.21	1.08	1.35	1.53	1.18	2.07	2.22
CaO	0.07	0.09	0.01	0.03	0	1.86	0.01	0
Na2O	0.47	0.49	0.45	0.4	0.45	0.38	0.19	0.14
K2O	9.88	10.03	9.29	9.97	10.46	9.42	11.12	11.14
BaO	0.98	1.02	0.88	1.11	1.46	1.04	0.68	0.64
Rb2O	-	-	-	-	-	-	-	-
Cs2O	-	-	-	-	-	-	-	-
SrO	0	0	0	0	0	0	0	0
NiO	0	0	0	0	0	0	0.04	0.03
F	0.39	0.24	0.28	0.34	0.4	0.27	0.19	0.19
Cl	0.03	0.01	0.02	0.01	0.01	0.01	0	0.01
H2O(c)	4.33	4.42	4.39	4.28	4.31	4.35	4.49	4.41
O=F	0.17	0.1	0.12	0.14	0.17	0.11	0.08	0.08
O=Cl	0.01	0	0	0	0	0	0	0
Sum Ox%	100.25	100.67	100.05	98.52	100.82	99.49	102.13	100.77
Si	6.343	6.279	6.4	6.559	6.189	6.404	6.485	6.531
Ti	0.037	0.017	0.36	0.029	0.034	0.099	0	0.001
Al/Al IV	1.657	1.721	1.6	1.441	1.811	1.596	1.515	1.469
Al VI	3.605	3.663	3.258	3.529	3.58	3.417	3.429	3.358
Cr	0.005	0	0.001	0.011	0.003	0.004	0.003	0.004
Fe2+	0.081	0.085	0.061	0.075	0.101	0.052	0.204	0.236
V	0.018	0.023	0.01	0.015	0.025	0.003	0	0
Zn	0	0	0.008	0.009	0	0	0	0.002
Mn2+	0.004	0	0.002	0	0	0	0.006	0.01
Mg	0.271	0.239	0.214	0.271	0.303	0.235	0.405	0.44
Ca	0.011	0.013	0.001	0.005	0	0.268	0.001	0.001
Na	0.121	0.126	0.117	0.103	0.116	0.098	0.049	0.035
K	1.67	1.69	1.571	1.715	1.776	1.61	1.859	1.893
Ba	0.051	0.053	0.046	0.059	0.076	0.055	0.035	0.034
Rb	-	-	-	-	-	-	-	-
Cs	-	-	-	-	-	-	-	-
Sr	0	0	0	0	0	0	0	0
Ni	0	0	0	0	0	0	0.004	0.003
F	0.165	0.101	0.118	0.144	0.168	0.114	0.078	0.081
Cl	0.006	0.002	0.004	0.001	0.003	0.003	0	0.001
OH	3.829	3.897	3.878	3.855	3.829	3.883	3.922	3.918
Sum Cat#	17.873	17.908	17.649	17.823	18.015	17.841	17.995	18.016
XMg	0.77	0.738	0.778	0.783	0.749	0.819	0.665	0.651
Oct	4.003	4.005	3.905	3.926	4.021	3.807	4.051	4.054
Int	1.852	1.881	1.734	1.882	1.969	2.031	1.944	1.962

Appendix 6.2
White mica microprobe analyses

	White mica in rhy-sst South Flank				White mica in mixed volcaniclastics 43 Block, HW Mine			
Catalogue #								
Field #	SJ600-T6	SJ600-T6	SJ600-T6	SJ600-T6	SJ558A-T12	SJ558A-T12	SJ558A-T12	SJ558A-T12
Location	16-33	16-33	16-33	16-33	20-675	20-675	20-675	20-675
SiO2	47.61	48.68	48.63	47.01	46.39	47.36	48.05	47.72
TiO2	0.13	0.01	0.11	0.13	0.05	0.04	0.12	0.03
Al2O3	32.82	32.89	32.52	33.35	31.97	32.14	30.19	33
Cr2O3	0.05	0.04	0	0.03	0.03	0.06	0	0
FeO	1.51	1.59	1.93	1.71	2.75	2.45	2.37	1.66
V2O3	0	0	0.03	0	0	0	0	0.06
ZnO	0	0	0	0	0.16	0.2	0.06	0.17
MnO	0	0	0.06	0	0	0.02	0	0.03
MgO	1.79	1.44	2.18	1.56	1.89	1.81	2	1.46
CaO	0	0	0	0	0.01	0.01	0.03	0.07
Na2O	0.19	0.24	0.15	0.23	0.18	0.14	0.22	0.37
K2O	11.16	10.8	11.08	11.19	10.9	11.01	10.35	10.59
BaO	0.73	0.68	0.62	0.74	1.37	0.97	0.99	0.71
Rb2O	-	-	-	-	-	-	-	-
Cs2O	-	-	-	-	-	-	-	-
SrO	0	0	0	0	-	-	-	-
NiO	0.08	0	0.03	0	-	-	-	-
F	0.15	0.17	0.18	0.11	0.15	0.1	0.2	0.13
Cl	0	0.02	0	0.01	0	0	0	0
H2O(c)	4.43	4.45	4.47	4.43	4.35	4.43	4.32	4.44
O=F	0.07	0.07	0.08	0.05	0.06	0.04	0.09	0.05
O=Cl	0	0	0	0	0	0	0	0
Sum Ox%	100.59	100.94	101.92	100.45	100.13	100.7	98.81	100.39
Si	6.345	6.435	6.394	6.283	6.288	6.348	6.53	6.36
Ti	0.013	0.001	0.011	0.013	0.005	0.004	0.012	0.003
Al/Al IV	1.655	1.565	1.606	1.717	1.712	1.652	1.47	1.64
Al VI	3.5	3.558	3.432	3.536	3.395	3.425	3.365	3.543
Cr	0.005	0.005	0	0.003	0.003	0.006	0	0
Fe2+	0.168	0.176	0.212	0.191	0.312	0.275	0.269	0.186
V	0	0	0.003	0	0	0	0	0.007
Zn	0	0	0	0	0.016	0.02	0.006	0.017
Mn2+	0	0	0.006	0	0	0.002	0	0.004
Mg	0.355	0.284	0.427	0.311	0.381	0.362	0.406	0.29
Ca	0	0	0	0	0.001	0.001	0.005	0.01
Na	0.049	0.06	0.038	0.059	0.049	0.038	0.057	0.095
K	1.898	1.821	1.858	1.908	1.885	1.882	1.794	1.8
Ba	0.038	0.035	0.032	0.039	0.073	0.051	0.053	0.037
Rb	-	-	-	-	-	-	-	-
Cs	-	-	-	-	-	-	-	-
Sr	0	0	0	0	-	-	-	-
Ni	0.009	0	0.003	0	-	-	-	-
F	0.065	0.07	0.076	0.047	0.064	0.041	0.088	0.054
Cl	0	0.005	0.001	0.003	0	0	0	0
OH	3.935	3.925	3.923	3.95	3.936	3.959	3.912	3.946
Sum Cat#	18.036	17.94	18.023	18.06	18.119	18.066	17.966	17.99
XMg	0.679	0.618	0.668	0.619	0.55	0.568	0.601	0.61
Oct	4.05	4.024	4.091	4.054	4.112	4.095	4.058	4.041
Int	1.985	1.916	1.928	2.006	2.007	1.972	1.908	1.942

Appendix 6.2
White mica microprobe analyses

	White mica in mixed volcaniclastics 43 Block, HW Mine						White mica in arg/sst Thelwood Valley	
Catalogue #								
Field #	SJ558A-T12	SJ558A-T12	SJ558A-T12	SJ558A-T12	SJ558A-T12	SJ558A-T12	SJ261-T1	SJ261-T1
Location	20-675	20-675	20-675	20-675	20-675	20-675	PR124	PR124
SiO2	46.35	47.68	47.35	46.8	47.65	45.77	46.13	46.38
TiO2	0.01	0.05	0.01	0.07	0	0.08	0.41	0.22
Al2O3	33.75	33.01	32.13	34.21	32.45	32.32	34.65	33.9
Cr2O3	0.04	0.03	0	0	0.03	0	0	0
FeO	1.51	1.95	2.74	2.01	2.39	4.21	1	0.94
V2O3	0	0	0.01	0	0	0	0	0
ZnO	0.03	0.2	0.04	0	0.08	0	0.07	0.06
MnO	0.06	0.01	0	0	0.07	0.04	0.04	0.09
MgO	1.47	1.58	1.61	0.91	1.58	1.45	1.91	2.19
CaO	0	0.01	0.02	0	0	0	0	0
Na2O	0.24	0.26	0.23	0.2	0.25	0.28	0.38	0.37
K2O	10.71	10.62	10.9	10.48	11.01	10.39	10.13	9.91
BaO	1.74	1.03	1.23	1.24	0.96	1.7	1.63	1.43
Rb2O	-	-	-	-	-	-	-	-
Cs2O	-	-	-	-	-	-	-	-
SrO	-	-	-	-	-	-	0	0
NiO	-	-	-	-	-	-	0.1	0
F	0.1	0.15	0.19	0.15	0.14	0.06	0.3	0.28
Cl	0	0	0	0.02	0.01	0.02	0	0
H2O(c)	4.42	4.44	4.38	4.41	4.42	4.39	4.36	4.35
O=F	0.04	0.06	0.08	0.06	0.06	0.03	0.13	0.12
O=Cl	0	0	0	0	0	0	0	0
Sum Ox%	100.39	100.97	100.75	100.44	100.98	100.68	100.99	100.01
Si	6.229	6.341	6.354	6.256	6.36	6.213	6.134	6.205
Ti	0.001	0.005	0.001	0.007	0	0.008	0.041	0.022
Al/Al IV	1.771	1.659	1.646	1.744	1.64	1.787	1.866	1.795
Al VI	3.575	3.515	3.437	3.645	3.465	3.382	3.565	3.551
Cr	0.004	0.003	0	0	0.003	0	0	0
Fe2+	0.169	0.217	0.307	0.225	0.267	0.478	0.111	0.105
V	0	0	0.001	0	0	0.001	0	0
Zn	0.003	0.02	0.004	0	0.008	0	0.007	0.006
Mn2+	0.007	0.001	0	0	0.008	0.005	0.005	0.01
Mg	0.295	0.314	0.322	0.181	0.315	0.294	0.378	0.437
Ca	0	0.002	0.002	0	0	0	0	0
Na	0.063	0.068	0.061	0.051	0.064	0.074	0.098	0.095
K	1.836	1.801	1.867	1.787	1.874	1.8	1.718	1.692
Ba	0.092	0.054	0.064	0.065	0.05	0.09	0.085	0.075
Rb	-	-	-	-	-	-	-	-
Cs	-	-	-	-	-	-	-	-
Sr	-	-	-	-	-	-	0	0
Ni	-	-	-	-	-	-	0.011	0
F	0.041	0.064	0.08	0.065	0.061	0.026	0.128	0.12
Cl	0	0.001	0	0.004	0.001	0.004	0.001	0.001
OH	3.959	3.935	3.92	3.931	3.938	3.97	3.871	3.879
Sum Cat#	18.045	18	18.067	17.962	18.055	18.131	18.018	17.993
XMg	0.635	0.591	0.512	0.447	0.541	0.381	0.773	0.806
Oct	4.054	4.075	4.072	4.058	4.066	4.167	4.117	4.131
Int	1.991	1.925	1.994	1.904	1.989	1.964	1.902	1.862

Appendix 6.2
White mica microprobe analyses

	White mica in arg/sst Thelwood Valley				White mica in argillite/sandstone Battle South			
Catalogue #								
Field #	SJ261-T1	SJ261-T1	SJ261-T1	SJ261-T1	SJ765-169	SJ765-169	SJ765-169	SJ765-169
Location	PR124	PR124	PR124	PR124	L14-676	L14-676	L14-676	L14-676
SiO2	46.31	47.19	47.7	46.52	48.01	49.78	46.92	47.64
TiO2	0.41	0.33	0.25	0.29	0.05	0.24	0.34	0.07
Al2O3	34.99	35.54	33.88	34.53	31.35	31	32.51	37.41
Cr2O3	0	0	0.02	0.02	0.07	0.09	0.06	0
FeO	0.51	0.67	0.75	0.74	0.86	0.69	0.8	0.93
V2O3	0	0.03	0	0	1.01	1.17	1	0.08
ZnO	0.04	0.06	0	0.01	0	0	0.07	0
MnO	0	0.02	0.07	0	0.04	0	0	0.01
MgO	1.18	1.27	1.62	1.33	2.23	1.7	1.85	0.58
CaO	0	0.01	0.03	0	0.01	0	0	0
Na2O	0.45	0.4	0.35	0.44	0.15	0.2	0.23	0.51
K2O	10.09	10.31	10.15	10.49	10.96	10.52	10.75	10.46
BaO	1.45	1.65	1.39	1.64	1.41	1.12	0.96	0.13
Rb2O	-	-	-	-	-	-	-	-
Cs2O	-	-	-	-	-	-	-	-
SrO	0	0	0	0	0	0	0	0
NiO	0.01	0	0.02	0	0	0	0.04	0.01
F	0.22	0.28	0.27	0.2	0.18	0.14	0.15	0.02
Cl	0	0.02	0.01	0	0.01	0.01	0	0
H2O(c)	4.39	4.44	4.4	4.4	4.4	4.48	4.4	4.63
O=F	0.09	0.12	0.11	0.09	0.08	0.06	0.06	0.01
O=Cl	0	0	0	0	0	0	0	0
Sum Ox%	99.95	102.11	100.81	100.54	100.66	101.08	100.02	102.49
Si	6.184	6.183	6.314	6.206	6.417	6.57	6.292	6.147
Ti	0.041	0.033	0.025	0.029	0.005	0.023	0.034	0.007
Al/Al IV	1.816	1.817	1.686	1.794	1.583	1.43	1.708	1.853
Al VI	3.691	3.672	3.599	3.635	3.356	3.392	3.429	3.836
Cr	0	0	0.002	0.002	0.007	0.01	0.007	0
Fe2+	0.057	0.074	0.083	0.083	0.096	0.076	0.09	0.1
V	0	0.003	0	0	0.108	0.124	0.108	0.008
Zn	0.004	0.006	0	0.001	0	0	0.007	0
Mn2+	0	0.003	0.008	0	0.005	0	0	0.002
Mg	0.236	0.248	0.32	0.264	0.445	0.334	0.371	0.112
Ca	0	0.002	0.005	0	0.001	0	0	0
Na	0.116	0.103	0.09	0.114	0.039	0.05	0.059	0.126
K	1.718	1.723	1.714	1.785	1.869	1.772	1.838	1.721
Ba	0.076	0.085	0.072	0.086	0.074	0.058	0.051	0.007
Rb	-	-	-	-	-	-	-	-
Cs	-	-	-	-	-	-	-	-
Sr	0	0	0	0	0	0	0	0
Ni	0.001	0	0.002	0	0	0	0.004	0.001
F	0.093	0.115	0.113	0.086	0.077	0.059	0.063	0.01
Cl	0	0.005	0.001	0	0.002	0.002	0	0.001
OH	3.907	3.88	3.885	3.914	3.921	3.94	3.937	3.989
Sum Cat#	17.939	17.95	17.92	17.999	18.005	17.84	17.997	17.921
XMg	0.806	0.772	0.793	0.761	0.823	0.814	0.806	0.528
Oct	4.029	4.036	4.039	4.014	3.914	3.836	3.941	4.059
Int	1.91	1.911	1.881	1.985	1.983	1.88	1.948	1.854

Appendix 6.2
White mica microprobe analyses

	White mica in arg/sst Battle South			White mica in rhy-sst/argillite HW North		
Catalogue #						
Field #	SJ765-169	SJ765-169	SJ765-169	SJ66-47	SJ66-47	SJ66-47
Location	L14-676	L14-676	L14-676	W202	W202	W202
SiO2	49.77	47.01	49.17	46.67	46.78	47.14
TiO2	0.15	0.34	0	0.11	0.06	0.1
Al2O3	33.18	36.7	31.93	32.24	32.34	30.33
Cr2O3	0.03	0.08	0.06	0.01	0.03	0.07
FeO	0.82	0.91	1.89	2.27	2.76	2.38
V2O3	0.74	0.09	0.66	0.08	0	0.03
ZnO	0.13	0	0	0	0.01	0.15
MnO	0	0	0.01	0.07	0	0
MgO	1.71	0.7	1.56	1.68	1.58	1.69
CaO	0.01	0.01	0	0.03	0.01	0.04
Na2O	0.19	0.71	0.2	0.26	0.28	0.25
K2O	10	10.26	10.76	10.8	10.55	10.14
BaO	0.52	0.29	0.32	0.94	1.22	1.23
Rb2O	-	-	-	-	-	-
Cs2O	-	-	-	-	-	-
SrO	0	0	0	0	0	0
NiO	0	0	0	0.08	0	0.09
F	0.1	0.09	0.12	0.17	0.15	0.11
Cl	0	0.01	0	0.01	0.06	0.03
H2O(c)	4.57	4.56	4.49	4.35	4.36	4.3
O=F	0.04	0.04	0.05	0.07	0.06	0.05
O=Cl	0	0	0	0	0.01	0.01
Sum Ox%	101.88	101.71	101.14	99.69	100.1	98.01
Si	6.461	6.128	6.487	6.312	6.314	6.478
Ti	0.015	0.033	0	0.011	0.006	0.01
Al/Al IV	1.539	1.872	1.513	1.688	1.686	1.522
Al VI	3.538	3.766	3.452	3.451	3.458	3.392
Cr	0.003	0.008	0.006	0.001	0.003	0.007
Fe2+	0.088	0.099	0.209	0.256	0.311	0.273
V	0.077	0.009	0.069	0.008	0	0.003
Zn	0.012	0	0	0	0.001	0.015
Mn2+	0	0	0.002	0.009	0	0
Mg	0.331	0.136	0.307	0.338	0.317	0.346
Ca	0.002	0.002	0	0.004	0.001	0.005
Na	0.049	0.18	0.052	0.068	0.074	0.065
K	1.655	1.706	1.811	1.864	1.815	1.777
Ba	0.026	0.015	0.016	0.05	0.065	0.066
Rb	-	-	-	-	-	-
Cs	-	-	-	-	-	-
Sr	0	0	0	0	0	0
Ni	0	0	0	0.009	0	0.01
F	0.04	0.036	0.052	0.071	0.064	0.048
Cl	0.001	0.002	0	0.002	0.014	0.008
OH	3.959	3.962	3.948	3.927	3.923	3.944
Sum Cat#	17.798	17.954	17.925	18.069	18.051	17.971
XMg	0.789	0.579	0.595	0.569	0.505	0.559
Oct	3.988	4.042	3.975	4.075	4.096	4.053
Int	1.733	1.903	1.88	1.986	1.955	1.915

Appendix 6.3

Microprobe analyses - Sphalerite

	Battle mine - shalerite in chert and altered argillite above massive sulphides								HW Mine - sphalerite in argillite above massive sulphides		
Catalogue #											
Field #	**SJ754-106**	**SJ754-106**	**SJ754-106**	**SJ754-106**	**SJ754-106**	**SJ754-106**	**SJ754-106**	**SJ754-106**	**SJ639-91**	**SJ639-91**	**SJ639-91**
Drive	G171XS	G171XS	G171XS	G171XS	G171XS	G171XS	G171XS	G171XS	S335C	S335C	S335C
Location	Gopher Zone	Gopher Zone	Gopher Zone	Gopher Zone	Gopher Zone	Gopher Zone	Gopher Zone	Gopher Zone	HW Mine	HW Mine	HW Mine
mineral	sphalerite	sphalerite	sphalerite	sphalerite	sphalerite	sphalerite	sphalerite	sphalerite	sphalerite	sphalerite	sphalerite
Wt.%											
S	32.92	33.00	33.01	33.17	33.09	33.00	32.74	32.99	33.14	33.15	33.13
Mn	0.01	0.00	0.00	0.00	0.00	0.00	0.03	0.00	0.06	0.02	0.01
Fe	1.03	0.35	0.32	0.33	0.22	0.42	0.49	0.47	2.62	2.78	1.63
Cu	0.69	0.06	0.05	0.02	0.03	0.01	0.01	0.03	0.00	0.10	0.01
Zn	63.13	65.25	65.36	66.06	64.40	65.80	65.84	65.39	63.69	63.37	64.01
Se	0.05	0.04	0.14	0.04	0.02	0.02	0.01	0.00	0.01	0.00	0.00
Cd	0.36	0.35	0.37	0.38	0.37	0.35	0.34	0.34	0.28	0.30	0.29
Pb	0.00	0.00	0.00	0.00	0.00	0.00	0.00	0.02	0.00	0.00	0.00
At.%											
S	50.68	50.49	50.44	50.33	50.95	50.28	50.03	50.41	50.21	50.25	50.54
Mn	0.01	0.00	0.00	0.00	0.00	0.00	0.02	0.00	0.05	0.02	0.01
Fe	0.91	0.31	0.28	0.28	0.20	0.37	0.43	0.41	2.28	2.42	1.42
Cu	0.53	0.05	0.04	0.02	0.02	0.01	0.00	0.02	0.00	0.07	0.01
Zn	47.67	48.98	48.99	49.17	48.65	49.18	49.35	49.01	47.33	47.11	47.90
Se	0.03	0.03	0.09	0.03	0.01	0.01	0.01	0.00	0.00	0.00	0.00
Cd	0.16	0.15	0.16	0.16	0.16	0.15	0.15	0.15	0.12	0.13	0.13
Pb	0.00	0.00	0.00	0.00	0.00	0.00	0.00	0.01	0.00	0.00	0.00

Appendix 7:
Fluid inclusion results

Fluid inclusions were analysed on a Linkam MDS-600 heating freezing stage at CODES, University of Tasmania. The data reported here was reproducible to ± 2°C for heating and ± 3°C for freezing runs.

Appendix 7
Fluid Inclusion data

Inclusions in spherical megaquartz patches in chert

Sample #	Area	Drillhole	Depth (m)	Host	Position	Te	Tm (H2O)	wt.% NaCl	Th oC
SJ161	Battle mine	18-1127	38	quartz	caprocks		-5	7.9	145
SJ161	Battle mine	18-1127	38	quartz	caprocks		-3.5	5.7	146
SJ161	Battle mine	18-1127	38	quartz	caprocks		-3.5	5.7	140
SJ161	Battle mine	18-1127	38	quartz	caprocks	-21.3	-5.1	8.0	140
SJ161	Battle mine	18-1127	38	quartz	caprocks		-3.8	6.1	120
SJ161	Battle mine	18-1127	38	quartz	caprocks		-2.9	4.8	172
SJ161	Battle mine	18-1127	38	quartz	caprocks		-4	6.4	161
SJ161	Battle mine	18-1127	38	quartz	caprocks		-3.8	6.1	186
SJ161	Battle mine	18-1127	38	quartz	caprocks		-7.6	11.2	148
SJ152	Battle mine	18-1126	61.4	quartz	caprocks		-4	6.4	145
SJ152	Battle mine	18-1126	61.4	quartz	caprocks		-2.7	4.5	210
SJ152	Battle mine	18-1126	61.4	quartz	caprocks		-2.3	3.9	175
SJ152	Battle mine	18-1126	61.4	quartz	caprocks		-5.3	8.3	142
SJ152	Battle mine	18-1126	61.4	quartz	caprocks		-2.8	4.6	140
SJ152	Battle mine	18-1126	61.4	quartz	caprocks		-3.7	6.0	155
SJ152	Battle mine	18-1126	61.4	quartz	caprocks		-3.6	5.8	157
SJ152	Battle mine	18-1126	61.4	quartz	caprocks		-4.2	6.7	140
SJ152	Battle mine	18-1126	61.4	quartz	caprocks		-3.5	5.7	137
SJ152	Battle mine	18-1126	61.4	quartz	caprocks		-2.9	4.8	155
SJ152	Battle mine	18-1126	61.4	quartz	caprocks		-3.2	5.2	156
SJ152	Battle mine	18-1126	61.4	quartz	caprocks		-3.6	5.8	155
SJ152	Battle mine	18-1126	61.4	quartz	caprocks		-2.9	4.8	155
SJ152	Battle mine	18-1126	61.4	quartz	caprocks		-3.1	5.1	156
SJ152	Battle mine	18-1126	61.4	quartz	caprocks		-2.9	4.8	162
SJ152	Battle mine	18-1126	61.4	quartz	caprocks		-2.9	4.8	150
SJ152	Battle mine	18-1126	61.4	quartz	caprocks		-3.2	5.2	138
SJ152	Battle mine	18-1126	61.4	quartz	caprocks		-3	4.9	169
SJ152	Battle mine	18-1126	61.4	quartz	caprocks		-4.9	7.7	180
SJ152	Battle mine	18-1126	61.4	quartz	caprocks		-4.4	7.0	220
SJ152	Battle mine	18-1126	61.4	quartz	caprocks		-4.3	6.9	210
SJ152	Battle mine	18-1126	61.4	quartz	caprocks		-4.8	7.6	250
SJ152	Battle mine	18-1126	61.4	quartz	caprocks		-6.9	10.4	197
SJ152	Battle mine	18-1126	61.4	quartz	caprocks		-3	4.9	147
SJ152	Battle mine	18-1126	61.4	quartz	caprocks		-4.3	6.9	140
SJ152	Battle mine	18-1126	61.4	quartz	caprocks		-4.3	6.9	159
SJ152	Battle mine	18-1126	61.4	quartz	caprocks		-1.3	2.2	165
SJ152	Battle mine	18-1126	61.4	quartz	caprocks		1.8	0.0	130
SJ152	Battle mine	18-1126	61.4	quartz	caprocks		-1.4	2.4	114
SJ152	Battle mine	18-1126	61.4	quartz	caprocks		2.6	0.0	136
SJ152	Battle mine	18-1126	61.4	quartz	caprocks		-1.3	2.2	113
SJ152	Battle mine	18-1126	61.4	quartz	caprocks		-0.2	0.4	102
SJ152	Battle mine	18-1126	61.4	quartz	caprocks		-1.4	2.4	126

Inclusions in spherical megaquartz patches in chert

Sample #	Area	Drillhole	Depth (m)	Host	Position	Te	Tm (H2O)	wt.% NaCl	Th oC
SJ160	Battle mine	18-1127	40	quartz	top of ore		-2.7	4.5	133
SJ160	Battle mine	18-1127	40	quartz	top of ore		-3.2	5.2	160
SJ160	Battle mine	18-1127	40	quartz	top of ore		-3.8	6.1	186
SJ160	Battle mine	18-1127	40	quartz	top of ore		-2.9	4.8	140
SJ160	Battle mine	18-1127	40	quartz	top of ore		-3.3	5.4	133
SJ160	Battle mine	18-1127	40	quartz	top of ore		-2.8	4.6	150
SJ160	Battle mine	18-1127	40	quartz	top of ore		-3.7	6.0	147
SJ160	Battle mine	18-1127	40	quartz	top of ore		-3	4.9	138
SJ160	Battle mine	18-1127	40	quartz	top of ore		-3.5	5.7	138
SJ160	Battle mine	18-1127	40	quartz	top of ore		-3.4	5.5	154
SJ160	Battle mine	18-1127	40	quartz	top of ore		-3.9	6.3	142
SJ160	Battle mine	18-1127	40	quartz	top of ore		-5.8	8.9	128
SJ160	Battle mine	18-1127	40	quartz	top of ore		-5.6	8.7	120
SJ160	Battle mine	18-1127	40	quartz	top of ore		-2.6	4.3	128
SJ160	Battle mine	18-1127	40	quartz	top of ore		-2.2	3.7	135
SJ160	Battle mine	18-1127	40	quartz	top of ore		-2.8	4.6	139
SJ160	Battle mine	18-1127	40	quartz	top of ore		-3.3	5.4	135
SJ160	Battle mine	18-1127	40	quartz	top of ore		-3	4.9	138
SJ160	Battle mine	18-1127	40	quartz	top of ore		-3.5	5.7	147
SJ160	Battle mine	18-1127	40	quartz	top of ore		-3.4	5.5	123
SJ160	Battle mine	18-1127	40	quartz	top of ore		-4.5	7.2	130
SJ160	Battle mine	18-1127	40	quartz	top of ore		-2.5	4.2	137
SJ160	Battle mine	18-1127	40	quartz	top of ore		-3.9	6.3	158

Inclusions in quartz interstital to ore (top ore contact with overlying chert)

Sample #	Area	Drillhole	Depth (m)	Host	Position	Te	Tm (H2O)	wt.% NaCl	Th
SJ160	Battle mine	18-1127	40	quartz	top of ore		-4.3	6.9	126
SJ160	Battle mine	18-1127	40	quartz	top of ore		-3.2	5.2	157
SJ160	Battle mine	18-1127	40	quartz	top of ore		-4.5	7.2	137
SJ160	Battle mine	18-1127	40	quartz	top of ore		-3.3	5.4	129
SJ160	Battle mine	18-1127	40	quartz	top of ore		-2.6	4.3	125
SJ160	Battle mine	18-1127	40	quartz	top of ore		-3.5	5.7	120
SJ160	Battle mine	18-1127	40	quartz	top of ore		-3.9	6.3	144
SJ160	Battle mine	18-1127	40	quartz	top of ore		-3.1	5.1	140
SJ160	Battle mine	18-1127	40	quartz	top of ore		-3.3	5.4	125
SJ160	Battle mine	18-1127	40	quartz	top of ore		-2.9	4.8	125
SJ160	Battle mine	18-1127	40	quartz	top of ore		-3.8	6.1	152
SJ160	Battle mine	18-1127	40	quartz	top of ore		-3.4	5.5	112
SJ160	Battle mine	18-1127	40	quartz	top of ore		-3	4.9	127
SJ160	Battle mine	18-1127	40	quartz	top of ore		-3.3	5.4	182
SJ160	Battle mine	18-1127	40	quartz	top of ore		-2.7	4.5	144
SJ160	Battle mine	18-1127	40	quartz	top of ore		-2.5	4.2	150
SJ160	Battle mine	18-1127	40	quartz	top of ore		-2.5	4.2	179
SJ160	Battle mine	18-1127	40	quartz	top of ore		-3	4.9	140
SJ160	Battle mine	18-1127	40	quartz	top of ore		-3.3	5.4	148
SJ160	Battle mine	18-1127	40	quartz	top of ore		-3.2	5.2	147
SJ160	Battle mine	18-1127	40	quartz	top of ore		-3.1	5.1	120
SJ160	Battle mine	18-1127	40	quartz	top of ore		-3.1	5.1	142
SJ160	Battle mine	18-1127	40	quartz	top of ore		-3.7	6.0	138
SJ160	Battle mine	18-1127	40	quartz	top of ore		-2.8	4.6	150
SJ160	Battle mine	18-1127	40	quartz	top of ore		-3.3	5.4	130
SJ160	Battle mine	18-1127	40	quartz	top of ore		-3.5	5.7	132
SJ160	Battle mine	18-1127	40	quartz	top of ore		-3.9	6.3	127
SJ160	Battle mine	18-1127	40	quartz	top of ore		-2.5	4.2	128
SJ160	Battle mine	18-1127	40	quartz	top of ore		-2.6	4.3	130
SJ160	Battle mine	18-1127	40	quartz	top of ore		-3	4.9	132
SJ160	Battle mine	18-1127	40	quartz	top of ore		-0.1	0.2	111
SJ160	Battle mine	18-1127	40	quartz	top of ore		-0.1	0.2	118
SJ160	Battle mine	18-1127	40	quartz	top of ore		-0.2	0.4	112
SJ160	Battle mine	18-1127	40	quartz	top of ore		-0.2	0.4	108
SJ160	Battle mine	18-1127	40	quartz	top of ore		-0.1	0.2	110
SJ160	Battle mine	18-1127	40	quartz	top of ore		-1.8	3.1	136
SJ160	Battle mine	18-1127	40	quartz	top of ore		-0.1	0.2	122
SJ160	Battle mine	18-1127	40	quartz	top of ore		-0.1	0.2	129
SJ160	Battle mine	18-1127	40	quartz	top of ore		-0.2	0.4	125
SJ160	Battle mine	18-1127	40	quartz	top of ore		-1.8	3.1	142
SJ160	Battle mine	18-1127	40	quartz	top of ore		-1.9	3.2	148
SJ160	Battle mine	18-1127	40	quartz	top of ore		0.2	0.0	125
SJ160	Battle mine	18-1127	40	quartz	top of ore		-1.8	3.1	155
SJ160	Battle mine	18-1127	40	quartz	top of ore		-1.4	2.4	124
SJ160	Battle mine	18-1127	40	quartz	top of ore		-0.1	0.2	129
SJ160	Battle mine	18-1127	40	quartz	top of ore		-0.9	1.6	121
SJ160	Battle mine	18-1127	40	quartz	top of ore		-0.1	0.2	122

Inclusions in quartz interstital to ccp-rich ore (middle of Battle main lens)

Sample #	Area	Drillhole	Depth (m)	Host	Position	Te	Tm (H2O)	wt.% NaCl	Th
F22	Battle mine	18-1006	101.7	quartz	main ore lens		-3.3	5.4	115
F22	Battle mine	18-1006	101.7	quartz	main ore lens		-8.6	12.4	124
F22	Battle mine	18-1006	101.7	quartz	main ore lens		-8.3	12.1	126
F22	Battle mine	18-1006	101.7	quartz	main ore lens		-4.6	7.3	127
F22	Battle mine	18-1006	101.7	quartz	main ore lens		-8.6	12.4	115
F22	Battle mine	18-1006	101.7	quartz	main ore lens		-5.5	8.5	113
F22	Battle mine	18-1006	101.7	quartz	main ore lens		-4.2	6.7	132
F22	Battle mine	18-1006	101.7	quartz	main ore lens		-6.6	10.0	142
F22	Battle mine	18-1006	101.7	quartz	main ore lens		-5.2	8.1	160
F22	Battle mine	18-1006	101.7	quartz	main ore lens		-5.5	8.5	138
F22	Battle mine	18-1006	101.7	quartz	main ore lens		-5	7.9	140
F22	Battle mine	18-1006	101.7	quartz	main ore lens		-3.4	5.5	130
F22	Battle mine	18-1006	101.7	quartz	main ore lens		-2.3	3.9	128
F22	Battle mine	18-1006	101.7	quartz	main ore lens		-2.1	3.5	148
F22	Battle mine	18-1006	101.7	quartz	main ore lens		-5	7.9	138
F22	Battle mine	18-1006	101.7	quartz	main ore lens		-5.4	8.4	137
F22	Battle mine	18-1006	101.7	quartz	main ore lens		-4.9	7.7	133
F22	Battle mine	18-1006	101.7	quartz	main ore lens		-3.3	5.4	134
F22	Battle mine	18-1006	101.7	quartz	main ore lens		-3.2	5.2	128
F22	Battle mine	18-1006	101.7	quartz	main ore lens		-4.7	7.4	202
F22	Battle mine	18-1006	101.7	quartz	main ore lens		-3.3	5.4	142

Inclusions in quartz interstital to ccp-rich ore (middle of Battle main lens)

Sample #	Area	Drillhole	Depth (m)	Host	Position	Te	Tm (H2O)	wt.% NaCl	Th
F22	Battle mine	18-1006	101.7	quartz	main ore lens		-3.3	5.4	122
F22	Battle mine	18-1006	101.7	quartz	main ore lens		-3	4.9	118
F22	Battle mine	18-1006	101.7	quartz	main ore lens		-3.7	6.0	138
F22	Battle mine	18-1006	101.7	quartz	main ore lens		-1.2	2.1	120
F22	Battle mine	18-1006	101.7	quartz	main ore lens		-0.9	1.6	100
F22	Battle mine	18-1006	101.7	quartz	main ore lens		-1.7	2.9	140
F22	Battle mine	18-1006	101.7	quartz	main ore lens		-2	3.4	100
F22	Battle mine	18-1006	101.7	quartz	main ore lens		-1.5	2.6	101

Inclusions in quartz interstital to sphal-rich ore (middle of Battle main lens)

Sample #	Area	Drillhole	Depth (m)	Host	Position	Te	Tm (H2O)	wt.% NaCl	Th
F18	Battle mine	18-979	93.1	quartz	main ore lens		-2.6	4.3	175
F18	Battle mine	18-979	93.1	quartz	main ore lens		-4.4	7.0	153
F18	Battle mine	18-979	93.1	quartz	main ore lens		-5.1	8.0	129
F18	Battle mine	18-979	93.1	quartz	main ore lens	-22	-4.2	6.7	127
F18	Battle mine	18-979	93.1	quartz	main ore lens		-6	9.2	150
F18	Battle mine	18-979	93.1	quartz	main ore lens		-7.1	10.6	155
F18	Battle mine	18-979	93.1	quartz	main ore lens		-5.6	8.7	158
F18	Battle mine	18-979	93.1	quartz	main ore lens		-5.3	8.3	162
F18	Battle mine	18-979	93.1	quartz	main ore lens		-4.9	7.7	167
F18	Battle mine	18-979	93.1	quartz	main ore lens		-4.8	7.6	152
F18	Battle mine	18-979	93.1	quartz	main ore lens		-5.5	8.5	176
F18	Battle mine	18-979	93.1	quartz	main ore lens		-3.7	6.0	177
F18	Battle mine	18-979	93.1	quartz	main ore lens		-5.7	8.8	175
F18	Battle mine	18-979	93.1	quartz	main ore lens		-5.7	8.8	174
F18	Battle mine	18-979	93.1	quartz	main ore lens		-4.4	7.0	170
F18	Battle mine	18-979	93.1	quartz	main ore lens		-3.7	6.0	171
F18	Battle mine	18-979	93.1	quartz	main ore lens		-4.9	7.7	145
F18	Battle mine	18-979	93.1	quartz	main ore lens		-4.9	7.7	155
F18	Battle mine	18-979	93.1	quartz	main ore lens		-4.2	6.7	140
F18	Battle mine	18-979	93.1	quartz	main ore lens		-4.8	7.6	158
F18	Battle mine	18-979	93.1	quartz	main ore lens		-4.5	7.2	140
F18	Battle mine	18-979	93.1	quartz	main ore lens		-4.3	6.9	142
F18	Battle mine	18-979	93.1	quartz	main ore lens		-4.2	6.7	148
F18	Battle mine	18-979	93.1	quartz	main ore lens		-5	7.9	153
F18	Battle mine	18-979	93.1	quartz	main ore lens		-4.1	6.6	152
F18	Battle mine	18-979	93.1	quartz	main ore lens		-5.4	8.4	160
F18	Battle mine	18-979	93.1	quartz	main ore lens		-5.6	8.7	182
F18	Battle mine	18-979	93.1	quartz	main ore lens		-5.3	8.3	190
F18	Battle mine	18-979	93.1	quartz	main ore lens		-5.8	8.9	188
F18	Battle mine	18-979	93.1	quartz	main ore lens		-6.3	9.6	185
F18	Battle mine	18-979	93.1	quartz	main ore lens		-5.5	8.5	210
F18	Battle mine	18-979	93.1	quartz	main ore lens		-5.3	8.3	172
F18	Battle mine	18-979	93.1	quartz	main ore lens		-5	7.9	180
F18	Battle mine	18-979	93.1	quartz	main ore lens		-5.3	8.3	189
F18	Battle mine	18-979	93.1	quartz	main ore lens		-4.8	7.6	179
F18	Battle mine	18-979	93.1	quartz	main ore lens		-4.7	7.4	174
F18	Battle mine	18-979	93.1	quartz	main ore lens		-5	7.9	172
F18	Battle mine	18-979	93.1	quartz	main ore lens		-5.3	8.3	176
F18	Battle mine	18-979	93.1	quartz	main ore lens		-1.7	2.9	125
F18	Battle mine	18-979	93.1	quartz	main ore lens		-1.3	2.2	142
F18	Battle mine	18-979	93.1	quartz	main ore lens		-0.6	1.0	143
F18	Battle mine	18-979	93.1	quartz	main ore lens		-1.4	2.4	135
F18	Battle mine	18-979	93.1	quartz	main ore lens		-1.7	2.9	132
F18	Battle mine	18-979	93.1	quartz	main ore lens		-1.4	2.4	138
F18	Battle mine	18-979	93.1	quartz	main ore lens		-0.3	0.5	142
F18	Battle mine	18-979	93.1	quartz	main ore lens		0.6	0.0	167
F18	Battle mine	18-979	93.1	quartz	main ore lens		2.3	0.0	118

Inclusions in crosscutting quartz-pyrite zone at ore contact

Sample #	Area	Drillhole	Depth (m)	Host	Position	Te	Tm (H2O)	wt.% NaCl	Th
F15	Battle mine	18-1003	93.4	quartz	near ore top		-2.3	3.9	103
F15	Battle mine	18-1003	93.4	quartz	near ore top		2.3	0.0	102
F15	Battle mine	18-1003	93.4	quartz	near ore top		-0.7	1.2	110
F15	Battle mine	18-1003	93.4	quartz	near ore top		-0.7	1.2	95
F15	Battle mine	18-1003	93.4	quartz	near ore top		-0.5	0.9	120
F15	Battle mine	18-1003	93.4	quartz	near ore top		-1.2	2.1	105
F15	Battle mine	18-1003	93.4	quartz	near ore top		-1	1.7	108
F15	Battle mine	18-1003	93.4	quartz	near ore top		-0.5	0.9	112
F15	Battle mine	18-1003	93.4	quartz	near ore top		-0.6	1.0	120
F15	Battle mine	18-1003	93.4	quartz	near ore top		-0.3	0.5	118
F15	Battle mine	18-1003	93.4	quartz	near ore top		-0.3	0.5	126

Inclusions in crosscutting quartz-pyrite zone at ore contact

Sample #	Area	Drillhole	Depth (m)	Host	Position	Te	Tm (H2O)	wt.% NaCl	Th
F15	Battle mine	18-1003	93.4	quartz	near ore top		1.6	0.0	104
F15	Battle mine	18-1003	93.4	quartz	near ore top		-1.1	1.9	95
F15	Battle mine	18-1003	93.4	quartz	near ore top		-1	1.7	115
F15	Battle mine	18-1003	93.4	quartz	near ore top		-0.5	0.9	110
F15	Battle mine	18-1003	93.4	quartz	near ore top		-0.9	1.6	102
SJ513	Battle mine	ST183A	Face B	quartz	ore top contact		-2.1	3.5	130
SJ513	Battle mine	ST183A	Face B	quartz	ore top contact		-3.9	6.3	158
SJ513	Battle mine	ST183A	Face B	quartz	ore top contact		-2.2	3.7	158
SJ513	Battle mine	ST183A	Face B	quartz	ore top contact		-5.4	8.4	149
SJ513	Battle mine	ST183A	Face B	quartz	ore top contact		-2.4	4.0	160
SJ513	Battle mine	ST183A	Face B	quartz	ore top contact		-2.2	3.7	170
SJ513	Battle mine	ST183A	Face B	quartz	ore top contact		-1	1.7	132
SJ513	Battle mine	ST183A	Face B	quartz	ore top contact		0.8	1.4	148
SJ513	Battle mine	ST183A	Face B	quartz	ore top contact		-1.9	3.2	130
SJ513	Battle mine	ST183A	Face B	quartz	ore top contact		-1.9	3.2	145
SJ513	Battle mine	ST183A	Face B	quartz	ore top contact		-1.4	2.4	155
SJ513	Battle mine	ST183A	Face B	quartz	ore top contact		-1.8	3.1	142
SJ513	Battle mine	ST183A	Face B	quartz	ore top contact		-1.9	3.2	151
SJ513	Battle mine	ST183A	Face B	quartz	ore top contact		-1.4	2.4	161
SJ513	Battle mine	ST183A	Face B	quartz	ore top contact		-1.4	2.4	150
SJ513	Battle mine	ST183A	Face B	quartz	ore top contact		-1.8	3.1	
SJ513	Battle mine	ST183A	Face B	quartz	ore top contact		-1.8	3.1	
SJ513	Battle mine	ST183A	Face B	quartz	ore top contact		-1.7	2.9	169
SJ513	Battle mine	ST183A	Face B	quartz	ore top contact		-1.6	2.7	
SJ513	Battle mine	ST183A	Face B	quartz	ore top contact		-1.8	3.1	133
SJ513	Battle mine	ST183A	Face B	quartz	ore top contact		-1.7	2.9	145

Inclusions in quartz interstitial to barite-rich Upper Zone ore

Sample #	Area	Drillhole	Depth (m)	Host	Position	Te	Tm (H2O)	wt.% NaCl	Th
SJ160	Battle mine	18-975	77.5	quartz	Upper Zone mz		-5.3	8.3	172
SJ160	Battle mine	18-975	77.5	quartz	Upper Zone mz		-3.4	5.5	166
SJ160	Battle mine	18-975	77.5	quartz	Upper Zone mz		-3.6	5.8	
SJ160	Battle mine	18-975	77.5	quartz	Upper Zone mz		-6.2	9.5	167
SJ160	Battle mine	18-975	77.5	quartz	Upper Zone mz		-3.5	5.7	182
SJ160	Battle mine	18-975	77.5	quartz	Upper Zone mz		-2.4	4.0	173
SJ160	Battle mine	18-975	77.5	quartz	Upper Zone mz		-2.7	4.5	201
SJ160	Battle mine	18-975	77.5	quartz	Upper Zone mz		-2.1	3.5	190
SJ160	Battle mine	18-975	77.5	quartz	Upper Zone mz		-2.3	3.9	171
SJ160	Battle mine	18-975	77.5	quartz	Upper Zone mz		-2.3	3.9	157
SJ160	Battle mine	18-975	77.5	quartz	Upper Zone mz		-2.1	3.5	155
SJ160	Battle mine	18-975	77.5	quartz	Upper Zone mz		-2.1	3.5	
SJ160	Battle mine	18-975	77.5	quartz	Upper Zone mz		-1.9	3.2	140
SJ160	Battle mine	18-975	77.5	quartz	Upper Zone mz		-4.8	7.6	210
SJ160	Battle mine	18-975	77.5	quartz	Upper Zone mz		-4.2	6.7	278
SJ160	Battle mine	18-975	77.5	quartz	Upper Zone mz		-3.5	5.7	242
SJ160	Battle mine	18-975	77.5	quartz	Upper Zone mz		-3.9	6.3	145
SJ160	Battle mine	18-975	77.5	quartz	Upper Zone mz		-1.9	3.2	160
SJ160	Battle mine	18-975	77.5	quartz	Upper Zone mz		-1.8	3.1	157
SJ160	Battle mine	18-975	77.5	quartz	Upper Zone mz		-1.9	3.2	150
SJ160	Battle mine	18-975	77.5	quartz	Upper Zone mz		-1.6	2.7	160
SJ160	Battle mine	18-975	77.5	quartz	Upper Zone mz		-1.4	2.4	173
SJ160	Battle mine	18-975	77.5	quartz	Upper Zone mz		-1.5	2.6	
SJ160	Battle mine	18-975	77.5	quartz	Upper Zone mz		-1.8	3.1	177
SJ160	Battle mine	18-975	77.5	quartz	Upper Zone mz		-2.1	3.5	165
SJ160	Battle mine	18-975	77.5	quartz	Upper Zone mz		-0.3	0.5	140
SJ160	Battle mine	18-975	77.5	quartz	Upper Zone mz		-1.9	3.2	139
SJ160	Battle mine	18-975	77.5	quartz	Upper Zone mz		-1.8	3.1	164
SJ160	Battle mine	18-975	77.5	quartz	Upper Zone mz		-1.7	2.9	177
SJ160	Battle mine	18-975	77.5	quartz	Upper Zone mz		-1.8	3.1	149
SJ160	Battle mine	18-975	77.5	quartz	Upper Zone mz		-1.8	3.1	157
SJ160	Battle mine	18-975	77.5	quartz	Upper Zone mz		-1.9	3.2	155
SJ160	Battle mine	18-975	77.5	quartz	Upper Zone mz		-1.7	2.9	
SJ160	Battle mine	18-975	77.5	quartz	Upper Zone mz		-1.8	3.1	142
SJ160	Battle mine	18-975	77.5	quartz	Upper Zone mz		-2.1	3.5	148
SJ160	Battle mine	18-975	77.5	quartz	Upper Zone mz		-1.7	2.9	152
SJ160	Battle mine	18-975	77.5	quartz	Upper Zone mz		-1.8	3.1	152
SJ160	Battle mine	18-975	77.5	quartz	Upper Zone mz		-1.6	2.7	153
SJ160	Battle mine	18-975	77.5	quartz	Upper Zone mz		-3.3	5.4	155
SJ160	Battle mine	18-975	77.5	quartz	Upper Zone mz		-3.1	5.1	182
SJ160	Battle mine	18-975	77.5	quartz	Upper Zone mz		-3.3	5.4	176
SJ160	Battle mine	18-975	77.5	quartz	Upper Zone mz		-3.4	5.5	168
SJ160	Battle mine	18-975	77.5	quartz	Upper Zone mz		-3.4	5.5	172

Inclusions in quartz interstitial to barite-rich Upper Zone ore

Sample #	Area	Drillhole	Depth (m)	Host	Position	Te	Tm (H2O)	wt.% NaCl	Th
SJ160	Battle mine	18-975	77.5	quartz	Upper Zone mz		-3.8	6.1	177
SJ160	Battle mine	18-975	77.5	quartz	Upper Zone mz		-3.7	6.0	168
SJ160	Battle mine	18-975	77.5	quartz	Upper Zone mz		-3.7	6.0	169
SJ160	Battle mine	18-975	77.5	quartz	Upper Zone mz		-3.4	5.5	175
SJ160	Battle mine	18-975	77.5	quartz	Upper Zone mz		-2.5	4.2	174
SJ160	Battle mine	18-975	77.5	quartz	Upper Zone mz		-2.6	4.3	183
SJ160	Battle mine	18-975	77.5	quartz	Upper Zone mz		-2.6	4.3	187
SJ160	Battle mine	18-975	77.5	quartz	Upper Zone mz		-2.6	4.3	167

Inclusions in quartz interstitial to barite-rich Upper Zone ore

Sample #	Area	Drillhole	Depth (m)	Host	Position	Te	Tm (H2O)	wt.% NaCl	Th
F16	Battle mine	18-975	77.5	quartz	Upper Zone mz		-3.2	5.2	175
F16	Battle mine	18-975	77.5	quartz	Upper Zone mz		-3.2	5.2	177
F16	Battle mine	18-975	77.5	quartz	Upper Zone mz		-3.5	5.7	186
F16	Battle mine	18-975	77.5	quartz	Upper Zone mz		-3.3	5.4	179
F16	Battle mine	18-975	77.5	quartz	Upper Zone mz		-3.2	5.2	165
F16	Battle mine	18-975	77.5	quartz	Upper Zone mz		-3.3	5.4	171
F16	Battle mine	18-975	77.5	quartz	Upper Zone mz		-2.5	4.2	164
F16	Battle mine	18-975	77.5	quartz	Upper Zone mz		-3.2	5.2	173
F16	Battle mine	18-975	77.5	quartz	Upper Zone mz		-3.3	5.4	170
F16	Battle mine	18-975	77.5	quartz	Upper Zone mz		-3.3	5.4	181
F16	Battle mine	18-975	77.5	quartz	Upper Zone mz		-3.8	6.1	171
F16	Battle mine	18-975	77.5	quartz	Upper Zone mz		-3.4	5.5	178
F16	Battle mine	18-975	77.5	quartz	Upper Zone mz		-3.3	5.4	170
F16	Battle mine	18-975	77.5	quartz	Upper Zone mz		-5	7.9	127
F16	Battle mine	18-975	77.5	quartz	Upper Zone mz		-4.7	7.4	125
F16	Battle mine	18-975	77.5	quartz	Upper Zone mz		-4.3	6.9	127
F16	Battle mine	18-975	77.5	quartz	Upper Zone mz		-4.3	6.9	108
F16	Battle mine	18-975	77.5	quartz	Upper Zone mz		-4.2	6.7	109
F16	Battle mine	18-975	77.5	quartz	Upper Zone mz		-3.1	5.1	101
F16	Battle mine	18-975	77.5	quartz	Upper Zone mz		-4.9	7.7	102
F16	Battle mine	18-975	77.5	quartz	Upper Zone mz		-2.7	4.5	177
F16	Battle mine	18-975	77.5	quartz	Upper Zone mz		-2.4	4.0	188

Inclusions in quartz interstitial to sulphides at top contact

Sample #	Area	Drillhole	Depth (m)	Host	Position	Te	Tm (H2O)	wt.% NaCl	Th
SJ638	HW mine	S335C	Face A	quartz	ore top contact		-1.9	3.2	159
SJ638	HW mine	S335C	Face A	quartz	ore top contact		-2.7	4.5	
SJ638	HW mine	S335C	Face A	quartz	ore top contact		-1.9	3.2	157
SJ638	HW mine	S335C	Face A	quartz	ore top contact		-1.8	3.1	154
SJ638	HW mine	S335C	Face A	quartz	ore top contact		-0.9	1.6	160
SJ638	HW mine	S335C	Face A	quartz	ore top contact	-22	-2.2	3.7	161
SJ638	HW mine	S335C	Face A	quartz	ore top contact		-2.8	4.6	168
SJ638	HW mine	S335C	Face A	quartz	ore top contact		-2.6	4.3	152
SJ638	HW mine	S335C	Face A	quartz	ore top contact		-1.6	2.7	130
SJ638	HW mine	S335C	Face A	quartz	ore top contact		-2.3	3.9	172
SJ638	HW mine	S335C	Face A	quartz	ore top contact		-2.3	3.9	162
SJ638	HW mine	S335C	Face A	quartz	ore top contact		-2.1	3.5	158
SJ638	HW mine	S335C	Face A	quartz	ore top contact		-1.7	2.9	148
SJ638	HW mine	S335C	Face A	quartz	ore top contact		1.7	0.0	
SJ638	HW mine	S335C	Face A	quartz	ore top contact		-2.2	3.7	142
SJ638	HW mine	S335C	Face A	quartz	ore top contact		1.2	0.0	127
SJ638	HW mine	S335C	Face A	quartz	ore top contact		2.5	0.0	143
SJ638	HW mine	S335C	Face A	quartz	ore top contact		-1.6	2.7	120
SJ638	HW mine	S335C	Face A	quartz	ore top contact		-1.8	3.1	129
SJ638	HW mine	S335C	Face A	quartz	ore top contact		-2.9	4.8	137
SJ638	HW mine	S335C	Face A	quartz	ore top contact		2.6	0.0	135
SJ638	HW mine	S335C	Face A	quartz	ore top contact		0.3	0.0	121
SJ638	HW mine	S335C	Face A	quartz	ore top contact		-2.4	4.0	130
SJ638	HW mine	S335C	Face A	quartz	ore top contact		2.5	0.0	144
SJ85	HW mine	23-488	14.3	quartz	ore top contact		-3.2	5.2	172
SJ85	HW mine	23-488	14.3	quartz	ore top contact		-2.6	4.3	174
SJ85	HW mine	23-488	14.3	quartz	ore top contact		-2.4	4.0	180
SJ85	HW mine	23-488	14.3	quartz	ore top contact		-3.8	6.1	172
SJ85	HW mine	23-488	14.3	quartz	ore top contact		-2.6	4.3	167
SJ85	HW mine	23-488	14.3	quartz	ore top contact		-4.2	6.7	169
SJ85	HW mine	23-488	14.3	quartz	ore top contact		-2	3.4	210
SJ85	HW mine	23-488	14.3	quartz	ore top contact		-2.8	4.6	180
SJ85	HW mine	23-488	14.3	quartz	ore top contact		-2.3	3.9	195
SJ85	HW mine	23-488	14.3	quartz	ore top contact		-2.2	3.7	195
SJ85	HW mine	23-488	14.3	quartz	ore top contact	-21	-2.8	4.6	170
SJ85	HW mine	23-488	14.3	quartz	ore top contact		-2.4	4.0	215
SJ85	HW mine	23-488	14.3	quartz	ore top contact		-3.3	5.4	176

Inclusions in quartz interstitial to sulphides at top contact

Sample #	Area	Drillhole	Depth (m)	Host	Position	Te	Tm (H2O)	wt.% NaCl	Th
SJ85	HW mine	23-488	14.3	quartz	ore top contact		-2.9	4.8	182
SJ85	HW mine	23-488	14.3	quartz	ore top contact		-0.3	0.5	140
SJ85	HW mine	23-488	14.3	quartz	ore top contact		0.3	0.0	143
SJ85	HW mine	23-488	14.3	quartz	ore top contact		-2.5	4.2	156
SJ85	HW mine	23-488	14.3	quartz	ore top contact		-2.6	4.3	149
SJ85	HW mine	23-488	14.3	quartz	ore top contact		-2.3	3.9	140
SJ85	HW mine	23-488	14.3	quartz	ore top contact		-2.4	4.0	190
SJ85	HW mine	23-488	14.3	quartz	ore top contact		-2	3.4	164
SJ85	HW mine	23-488	14.3	quartz	ore top contact		-2.1	3.5	170
SJ80	HW mine	23-488	1	quartz	ore top contact		-3.3	5.4	162
SJ80	HW mine	23-488	1	quartz	ore top contact		-3	4.9	148
SJ80	HW mine	23-488	1	quartz	ore top contact		-1.5	2.6	144
SJ80	HW mine	23-488	1	quartz	ore top contact		-2.5	4.2	148
SJ80	HW mine	23-488	1	quartz	ore top contact		-2.2	3.7	152
SJ80	HW mine	23-488	1	quartz	ore top contact		-2.2	3.7	164
SJ80	HW mine	23-488	1	quartz	ore top contact		-2.3	3.9	142

Inclusions in quartz interstitial to sulphides near base of HW main lens

Sample #	Area	Drillhole	Depth (m)	Host	Position	Te	Tm (H2O)	wt.% NaCl	Th
F20	HW mine	N357RP	23 Level	quartz	near ore base		-3.7	6.0	128
F20	HW mine	N357RP	23 Level	quartz	near ore base		-4.4	7.0	122
F20	HW mine	N357RP	23 Level	quartz	near ore base		-4.2	6.7	177
F20	HW mine	N357RP	23 Level	quartz	near ore base		-5.7	8.8	180
F20	HW mine	N357RP	23 Level	quartz	near ore base		-3.9	6.3	202
F20	HW mine	N357RP	23 Level	quartz	near ore base		-5.2	8.1	128
F20	HW mine	N357RP	23 Level	quartz	near ore base		-3.9	6.3	162
F20	HW mine	N357RP	23 Level	quartz	near ore base		-5	7.9	171
F20	HW mine	N357RP	23 Level	quartz	near ore base		-4.2	6.7	170
F20	HW mine	N357RP	23 Level	quartz	near ore base		-4.1	6.6	163

Inclusions in late crosscutting quartz vein

Sample #	Area	Drillhole	Depth (m)	Host	Position	Te	Tm (H2O)	wt.% NaCl	Th
F20	HW mine	N357RP	23 Level	quartz	near ore base		-2	3.4	136
F20	HW mine	N357RP	23 Level	quartz	near ore base		-2.8	4.6	137
F20	HW mine	N357RP	23 Level	quartz	near ore base		-2.7	4.5	165
F20	HW mine	N357RP	23 Level	quartz	near ore base		-2.1	3.5	150
F20	HW mine	N357RP	23 Level	quartz	near ore base		-2.3	3.9	137
F20	HW mine	N357RP	23 Level	quartz	near ore base		-0.2	0.4	
F20	HW mine	N357RP	23 Level	quartz	near ore base		-2	3.4	154
F20	HW mine	N357RP	23 Level	quartz	near ore base		-2.1	3.5	152
F20	HW mine	N357RP	23 Level	quartz	near ore base		-2	3.4	168
F20	HW mine	N357RP	23 Level	quartz	near ore base		-1.9	3.2	129
F20	HW mine	N357RP	23 Level	quartz	near ore base		-2.2	3.7	149
F20	HW mine	N357RP	23 Level	quartz	near ore base		-2.1	3.5	138
F20	HW mine	N357RP	23 Level	quartz	near ore base		-1.8	3.1	172
F20	HW mine	N357RP	23 Level	quartz	near ore base		-1.9	3.2	124
F20	HW mine	N357RP	23 Level	quartz	near ore base		-1.8	3.1	167
F20	HW mine	N357RP	23 Level	quartz	near ore base		-1.9	3.2	138
F20	HW mine	N357RP	23 Level	quartz	near ore base		-2.5	4.2	166
F20	HW mine	N357RP	23 Level	quartz	near ore base		-2.3	3.9	142
F20	HW mine	N357RP	23 Level	quartz	near ore base	-24	-2.5	4.2	164
F20	HW mine	N357RP	23 Level	quartz	near ore base		-2.4	4.0	138
F20	HW mine	N357RP	23 Level	quartz	near ore base		-2	3.4	174
F20	HW mine	N357RP	23 Level	quartz	near ore base		-1.6	2.7	165
F20	HW mine	N357RP	23 Level	quartz	near ore base		-1.3	2.2	166
F20	HW mine	N357RP	23 Level	quartz	near ore base		-1	1.7	168
F20	HW mine	N357RP	23 Level	quartz	near ore base		-1.7	2.9	148
F20	HW mine	N357RP	23 Level	quartz	near ore base		-1.4	2.4	168
F20	HW mine	N357RP	23 Level	quartz	near ore base		-1.7	2.9	166
F20	HW mine	N357RP	23 Level	quartz	near ore base		-1.5	2.6	166
F20	HW mine	N357RP	23 Level	quartz	near ore base		-1.7	2.9	92
F20	HW mine	N357RP	23 Level	quartz	near ore base		-1.5	2.6	146
F20	HW mine	N357RP	23 Level	quartz	near ore base		-1.6	2.7	132
F20	HW mine	N357RP	23 Level	quartz	near ore base		0	0.0	110
F20	HW mine	N357RP	23 Level	quartz	near ore base		-1.8	3.1	155
F20	HW mine	N357RP	23 Level	quartz	near ore base		-1.8	3.1	177
F20	HW mine	N357RP	23 Level	quartz	near ore base		-1.7	2.9	177
F20	HW mine	N357RP	23 Level	quartz	near ore base		-1.9	3.2	150
F20	HW mine	N357RP	23 Level	quartz	near ore base		-0.1	0.2	116
F20	HW mine	N357RP	23 Level	quartz	near ore base		0.5	0.0	118
F20	HW mine	N357RP	23 Level	quartz	near ore base		1	0.0	108
F20	HW mine	N357RP	23 Level	quartz	near ore base		0.8	0.0	162
F20	HW mine	N357RP	23 Level	quartz	near ore base		0.2	0.0	192